CLIMATIC, OCEANOGRAPHIC AND ENVIRONMENTAL CHANGE IN THE EARLY TO MIDDLE EOCENE

by

NICOLA JANE KIRBY

A thesis submitted to the University of Birmingham for the degree of

DOCTOR OF PHILOSOPHY

School of Geography, Earth and Environmental Sciences

College of Life and Environmental Sciences

University of Birmingham

December 2022

UNIVERSITY OF
BIRMINGHAM

University of Birmingham Research Archive

e-theses repository

This unpublished thesis/dissertation is copyright of the author and/or third parties. The intellectual property rights of the author or third parties in respect of this work are as defined by The Copyright Designs and Patents Act 1988 or as modified by any successor legislation.

Any use made of information contained in this thesis/dissertation must be in accordance with that legislation and must be properly acknowledged. Further distribution or reproduction in any format is prohibited without the permission of the copyright holder.

ABSTRACT

The early to middle Eocene (~56 – 37 Ma) 'hothouse' was a dynamic interval of Earth's history. Global mean surface temperatures were much warmer than today, atmospheric pCO_2 levels likely exceeded ~1,000 ppm at their highest, and large polar ice sheets did not exist. A number of global warming events of varying timescales and magnitudes were superimposed on background Eocene global warmth. Global warming events in the Eocene were likely forced by changing atmospheric pCO_2 concentrations, however the exact mechanisms and carbon sources involved in each case are unknown. Constraining the parameters of Eocene climate change is important for informing estimates of Earth system sensitivity under greenhouse or hothouse conditions, which feeds into modelling studies of future warming.

In Chapter 2, new, high-resolution (~3 – 5 kyr) X-ray fluorescence records of sediment geochemistry are presented from IODP Site U1514, Mentelle Basin, Southern Indian Ocean, across the EECO. Site U1514 was located at a high palaeolatitude, ~60 °S, in the early Eocene. It is therefore well-situated to record the influence of changing Southern Ocean circulation, particularly any response to the early surface water connection through the Tasmanian Gateway, ~49 Ma. Changing balances between biogenic and lithogenic elements in Site U1514 sediments indicate local variations in hydrological cycling and weathering rates on the nearby Australian continent in response to sustained high temperatures of the EECO. The initiation of a surface water connection through the Tasmanian Gateway may have stimulated a ~1 Myr interval of increased local primary productivity in the southern Indian Ocean at the end of the EECO, however it is unlikely to have contributed significantly to post-EECO pCO_2 drawdown.

In Chapter 3, a new benthic stable isotope ($\delta^{18}O$ and $\delta^{13}C$) record is presented across ~50 – 51 Ma from IODP Site U1514. These are the first climate records of early Eocene

hyperthermal events P to U from the Indian Ocean, a relatively understudied ocean basin with respect to the early Eocene. Time-series analysis on these high-resolution (~4 kyr) records is used to assess the impact of orbital forcing on the timing and magnitude of early Eocene hyperthermals. Hyperthermal events P to U in the Indian Ocean are driven by the 100-kyr eccentricity cycle in line with previous studies of early Eocene hyperthermals, while transient obliquity influence may indicate weak high-latitude forcing periodically throughout the EECO. A longer XRF Ca/Fe record also shows the influence of the 405-kyr eccentricity cycle on hyperthermal variations. Orbital conditions do not correlate with hyperthermal magnitude, which may instead reflect local, site-specific variations in climate records.

In Chapter 4, a compilation of sea surface temperature records from 17 sites with a global geographic spread is presented across the Middle Eocene Climatic Optimum. Records are compiled from three proxies: planktic foraminiferal $\delta^{18}O$, planktic foraminiferal Mg/Ca and isoprenoidal GDGTs (TEX_{86}). This compilation is the first such collection of all available $\delta^{18}O$, Mg/Ca and TEX_{86} data to show the geographic variation of MECO warming, which may contribute to future estimations of global climate sensitivity for the middle Eocene. Proxies are biased to different extents due to post-depositional alteration, uncertainties in middle Eocene ocean chemistry and GDGT distribution quality. Surface warming is constrained to ~1 – 7.5 °C. The reduced latitudinal temperature gradient of the middle Eocene is reconstructed, though MECO warming does not appear to impact latitudinal temperature gradients based on the datasets presented in this compilation.

In summary, this thesis presents new stable isotope data (Chapter 3) alongside re-analysis of existing datasets (Chapters 2 and 4) from the early and middle Eocene to provide insight into the environmental dynamics of the early Eocene 'hothouse', with a particular focus on the relatively understudied Indian Ocean.

ACKNOWLEDGEMENTS

Firstly, I would like to thank my supervisor Kirsty Edgar, who has provided unlimited support, encouragement and feedback throughout my four years at Birmingham. Despite the difficulties of the Covid-19 pandemic, she has consistently maintained enthusiasm for my research and kept me moving forward. She has always been willing to discuss Eocene climate and provide feedback on the many, many drafts I have sent her way and for that I am hugely grateful.

Thanks also to Tom Dunkley Jones, for the additional conversations, feedback and ideas which have helped shape my research and helped me to see the bigger picture outside of my datasets.

A big thanks to Sietske Batenburg, who generously hosted me at the University of Barcelona and providing training in time series analysis. She made the complexities of astronomical theory accessible from the beginning and her help contributed greatly to the third chapter of this work. Additional thanks to the rest of the IODP Expedition 369 Scientific Party, for welcoming me among them in Japan and inspiring the future direction of my research, as well as providing the data on which a portion of this work is based.

Thanks to those who have provided essential training and technical help throughout this project. Hans-Jürgen Brumsack, who analysed bulk chemical composition of Site U1514 samples for me. Melanie Leng at the British Geological Survey, who ran my samples for stable isotope analysis and invited me to the BGS to assist in sample preparation. Jonathan Hall, who provided GDGT distributions and training in BAYSPAR and OPTIMAL for my final chapter, and Sophie Manners, whose initial compilation of MECO datasets for her BSc formed the foundation of this chapter. Megan Wilding and the rest of the University of

Southampton Palaeoclimate laboratory technicians for introducing me to palaeoclimate sample preparation.

Special thanks to Vicki Taylor, who first introduced me to foraminifera and the microscope, and always had time to help despite her own PhD workload – whether for identifying species, or just to lend an ear. Your patience and companionship during long days in the lab inspired me to pursue science further. I would never have started this PhD without your encouragement.

Thanks to the friends I made along the way who made Birmingham the place to be, even during lockdowns: Alastair Hodgetts, Luke Meade, Murray Hoggett, Lisa Schnetz, Emma Hanson and Bridget Warren.

Thanks to my parents, for keeping my cupboards stocked with chocolate in the last few hectic months, and my brothers, Simon and Matt, for programming advice and last-minute dog sitting. Finally, thanks to my little family, Alex, Alfie and Rusty, for always being there for me at the end of the day.

This research was funded by the Natural Environmental Research Council (NERC) thorough a Central England NERC Training Alliance (CENTA) studentship, and by the European Consortium for Ocean Research Drilling (ECORD). This research uses samples from the International Ocean Discovery Program (IODP).

CONTENTS

ABSTRACT *1*

ACKNOWLEDGEMENTS *3*

CONTENTS *5*

LIST OF FIGURES *8*

LIST OF TABLES *10*

CHAPTER 1: INTRODUCTION **1**

1.1 Eocene climate evolution *1*

1.2 Importance of Eocene climate research *3*

1.3 Thesis structure and outline *4*

1.3.1 Chapter 2: Sediment chemistry at IODP Site U1514: Implications for environmental dynamics of the early Eocene 'hothouse' in the high latitude Indian Ocean *4*

1.3.2 Chapter 3: Orbital forcing of early Eocene hyperthermal events: A new benthic foraminiferal stable isotope record from the Indian Ocean, 50-51 Ma *6*

1.3.3 Chapter 4: Proxy constraints on sea surface temperature evolution across the Middle Eocene Climatic Optimum *7*

CHAPTER 2: SEDIMENT CHEMISTRY AT IODP SITE U1514: IMPLICATIONS FOR ENVIRONMENTAL DYNAMICS OF THE EARLY EOCENE 'HOTHOUSE' IN THE HIGH LATITUDE INDIAN OCEAN **10**

2.1 INTRODUCTION *10*

2.2 MATERIALS AND METHODS *14*

2.2.1 Materials *14*

2.2.2 Age model *15*

2.2.3 X-ray fluorescence core scanning and processing *15*

2.2.4 Converting XRF data to concentration and mass accumulation rates *17*

2.2.5 Strength of XRF intensity-concentration calibrations *19*

2.2.6 Normalisation of XRF data *20*

2.2.7 Additional data from Site U1514 ..... *21*

2.2.8 Principal component analysis *22*

2.3 RESULTS *23*

2.3.1 Downcore changes in elements *23*

2.3.1.1 55 – 52 Ma: pre-EECO and EECO onset *24*

2.3.1.2 52 – 49.1 Ma: Peak EECO and initial cooling *24*

2.3.1.3 49.1 – 46 Ma: Post-EECO cooling *26*

2.3.2 Principal component analysis results *27*

2.4 DISCUSSION *28*

2.4.1 Variable weathering response to warm EECO temperatures *28*
2.4.2 Increased Indian Ocean primary productivity across the EECO *31*
2.4.3 Signals of early Eocene hyperthermal events *35*
2.4.4 Controls on Sr/Ca variation across the EECO *37*
2.4.5 Impact of an early surface water connection through the Tasmanian Gateway *38*
2.5 CONCLUSIONS *40*

CHAPTER 3: ORBITAL FORCING OF EARLY EOCENE HYPERTHERMAL EVENTS: A NEW BENTHIC FORAMINIFERAL STABLE ISOTOPE RECORD FROM THE INDIAN OCEAN, 50-51 MA **43**

3.1 INTRODUCTION *43*
3.2 MATERIALS AND METHODS *49*
3.2.1 Materials *49*
3.2.2 Stable isotopes *50*
3.2.3 Palaeotemperature estimates from $\delta^{18}O$ *52*
3.2.4 X-ray fluorescence *53*
3.2.5 Time series analysis *53*
3.3 RESULTS *55*
3.3.1 Early Eocene stable isotopes and Ca/Fe *55*
3.3.2 Spectral analysis *60*
3.3.3 Coherence and phase relationships *65*
3.3.4 Filtering *67*
3.4 DISCUSSION *69*
3.4.1 Isotopic and lithologic signature of hyperthermals P – U in the Indian ocean *69*
3.4.2 Orbital characteristics of the early Eocene and forcing of hyperthermal events *75*
3.4.3 Phasing between environmental records *79*
3.4 CONCLUSIONS AND AVENUES FOR FUTURE WORK *83*

CHAPTER 4: PROXY CONSTRAINTS ON SEA SURFACE TEMPERATURE EVOLUTION ACROSS THE MIDDLE EOCENE CLIMATIC OPTIMUM **86**

4.1 INTRODUCTION *86*
4.2 MATERIALS AND METHODS *91*
4.2.1 Site selection and data collection *91*
4.2.2 Age models *94*
4.2.3 Oxygen isotope palaeothermometry *95*
4.2.4 Mg/Ca palaeothermometry *99*
4.2.5 Isoprenoidal GDGT palaeothermometry (TEX_{86}) *102*
4.2.6 Identifying pre-MECO, MECO onset, peak-MECO and post-MECO intervals *106*
4.3 RESULTS *107*

4.3.1 Palaeotemperature reconstructions across the MECO 107
4.3.1.1 $\delta^{18}O$-based SST reconstructions 110
4.3.1.2 Mg/Ca-based SST reconstructions 114
4.3.1.3 TEX_{86}-based SST reconstructions 117
4.3.2 SST change across intervals of the MECO 123
4.3.3 Latitudinal SST change across the MECO 128
4.4 DISCUSSION 131
4.4.1 Eocene climate reconstructions with $\delta^{18}O$, Mg/Ca and TEX_{86} 131
4.4.1.1 Impact of diagenesis on planktic foraminiferal $\delta^{18}O$ 131
4.4.1.2 Impact of middle Eocene seawater chemistry on SST estimates 133
4.4.1.3 Comparison of the Bayfox and Equation 4.1 $\delta^{18}O$ palaeothermometry approach 135
4.4.1.4 Impact of calibration and middle Eocene ocean chemistry on Mg/Ca 136
4.4.1.5 Comparison of BAYSPAR and OPTiMAL temperature calibrations 137
4.4.1.6 High variability in TEX_{86} SST reconstructions 139
4.4.2 Site specific responses to MECO warming 141
4.4.3 Polar amplification and the role of pCO_2 142
4.5 CONCLUSIONS AND AREAS FOR FUTURE WORK 145

CHAPTER 5: CONCLUSIONS 148

5.4 Summary of main findings 148
5.4.1 Chapter 2: Sediment chemistry at IODP Site U1514: Implications for environmental dynamics of the early Eocene 'hothouse' in the high latitude Indian Ocean 148
5.4.2 Chapter 3: Orbital forcing of early Eocene hyperthermal events: A new benthic foraminiferal record from the Indian Ocean, 50-51 Ma 149
5.4.3 Chapter 4: Proxy constraints on sea surface temperature evolution across the Middle Eocene Climatic Optimum 150
5.5 Future directions for Eocene palaeoclimate research 151

References 154

Appendices 173

Appendix 1: Supplementary material for Chapter 2 173
Appendix 2: Supplementary material for Chapter 3 180
Appendix 3: Supplementary material for Chapter 4 198

LIST OF FIGURES

1.1	CENOGRID isotope compilation of the Eocene	2
2.1	Palaeogeographic reconstruction at 55 Ma showing location of IODP Site U1514	13
2.2	Correlation between XRF intensities and element concentrations	18
2.3	Chron boundaries, spliced core sections, linear sedimentation rates and magnetic susceptibility (46 – 55 Ma) at IODP Site U1514	22
2.4	XRF ratios from 46 – 55 Ma at IODP Site U1514	23
2.5	Element concentrations and mass accumulation rates from 46 – 55 Ma at IODP Site U1514	25
2.6	Principle component analysis of XRF data from IODP Site U1514	26
2.7	Loadings plots for PCA analysis of XRF data	27
2.8	Shipboard smear slide results from IODP Site U1514	35
2.9	Sr/Ca variation from 46 – 55 Ma, IODP Site U1514	36
3.1	CENOGRID isotope compilation of the Eocene, showing climatic context for Ch. 3	44
3.2	Published isotope records across the early Eocene	47
3.3	Palaeogeographic reconstruction at 50 Ma showing location of IODP Site U1514 and other sites referenced in this chapter	49
3.4	Stable isotope and XRF results from 50 – 51 Ma, IODP Site U1514	55
3.5	Cross-plot of $\delta^{18}O$ and $\delta^{13}C$ data	56
3.6	Comparison of new data from IODP Site U1514 with published datasets	57
3.7	$\delta^{18}O$ – $\delta^{13}C$ regression lines for hyperthermals P – U at IODP Site U1514	60
3.8	Basic frequency spectra for $\delta^{18}O$, $\delta^{13}C$ and Ca/Fe data at IODP Site U1514	61
3.9	Evolutive spectra for $\delta^{18}O$, $\delta^{13}C$ and Ca/Fe data at IODP Site U1514	62
3.10	Wavelet spectra for $\delta^{18}O$, $\delta^{13}C$ and Ca/Fe data at IODP Site U1514	64
3.11	Coherence and phasing between records at IODP Site U1514	66
3.12	Filtered $\delta^{18}O$ data from IODP Site U1514	68
3.13	Filtered $\delta^{13}C$ data from IODP Site U1514	68
3.14	Filtered Ca/Fe data from IODP Site U1514	69

3.15	Comparison of new records from IODP Site U1514 with the La2010C eccentricity solution between 50 – 51 Ma	79
3.16	Summary of main findings from Chapter 3	82
4.1	CENOGRID isotope compilation of the Eocene, showing climatic context for Ch. 4	87
4.2	Palaeogeographic reconstruction at 40 Ma showing locations of sites included in this compilation	93
4.3	Sea surface temperature records across the MECO for DSDP Site 516, ODP Site 913, ODP Site 959	108
4.4	Sea surface temperature records across the MECO for ODP Site 647	109
4.5	Sea surface temperature records across the MECO for ODP Site 702	111
4.6	Sea surface temperature records across the MECO for ODP Site 748	112
4.7	Sea surface temperature records across the MECO for ODP Site 865	113
4.8	Sea surface temperature records across the MECO for ODP Site 1051	114
4.9	Sea surface temperature records across the MECO for ODP Site 1052	115
4.10	Sea surface temperature records across the MECO for ODP Sites 1172 and 1209	116
4.11	Sea surface temperature records across the MECO for ODP Site 1170	117
4.12	Sea surface temperature records across the MECO for ODP Site 1260	118
4.13	Sea surface temperature records across the MECO for ODP Site 1263	119
4.14	Sea surface temperature records across the MECO for the Baskil Section	120
4.15	Sea surface temperature records across the MECO for the Belaya River Section	121
4.16	Sea surface temperature records across the MECO for IODP Site U1408	122
4.17	SST change across intervals of the MECO for all sites	124
4.18	Latitudinal patterns in MECO temperature change	127
4.19	Average SSTs across each interval of the MECO, with latitude	128
4.20	Average SSTs across each MECO interval, poor quality data excluded	130

LIST OF TABLES

3.1	Hyperthermal excursions in $\delta^{18}O$ and $\delta^{13}C$ at IODP Site U1514 and in other published records	59
4.1	Summary of sites, proxies, parameters and references for sites included in this compilation	92
4.2	Palaeoecologies of foraminifera used in $\delta^{18}O$ SST reconstructions	94
4.3	Case study of geochemical impacts on final $\delta^{18}O$-derived SSTs	99
4.4	Change in SST over intervals of the MECO for sites in this compilation	126

CHAPTER 1: INTRODUCTION

1.1 Eocene climate evolution

The Eocene (56 – 34 Ma) was a pivotal time in Earth's climate history, characterised by high temperature greenhouse conditions, dynamic shifts in global temperature and fundamental tectonic and oceanographic reorganisations (Fig.1.1, Cramer et al., 2009; Westerhold et al., 2020; Zachos et al., 2001). The beginning of the Eocene is marked by the Palaeocene-Eocene Thermal Maximum (PETM), expressed in sedimentary records by a large negative carbon isotope excursion (CIE) associated with extensive sedimentary carbonate dissolution and >5 °C average global warming (Inglis et al., 2020; McInerney & Wing, 2011). From ~50 – 53 Ma, following post-PETM recovery, atmospheric pCO_2 concentrations and global temperatures continued to rise, reaching average surface temperatures of ~27 °C and pCO_2 concentrations of 1,000 – 2,000 ppm during the Early Eocene Climatic Optimum (EECO, Anagnostou et al., 2016; Inglis et al., 2020; Rae et al., 2021) . Superimposed on this background 'hothouse' global climate state were a series of short-lived (<200 kyr), repeated global warming events known as early Eocene hyperthermals (Cramer et al., 2003; Kirtland Turner et al., 2014; Sexton et al., 2011). Following the EECO, atmospheric CO_2 concentrations and global temperatures began to decline (Bornemann et al., 2016; Westerhold et al., 2020). Cooling was interrupted at ~40 Ma by the Middle Eocene Climatic Optimum (MECO), a ~400 – 700 kyr warming event (Bohaty et al., 2009; Bohaty & Zachos, 2003), yet continued following MECO recovery, eventually leading to the Eocene-Oligocene transition (EOT) at ~34 Ma and the rapid expansion of ice sheets on Antarctica (Coxall et al., 2005; Liu et al., 2009; Miller et al., 1991; Zachos et al., 1992). This transition from the ice-free, early Eocene 'hothouse' planet to the cooler, glaciated state that has persisted to the present day is

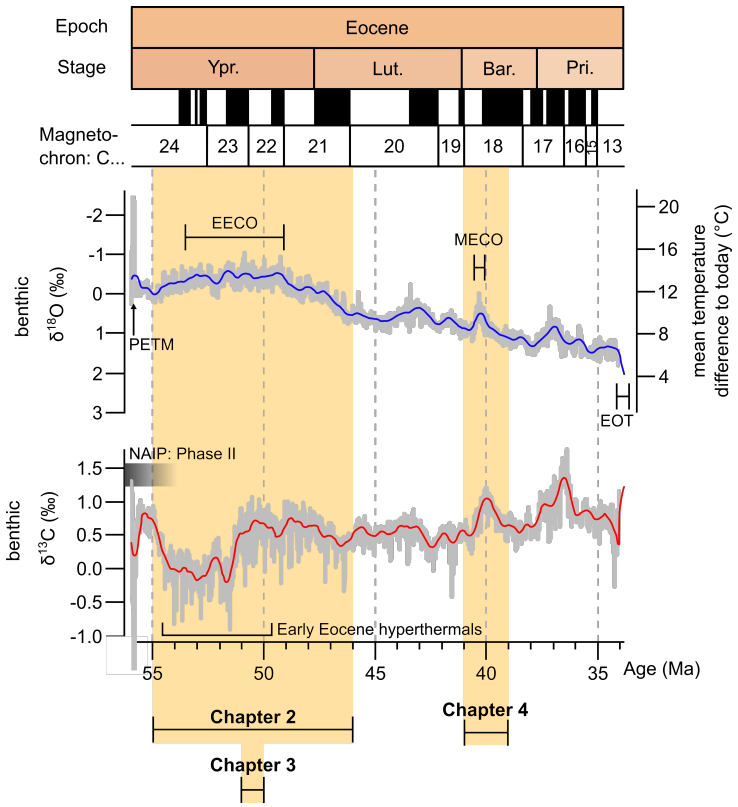


Figure 1.1 *Eocene section of the Cenozoic Global Reference benthic foraminiferal carbon and oxygen Isotope Dataset (CENOGRID, Westerhold et al., 2020) showing the 20 kyr (grey) and 1 Myr smoothed composite benthic $\delta^{18}O$ record (blue) and benthic $\delta^{13}C$ record (red) alongside relevant climatic events for the Eocene and oxygen isotope temperature conversion, relative to today. Study intervals in this thesis are highlighted with the yellow bars. Figure modified from Fig. 1, Westerhold et al. (2020). Climatic event labels: Early Eocene Climatic Optimum (EECO), Paleocene-Eocene Thermal Maximum (PETM), Active Phase II of the North Atlantic Igneous Province (NAIP: Phase II), Middle Eocene Climatic Optimum (MECO), Eocene/Oligocene Transition (EOT).*

associated with the appearance of many features of the modern Earth system. In particular, the Antarctic ice sheet (AIS, Coxall et al., 2005; Lear et al., 2008), the Antarctic Circumpolar Current (ACC, Barker et al., 2007) and Atlantic Meridional Overturning Circulation (AMOC, Borrelli et al., 2014) each have their roots in oceanographic and environmental changes that occurred alongside post-EECO cooling and pCO_2 decline.

Key climate events and transitions in the Eocene were likely to have been forced by carbon cycle perturbations and changes in atmospheric pCO_2 concentrations. For example, the PETM may have been triggered by release of volcanic gases from activity in the North Atlantic Igneous Province (Gutjahr et al., 2017; Jones et al., 2019), while early Eocene hyperthermal

events are likely linked to changes in Earth's orbital eccentricity, periodically releasing isotopically light carbon from a temperature sensitive reservoir (Barnet et al., 2019; Cramer et al., 2003; Galeotti et al., 2010; Kirtland Turner et al., 2014; Lauretano et al., 2015; Littler et al., 2014; Lourens et al., 2005; Westerhold et al., 2018; Zachos et al., 2010). Post-EECO cooling has also been attributed primarily to pCO_2 drawdown (Anagnostou et al., 2016; DeConto & Pollard, 2003; Lauretano et al., 2021; Pagani et al., 2005; Speelman et al., 2009). The MECO is also associated with pCO_2 change (Bijl et al., 2009; Henehan et al., 2020), and warming may be linked to volcanism (van der Boon et al., 2021) or have an orbital component (Westerhold & Röhl, 2013). However, while the PETM, EECO, early Eocene hyperthermal and MECO global warming events are each attributed to carbon release from different potential reservoirs, the particular source of carbon and exact forcing mechanism in each case remain elusive.

1.2 Importance of Eocene climate research

Many authors point to the importance of understanding Eocene climate as an analogue for a potential future greenhouse world. Modelling studies of future warming suggest that under the Representative Concentration Pathway (RCP) 8.5 unmitigated emissions scenario, global climate may closely resemble that of the Eocene by the year 2150 (Burke et al., 2018). The Intergovernmental Panel on Climate Change (IPCC) also uses palaeoclimate data from past warm and cool periods to inform reports on climate change which are directly relevant to policymakers (Forster et al., 2021). Eocene climate data is particularly useful for modelling projections of future warming, where models based on modern data are not necessarily accurate when extrapolated beyond modern temperatures or pCO_2 levels (Lunt et al., 2013). Additionally, discrepancies between proxy data and climate models highlight the need for a

better understanding of Earth system sensitivity to pCO_2 change (Anagnostou et al., 2020; Haywood et al., 2013). Constraining the parameters of past warming events, such as the volume and source of CO_2 released, the overall magnitude of warming, and the impact of warming on latitudinal temperature gradients, allows for a better understanding of past Earth system sensitivity and therefore improves our ability to inform boundary conditions in climate models (Anagnostou et al., 2020; Hollis et al., 2019). However, there are still many unknowns surrounding Eocene climate and carbon cycle dynamics which need to be better constrained to improve model parameters and assessment of future climate change.

1.3 Thesis structure and outline

This thesis has been written in a paper style, with the aim to submit independent chapters for publication. Throughout this thesis the author has used first person plural language ('we' and 'our') to honour the contributions of other researchers within each chapter, as would be correct for a published paper. However, the majority of the research in this thesis was carried out by the primary author, Nicola Kirby. Additional researchers who have contributed to this thesis have been listed in the Acknowledgements section prior to this chapter. Specific author contibutions for each chapter are also summarised below, along with the specific aims addressed in this thesis:

1.3.1 Chapter 2: Sediment chemistry at IODP Site U1514: Implications for environmental dynamics of the early Eocene 'hothouse' in the high latitude Indian Ocean

Aim: Document the environmental and geochemical signals across the build-up, peak and close of the EECO, and assess any impacts of Southern Ocean circulation on the high latitude Indian Ocean.

Extreme global warmth of the early Eocene peaked during the Early Eocene Climatic Optimum (EECO, ~49 – 53 Ma). By ~49 Ma, temperatures began to decline and global cooling continued, with some interruptions, until the Eocene-Oligocene Transition and Oi-1 glaciation event, ~34 Ma (Westerhold et al., 2020). The Southern Ocean connects the atmospheric carbon reservoir to the global deep ocean through processes such as deep-water formation, upwelling and carbon sequestration through the biological pump (Fogwill et al., 2020; Marinov et al., 2006; Sigman & Boyle, 2000). Over geological timescales, the relative strength of these processes and associated feedbacks can influence atmospheric pCO_2 concentrations (e.g. Schmittner & Galbraith, 2008; Toggweiler et al., 2006) however the role of Southern Ocean dynamics in post-EECO cooling is unknown. Here, we present high resolution X-ray fluorescence (XRF) records of sediment chemistry from the Indian Ocean, IODP Site U1514. This site was located at a high palaeolatitude in the early Eocene, ~60 °S. It is therefore well-situated for recording environmental change in the Indian Ocean sector of the Southern Ocean across the build-up and decline of the EECO. XRF records show that geochemical variation at Site U1514 are largely driven by changes in lithogenic elements, likely through local weathering inputs. We identify a rise in potassium in sediments as temperatures increase into the EECO, which suggests an enhanced weathering response to warming on the Australian continent. Subsequent potassium decline across peak EECO temperatures may indicate a decline in continental 'weatherability' over time (e.g. van der Ploeg et al., 2018). Calcium and barium concentrations are high and variable throughout the EECO, implying high yet unstable calcareous and export productivity related to peak EECO warmth. A ~1 Myr-long productivity 'spike' occurs at the end of the EECO, ~49 Ma, however it is unlikely that this temporary increase would have been great enough to contribute to post-EECO pCO_2 drawdown and cooling. Further evidence of C-sequestration at

high latitudes following EECO warmth is needed to confirm whether Southern Ocean dynamics contributed to cooling.

Author contributions: XRF datasets were generated by the IODP Expedition 369 Scientific Party. The bulk sedimentary composition dataset was generated by Hans-Jürgen Brumsack (University of Oldenburg). Data analysis, presentation and interpretation was done by Nicola Kirby with support from Kirsty Edgar (University of Birmingham) and Tom Dunkley Jones (University of Birmingham). Nicola Kirby wrote this manuscript with editorial support from Kirsty Edgar and Tom Dunkley Jones.

1.3.2 Chapter 3: Orbital forcing of early Eocene hyperthermal events: A new benthic foraminiferal stable isotope record from the Indian Ocean, 50-51 Ma

Aim: Identify the impact, phasing and evolution of Earth's orbital cycles on benthic foraminiferal stable isotope records of Early Eocene hyperthermals.

During the late Palaeocene-early Eocene, global mean surface temperatures were high, reaching ~27 °C during the Early Eocene Climatic Optimum (EECO, Inglis et al., 2020). A series of transient, <200 kyr-long global warming 'hyperthermal' events occur superimposed on this background warmth. While the cause of early Eocene hyperthermals remains unknown, previous studies have identified that hyperthermals are paced by Earth's orbital variations, in particular the long (405 kyr) and short (100 kyr) eccentricity cycles (Barnet et al., 2019; Cramer et al., 2003; Galeotti et al., 2010; Kirtland Turner et al., 2014; Lauretano et al., 2015; Littler et al., 2014; Lourens et al., 2005; Westerhold et al., 2018; Zachos et al., 2010). We present the first high-resolution benthic foraminiferal stable isotope record from IODP Site U1514, high latitude Indian Ocean, between 50 – 51 Ma from *Nuttalides truempyi*.

We document hyperthermal events P to U within this interval, and use time series analysis to identify that hyperthermals are paced dominantly by the 100-kyr short eccentricity cycle. We also perform time series analysis on a longer XRF Ca/Fe record from this site to capture the influence of longer orbital periodicities, which captures the influence of the 405-kyr long eccentricity cycle. Hyperthermal events in the Indian Ocean therefore fit the global pattern and are controlled dominantly by eccentricity variation. However, we do not find any correlation between orbital parameters and relative hyperthermal magnitude at this site. High coherence between benthic $\delta^{18}O$ and $\delta^{13}C$ across the study interval indicates close coupling of climate and carbon cycling across the EECO in the Indian Ocean, as has been documented in other ocean basins (Cramer et al., 2003; Kirtland Turner et al., 2014). Records from Site U1514 also show transient influence of obliquity-scale signals, which suggests weak high-latitude forcing on Indian Ocean climate across the EECO.

Author contributions: Sedimentary samples were obtained from IODP, and laboratory work to obtain microfossils for analysis was done by Nicola Kirby with methodological advice from Kirsty Edgar (University of Birmingham). Microfossils were run for stable isotope analysis by Melanie Leng (British Geological Survey). Sietske Batenburg (University of Barcelona) trained Nicola Kirby in time series analysis techniques and subsequent data analysis, presentation and interpretation was done by Nicola Kirby, with input from Sietske Batenburg. Nicola Kirby wrote this manuscript with support from Kirsty Edgar and Sietske Batenburg.

1.3.3 Chapter 4: Proxy constraints on sea surface temperature evolution across the Middle Eocene Climatic Optimum

Aim: Compile existing sea surface temperature data across the MECO from $\delta^{18}O$, Mg/Ca and TEX_{86} proxies to assess latitudinal and methodological variation in MECO warming.

Middle to late Eocene climate is characterised by global cooling from peak warmth of the Early Eocene Climatic Optimum (EECO, ~49 – 53 Ma) to the rapid expansion of Antarctic ice-sheets at the Eocene-Oligocene Transition (EOT, ~34 Ma). Cooling was temporarily interrupted at ~40 Ma by the Middle Eocene Climatic Optimum (MECO), a ~400 – 700 kyr-long warming event (Bohaty et al., 2009; Bohaty & Zachos, 2003). Here, we compile sea surface temperature (SST) records of the MECO from 17 sites with a global spread to assess latitudinal and inter-basinal variations in warming. We include SST measurements from planktic foraminiferal $\delta^{18}O$, planktic foraminiferal Mg/Ca and isoprenoidal GDGTs (TEX_{86}). MECO warming in this compilation ranges from ~1 – 7.5 °C, and may therefore be more variable than previously identified. We demonstrate the reduced latitudinal temperature gradient of the middle Eocene (Inglis et al., 2015), however we do not identify any change of latitudinal temperature gradients in response to MECO warming. Our compilation highlights significant method-specific uncertainties in Eocene palaeotemperature calculations. In particular, $\delta^{18}O$-derived SSTs are strongly affected by post-depositional recrystallisation and poor characterisation of middle Eocene ice volumes. Additionally, TEX_{86} SST data for the middle Eocene is influenced both by GDGT quality and by calibration strength at high temperatures. Lack of quantification of pH change across the MECO also limits the accuracy of the Mg/Ca SST proxy. Analysis of geographic variation in MECO SST evolution would be improved by better characterisation of middle Eocene ocean chemistry, additional SST records from $\delta^{18}O$, Mg/Ca and TEX_{86}, and further SST data from additional proxies.

Author contributions: Nicola Kirby compiled stable isotope and Mg/Ca datasets (see chapter for original authors of these datasetds). Johnathan Hall (University of Birmingham) compiled GDGT distributions and taught Nicola Kirby OPTiMAL and BAYSPAR methods. Nicola Kirby converted stable isotope, Mg/Ca and TEX_{86} data to SSTs. Subsequent data

analysis, presentation and interpretation was done by Nicola Kirby. Nicola Kirby wrote this manuscript with support from Kirsty Edgar (University of Birmingham).

CHAPTER 2: SEDIMENT CHEMISTRY AT IODP SITE U1514: IMPLICATIONS FOR ENVIRONMENTAL DYNAMICS OF THE EARLY EOCENE 'HOTHOUSE' IN THE HIGH LATITUDE INDIAN OCEAN

2.1 INTRODUCTION

The early Eocene, ~56 – 48 Ma, is characterised by high atmospheric pCO_2 levels up to 1,000 – 2,000 ppm (Rae et al., 2021), warm polar regions free from continental-scale ice sheets (Cramer et al., 2011) and extreme global warmth which culminated in the Early Eocene Climatic Optimum (EECO, ~53 – 49 Ma). During the EECO, sea surface temperatures reached ~18 °C at high latitudes and likely exceeded 30 °C in tropical regions (Hollis et al., 2019). However, at ~49 Ma, temperatures began to decline and global climate gradually cooled over the next ~15 million years (albeit with some interruptions) until the rapid expansion of continental ice sheets on Antarctica at the Eocene-Oligocene Transition, ~34 Ma (Westerhold et al., 2020). A number of major oceanographic changes in the Southern Ocean accompany the transition out of the 'hothouse' conditions of the EECO and across the Early Middle Eocene Transition (EMET, ~51 – 47 Ma). Most notably, the earliest evidence of surface water throughflow from the Pacific to the Southern Indian Ocean occurs at ~49 – 48 Ma (Bijl et al., 2013) indicating that the Tasmanian Gateway between Australia and Antarctica had opened to the passage of shallow waters. Globally, deep water temperatures began to decline at ~49 Ma (Ortiz & Thomas, 2015; Westerhold et al., 2020). Around the same time, ~50 – 48 Ma, a neodymium isotope excursion in several Southern Ocean sites indicates a significant erosional event on Antarctica, potentially related to a perturbation in the Antarctic hydrological cycle (Huck et al., 2017). The coincident timing of oceanographic and climatic changes suggests that these responses are linked, but the role of Southern Ocean

biogeochemistry in early Eocene global carbon-cycle dynamics is unclear. Well-dated proxy records of biogeochemical changes are needed in order to determine the relative timing and links between tectonic and oceanographic changes in the Southern Ocean and wider Cenozoic climate evolution. Additionally, with the Drake Passage and Tasman Gateway closed to deep water flow throughout the early Eocene (Scher & Martin, 2006; Stickley et al., 2004) adjacent sectors of the Southern Ocean were isolated from each other and environmentally heterogenous (Judd et al., 2019). It is therefore important to determine regional climate history for the Pacific, Atlantic and Indian sectors of the Southern Ocean across key climate transitions of the early Eocene.

Many studies have highlighted the role of the Southern Ocean in influencing global atmospheric pCO_2 levels and global carbon cycling on a wide range of timescales through several circulatory and biogeochemical processes. For example, the biological pump sequesters carbon through surface primary productivity and remineralisation at depth, while deep water formation and upwelling of deep waters connect the surface and atmospheric carbon reservoirs to the global deep ocean (Fogwill et al., 2020; Marinov et al., 2006; Sigman & Boyle, 2000). The overall magnitude of these processes relative to one another has been shown to affect atmospheric pCO_2 concentrations over glacial-interglacial cycles (Anderson et al., 2009; Gottschalk et al., 2016; Schmittner & Galbraith, 2008). Feedback cycles involving global temperature, the latitudinal position of westerly winds and iron fertilisation are also at play, acting to both strengthen or dampen the role of the Southern Ocean as a carbon source or sink on a range of timescales (Fogwill et al., 2020; Schmittner & Galbraith, 2008; Toggweiler et al., 2006). In the case of the Eocene, stratification of the Southern Ocean prior to the Eocene Oligocene Transition (EOT, ~34 Ma) and associated strengthening of Atlantic Meridional Overturning Circulation (AMOC) may have led to Northern Hemisphere

warming, greater precipitation over land and CO_2 drawdown through silicate weathering, enhancing Antarctic ice sheet (AIS) growth (Elsworth et al., 2017). The Southern Ocean is also identified as a key sink for current and future anthropogenic CO_2 (e.g. Frölicher et al., 2015; Sabine et al., 2004).

Existing research into the impact of Southern Ocean circulation and biogeochemistry on the global carbon cycle focuses primarily on the Pleistocene (~2.6 – 0.01 Ma), particularly the last glacial and deglacial period (e.g. Anderson et al., 2009; Fogwill et al., 2020; Gottschalk et al., 2016), and the Eocene-Oligocene Transition (e.g. DeConto & Pollard, 2003; Elsworth et al., 2017; Huber et al., 2004). However, the impact of Southern Ocean dynamics on the early Eocene greenhouse is unknown. This is in part due to a large-scale hiatus in carbonate deposition around this time (Payros et al., 2009; van Andel et al., 1975), coupled with a relatively shallow global carbonate compensation depth (CCD) which resulted in carbonate-poor deep-sea sediments in most ocean basins (Greene et al., 2019; Pälike et al., 2012). This has led to a lack of high-resolution, long-term and continuous climate records across the early Paleogene. Neodymium isotope and other geochemical studies show that the Southern Ocean was a source of global deep waters from the early Eocene through Oligocene (Cramer et al., 2009; Huck et al., 2017; Scher & Martin, 2004; Thomas et al., 2014; Wright et al., 2018). Changes in Southern Ocean conditions across the Eocene would have been exported to other ocean basins via deep water formation and convection.

Several high-resolution climate records exist for the latest Palaeocene to early Eocene interval, including the northwest Pacific (Luciani et al., 2016; Westerhold et al., 2018), equatorial Pacific (Leon-Rodriguez & Dickens, 2010), southeast Atlantic (Barnet et al., 2019; Lauretano et al., 2015; Littler et al., 2014; Zachos et al., 2010), equatorial Atlantic (Sexton et al., 2011), Mead Stream, New Zealand (Nicolo et al., 2007; Slotnick et al., 2012) and Tethyan

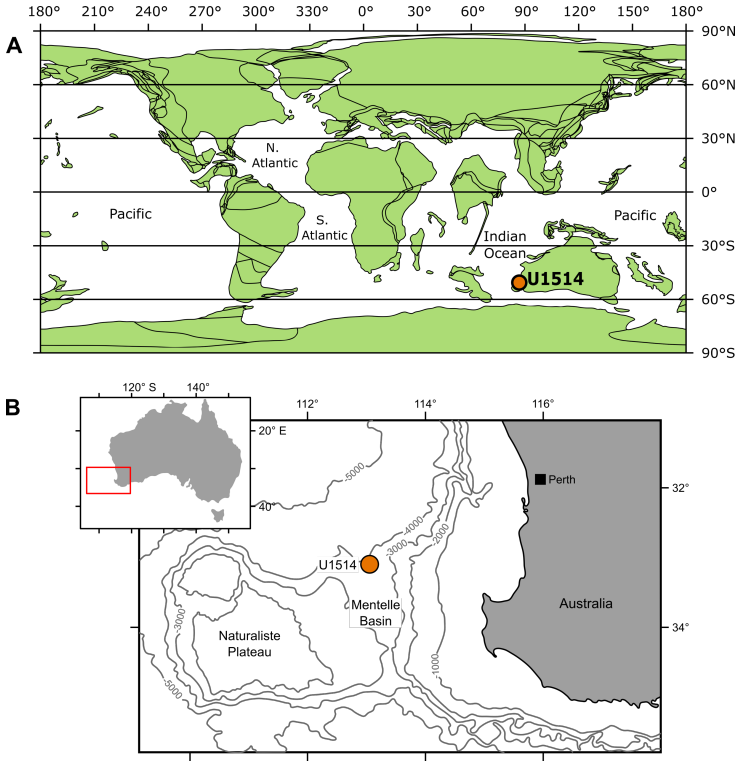


Figure 2.1 A. *Paleogeographic reconstruction of the Eocene at 55 Ma from the Ocean Drilling Stratigraphic Network (www.odsn.de). Red circle shows the palaeolocation of IODP Site U1514.* ***B.*** *Modern-day position of IODP Site U1514 relative to the Australian continent and the Mentelle Basin. Modified from Huber et al. (2019).*

sections (Francescone et al., 2019; Galeotti et al., 2010). However, few of these records are from high latitudes and there are no published high-resolution records from the Indian Ocean across this interval.

Site U1514 was cored in 2017 during International Ocean Discovery Program (IODP) Expedition 369 to the Indian Ocean (Hobbs et al., 2019). Site U1514 is located in the northern part of the Mentelle Basin on the southwest Australian continental margin (Fig. 2.1). A semi-continuous, 518 m long sedimentary sequence spanning the Upper Cretaceous through Holocene was recovered (Huber et al., 2019). During the early Eocene, Site U1514 was located at a relatively high palaeolatitude, ~60°S, carbonate content in sediments was high (45.6 – 77.1 %, mean 63.8 %) and recovery was good, 88 % in total across the study interval (Huber et al., 2019). With a high palaeolatitude, good carbonate recovery and location close

to the Tasman Gateway in the relatively understudied Indian Ocean, Site U1514 is ideally situated for investigating high latitude climatic and oceanographic responses across a highly dynamic period of Earth's climate history.

Here, we present new high-resolution X-ray fluorescence (XRF) records from Site U1514 spanning ~55-46 Ma. We use these records to determine biogeochemical changes associated with the rise and fall of the EECO and how this is linked to local and global climate and oceanographic changes.

2.2 MATERIALS AND METHODS

2.2.1 Materials

IODP Site U1514 is located at 33° 7.2327′ S, 113° 5.4672′ E at 3850 m modern water depth in the Mentelle Basin, southeast Indian Ocean (Fig. 2.1). Benthic foraminiferal assemblages indicate a similar palaeowater depth of lower to middle bathyal for the Eocene (Huber et al., 2019). Sediments recovered span the Late Cretaceous to the Pleistocene, with overall recovery of 87.5 %. A shipboard splice was generated across Lower Eocene sediments between the two main holes, U1514 A and U1514 C, covering 253.82 – 280.2 m CSF-A in Hole U1514A, and 195.6 – 264.31 m CSF-A in Hole U1514 C (Huber et al., 2019). Shipboard splice tie points were subsequently refined by Vahlenkamp et al. (2020). We focus on sediments between 186.8 – 270.4 m core composite depth below seafloor (CCSF), corresponding to ~46.0 – 55.0 Ma and comprising of nannofossil oozes, nannofossil-rich clays and nannofossil chalk (Huber et al., 2019). The splice maximises the length of the record however there are still some minor gaps (<2 m) in the lower portion, below 248 m CCSF. The core depth below seafloor (CSF-A) scale was converted to CCSF following

Vahlenkamp et al. (2020) in order to use the revised core splice and allow correlation of depths between holes U1514 A and C.

2.2.2 Age model

The initial age model for Site U1514 was based on shipboard magneto- and bio-stratigraphic age-depth tie points (Huber et al., 2019) reported on the Geomagnetic Polarity Time Scale (GPTS) 2012 (Gradstein et al., 2012). Subsequently, an astronomically tuned timescale for the middle Eocene (~40 – 56 Ma) was created by Vahlenkamp et al. (2020) using cyclic variations in XRF-derived Ca/Fe ratios. In this astronomical age model, tie points for the middle-lower Eocene were generated by tuning the Ca/Fe record to the La2010c full astronomical solution (Laskar et al., 2011; Vahlenkamp et al., 2020). See Supplementary Table 4 of Vahlenkamp et al. (2020) for Site U1514 age-depth tie points. Vahlenkamp et al. (2020) also identified hyperthermal events between the PETM and the W event on the basis of Ca/Fe excursions, as available stable isotope records for the site are of insufficient resolution to resolve these events (Edgar et al., 2022). All of the Site U1514 datasets are presented here on this site-specific age model.

2.2.3 X-ray fluorescence core scanning and processing

X-ray fluorescence (XRF) core scanning generates a continuous, semi-quantitative record of sediment chemistry (Rothwell & Croudace, 2015). Due to the rapid and non-destructive nature of this method, XRF records have been widely applied as palaeoenvironmental proxies in a variety of different sedimentary environments and ages (e.g. Ellis et al., 2019; Evans et al., 2021; Spofforth et al., 2008). Here, Paleogene sediments from Site U1514 were XRF-scanned during the IODP Exp. 369 shipboard sampling party on third generation Avaatech machines at the AVAATECH XRF Core Scanning Facility in the IODP Gulf Coast Repository, Texas (Bogus et al., 2019; Huber et al., 2019). XRF scanning followed the core

splice between 186.7 – 270.3 m CSF-A, with two different XRF machines used to maximise throughput. Split core surfaces were cleaned and flattened, and a SPEX-Certi Prep Ultralene foil (4 μm thick) was applied to prevent desiccation and contamination of the XRF instrument between measurements. Measurements were made over an area of 1 cm^2 with a 6-second count time, at source energies and currents of 10 kV at 0.16 mA with no filter, 30 kV at 1.25 mA with a copper filter, and 50 kV at 0.75 mA with a palladium filter. Different elements were detected at different source energies: Al, Ar, Cl, Cr, K, Mg, P, S, Si and Ti at 10 kV; Br, Cu, K, Mo, Ni, Rb, Sr, Ti, Y, Zn and Zr at 30 kV; Ag, Ba, Ni, Rb, Sr, Y and Zr at 50 kV. Elements Ca, Fe and Mn were detected at all three source energies. In this study, we focus only on XRF data from the elements Fe, Si, Ti, Ca, Ba, K and Sr. A powdered standard was also scanned multiple times throughout the analysis sessions to check for instrument drift or any other issues. The resulting raw spectra were converted to elemental intensities using the bAxil software (BrightSpec NV/SA, Belgium). Measurement resolution varied over the study interval due to variable lithological and core quality, but averaged ~3 cm spacing between 186.7 – 220.0 m CSF-A and ~2 cm spacing between 220.0 – 270.3 m CSF-A. High-resolution spacing was maintained in order to capture orbital-scale climate variability (Bogus et al., 2019). Anomalous peaks (sharp, single point drops) evident in intensities of all elements or extreme spikes followed by drops typically corresponded to cracks or gaps in the core surface, visible in core photographs. These anomalous data points were removed from the dataset. The 'cleaned' dataset employed in this study is shown in Supplementary Table 2.1, and the raw dataset is available online at the IODP Laboratory Information Management System (LIMS) database (IODP Joides Resolution Science Operator, 2018).

Due to using two separate XRF instruments during scanning (Bogus et al., 2019), a strong instrumental offset is seen at the switch point in raw XRF datasets for elements with lower

overall intensities. Out of the elements described in this study, instrumental offset affected Sr and Ba while Ca, Fe, Si and Ti were unaffected (Supplementary Fig. 2.1).

2.2.4 Converting XRF data to concentration and mass accumulation rates

As XRF-derived elemental intensities only return a semi-quantitative representation of sediment composition, we used discrete, low-resolution measurements of elemental concentrations to calibrate the calculated high-resolution XRF intensities to concentrations. In total, 138 bulk sediment samples spanning 61.5 – 397.3 m CSF-A were analysed for concentrations of a range of elements including the focal elements studied here: SiO_2, TiO_2, Al_2O_3, Fe_2O_3, CaO, K_2O, Ba and Sr (Supplementary Tables 2.1, 2.4). The majority of the discrete samples (134) correspond to the same lithological unit (nannofossil oozes, nannofossil-rich clays and nannofossil chalk, Huber et al., 2019) that we focus on in this study.

Samples were analysed for elemental concentrations at the University of Oldenburg using a wave-length dispersive X-ray fluorescence (WD-XRF) spectrometer (Axios Plus, Panalytical). ~700 mg of powdered sample was mixed with 4,200 mg of lithium tetraborate powder and ammonium nitrate (NH_4NO_3) then pre-oxidised in an oven overnight at 500 °C. Samples were then fused into glass beads in platinum crucibles. Beads were analysed using a WD-XRF spectrometer equipped with a rhodium tube. Measurements of element concentrations are based on calibration of resulting XRF measurements with 56 international standard reference samples covering multiple types of known sediment composition. Two in-house standards were used to check analytical precision: Peru-1, a Peruvian margin fine-grained sediment, and PS-S, Lower Jurassic Posidonia Shale. Analytical precision is <1 % for Si, Ti, Fe, Ca, K, Sr and is <2 % for Ba.

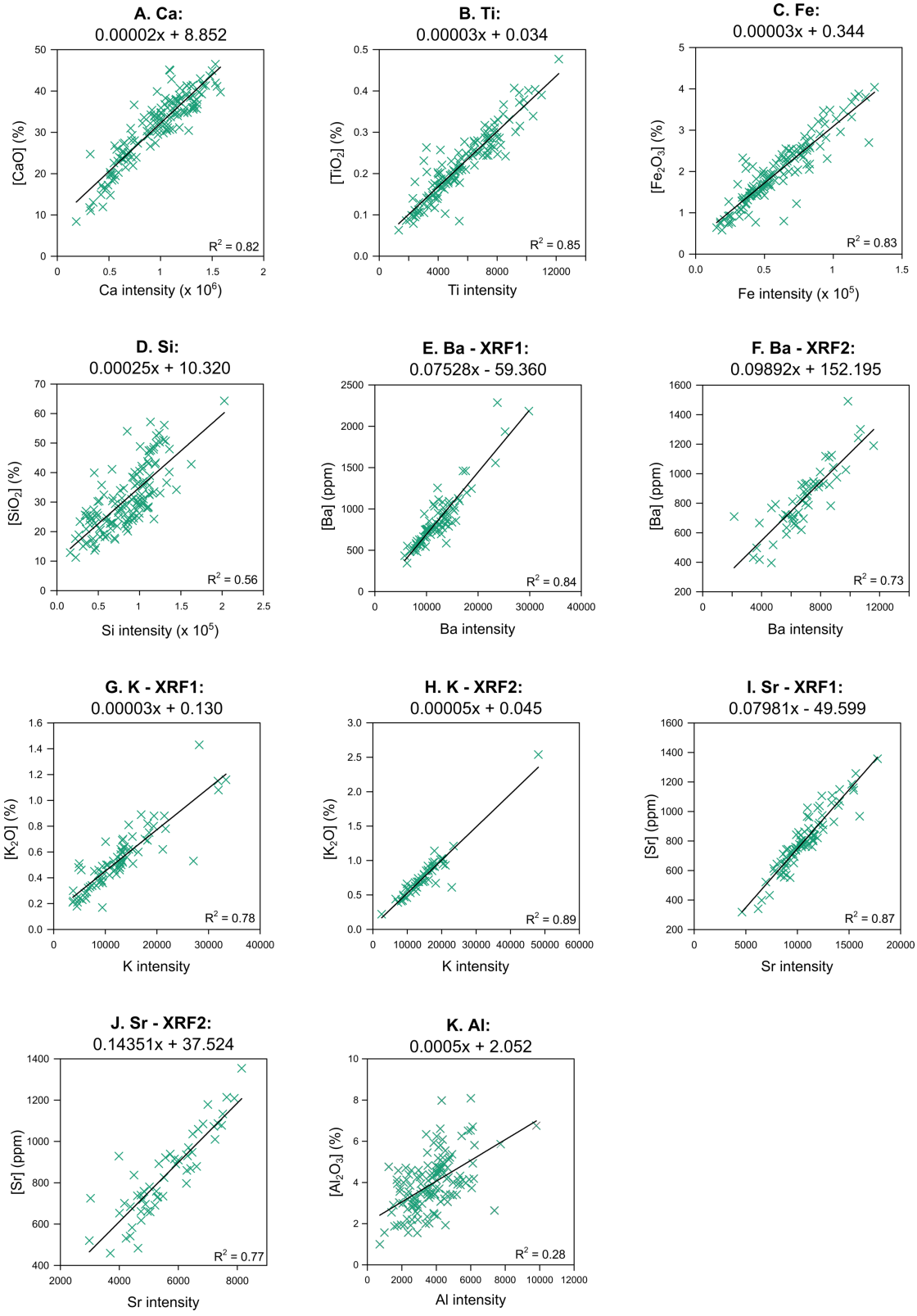


Figure 2.2 *Correlations between raw XRF intensities and actual concentrations for elements used in this study. Correlation equations used for calibration of full XRF results to concentration are presented above the plot for each element. For Ba, K and Sr (panels E-J), a separate calibration is provided for XRF machines 1 and 2.*

Relationships between XRF intensities and concentrations were determined using linear regression analysis for individual elements (Fig. 2.2). The impact of different XRF instruments was also tested. For elements which were strongly affected by instrumental offset, Ba and Sr, instrument-specific calibrations improve the R^2 values of regression. We also found that instrument-specific calibrations improved the overall relationship for K than a general calibration, despite no obvious instrumental offset in XRF intensities for this element. Mass accumulation rates (MARs) were calculated following Equation 2.1 (Lyle et al., 2005):

Equation 2.1

$$Bulk\ MAR\ (g\ cm^{-2}/kyr = LSR\ (cm/kyr)\ \times\ DBD\ (g\ cm^{-3})$$

Where bulk MAR = bulk mass accumulation rate, LSR = linear sedimentation rate calculated from the high resolution orbitally tuned age model (Vahlenkamp et al., 2020) and DBD = dry bulk densities. We created a high resolution DBD record for each point in our record by first assessing the relationship between low resolution wet and dry bulk densities from the shipboard moisture and density dataset (Supplementary Fig. 2.2; Huber et al., 2019). We then applied this relationship to the shipboard gamma ray attenuation (GRA) bulk density dataset (Hobbs et al., 2019; available online at the IODP Laboratory Information Management System (LIMS) database, IODP Joides Resolution Science Operator, 2018) to obtain a high-resolution dry bulk density record. MARs for individual elements are calculated from the bulk MAR and element weight percentages. Element concentrations and MARs calculated from Equation 2.1 are included in Supplementary Table 2.2.

2.2.5 Strength of XRF intensity-concentration calibrations

Linear relationships between XRF intensities and concentrations for Ca, Ti, Fe, Si, Ba, K, Sr and Al, along with respective calibration equations and correlation coefficients, are shown

in Fig. 2.2. A strong positive relationship between XRF intensities and element concentrations (R^2 >0.7) is indicated for Ca, Ti, Fe, Ba, K and Sr. This suggests that for these elements, the XRF intensity record gives a good representation of actual variations in element concentrations. Elements with relatively poor correlations are Si and Al, with R^2 values of 0.56 and 0.28 respectively (Fig. 2.2 D, K), implying that other factors than concentration are affecting XRF intensity measurements. This is a known issue for lighter elements, which are vulnerable to artificial shifts in intensity caused by changes in core water content and physical properties (Tjallingii et al., 2007). The concentration record for Si should therefore be interpreted with this caveat. Based on the poor relationship between Al XRF intensity and concentration, we do not consider the quality of Al data good enough to analyse further in this study.

2.2.6 Normalisation of XRF data

While the intensity of an element returned by XRF analysis is related to the concentration of that element within the sediment, this relationship is not directly proportional and can be complicated by physical and chemical irregularities within the core and on the surface being analysed (Rothwell & Croudace, 2015). Hence the concentration records derived above based on XRF intensity for each element should not be considered fully quantitative, though the calibration does present a good representation for most elements as discussed above. To get around this semi-quantitative behaviour, we also present normalised XRF datasets for each element. Elements are typically normalised to a more conservative element and reported as ratios to this common divisor (e.g. Spofforth et al., 2008; Weltje & Tjallingii, 2008). This allows for relative changes in different elements to be investigated. Al, Fe and Ti are commonly used normalising elements on the assumption that they act as proxies for the

detrital sediment fraction in a deep ocean environment, thus revealing changes in biogenic inputs against the background detrital sedimentation rate.

To choose an appropriate normalising element for Site U1514, an assessment was made of how conservatively Al, Fe and Ti each behaved over the study interval. The Al XRF record shows a very poor correlation ($R^2 = 0.28$, Fig. 2.2 K) to measured concentration data in comparison to Fe and Ti ($R^2 = 0.83$ and 0.85 respectively, Fig. 2.2 B, C), suggesting that XRF intensities for Al do not accurately reflect Al concentrations in the sediment. In light elements such as Al, this is typically a result of water in the core or at the core surface interfering with the Al XRF signal (Rothwell & Croudace, 2015). Fe and Ti both show a better relationship between XRF intensities and concentrations, though Fe does not behave conservatively under changing redox conditions and can be sensitive to diagenesis (Rothwell & Croudace, 2015). At Site U1514, organic matter concentrations are very low throughout the study interval and Fe strongly correlates with Ti ($R^2 = 0.94$, Supplementary Fig. 2.3) which is not sensitive to redox variations. These observations suggest that both Fe and Ti are behaving conservatively at Site U1514 and are appropriate normalising elements. Though the effects of redox conditions on Fe appear to be minimal over the study interval, Ti was chosen as a normalising element as it is not vulnerable to these effects.

2.2.7 Additional data from Site U1514

We also present the magnetic susceptibility record for Site U1514 (Hobbs et al., 2019), available online at the IODP LIMS database (IODP Joides Resolution Science Operator, 2018) which was made at a high spatial resolution, typically 2 – 3 cm. Core sections, magnetostratigraphy, linear sedimentation rates and magnetic susceptibility across the study interval are shown in Fig. 2.3. We compare new XRF and MAR datasets from Site U1514 with a published bulk carbonate $\delta^{18}O$ and $\delta^{13}C$ records from Site U1514 (Edgar et al., 2022)

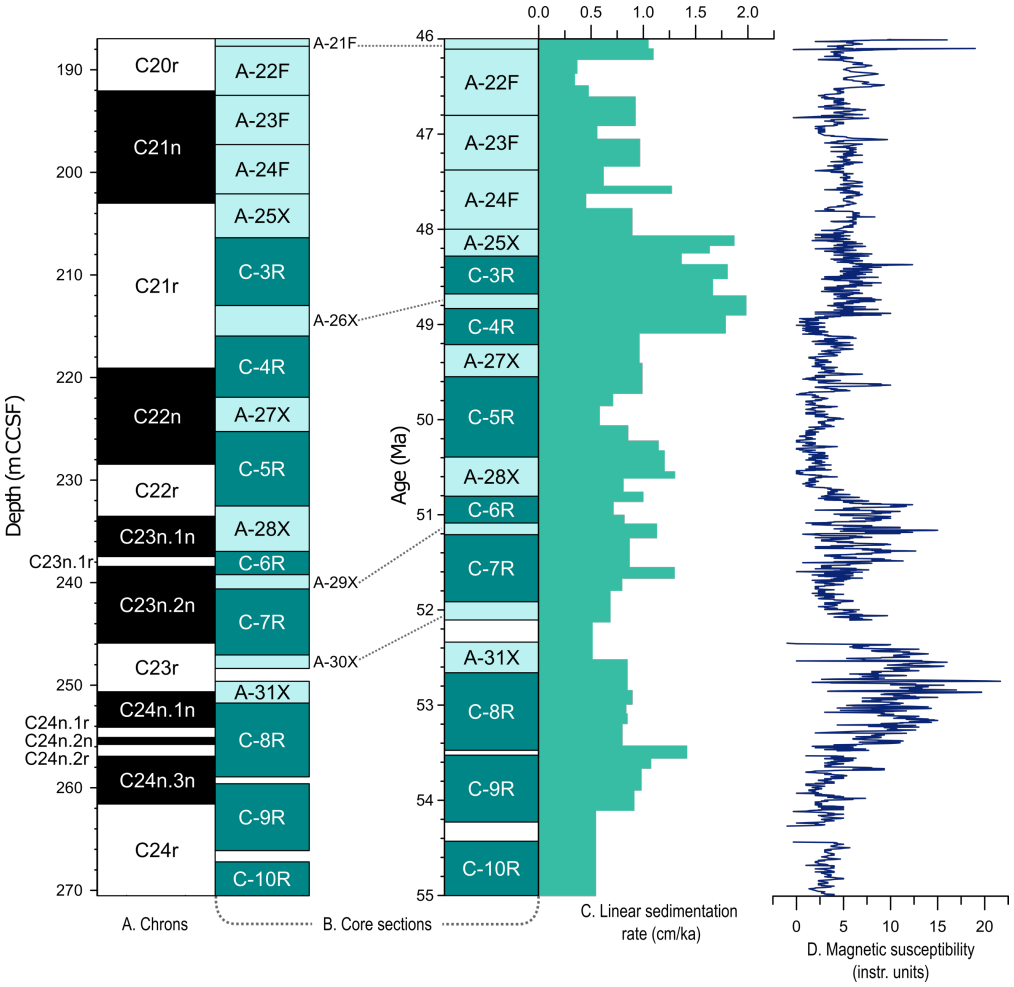


Figure 2.3 *Chron boundaries (A), spliced core sections (B), linear sedimentation rates (C) and magnetic susceptibility data (D) across the study interval. Core sections are labelled in the form 'Hole-Section Type' and are presented on both the depth scale and age scale. C and D are on the age scale.*

and a high resolution benthic $\delta^{18}O$ and $\delta^{13}C$ record from northwest Pacific ODP Site 1209 (Westerhold et al., 2018) to compare sedimentary trends at Site U1514 with local and global climate and carbon cycle evolution.

2.2.8 Principal component analysis

A principal component analysis (PCA) was undertaken to extract the main patterns of variability amongst elements in U1514 sediments. This was done using PAST4 software (Hammer et al., 2001) on the non-normalised elemental data, to prevent loss of trends through normalisation to Ti. Element concentrations as calibrated from XRF data were converted to

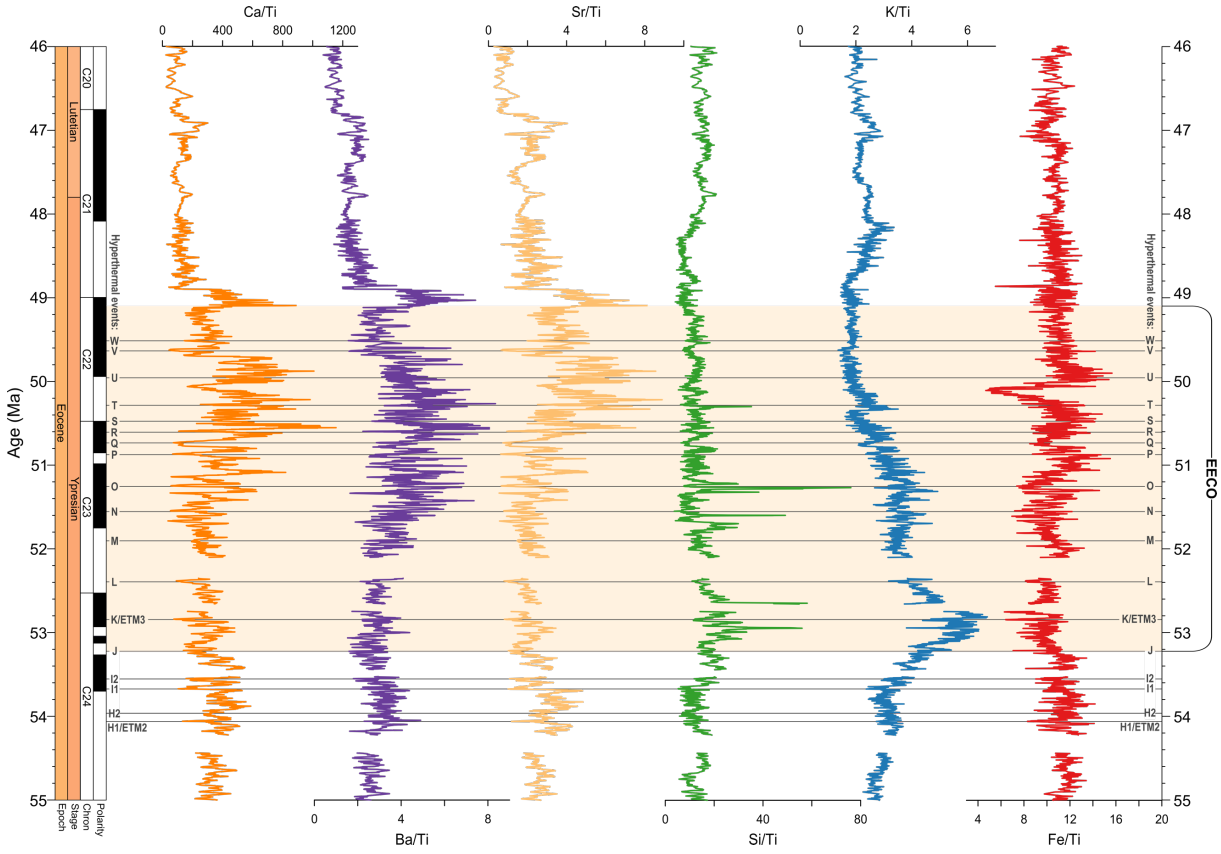


Figure 2.4 *Ratios of XRF data normalised to Ti for the study interval: 46 – 55 Ma. The EECO has been highlighted in the yellow box. Hyperthermal events are marked with horizontal black lines and labelled using the lettering scheme of Cramer et al. (2003). Units for all XRF data are counts/counts.*

weight % (wt%) and the major elements considered here (Ca, Ba, Sr, Si, K, Fe, Ti) were rescaled to 100%. A natural logarithmic (ln) transformation was then applied to wt% records before principal component analysis in PAST4 (Supplementary Table 2.3).

2.3 RESULTS

2.3.1 Downcore changes in elements

To assess how elements at Site U1514 vary across the early Eocene Climatic Optimum, we present both ratios of elements normalised to Ti (Fig. 2.4) and the mass accumulation rates (MAR) for CaO, Ba, Sr, SiO_2, K_2O, Fe_2O_3 and TiO_2 from ~46 – 55 Ma (Fig. 2.5).

We separate our ~9 Myr long record into three intervals in which major changes in these elements occur: (1) the pre-EECO and EECO onset from 55 – 52 Ma; (2) peak EECO conditions and initial post-EECO cooling from 52 – 49.1 Ma; (3) post-EECO from 49.1-46 Ma, covering the transition out of the EECO. We follow Hollis et al. (2019) and define the EECO interval as between ~53.2 (the J event) and 49.1 Ma.

2.3.1.1 55 – 52 Ma: pre-EECO and EECO onset

Bulk sediment MARs are consistently low prior to ~54 Ma (<1 g/cm^{2}ka). The transition into the EECO is associated with a rise in bulk sediment MARs, mainly due to Ca and Ba MARs increasing, with smaller increases in Sr and Si MARs (Fig. 2.5). Between ~52.5 – 53 Ma, K and Si MARs show strong peaks which are not seen in any other elements. This is related to a transient rise and fall in K and Si concentrations, peaking at ~52.8 Ma (Fig. 2.4). The peak in K and Si in sediments is accompanied by an increase in magnetic susceptibility (Fig. 2.3). The K-peak between ~52.5 – 53.5 Ma is also associated with a brief change in sediment colour, from light greenish grey to pale yellow and yellow-brown (Huber et al., 2019). Following this peak, K and Si then steadily decline as the EECO progresses.

2.3.1.2 52 – 49.1 Ma: Peak EECO and initial cooling

Bulk MARs are high (~0.75 – 1.75 g/cm^{2}ka) yet also highly variable throughout this interval. High bulk MARs over this interval are driven primarily by high input of Ca and Ba to sediments (Fig. 2.5), with peaks in Si and K also occurring between 51 and 52 Ma. Fe and Ti MARs remain relatively low and stable throughout. Superimposed on the long-term pattern are shorter cycles in Ca (<200 kyrs) that occur throughout the EECO and are strongly expressed in the Ca/Ti record (Fig. 2.4). Cycles are most pronounced during the peak EECO, and largely correlate with known early Eocene hyperthermal events as identified in the Ca/Fe record by Vahlenkamp et al. (2020). These events are associated with transient declines in Ca

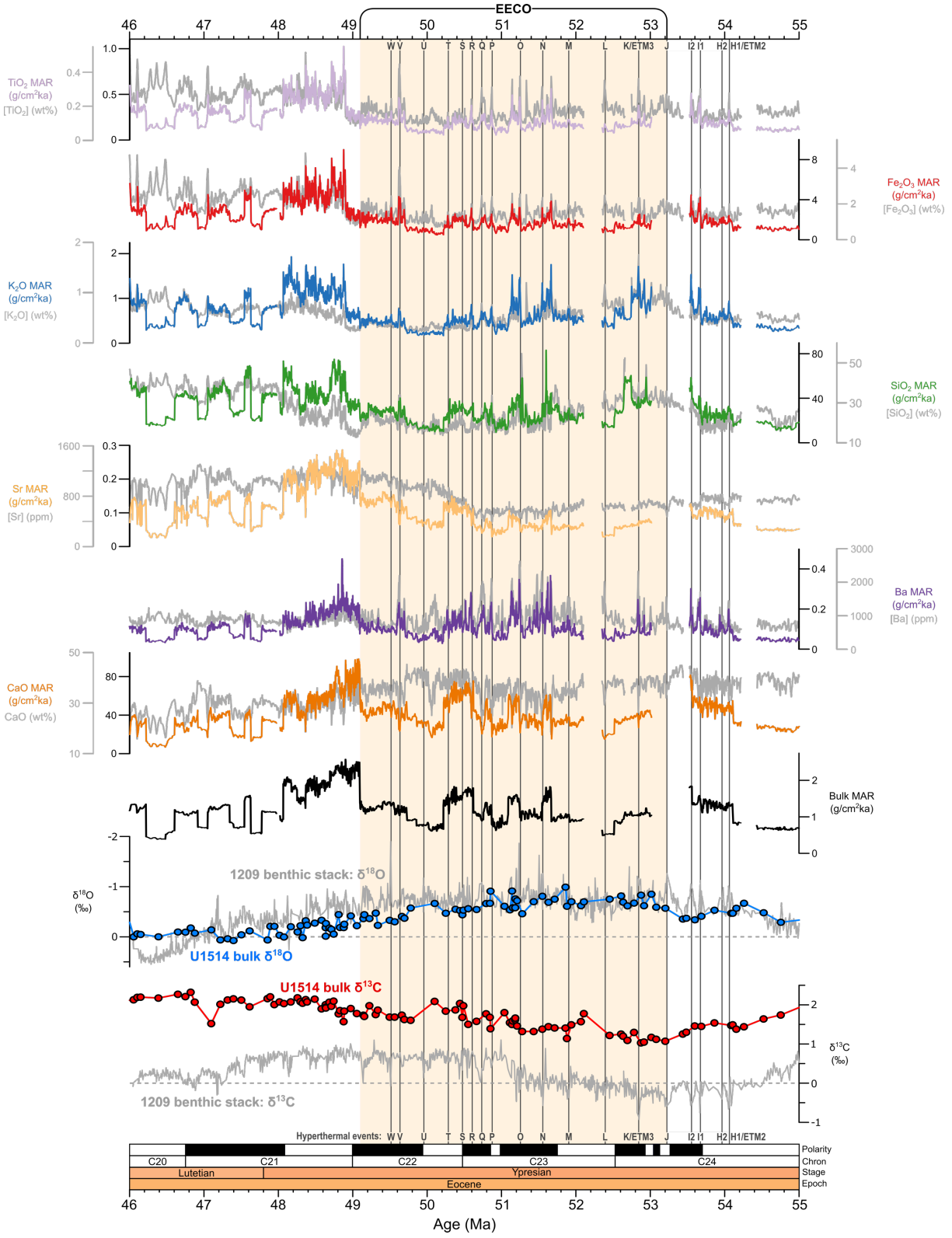


Figure 2.5 *Mass accumulation rates (MARs, coloured lines) and concentrations in wt% (grey lines) for oxides of Ti, Fe, K, Si, Sr, Ba, Ca. Bottom panels: Bulk MAR for Site U1514 (black), Bulk carbonate $\delta^{18}O$ for Site U1514 (Edgar et al., 2022, blue circles) and benthic $\delta^{18}O$ stack from IODP Site 1209 (Westerhold et al., 2018, grey line), Bulk carbonate $\delta^{13}C$ for Site U1514 (Edgar et al., 2022, red circles) and benthic $\delta^{13}C$ stack for Site 1209 (Westerhold et al., 2018, grey line). The EECO is highlighted by the yellow box and hyperthermal events are marked as vertical black lines and labelled according to Vahlenkamp et al., 2020.*

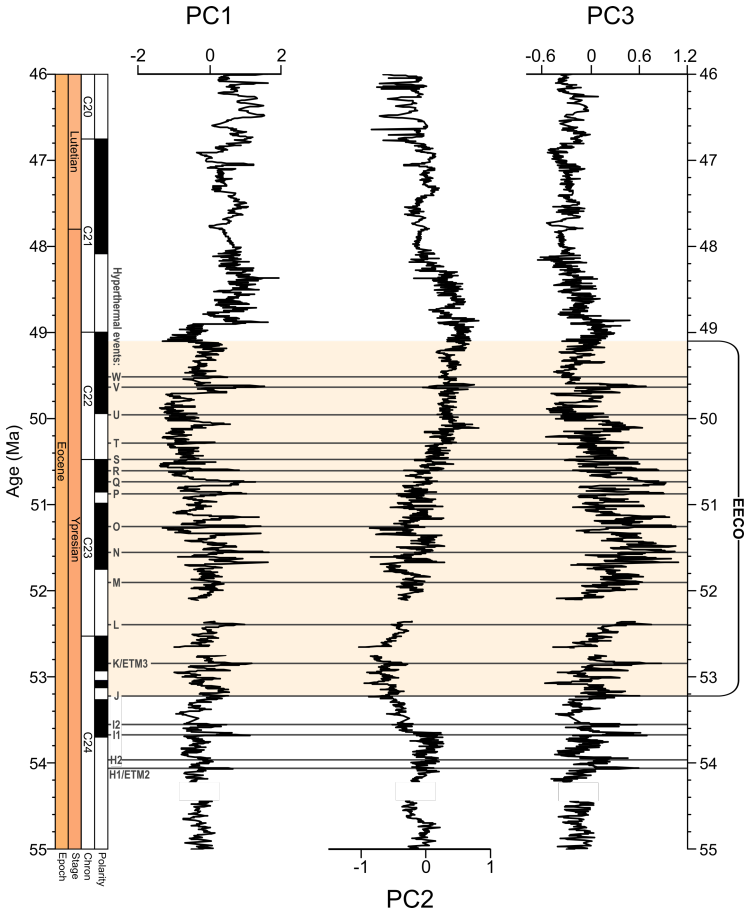


Figure 2.6 *Principal components 1, 2 and 3 from principal component analysis of Ca, Ba, Sr, Si, K, Fe and Ti weight % at Site U1514. The EECO has been highlighted with the yellow box, and early Eocene hyperthermals are labelled with horizontal black lines according to Vahlenkamp et al. (2020).*

MARs and peaks in Ba MARs followed by rapid recovery to pre-event values. Similar cyclical, high-amplitude, high-frequency variations are not evident in other elements, though Si, K, Fe and Ti show minor MAR peaks across some hyperthermals. The available bulk carbonate $\delta^{13}C$ record from Site U1514 is currently not of sufficiently high temporal resolution to capture these sub-million-year events.

2.3.1.3 49.1 – 46 Ma: Post-EECO cooling

At 49.1 Ma, as the EECO closes (Hollis et al., 2019), bulk, Ca, Ba and Sr MARs at Site U1514 increase twofold to ~2 g/cm^{2}ka and remain high for ~1 Myr, before recovering to pre-EECO MARs at ~48 Ma (Fig. 2.5). MARs for Si, K, Fe and Ti also show a similar large

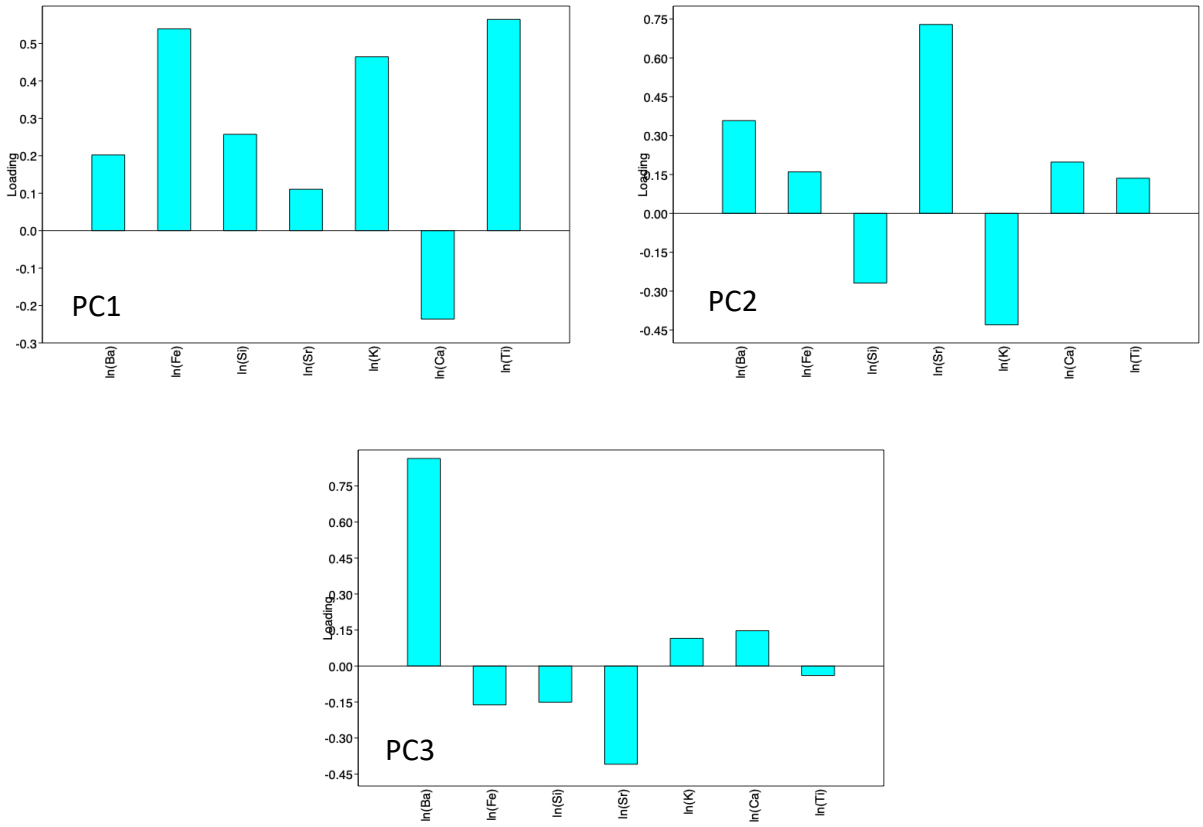


Figure 2.7 *Loadings plots for principle components 1, 2 and 3 showing the loading of the natural logarithm of each element for each principal component.*

increase in concentrations but ~200 kyrs later, at ~48.9 Ma. Bulk MARs then remain low from ~48 – 46 Ma, <1 g/cm^{2}ka.

2.3.2 Principal component analysis results

Principal component analysis demonstrates that the majority of the variance in the elemental concentration dataset can be explained by PCs 1 to 3 (combined eigenvalues = 93.4 %; Fig. 2.6), which account for 60.5 %, 18.5 % and 14.4 % of the total variance, respectively. We therefore consider only PC1, 2 and 3 in this analysis. Loadings plots for PCs 1-3 (Fig. 2.7, Supplementary Fig. 2.4) show that PC1, which explains the majority of the variance in the dataset, is correlated with patterns in elements Ti, Fe, K and Si, while PC2 is correlated with patterns in Sr, Ba and Ca. PC3 correlates dominantly with Ba.

2.4 DISCUSSION

2.4.1 Variable weathering response to warm EECO temperatures

At ~53.3 Ma around the EECO onset, MARs and concentrations of Si, K, Fe and Ti rise where other elements decrease or show little change. This is particularly pronounced for K and Si, which show strong increases when normalised to Ti (Fig. 2.4). In a deep ocean sedimentary setting, K, Si, Ti and Fe have been linked to the terrigenous sedimentary component, with K and Si indicating increased aluminosilicate or clay mineral input to sites (e.g. Hodell et al., 2010; Kleiven et al., 2008; Kuhlmann et al., 2004; Richter et al., 2006). PCA analysis indicates that the majority of variance in the dataset correlates with patterns in terrigenous elements Ti, Fe, K and Si, hence variability in the detrital input to Site U1514 is an important factor to consider. The terrigenous component of Site U1514 sediments comprises of dust input and riverine runoff from the nearby Australian continent (Fig. 2.1, Quilty, 1994). A first order explanation for increased Si, K, Ti and Fe concentrations at Site U1514 is an increase in continental weathering fluxes associated with EECO warming, whereby more terrigenous material is being delivered into the Mentelle Basin overall. The interval of higher K and Si MARs (53.3 – 52.4 Ma) also coincides with increased bulk sediment magnetic susceptibility (Fig. 2.5) and a colour change from light greenish grey to light yellowish brown (Huber et al., 2019), both supporting higher input of detrital clay minerals associated with greater K and Si concentrations. Linear sedimentation rates (LSR) overall are higher over this interval than at the very start of the study interval (Fig. 2.3), however the increase in LSR occurs earlier than the rise in K/Ti and may therefore partially relate to input of other material to the site, as discussed further below.

Intensified continental weathering regimes have been identified in early Eocene warm periods, including the PETM (Chen et al., 2016; Pogge von Strandmann et al., 2021) and the

EECO (Elliot Smith et al., 2008). Late Palaeocene Australian climate was relatively warm and wet compared to widespread modern aridity (Martin, 2006; McGowran & Hill, 2015) and southern Australian palaeosols dated to ~52 Ma show that high rainfall levels occurred during the EECO (Zhou et al., 2015). Climate models also simulate an intensified hydrological cycle for SW Australia in the early Eocene relative to the preindustrial, likely due to higher atmospheric CO_2 concentrations (Carmichael et al., 2016, 2017). Higher siliclastic input to the Mentelle Basin during the EECO, which is consistent with an intensified hydrological cycle on the Australian continent due to global warmth. Greater chemical weathering of silicate rocks is driven by greater atmospheric pCO_2 levels (Berner, 1992; Walker et al., 1981), and higher temperatures can lead to increased weathering fluxes through an intensified continental hydrological cycle (Zhou et al., 2015). Sedimentary potassium content has been widely used as a proxy for variations in weathering flux through geological time, with K-depletion related to input of more mature, intensively weathered sediments (Colin et al., 2014; Gaillardet et al., 1999; Matys Grygar et al., 2017, 2019). In the case of the PETM, large clay mineral input to the oceans has been linked to a shift in the continental weathering regime towards higher physical erosion rates and sediment fluxes (Pogge von Strandmann et al., 2021).

Western Australia has a relatively flat relief (Quilty, 1994) and bedrock geology is largely Archaean to Proterozoic metamorphosed granites and greenstones (Spaggiari et al., 2009) with extensive regolith cover and deep weathering profiles (Anand & Paine, 2002). Prior to EECO warming, terrigenous source sediment to Site U1514 is likely mature and intensively weathered. High temperatures and pCO_2 across the EECO are associated with increased chemical weathering (Elliot Smith et al., 2008), so we would expect detrital minerals at Site U1514 to become progressively more K-depleted as temperatures increase. However, we see

a gradual rise in K content. This suggests an influx of less mature material, either through a change in source sediment region or a change in weathering regime on land.

We suggest that the increase in K and Si here is related to an influx of clay minerals to the site associated with increased continental rainfall (Carmichael et al., 2016; Zhou et al., 2015) and greater physical weathering rates which are not initially balanced by enhanced chemical weathering rates. K and Si content in sediments begins to drop off around 52.7 Ma, despite continued high temperatures in the EECO inferred from the Site 1209 benthic $\delta^{18}O$ and the Site U1514 bulk $\delta^{18}O$ records (Figs. 2.4, 2.5). As this change is not directly linked to temperature, it may indicate a change in the weathering response on Australia as high temperatures are maintained across the EECO. The 'weatherablity' of continental surfaces, and thus the supply of weathering products to marine sediments, is reduced over time despite continued high temperatures and precipitation as the supply of new weatherable minerals is depleted, and mature soil horizons build up (Froelich & Misra, 2014; van der Ploeg et al., 2018; West et al., 2005). In-keeping with this process, we suggest that at Site U1514, as temperatures continue to increase in the EECO, the source sediment exposed on the continental surface becomes progressively more mature and K-depleted. This is supported by the K/Ti record, which progressively decreases throughout the EECO until ~49.8 Ma, when temperatures begin to decline. While the K-profile across the EECO may also relate to a change in the source region for terrigenous sediments to Site U1514, this is difficult to assess without a full study of the mineralogy of U1514 sediments.

Towards the end of our study interval, ~48.9 Ma, we see an increase in terrigenous elements (Fe, K and Ti) along with magnetic susceptibility supporting an increase in overall detrital sediment content delivered to the site. This coincides with neodymium isotope evidence for an erosional event on Antarctica between 48 – 49 Ma (Huck et al., 2017). While

the signal at Site U1514 may be more local in origin, it could also reflect the influence of Antarctic-derived detrital material. Alternatively, the erosional event in Antarctica and the increase in lithogenic input to the southern Indian Ocean may have had a common driver. Mineralogical comparisons are needed to identify alternative source sediment regions at Site U1514.

Principal component analysis indicates that PC1, which accounts for >60 % of the variance of the dataset, correlates best with patterns in dominantly lithogenic elements Ti, Fe, K and Si (Fig. 2.6, 2.7). This suggests that geochemical variability at Site U1514 is largely influenced by changes in weathering inputs, likely driven by warming and cooling at the build-up and decline of the EECO.

2.4.2 Increased Indian Ocean primary productivity across the EECO

The warmest interval of the early Eocene occurred within the EECO ('peak EECO' conditions) both globally and in our record from ~52 – 49.1 Ma (Hollis et al., 2019; Westerhold et al., 2020). Across peak EECO conditions, bulk MARs, Ca/Ti, Ba/Ti and Sr/Ti increase both in magnitude and variability (Fig. 2.4, 2.5).

The main source of barium to marine sediments is in the form of barite ($BaSO_4$) microcrystals, which precipitate within sinking organic matter (McManus et al., 1999). A positive correlation between barite accumulation in sediments and export productivity in modern sediments has led to the use of barium as a palaeoproductivity indicator, specifically export productivity (Carter et al., 2020; Dymond et al., 1992; Eagle et al., 2003; McManus et al., 1998; Paytan & Kastner, 1996). The nature of the relationship between biogenic barite accumulation rates and primary productivity has not been investigated in the Indian Ocean across the Eocene as it has in the modern Atlantic, Pacific and Southern Oceans (Eagle et al., 2003), hindering quantitative reconstruction of Indian Ocean palaeoproductivity levels.

Further, caution is warranted when interpreting the signal, as primary productivity and export productivity (as indicated by Ba content) are not always coupled because of secondary controls on Ba in sediments such as sedimentary accumulation rates and bottom water oxygenation (Carter et al., 2020; Faul & Delaney, 2010; Griffith et al., 2021). Evidence of bioturbation and very low organic matter content (<0.2 wt%, Huber et al., 2019) supports a primarily oxygenated depositional setting across the study interval. We therefore interpret Ba content here as a signal of export productivity. We also assess productivity using Ca, as the dominant biogenic component making up U1514 sediments across the early Eocene is calcareous nannofossils, with a small contribution from foraminifera (Huber et al., 2019). Calcium concentrations are therefore driven primarily by biogenic Ca input from calcareous nannofossil productivity.

Across peak EECO conditions, high and variable Ca and Ba concentrations and MARs reflect variations in carbonate productivity and export productivity. Given their dominance in the sediment overall, Ca and Ba variation in this interval lead to similar variations in bulk MARs across peak EECO temperatures. An increase in primary productivity requires an increase in nutrient supply, most likely either through enhanced riverine runoff or increased upwelling of deep nutrient rich waters. During the peak EECO interval, the ocean gateway between Australia and Antarctica was still likely closed and southern Indian Ocean productivity was driven by local circulation patterns and nutrient inputs (Bijl et al., 2013). The productivity response to warming at high latitudes varies in proxy records, with different sectors of the Southern Ocean showing different productivity patterns across the early Eocene (Diester-Haass & Faul, 2019). However, in the Indian Ocean sector of the Southern Ocean (ODP Site 738, Kerguelen Plateau), reconstructions from accumulation rates of benthic foraminifera and biological barium imply productivity rises from the late Palaeocene into the

early Eocene, peaking in the EECO before dropping off at ~50 Ma (Diester-Haass & Faul, 2019). We confirm this finding and suggest that high productivity in the Indian Ocean may be maintained until ~49.6 Ma, where our records show a strong decline in Ca/Ti and Ba/Ti. High primary productivity in the surface ocean is initiated and sustained by increased local nutrient inputs, through greater rainfall and weathering on the Australian continent (e.g. Carmichael et al., 2016).

The largest increase in both Ca and Ba relative to Ti occurs after ~51.6 Ma (Fig. 2.4). This interval of high Ca and Ba variability is shortly followed by a global stepped increase in benthic foraminiferal $\delta^{13}C$ values at 51.2 – 51.0 Ma that is observed at ODP Sites 1209, 1258, 1263 and the Tethyan sections of Italy (Kirtland Turner et al., 2014; Lauretano et al., 2016; Luciani et al., 2016; Westerhold et al., 2018). Bulk $\delta^{13}C$ records from Site U1514 do not show a similar step change as the global benthic foraminiferal signal (Fig. 2.5), however from 51.6 – 50.0 Ma, Ca and Ba MARs, along with Ca/Ti, Ba/Ti and Sr/Ti do show dramatic variations (Fig. 2.4). High-amplitude, high-frequency variations in $\delta^{13}C$, pCO_2 and SSTs are evident in both marine and terrestrial records between ~51.5 – 50.9 Ma (Hyland & Sheldon, 2013; Westerhold et al., 2018). Increased environmental instability associated with peak EECO conditions may have been an early warning signal that the planet was approaching a critical climatic tipping point, beyond which the high-temperature EECO state could not be sustained (Crowley & Hyde, 2008; Scheffer et al., 2009; Westerhold et al., 2018). Our records demonstrate that this period of enhanced variability is also expressed in productivity proxies and carbonate chemistry records from the Mentelle Basin. The period of instability in the Indian Ocean represented by our Site U1514 records persists for ~1.5 Myrs, compared to ~0.6 Myrs in benthic $\delta^{13}C$ (Westerhold et al., 2018). The impact of environmental instability recorded in sedimentary records may be highly variable in different proxies, environmental

settings and localities. At Site U1514, instability may be promoted relative to other sites due to increased variability in local environmental conditions on top of background high pCO_2 levels. For example, the tectonic opening of the Tasmanian Gateway may cause associated impacts on local oceanography and productivity patterns (Bijl et al., 2013) while seasonal variability in precipitation due to Eocene monsoon weather patterns (Carmichael et al., 2016; Huber & Goldner; 2012) could cause fluctuations in weathering flux and primary productivity in the southern Indian Ocean.

Si can also be used as a palaeoproductivity indicator as it can indicate input of biogenic silica from siliceous microfossils (e.g. Ingall et al., 2013; Johnson et al., 2011). A number of brief (<100 kyrs), high-amplitude peaks in Si/Ti occur across the peak EECO interval (Fig. 2.4). Two of these excursions are particularly prominent in Si/Ti, SiO_2 concentration and Si MARs (Figs. 2.4, 2.5): at ~51.6 Ma, just before the N hyperthermal event, and at ~51.25 Ma, coinciding with the O hyperthermal event. Outside of these transient excursions Si/Ti remains relatively constant, suggesting that Si closely follows the pattern of other lithogenic elements and that background biogenic Si input is thus relatively minor. However, Si peaks indicate transient periods where Si is decoupled from background detrital input, which we infer here using Ti. Si peaks may relate to increased biogenic silica input, perhaps due to short-lived blooms of siliceous organisms such as radiolarians and/or benthic sponges. Shipboard smear slide records (Huber et al., 2019) are not of sufficiently high resolution to capture such short-term changes; however, they do provide some insights (Fig. 2.8). Calcareous microfossils dominate at Site U1514 throughout the early Eocene and diatoms are not present. Prior to peak EECO conditions (~52.4 Ma), there are no sponge spicules present and only trace amounts of radiolarians (<1% of total grains). However, across peak EECO conditions, from

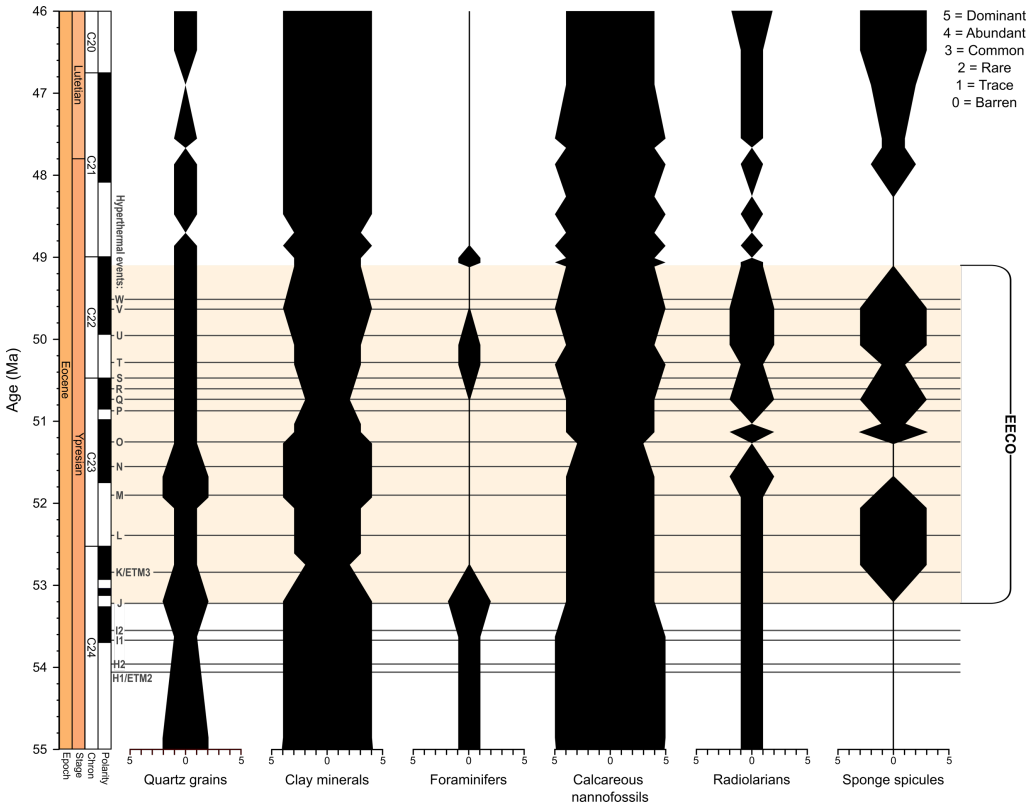


Figure 2.8 *Shipboard smear slide data in the study interval highlighting key lithogenic and biogenic sedimentary components at Site U1514.*

~52.4 – 49.1 Ma, sponge spicules vary between none to common (0 – 15 % total grains) and radiolarians vary from none to rare (0 – 5 % total grains). Transient blooms in sponge and radiolarian populations may therefore be responsible for brief Si peaks in sediments. Alternatively, inorganic mechanisms for Si accumulation in sediments have been proposed for the early Eocene and may play a role at Site U1514 meaning that Si peaks at this site are not linked to siliceous microorganism productivity (Witkowski et al., 2020). Higher-resolution analysis of siliceous microfossil assemblages is needed to investigate whether Si/Ti peaks across the EECO are biogenic or abiotic in origin.

2.4.3 Signals of early Eocene hyperthermal events

The peak-EECO interval also encompasses many of the so-called early Eocene hyperthermal events (J through X), which are characteristic of the early Eocene 'hothouse'

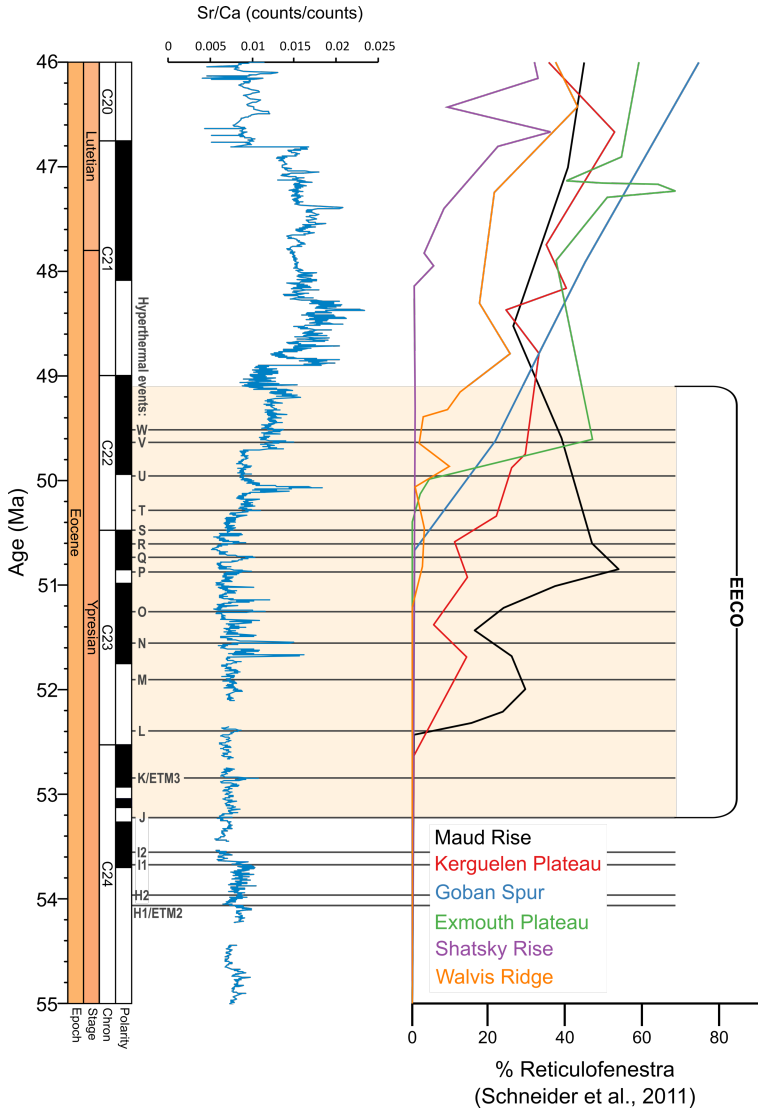


Figure 2.9 *Sr/Ca variation throughout the study interval. Hyperthermals and EECO labelled as in Figs. 2.4 and 2.5. The percentage of nannofossil assemblages made up of the group* Reticulofenestra *in different ocean basins is also shown (Schneider et al., 2011).*

climate state and represent transient periods (~200 kyrs) of higher temperatures relative to background EECO warmth, with associated negative $\delta^{13}C$ excursions (e.g. Kirtland Turner et al., 2014; Sexton et al., 2011; Westerhold et al., 2018). Unlike earlier hyperthermal events (ETM-2 to L), the J – X events are strongly expressed at Site U1514 in the Ca/Fe record (Vahlenkamp et al., 2020) and in our Ca/Ti record (Fig. 2.4), due to transient large reductions followed by rapid recovery in bulk sediment Ca content. Ba concentration or Ba/Ti does not consistently decline across hyperthermal events, indicating that overall export productivity is

either maintained or increased, so Ca reduction is unlikely to be related to strong declines in primary productivity, and is more likely to be dissolution-controlled. Additionally, Sr/Ca increases across the majority of hyperthermal events (Fig. 2.9) supporting continued or increased carbonate productivity in most cases (Stoll & Schrag, 2000, 2001). Dissolution horizons are well-known from early Eocene hyperthermal events in sedimentary records from both high and low latitudes as the carbonate compensation depth (CCD) shoals in response to greater atmospheric pCO_2 and ocean acidification (Galeotti et al., 2010; Kirtland Turner et al., 2014; Lourens et al., 2005; Zachos et al., 2010). Pronounced carbonate dissolution at Site U1514 adds further evidence for a CO_2-driven (i.e., global) warming mechanism for early Eocene hyperthermals, causing deep ocean acidification in multiple ocean basins.

2.4.4 Controls on Sr/Ca variation across the EECO

Sr in seawater is co-precipitated with biogenic calcium carbonate through substitution of Sr^{2+} with Ca^{2+} within the carbonate crystal structure (Pingitore et al., 1992; Stoll & Ziveri, 2004). Hence, Sr variations in carbonate-rich sediments are closely related to variations in biogenic calcite accumulation. This is seen in the geochemistry of Site U1514, where Sr/Ti and Ca/Ti are closely coupled throughout the early Eocene (Fig. 2.4). However, the amount of Sr incorporated into carbonates does not remain equal throughout the study interval. Prior to 51 Ma, Sr concentrations (Fig. 2.5) are relatively low and stable at Site U1514. Sr/Ca then shows a steady increase from 51 – 49 Ma (Fig. 2.9). The majority of marine carbonate Sr/Ca variations are caused by changes in global sea level, seawater Sr/Ca, temperature or Sr partitioning in the dominant biogenic calcifiers (Stoll et al., 2002; Stoll & Schrag, 2001; Stoll & Ziveri, 2004). There is no independent temperature record available at Site U1514, however the bulk $\delta^{18}O$ record (Fig. 2.5) does not covary with the Sr/Ca record, so temperature is unlikely to be an important control here. The series of transient Sr peaks between ~50.5 –

52 Ma may be related to carbonate dissolution across the hyperthermal events, as discussed above (Fig. 2.9). Core top studies show high Sr/Ca in marine carbonates also corresponds to high surface productivity (Stoll & Schrag, 2000). However, elevated carbonate productivity is unlikely to account for the long-term Sr/Ca increase from 51 – 49 Ma, where Ca concentrations and carbonate productivity are much more variable. This long-term Sr/Ca increase coincides with a global shift in nannoplankton assemblages which began at 52 Ma in the Southern Ocean, and expanded into the Indian Ocean by 51 Ma (Schneider et al., 2011). Global cooling and the collapse of thermal stratification allowed the calcareous nannofossil genus *Reticulofenestra* to expand rapidly, almost entirely replacing the previously abundant *Toweius* at high latitudes by 51 Ma (Schneider et al., 2011; Stoll & Ziveri, 2004). Different species of nannofossils fractionate Sr to different extents, whereby larger and faster-growing coccolithophore species incorporate higher Sr/Ca in their carbonate (Stoll & Ziveri, 2004). As calcareous nannofossils are the dominant source of calcium carbonate at Site U1514, the increase in Sr/Ca may reflect this assemblage change. Nannofossil assemblage studies are needed to clarify the timing of *Reticulofenestra* appearance at Site U1514 and link it to the Sr/Ca variation.

2.4.5 Impact of an early surface water connection through the Tasmanian Gateway

Following the termination of the EECO and a cooling indicated by a strong increase in global benthic foraminiferal $\delta^{18}O$ records (Fig. 2.5, Westerhold et al., 2020), a suite of bulk sediment geochemical changes occur at Site U1514. A period of elevated linear sedimentation rates and bulk MARs begins at ~49.1 Ma and lasts for ~1 Myrs (Fig. 2.5). Increases in elemental MARs are, however, not synchronous across all elements: biogenic elements Ca, Ba and Sr increase at ~49.1 Ma, closely followed by detrital elements K, Ti and Fe at ~48.9

Ma. The timing of these shifts closely coincides with the onset of post-EECO cooling in the NW Pacific at 49.14 Ma (Westerhold et al., 2018) and the initiation of a surface water connection through the Tasmanian Gateway, ~49 Ma (Bijl et al., 2013). The surface water connection through the Tasmanian Gateway may have strengthened surface ocean current activity in the southern Indian Ocean, providing nutrients for a higher productivity regime and increasing Ca and Ba MARs at Site U1514. However, productivity may also be stimulated by more local oceanographic changes such as upwelling strength (e.g. Sarkar et al., 2019), or the global temperature and carbon-cycle shifts at the close of the EECO (Westerhold et al., 2020; Zachos et al., 2001). Further evidence is needed to conclusively link post-EECO cooling, Tasmanian Gateway and geochemical changes in the southern Indian Ocean, but the coincident nature of these events warrants analysis.

The main driving mechanism for post-EECO cooling is likely to be atmospheric pCO_2 decline (DeConto & Pollard, 2003; Huber et al., 2004), though studies have suggested that the opening of the Tasmanian Gateway and associated development of the Antarctic Circumpolar played a role (Kennett, 1977; Sijp et al., 2009). Proxy records from multiple ocean basins show a synchronous temperature decline at ~49.1 Ma (Crouch et al., 2020; Hollis et al., 2019; Sexton et al., 2011; Westerhold et al., 2018, 2020), suggesting a global driver with local oceanographic changes playing a minor role (Cramer et al., 2009; DeConto & Pollard, 2003; Inglis et al., 2015; Westerhold et al., 2018). Additionally, deep water throughflow through the Tasmanian Gateway was likely inhibited until ~35.5 Ma (Scher et al., 2015; Stickley et al., 2004), well after post-EECO cooling began (~49.1 Ma, Hollis et al., 2019 and references therein). Our geochemical records suggest that an early, surface-level connection through the Tasman Gateway may be linked to increased primary productivity in the Indian Ocean and a temporary, local pCO_2 drawdown mechanism. This interval of increased productivity at Site

U1514 lasts only ~1 Myr and post-dates the onset of cooling which continues throughout the Eocene (with a few reversals, e.g., MECO) as shown by benthic $\delta^{18}O$ records (Fig. 2.5; Westerhold et al., 2018). Taken together, this suggests that the inferred increase in productivity associated with the end of the EECO would not have contributed significantly to post-EECO cooling. After ~48.5 Ma, the bulk carbonate $\delta^{13}C$ record at Site U1514 becomes decoupled from the Site 1209 benthic foraminiferal $\delta^{13}C$ record: whilst bulk carbonate $\delta^{13}C$ values remain high and even increase, Site 1209 benthic $\delta^{13}C$ values decline by ~1‰ (Fig. 2.5). High bulk carbonate $\delta^{13}C$ values being maintained following the EECO may indicate a strong biological pump in the southern Indian Ocean continuing to transfer carbon from surface waters to deep, suggesting strong primary productivity continues past 48.5 Ma despite the decline in Ca/Ti, Ba/Ti and Sr/Ti (Fig. 2.4). However, there are a number of caveats associated with interpreting bulk carbonate $\delta^{13}C$ records in this manner as benthic $\delta^{13}C$ records for Site U1514 are not available to assess the balance between primary productivity and export productivity. The Site 1209 benthic $\delta^{13}C$ record decreases at this time, which may suggest that globally, the biological pump is weakening as organic matter with a lighter $\delta^{13}C$ signature is not being transferred to deep waters which become enriched in organic matter with a heavier $\delta^{13}C$ signature instead. Independent palaeoproductivity proxies (e.g. Griffith et al., 2021) are needed to fully assess how productivity might have impacted the carbon cycling in the post-EECO Indian Ocean.

2.5 CONCLUSIONS

Geochemical signals from Site U1514 reveal that palaeoenvironmental conditions in the high latitude southern Indian Ocean were highly dynamic over the development and collapse

of the EECO. We identify sedimentary evidence for a variable weathering response on continental Australia across the build-up to peak EECO temperatures, where increasing temperatures drive an intensified hydrological cycle. Higher rainfall on land (Carmichael et al., 2016) drives an initial physical weathering pulse, depositing immature, high-K sediments into the Mentelle Basin, followed by more mature, K-depleted sediments as high temperatures are maintained and the weatherability of the surface declines. Following initial temperature increase, peak-EECO temperatures are associated with increased Ca and Ba in Site U1514 sediments. We suggest that higher carbonate and export productivity are driven by greater nutrient input to the southern Indian Ocean, linked to an intensified hydrological cycle on land causing higher overall nutrient delivery to surface waters. We also show additional evidence for increased environmental instability across peak EECO conditions (Hyland & Sheldon, 2013; Westerhold et al., 2018), as concentrations of biogenic elements show high-magnitude, high-variability excursions.

Site U1514 also yields the first high-resolution XRF records of early Eocene hyperthermals in the Indian Ocean (Vahlenkamp et al., 2020). Here, we confirm that transient Ca reduction associated with hyperthermal events is the result of carbonate dissolution and not periodic carbonate productivity collapse, providing further evidence that carbon-cycle perturbations across hyperthermal events were a global phenomenon (Kirtland Turner et al., 2014; Lourens et al., 2005; Sexton et al., 2011; Zachos et al., 2005). However, from the elements assessed in this study, there are no other high-amplitude, consistent geochemical responses to hyperthermals in the southern Indian Ocean.

At 49.1 Ma, cooling out of the EECO is accompanied by a ~1 Myr long spike in primary productivity at Site U1514. This coincides with the initiation of a surface water connection through the Tasmanian Gateway (Bijl et al., 2013), and may reflect a southern Indian Ocean

response to incursion of southwest Pacific surface waters through the gateway. The impact of increased productivity is temporary and may be localised to Site U1514, suggesting that C-sequestration associated with increased productivity would not have been a significant contributor to post-EECO pCO_2 drawdown and cooling. If Southern Ocean dynamics played a significant role in post-EECO cooling, evidence of sustained high latitude productivity and associated carbon sequestration is needed.

CHAPTER 3: ORBITAL FORCING OF EARLY EOCENE HYPERTHERMAL EVENTS: A NEW BENTHIC FORAMINIFERAL STABLE ISOTOPE RECORD FROM THE INDIAN OCEAN, 50-51 MA

3.1 INTRODUCTION

During the early Palaeogene (~66 – 34 Ma), Earth's climate was in an extended greenhouse state which featured the warmest average global temperatures of the Cenozoic (Fig. 3.1, Cramer et al., 2009; Westerhold et al., 2020; Zachos et al., 2001). From the late Palaeocene to early Eocene (~62 – 54 Ma), Earth was under the influence of the most active phase of North Atlantic Igneous Province formation (NAIP, Jolley & Bell, 2002; Wilkinson et al., 2017). Atmospheric pCO_2 concentrations rose to between 1,000 – 2,000 ppm (Anagnostou et al., 2016; Rae et al., 2021) and global mean surface temperatures (GMST) increased to ~27 °C (Inglis et al., 2020), culminating at the Early Eocene Climatic Optimum (EECO), ~53 – 49 Ma (Hollis et al., 2019). Following the EECO, global temperatures and atmospheric CO_2 concentrations declined and by the end of the Eocene (~34 Ma) major ice sheets were present on Antarctica (Coxall et al., 2005; Lear et al., 2008; Westerhold et al., 2020; Zachos et al., 2008).

Superimposed upon the background warmth of the late Palaeocene-early Eocene are a number of transient (<200 kyr) global warming events, or 'hyperthermals' (Barnet et al., 2019; Cramer et al., 2003; Kirtland Turner et al., 2014; Lauretano et al., 2015, 2016; Sexton et al., 2011), of which the Palaeocene-Eocene Thermal Maximum (PETM, ~55.9 Ma) is the largest and most well-studied (McInerney & Wing, 2011). These events are expressed more or less globally and show rapid, negative carbon and oxygen isotope ($\delta^{13}C$ and $\delta^{18}O$, respectively) excursions associated with carbonate dissolution horizons (Kirtland Turner et

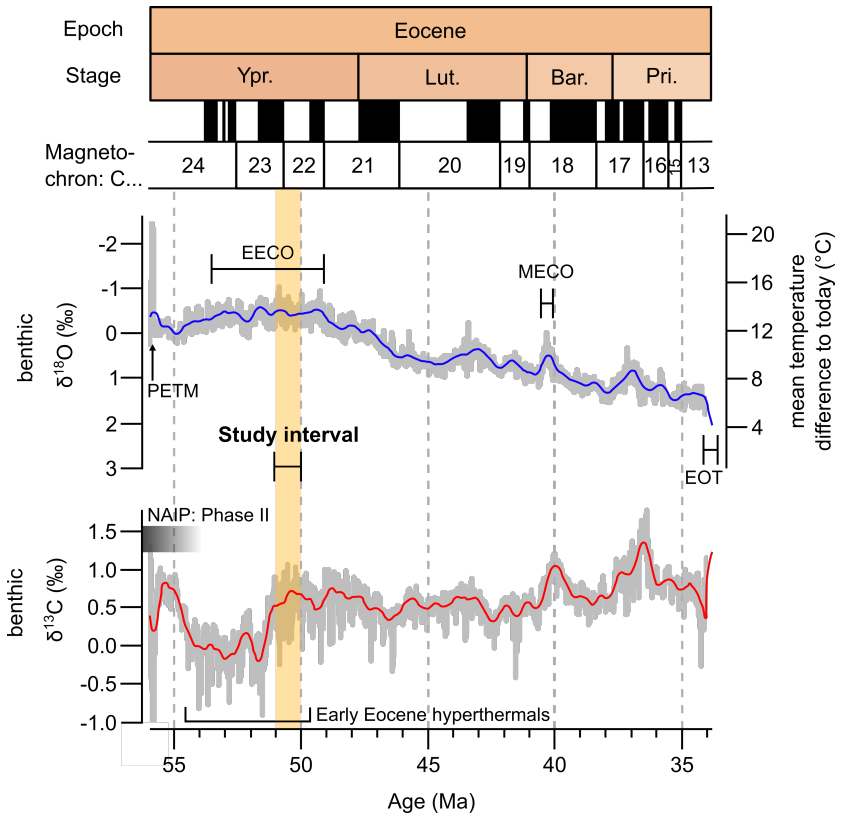


Figure 3.1 *Eocene section of the Cenozoic Global Reference benthic foraminiferal carbon and oxygen Isotope Dataset (CENOGRID, Westerhold et al., 2020) showing the 20 kyr (grey) and 1 Myr smoothed composite benthic $\delta^{18}O$ record (blue) and benthic $\delta^{13}C$ record (red) alongside relevant climatic events for the Eocene and oxygen isotope temperature conversion, relative to today. Our study interval is highlighted in the yellow bar. Figure modified from Fig. 1, Westerhold et al. (2020). Climatic event labels: Early Eocene Climatic Optimum (EECO), Paleocene-Eocene Thermal Maximum (PETM), North Atlantic Igneous Province (NAIP), Middle Eocene Climatic Optimum (MECO), Eocene/Oligocene Transition (EOT).*

al., 2014; Littler et al., 2014; Nicolo et al., 2007; Sexton et al., 2011). They are also associated with pronounced hydrological and ecological perturbations, the scale of which depends on the magnitude of the carbon isotope excursion (CIE) and varies among hyperthermal events and location (Carmichael et al., 2017; Gibbs et al., 2012; McInerney & Wing, 2011; Speijer et al., 2012). Nevertheless, the consistent sedimentary expression of hyperthermals and associated coherent negative $\delta^{13}C$ and $\delta^{18}O$ excursions shows that they each represent rapid, massive greenhouse gas input to the atmosphere, elevated global temperatures and widespread deep ocean acidification (Zachos et al., 2008). These carbon cycle perturbations therefore represent

the best, albeit not perfect, analogues for understanding carbon cycle processes and feedbacks during current anthropogenic climate change (Lunt et al., 2013).

The forcing mechanism behind early Eocene hyperthermals is not fully understood. In particular, the source of isotopically light carbon driving Eocene hyperthermal events has been the subject of much controversy since their discovery. For example, hypotheses for the source of greenhouse gases driving PETM warming include: volcanism, a meteorite impact, dissociation of oceanic methane hydrates, orbitally-induced thawing of permafrost and changes in ocean ventilation (Bice & Marotzke, 2002; DeConto et al., 2012; Dickens, 2011; Gutjahr et al., 2017; Jones et al., 2019; Schaller & Fung, 2018; Thomas et al., 2002). The past two decades of scientific ocean drilling has led to the recovery of more continuous sedimentary records over the Eocene, and we now know that early Eocene hyperthermals are paced by the 100 kyr (short) and 405 kyr (long) eccentricity cycles and that warming leads the CIE (Barnet et al., 2019; Cramer et al., 2003; Galeotti et al., 2010; Kirtland Turner et al., 2014; Littler et al., 2014; Lourens et al., 2005; Westerhold et al., 2018; Zachos et al., 2010). Changes in the Earth's orbital parameters have therefore played a key role in driving warming by triggering release of isotopically light carbon from a temperature sensitive reservoir. This necessitates carbon release from a readily exchangeable (and easily replenished) surficial carbon reservoir (e.g., atmosphere, biosphere, oceans), thus ruling out discrete events such as impacts and those requiring regular 'refilling' such as methane hydrates (Kirtland Turner et al., 2014; Westerhold et al., 2018; Zachos et al., 2010). The PETM is likely an exception to this, as it is much larger than other early Eocene hyperthermals and likely augmented by NAIP volcanism (Barnet et al., 2019; Gutjahr et al., 2017; Jones et al., 2019).

Previously, research has primarily focused on constraining the nature and causes of the earliest and most well-expressed Eocene hyperthermals, including the PETM, Eocene

Thermal Maximum 2 (ETM-2) and ETM-3. Much less attention has been given to the latest Palaeocene (e.g., the Dan-C2 event, ~65.2 Ma) and early Eocene warming events (named I-W, between ~54 – 49.5 Ma). Additionally, while hyperthermal events are generally associated with the early Eocene, hyperthermal-like $\delta^{13}C$ excursions continue to occur in the middle Eocene, between ~49 – 46.5 Ma (Sexton et al., 2011; Westerhold et al., 2018). Many existing records focus on understanding single events rather than the long-term series of climate perturbations through the Eocene. Research has also been limited by the scarcity of continuous, carbonate-rich sedimentary sequences from the early Eocene high-CO_2 world, as these records are necessary to fully characterise climate change and orbital-climate links (Boulila et al., 2018; Vahlenkamp et al., 2020; Westerhold et al., 2017, 2018). This is largely due to frequent hiatuses found in early-middle Eocene sediments (~50-48 Ma, Payros et al., 2009) and the relatively shallow carbonate compensation depth (CCD) at the time (Pälike et al., 2012; van Andel et al., 1975), as well as the high analytical and time costs of generating such records. Thus, few continuous, high-resolution single-site records exist at present to assess the relative magnitude of the full sequence of hyperthermals, their relationship to one another and the role of changing background conditions, e.g., continental configuration and atmospheric CO_2 levels, on the nature of these events.

We highlight two key benthic stable isotope records which document the synchronous expression of long and short-term early Eocene climate trends in the Pacific and Atlantic Oceans (Fig. 3.2, Barnet et al., 2019; Westerhold et al., 2018). Westerhold et al. (2018) present a high-resolution (4 – 5 kyr), 12 Myr long benthic foraminiferal $\delta^{18}O$ and $\delta^{13}C$ record from Ocean Drilling Program (ODP) Site 1209, northwest Pacific Ocean spanning 56 – 44 Ma. Barnet et al. (2019) present a high-resolution (1.5 – 4 kyr), 14.75 Myr long benthic foraminiferal $\delta^{18}O$ and $\delta^{13}C$ record from ODP Site 1262, South Atlantic Ocean spanning ~67

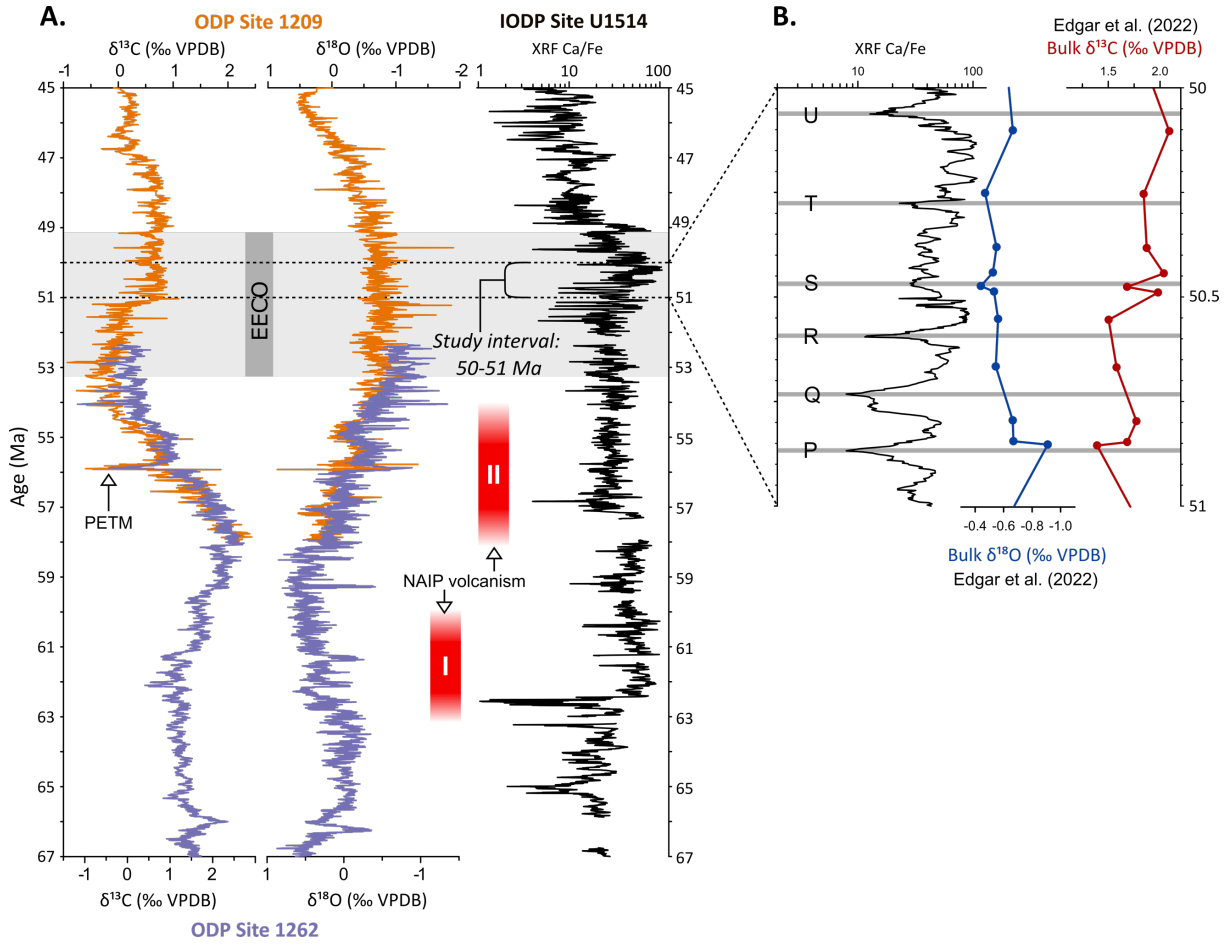


Figure 3.2 *Published benthic stable isotope records over 45-67 Ma from ODP Site 1209, Pacific (orange line, Westerhold et al., 2018) and Site 1262, Atlantic (purple line, Barnet et al., 2019), and XRF Ca/Fe record from Site U1514, Indian Ocean (black line). The Early Eocene Climatic Optimum is highlighted with a grey bar. B. Close-up of the study interval, 50-51 Ma, showing published bulk stable isotope records from Site U1514 (Edgar et al., 2022) and XRF Ca/Fe. Hyperthermals as identified in Vahlenkamp et al. (2020) are marked with black horizontal lines. Climatic event labels: Early Eocene Climatic Optimum (EECO), Paleocene-Eocene Thermal Maximum (PETM), North Atlantic Igneous Province (NAIP Phases I and II).*

– 52 Ma. While the Site 1209 record includes almost all of the early Eocene hyperthermals events, it is condensed in intervals within magnetochron C24r, in the latest Palaeocene to earliest Eocene, which prevents it from being directly astronomically tuned and limits assessment of phase relationships with other records (Westerhold et al., 2018). The Site 1262 record is more stratigraphically continuous and covers many of the larger early Eocene hyperthermals (e.g., PETM, ETM-2), but it does not extend high enough to include the lesser known L through W events from the peak of the EECO. Supplementary to this stable isotope

record from ODP Site 1262, an additional, ~5 Myr-long benthic foraminiferal stable isotope record exists for South Atlantic ODP Site 1263 (Lauretano et al., 2016, 2018; Westerhold et al., 2017) and spans the interval between ~49 – 54 Ma, including the hyperthermal events within our study interval. A high-resolution bulk stable isotope record has also been created across this period from ODP Site 1258, equatorial Atlantic (Kirtland Turner et al., 2014). To confidently understand the nature and causes of early to middle Eocene climate variability within an orbital framework, high-resolution climatic records of carbon and oxygen stable isotopes are needed across the full spectrum of hyperthermal events and from a range of different ocean basins, in particular the Indian Ocean, from which no high-resolution, long-term climate records have been generated so far.

Here, we focus on the interval between ~50 – 51 Ma from Site U1514, in the Indian Ocean, corresponding to ~10 m of core between ~228 – 238 m core composite depth below sea floor (CCSF). This interval captures six hyperthermal events (events P to U) across peak temperatures of the Early Eocene Climatic Optimum (EECO), which show differing magnitudes and characters in their X-ray fluorescence (XRF) Ca/Fe expressions (Fig. 3.2). We generate a new high-resolution benthic foraminiferal $\delta^{18}O$ and $\delta^{13}C$ stable isotope record within the study interval. We conduct spectral analyses on this new dataset alongside published XRF data from the same interval to: [1] Constrain the nature and magnitude of environmental change across hyperthermal events in the Indian Ocean; [2] Identify the dominant forcing mechanism of these smaller hyperthermal events; [3] Determine the phasing between individual environmental records to contribute to understanding of the origin of the events; [4] Test the synchronicity of climatic and carbon cycle changes during the early Eocene hyperthermals between different ocean basins.

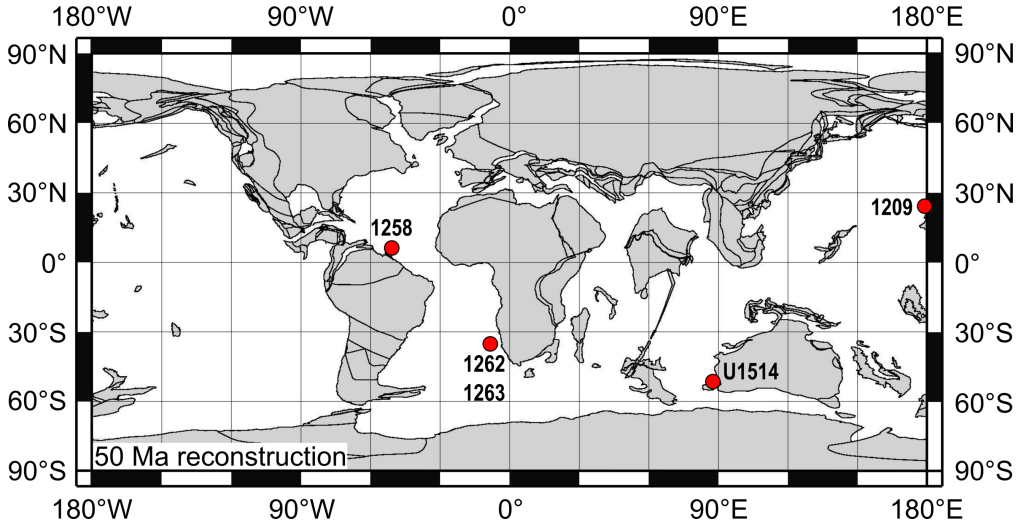


Figure 3.3 *Paleogeography at 50 Ma showing the location of Site U1514 and other sites referenced in this study. Reconstruction from www.odsn.de.*

3.2 MATERIALS AND METHODS

3.2.1 Materials

Site U1514 was cored during International Ocean Discovery Program (IODP) Expedition 369 in the Mentelle Basin on the southwest Australian continental margin in the Indian Ocean (Fig. 3.3; 33° 7.2327′ S, 113° 5.4672′ E). Modern water depth at Site U1514 is 3850 m, and benthic foraminiferal assemblages indicate a similar palaeowater depth of lower to middle bathyal for the focal Paleogene interval (Huber et al., 2019). At 50 Ma, Site U1514 was located at a palaeolatitude of ~60°S. Sediments recovered span the Late Cretaceous to the Pleistocene and include >200 m of carbonate-rich Eocene sediments, with well-expressed regular alterations between paler clayey nannofossil chalk and darker nannofossil-rich claystone (Huber et al., 2019). Core recovery was very good for Site U1514 (87.5 % overall) and the two main holes drilled, Holes A and C, stratigraphically overlap during the early to middle Eocene, creating a continuous ~50 m sedimentary section.

High-resolution (~3 cm) XRF records of bulk elemental composition developed for the Eocene from Site U1514 demonstrated that lithological variations were mostly paced by obliquity and eccentricity cycles (Bogus et al., 2019; Huber et al., 2019), allowing for an astronomically tuned age model for the lower to middle Eocene (56 – 40 Ma) to be developed (Vahlenkamp et al., 2020). Hyperthermal events from the PETM to W were identified within the early Eocene using the high-resolution Ca/Fe records by short-term negative excursions in Ca/Fe, caused by reduced $CaCO_3$ content in sediments across hyperthermal events.

The linear sedimentation rate for the study interval is calculated using age-depth tie-points reported in Vahlenkamp et al. (2020) and varies between 0.76 – 1.11 cm/kyr (Supplementary Fig. 3.1). The average sedimentation rate across the study interval is 0.97 cm/kyr.

3.2.2 Stable isotopes

246 samples were taken at an average spacing of 4 cm (~4.5 kyrs temporal resolution) between 228.7 – 238.8 m core composite depth below sea floor (CCSF). This interval includes the spliced portion of Site U1514 sediments (see Supplementary Table 4 of Vahlenkamp et al., 2020 for the revised shipboard splice), so samples were taken from Holes U1514 A and C.

Sediment samples were weighed and then dried in a 40°C oven for ~48 hours until no further change in sample weight was recorded in order to obtain a dry weight. Samples were then disaggregated in a solution of 45 mg/L sodium hexametaphosphate (calgon) and deionised water for 2 – 6 hours. Disaggregated samples were then washed over a 63 μm sieve and dried overnight before being vialled up. Three samples (at depths of 231.41, 231.45 and 231.49 m CCSF) required additional treatment in 80% acetic acid solution to aid disaggregation, following the method of Beasley et al. (2020) and references therein. There is no apparent offset in stable isotope results between the samples treated with acetic acid and

those treated with only calgon (Supplementary Fig. 3.2). The resulting dry coarse fraction (>63 μm) for each sample was sieved to separate out the 150-250 μm size fraction, from which up to 20 individuals of the epifaunal benthic foraminifera *Nuttallides truempyi* were picked following taxonomy in Holbourn et al. (2013). This species of benthic foraminifera was present in all samples across the study interval, however low numbers of tests where the total mass of carbonate was below analytical limits prevented data collection at depths 229.09 – 229.21 m CCSF and 234.39 m CCSF. Mechanical preservation ranged from poor to moderate (see Expedition 369 Methods for preservation scheme used, Huber et al., 2019), however in most cases we were able to select the most well-preserved, complete tests for stable isotope analyses. Test preservation was frosty under the light microscope.

Benthic foraminifera tests were analysed for stable carbon and oxygen isotope ratios ($\delta^{13}C$ and $\delta^{18}O$ respectively) at the National Environmental Isotope Facility, British Geological Survey (BGS; Nottingham, UK). Between 2 and 20 individual *Nuttallides truempyi* tests were pooled in each sample giving a combined weight of approximately 15 – 170 μg (mean = 123 μg), and analysed on the IsoPrime dual inlet mass spectrometer and Multiprep device. Samples were loaded into glass vials, sealed and evacuated. Anhydrous phosphoric acid was added to the carbonate at 90 °C, and the CO_2 released was collected for 15 minutes, cryogenically cleaned and delivered to the mass spectrometer for isotope analysis. A calcite-acid fractionation factor of 1.00798 is applied, along with drift correction calculated using repeated standards within each run. The Craig correction (Craig, 1957) is applied to account for $\delta^{17}O$. Average analytical reproducibility of the calcite standard (KCM) based on repeated in-house standard analyses was 0.05 ‰ for samples >20 μg, and 0.1 ‰ for samples <20 μg for both $\delta^{13}C$ and $\delta^{18}O$ values. $\delta^{13}C$ and $\delta^{18}O$ values are reported as per mille (‰) deviations of the isotopic ratios ($^{13}C/^{12}C$ and $^{18}O/^{16}O$) relative to the Vienna Peedee Belemnite (‰

VPDB) standard after calibration with the laboratory standard calcite, KCM. The laboratory standard, KCM, has been calibrated against the NBS-19 standard. Stable isotope data generated in this study is presented in Supplementary Table 3.1.

3.2.3 Palaeotemperature estimates from $\delta^{18}O$

We convert our benthic foraminiferal stable isotope $\delta^{18}O$ measurements to palaeotemperature to provide an estimate of temperature changes at Site U1514 across hyperthermal events. We follow the recommendation of Hollis et al. (2019) in using the palaeotemperature calibration derived by Kim & O'Neil (1997) and modified by Bemis et al. (1998):

$$T\ (℃) = 16.1 - 4.64(\delta^{18}O_c - \ \delta^{18}O_{sw}) + 0.09(\delta^{18}O_c - \delta^{18}O_{sw})^2$$

Where T = palaeotemperature, $\delta^{18}O_c$ = the stable oxygen isotope measurement of calcite (‰ VPDB) and $\delta^{18}O_{sw}$ = the stable oxygen isotope measurement of ambient seawater (‰ VSMOW). $\delta^{18}O_{sw}$ was estimated using a MATLAB script published with Hollis et al. (2019), which estimates past $\delta^{18}O_{sw}$ based on palaeolocation using a modern global gridded $\delta^{18}O_{sw}$ dataset (LeGrande & Schmidt, 2006) and applies a correction of -1.0 ‰ for the ice-free early Eocene. Palaeocoordinates for Site U1514 were generated using the GPlates Web Service (Müller et al., 2018) and the mantle reference plate deformation model of Müller et al. (2019). This gives us an estimate of -1.31 ‰ VSMOW, assuming ice-free conditions. The above palaeotemperature equation shows good agreement with benthic foraminifera *Cibicidoides* measurements (Bemis et al., 1998), so we convert our *N. truempyi* $\delta^{18}O$ values to equivalent *Cibicidoides* $\delta^{18}O$ values using the correction factor from Katz et al. (2003) for the Palaeogene:

$$\delta^{18}O_{Cib} = \frac{(\delta^{18}O_{Nutt} + 0.1)}{0.89}$$

3.2.4 X-ray fluorescence

XRF scanning of Site U1514 sediments was done on third generation Avaatech machines at the AVAATECH XRF Core Scanning Facility, IODP Gulf Coast Repository, Texas. The XRF scanning method allows for high resolution measurements to be made in a relatively short period of time. Average measurement resolution across the study interval was 2 cm, equating to roughly ~2.2 kyr based on the average sedimentation rate across the interval. The full XRF method for Site U1514 is reported in the IODP Expedition 369 Methods (Bogus et al., 2019; Huber et al., 2019) In brief: measurements were made over a 1 cm^2 area for a 6-second count time, at source energies and currents of 10 kV at 0.16 mA (no filter), 30 kV at 1.25 mA (copper filter), and 50 kV at 0.75 mA (palladium filter). Anomalous peaks, which typically correspond to cracks or gaps in the core surface, were removed from the dataset and the 'cleaned' dataset used in this study is given in Supplementary Table 3.2. The raw dataset is available online at the IODP Laboratory Information Management System (LIMS) database (IODP Joides Resolution Science Operator, 2018). Here we use the Fe and Ca intensity data, reported as a ratio of Ca counts per second (cps) to Fe cps, and presented on a logarithmic scale to highlight known hyperthermal events and other prominent excursions. Ca and Fe were detected at all source energies. We use the 10 kV dataset here as the resulting Ca/Fe ratio is the same regardless of the energy at which it was measured.

3.2.5 Time series analysis

To identify cycles within the Site U1514 sedimentary record that are not captured within the relatively short study interval (~10 m between ~228.7 – 238.8 m CCSF), we selected a wider depth interval for time series analysis on the Ca/Fe record that incorporates the original study interval (~30 m between 218 – 248 m CCSF).

Time series analysis was performed using the Acycle software, version 2.4.1 (Li et al., 2019). $\delta^{18}O$, $\delta^{13}C$ and Ca/Fe XRF records were detrended using a locally weighted scatterplot smoothing (LOWESS) curve-fitting model with a window at 50 %. The detrended datasets were then linearly interpolated to create new data points at regular 2 cm intervals. This is necessary as the Acycle software requires equal spacing between data points before time series analysis. The new 2 cm sampling resolution after interpolation is sufficiently high to prevent any loss of trends within the dataset and is equivalent to the average XRF record spacing. A comparison of the new detrended and interpolated dataset with the original dataset is shown in Supplementary Fig. 3.3.

Basic spectral analysis was performed on the $\delta^{18}O$, $\delta^{13}C$ and Ca/Fe records using a 2π-multi-taper method with a robust, first order autoregressive (AR1) red noise model (Mann & Lees, 1996). Confidence limits above the AR1 red noise model were auto-generated by Acycle at 99 %, 95 % and 90 %. To assess how the periodicities in the signal vary over the length of the record, evolutive spectral analysis and wavelet analysis were also performed. The evolutive spectral analysis method uses the evolutionary Fast Fourier Transform by Linda A. Hinnov (Kodama & Hinnov, 2014) with a window length of 2.02 m for $\delta^{18}O$ and $\delta^{13}C$, and 3 m for Ca/Fe. Evolutive wavelet analysis is also used to decompose spectral features of the record over the length of the time series. For wavelet analysis, we used the wavelet transform script published in Grinsted et al. (2004) in MATLAB.

Bandpass filters are used to analyse how the amplitude of specific frequencies changes over time within the study interval. We employ the Acycle Gaussian filtering tool (Kodama & Hinnov, 2014; Li et al., 2019) using a wide range of frequencies for each filter in order to capture variation in certain periodicities. The upper and lower bounds for each frequency band are $^1/_3$ above and $^1/_3$ below the chosen frequency, respectively.

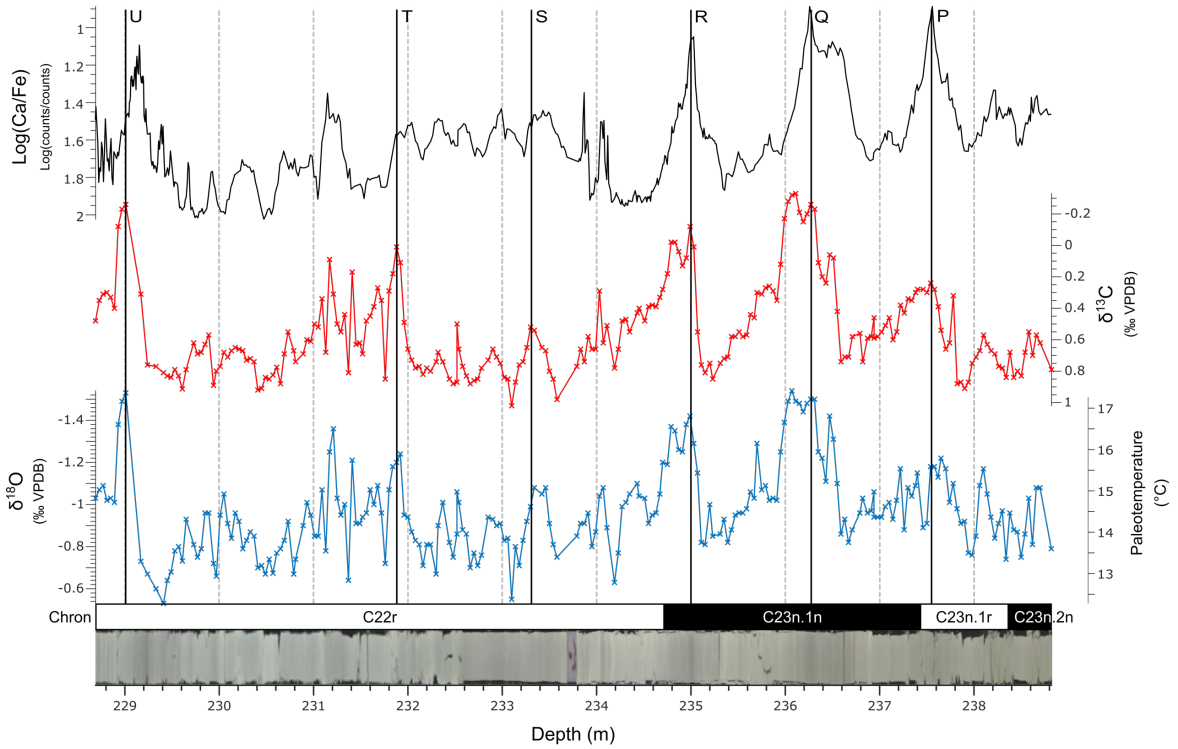


Figure 3.4 *Stable isotope and XRF records from Site U1514 alongside core photos and magnetostratigraphic chron boundaries. A: XRF Log(Ca/Fe), B: stable isotope $\delta^{13}C$ (red), C: stable isotope $\delta^{18}O$ (blue) with paleotemperature conversion on separate axis. The locations of hyperthermals P, Q, R, S, T and U are shown with solid vertical lines. Spliced core images were created using IODPCoreImage (Drury et al., 2018).*

Once periodicities were identified within our datasets, these were further interrogated using coherence, phase and lead/lag analysis. These are also performed using the built-in tools for these functions within Acycle (Li et al., 2019).

3.3 RESULTS

3.3.1 Early Eocene stable isotopes and Ca/Fe

Across the study interval between 228.7 and 238.8 m CCSF, $\delta^{13}C$ values vary between -0.33 and 1.02 ‰ and $\delta^{18}O$ between -1.54 and -0.33 ‰ (Fig. 3.4). $\delta^{13}C$ and $\delta^{18}O$ values show a strong positive linear correlation at all depths across the study interval ($r^2 = 0.79$, Fig. 3.5). The most prominent feature of the new benthic foraminiferal $\delta^{13}C$ and $\delta^{18}O$ records are multiple negative excursions of ~0.4 – 1 ‰ in $\delta^{13}C$ and 0.3 – 1 ‰ in $\delta^{18}O$, which individually

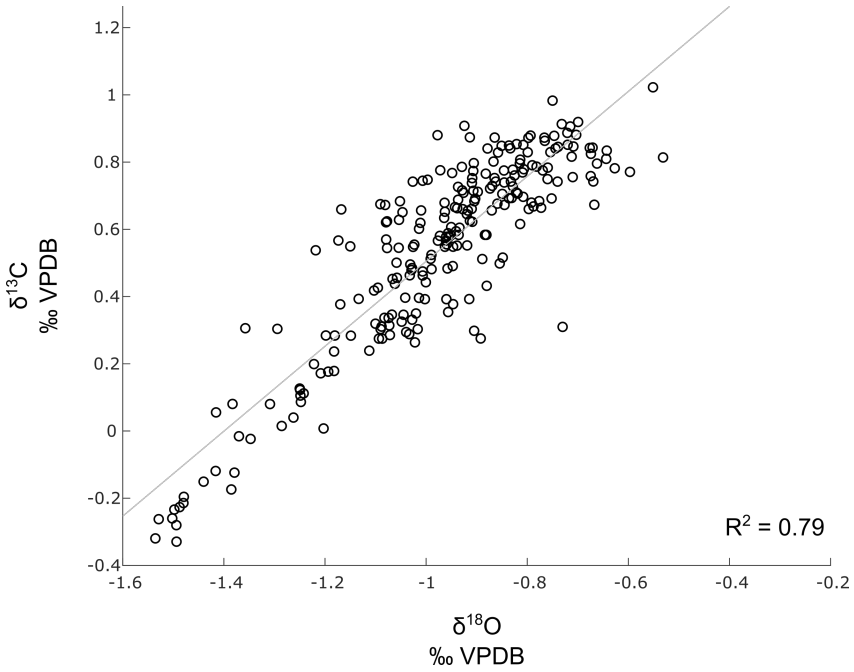


Figure 3.5 *Cross-plot between $\delta^{18}O$ and $\delta^{13}C$ results at Site U1514, showing the strength of the relationship ($R^2 = 0.79$).*

span ~0.4 – 0.7 m of sediment. These correlate with pronounced negative excursions in the Ca/Fe record associated with the early Eocene hyperthermal events P, Q, R, S, T and U identified at Site U1514 based on the Ca/Fe records by Vahlenkamp et al. (2020). We refined the exact positions of hyperthermals in all records is based on the initial onset of strong, sustained $\delta^{13}C$ decline and 'peak' hyperthermal conditions are marked at the earliest $\delta^{13}C$ minimum, as shown in Supplementary Fig. 3.4. We follow the alphabetical naming system for hyperthermal events established by Cramer et al. (2003) and extended by Laurentano et al. (2016). Notably, the onset of hyperthermal $\delta^{13}C$ and $\delta^{18}O$ excursions are ~10 – 30 cm higher in the sediment column than the shift to lower Ca/Fe ratios in the XRF dataset. There is some variation in the size and character of hyperthermal events across the study interval as expressed by both the stable isotope and Ca/Fe records. Hyperthermal events P, W and R in the lower portion of the record, below ~234 m, show pronounced excursions in all three records, with $\delta^{13}C$ and $\delta^{18}O$ negative excursions of 0.6 – 1 ‰ and 0.5 – 0.6 ‰ respectively.

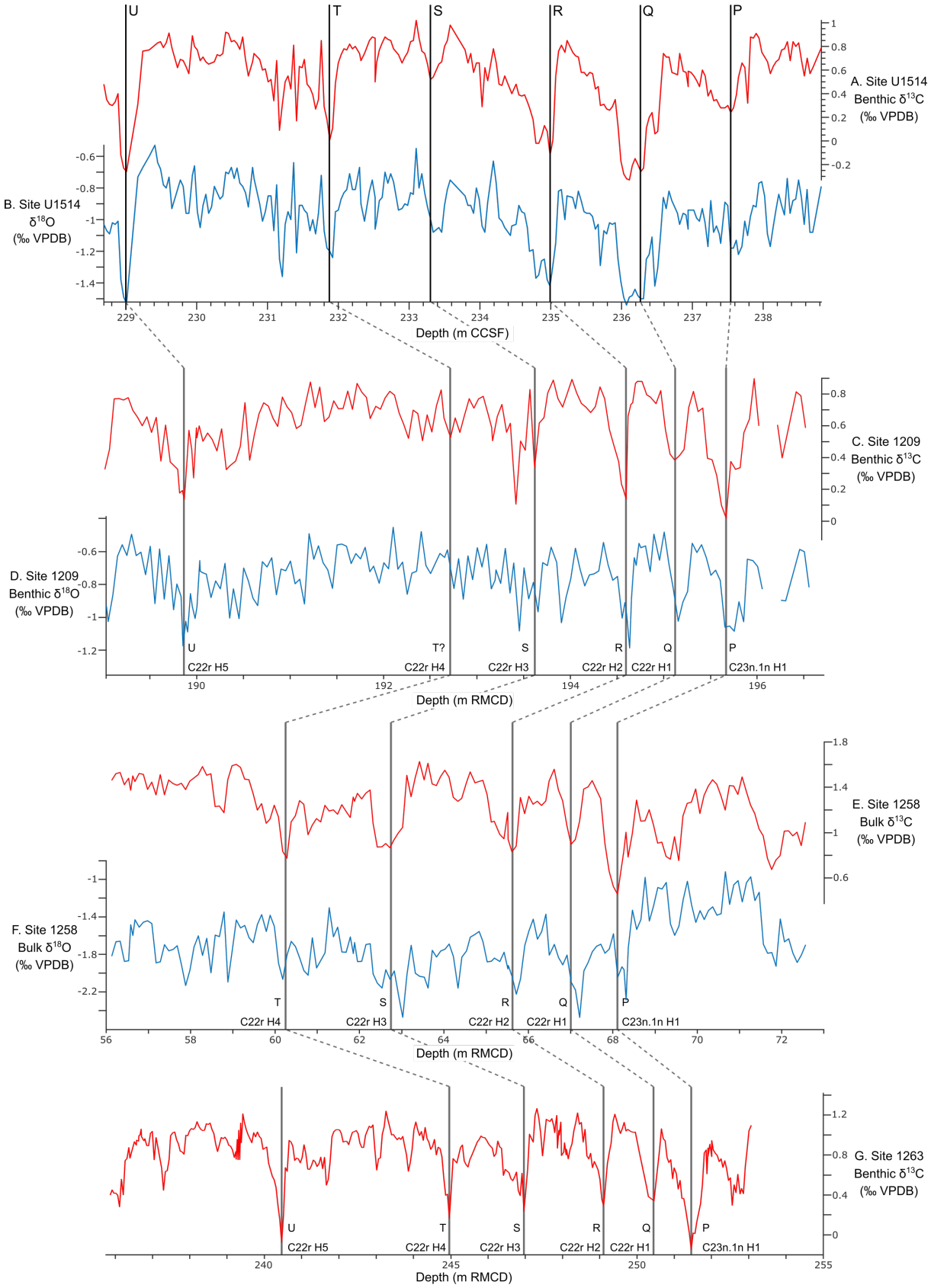


Figure 3.6 *Comparison of high-resolution records from other ocean basins across the study interval: benthic $\delta^{13}C$ and $\delta^{18}O$ from Site U1514 (A and B), benthic $\delta^{13}C$ and $\delta^{18}O$ from Site 1209 (C and D; Westerhold et al., 2018), bulk $\delta^{13}C$ and $\delta^{18}O$ from Site 1258 (E and F; Kirtland Turner et al., 2014) and benthic $\delta^{13}C$ from Site 1263 (G; Lauretano et al., 2016; Westerhold et al., 2017). All datasets are presented on site-specific depth scales. Hyperthermal events P to U, where present, are identified using these authors' original hyperthermal classifications and are marked using black vertical lines.*

Events S and T between 234 – 231 m depth show smaller excursions, of 0.4 – 0.8 ‰ in $\delta^{13}C$ and 0.3 – 0.5 ‰ in $\delta^{18}O$. The S and T events also appear less stable than earlier events, with higher variability in isotope values around the event and a greater mismatch between isotope and XRF Ca/Fe patterns. Event U, the highest in the record, is similar to early events P, Q and R, in terms of showing a pronounced negative excursion of ~1 ‰ in both $\delta^{13}C$ and $\delta^{18}O$ values and negative ~0.7 units in Ca/Fe. $\delta^{18}O$-based bottom water temperatures (Fig. 3.4) vary between ~12.5 – 17.5 °C across the study interval, with warmest temperatures occurring at the peak of hyperthermal events Q, R and U. Events P, Q and R represent temperature increases of ~2.5, 3.5 and 3 °C respectively, while events S and T show smaller rises of ~1.75 and 2.5 °C. The largest temperature increase occurs across the U event, ~4.5 °C, however high temperatures are not sustained for as long in sediments as other large events, Q and R. Excursions in stable isotopes have an abrupt onset and more gradual recovery, whereas excursions are more symmetrical in the Ca/Fe record.

We have correlated events P to U across published benthic foraminiferal stable isotope records from Site 1209 in the northwest Pacific (Westerhold et al., 2018) and Site 1263 in the southeast Atlantic (Lauretano et al., 2016; Westerhold et al., 2017) and bulk stable isotope records from Site 1258 in the equatorial Atlantic (Kirtland Turner et al., 2014) to compare the expression of these events in different proxies and ocean basins (Fig. 3.6). We present these records on a depth axis to avoid age model discrepancies. A summary of palaeodepths and source material used by these references is given in Supplementary Table 3.3. Mean benthic $\delta^{13}C$ across this interval is 0.54 ‰ at Site U1514, which is slightly lower than the mean of other benthic records, 0.61 ‰ at Site 1209 and 0.82 ‰ at Site 1263. Site U1514 also shows the most negative $\delta^{13}C$ values at the peak of hyperthermal events Q, R, T and U than other sites, while events P and S show similar values with other sites. Mean benthic $\delta^{18}O$ at Site

Table 3.1: *Summary of magnitude of $\delta^{13}C$ and $\delta^{18}O$ excursions across the onset of hyperthermal events at Sites U1514 (this study), 1209 (Westerhold et al., 2018), 1258 (Kirtland Turner et al., 2014) and 1263 (Lauretano et al., 2016; Westerhold et al., 2017). Stronger colours denote greater magnitude of change in $\delta^{13}C$ and $\delta^{18}O$. All magnitudes are in ‰ VPDB units and refer to a negative change of that amount in $\delta^{13}C$ or $\delta^{18}O$.*

		U1514	1209	1258 (bulks)	1263
$\delta^{13}C$ ‰	P	0.6	0.9	0.8	1.1
	Q	1.0	0.4	0.6	0.7
	R	1.0	0.7	0.5	0.9
	S	0.4	0.6	0.6	1.0
	T	0.8	0.2	0.5	0.8
	U	1.0	0.5		1.0
$\delta^{18}O$ ‰	P	0.5	0.4	1.0	
	Q	0.7	0.5	0.8	
	R	0.6	0.6	0.8	
	S	0.3	0.4	0.8	
	T	0.5	0.3	0.5	
	U	1.0	0.5		

U1514 is -0.97 ‰, which is also slightly more negative than the mean from Site 1209, -0.75 ‰. This indicates warmer average temperatures by ~1 °C. $\delta^{18}O$ at Site U1615 generally shows a greater magnitude change associated with hyperthermals (Table 3.1), where the $\delta^{18}O$ excursion at events P, Q, R, T and U is greater by 0.1 – 0.5 ‰ than equivalent events at Site 1209. Later hyperthermal events T and U are therefore relatively more strongly expressed in the high latitude Indian Ocean compared to the Atlantic and Pacific Oceans. Note that for Site 1258, only bulk carbonate stable isotope values are available (Fig. 3.6), which are incorporate the surficial water signal, and therefore show more positive $\delta^{13}C$ and more negative $\delta^{18}O$ than other sites where benthic records are available. The magnitude of environmental change associated with individual hyperthermal events is also not consistent across different sites. For example, at Site U1514 events Q, R and U show the largest benthic foraminiferal CIE, whereas the benthic CIE for the P event is largest at Sites 1209 and 1258.

Regression lines calculated for the $\delta^{13}C$ – $\delta^{18}O$ relationships across hyperthermal events are shown in Fig. 3.7 and indicate similar slopes for Events P, Q, R and T. Events that show similar expression in terms of the magnitude of stable isotope excursion do not necessarily

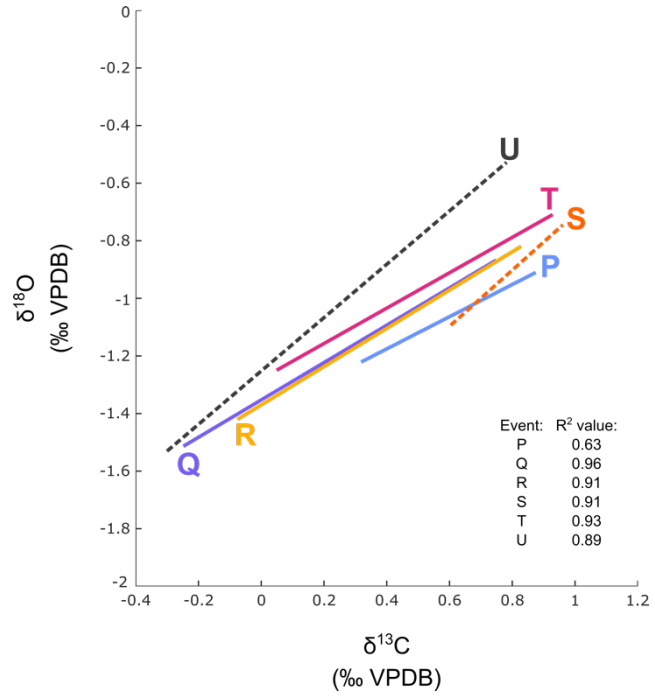


Figure 3.7 *$\delta^{18}O$ – $\delta^{13}C$ regression lines for hyperthermals P, Q, R, S, T and U at Site U1514. Hyperthermals with a flatter gradient are shown by solid lines (P, Q, R and T), and steeper hyperthermals are shown by dashed lines (S and U). The strength of the relationship for each hyperthermal is shown with R^2 values, bottom right.*

show the same gradient of their $\delta^{18}O$ – $\delta^{13}C$ regression. For example, event U has a much greater magnitude excursion than S in both $\delta^{13}C$ and $\delta^{18}O$, but the slope of the $\delta^{18}O$ – $\delta^{13}C$ regression line for events U and S is similar and notably steeper than other events.

3.3.2 Spectral analysis

To identify the dominant periodicities present in our records, we first performed basic spectral analysis on the records as a whole (Fig. 3.8). There are peaks in power at similar frequencies in all records, however the exact frequency varies slightly between records. In the $\delta^{13}C$ and $\delta^{18}O$ records, there are two main peaks in power above the 99 % confidence level, at frequencies of ~0.8 cycles/m and 4.5 cycles/m corresponding to periodicities of 1.24-1.27 m and 0.22 m, respectively. While the dominant periodicities in $\delta^{13}C$ and $\delta^{18}O$ are very similar, cycles generally have slightly smaller periods (i.e. higher frequencies) in $\delta^{13}C$ than $\delta^{18}O$. For

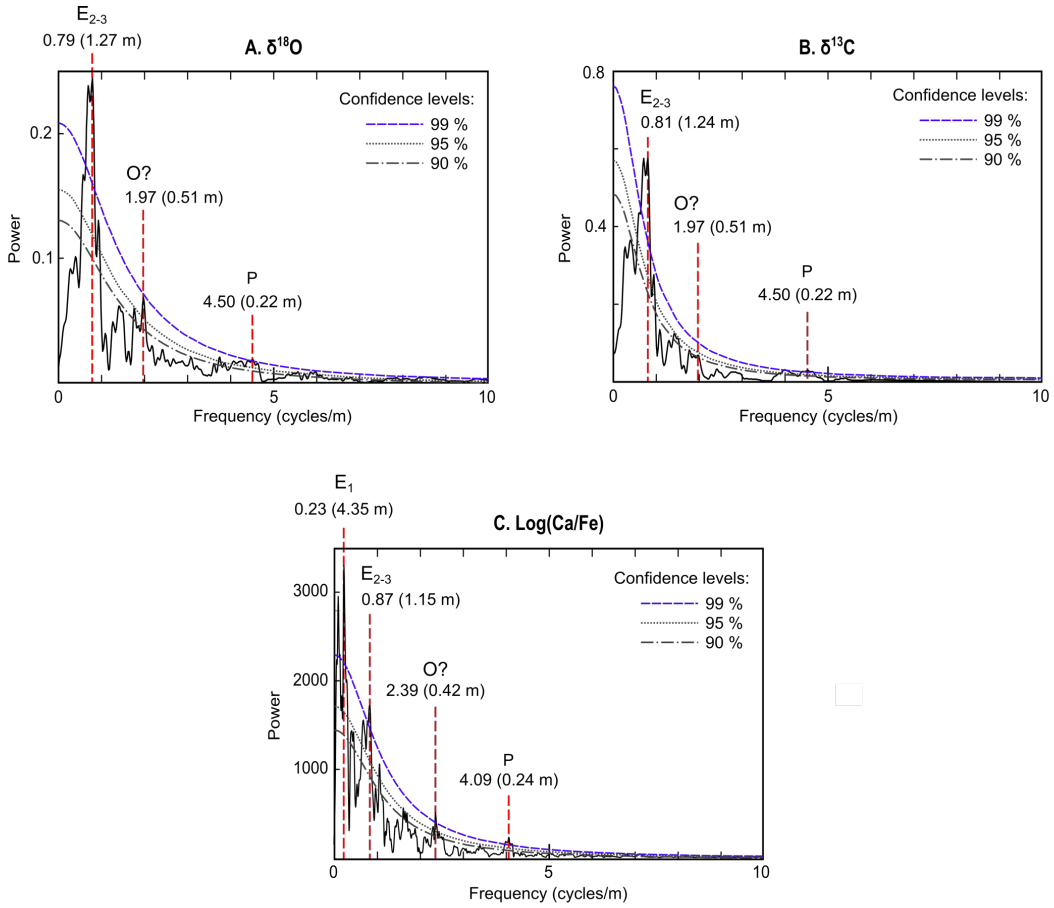


Figure 3.8 *Basic frequency spectra for $\delta^{18}O$ (A), $\delta^{13}C$ (B) and Log(Ca/Fe) (C) at Site U1514. 99 %, 95 % and 90 % confidence limits are indicated using blue and grey dashed lines. Significant peaks in spectra have been highlighted and where these correspond to likely orbital periodicities, a label has been added, where E1 = long eccentricity, E2-3 = short eccentricity, P = precession and O? = potential influence of obliquity.*

example, the cycle at ~0.8 cycles/m shows the greatest spectral power at 0.79 cycles/m in $\delta^{18}O$ and 0.81 cycles/m in $\delta^{13}C$. The Log(Ca/Fe) spectrum shows peaks at similar frequencies also above the 99% confidence level, at 0.87 cycles/m (period = 1.15 m) and 4.09 cycles/m (period = 0.24 m). There are additional peaks above the 95 % confidence level in $\delta^{18}O$ and between 90-95 % confidence in $\delta^{13}C$, around 1.97 cycles/m (period = 0.51 m). In Log(Ca/Fe), there are several mid-frequency peaks above the 90 % confidence level, but one above 99 % confidence at 2.39 cycles/m (period = 0.42 m). There is an additional high-powered peak in the Log(Ca/Fe) record at 0.23 cycles/m (period = 4.35 m), which is not captured in the shorter isotope records, but is well above the 99 % confidence level for Log(Ca/Fe).

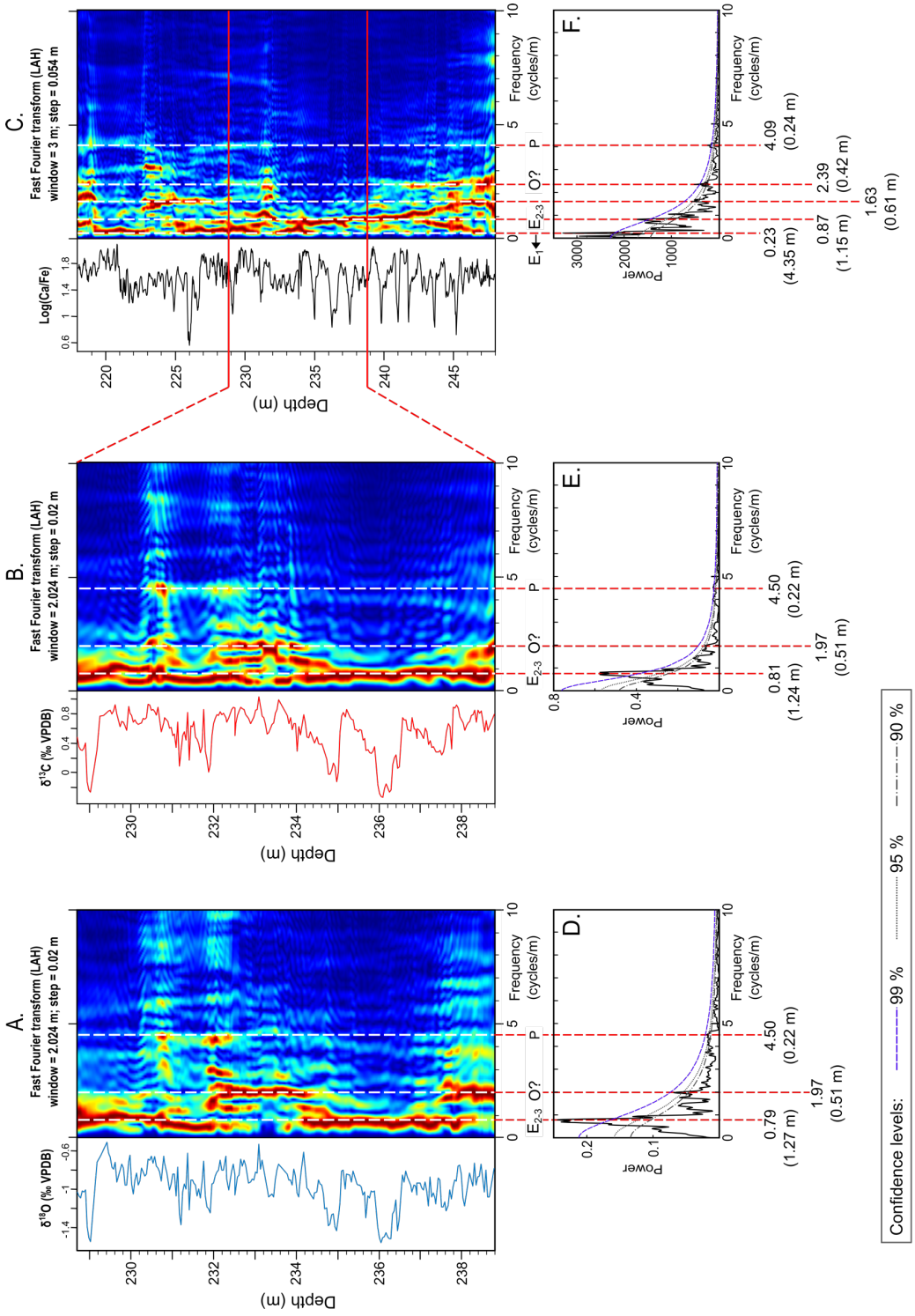


Figure 3.9 *Evolutive spectral analyses for $\delta^{18}O$ (A), $\delta^{13}C$ (B) and Ca/Fe (C) at Site U1514, alongside basic frequency spectra for these records (D, E and F, also see Fig. 3.8). Major periodicities that occur in basic non-evolutive spectra have been highlighted using vertical lines. Confidence levels of 99 %, 95 % and 90 % are shown using blue and grey dashed lines in D, E and F.*

To test for any changes in dominant periodicity through time, we also generated evolutionary frequency spectra for our datasets (Fig. 3.9). Notably, frequencies described above are not constant in power over the entire length of each record. In the stable isotope records, the lowest frequency cycle at ~0.8 cycles/m is dominant across most of the study interval. However, there are two intervals from ~237.4 – 238.8 m (the base of the record) and 232 – 234.4 m where power in this frequency is reduced and mid-frequency periodicities around ~2 cycles/m become more dominant. The highest frequency periodicity, at 4.5 cycles/m, only shows high power at brief points in $\delta^{18}O$ and $\delta^{13}C$, around 230.8 m and 232.2 m. The switch in power between low and mid-frequency periodicities is 'cleaner' in the $\delta^{18}O$ record, where an almost step-like change from ~0.8 to ~2 cycles/m can be observed at multiple points in the record. In $\delta^{13}C$ this change is less clear and there is more noise and interference between frequencies.

Periodicities do not evolve the same way for Log(Ca/Fe) as for the stable isotope records. Between 238.8 – 229 m, the frequency at 0.87 cycles/m is relatively constant in power, except for brief intervals of low power at 232 – 233 m and 229 – 230 m. The mid-frequency periodicity at 2.39 cycles/m shows power between 231 – 232 m, whereas the mid-frequency periodicity in isotopes at ~2 cycles/m shows highest power between 232 – 234.4 m. However, due to the longer Ca/Fe record, the evolutive spectrum for Log(Ca/Fe) shows sections above and below the study interval, from 222.5 – 227 m and 241.5 – 248 m where mid-frequency periodicities dominate the spectrum. Additionally, we see the evolution of the very low frequency cycle at 0.23 cycles/m in the Log(Ca/Fe) spectrum, which is not evident in stable isotopes. This frequency shows low/no power below 235 m, but high power relatively consistently between 225 – 235 m and 219 – 223 m. The highest frequency in Log(Ca/Fe), at 4.09 cycles/m, shows very little power across the entire Log(Ca/Fe) record, however there are

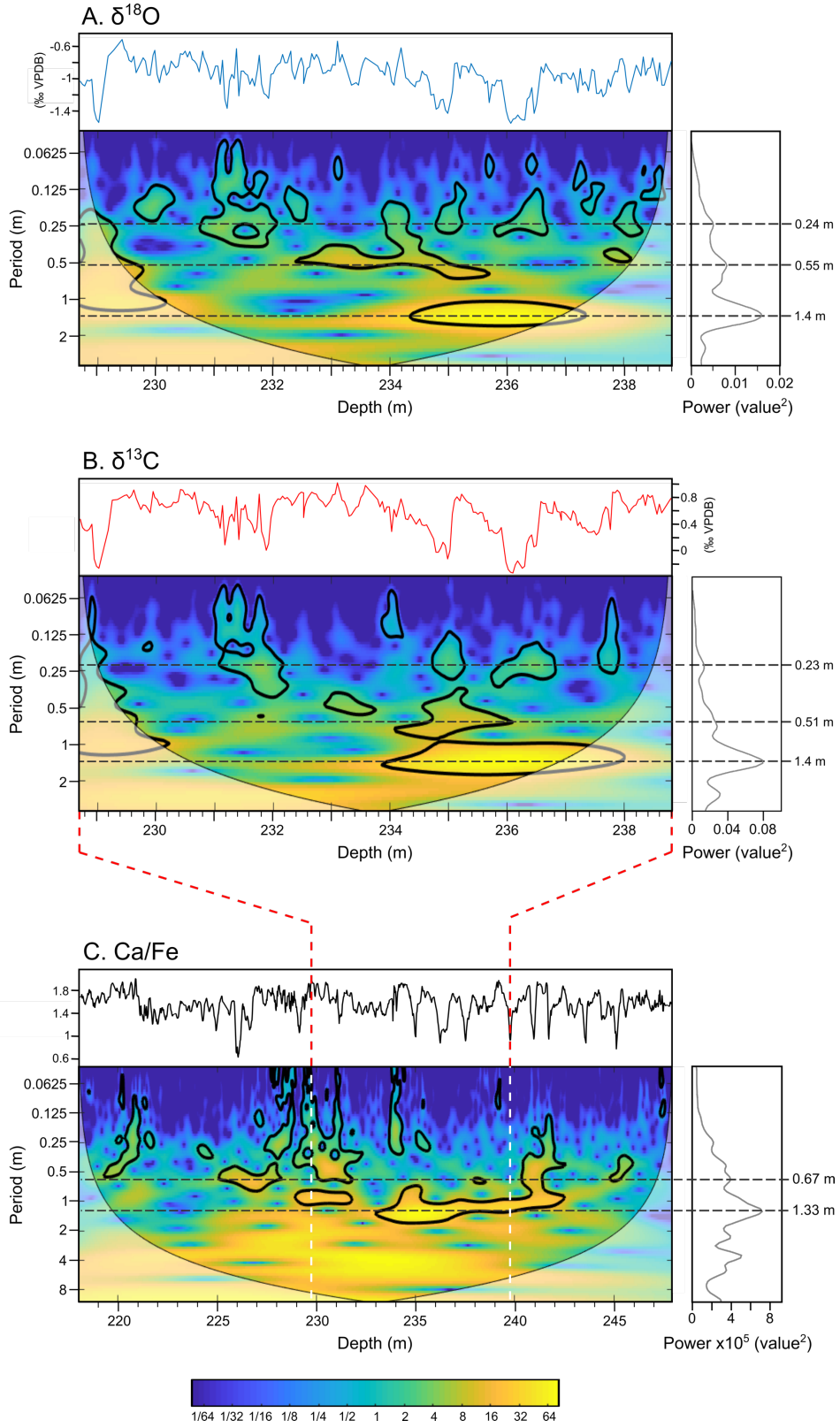


Figure 3.10 *Wavelet analysis for Site U1514: $\delta^{18}O$ (A), $\delta^{13}C$ (B) and Ca/Fe (C). The Morlet continuous wavelet transform script used is from Grinsted et al. (2004). Thick black contours indicate the 5 % significance level above background red noise. Lighter shading designates the area outside the cone of influence, which may be distorted by edge effects and is not included in interpretations. Colours indicate power values, with blue shades showing the lowest power and yellow shades the highest power.*

short intervals where it occurs in the upper portion of the record, above 232 m. One of these intervals, from 231.5 – 232 m, coincides with the emergence of the similar high frequency cycle (at 4.5 cycles/m) in the stable isotope records (~230.8 – 232.2 m). Wavelet analyses highlight the non-stationary characteristics of periodicities within the dataset (Fig. 3.10). Wavelet spectra show a similar pattern to evolutive spectra (Fig. 3.9), with lower frequencies dominating the bottom portion of the record below 234 m. In higher frequencies, power is distributed intermittently at semi-regular sections across the record. This is illustrated in the wavelet spectra for $\delta^{13}C$, where high power at the 0.23 m periodicity (frequency = 4.35 cycles/m) occurs around 237.8 m, 236.5 m, 235.0 m and 231.8 m, coinciding with negative carbon excursions at hyperthermal events P, Q, R and T. This reflects the influence of a lower frequency cycle, likely the periodicity at 1.4 m in $\delta^{13}C$, controlling power at higher frequencies.

Overall, there is a distinction in both evolutive and wavelet spectra between the lower portion of the record from ~234 – 238.8 m, where lower frequencies of ~0.8 cycles/m (period = ~1.25 m) dominate, and above 234 m, where mid-range and high frequencies, at 1.97 and 4.50 cycles/m (period = 0.51 and 0.22 m respectively), are introduced. These periodicities are not constant or consistent in frequency or power across the top half of the record. The longer Ca/Fe record shows the presence of an additional low frequency periodicity, at 0.23 cycles/m (period = 4.35 m) influencing this record. Wavelet analyses suggest that hyperthermal event excursions, particularly in $\delta^{13}C$, are associated with the low frequency periodicity at ~0.8 cycles/m.

3.3.3 Coherence and phase relationships

As suggested by the strong linear relationship between benthic foraminiferal $\delta^{13}C$ and $\delta^{18}O$ values (Fig. 3.5), cross-spectral analysis shows very high coherence of $\delta^{13}C$ relative to $\delta^{18}O$ at

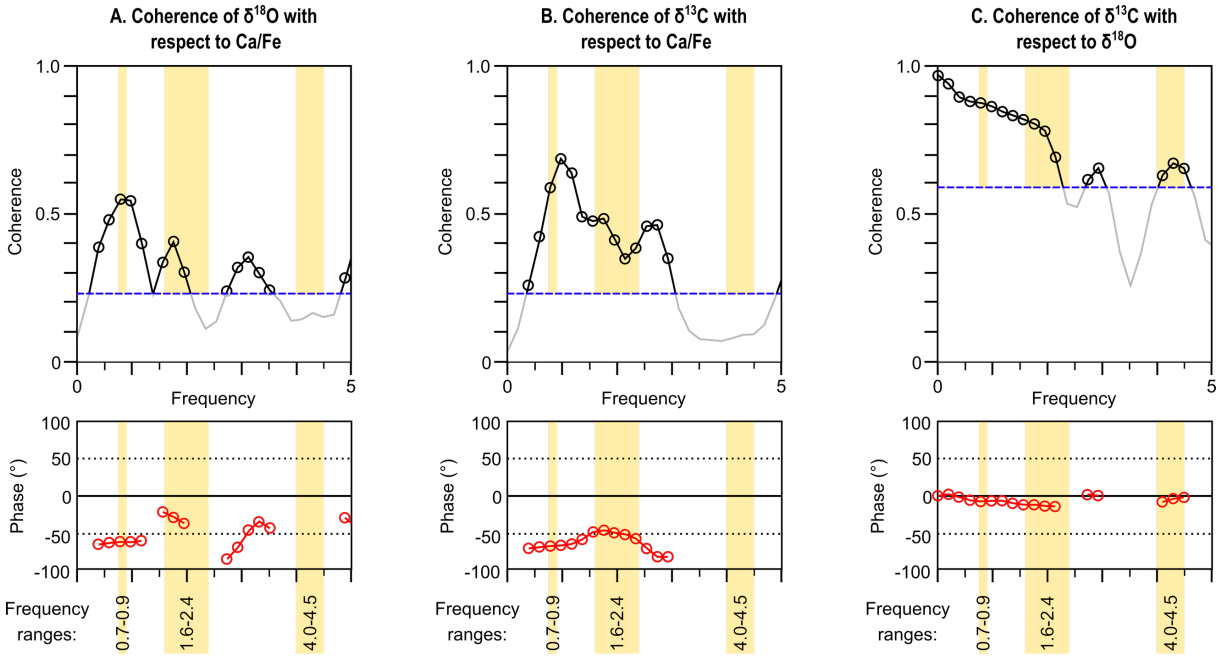


Figure 3.11 *Coherence and phase relationships between $\delta^{18}O$ and Ca/Fe (A), $\delta^{13}C$ and Ca/Fe (B), $\delta^{13}C$ and $\delta^{18}O$ (C). The coherence threshold is based on the 95 % confidence interval for each pairing (blue line). Phase relationships are plotted where coherence exceeds the threshold. Vertical yellow shading indicates dominant frequency ranges identified by spectral analysis (see Figs. 3.8 – 3.10). Window size is 2 m.*

the dominant frequencies identified in time series analysis (Fig. 3.11 C). Coherence is highest at the lowest frequencies and decreases as frequency increases, yet remains above the threshold for all of the dominant frequency ranges. The phase relationship between stable isotope records is slightly negative, with the $\delta^{13}C$ excursions occur slightly later (i.e. at a shallower depth) than $\delta^{18}O$ excursions. Lead/lag analysis between isotopes shows the average magnitude of the lag across the study interval is ~0.005 m (Supplementary Fig. 3.5). This is below the sampling resolution for stable isotopes in this study (0.04 m) and so the lag is considered negligible in this case. $\delta^{18}O$ and $\delta^{13}C$ are therefore considered in phase at key frequencies in this study.

Coherence of stable isotope records with the XRF Ca/Fe record is more variable than between isotopes (Fig. 3.11 A, B). With respect to Ca/Fe, coherence of $\delta^{18}O$ is above the threshold for the lower two frequency ranges, ~0.8 cycles/m and 1.6 – 2.4 cycles/m.

Coherence is low (below the threshold) for the highest frequency of interest, 4.0 – 4.5 cycles/m. The phase relationship of $\delta^{18}O$ with respect to Ca/Fe within our frequency bands is consistently negative, and thus cycles recognised in $\delta^{18}O$ records lag those in Ca/Fe. Phase is most negative at the lowest frequency band, ~0.8 cycles/m. The magnitude of this lag is ~0.085 m on average across the study interval (Supplementary Fig. 3.5).

Similar patterns are seen when the coherence and phase of $\delta^{13}C$ with respect to Ca/Fe is analysed as $\delta^{13}C$ and $\delta^{18}O$ strongly covary (Fig. 3.11 B). Coherence is highest in the lowest frequency band, ~0.8 cycles/m, and lower but still above the threshold in the mid-frequency band, 1.6 – 2.4 cycles/m. Coherence is low (below the threshold) at the highest frequency range, 4.0 – 4.5 cycles/m. However, where coherence is above the threshold between $\delta^{13}C$ and Ca/Fe, it is higher than coherence between $\delta^{18}O$ and Ca/Fe. Similar with $\delta^{18}O$, the phase relationship between $\delta^{13}C$ and Ca/Fe is consistently negative, and cycles at frequencies of ~0.8 and 1.6 – 2.4 cycles/m in $\delta^{13}C$ thus lag behind Ca/Fe. Phase is most negative at the lowest frequency band, ~0.8 cycles/m. The magnitude of this lag is ~0.115 m on average across the study interval, greater than the lag between $\delta^{18}O$ and Ca/Fe (Supplementary Fig. 3.5).

3.3.4 Filtering

Detrended and interpolated $\delta^{18}O$, $\delta^{13}C$ and Log(Ca/Fe) datasets were filtered by our major frequencies as identified in spectral analysis (Figs. 3.12 – 3.14). In all three proxies, hyperthermal events are associated with a periodicity between 0.7 – 0.9 cycles/m. The magnitude of cycles at this frequency is greatest at the base of the study interval, between ~234 – 238.8 m (Fig. 3.9). Whereas the magnitude of variability is greatest in the periodicity between 0.7 – 0.9 cycles/m in all three proxies (Figs. 3.12 – 3.14), with the highest frequency

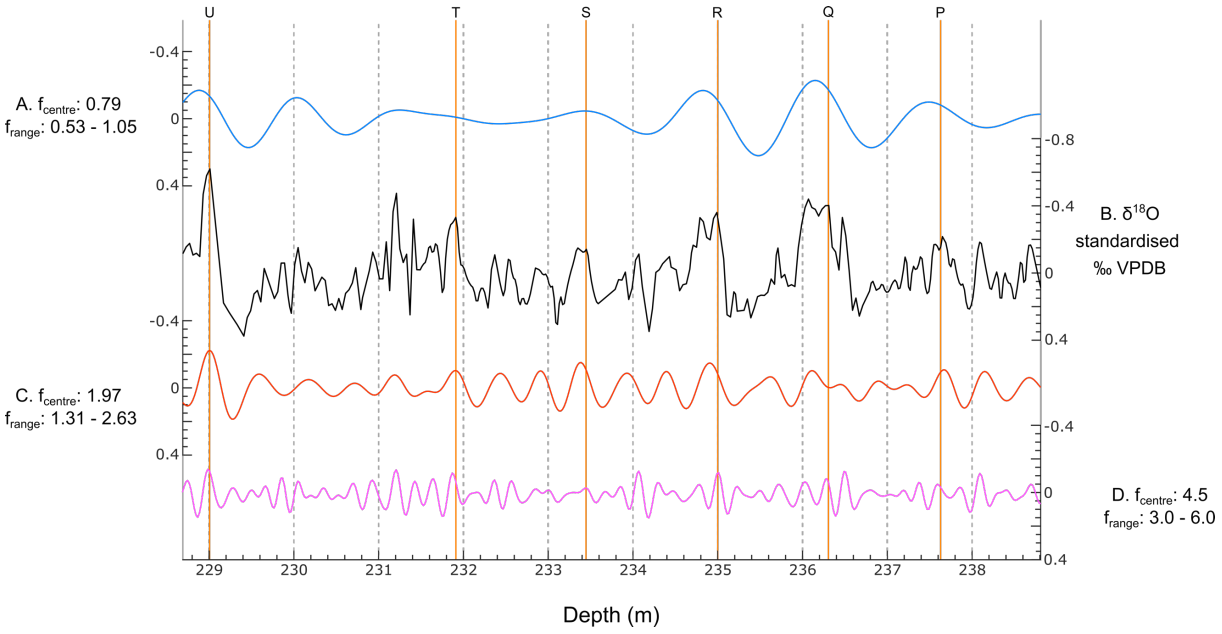


Figure 3.12 *De-trended and interpolated $\delta^{18}O$ dataset (B, black line) filtered by major periodicities at frequencies of 0.79, 1.97 and 4.5 cycles/m (A, C and D respectively). Gaussian filters are centered around major frequencies where the upper and lower frequency bounds are 1/3 above and below the centre frequency. Yellow vertical bars mark hyperthermal events P to U.*

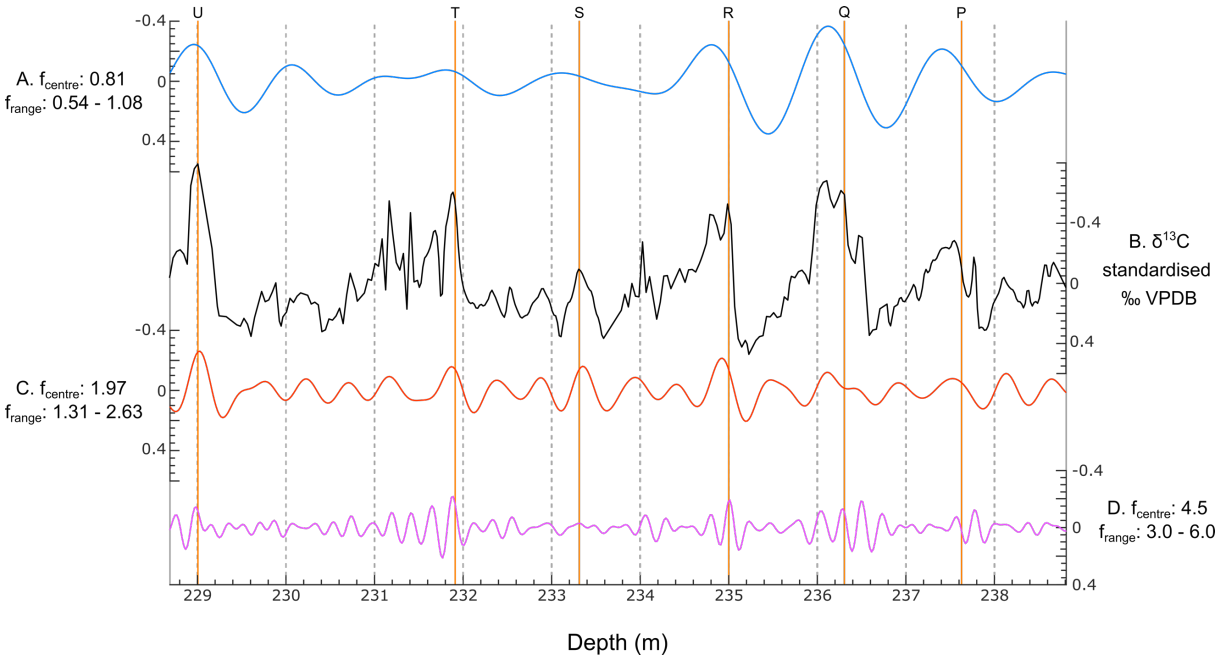


Figure 3.13 *De-trended and interpolated $\delta^{13}C$ dataset (B, black line) filtered by major periodicities at frequencies of 0.81, 1.97 and 4.5 cycles/m (A, C and D respectively). Gaussian filters are centered around major frequencies where the upper and lower frequency bounds are 1/3 above and below the centre frequency. Yellow vertical bars mark hyperthermal events P to U.*

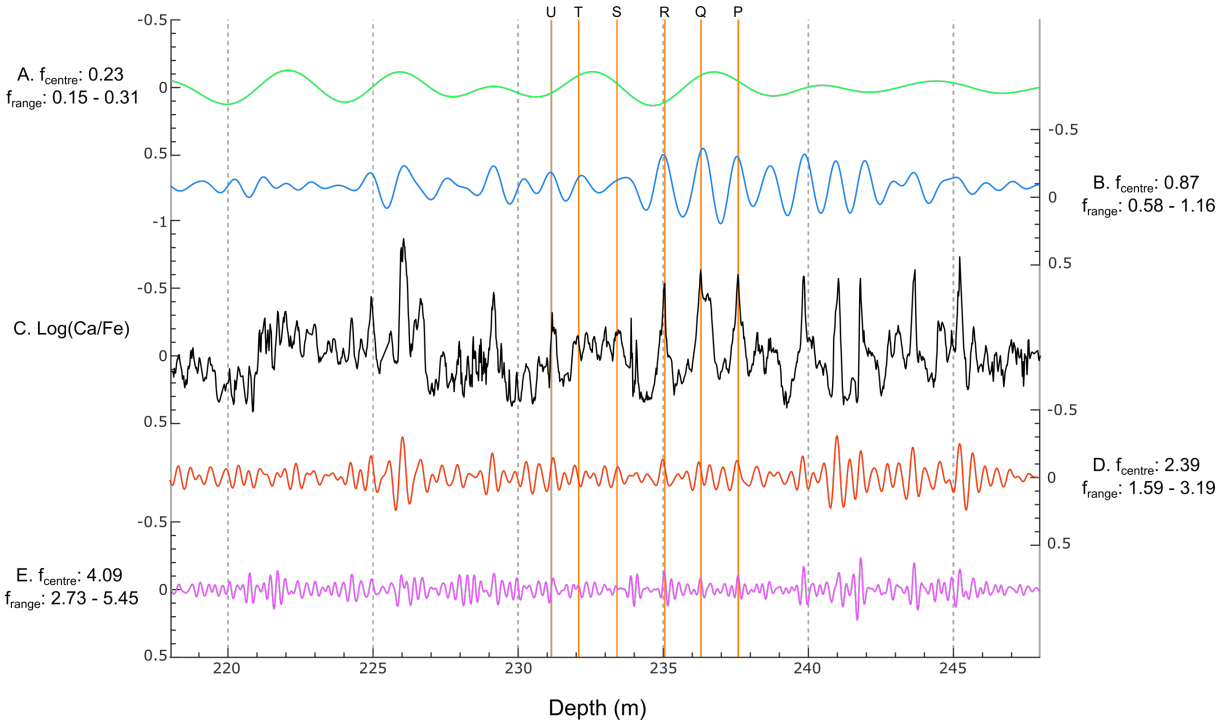


Figure 3.14 *De-trended and interpolated Log(Ca/Fe) dataset (C, black line) filtered by major periodicities at frequencies of 0.23, 0.87, 2.39 and 4.09 cycles/m (A, B, D and E respectively). Gaussian filters are centered around major frequencies where the upper and lower frequency bounds are 1/3 above and below the centre frequency. Yellow vertical bars mark hyperthermal events within the study interval, P to U.*

periodicity, between 4.09 – 4.5 cycles/m, showing the smallest amplitude of variability across the majority of the study interval.

3.4 DISCUSSION

3.4.1 Isotopic and lithologic signature of hyperthermals P – U in the Indian ocean

We have correlated events P to U across previously published bulk isotope and stable isotope records from Site 1209 in the northwest Pacific (Westerhold et al., 2018), Site 1258 in the equatorial Atlantic (Kirtland Turner et al., 2014) and Site 1263 in the southeast Atlantic (Lauretano et al., 2016; Westerhold et al., 2017) to compare the expression of these events (Fig. 3.6). Hyperthermal events at Site U514 are characterised by negative excursions in XRF

Ca/Fe, $\delta^{13}C$ and $\delta^{18}O$ (Fig. 3.4), consistent with previously published records of these events from other ocean basins (Kirtland Turner et al., 2014; Lauretano et al., 2016; Westerhold et al., 2017, 2018). Our records from the Indian Ocean confirm the global occurrence of these events, as well as the coupling of carbon cycling and bottom water temperatures throughout the EECO.

However, it is worth noting that the size, shape and apparent timing of hyperthermal excursions are not consistent between proxies and/or ocean basins. Methods used to identify hyperthermals also vary between publications. For example, hyperthermals have been defined variously as: (1) negative CIEs of 0.7–1.0 ‰ on a non-detrended benthic $\delta^{13}C$ record (Sexton et al., 2011), (2) CIEs more negative than one standard deviation below the mean of the detrended bulk $\delta^{13}C$ record (Kirtland Turner et al., 2014), (3) paired, coherent, negative CIEs and oxygen isotope excursions (OIEs) but with no reference to magnitude (Westerhold et al., 2017) and (4) abrupt negative Ca/Fe excursions in XRF records (e.g., Vahlenkamp et al., 2020). Based on our new records from Site U1514, hyperthermals P to U do not meet all of the above criteria. While all events are associated with a paired, coherent negative CIE and OIE, as mentioned in point (4) above, the CIE associated with the S event is less than one standard deviation below our detrended record (Supplementary Fig. 3.6), and the S and P CIEs are smaller than 0.7 ‰ (Table 1). This does not mean that these events do not represent global perturbations in the carbon cycle, but that hyperthermals are expressed differently depending on the ocean basin, proxy being analysed and, where standard deviation is taken into consideration, the length of the record making it difficult to provide a precise quantitative definition. To fully characterise the nature, spatial variation and magnitude of environmental change for individual hyperthermal events, high resolution records of XRF Ca/Fe, benthic $\delta^{13}C$ and $\delta^{18}O$ and other proxies from a wide global spread of sites are needed. Our new stable

isotope record from Site U1514 provides the first such record of hyperthermal events P to U from the Indian Ocean, contributing to this effort.

Close agreement in terms of overall pattern and values in benthic foraminiferal stable isotope records from the Indian, Atlantic and Pacific Oceans show that environmental change in these basins are closely coupled before 50 Ma (Sexton, Wilson, & Norris, 2006). However, the magnitude of hyperthermals varies between records. For events Q, R, T and U, Site U1514 shows the most negative $\delta^{13}C$ and $\delta^{18}O$ values at the peak of the event, as well as the largest hyperthermal CIE when compared to Sites 1209 (Pacific), 1258 and 1263 (Atlantic). Benthic foraminiferal stable isotope records from Sites 1209 (Pacific) and 1263 (Atlantic) were also generated using *N. truempyi,* so inter-basin variations are not the result of inter-species offsets (Supplementary Table 3.5). Site palaeowater depths indicate all are within the bathyal zone, ~ 1,500 m for Site 1263, 2,387 m for 1209 and >2,500 m for Site U1514. While $\delta^{13}C$ and $\delta^{18}O$ values across hyperthermal events differ between Sites U1514, 1263 and 1209, values between hyperthermal events are similar. Palaeowater depth is unlikely to account for differences between absolute values as this would show a consistent offset between sites across the entire record. However, palaeowater depth may account for differences in the magnitude of hyperthermals and the carbon and oxygen isotopic minima reached across events. The expression of a warming event in carbon isotope records can be influenced by the relationship between sedimentation rate and the depth of the CCD (McCarren et al., 2008). Sites that are above the local CCD with higher sedimentation rates can record an event in greater 'detail', producing larger excursions. Carbonate is consistently present at Site U1514 across the study interval, therefore this site is above the local CCD at this time. The average sedimentation rate across the study interval at Site U1514 is relatively low for the deep sea at 0.97 cm/ka. Sedimentation rates at Sites 1209 and 1263 are 0.64 and 1.21 cm/ka respectively

for the same interval (Lauretano et al., 2016; Westerhold et al., 2017, 2018). Thus, assuming average sedimentation rates are accurate across the study interval, they cannot explain why excursions at Site U1514 are slightly larger than recorded elsewhere. Despite low sedimentation rates, low resolution measurements of bulk carbonate $\delta^{13}C$ from Site U1514 (Supplementary Fig. 3.7, Edgar et al., 2022) are consistently more positive than benthic $\delta^{13}C$ values by ~1 - 1.5 ‰, indicating that surface productivity and the surface-deep $\delta^{13}C$ gradient is likely maintained throughout this interval.

For benthic foraminiferal $\delta^{18}O$, we compare our record with the previously published benthic $\delta^{18}O$ record from Site 1209 (Pacific). Stable oxygen isotope values are higher at Site U1514 than 1209 for events P, Q, T and U. Site 1209 has the lowest sedimentation rate across the study interval, which may account for smaller $\delta^{18}O$ excursions, especially as the differences between excursions from Site 1209 and Site U1514 are relatively small for all events apart from the U event, only ~0.1 – 0.2 ‰. Alternatively, the higher palaeolatitude of Site U1514 (~56 °S vs ~30 °N at Site 1209) may show a greater temperature change due to hyperthermal warming compared to sites at lower latitudes because of a heightened response of high latitudes to global warming events in the early Cenozoic. For example, mean surface air temperature during the PETM was higher than the pre-PETM background state by ~8 – 10 °C at high latitudes (above 60 °S and N), and ~4 – 6 °C at lower latitudes (Tierney et al., 2022). In contrast, the full record of XRF Ca/Fe for hyperthermal events at Site U1514 suggests that earlier hyperthermal events (E2 – L; ~55.5 – 52.5 Ma) show a weak expression compared to lower latitude Atlantic records (Vahlenkamp et al., 2020). Amplification of the later hyperthermals at Site U1514 may therefore be a more local phenomenon within the Indian Ocean. We do not have benthic $\delta^{13}C$ and $\delta^{18}O$ records for the full suite of hyperthermals from the Indian Ocean, so we cannot compare if earlier events E2 – L are also

larger than recorded elsewhere as with events P to U using benthic isotopes rather than Ca/Fe only.

The relationship between $\delta^{13}C$ and $\delta^{18}O$ remains consistently linear throughout the study interval (Fig. 3.5), indicating that climate and the carbon cycle remain tightly coupled across the build-up and recovery of each hyperthermal event between 50-51 Ma. However, there is variation among the slope of the linear relationship between $\delta^{13}C$ and $\delta^{18}O$ for individual hyperthermal events. The slope of linear regression lines between $\delta^{13}C$ and $\delta^{18}O$ has been used to infer differences in the forcing mechanism of hyperthermals, particularly in the isotopic signature of the carbon input to the atmosphere (Lauretano et al., 2015; Stap et al., 2010; Westerhold et al., 2018). At Site 1209 in the equatorial Pacific, events P, S and T show a flatter slope than other early Eocene hyperthermals (Westerhold et al., 2018). Assuming climate sensitivity is constant across the study interval, and no secondary controls on these records, one explanation for a change in the $\delta^{18}O - \delta^{13}C$ gradient is that the carbon source forcing these events is more isotopically depleted than for other hyperthermals (Lauretano et al., 2015; Westerhold et al., 2018). If this is the case, then the P, S and T events $\delta^{13}C$ and $\delta^{18}O$ excursions should show a flatter linear regression slope than other hyperthermal events globally. Our record from Site U1514 shows that this is not the case: events P and T do fit into this pattern, events Q and R have the same gradient as events P and T, and are much steeper than at Site 1209. Additionally, whilst the S event at Site 1209 can be grouped with the flatter-slope group, it shows a steeper $\delta^{13}C - \delta^{18}O$ relationship along with the U event at Site U1514. The isotopic composition of carbon input to the atmosphere may play a role, particularly in the case of larger hyperthermal events such as the PETM and ETM2 (Lauretano et al., 2015; Westerhold et al., 2018) however it cannot explain variations in individual events between different ocean basins. The size of carbon isotope excursions is

also not consistent with linear regression patterns, where our steeper hyperthermals, S and U, represent both the smallest and largest excursions in our record. $\delta^{13}C$ is a complicated proxy to interpret, as it is influenced by multiple parameters, including biological productivity, ocean circulation, atmospheric composition, and sea level variations (Mackensen & Schmiedl, 2019). Our comparison shows that the isotopic expression of hyperthermals, both in terms of absolute magnitudes and relative $\delta^{13}C$ – $\delta^{18}O$ relationships, is site-specific and that variations are unlikely to be explained by the source of atmospheric carbon alone. Variability in the CIE shape between different records and events has been observed for early Eocene hyperthermals before, particularly in the case of the PETM, where the character of the CIE in records varies widely depending on location, proxy and sedimentary environment (McCarren et al., 2008; McInerney & Wing, 2011; Zachos et al., 2005). Our study interval is also within a period characterised by high amplitude climate fluctuations with large fluctuations in deep sea temperatures and shifts in terrestrial environmental conditions (Hyland & Sheldon, 2013; Westerhold et al., 2018). Inconsistencies in the expression of hyperthermal events across ocean basins may thus represent further instability in the global climate system across peak temperatures of the EECO, before global temperatures begin to decline.

Estimates of deep ocean temperatures from Site U1514 benthic $\delta^{18}O$ values in the southeast Indian Ocean vary between 12.5 – 17.5 °C across the study interval (Fig. 3.4). At first glance, this seems high for bottom water temperatures at high latitudes relative to today (~ -1 – 4 °C), however it is within the range of other ice-free temperature estimations from benthic foraminiferal $\delta^{18}O$ across the EECO, e.g., ~12 – 16 °C between 54 – 52 Ma in the South Atlantic Ocean (Site 1262, Barnet et al., 2019), and a new independent record from clumped stable oxygen isotopes, which estimates deep ocean temperatures from ~15 to 21 °C between 52 – 49 Ma, albeit at low temporal resolution (Meckler et al., 2022). Similarly, the

CENOGRID global benthic stable isotope compilation puts temperatures across the EECO at ~12 – 16 °C higher than modern (Westerhold et al., 2020), reaching peak temperatures ~16 °C higher than modern briefly at the peak of hyperthermal events. Hyperthermal events cause bottom water warming of at least ~1.5 °C (S event), up to ~4.5 °C (U event) at Site U1514 (Fig. 3.4). Bottom water temperature change across hyperthermals is therefore relatively consistent across ocean basins, further supporting the global nature of hyperthermal warming and the overarching orbital control on hyperthermal events.

3.4.2 Orbital characteristics of the early Eocene and forcing of hyperthermal events

Previous studies of the relationships between early Eocene hyperthermals and astronomical cycles from multiple ocean basins have demonstrated that they are dominantly paced by the long (405 kyr) and short (100 kyr) eccentricity cycles (Cramer et al., 2003; Galeotti et al., 2010; Kirtland Turner et al., 2014; Lauretano et al., 2015, 2016; Littler et al., 2014; Lourens et al., 2005; Sexton et al., 2011; Westerhold et al., 2017; Zachos et al., 2010). This pacing appears consistent throughout the early Eocene, despite variations in the magnitude and expression of individual events. At Site U1514, evolutive and wavelet spectra of $\delta^{13}C$, $\delta^{18}O$ and XRF Ca/Fe show spectral peaks in frequencies that can be linked confidently to eccentricity cycles. A strong peak in spectral power at 0.80 – 0.82 cycles/m is present in all three proxies, equating to a period of 1.22 – 1.25 m which is the dominant periodicity controlling hyperthermal cycles across this interval. When converted to time using the average sedimentation rate across the interval, this gives a periodicity of 126 – 129 kyr, close to the ~100 kyr periodicity of the short eccentricity cycle. Hyperthermals in the Indian Ocean therefore follow the established pattern (Cramer et al., 2003; Galeotti et al., 2010; Kirtland Turner et al., 2014; Lauretano et al., 2015, 2016; Littler et al., 2014; Lourens et al., 2005;

Sexton et al., 2011; Westerhold et al., 2017; Zachos et al., 2010) and are paced dominantly by the short eccentricity cycle. This is further confirmed when our records are filtered, as the greatest amplitude of variability is seen in the records filtered by the 0.79 – 0.81 cycles/m frequency (Figs. 3.12 – 3.14). Our $\delta^{13}C$ and $\delta^{18}O$ records are too short to resolve any influence of the long eccentricity cycle (~405 kyrs), however the longer XRF Ca/Fe record shows the influence of an additional periodicity of 5 m. This is equal to a cycle length of ~500 kyr and likely represents the imprint of long eccentricity. The 23 kyr precession cycle is also present in our dataset. Peaks in spectral power at 4.0 – 4.5 cycles/m occur in all three proxies, which equates to a periodicity of 0.22 – 0.25 m, or 23 – 26 kyr. Filters show that the strongest precessional cycles occur at eccentricity maxima (Fig. 3.12 – 3.14). This is due to the eccentricity modulation of precession, and provides further evidence that the frequencies in our datasets can be tied to orbital periodicities.

The periodicities described above are consistently longer than typical for eccentricity and precession. This is most likely caused by an underestimation of sedimentation rate across our study interval due to carbonate dissolution across hyperthermals truncating the record. If this is the case, disagreement between our estimated average sedimentation rate and the true sedimentation rate will be greater for larger intervals, and hence we see a greater offset between longer orbital periodicities and their typical values. For example, we find a periodicity of 23 – 26 kyr for precession (typically 23 kyr) vs. ~500 kyr for long eccentricity (typically 405 kyr). The hierarchy of periodicities in our dataset is consistent with the established hierarchy of precession and eccentricity, so we are confident in linking these cycles to spectral peaks at Site U1514. Although an astronomically tuned age model for Site U1514 exists (Vahlenkamp et al., 2020) and may improve the match between periodicities in

our dataset and orbital periodicities, we do not perform time series analysis initially on the tuned dataset to avoid introducing power into certain orbital frequencies artificially.

Benthic foraminiferal $\delta^{13}C$ and $\delta^{18}O$ records at Site U1514 both show a strong peak in spectral power at 1.97 cycles/m, at a period of 0.51 m or 53 kyr. Ca/Fe shows a number of peaks ranging from 1.64 – 2.38 cycles/m, at a period of 0.42 – 0.61 m or 43 – 63 kyr. Though eccentricity dominates across this interval, these peaks may indicate some influence of the 41 kyr obliquity cycle on the Eocene Indian Ocean. As with our eccentricity and precession frequencies, this periodicity is longer than expected for a perfect obliquity cycle, however its relationship with other periodicities is consistent with the hierarchy of eccentricity, obliquity and precession. Though obliquity signals are usually more strongly expressed in high latitude records during intervals when the world is glaciated due to the high sensitivity of ice sheets to orbital forcing (Mantsis et al., 2011) the impact of obliquity is typically thought to be minor in an ice-free world (Littler et al., 2014). Indeed, many high-resolution (~5 kyrs) climate records for the early Eocene typically show weak expression of obliquity in Ca/Fe and stable isotope records, e.g. Shatsky Rise in the northwest Pacific and Walvis Ridge in the south Alantic (Barnet et al., 2019; Lauretano et al., 2015, 2016; Littler et al., 2014) but strong obliquity cycles are documented in the late Palaeocene-early Eocene (50.1 – 59.4 Ma) at Site 1258, equatorial Atlantic Ocean (Westerhold & Röhl, 2009). However, the wide range of obliquity-scale frequencies (between 43 – 63 kyr) in Ca/Fe at this site may actually imply that obliquity overall has a relatively weak influence on climate at this time. Hence, there remains some ambiguity. The influence of obliquity is strongest in our $\delta^{18}O$ records, rather than $\delta^{13}C$ records, but is inconsistent through time, occurring at 50.58 Ma and at the base of our record, at 51 Ma. This indicates only transient periods of high latitude insolation forcing on Indian Ocean climate. One interpretation of this record is that it may be linked to the presence of

early, small-scale ephemeral ice sheets in Antarctica (e.g. DeConto & Pollard, 2003; Miller et al., 2005). However, as previously mentioned, high latitudes are assumed to be ice-free throughout the early Eocene and bottom water temperatures were very warm globally, ~15 – 20 °C (Barnet et al., 2019; Meckler et al., 2022; Westerhold et al., 2020), which might preclude ice from the equation given that bottom waters form at high latitudes through downwelling of surface waters. Notably, at Site U1514 the obliquity signal is strongest where bottom water temperatures are at their lowest in the record (< ~15 °C; Fig. 3.4) which might support the presence of minor high latitude ice in these relatively cool periods. Alternatively, climate modelling results show that obliquity can induce climate change even at low latitudes without invoking ice-sheet dynamics, via changes in the solar insolation gradient and its effect on seasonality, for example changing monsoon cycle strength (Bosmans, Drijfhout, et al., 2015; Bosmans, Hilgen, et al., 2015). Monsoon-like rainfall patterns in mainland Asia, continental Antarctica and continental Australia have been identified in fossil and geochemical records for the Eocene (Jacques et al., 2014; Licht et al., 2014; Spicer et al., 2016). Modelling studies of early Eocene climate also support the presence of an Australian monsoon (Carmichael et al., 2016; Huber & Goldner; 2012). Further study of astronomical forcing of seasonal monsoon patterns over continental Australia in the early Eocene is needed to identify the role of obliquity cycle variations in Site U1514 records.

To identify whether variations in hyperthermal magnitude coincide with variations in Earth's orbital parameters, we used the astronomically tuned age model from Vahlenkamp et al. (2020) to compare the timing of our hyperthermals to the La2010c eccentricity solution (Fig. 3.15). Events P, Q, R and T, with flatter $\delta^{13}C - \delta^{18}O$ linear regression slopes, do not have a consistent relationship with eccentricity. This suggests that, while orbital conditions have an influence on the timing of hyperthermals, it does not fully explain their magnitude

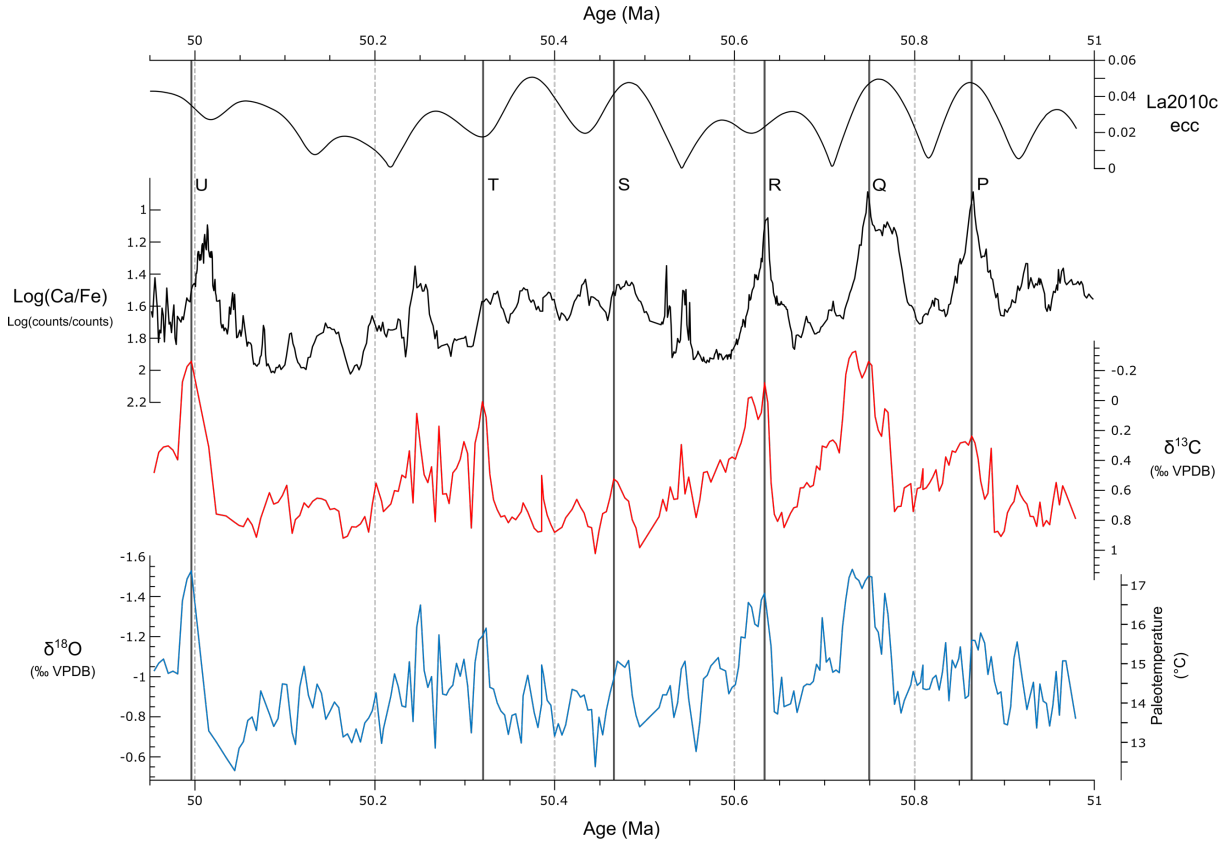


Figure 3.15 *Stable isotope and Ca/Fe results from Site U1514 on the astronomically tuned age model from Vahlenkamp et al., 2020 alongside the La2010c eccentricity solution (Laskar et al., 2011).*

and expression, and that site-specific parameters, such as ocean circulation, water depth, sedimentation rate and productivity must also play a role. In benthic stable isotope records from South Atlantic ODP Site 1262 across the latest Palaeocene, 405-kyr paced cycles show 2 – 4 °C temperature change in bottom waters, while 100-kyr paced cycles show temperature change of 1.5 °C (Littler et al., 2014). Our documented warming of 1.5 – 4.5 °C agrees with the magnitude of temperature change in the latest Palaeocene, however our records do not show any consistent relationship between hyperthermal magnitude and orbital conditions.

3.4.3 Phasing between environmental records

Our records show high coherence and a positive, stable phase relationship between benthic foraminiferal $\delta^{13}C$ and $\delta^{18}O$ values. While benthic stable isotopes are generally thought to be less susceptible to post-depositional diagenetic alteration than their planktic counterparts

(Edgar et al., 2013), long-term alteration processes may still affect benthic foraminiferal stable isotopes, particularly $\delta^{18}O$ (Bernard et al., 2017). However, based on the strength of the linear relationship between $\delta^{13}C$ and $\delta^{18}O$, along with the high coherence over our ~1 Ma timescale, the relationship here is more likely to show tight coupling of climate and the carbon cycle through hyperthermal variation. High coherence between $\delta^{13}C$ and $\delta^{18}O$ at eccentricity frequencies in particular suggests an almost instantaneous temperature response to carbon-cycle changes, induced by orbital forcing. The close link between temperature and the carbon cycle is not unique to Site U1514 and high coherence between the $\delta^{13}C$ and $\delta^{18}O$ response across hyperthermals has been observed in other records of early Eocene hyperthermals (Cramer et al., 2003; Kirtland Turner, 2014; Kirtland Turner et al., 2014). Our results suggest only a minor lag of $\delta^{13}C$ behind $\delta^{18}O$ of <1 kyr, however as this is smaller than our sampling resolution (~ 4kyrs), this is not resolvable with our dataset and additional measurements at higher resolution would be needed to confirm this. A lag of ~3 – 23 kyr between benthic $\delta^{13}C$ and benthic $\delta^{18}O$ at eccentricity frequencies is documented in records the Late Cretaceous – early Paleogene from the Atlantic Ocean (Barnet et al., 2019). In our study interval, a lag between $\delta^{13}C$ and $\delta^{18}O$ suggests that orbital changes induced an initial climatic warming response, and fast-acting positive feedbacks from temperature-sensitive carbon reservoirs further amplified warming (e.g. DeConto et al., 2012; Zachos et al., 2010) leading to repeated hyperthermal events.

Coherence between Ca/Fe and stable isotopes is also relatively high at Site U1514 within the eccentricity and obliquity frequencies. Coherence is greater between $\delta^{13}C$ and Ca/Fe than $\delta^{18}O$, which is likely because Ca/Fe patterns are caused by carbonate dissolution, and therefore records primarily a carbon cycle signal, as opposed to the temperature signal recorded by $\delta^{18}O$. The phase relationship for $\delta^{13}C$ and $\delta^{18}O$ relative to Ca/Fe is negative for

both eccentricity and obliquity. While consistent phase relationships between these stable isotopes and Ca/Fe occur in the early pre-EECO Eocene, published records from the EECO itself suggest inconsistent phasing and decoupling of the lithological response evidenced by Ca/Fe from the isotopic response (Lauretano et al., 2016; Westerhold & Röhl, 2009). Our record shows that in the Indian Ocean, at eccentricity and obliquity frequencies, a negative phase relationship between isotopes and Ca/Fe persists across at least the latest portion of the EECO.

CIE's and OIE's linked to hyperthermal events in benthic foraminiferal isotope records lag behind XRF Ca/Fe excursions by ~0.09 m, equivalent to ~10 kyr based on the U1514 age model. This lag, while small in the context of the total study interval length (~10 m or 1 Myr), is considered significant as is it ~2x the sampling resolution, ~4 cm. OIE's may lag Ca/Fe excursions because carbon cycle perturbations precede temperature change. However, this does not explain the similar lag seen of $\delta^{13}C$ behind Ca/Fe. Marine records from the Cretaceous (Batenburg et al., 2012), Oligocene-Miocene (Pälike et al., 2006) and Palaeocene (Westerhold et al., 2011) show a lag of $\delta^{13}C$ behind Ca/Fe, which may reflect a more rapid response of the Ca/Fe proxy to environmental change, as this proxy dominantly reflects changing local lithological conditions as opposed to changes in the global carbon cycle (Batenburg et al., 2012). However, in the above cases, the lag time is on the order of 35 – 60 kyrs and is usually identified with respect to the 405-kyr eccentricity cycle (Batenburg et al., 2012; Pälike et al., 2006; Westerhold et al., 2011).

The relatively small-scale lag of $\delta^{13}C$ behind Ca/Fe in our records may be instead related to carbonate dissolution or 'burndown' (e.g. Bralower et al., 2014; Dickens et al., 1997). Large input of isotopically light CO_2 or CH_4 to the atmosphere during hyperthermal events leads to CCD and lysocline shoaling and carbonate dissolution in deep ocean sediments

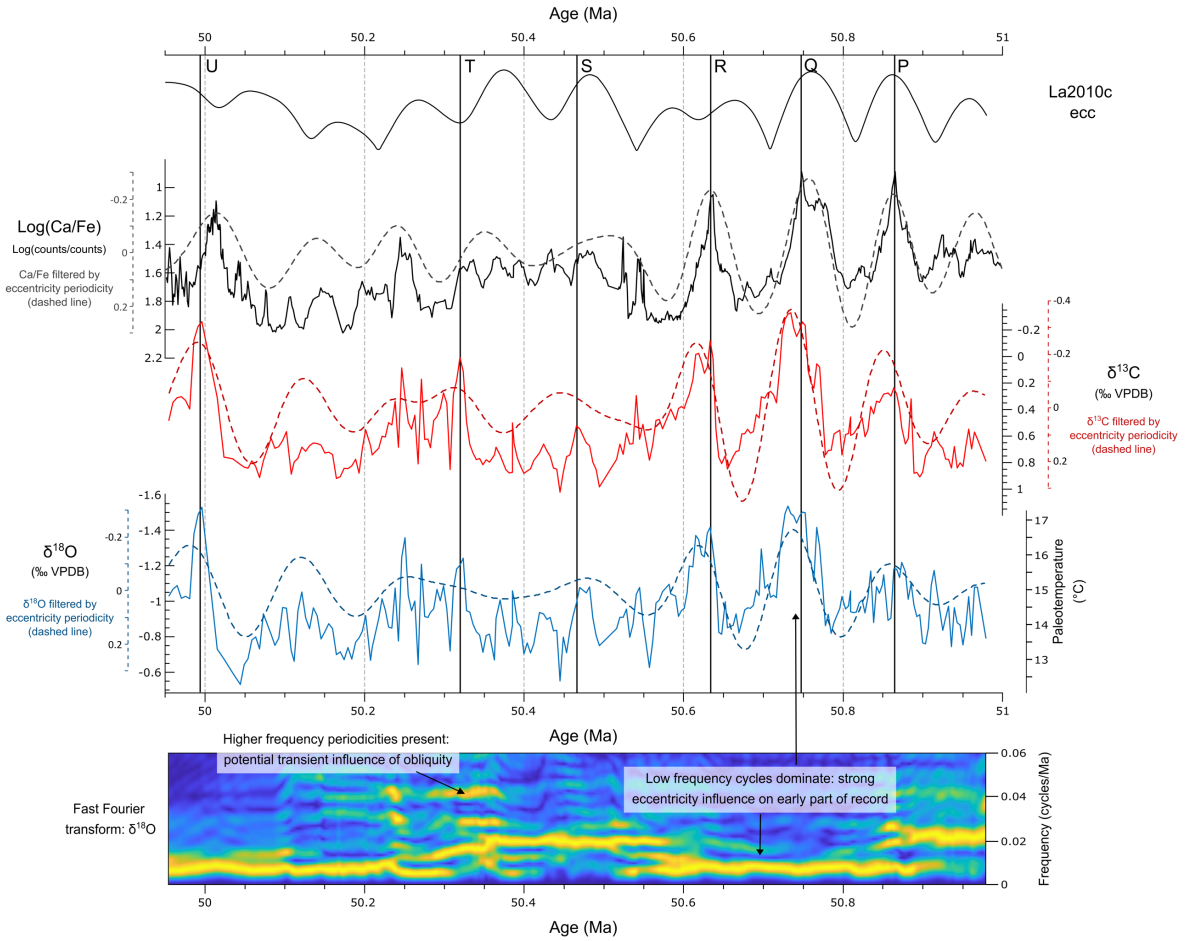


Figure 3.16 *Summary of new datasets presented in this chapter and key time series analysis results, on the astronomically tuned age model from Vahlenkamp et al. (2020). From top to bottom: La2010c eccentricity solution (Laskar et al., 2011), XRF Ca/Fe record from Site U1514 (black) with XRF Ca/Fe record filtered by eccentricity periodicity (dashed line), benthic foraminiferal $\delta^{13}C$ record from Site U1514 (red) with benthic $\delta^{13}C$ record filtered by eccentricity periodicity (dashed line), benthic foraminiferal $\delta^{18}O$ record from Site U1514 (blue) with benthic $\delta^{18}O$ record filtered by eccentricity periodicity (dashed line), evolutive spectrum of benthic $\delta^{18}O$ record from Site U1514 (high power at frequencies represented in yellow, low power in blue) with key transitions in frequencies labelled.*

(DeConto et al., 2012; Dickens et al., 1995; Kirtland Turner et al., 2014; McInerney & Wing, 2011; Zachos et al., 2005). As carbonate is never fully absent from sediments across the study interval, Site U1514 likely remains above the CCD throughout despite shoaling during the hyperthermals. However, there is a reduction in sedimentary carbonate content over hyperthermal events evidenced by reduced XRF Ca/Fe at Site U1514 (Fig. 3.4). Carbonate 'burndown' occurs when carbonate dissolution propagates below the seafloor into the top few

centimetres of sediment (Bralower et al., 2014; Dickens et al., 1997). It is usually invoked when interpreting the sedimentary history of the PETM, where intense carbonate dissolution can condense the chemical expression of the event in sediments and lead to offsets between the stable isotope and sedimentological signals of the event (e.g. Murphy et al., 2010). In the case of the PETM, the first and largest of the early Eocene hyperthermals, records from the southeast Atlantic and Southern Ocean show the $CaCO_3$ wt % minimum occurs earlier (~40 kyrs) than the minimum in bulk $\delta^{13}C$ (Röhl et al., 2007; Zachos et al., 2005). For a smaller hyperthermal event with less extreme carbonate dissolution, the offset between $\delta^{13}C$ and carbonate content is likely to be much smaller, as is the case at Site U1514, where the lag is equivalent to ~10 kyr. The lag between isotopes and Ca/Fe at Site U1514 is therefore unlikely to be a true time lag between climatic and lithological responses to hyperthermal event warming. Instead, it is the effect of carbonate burndown, where $CaCO_3$ content is decreased below the horizon of the event. However, our record does not show how the 405-kyr eccentricity cycle influences benthic isotopes.

3.4 CONCLUSIONS AND AVENUES FOR FUTURE WORK

In this study, we created a new, high resolution benthic foraminiferal stable $\delta^{13}C$ and $\delta^{18}O$ records between ~50 – 51 Ma from IODP Site U1514 in the high latitude Indian Ocean, documenting hyperthermal events P to U in this ocean basin for the first time. This record provides new evidence for environmental change, including perturbation of the global carbon cycle, dissolution and deep ocean warming of up to ~4 °C across these relatively understudied hyperthermal events. We document the influence of the long and short eccentricity cycles on our datasets, confirming the global nature of orbital climate variations in the early Eocene

(Barnet et al., 2019; Cramer et al., 2003; Galeotti et al., 2010; Kirtland Turner et al., 2014; Littler et al., 2014; Lourens et al., 2005; Westerhold et al., 2018; Zachos et al., 2010).

In particular, we show that whilst the timing of hyperthermal events is controlled by the 100-kyr eccentricity cycle, their relative magnitude cannot be tied to any particular orbital condition. We also identify the imprint of obliquity on these high latitude records at a time when the planet is generally considered free from Antarctic ice sheets. Despite the lack of ice sheets, processes driven by high latitudes were able to influence environmental change in the Indian Ocean across the EECO. Close coupling of global deep ocean temperature change and the carbon cycle across our study interval suggests that carbon is released from a reservoir that responds very quickly to initial orbital forcing across hyperthermals. We recommend that future studies of early Eocene hyperthermals define events using the paired, coherent negative excursions in $\delta^{13}C$ and $\delta^{18}O$ where possible, as other definitions (e.g. Kirtland Turner et al., 2014; Sexton et al., 2011) do not necessarily hold up between different ocean basins or proxies.

Our isotopic records show that hyperthermal expression in the Indian Ocean varies from the Atlantic and Pacific Oceans, both in terms of event magnitude and $\delta^{13}C - \delta^{18}O$ relationships. To improve our understanding of the relationship between isotopic records and the many parameters that influence proxies, including latitude, depth, sedimentation rate, ocean circulation rate and orbital configuration, our record of Indian Ocean hyperthermals needs to be extended back to at least the PETM to provide a record across a wider range of events. New records of later, less well-studied hyperthermals from other ocean basins, including events P – U, would allow us to identify how closely patterns seen in our records reflect the global case. Additionally, a longer stable isotope record may show the imprint of the 405-kyr eccentricity cycle and potentially the 2.4-Myr component. This would add to our

understanding of the overall astronomical effect on hyperthermals and early Eocene climate evolution and contribute to evidence that the global carbon cycle lags behind environmental change recorded by Ca/Fe at longer periodicities. We could also employ additional sedimentological techniques at Site U1514 such as grain size analysis, to provide further evidence of carbonate burndown and quantify the extent to which it is occurring here (e.g. Bralower et al., 2014).

The current astronomical age model for Site U1514 is based on tuning to the 405-kyr eccentricity cycle (Vahlenkamp et al., 2020). The resolution of the existing astronomical age model could be improved between 50-51 Ma by tuning to the 100-kyr eccentricity cycle as well. This interval is at the ~50 Ma limit for application of current astronomical solutions, beyond which the precision of solution declines and behaviour of solutions becomes chaotic (Laskar et al., 2011). Comparing geochemical data with orbital solutions can help constrain orbital behaviour beyond this limit. The impact of this strategy is likely to be minor between 50 – 51 Ma, where the difference between published solutions is relatively minor, but an extended record of hyperthermals from Site U1514 could allow us to improve the precision of orbital reconstructions back to the beginning of the Eocene at ~56 Ma.

CHAPTER 4: PROXY CONSTRAINTS ON SEA SURFACE TEMPERATURE EVOLUTION ACROSS THE MIDDLE EOCENE CLIMATIC OPTIMUM

4.1 INTRODUCTION

Middle to late Eocene climate is characterised by a long-term cooling trend, beginning at the end of the Early Eocene Climatic Optimum (EECO, ~49 – 53 Ma) and culminating with the rapid expansion of continental ice-sheets on Antarctica at the Eocene-Oligocene boundary, ~34 Ma (Westerhold et al., 2020; Zachos et al., 2001). The Middle Eocene Climatic Optimum (MECO, Fig. 4.1) is a transient global warming event that occurred at ~40 Ma, interrupting long-term Eocene cooling (Bohaty et al., 2009; Bohaty & Zachos, 2003; Boscolo Galazzo et al., 2014; Cramwinckel et al., 2018; Cramwinckel, Woelders, et al., 2020; Edgar et al., 2010; Giorgioni et al., 2019; Rivero-Cuesta et al., 2019). The MECO is observed in geochemical records from multiple sites globally, and is primarily identified by a negative excursion of ~0.5 – 1.0 ‰ in benthic foraminiferal and bulk oxygen stable isotope records (Bohaty et al., 2009; Boscolo Galazzo et al., 2014; Edgar et al., 2010, 2020; Rivero-Cuesta et al., 2019). This distinctive oxygen isotope signal suggests gradual bottom water warming of up to ~3 – 6 °C (Bijl et al., 2010; Bohaty et al., 2009; Cramwinckel et al., 2018; Rivero-Cuesta et al., 2019) occurring over 400 – 700 kyr (Bohaty & Zachos, 2003; Boscolo Galazzo et al., 2014; Edgar et al., 2020). The peak of the MECO is associated with a small negative stable carbon isotope excursion (CIE) of <0.5 ‰ superimposed on a gradual long-term trend of rising $\delta^{13}C$ values through the event (Bohaty & Zachos, 2003; Henehan et al., 2020). The magnitude and timing of the CIE associated with the MECO varies widely with site location (Bohaty et al., 2009; Boscolo Galazzo et al., 2014). In contrast to the muted $\delta^{13}C$ signal, in

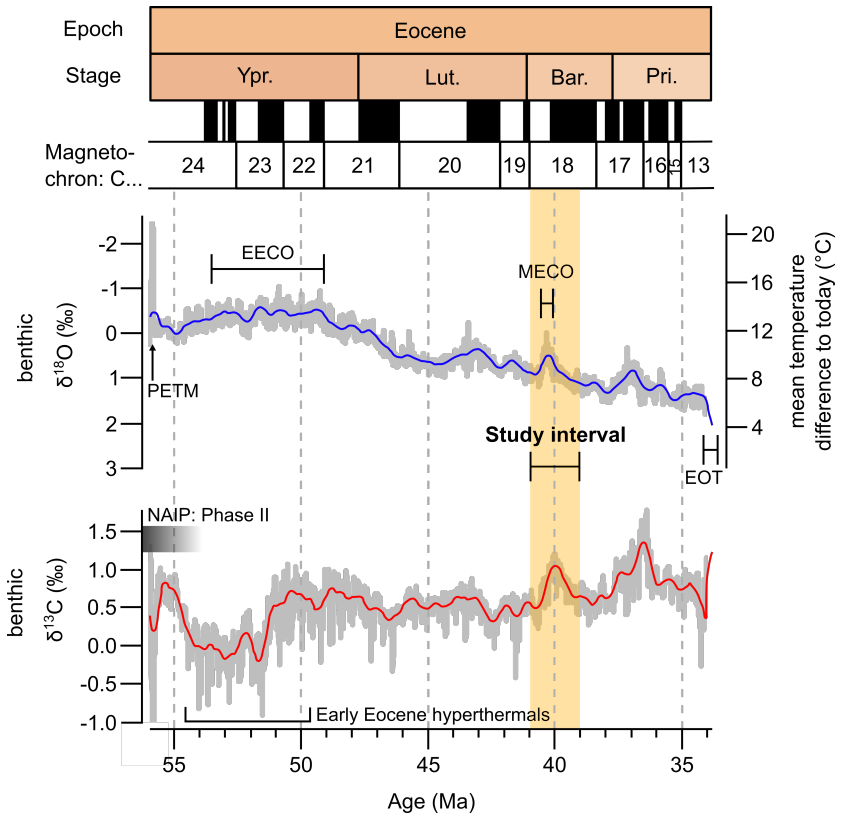


Figure 4.1 *Eocene section of the Cenozoic Global Reference benthic foraminiferal carbon and oxygen Isotope Dataset (CENOGRID, Westerhold et al., 2020) showing the 20 kyr (grey) and 1 Myr smoothed composite benthic $\delta^{18}O$ record (blue) and benthic $\delta^{13}C$ record (red) alongside relevant climatic events for the Eocene and oxygen isotope temperature conversion, relative to today. Our study interval is highlighted in the yellow bar. Figure modified from Fig. 1, Westerhold et al. (2020). Climatic event labels: Early Eocene Climatic Optimum (EECO), Paleocene-Eocene Thermal Maximum (PETM), North Atlantic Igneous Province (NAIP), Middle Eocene Climatic Optimum (MECO), Eocene/Oligocene Transition (EOT).*

many records of the MECO there is evidence for CCD shoaling by >1 km indicating deep ocean acidification across the event and a significant perturbation to the global carbon cycle (Bohaty et al., 2009; Edgar et al., 2020; Henehan et al., 2020; Pälike et al., 2012). A transient rise in atmospheric pCO_2 has also been identified across the event (Bijl et al., 2010; Pälike et al., 2012), with boron isotope evidence suggesting that pCO_2 rose from pre-MECO levels of ~550 µatm to peak at ~870 µatm across the peak of the MECO (Henehan et al., 2020). The MECO is distinct from other early Eocene warming events such as the Palaeocene Eocene Thermal Maximum (PETM, ~55.5 Ma) and early Eocene hyperthermals (between ~49 – 55 Ma) as it represents a more sustained warming over ~400 – 700 kyrs, with an asymmetrical

character in geochemical records indicating gradual onset of warming, and an abrupt recovery from peak warmth to pre-MECO values (Bohaty et al., 2009).

Significant unknowns remain surrounding the causes of the MECO. While increased atmospheric pCO_2 likely played a role in MECO warming (Bijl et al., 2010; Henehan et al., 2020; Pälike et al., 2012), the small and inconsistent expression of the MECO in benthic foraminiferal stable carbon isotope records suggests that unlike the PETM and other early Eocene hyperthermals, MECO warming is not linked to input of CO_2 into the atmosphere from an isotopically light source, e.g. dissociation of methane hydrates (Bohaty et al., 2009; Dickens et al., 1995; Westerhold et al., 2018). The most viable potential carbon source at present may be volcanism (Bohaty et al., 2009). In particular, the MECO may be related to an increase in continental arc volcanism in the Azerbaijan–Bazman Arc in Iran, associated with the Neotethys subduction zone (van der Boon et al., 2021). Argon dating of volcanic rocks show an increase in activity ~40 Ma, however more precise dating is still needed to conclusively link this event with the MECO (van der Boon et al., 2021). MECO warming may also have had an orbital component, as it has been tied to the 2.4 Myr (very long) eccentricity cycle (Westerhold & Röhl, 2013).

Several problems complicate studies of middle Eocene climate and the environmental impact of the MECO. Firstly, global carbon cycle dynamics across the MECO are not fully understood. Geochemical records of the MECO have raised the 'middle Eocene carbon cycle conundrum', whereby the silicate weathering feedback should have kept pace with the gradual nature of climate change at the onset of the MECO, leading to CCD deepening and increased carbonate burial (Sluijs et al., 2013). However, CCD shoaling and carbonate dissolution is observed (Bohaty et al., 2009; Edgar et al., 2020; Henehan et al., 2020; Pälike et al., 2012). Osmium isotope records suggest that the strength of the silicate weathering

feedback was reduced over the middle Eocene due to the warm, greenhouse climate of the early Eocene and reduced weatherability of the earth's surface (Kump et al., 2000; van der Ploeg et al., 2018). The MECO could therefore have been forced by a comparatively minor increase in atmospheric pCO_2, and a suppressed silicate weathering feedback would not have been able to buffer the change. Alternatively, pCO_2 release may have occurred via a short, <10 kyr-long pulse, outpacing the silicate weathering feedback and leading to CCD shoaling and dissolution (Henehan et al., 2020). Characterisation of the scale of MECO climate change is also hindered by uncertainty in middle Eocene global ice volumes, a powerful climate feedback. Whilst there is not compelling evidence for large volumes of continental ice until the Eocene-Oligocene Transition, ~34 Ma, several studies suggest that small ice volumes may have existed on Antarctica and/or the Arctic in the middle Eocene (Browning et al., 1996; Cramer et al., 2011; Dawber & Tripati, 2011; Stickley et al., 2009; Tripati & Darby, 2018; Tripati et al., 2008). However, the magnitude of this ice, and thus any impact on geochemical records, remains highly uncertain (Cramer et al., 2011; Rohling et al., 2021). Poor constraints on middle Eocene ice volume introduces uncertainty to absolute palaeotemperature estimations and relative changes in the middle Eocene derived from the widely used carbonate $\delta^{18}O$ proxy via the assumption of the $\delta^{18}O_{sw}$ parameter.

The MECO represents a period of sustained global warming at a time when background pCO_2 levels were high (~1,000 ppm, Rae et al., 2021) that is still associated with many unanswered questions. To fully characterise the role of pCO_2, i.e. earth system sensitivity, and associated feedbacks in forcing MECO warming, a full assessment of the magnitude of warming across a wide range of latitudes, environments and proxies is needed. The geographic variation of warming is not usually considered in studies which often focus on generating new records for a single site (e.g. Cramwinckel et al., 2022) or compare a small

spread of sites (e.g. Edgar et al., 2013). Additionally, comparing published assessments of climate events introduces additional uncertainty where records are published on different age scales or use different proxy-temperature calibration methods. Thus, compilations of palaeoclimate data, where records are analysed on a single age model and with consistent methods, are highly valuable for assessment of past latitudinal thermal gradients and latitudinal variations in warming. This contributes to our understanding of important earth system parameters, including the magnitude of polar amplification and past climate sensitivity, which are vital for informing climate models (Haywood et al., 2013; Hollis et al., 2019; Lunt et al., 2012) as well as understanding impacts of regional versus global drivers of environmental and ecological change. To this end, there have been many Eocene temperature compilations comparing marine and/or terrestrial geochemical data. For example, Dunkley Jones et al. (2013) compiled and synthesised benthic and planktic foraminiferal $\delta^{18}O$ and Mg/Ca SST records alongside organic lipid biomarker palaeothermometry from 16 sites across the PETM to constrain the geographical pattern of ocean warming, identify inter-proxy variation, and compare with global climate model (GCM) simulation results to better constrain PETM warming. Evans et al. (2018) combine new clumped isotope and Mg/Ca palaeotemperature estimates with previously published data from 22 sites globally to analyse sea surface temperature evolution with latitude across the entire Eocene to quantify the magnitude of Eocene polar amplification. As part of the Deep-Time Model Intercomparison Project (DeepMIP), Hollis et al. (2019) present an initial compilation of available marine surface temperature records from three time slices, including data from 27 sites across the PETM and 16 sites across the EECO, and combine these with estimates of land air temperatures and atmospheric pCO_2 reconstructions to inform future climate modelling studies. Data from this compilation has been recently utilised to re-assess the geographic

variation of PETM warming and hydrological cycles (Tierney et al., 2022). Overall, proxy data compilations have many advantages and high potential for re-use, improving our understanding of deep time climate evolution.

The aim of this study is to generate the first such compilation of available sea surface temperature records across the enigmatic MECO event. We combine oxygen stable isotope ($\delta^{18}O$) and Mg/Ca palaeothermometry from planktic foraminifera with organic lipid biomarker (TEX_{86}) palaeothermometry collected over the past 15 years. We apply consistent methodologies for identification of the MECO and palaeotemperature calculation with all data placed on a common timescale (GTS2012). This allows us to: [1] assess the sensitivity of palaeotemperature estimates to different calibration methods and inter-proxy sea surface temperature (SST) variability, [2] assess SST change across the MECO at individual sites, [3] generate a more complete picture of geographic variation in MECO surface ocean warming and the nature and evolution of the latitudinal temperature gradient at ~40 Ma.

4.2 MATERIALS AND METHODS

4.2.1 Site selection and data collection

We compiled published sea surface temperature proxy records (planktic foraminiferal $\delta^{18}O$ and Mg/Ca, and TEX_{86}) spanning ~42 – 38 Ma, including the MECO event. These records are from 17 DSDP, ODP and IODP sites, as well as marine sediments from land sections. A summary of sites referenced in this compilation, along with their references, modern locations, palaeolocations, depths and proxy data collected from these sites is presented in Table 4.1. Palaeolongitudes and palaeolatitudes for all sites were determined using the GPlates Web Service (Müller et al., 2018) and the mantle reference frame plate motion model

Site name/number	Datasets used in this study	Data reference	Location	Latitude (°)	Longitude (°)	Palaeolatitude at 40 Ma, Müller et al., 2019 (°)	Palaeolongitude at 40 Ma, Müller et al., 2019 (°)	Modern depth (m)	Eocene palaeodepth (m) or depositional setting	Age model and reference	Foraminiferal preservation
DSDP 516	TEX_{86}	Auderset et al. (2022)	Rio Grande Rise, Southwest Atlantic	-30.28	-35.29	-33.35	-27.97	1313	1000	GTS2012, Auderset et al. (2022)	N/A
ODP 647	TEX_{86}, $\delta^{18}O$	Cramwinckel et al. (2020a)	Labrador Sea, North Atlantic	53.33	-45.26	48.69	-36.16	3861.8	2000 - 3000	GTS2012, Firth et al. (2012)	Glassy to recrystallised
ODP 702	Mg/Ca, $\delta^{18}O$	Henehan et al. (2020)	Islas Orcadas Rise, Southern Ocean	-50.95	-26.37	-53.51	-16.65	3083.7	2000 - 2200	GTS2012, Henehan et al. (2020)	Recrystallised
ODP 748	$\delta^{18}O$	Edgar et al. (2013)	Kerguelen Plateau, Southern Ocean	-58.44	79.98	-58.15	74.12	1290.9	725	CK95, Edgar et al. (2013)	Recrystallised
ODP 865	Mg/Ca, $\delta^{18}O$	$\delta^{18}O$ - Henehan et al. (2020) Mg/Ca - Henehan et al. (2020), Badger et al. (unpublished)	Allison Guyot, Equatorial Pacific	18.44	-179.56	11.18	-158.43	1517	1300 - 1500	GTS2012, Henehan et al. (2020)	Recrystallised
ODP 913	TEX_{86}	Inglis et al. (2015)	Greenland Basin, North Atlantic	75.49	-6.95	68.67	-2.02	3318	>1000, poorly constrained	GTS2012, Inglis et al. (2015)	N/A
ODP 959	TEX_{86}	Cramwinckel et al. (2018)	Cote d'Ivoire-Ghana Marginal Ridge, eastern equatorial Atlantic	3.63	-2.74	-1.98	-10.65	2100	>1000	GTS2012, Cramwinckel et al. (2018)	N/A
ODP 1051	$\delta^{18}O$	Edgar et al. (2013)	Blake Nose Plateau, western N. Atlantic	30.05	-76.36	28.33	-69.07	1980.6 - 1982.7	1000 - 2000	CK95, Edgar et al. (2013)	Recrystallised
ODP 1052	$\delta^{18}O$	Wade et al. (2008)	Blake Nose Plateau, western N. Atlantic	29.95	-76.63	28.26	-69.34	1342 - 1345	600 - 1000	Berggren 1995, Wade et al. (2008)	Recrystallised
ODP 1170	TEX_{86}	Cramwinckel et al. (2020b)	South Tasman Rise, southwest Pacific	-47.15	146.05	-66.14	150.23	2704	Shallow marine setting	No age model	N/A
ODP 1172	TEX_{86}	Bijl et al. (2009, 2021)	East Tasman Plateau, southwest Pacific	-43.96	149.93	-62.21	153.60	2620	Shallow marine setting	GTS2012, Bijl et al. (2021)	N/A
ODP 1209	TEX_{86}	Kast et al. (2019)	Shatsky Rise, central Pacific	32.65	158.51	27.04	-177.98	2387	1900	GTS2012, Kast et al. (2019)	N/A
ODP 1260	Mg/Ca, $\delta^{18}O$	Henehan et al. (2020)	Demerara Rise, Equatorial Atlantic	9.27	-54.54	5.49	-49.03	2549	2500 - 3200	GTS2012, Henehan et al. (2020)	Recrystallised
ODP 1263	Mg/Ca, $\delta^{18}O$	$\delta^{18}O$ - Boscolo Galazzo et al. (2014), Henehan et al. (2020) Mg/Ca - Henehan et al. (2020)	Walvis Ridge, Southeast Atlantic	-28.53	2.78	-34.47	-7.90	2717	2000	GTS2012, Henehan et al. (2020)	Recrystallised
Baskil Section	$\delta^{18}O$	Giorgioni et al. (2019)	Elazığ Basin, eastern Turkey, western Neotethys	30.61	38.60	21.39	29.85	N/A	300 - 600	GTS2012, Rodelli et al. (2018)	Recrystallised
Belaya River	TEX_{86}	Cramwinckel et al. (2022)	Northern Peri-Tethys, North Caucasus, Russia	44.37	40.20	42.57	31.89	N/A	Middle shelf setting	GTS2012, Cramwinckel et al. (2022)	N/A
IODP U1408	$\delta^{18}O$	Arimoto et al. (2020)	Newfoundland Ridge, Northwest Atlantic	41.44	-49.79	37.20	-42.10	3022	2600	Orbitally tuned, Boulila et al. (2018)	Recrystallised

Table 4.1 *Summary of main properties for sites used in this compilation and the datasets collected from these sites. Palaeocoordinates are collected using the Gplates Web Service (Müller et al., 2018) and the Müller et al. (2019) mantle reference plate model. Depositional settings are reported where approximate palaeodepths in m have not been estimated for these sites.*

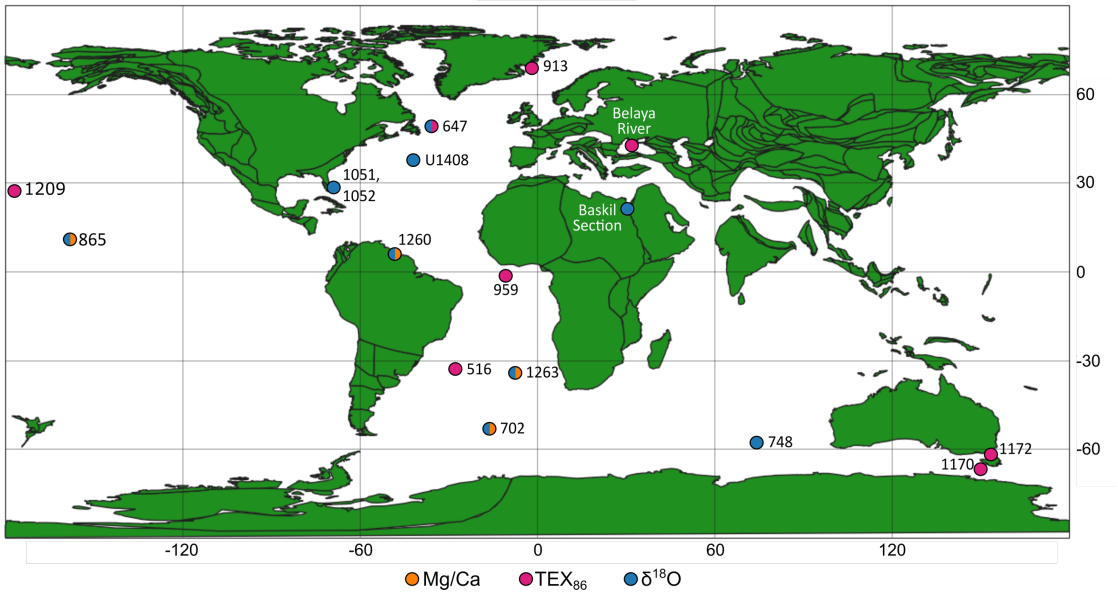


Figure 4.2 *Paleogeographic reconstruction at 40 Ma showing palaeocoordinates of sites included in this compilation. Palaeocoordinates are reconstructed using the Gplates Web Service (Müller et al., 2018) and Müller et al. (2019) mantle reference frame plate motion model. Site colours reflect the proxies available across the MECO from these sites: orange = Mg/Ca, pink = TEX_{86} and blue = $\delta^{18}O$. Split colours show sites where data from two proxies are available. Site numbers refer to DSDP Site 516, ODP Sites 647, 702, 748, 865, 913, 959, 1051, 1052, 1170, 1172, 1209, 1260, 1263 and IODP Site U1408.*

of Müller et al. (2019). Palaeolocations for all sites are shown on a plate tectonic reconstruction for 40 Ma (Fig. 4.2). While additional data exists over this interval, we prioritised selection of sites with "good" data coverage across the pre-, onset, peak and post-MECO in order to characterise sea surface temperature evolution across the event. We have re-calculated all published SST estimates using a common approach detailed below.

For planktic foraminiferal $\delta^{18}O$ and Mg/Ca-based SST reconstructions, we focus on collecting data from dominantly surface dwelling, photosymbiont-hosting species, e.g., primarily *Morozovelloides*, *Acarinina* and *Globigerinatheka* (Aze et al., 2011; Table 4.2). We have not included $\delta^{18}O$ or Mg/Ca data from deep dwelling or benthic foraminiferal species. Foraminifera were described as recrystallised at all sites in original publications, except for well-preserved, 'glassy' specimens found outside the MECO interval at ODP Site 647

Sites	Species	Habitat	Reference
647, 1263, Baskil	*Acarinina spp.*		
647, U1408	*Acarinina bullbrooki*		
647	*Acarinina cf. collactea 5-chambers*		
647	*Acarinina cf. mcgowrani 4-chambers*	Open ocean mixed layer tropical/subtropical, with symbionts	Aze et al., 2011
865, U1408	*Acarinina praetopilensis*		
748	*Acarinina primitiva*		
1051	*Acarinina topilensis*		
647	*Chiloguembelina ototara*	Thermocline; surface mixed layer	Fucek et al., 2018
1263, 1051	*Globigerinatheka spp.*		
647, 702, U1408, 748	*Globigerinatheka index*	Open ocean mixed layer tropical/subtropical, with symbionts	Aze et al., 2011
1263	*Globigerinatheka kugleri*		
U1408	*Globigerinatheka mexicana*		
647	*Globorotaloides quadrocameratus*	Open ocean sub−thermocline	Aze et al., 2011
647	*Globoturborotalita cf. ouachitaensis*	Open ocean mixed layer tropical/subtropical, with symbionts	Aze et al., 2011
647	*Hantkenina australis*	Open ocean thermocline	Aze et al., 2011
865, 1052, 1260, 1051	*Morozovelloides crassatus*	Open ocean mixed layer tropical/subtropical, with symbionts	Aze et al., 2011
647	*Pseudohastigerina micra*	Open ocean mixed layer tropical/subtropical, without symbionts	Aze et al., 2011
1051, 748	*Subbotina spp.*	Uncertain palaeoecology but likely mixed-layer dwelling, without symbionts	Aze et al., 2011

Table 4.2 *Summary of palaeoecologies for extinct Eocene species and the sites in which these species are present in our compilation.*

(Cramwinckel et al., 2020). Post-burial diagenesis can cause artificially high $\delta^{18}O$ values in planktic foraminifera, leading to cooler SST reconstructions (Pearson et al., 2001; Sexton et al., 2006). We therefore consider the impact of diagenesis on planktic $\delta^{18}O$ SSTs in our analysis.

4.2.2 Age models

As compiled records are published on different age models, we bring all included records here onto the GTS2012 age scale to aid direct comparisons (Gradstein et al., 2012). For the majority of sites, published ages are reported relative to the GTS2012 age scale so no age conversion was required. However, datasets from Sites 748 and 1051 are reported relative to the Cande & Kent (1995) geomagnetic polarity timescale (Edgar, Bohaty, et al., 2013) and Site 1052 is reported relative to the Berggren et al. (1995) timescale (Wade et al., 2008). Data from these three sites were converted to GTS2012 using the Ocean Drilling Stratigraphic

Network (ODSN) online timescale converter (www.odsn.de). Records from Site U1408 were reported on a site-specific, orbitally-tuned age model (Boulila et al., 2018). We adjusted the age-depth tie points from this paper to the GTS2012 reference frame and interpolated between these to obtain new ages for the depth of each sample. TEX_{86} records from Site 1170 are not published against an age model because a lack of magnetostratigraphic and calcareous nannofossil tie points prevent a detailed age model from being created (Stickley et al., 2004). However, correlation of biostratigraphic datums and temperature correlations with other records place the MECO confidently within the interval analysed (Cramwinckel et al., 2018). We therefore present the temperature reconstructions from this site on a depth scale.

4.2.3 Oxygen isotope palaeothermometry

The stable oxygen isotope ratio of foraminiferal calcite, $\delta^{18}O$, is widely used as a palaeothermometer (Pearson, 2012). We use two different methods to generate SST estimates from planktic foraminiferal $\delta^{18}O$ measurements. Firstly, we follow the recommended methodology in Hollis et al. (2019) and use the calibration of Kim and O'Neil (1997) for inorganic calcite calibrated over 15 – 25 °C, as modified by Bemis et al. (1998). In this calibration, temperature is derived from Equation 4.1:

Equation 4.1

$$T = 16.1 - 4.64(\delta^{18}O_c - \delta^{18}O_{sw}) + 0.09(\delta^{18}O_c - \delta^{18}O_{sw})^2$$

Where T = temperature in degrees Celsius, $\delta^{18}O_c$ = the measured $\delta^{18}O$ value of foraminiferal calcite relative to the Vienna Peedee Belemnite reference (VPDB) and $\delta^{18}O_{sw}$ = the $\delta^{18}O$ value of seawater at the time of test formation (converted from VSMOW to VPDB for use in this equation).

Secondly, we calculate palaeotemperatures using a Bayesian calibration model, *Bayfox* (Malevich et al., 2019), using R statistical software, Version 1.3.1093. We use the pooled

annual calibration model option for our calibrations as this is the most appropriate option for deep-time applications where seasonality and species differences are largely unknown, however this does not account for any impacts that these factors may have had on our $\delta^{18}O$ records. Bayfox fits a linear Bayesian regression model to core-top measurements for a number of planktic foraminiferal species to produce a prediction distribution for sea surface temperature (Malevich et al., 2019). We report the median (50th percentile), 5th and 95th percentile intervals of this distribution to provide a range of viable SSTs from $\delta^{18}O_c$ values, which captures the uncertainty in the modelled temperature predictions. We use a weakly informed prior distribution for sea surface temperature, where we input both the prior mean and prior standard deviation as 20°C.

One of the principal shortcomings of the $\delta^{18}O$ palaeothermometer is substantial uncertainty in past $\delta^{18}O$ values of ancient seawater (Pearson, 2012). Three "corrections" must be made to the modern $\delta^{18}O_{sw}$ value to provide an appropriate estimate of $\delta^{18}O_{sw}$ for the middle Eocene. Firstly, a latitudinal correction is applied to account for local hydrological effects on $\delta^{18}O_{sw}$ at each site caused by variations in the ratio of evaporation and precipitation. We use a published MATLAB script from Hollis et al. (2019) which uses a globally gridded $\delta^{18}O_{sw}$ dataset (LeGrande & Schmidt, 2006) to correct $\delta^{18}O_{sw}$ based on the palaeolatitude and palaeolongitude of each site. This improves upon the long-used and data-poor latitudinal correction of Zachos et al. (1994), as discussed in Hollis et al. (2019). Secondly, an ice volume correction is applied to $\delta^{18}O_{sw}$ values to account for differences in global ice volume in the Eocene relative to modern. While it is generally accepted that the early Eocene was dominantly ice-free and major ice sheets on Antarctica did not build up until the Eocene-Oligocene Transition at ~34 Ma, several studies suggest that small-scale ice volumes may have existed on Antarctica and/or the Arctic by the middle Eocene (Cramer et al., 2011;

Dawber & Tripati, 2011; Tripati & Darby, 2018; Tripati et al., 2008). However, the volume and variability of ice present across the MECO, as well as the $\delta^{18}O$ of this ice, remains highly uncertain (Cramer et al., 2011; Henehan et al., 2020; Rohling et al., 2021; Tripati et al., 2008). We estimate an ice volume correction of -0.6 ‰ based on sea level-derived ice volume reconstructions from Cramer et al. (2011) for the middle Eocene. On a first order interpretation, this is a realistic assumption as it is between the ~ -1 ‰ correction required for the ice-free early Eocene case (Cramer et al., 2011; L'Homme, 2005; Shackleton & Kennett, 1975) and 0 ‰ correction required for the modern, full ice-sheet case. However, as middle Eocene ice volumes are poorly constrained, our ice-volume correction factor is based on very little evidence and is likely to be the greatest uncertainty in our palaeotemperature calculations. Additionally, we do not account for any change in $\delta^{18}O_{sw}$ caused by ice melt across the MECO warming event due to lack of evidence for ice volume change at present. Our $\delta^{18}O$-based palaeotemperature records should therefore be interpreted in the context of these significant unknowns. Thirdly, we apply a correction factor of -0.27 ‰ (Kim & O'Neil, 1997) to convert our $\delta^{18}O_{sw}$ estimates from the Vienna Standard Mean Ocean Water (VSMOW) reference scale to the VPDB reference scale for use in Equation 4.1.

Past seawater carbonate ion concentrations, $[CO_3^{2-}]$, were likely significantly lower than modern (Tyrrell & Zeebe, 2004; Zeebe & Tyrrell, 2019). $\delta^{18}O$-based temperature reconstructions can be biased by the negative relationship between $[CO_3^{2-}]$ and $\delta^{18}O$ of foraminiferal calcite (Bijma et al., 1999; Spero et al., 1997, 1999). We therefore correct $\delta^{18}O$ measurements for past $[CO_3^{2-}]$ using Equation 4.2:

Equation 4.2

$$\delta^{18}O_c' = \delta^{18}O_c - (s[CO_3^{2-}] - 200s)$$

Where $\delta^{18}O_c$' = corrected $\delta^{18}O$ of foraminiferal calcite, $\delta^{18}O_c$ = measured $\delta^{18}O$ of foraminiferal calcite, s = the mean slope of the relationship between $[CO_3^{2-}]$ and $\delta^{18}O$ for planktic foraminifera from Spero et al. (1997), and $[CO_3^{2-}]$ is calculated across the MECO using linear interpolation between $[CO_3^{2-}]$ values in the long-term record from Zeebe and Tyrrell (2019). While this equation provides a basic estimate of the carbonate ion effect on $\delta^{18}O_c$, there are many significant unknowns which cannot yet be accounted for in our palaeotemperature reconstructions. Firstly, the relationship between $[CO_3^{2-}]$ and $\delta^{18}O$ of foraminiferal calcite has only been measured for a few species of extant planktic foraminifera in culture experiments (Bijma et al., 1999; Spero et al., 1997, 1999). For extinct species, we assume that the relationships for extant, surface-dwelling and symbiont-bearing foraminifera can be applied, despite uncertainties in palaeoecology. Secondly, we choose to use the Cenozoic carbonate ion record created by Zeebe and Tyrrell (2019), a global ocean record at ~10 Ma resolution, which does not account for latitudinal or short-term variation in $[CO_3^{2-}]$. Boron isotope records across the MECO show that pH, which is linked to $[CO_3^{2-}]$, varied by up to 0.2 pH units across the event and in magnitude between sites (Henehan et al., 2020). As pH reconstruction requires temperature records, using these pH records to then correct our SST records introduces a degree of circularity into our palaeotemperature reconstructions. Additionally, these pH records only exist for four sites (Henehan et al., 2020) and are not necessarily applicable to the full range of $\delta^{18}O$ records in our compilation. We therefore exclude a short-term pH correction from our records, but note that temperatures across the peak of the MECO are likely to be underestimated due to the pH effect (Henehan et al., 2020). This has previously been demonstrated for the PETM where including a pH correction results in temperatures ~1.5 °C higher than uncorrected records (Aze et al., 2014). We explore the

	Ice-volume correction applied to $\delta^{18}O_{sw}$ (VSMOW)	A. No carbonate ion correction		B. Carbonate ion correction applied	
		SST estimate from Equation 4.1 (°C)	SST estimate from Bayfox (°C)	SST estimate from Equation 4.1 (°C)	SST estimate from Bayfox (°C)
1. Full ice sheets (modern case)	0 ‰	20.44	22.10 (18.18 – 25.99)	21.41	22.26 (18.41 – 26.14)
2. Some ice (hypothetical middle Eocene case)	-0.6 ‰	17.59	18.84 (14.93 – 22.74)	18.54	19.62 (15.78 – 23.53)
3. Ice-free (early Eocene case)	-1.0 ‰	15.72	17.10 (13.34 – 20.95)	16.66	18.04 (14.12 – 21.87)

Table 4.3 *Matrix of final temperature values derived from a case study $\delta^{18}O_c$ starting value of -1.66 ‰ VPDB, from a well-preserved* Chiloguembelina ototara *sample from 41.1 Ma (pre-MECO), 480.59 mbsf. Final temperatures are derived through Equation 4.1 and Bayfox when different ice-volume corrections are applied to $\delta^{18}O_{sw}$ (rows 1 – 3) and when a carbonate ion correction is/is not applied to $\delta^{18}O_c$ (columns A – B). For Bayfox temperature estimates, unbracketed numbers indicate the median returned by Bayfox while the numbers in brackets show the 5% and 95% confidence intervals. Darker colours indicate higher temperatures.*

impact of choosing different ice volume and carbonate ion corrections on estimated $\delta^{18}O$ SSTs in a case study from Site 647 in Table 4.3.

4.2.4 Mg/Ca palaeothermometry

The Mg/Ca ratio of foraminiferal calcite varies depending on the temperature of calcification in both core top studies and laboratory culture experiments (e.g. Anand et al., 2003; Elderfield & Ganssen, 2000; Lea et al., 1999; Nürnberg et al., 1996; Rosenthal et al., 1997). We generate SST records from Mg/Ca data following the recommendations of Hollis et al. (2019), using Equation 4.3:

Equation 4.3

$$T = \frac{\ln\left(\frac{Mg/Ca_c}{B}\right)}{A}$$

Where T = temperature in °C, Mg/Ca_c = Mg/Ca of foraminiferal calcite, and A and B are constants derived from published calibrations that can be determined based on the time

interval and species/group of study. Due to the absence of species-specific calibrations for extinct Eocene planktic foraminiferal species, we use the core-top multi-species calibration of Anand et al. (2003), where A = 0.09 and B = 0.38 as this calibration shows a good fit with a range of extant species and is therefore likely a good approximation of the relationship for a range of extinct species.

Before calculating temperature, we first correct for a different past Mg/Ca of seawater, Mg/Ca_{sw} as this has not remained constant through the Cenozoic. We follow Hollis et al. (2019) and apply Equation 4.4 according to relationships derived by Hasiuk & Lohmann (2010) and Evans & Müller (2012):

Equation 4.4

$$B' = \left(\frac{Mg/Ca_{sw}{}^{H}}{5.2^{H}}\right) \times B$$

Where B' = corrected value of B to be used in Equation 4.3, B = 0.38 as described above (Anand et al., 2003), Mg/Ca_{sw} = Mg/Ca of past seawater based on reconstructions in Evans et al. (2018), 5.2 = modern seawater Mg/Ca in mol/mol, and H = the degree of nonlinearity of the relationship between Mg/Ca_{sw} and Mg/Ca_c. This is done as the partition coefficient of magnesium, D_{Mg}, varies with Mg/Ca_{sw} (Cramer et al., 2011; Evans & Müller, 2012). There are few published estimates of H for modern planktic foraminifera and none for extinct Eocene species. Thus, here we use a value of 0.42 for H based on analyses of cultured *G. sacculifer* (Delaney et al., 1985; Hasiuk & Lohmann, 2010) as this is a representative value for shallow-dwelling, planktic foraminifera.

Mg/Ca values are also sensitive to pH change, where foraminifera that calcify in lower pH waters have higher Mg/Ca (Evans et al., 2016; Lea et al., 1999). Records that do not correct for pH change likely overestimate temperatures by ~1 °C per 0.1 units pH decrease. Boron isotope-based pH records generated by Henehan et al. (2020) show pH declining by up to

0.22 units across the MECO. However, these authors estimate absolute pH values and thus relative changes using Mg/Ca-based temperature records, as the carbonate system and temperature are interlinked. Thus, to avoid introducing circularity by correcting our Mg/Ca temperature records using pH records that have already been corrected by the same Mg/Ca records we do not apply any pH correction to our Mg/Ca SST estimates. Our Mg/Ca-based temperatures could therefore be ~2 – 3 °C warmer across the peak of the MECO than true temperatures. To demonstrate potential differences between the SST estimates of Henehan et al. (2020), which account for pH change, and this study, we show both records in this compilation.

Post-depositional dissolution of foraminiferal carbonate can also cause temperature underestimates due to preferential dissolution of $MgCO_3$, artificially decreasing Mg/Ca (Regenberg et al., 2014; Rosenthal & Lohmann, 2002). We do not correct for potential dissolution effects on foraminiferal calcite as this is difficult to quantify without knowing the weights of individual tests (e.g. Rosenthal & Lohmann, 2002). We also do not account for changes in ocean salinity across the MECO, as these changes are likely to be highly site-specific and there are no high-resolution data or model reconstructions available. Finally, previous studies have identified that the foraminiferal cleaning method can impact the final measured Mg/Ca_c values, whereby Mg/Ca values are reduced with the more intense reductive cleaning approaches (Barker et al., 2003; Khider et al., 2015). The same oxidative cleaning method was used to generate all of the Mg/Ca records in this study (Henehan et al., 2020) therefore we do not consider cleaning method a concern here. We note that analytical uncertainty on Mg/Ca values (±2% of the measured value) is minor relative to the combination of many unknowns in the Mg/Ca palaeothermometer, so we do not report this here.

4.2.5 Isoprenoidal GDGT palaeothermometry (TEX_{86})

Glycerol dialkyl glycerol tetraether (GDGT) membrane lipids from marine Thaumarchaeota, a phylum of Arachaea, are abundant in sediments and found in a wide range of environmental conditions (Schouten et al., 2002). The chemical structure of GDGT membrane lipids varies depending on temperature, where higher growth temperatures correlate with higher numbers of cyclopentane rings within GDGT lipids (Schouten et al., 2002). This structural distribution can be summarised by the 'tetraether index' of GDGTs in sediments, and is referred to as TEX_{86}. While marine Thaumarchaeota can live at a wide range of depths within the water column (Church et al., 2010), TEX_{86} has been shown from core top studies to correlate best with annual mean sea surface temperatures (Kim et al., 2008; Schouten et al., 2002; Tierney et al., 2017). TEX_{86}-derived sea surface temperature estimates are available as far back as the Jurassic (Jenkyns et al., 2012) and the proxy has been widely applied in Palaeocene – Eocene sedimentary records where foraminifera are often poorly preserved (e.g. Cramwinckel et al., 2018; Cramwinckel, Woelders, et al., 2020; Inglis et al., 2015; Sluijs et al., 2009; Zachos et al., 2006).

A number of different calibrations exist describing the TEX_{86}-temperature relationship, in both linear (e.g. Kim et al., 2008; Schouten et al., 2002) and exponential forms (e.g. Kim et al., 2010). Whether this relationship is linear or exponential is still unclear, and both types of calibration are commonly shown in TEX_{86} surface temperature reconstructions (e.g. Cramwinckel et al., 2018; Tierney & Tingley, 2014). We collected published fractional abundances of GDGTs and quality control indices, described below, from nine sites and used these to re-calculate TEX_{86}. We then estimated sea surface temperature and associated uncertainties from TEX_{86} and GDGT fractional abundances using two tools: OPTiMAL (Dunkley Jones et al., 2020) and BAYSPAR (Tierney & Tingley, 2014, 2015).

OPTiMAL (Optimised Palaeothermometry from Tetraethers via Machine Learning) is a Gaussian process regression tool, which uses the fractional abundances of GDGTs and core-top datasets to estimate SST and uncertainties (Dunkley Jones et al., 2020). Instead of relying on the TEX_{86} index, which reduces the variability of GDGTs to a single figure (discussed further below), OPTiMAL inputs the original fractional abundances of GDGTs to predict temperature based on the modern core-top dataset (Dunkley Jones et al., 2020). OPTiMAL also derives the $D_{nearest}$ metric for each temperature predicted, which is based on the distance between the nearest neighbour in the modern compilation and GDGT abundances in ancient records. $D_{nearest}$ values of >0.5 suggest some degree of non-analogue behaviour, i.e. the modern calibration dataset does not appropriately constrain temperatures for the ancient GDGT distribution for this particular sample (Dunkley Jones et al., 2020). This is particularly important for Eocene calibrations, where higher average global temperatures mean that GDGT distributions are either at or outside the limits of the modern calibration database and there are no suitable analogues in modern GDGT distributions. We use the OPTiMAL script with R statistical software, Version 1.3.1093, to generate SST estimates, $D_{nearest}$ values and standard deviation.

We also estimate sea surface temperatures from our GDGT data using BAYSPAR. BAYSPAR (Bayesian Spatially-varying Regression) is a Bayesian calibration model for TEX_{86} temperature reconstructions (Tierney & Tingley, 2014, 2015). Similar to OPTiMAL, BAYSPAR uses a modern core-top GDGT and temperature dataset to account for spatial variation in the response of GDGT distribution with temperature. We input the TEX_{86} index, calculated using Equation 4.5 (Schouten et al., 2002):

Equation 4.5

$$TEX_{86} = \frac{GDGT2 + GDGT3 + cren'}{GDGT1 + GDGT2 + GDGT3 + cren'}$$

Where GDGT1, GDGT2 and GDGT3 refer to the fractional abundances of GDGT's with 1, 2 and 3 cyclopentane rings within their structure, and cren' refers to the fractional abundance of the structural regioisomer of the GDGT crenarchaeol. We also specify a prior mean, calculated as the mean TEX_{86} of the entire time series at each site and a wide prior standard deviation of 20 °C. The BAYSPAR script is run on the MATLAB programming platform. BAYSPAR outputs a Bayesian distribution array of temperature predictions for each TEX_{86} data point. We use the 50th percentile of this distribution as our median SST for each sample, with the 5th and 95th percentiles also recorded to account for uncertainty.

To screen for non-thermal influences on GDGT distribution for each sample, we use a number of different indices: the branched and isoprenoid tetraether index (BIT), methane index (MI), GDGT-0 % and deviation between TEX_{86} and the ring index (ΔRI). BIT shows the ratio of branched GDGTs to crenarchaeol, where high BIT (>0.5) suggests significant terrestrial input to the site (Hopmans et al., 2004) which can cause the TEX_{86} palaeothermometer to overestimate SSTs. BIT is reported alongside GDGT fractional abundances by the original authors of these data for all sites in our compilation except for the Balaya River section (Cramwinckel et al., 2022) and ODP Site 959 (Cramwinckel et al., 2018). The methane index (MI) indicates input of GDGTs to sediment from methanotrophic archaea, where high MI (>0.5) suggests strong influence of methanotropic archaeal GDGTs on overall abundances (Zhang et al., 2011). MI is calculated from GDGT fractional abundances following Equation 4.6 (Zhang et al., 2011):

Equation 4.6

$$MI = \frac{GDGT1 + GDGT2 + GDGT3}{GDGT1 + GDGT2 + GDGT3 + cren + cren'}$$

Where GDGT1, GDGT2 and GDGT3 are the fractional abundances of GDGTs with 1, 2 and 3 cyclopentane rings within their structure, cren refers to the fractional abundance of the

GDGT crenarchaeol, and cren' refers to the fractional abundance of the structural regioisomer of crenarchaeol. Methanogenic archaea can also produce GDGT-0, so we use the percentage of GDGT-0 to assess the impact of methanogenic communities on our TEX_{86} values (Weijers et al., 2006). Where GDGT-0 is >67 %, GDGT distributions are likely to be strongly influenced by methanogenic arachaea and resulting temperatures are unreliable (Inglis et al., 2015; Sinninghe Damsté et al., 2012). GDGT-0 abundances are reported alongside other GDGT abundances by the original authors for the sites in our compilation. Finally, ΔRI is used to characterise any effects of nutrient levels and microbial community structure on overall GDGT abundances (Zhang et al., 2016). Where ΔRI >0.3, TEX_{86} values are likely to be biased by these non-thermal influences. RI and ΔRI are calculated via Equations 4.7 and 4.8 (Zhang et al., 2016):

Equation 4.7

$$RI = (0 \times GDGT0) + (1 \times GDGT1) + (2 \times GDGT2) + (3 \times GDGT3) + (4 \times cren) + (4 \times cren')$$

Equation 4.8

$$\Delta RI = (-0.77 \times TEX_{86}) + \left(3.22 \times TEX_{86}{}^{2}\right) + 1.59 - RI$$

Where GDGT0, GDGT1, GDGT2 and GDGT3 refer to the fractional abundances of GDGTs with 0, 1, 2 and 3 cyclopentane rings within their structure, cren refers to the fractional abundance of the GDGT crenarchaeol, and cren' refers to the fractional abundance of the regioisomer of crenarchaeol. Where TEX_{86} sea surface temperatures are plotted we highlight samples where $D_{nearest}$, BIT, MI, %GTGD-0 and/or ΔRI are above the thresholds described, indicating poor quality data where caution should be employed in taking SST estimates at face value.

4.2.6 Identifying pre-MECO, MECO onset, peak-MECO and post-MECO intervals

All datasets are presented relative to the GTS2012 age scale so that the timing of the MECO is comparable between sites, except one. There is no age model available for ODP Site 1170 so data are presented in depth space only (Cramwinckel, Woelders, et al., 2020). When comparing individual records in age space, it is notable that the shape, size and timing of proxy excursions across the MECO vary depending on inter-site differences due to, e.g., depositional environment, sedimentation rate, proxy and age model resolution. Comparing datasets from multiple sites on age models alone can create significant noise by, for instance, bringing in peak versus post-MECO intervals to the same window. To mitigate this, we break the MECO up into four intervals: pre-, onset, peak- and post-MECO. We identify these intervals at each site based on the high-resolution bulk or benthic foraminiferal $\delta^{18}O$ records record as this is how the event was initially recognised and most commonly defined (Bohaty & Zachos, 2003). Where high resolution $\delta^{18}O$ records are not available, we compare individual sites to the CENOGRID global benthic oxygen isotope stack also on the GTS2012 timescale (Westerhold et al., 2020) to aid MECO identification. The timing and magnitude of the CIE associated with the MECO is inconsistent between sites therefore the $\delta^{13}C$ signal is not highly diagnostic for recognising the structure of the MECO event.

The pre-MECO interval is defined here as the interval of ~250 kyr prior to the MECO onset, i.e., before the continuous and gradual shift to lower bulk or benthic foraminiferal $\delta^{18}O$ values. The MECO onset interval begins at the point of initial $\delta^{18}O$ decrease and incorporates the subsequent rapid rise in $\delta^{18}O$. We follow Bohaty et al. (2009) and define the peak-MECO interval as the period of ~100 kyrs of sustained minimum $\delta^{18}O$ values, which lasts until the

beginning of $\delta^{18}O$ increase signifying cooling. The post-MECO interval begins at this point of rapid increase in $\delta^{18}O$ values and is ~250 kyrs in duration.

Site 1172 is not presented here on an age model. In this case, we refer to the original authors' description of the MECO to aid in identifying onset, peak and post-MECO intervals. Due to the lack of age-depth tie points, we are avoid delimiting the widths of these intervals at this site and only define the width of the peak MECO interval. For Site 647, we define the intervals of the MECO using TEX_{86} records, as benthic and planktic $\delta^{18}O$ records do not show the temperature rise clearly. For Site 748, we use the interpretation of Edgar et al. (2013) to inform the widths of the MECO onset and pre-MECO intervals, as a gap in the Site 748 benthic $\delta^{18}O$ record (Bohaty et al., 2009) prevents identification of these intervals based on this record alone.

4.3 RESULTS

4.3.1 Palaeotemperature reconstructions across the MECO

Figures 4.3 – 4.16 show raw sea surface temperature proxy ($\delta^{18}O$, Mg/Ca and TEX_{86}) and temperature estimates alongside other relevant records including benthic foraminiferal and bulk stable isotope records, with pre-, onset, peak and post-MECO intervals highlighted. Sea surface temperatures across the MECO vary across different sites, but also depending on the proxy and method used. Out of the 17 sites included in this compilation, the majority of sites have single proxy records (either $\delta^{18}O$ or TEX_{86}), four sites have both $\delta^{18}O$ and Mg/Ca records, and only one site has both $\delta^{18}O$ and TEX_{86} (Fig. 4.2). No site has both TEX_{86} and Mg/Ca or all three proxies available. Before describing MECO SST patterns, we first

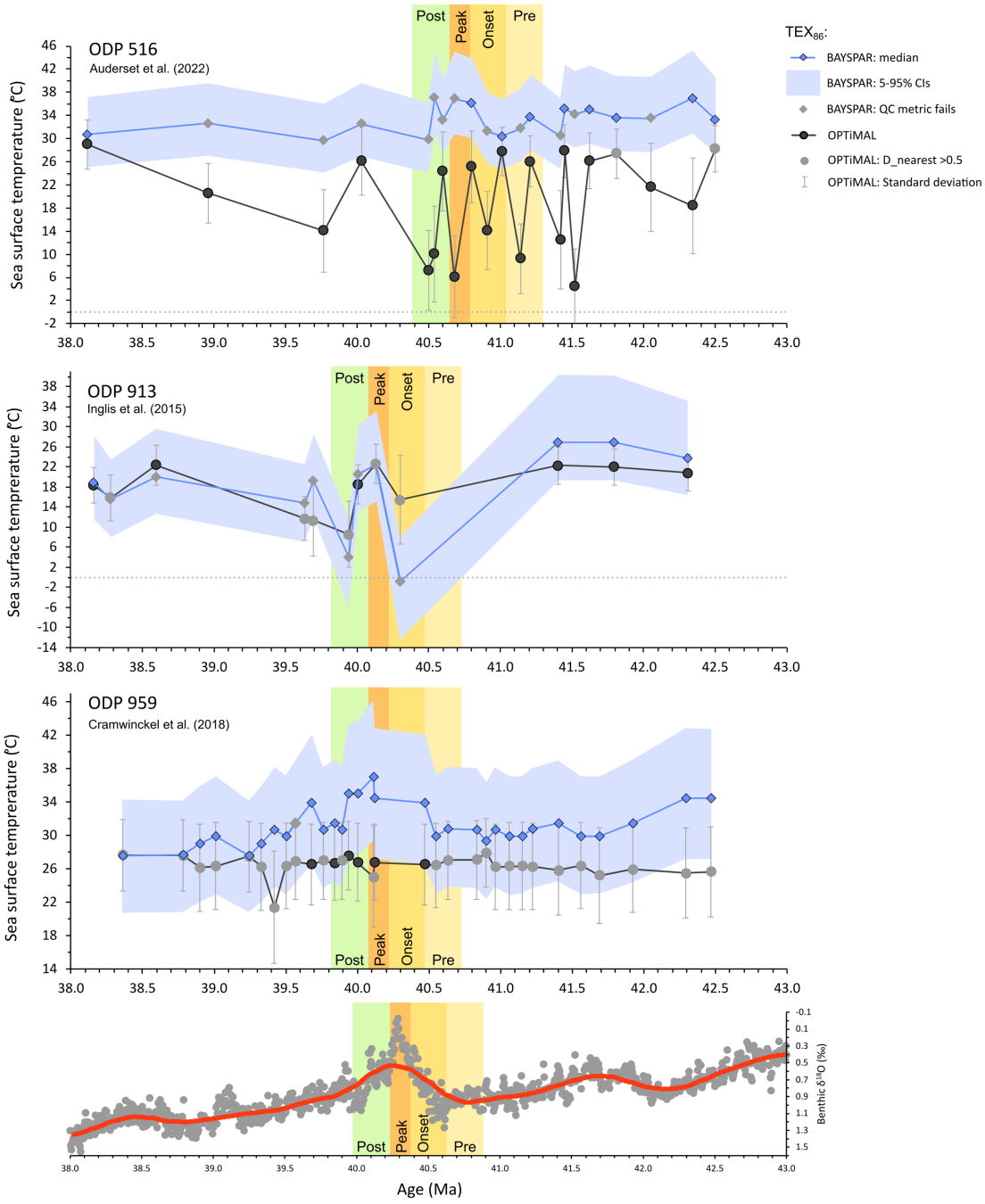


Figure 4.3 *TEX_{86} temperature records for ODP Sites 516, 913 and 959, alongside the CENOGRID global benthic oxygen isotope stack (Westerhold et al., 2020; bottom, red line shows 250 kyr smoothed values). BAYSPAR reconstructions are shown in blue, and OPTiMAL reconstructions are shown in grey. Pre-MECO, MECO onset, Peak MECO and Post-MECO intervals are highlighted in orange and green and labelled Pre, Onset, Peak and Post.*

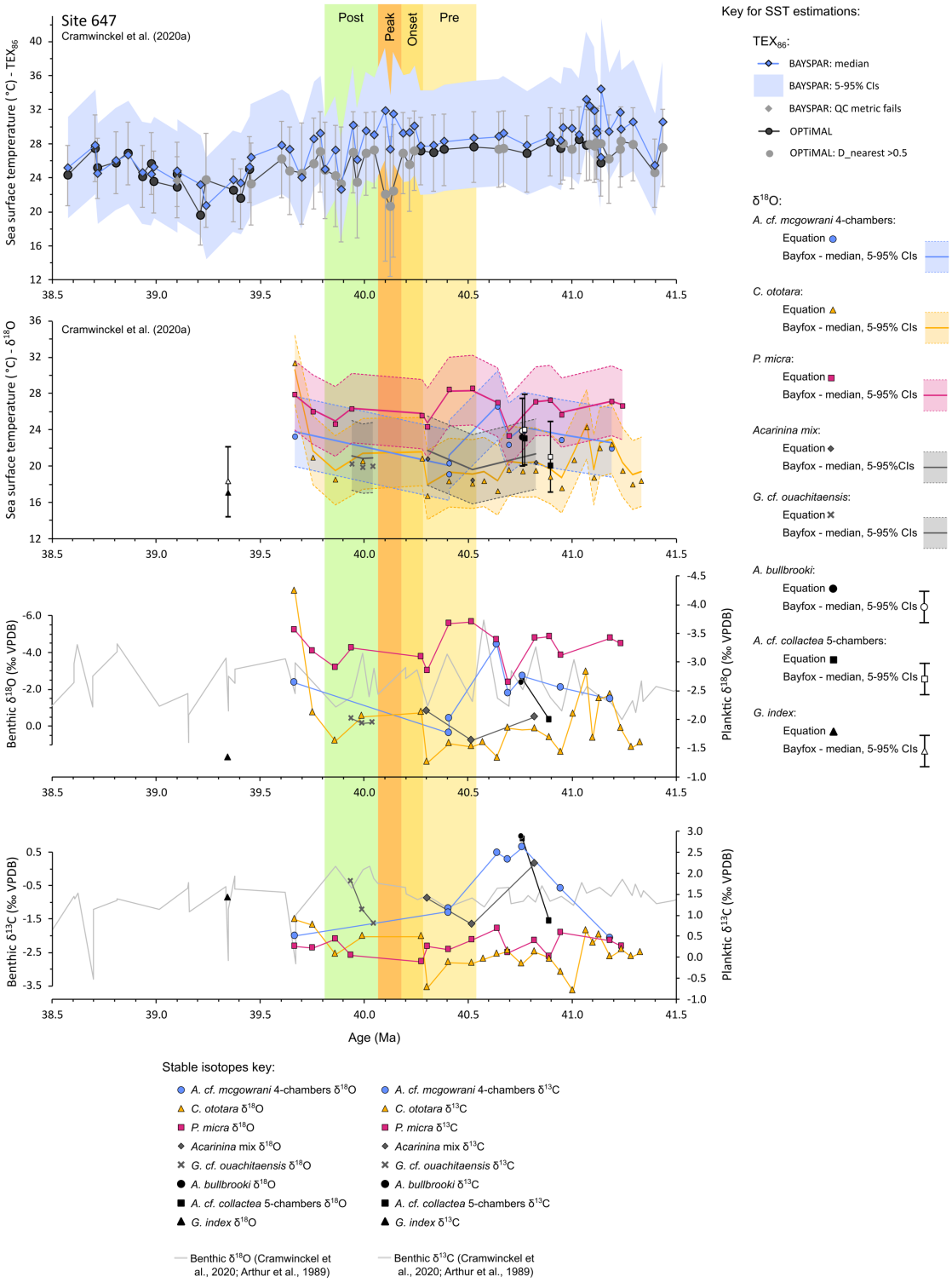


Figure 4.4 *TEX_{86} and planktic $\delta^{18}O$ temperature reconstructions for ODP Site 647, alongside planktic and benthic stable oxygen and carbon isotope records. For TEX_{86} temperature reconstructions, BAYSPAR reconstructions are shown in blue, and OPTiMAL reconstructions are shown in grey. For $\delta^{18}O$ temperature reconstructions, symbols show temperature values derived from Equation 4.1 and lines with shaded areas show Bayfox temperature estimates with confidence intervals. Benthic stable isotope records are sourced from (cont. on next page)*

Figure 4.4 (cont.) *Cramwinckel et al. (2020) and Arthur et al. (1989). Pre-MECO, MECO onset, Peak MECO and Post-MECO intervals are highlighted in orange and green and labelled Pre, Onset, Peak and Post. Species abbreviations refer to species:* Acarinina cf. mcgowrani (A. cf. mcgowrani), Chiloguembelina ototara (C. ototara), Pseudohastigerina micra (P. micra), Globoturborotalita cf. ouachitaensis (G. cf. ouachitaensis), Acarinina bullbrooki (A. bullbrooki), Acarinina cf. collactea (A. cf. collactea), Globigerinatheka index (G. index).

summarise the similarities and differences between temperature reconstructions for each of the different proxies.

4.3.1.1 $\delta^{18}O$-based SST reconstructions

We have compiled planktic foraminiferal $\delta^{18}O$ records across the MECO from ten sites: ODP Sites 647 (Fig. 4.4), 702 (Fig. 4.5), 748 (Fig. 4.6), 865 (Fig. 4.7), 1051 (Fig. 4.8), 1052 (Fig. 4.9), 1260 (Fig. 4.12), 1263 (Fig. 4.13), IODP Site U1408 (Fig. 4.16) and the Baskil Section (Fig. 4.14), which span all ocean basins (Fig. 4.2; Supplementary Table 4.1). We present SSTs calculated using both $\delta^{18}O$ palaeothermometry methods described in Methods Section 4.2.3: Equation 4.1 and Bayfox. We include the 5 – 95 % confidence intervals of the Bayfox temperature prediction to show the full range of possible temperatures. For the majority of sites, we plot the median of the Bayfox temperature prediction, however for ODP Sites 748 and 1051 multiple samples from each depth were measured. In these cases, we do not include the Bayfox median, but plot the range between the lowest 5 % interval and highest 95 % interval out of all the predictions for a single depth/age value. For all sites, planktic foraminifera tests were described as recrystallised in original publications (Table 4.1), except for ODP Site 647, where preservation ranged from glassy to recrystallised (Cramwinckel, Coxall, et al., 2020). Six sites have multi-species records, with $\delta^{18}O$ data generated from two or more surface-dwelling planktic foraminiferal species: ODP Sites 647 (Fig. 4.4), 748 (Fig. 4.6), 865 (Fig. 4.7), 1051 (Fig. 4.8), 1263 (Fig. 4.13), and IODP Site U1408 (Fig. 4.16). For these sites, separate SST records for each species were created. For the remaining four sites,

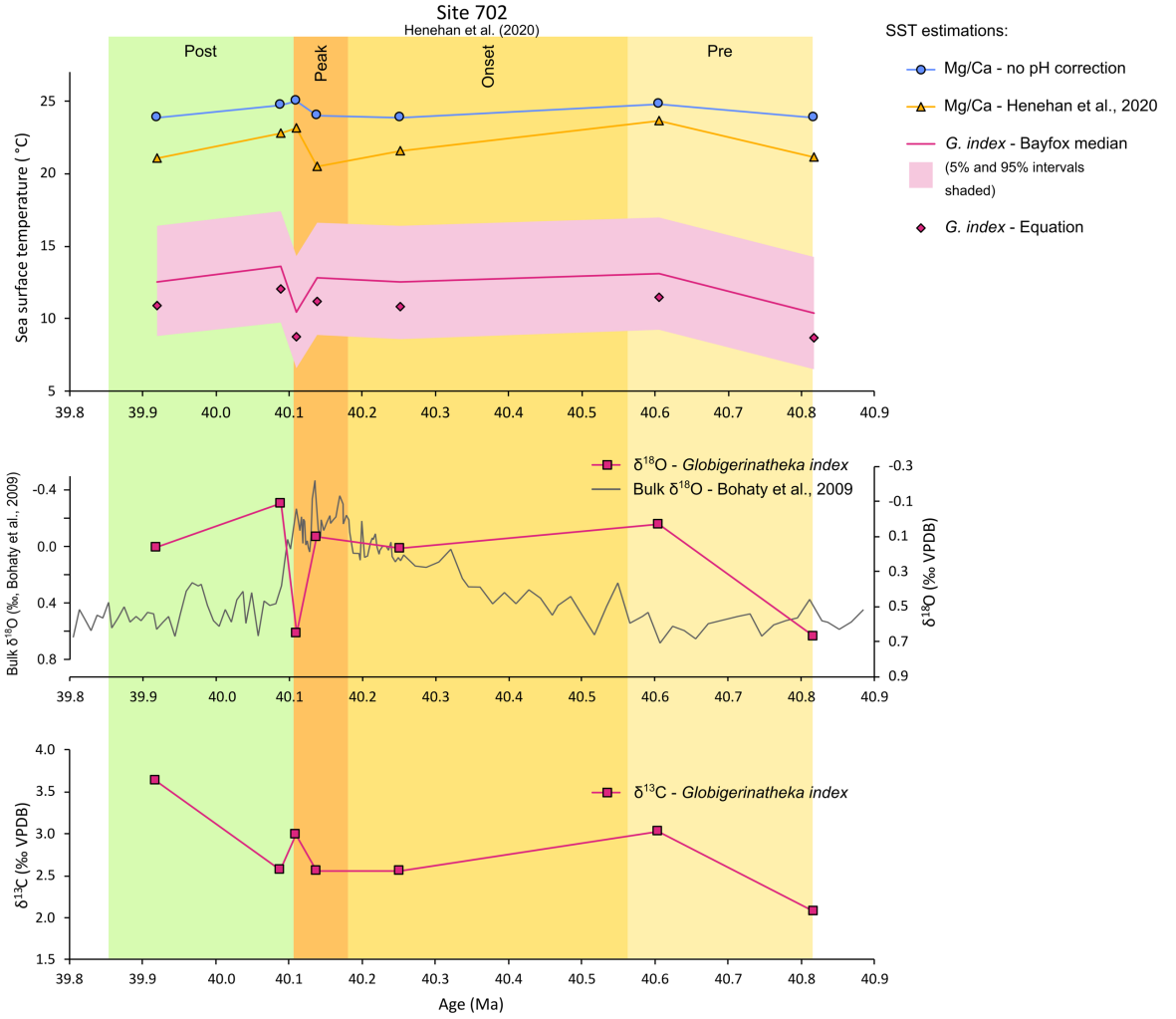


Figure 4.5 *Mg/Ca and planktic $\delta^{18}O$ temperature reconstructions for ODP Site 702, alongside planktic and bulk stable oxygen and carbon isotope records. For Mg/Ca temperature reconstructions, temperatures derived by Equation 4.3 are shown in blue while temperatures published in Henehan et al. (2020) are shown in yellow. For $\delta^{18}O$ temperature reconstructions, symbols show temperature values derived from Equation 4.1 and lines with shaded areas show Bayfox temperature estimates with confidence intervals. Bulk $\delta^{18}O$ record (grey line) is sourced from Bohaty et al. (2009). Pre-MECO, MECO onset, Peak MECO and Post-MECO intervals are highlighted in orange and green and labelled Pre, Onset, Peak and Post. Species abbreviation* G. index *refers to species* Globigerinatheka index.

ODP Sites 702 (Fig. 4.5), 1052 (Fig. 4.9), 1260 (Fig. 4.12) and the Baskil Section (Fig. 4.14), $\delta^{18}O$-based SSTs are presented here from a single species, despite additional non-surface dwellers included in original publications.

For most sites, median Bayfox SST estimates are higher than SSTs from Equation 4.1, though Equation 4.1 SST estimates are usually within the 5 – 95 % intervals of Bayfox predictions. Exceptions include the *Pseudohastigerina micra* SST record from ODP Site 647

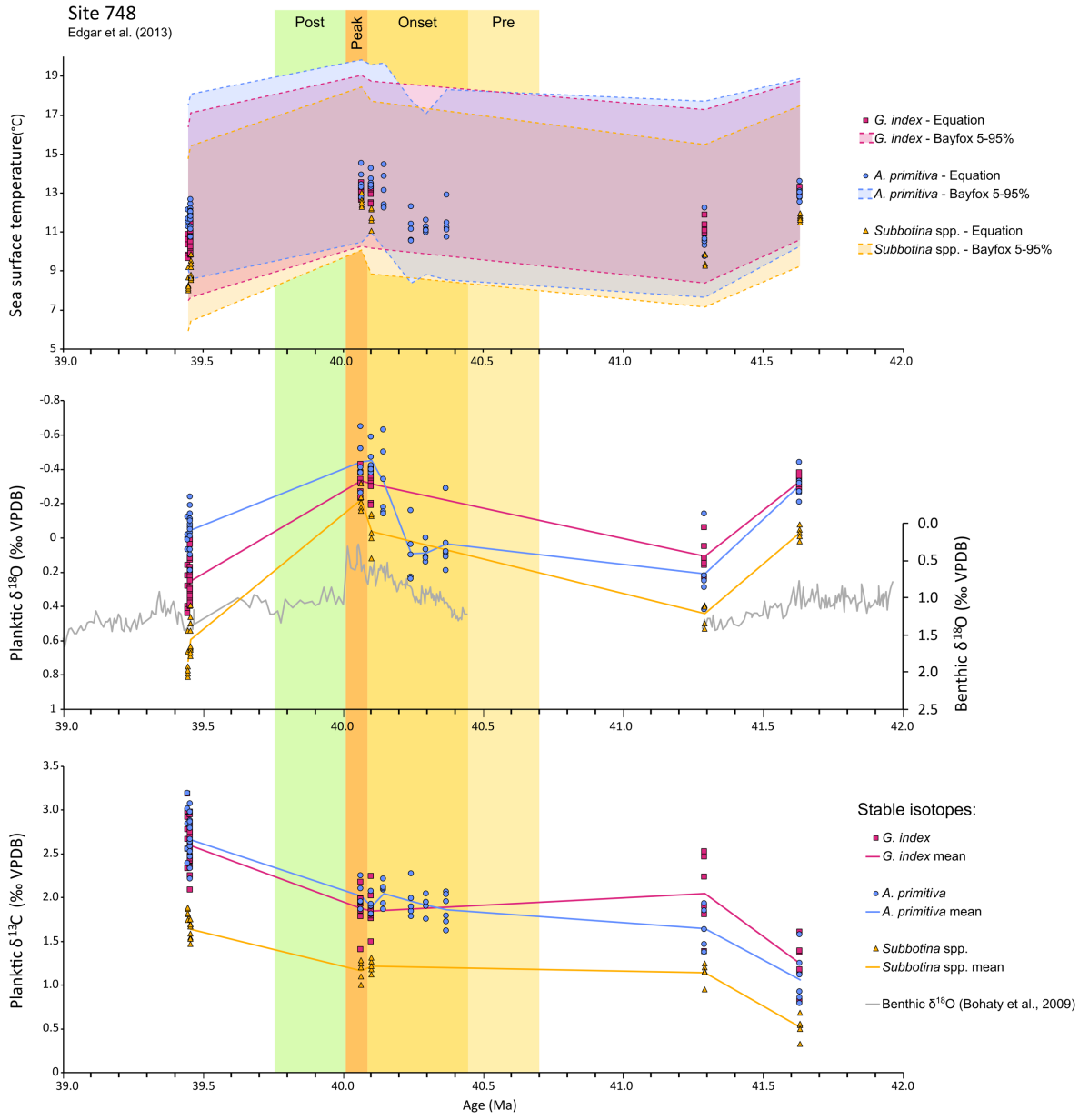


Figure 4.6 *Planktic $\delta^{18}O$ reconstructions for ODP Site 748, alongside the benthic stable oxygen isotope record for this site. Symbols show temperature values derived from Equation 4.1 and lines with shaded areas show Bayfox temperature estimates with confidence intervals. Benthic $\delta^{18}O$ record (grey line) is sourced from Bohaty et al. (2009). Pre-MECO, MECO onset, Peak MECO and Post-MECO intervals are highlighted in orange and green and labelled Pre, Onset, Peak and Post. Species abbreviations refer to:* G. index *(*Globigerinatheka index*)* A. primitiva (Acarinina primitiva).

and the Baskil Section record generated from *Acarinina* specimens. At ODP Site 647, SST estimates using both methods for *Pseudohastigerina micra* are in close agreement. In the Baskil Section record, SSTs derived from Equation 4.1 are up to 2 °C higher than the Bayfox median for some samples. Across all sites, the agreement between SST estimates derived

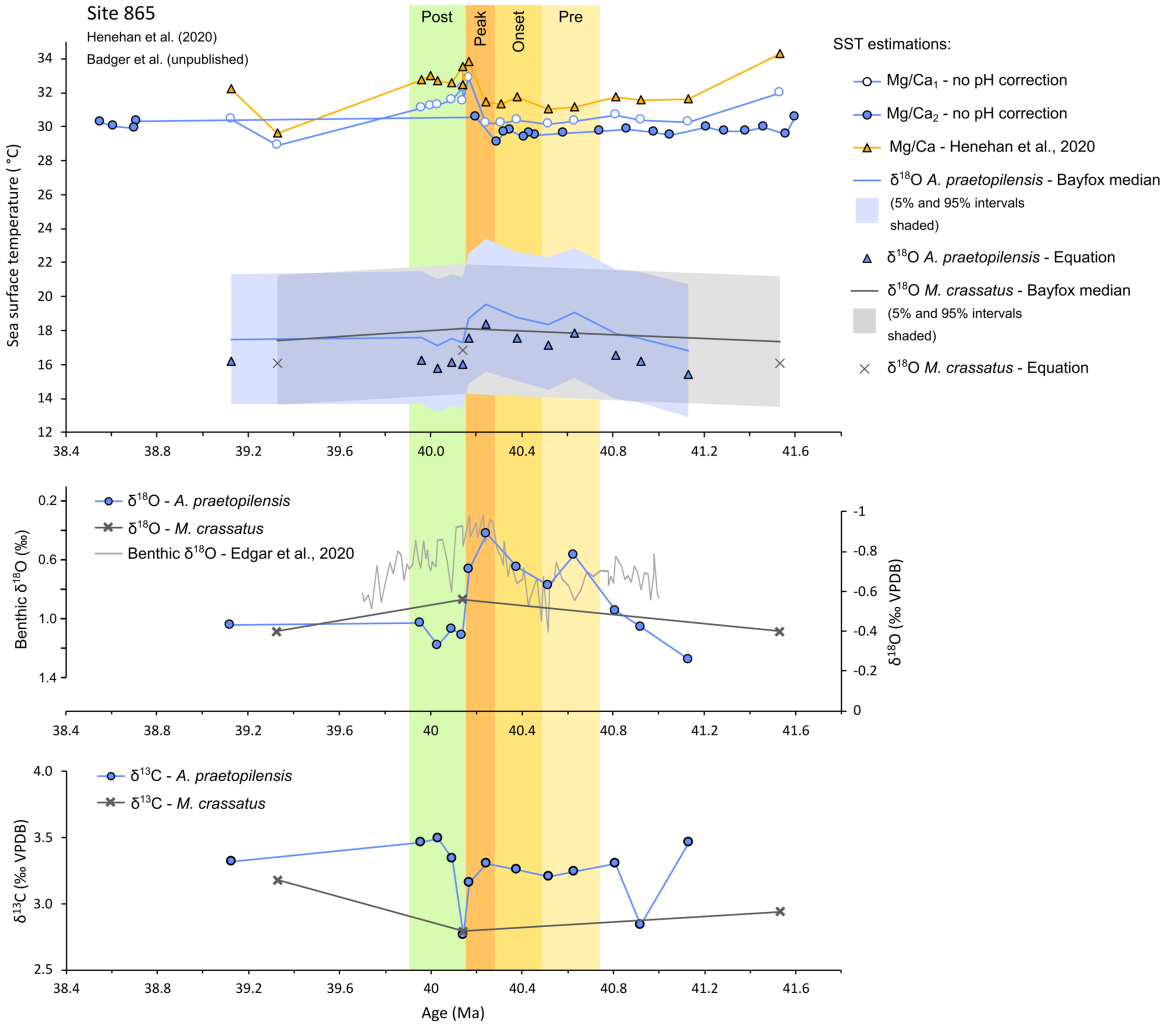


Figure 4.7 *Mg/Ca and planktic $\delta^{18}O$ temperature reconstructions for ODP Site 865, alongside planktic stable oxygen and carbon isotope records. For Mg/Ca temperature reconstructions, temperatures derived by Equation 4.3 are shown in blue while temperatures published in Henehan et al. (2020) are shown in yellow. Mg/Ca_1 refers to data collected by Henehan et al. (2020) and Mg/Ca_2 refers to data collected by Badger et al. (unpublished). For $\delta^{18}O$ temperature reconstructions, symbols show temperature values derived from Equation 4.1 and lines with shaded areas show Bayfox temperature estimates with confidence intervals. Benthic $\delta^{18}O$ record (grey line) is sourced from Edgar et al. (2020). Pre-MECO, MECO onset, Peak MECO and Post-MECO intervals are highlighted in orange and green and labelled Pre, Onset, Peak and Post. Species abbreviations refer to species:* Acarinina praetopilensis (A. praetopilensis), Morozovelloides crassatus (M. crassatus).

from Equation 4.1 and Bayfox appears to increase with temperature. For example, at ODP Site 1260, SSTs within the pre-MECO and MECO onset intervals estimated from Equation 4.1 are ~1 °C cooler than Bayfox estimates. Across the peak MECO and post-MECO intervals, overall SSTs are higher, and SST estimates from Equation 4.1 are <0.5 °C cooler than Bayfox estimates. Where multiple proxies exist for the same site, SSTs estimated

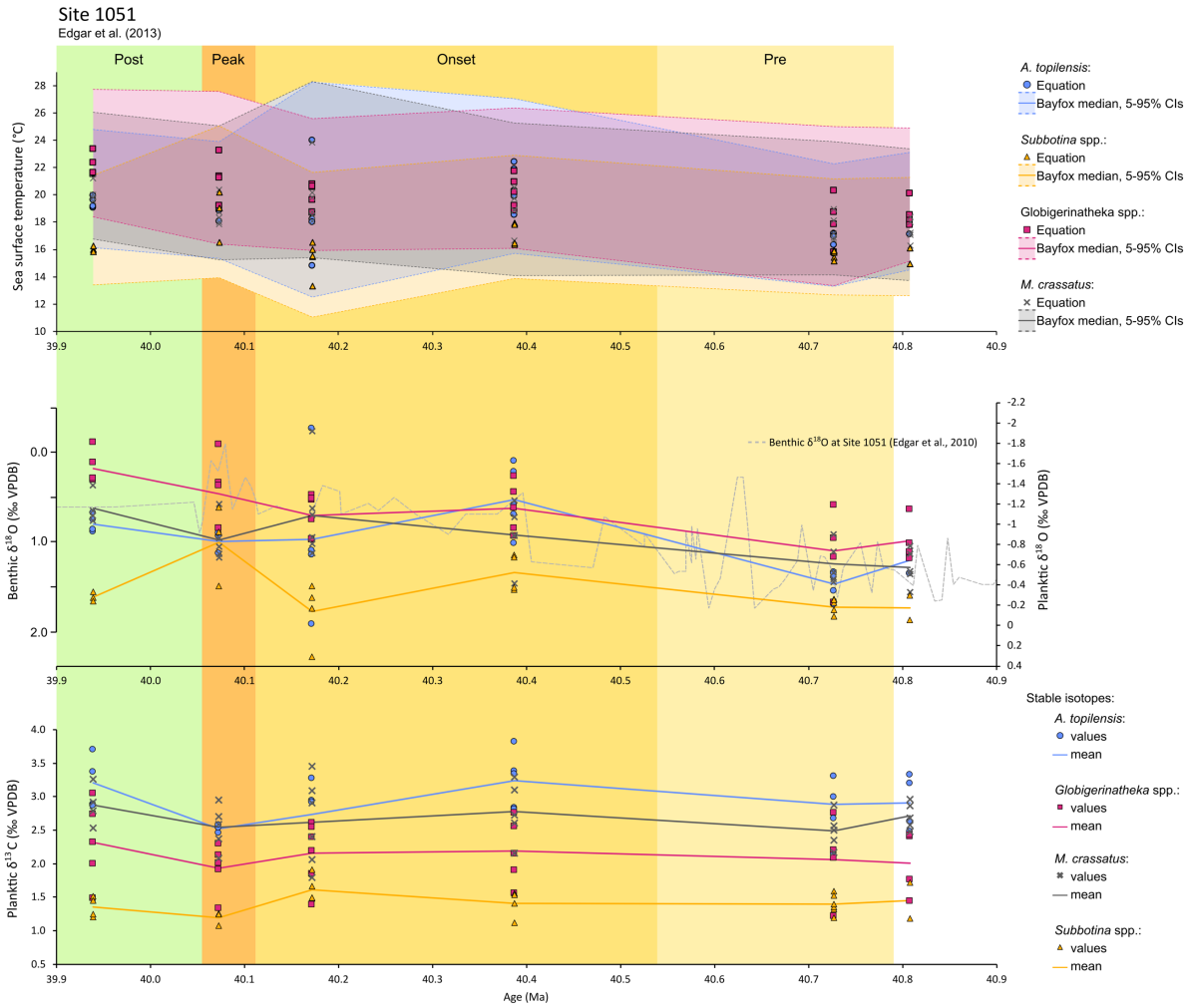


Figure 4.8 *Planktic $\delta^{18}O$ temperature reconstructions for ODP Site 1051, alongside the benthic $\delta^{18}O$ record for this site. Symbols show temperature values derived from Equation 4.1 and lines with shaded areas show Bayfox temperature estimates with confidence intervals. Benthic $\delta^{18}O$ record (grey line) is sourced from Edgar et al. (2010). Pre-MECO, MECO onset, Peak MECO and Post-MECO intervals are highlighted in orange and green and labelled Pre, Onset, Peak and Post. Species abbreviations refer to species:* Acarinina topilensis (A. topilensis), Morozovelloides crassatus (M. crassatus).

through $\delta^{18}O$ (both methods) are cooler than SSTs estimated using Mg/Ca and TEX_{86}. $\delta^{18}O$ temperatures are between 8 – 16 °C cooler than Mg/Ca estimates at ODP Sites 702, 865, 1260 and 1263 across the MECO. For ODP Site 647, $\delta^{18}O$ temperature estimates are ~4 °C cooler than TEX_{86} temperatures across the intervals of the MECO.

4.3.1.2 Mg/Ca-based SST reconstructions

Four sites have Mg/Ca records available across the MECO (Supplementary Table 4.2): ODP Sites 702 (Fig. 4.5), 865 (Fig. 4.7), 1260 (Fig. 4.12) and 1263 (Fig. 4.13). For each site

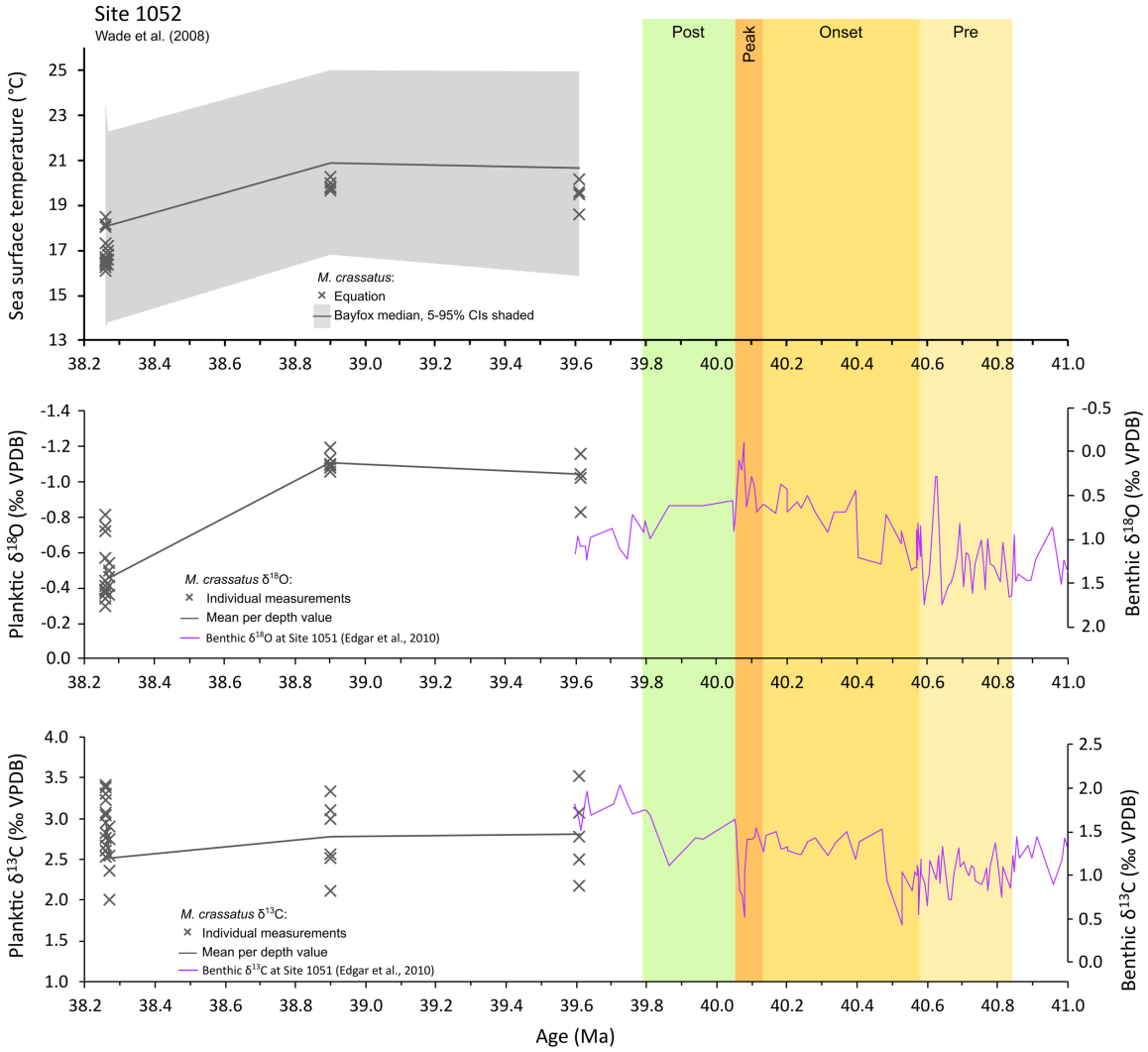


Figure 4.9 *Planktic $\delta^{18}O$ temperature reconstructions for ODP Site 1052, alongside benthic stable oxygen and carbon isotope records. Symbols show temperature values derived from Equation 4.1 and lines with shaded areas show Bayfox temperature estimates with confidence intervals. Benthic $\delta^{18}O$ and $\delta^{13}C$ records (purple line) are sourced from Edgar et al. (2010). Pre-MECO, MECO onset, Peak MECO and Post-MECO intervals are highlighted in orange and green and labelled Pre, Onset, Peak and Post. Species abbreviation* M. crassatus *refers to species* Morozovelloides crassatus.

we present two SST estimates from Mg/Ca data: our SST calculation using Equation 4.3, which does not include a pH correction, and the temperature reconstruction from Henehan et al. (2020) which includes a pH correction. All sites with Mg/Ca temperature records also have planktic foraminiferal $\delta^{18}O$ temperature records as these two proxies were generated from the same planktic foraminifera species at each site. Foraminifera tests were recrystallised in all cases. At ODP Site 702, Mg/Ca SSTs vary between 20 – 25 °C across the MECO, and are

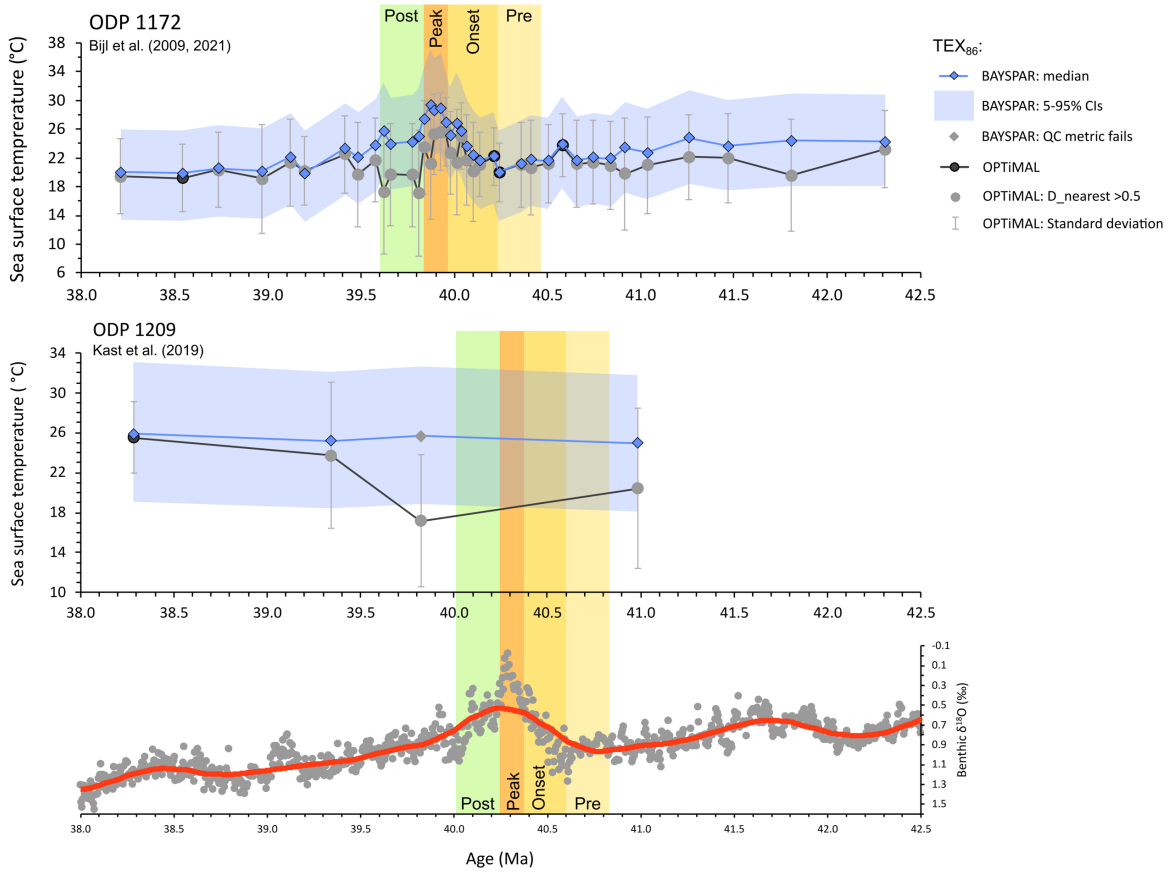


Figure 4.10 *TEX_{86} temperature records for ODP sites 1172 and 1209, alongside the CENOGRID global benthic oxygen isotope stack (bottom, red line shows 250 kyr smoothed values). BAYSPAR reconstructions are shown in blue, and OPTiMAL reconstructions are shown in grey. Pre-MECO, MECO onset, Peak MECO and Post-MECO intervals are highlighted in orange and green and labelled Pre, Onset, Peak and Post.*

between 7.5 to 16 °C warmer than temperatures derived from $\delta^{18}O$ at this site. For ODP Site 865, SSTs vary between 29 – 34 °C across the MECO and are 15 – 17 °C warmer than temperatures derived from $\delta^{18}O$. At ODP Site 1260, Mg/Ca SSTs vary between 27.5 – 32 °C across the MECO, however, unlike other sites with Mg/Ca data, peak SSTs are not aligned with the peak MECO interval. Mg/Ca SSTs are 2 – 12 °C warmer than $\delta^{18}O$ temperatures from Site 1260. At ODP Site 1263, temperatures vary between 25 – 29 °C across the MECO and Mg/Ca SSTs are 8 – 12 °C warmer than temperatures derived from $\delta^{18}O$ for the same species of foraminifera.

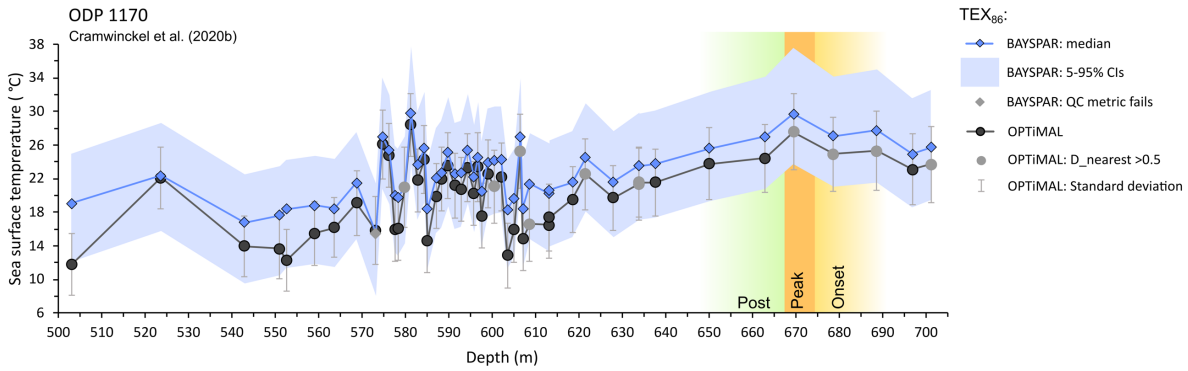


Figure 4.11 *TEX_{86} temperature record for ODP Site 1170. SST reconstructions are shown on the depth scale due to lack of age-depth tie points across the middle Eocene. BAYSPAR reconstructions are shown in blue, and OPTiMAL reconstructions are shown in grey. MECO onset, Peak MECO and Post-MECO intervals are highlighted in orange and green and labelled Onset, Peak and Post. Due to a lack of age model constraints we do not interpret the boundaries of the Post and Onset intervals here.*

Mg/Ca temperature reconstructions from Henehan et al. (2020) are within ~4 °C of SSTs from Equation 4.3, with no pH correction. However, the relationship between the two methods is not consistent. For ODP Sites 702 and 1263, the Henehan et al. (2020) temperature reconstruction is cooler than our reconstruction with no pH correction, by 1 – 4 °C for Site 702 and 0.5 – 1.5 °C for Site 1263. For ODP Site 865, the Henehan et al. (2020) reconstruction is 1 – 2 °C warmer than our reconstruction. For ODP Site 1260, the Henehan et al. (2020) record is 0.5 – 1.5 °C warmer than our reconstruction, except for one sample at the boundary between the peak MECO and post-MECO interval, where the Henehan et al. (2020) SST is cooler than our SST by <0.5 °C.

4.3.1.3 TEX_{86}-based SST reconstructions

TEX_{86} SST reconstructions across the MECO are presented for eight sites (Supplementary Table 4.3): DSDP Site 516 (Fig. 4.3), ODP sites 647 (Fig. 4.4), 913 (Fig. 4.3), 959 (Fig. 4.3), 1170 (Fig. 4.10), 1172 (Fig. 4.9), 1209 (Fig. 4.9) and the Belaya River section (Fig. 4.14). SSTs generated through BAYSPAR and OPTiMAL are presented for each site, along with the 5 – 95 % intervals of BAYSPAR reconstructions and the standard deviation as error bars on OPTiMAL reconstructions. For each reconstruction, we highlight samples which are lower in

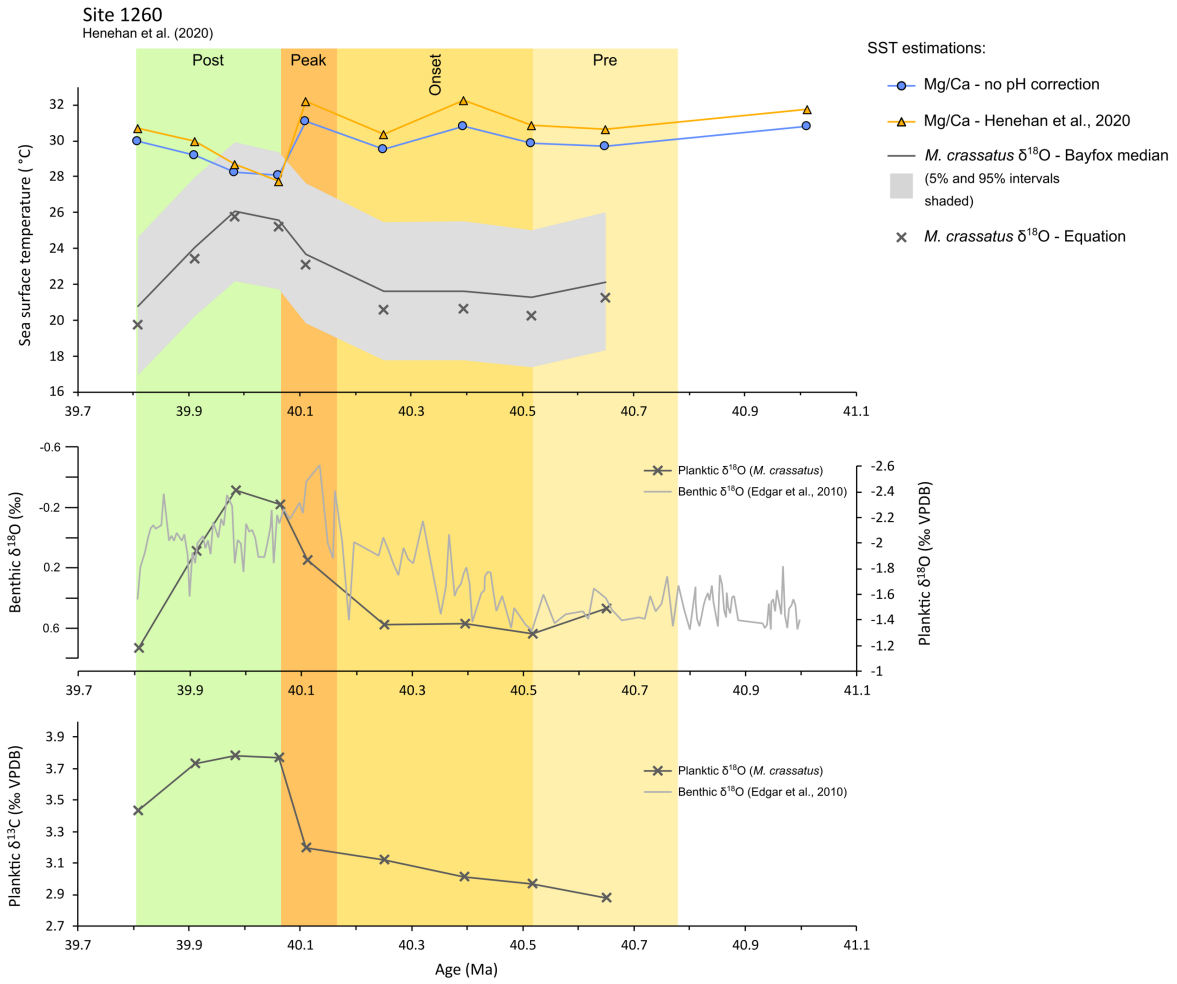


Figure 4.12 *Mg/Ca and planktic $\delta^{18}O$ temperature reconstructions for ODP Site 1260, alongside planktic and benthic stable oxygen isotope records. For Mg/Ca temperature reconstructions, temperatures derived by Equation 4.3 are shown in blue while temperatures published in Henehan et al. (2020) are shown in yellow. For $\delta^{18}O$ temperature reconstructions, symbols show temperature values derived from Equation 4.1 and lines with shaded areas show Bayfox temperature estimates with confidence intervals. Benthic $\delta^{18}O$ record (grey line with no symbols) is sourced from Edgar et al. (2010). Pre-MECO, MECO onset, Peak MECO and Post-MECO intervals are highlighted in orange and green and labelled Pre, Onset, Peak and Post. Species abbreviation* M. crassatus *refers to species* Morozovelloides crassatus*.*

quality according to the metrics described in Methods Section 4.2.5. Lower quality TEX_{86} samples are shown on all figures by the white symbol. As BAYSPAR and OPTiMAL rely on different metrics for quality assessment, different samples are often highlighted as lower quality in different reconstructions for the same site. While many samples are good quality according to the metrics used in BAYSPAR, the majority of samples returned by OPTiMAL have $D_{nearest}$ values >0.5, indicating a poor-quality temperature reconstruction. For example,

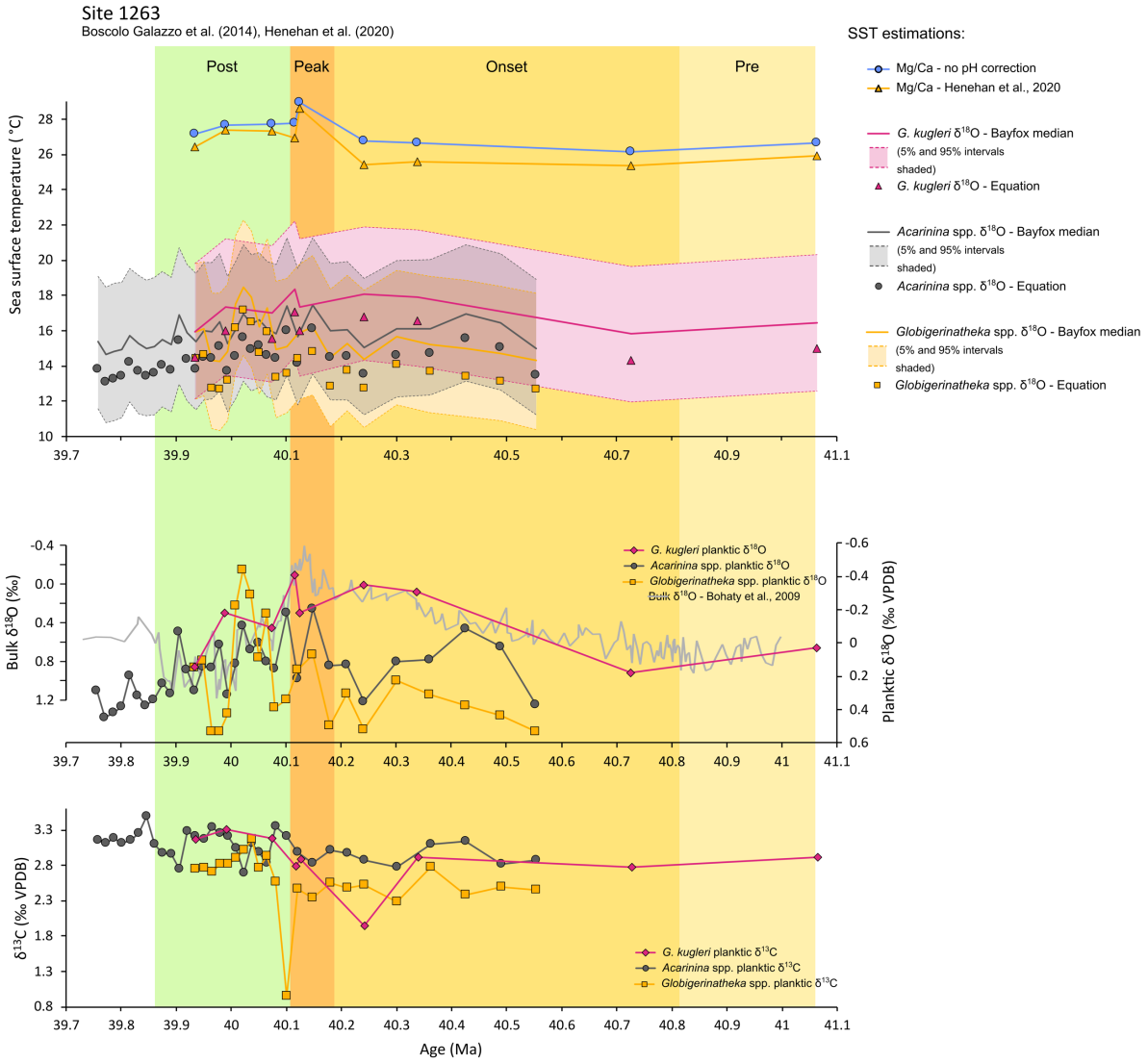


Figure 4.13 *Mg/Ca and planktic $\delta^{18}O$ temperature reconstructions for ODP Site 1263, alongside planktic and bulk carbonate stable oxygen isotope records. For Mg/Ca temperature reconstructions, temperatures derived by Equation 4.3 are shown in blue while temperatures published in Henehan et al. (2020) are shown in yellow. For $\delta^{18}O$ temperature reconstructions, symbols show temperature values derived from Equation 4.1 and lines with shaded areas show Bayfox temperature estimates with confidence intervals. Benthic $\delta^{18}O$ record (grey line with no symbols) is sourced from Bohaty et al. (2009). Pre-MECO, MECO onset, Peak MECO and Post-MECO intervals are highlighted in orange and green and labelled Pre, Onset, Peak and Post. Species abbreviation* G. kugleri *refers to species* Globigerinatheka kugleri.

all samples in the BAYSPAR reconstruction for ODP Site 1172 (Fig. 4.9) are considered "good" quality, while almost all of the same samples in the OPTiMAL reconstruction for this site are highlighted as "poor" quality. Absolute SSTs generated using OPTiMAL and BAYSPAR are not in good agreement for many sites. However, ODP Sites 913, 1172 and 1170 show generally good agreement between OPTiMAL and BAYSPAR across the lengths

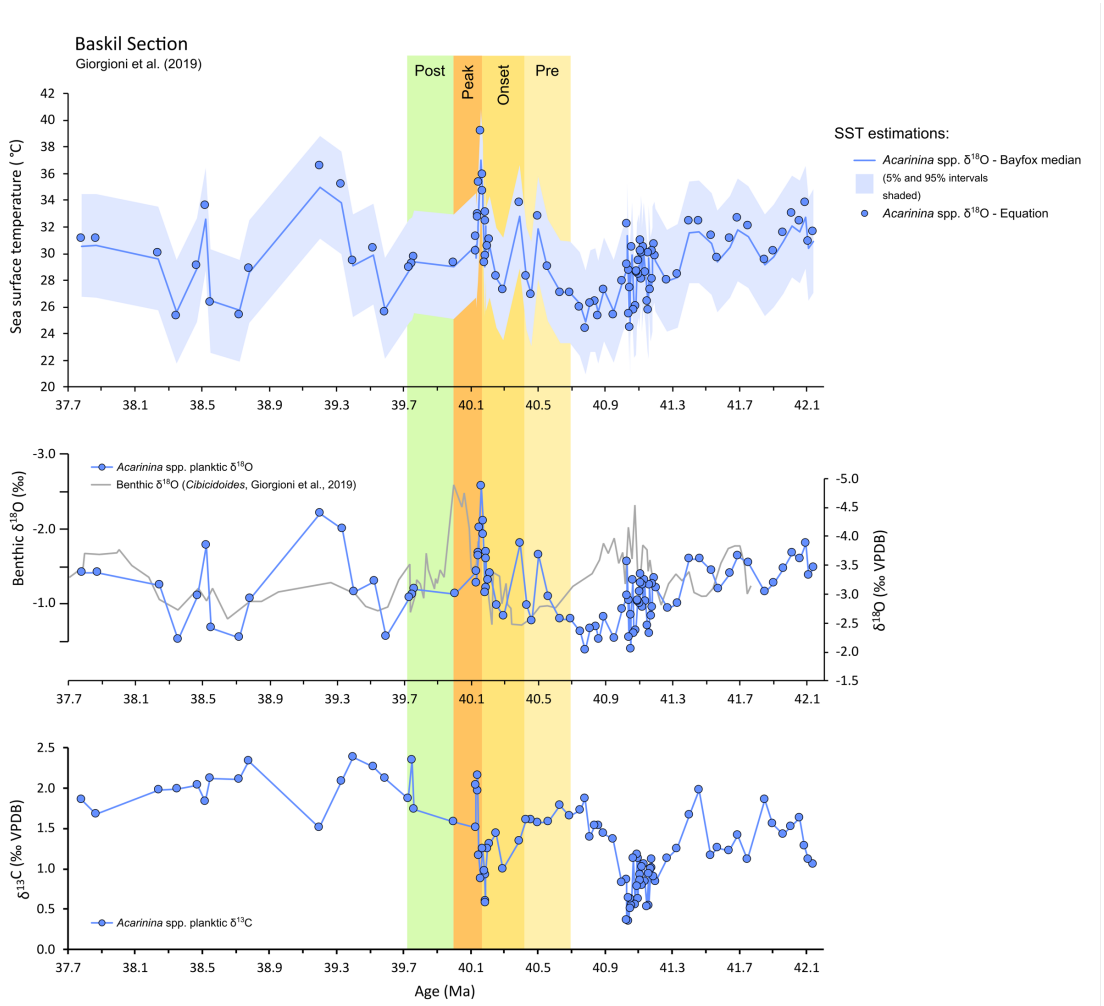


Figure 4.14 *Planktic $\delta^{18}O$ temperature reconstructions for the Baskil Section, alongside planktic and benthic oxygen and planktic carbon stable isotope records. Symbols show temperature values derived from Equation 4.1 and lines with shaded areas show Bayfox temperature estimates with confidence intervals. Benthic $\delta^{18}O$ record (grey line) is sourced from Giorgioni et al. (2019). Pre-MECO, MECO onset, Peak MECO and Post-MECO intervals are highlighted in orange and green and labelled Pre, Onset, Peak and Post.*

of these records, with temperatures from each reconstruction within ~5 °C of each other for most samples and showing similar general trends. ODP Sites 959, 647 and 1209 show relatively good agreement (OPTiMAL temperatures are within 8 °C of BAYSPAR) outside the MECO, but temperatures reconstructed via the two methods diverge across the MECO. For these sites, BAYSPAR temperature reconstructions show warming across the MECO, while OPTiMAL reconstructions show either no change or a cooling. DSDP Site 516 shows generally poor agreement between the two reconstructions across the entire record, where the

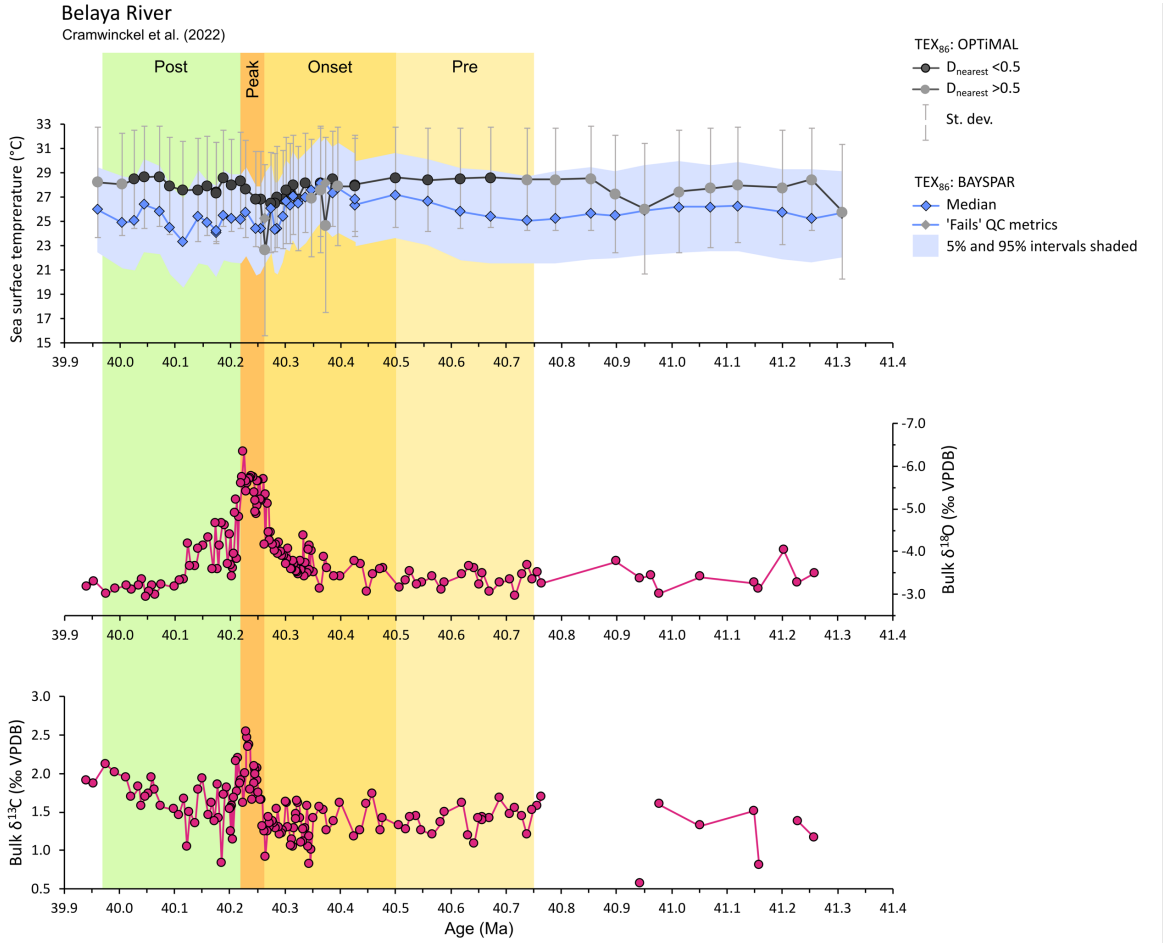


Figure 4.15 *TEX_{86} temperature records for the Belaya River section, alongside bulk stable oxygen and carbon isotopes. BAYSPAR reconstructions are shown in blue, and OPTiMAL reconstructions are shown in grey. Pre-MECO, MECO onset, Peak MECO and Post-MECO intervals are highlighted in orange and green and labelled Pre, Onset, Peak and Post.*

BAYSPAR reconstruction is between 2 and 30 °C warmer than the OPTiMAL reconstruction. The MECO warming trend shown by the BAYSPAR reconstruction is also not reproduced by OPTiMAL for this site. Across all sites, BAYSPAR reconstructions are usually warmer than OPTiMAL, by <1 to >20 °C depending on the site. The Belaya River section is an exception to this pattern, as OPTiMAL temperatures in this case are warmer than BAYSPAR temperatures by up to 4 °C. The two reconstructions otherwise agree well at this site, and temperatures show a similar pattern in both methods across the MECO.

TEX_{86} temperature reconstructions using both methods produce the warmest temperatures of all proxies used in this compilation, and SSTs across the MECO are 20 – 37 °C according

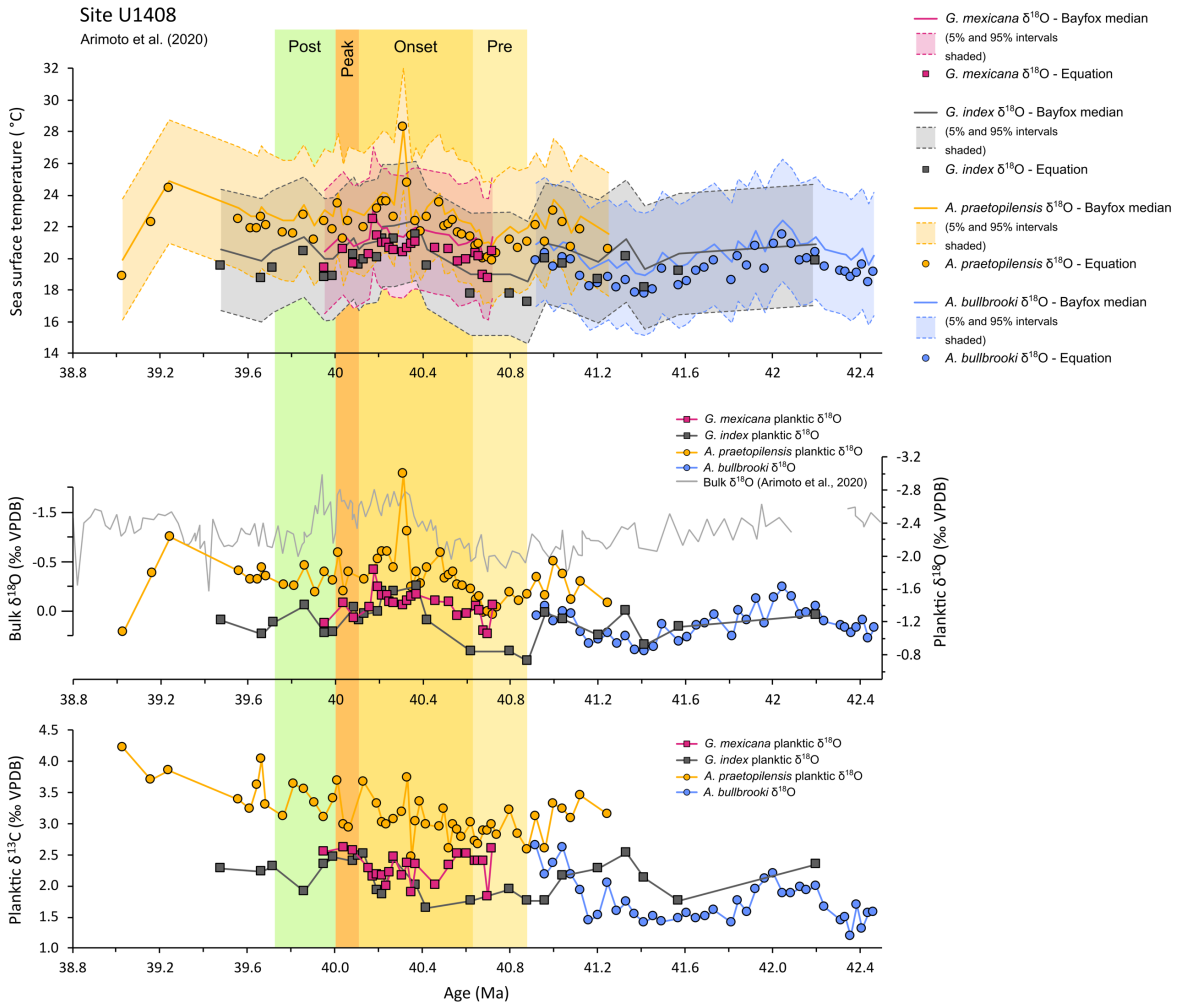


Figure 4.16 *Planktic $\delta^{18}O$ temperature reconstructions for IODP Site U1408, alongside planktic stable oxygen and carbon isotope records and bulk carbonate oxygen stable isotopes. Symbols show temperature values derived from Equation 4.1 and lines with shaded areas show Bayfox temperature estimates with confidence intervals. Bulk $\delta^{18}O$ record (grey line) is sourced from Arimoto et al. (2020). Pre-MECO, MECO onset, Peak MECO and Post-MECO intervals are highlighted in orange and green and labelled Pre, Onset, Peak and Post. Species abbreviations refer to species:* Acarinina bullbrooki (A. bullbrooki), Acarinina praetopilensis (A. praetopilensis), Globigerinatheka index (G. index) *and* Globigerinatheka mexicana (G. mexicana).

to this proxy. However, the TEX_{86} proxy also produces the coolest temperatures of the three proxies. The BAYSPAR method infers a temperature of -1 °C for one sample at ODP Site 913, though we note that this sample is poor quality according to both BAYSPAR and OPTiMAL metrics.

4.3.2 SST change across intervals of the MECO

For each site, SSTs for every sample within each MECO interval were averaged and plotted, along with the standard deviation of the group of samples averaged (Supplementary Table 4.4 and Fig. 4.17). Of the 17 sites included in this compilation, 11 sites (DSDP Site 516, ODP Sites 647, 702, 865, 959, 1051, 1172, 1260, Baskil Section, Belaya River section and IODP Site U1408) have at least one data point in each of the MECO intervals. ODP Sites 1052 and 1209 do not have any data points across the MECO but only background temperatures. For ODP Site 1170, which lacks an age model, we place our peak MECO interval based on the peak temperature identified by Cramwinckel, Woelders, et al. (2020).

We calculate the temperature change, ΔT, between MECO intervals for sites which have data points in two or more adjacent intervals (Table 4.4). According to our definitions of the MECO based on bulk carbonate or benthic foraminiferal stable isotope records, we would expect temperatures to progressively increase from the pre-MECO to the peak MECO, and then decrease rapidly from peak MECO to post MECO. Of the sites with data points across all four MECO intervals, this 'typical warming' pattern is observed in the SST records at eight sites: the TEX_{86} (BAYSPAR) record of ODP Site 647, the $\delta^{18}O$ (*Acarinina praetopilensis*) record for ODP Site 865, the TEX_{86} (BAYSPAR) record of ODP Site 959, the $\delta^{18}O$ (*Subbotina* spp.) records for ODP Sites 1051, both TEX_{86} records for ODP Site 1172, both Mg/Ca records (X and X) for ODP 1260, $\delta^{18}O$ (*Acarinina* spp.) records for the Baskil Section and the $\delta^{18}O$ (*Globigerinatheka index*) records for IODP Site U1408 (Fig. 4.17, Table 4.4). The greatest ΔT from MECO onset to peak MECO is in TEX_{86} records from ODP Site 913 (Table 4.4), where mean temperature rises by 7.2 °C (OPTiMAL) and -23.1 °C (BAYSPAR). The very high ΔT in the Site 913 TEX_{86} BAYSPAR record is strongly influenced by negative temperature values estimated in the MECO onset interval at this site, which is not realistic for

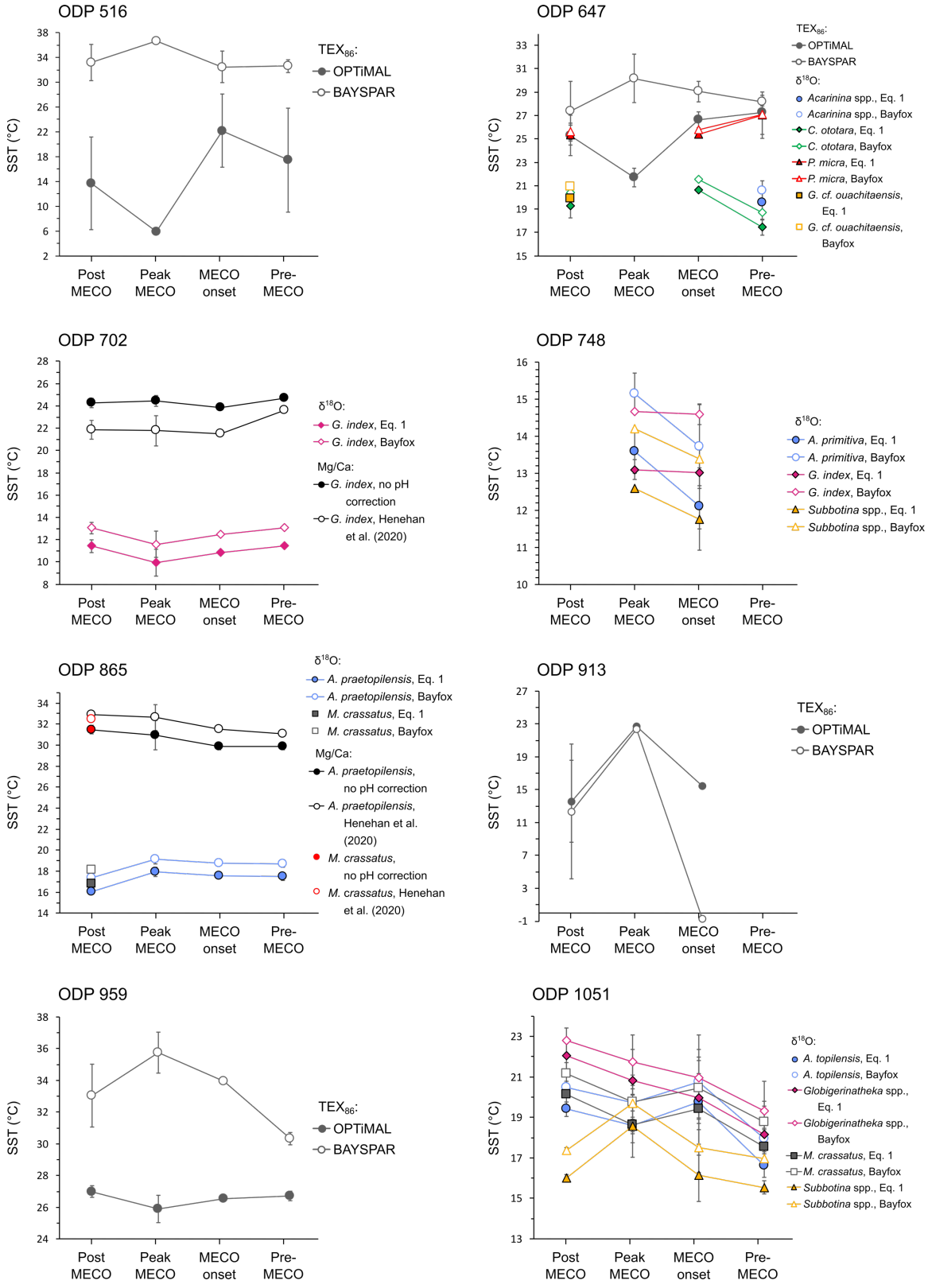


Figure 4.17 *Average SSTs over the pre-, onset, peak and post-MECO intervals. Error bars show standard deviation for each average SST value. Continued overleaf.*

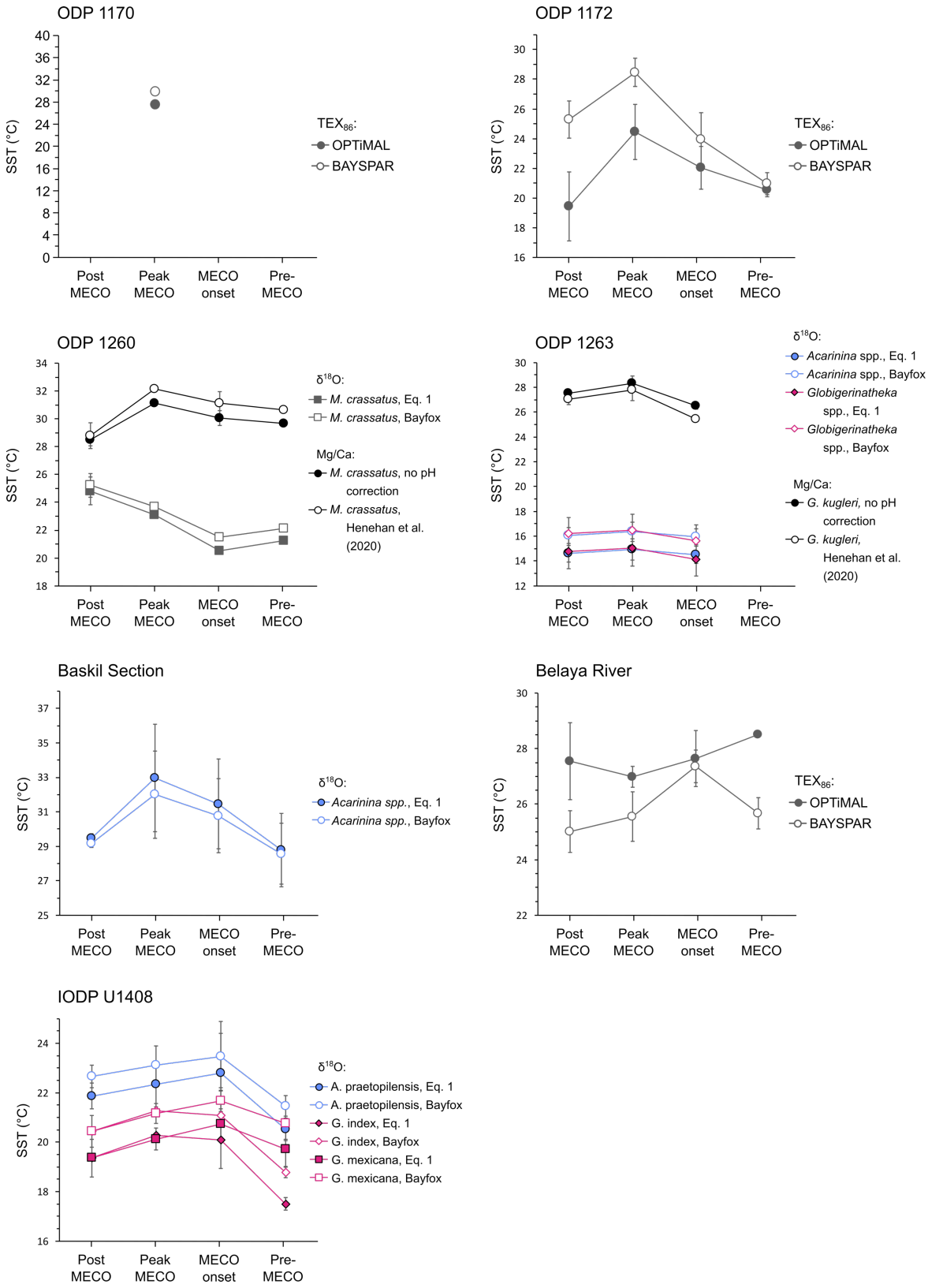


Figure 4.17 (cont.) *Average SSTs over the pre-, onset, peak and post-MECO intervals. Error bars show standard deviation for each average SST value*

Site	Proxy - Method	Species	ΔT (°C): Pre to Onset	ΔT (°C): Onset to Peak	ΔT (°C): Peak to Post
516	TEX86 - OPTiMAL	N/A	4.8	-16.3	7.8
	TEX86 - BAYSPAR	N/A	-0.2	4.3	-3.5
647	TEX86 - OPTiMAL	N/A	-0.6	-5.0	3.6
	TEX86 - BAYSPAR	N/A	0.9	1.1	-2.8
	d18O - Equation 1	C. ototara	3.2		
	d18O - Bayfox	C. ototara	2.8		
	d18O - Equation 1	P. micra	-1.6		
	d18O - Bayfox	P. micra	-1.3		
702	d18O - Equation 1	G. index	-0.7	-0.9	1.5
	d18O - Bayfox	G. index	-0.6	-0.9	1.5
	Mg/Ca - no pH correction	G. index	-0.8	0.6	-0.2
	Mg/Ca - Henehan et al. (2020)	G. index	2.1	0.3	0.1
748	d18O - Equation 1	A. primitiva		1.5	
	d18O - Bayfox	A. primitiva		1.5	
	d18O - Equation 1	G. index		0.1	
	d18O - Bayfox	G. index		0.1	
	d18O - Equation 1	Subbotina spp.		0.8	
	d18O - Bayfox	Subbotina spp.		0.8	
865	d18O - Equation 1	A. praetopilensis	0.1	0.3	-1.9
	d18O - Bayfox	A. praetopilensis	0.1	0.3	-1.7
	Mg/Ca - no pH correction	A. praetopilensis	0.0	1.0	0.6
	Mg/Ca - Henehan et al. (2020)	A. praetopilensis	0.4	1.1	0.3
913	TEX86 - OPTiMAL	N/A		7.2	-9.1
	TEX86 - BAYSPAR	N/A		23.1	-10.0
959	TEX86 - OPTiMAL	N/A	-0.2	-0.6	1.1
	TEX86 - BAYSPAR	N/A	3.6	1.8	-2.6
1051	d18O - Equation 1	A. topilensis	3.1	-1.1	0.8
	d18O - Bayfox	A. topilensis	2.8	-1.0	0.8
	d18O - Equation 1	Globigerinatheka spp.	1.8	0.8	1.2
	d18O - Bayfox	Globigerinatheka spp.	1.6	0.8	1.1
	d18O - Equation 1	M. crassatus	1.9	-0.8	1.5
	d18O - Bayfox	M. crassatus	1.6	-0.6	1.4
	d18O - Equation 1	Subbotina spp.	0.7	2.4	-2.6
	d18O - Bayfox	Subbotina spp.	0.5	2.2	-2.3
1172	TEX86 - OPTiMAL	N/A	1.4	2.4	-5.0
	TEX86 - BAYSPAR	N/A	2.9	4.6	-3.2
1260	d18O - Equation 1	M. crassatus	-0.8	2.6	1.7
	d18O - Bayfox	M. crassatus	-0.6	2.2	1.5
	Mg/Ca - no pH correction	M. crassatus	0.4	1.0	-2.6
	Mg/Ca - Henehan et al. (2020)	M. crassatus	0.4	1.1	-3.4
1263	Mg/Ca - no pH correction	G. kugleri		1.8	-0.8
	Mg/Ca - Henehan et al. (2020)	G. kugleri		2.4	-0.8
	d18O - Equation 1	Acarinina spp.		0.4	-0.3
	d18O - Bayfox	Acarinina spp.		0.4	-0.3
	d18O - Equation 1	Globigerinatheka spp.		0.9	-0.2
	d18O - Bayfox	Globigerinatheka spp.		0.9	-0.3
Baskil Section	d18O - Equation 1	Acarinina spp.	2.7	1.5	-3.5
	d18O - Bayfox	Acarinina spp.	2.2	1.2	-2.8
Belaya River	TEX86 - OPTiMAL	N/A	-0.9	-0.6	0.5
	TEX86 - BAYSPAR	N/A	1.6	-1.8	-0.5
U1408	d18O - Equation 1	A. praetopilensis	2.3	-0.5	-0.4
	d18O - Bayfox	A. praetopilensis	2.0	-0.4	-0.4
	d18O - Equation 1	G. index	2.6	0.2	-0.9
	d18O - Bayfox	G. index	2.3	0.2	-0.9
	d18O - Equation 1	G. mexicana	1.0	-0.6	-0.7
	d18O - Bayfox	G. mexicana	0.9	-0.5	-0.8

Table 4.4 *Temperature change (ΔT) between intervals of the MECO for sites which have data points in two or more adjacent intervals of the MECO. Pre, Onset, Peak and Post refer to the pre-MECO, MECO onset, peak MECO and post-MECO intervals.*

the middle Eocene surface ocean. Most sites show warming from the pre-MECO to peak MECO of between 0.1 – 4.6 °C. However, not every proxy, method of SST reconstruction or species analysed for these sites shows the same pattern. Other sites show a combination of cooling into the peak MECO interval, and/or warming into the post-MECO interval. Where

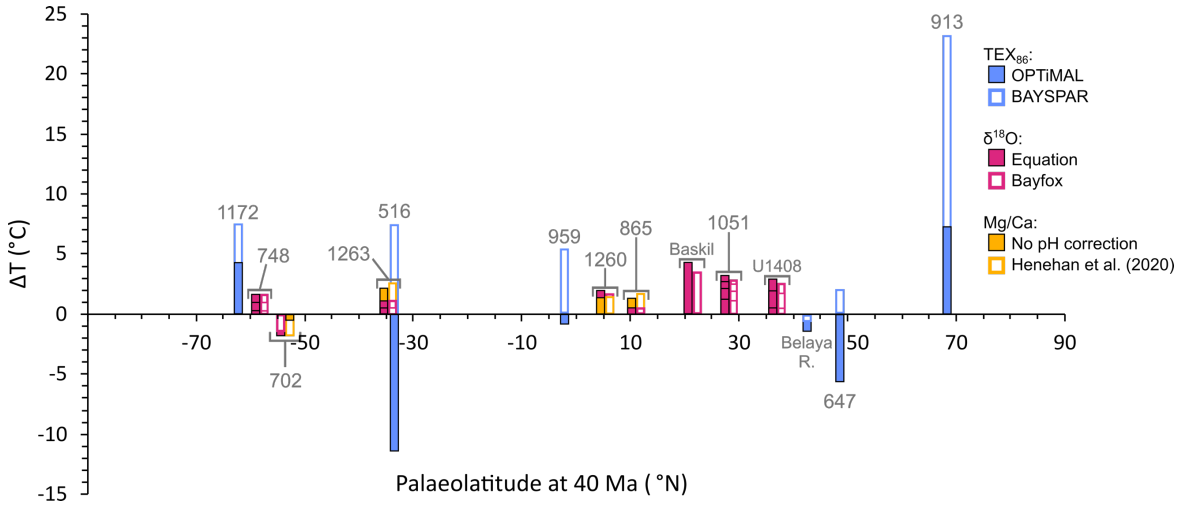


Figure 4.18 *Change in temperature, ΔT, between the pre/onset to peak MECO intervals by latitude. ΔT is the difference between average SSTs between the pre-MECO and peak MECO intervals. For Sites 748, 913 and 1263, there are no data points in the pre-MECO interval so ΔT for these sites is the difference between average SSTs between the MECO onset and peak MECO intervals. For $\delta^{18}O$ SST reconstructions (pink), horizontal lines across ΔT bars indicate different temperature reconstructions for different species.*

sites show a temperature decline across the peak MECO, this is between -0.4 to -5 °C, aside from the OPTiMAL TEX_{86} SST record from DSDP Site 516 which shows a large temperature decline of -16.3 °C from MECO onset to peak MECO. Apparent cooling across the MECO is presented at face-value here, however we discuss the validity of these datasets further in our discussion.

Temperature change, ΔT, between the pre- (or onset) and peak MECO intervals shows the average warming of surface waters at each site associated with the MECO (Fig. 4.18). The TEX_{86} proxy (both BAYSPAR and OPTiMAL methods) shows the most variability across the MECO, with ΔT across the MECO ranging from -11 °C (DSDP Site 516, palaeolatitude: -33.4 °) to 23 °C (ODP Site 913, palaeolatitude: 68.7 °). There is also variability in the SST reconstruction method used with TEX_{86} data, with many sites showing a cooling with OPTiMAL but a warming with BAYSPAR. The greatest ΔT from TEX_{86} is seen at the two highest latitude sites, ODP Site 913 (ΔT = 23 °C, palaeolatitude: 68.7) and ODP Site 1172 (ΔT = 7.5 °C, palaeolatitude: -62.2 °). However, there is no trend of increasing warming with

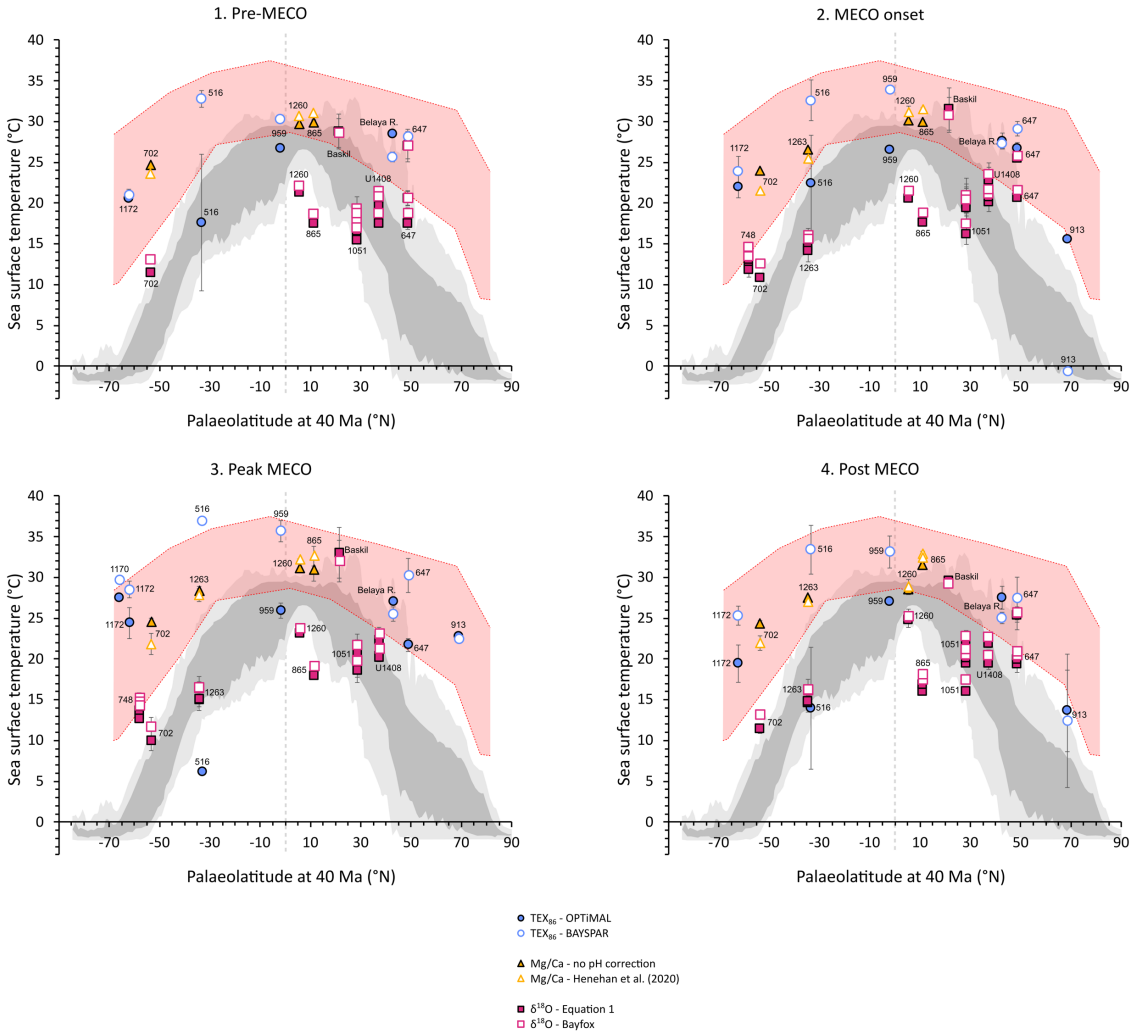


Figure 4.19 *Average sea surface temperatures with latitude for: 1. pre-MECO, 2. MECO onset, 3. Peak MECO and 4. Post MECO intervals, compared to the compilation of SST proxy data for the full middle Eocene (38 – 48 Ma, red shaded band with dashed boundaries, Evans et al., 2018) and modern mean annual temperature (dark grey) and seasonal SST ranges (pale grey). Error bars indicate standard deviation for each SST average data point.*

increasing latitude, and the next greatest magnitude warming (ΔT = 5.4 °C) is at the equatorial Atlantic site ODP 959 (palaeolatitude: -1.9 °C).

4.3.3 Latitudinal SST change across the MECO

Average SSTs for each MECO interval are plotted against latitude (Fig. 4.19) and compared with modern mean and seasonal SST ranges, as well as the temperature range of clumped isotope and Mg/Ca proxy data for the full middle Eocene (38 – 48 Ma, Evans et al.,

2018). There are two striking patterns here. First, TEX_{86} and Mg/Ca records span all latitudes and suggest warmer than modern tropics (~25 – 36 °C) throughout the MECO, and decreasing SSTs with increasing latitude in (Fig. 4.19). The majority of TEX_{86} and Mg/Ca SSTs are within or close to the range of the published middle Eocene compilation in all intervals, except for DSDP Site 516 and ODP Sites 959 and 913, where TEX_{86} SSTs are <1 to >20 °C cooler than the middle Eocene compilation. The latitudinal gradient is noticeably less steep than the modern SST gradient, where polar regions are ~25 °C cooler than tropics in the modern case and our compilation shows high latitudes ~5 – 15 °C cooler than tropics. Second, planktic foraminiferal $\delta^{18}O$ average SST records are consistently cooler than the Mg/Ca and TEX_{86} records from this study and the published middle Eocene compilation in all intervals. The exceptions are records from the Baskil Section and ODP Site 647 which are more consistent with the other proxies and the middle Eocene compilation. Notably, planktic foraminiferal $\delta^{18}O$ average SSTs do not decrease as latitude increases and instead group into two clusters. Mid-high latitude southern hemisphere sites (-30 – -65 °S), ODP 702, 748 and 1263, show relatively consistent SSTs of ~10 – 15 °C in all MECO intervals. The remaining sites are all located in the northern hemisphere, between latitudes of 0 – 55 ° and are overall at least several degrees higher than in the southern hemisphere, with SSTs ranging from 15 – 25 °C across all MECO intervals. Baskil Section SSTs are a little higher, up to 30 °C. There is no clear change in the shape or magnitude of the latitudinal gradient across the MECO in any of the proxy types but the spread of SSTs is greatest in the peak MECO interval.

There is also no clear latitudinal pattern to warming (ΔT) for temperatures derived from Mg/Ca via both methods (Fig. 4.18). ΔT for this proxy ranges from -0.2 °C (ODP Site 702, palaeolatitude: -53.5 °) to 2.4 °C (ODP Site 1263, palaeolatitude: -34.5 °). For $\delta^{18}O$, ΔT

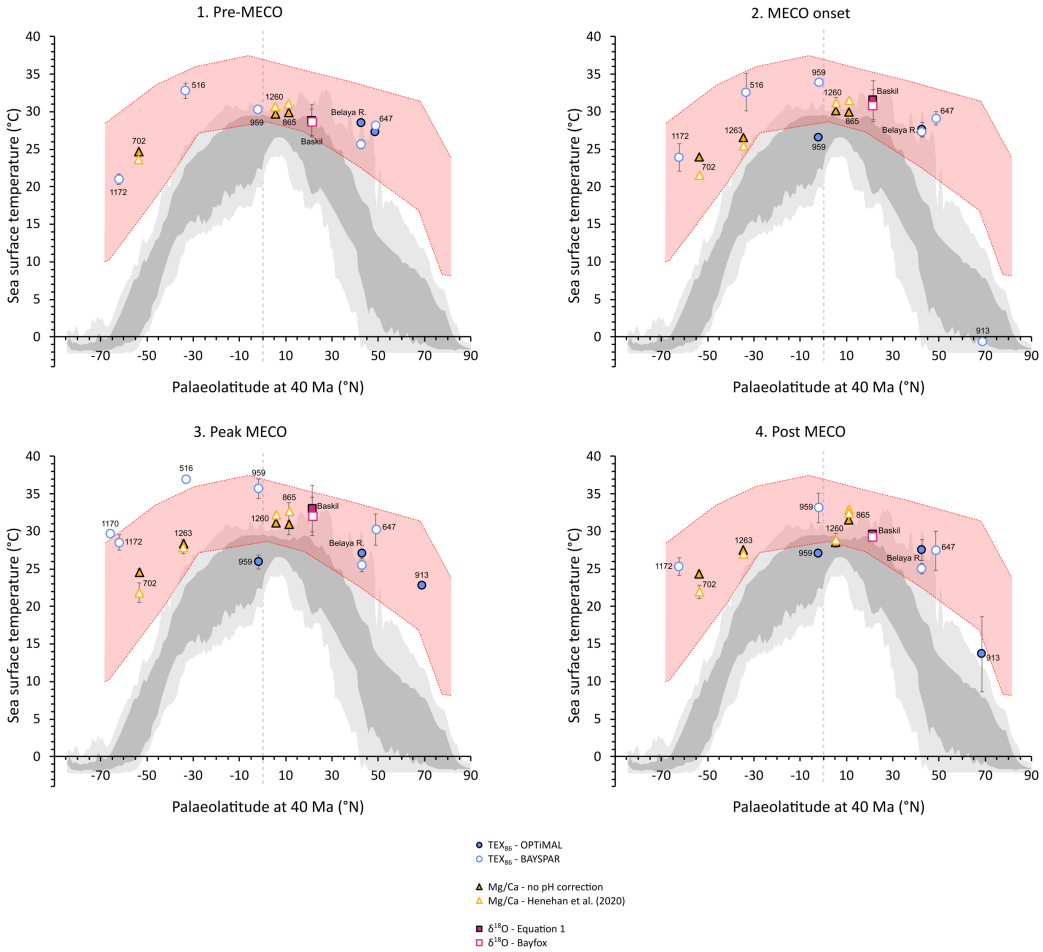


Figure 4.20 *Reproduction of average SSTs in MECO intervals as in Fig. 4.19, with poor quality data points removed. Compilation of SST proxy data for the full middle Eocene (38 – 48 Ma, red shaded band with dashed boundaries, Evans et al., 2018) and modern mean annual temperature (dark grey) and seasonal SST ranges (pale grey). Error bars indicate standard deviation for each SST average data point.*

ranges from -1.6 °C (ODP Site 702, palaeolatitude: -53.5 °) to 4.2 °C (Baskil Section, palaeolatitude: 21.4 °). Overall, while the greatest amount of surface water warming associated with the MECO is reconstructed by the TEX_{86} proxy at the two highest latitude sites in both the northern and southern hemispheres, ODP Sites 913 and 1172, the magnitude of warming is highly variable at all latitudes in-between.

Removing unreliable data points from this compilation, such as $\delta^{18}O$ from recrystallised foraminifera and poor quality TEX_{86} distributions, results in a better match between MECO SSTs and the middle Eocene SST compilation (Evans et al., 2018; Fig. 4.20).

4.4 DISCUSSION

4.4.1 Eocene climate reconstructions with $\delta^{18}O$, Mg/Ca and TEX_{86}

This study highlights the major differences between temperature reconstructions based on different proxies, and the importance of multi-proxy SST records in generating a full and accurate picture of SST change, both spatially and temporally. We discuss the impact of different uncertainties and assumptions involved in each proxy ($\delta^{18}O$, Mg/Ca and TEX_{86}) and method employed to ultimately assess how applicable these proxies are towards estimating middle Eocene SSTs.

4.4.1.1 Impact of diagenesis on planktic foraminiferal $\delta^{18}O$

Planktic foraminiferal carbonate is well-known to be susceptible to post-depositional diagenesis, which artificially increases $\delta^{18}O_c$ leading to cooler palaeotemperature estimates (e.g., Edgar et al., 2015; Pearson et al., 2001; Sexton et al., 2006). This problem is most pronounced in tropical and low latitude sites, leading to offsets >10 °C due to a large temperature difference between surface waters, where planktic foraminiferal carbonate is precipitated, and conditions at or beneath the seafloor where recrystallisation occurs. Diagenesis of $\delta^{18}O$ values is responsible for the so-called "cool-tropic paradox" whereby Cretaceous and Eocene planktic foraminiferal $\delta^{18}O$ indicates tropical temperatures similar or cooler than modern (Pearson et al., 2001; Sexton et al., 2006). Almost all $\delta^{18}O$ data points in this study were generated from recrystallised foraminiferal tests, so it is likely that persistently cooler overall SSTs estimated from $\delta^{18}O$ data compared to Mg/Ca and TEX_{86}, particularly in the tropical region, reflects an overprint of diagenesis (Fig. 4.19). Indeed, the agreement between SSTs from foraminiferal Mg/Ca, which is less susceptible to post-depositional diagenesis than $\delta^{18}O$ from the same carbonate (Sexton et al., 2006), with non-anomalous

TEX_{86} SSTs presented here (Fig. 4.19) and foraminiferal clumped isotope SSTs for the middle Eocene between 38 – 48 Ma (red shading in Fig. 4.19; Evans et al., 2018) suggests that the majority of available $\delta^{18}O$ data here does not accurately reflect middle Eocene SSTs. The notable exception is planktic foraminiferal SST estimates from the Baskil Section (Fig. 4.14), from which tests do not show evidence of significant post-depositional alteration, i.e., are well preserved or "glassy" (Giorgioni et al., 2019). These $\delta^{18}O$ values yield very warm temperatures throughout the MECO, ~32 – 33 °C at the peak of the MECO, in close agreement with Mg/Ca and TEX_{86} SSTs from nearby latitudes (Fig. 4.19). All other sites with $\delta^{18}O$ data show much cooler SSTs of <23 °C throughout the study interval, despite many data points at these sites deriving from the same group of surface dwelling planktic foraminifera as measured in the Baskil Section, *Acarinina,* ruling out species-specific offsets as an explanation.

Our records highlight large SST offsets, ~10 °C, observed between proxies at mid to high latitude sites where the effects of digenesis are expected to be less pronounced (e.g., Pearson et al., 2001; Schrag et al., 1995; Sexton et al., 2006). High southern latitude sites ODP 702 and 748 in the south Atlantic Ocean yield $\delta^{18}O$-derived SSTs of 10 – 16 °C across the MECO, much lower (~10 – 15 °C) than TEX_{86}-SSTs from equivalent latitude at southwest Pacific Ocean Sites 1170 and 1172 (Fig 4.19). At first glance, the inter-basin offset in SSTs observed here support previous reports of a much warmer middle Eocene south Pacific (SSTs >20°C; Bijl et al., 2009, 2021; Cramwinckel et al., 2020), than the high latitude South Atlantic, from which bivalve clumped $\delta^{18}O$ and TEX_{86} reconstruct temperatures of 10 – 17 °C (Seymour Island, ~67 °S; Douglas et al., 2014; Dutton et al., 2002). It is therefore possible that planktic foraminiferal $\delta^{18}O$ values at ODP Sites 702 and 748 are recording a surface temperature signal similar to that of Seymour Island, close to the Antarctic Peninsula, and that cool, polar

temperatures of the middle Eocene extended into the high latitude southern Atlantic and southern Indian oceans. However, foraminiferal Mg/Ca values at ODP Site 702 record SSTs between 21 – 25 °C, ~10 °C higher than $\delta^{18}O$-based SSTs implying that there may be a diagenetic bias operating here (Fig. 4.5) and that SSTs <20 °C were constrained to latitudes above ~60 °S, proximal to Antarctica. It is also worth noting that the SST estimates from Seymour Island are relatively low resolution and do not capture MECO variability (Douglas et al., 2014; Dutton et al., 2002) so peak MECO temperatures may be underestimated. New proxy records (Mg/Ca and/or TEX_{86}) from Site 748, along with other SST records from high latitude sites including the high latitude Indian Ocean (e.g. IODP Site U1514, Huber et al., 2019) would allow a better estimation of high southern latitude SST evolution across the MECO and allow us to better test the apparent temperature offset between the cool, high latitude South Atlantic and warm southwest Pacific from the literature and seen here.

4.4.1.2 Impact of middle Eocene seawater chemistry on SST estimates

The accuracy of $\delta^{18}O_{sw}$ values is limited by an incomplete understanding of Eocene ocean chemistry, which is a function of ice volume and carbonate ion concentration. This represents the largest source of uncertainty in our reconstructions. We correct for carbonate ion concentration based on a long-term, ocean-wide record of $[CO_3^{2-}]$ (Zeebe & Tyrrell, 2019). While this provides a reasonable estimate of the difference in whole ocean carbonate ion concentration in the middle Eocene compared to the modern ocean, it does not account for either site-specific differences or evolution of pH, and thus carbonate ion concentration, across the MECO itself (e.g. Henehan et al., 2020). Planktic foraminiferal $\delta^{18}O$ values from the PETM show that without accounting for pH change, peak PETM temperatures may be underestimated by ~1.5 °C (Aze et al., 2014). However, PETM surface water pH decline was ~0.25 – 0.45 pH units (Hönisch et al., 2012), much greater than the ~0.12 – 0.18 units decline

estimated at the MECO (Henehan et al., 2020). Thus, the impact of pH change on peak MECO temperatures is likely <1.5 °C, and pH change cannot account for the large offset between $\delta^{18}O$ SSTs and other proxies at any point across the MECO. ΔT estimates from Mg/Ca-Henehan et al. (2020), which account for pH change, are greater than ΔT from $\delta^{18}O$ for ODP Sites 865 and 1263, but lower for ODP Sites 702 and 1260. The impact of pH changes on the magnitude of MECO warming from $\delta^{18}O$ SSTs is therefore inconsistent between localities and not easy to interpret based on available data.

Our ice volume correction is within the range expected for the middle Eocene (Cramer et al., 2011) but middle Eocene ice volumes are contested (Cramer et al., 2011; Dawber & Tripati, 2011; Edgar et al., 2007; Rohling et al., 2021; Tripati & Darby, 2018) and different corrections have been proposed for this period (L'Homme, 2005; Shackleton & Kennett, 1975; Zachos et al., 1994). The ice volume correction that we apply represents a compromise and assumes that $\delta^{18}O_{sw}$ is influenced by the presence of 'some' ice in the northern and/or southern hemisphere. The case for at least some middle Eocene ice is supported by a number of proxy and modelling studies, summarised in Henehan et al. (2020). In brief: proxy comparisons suggest some influence of ice on $\delta^{18}O_{sw}$ (Bijl et al., 2009; Dawber & Tripati, 2011), general circulation models simulate Antarctic ice under middle Eocene boundary conditions (DeConto & Pollard, 2003; Gasson et al., 2014), low SSTs in the Antarctic peninsula imply a continental interior cold enough for ice accumulation (Douglas et al., 2014; Judd et al., 2019), sedimentological evidence suggests possible Arctic sea ice (Tripati et al., 2008) and finally, ice volume change has been linked to coincident $\delta^{18}O$ and sea level variations (Gasson et al., 2012). While there is no evidence as of yet to quantify the exact ice volume or its impact on $\delta^{18}O_{sw}$, evidence summarised above supports our assumption that the correction for ice volume required lies somewhere between the two end-member scenarios for

full, modern ice sheets and the ice-free early Eocene. But with little evidence quantifying middle Eocene ice volumes, we cannot account for the impact of warming on ice melt and $\delta^{18}O_{sw}$ across the MECO. Table 4.3 shows that as the inferred ice volume increases, the estimated SST increases, e.g. SSTs of 15.7 – 18.0 °C are reconstructed for an ice-free case, and 20.4 – 22.3 °C for the modern, full ice-sheet case based on the same initial $\delta^{18}O_c$ value. If global ice volume decreases across the peak MECO interval, absolute peak MECO temperatures and ΔT estimates from $\delta^{18}O$ estimated using a static correction (as applied here) may be too high. The magnitude of warming, ΔT, is not uniformly offset in $\delta^{18}O$ records from other proxies which are not impacted by ice volume change (Fig. 4.18), which may suggest that ice melt has a minor effect on our records. Indeed, Henehan et al. (2020) also note that initial MECO warming is associated with a very modest pCO_2 rise, so ice melt would require either a very high climate sensitivity or an alternative (and as yet unknown) trigger, such as a change in ocean circulation (Henehan et al., 2020). Ultimately, the effects of pH change and ice volume change on $\delta^{18}O$ SSTS are likely smaller than the effect of post-depositional diagenesis here, though these may introduce additional offset between $\delta^{18}O$ and other proxies.

4.4.1.3 Comparison of the Bayfox and Equation 4.1 $\delta^{18}O$ palaeothermometry approach

Both of the Bayfox and Equation 4.1 palaeotemperature methods require the same corrections and assumptions for $\delta^{18}O_{sw}$ and so have the same inherent uncertainties based on ice volumes and carbonate ion concentration described above. Equation 4.1 generates SSTs based on a simple calibration between temperature and $\delta^{18}O_c$ from precipitation of inorganic calcite between 10 – 40 °C (Bemis et al., 1998; Kim & O'Neil, 1997) while Bayfox uses a Bayesian regression to generate a predicted distribution of SSTs based on the modern core-

top dataset and a calibration equation based on laboratory cultures of planktic foraminifera between 0 – 29.5 °C (Malevich et al., 2019). SSTs generated with Equation 4.1 are within the 5 – 95% confidence limits of Bayfox throughout our records suggesting that the greatest uncertainties are related to the assumptions that we make before SST is calculated, as described above. The exception to this is SSTs within the peak MECO interval of the Baskil Section (Fig. 4.14), which are reconstructed to be >30 °C. The lack of agreement between Bayfox and Equation 4.1 SSTs here may be due to temperatures outside the upper limits of calibration for Bayfox (Bemis et al., 1998; Malevich et al., 2019).

4.4.1.4 Impact of calibration and middle Eocene ocean chemistry on Mg/Ca

Dissolution of foraminiferal shells artificially decreases Mg/Ca values and leads to temperature underestimates (Regenberg et al., 2014; Rosenthal & Lohmann, 2002). However, in general the impact of post-depositional diagenesis of planktic foraminifera is far greater for $\delta^{18}O$ than for Mg/Ca, hence the Mg/Ca proxy is more likely to reflect closer to original SSTs (Sexton et al., 2006). This is supported by our analysis. Where Mg/Ca and $\delta^{18}O$ SST estimates are present in the same sites and material (ODP Sites 702, 865, 1260 and 1263; Figs 4.5, 4.7, 4.12 and 4.13, respectively), Mg/Ca SSTs are ~2 – 17 °C warmer than $\delta^{18}O$ SSTs, are within the range of the middle Eocene compilation throughout the MECO interval (Fig. 4.19; Evans et al., 2018) and are similar to non-anomalous TEX_{86} SST estimates. Mg/Ca values therefore likely provide a better approximation of middle Eocene SSTs than $\delta^{18}O$. However, there are still some uncertainties in the Mg/Ca proxy that should be considered. The chosen calibration between Mg/Ca and temperature, and thus the constants A, B and H used in the Mg/Ca palaeotemperature equation rely on multi-species, core-top or cultured relationships, which may not hold true for extinct middle Eocene species (Anand et al., 2003; Evans & Müller, 2012; Hasiuk & Lohmann, 2010). Additionally, the relationship between

Mg/Ca_{sw} and Mg/Ca_c is complicated by the Mg distribution coefficient, D_{Mg}, which varies depending on Mg/Ca_{sw} according to a power law (Evans & Müller, 2012; Hasiuk & Lohmann, 2010) and the constant describing this power dependency itself is species specific (Lear et al., 2015; Evans et al., 2016). SSTs from Mg/Ca may therefore be offset from true values due to inaccuracies in any of the calibration constants.

Mg/Ca_c is also influenced by ocean pH, whereby not correcting for pH change can lead to SST overestimation on the order of ~1 °C per 0.1 units pH decrease (Evans et al., 2016; Lea et al., 1999). SSTs generated using Equation 4.3, without accounting for pH, are within 4 °C of SSTs generated by accounting for pH (Henehan et al., 2020). pH across these sites declines by ~0.12 – 0.18 units across the MECO (Henehan et al., 2020) suggesting that peak MECO SSTs generated from Equation 4.3 may be overestimated at Sites 702 and 1263 by up to 2 °C if pH corrections are included. However, the impact of including a pH correction is not consistent across sites. At ODP Sites 865 and 1260, Henehan et al. (2020) SSTs are warmer than SSTs estimated from Equation 4.3. Henehan et al. (2020) use iterative methods to simultaneously correct pH records (based on boron isotopes) and SST records (based on Mg/Ca) according to each other. While general trends in Mg/Ca SST records from Henehan et al. (2020) are reproduced by Equation 4.3, the magnitude of warming, ΔT, estimated by Henehan et al. (2020) is greater for all sites (Fig. 4.18). This shows that while excluding a pH correction from calculations can either under or overestimate absolute SSTs, the scale of MECO warming is underestimated in all cases without accounting for pH change.

4.4.1.5 Comparison of BAYSPAR and OPTiMAL temperature calibrations

BAYSPAR and OPTiMAL yield very different SSTs across most sites, both in terms of absolute temperatures and trends across the MECO. Despite this the apparent "quality" of MECO TEX_{86} data is generally good as defined in Methods Section 4.3.5 (Supplementary

Table 4.3). Most poor-quality samples have high ΔRI, thus likely significant non-thermal influences on GDGT distributions and are not suitable for temperature reconstructions (Zhang et al., 2016). In most sites this is only one or two samples, however at DSDP Site 516 and ODP Site 913, most samples across the MECO have high ΔRI, along with high BIT, MIT and %GDGT-0. The only other site with high BIT is ODP Site 647, where three samples following the MECO have high BIT, indicating the influence of terrestrial-derived GDGTs on overall GDGT distributions (Hopmans et al., 2004). Unlike BAYSPAR, OPTiMAL doesn't use GDGT data based on specific indices for quality screening but uses a single metric, $D_{nearest}$ (Dunkley Jones et al., 2020). The majority of records in this compilation yield high $D_{nearest}$ values, exceeding 0.5, indicating that the modern core-top dataset fails to appropriately constrain temperatures and resulting in low confidence temperature predictions (Dunkley Jones et al., 2020). Dunkley Jones et al. (2020) show that >60 % of Eocene GDGT assemblages are poorly constrained according to the $D_{nearest}$ metric, and this new compilation, which includes a portion of this dataset, confirms this assessment. While samples may be considered good quality according to traditional metrics assessed in our BAYSPAR reconstructions, OPTiMAL highlights that even these data points may not yield an accurate SST signal based on modern core-top calibrations. Ultimately, this means that in order to interpret data meaningfully there is a temptation to utilise BAYSPAR over Optimal in the middle Eocene. Furthermore, we use a blanket threshold value for each of the quality control indices used here with BAYSPAR records, yet recent studies suggest that it may be more appropriate to vary these thresholds at each site depending on the depositional setting (Bijl et al., 2021; Sluijs et al., 2020). Aside from the quality of GDGT distributions, TEX_{86} SST reconstructions can be influenced by the selected temperature calibration (Kim et al., 2008; Schouten et al., 2002; Tierney & Tingley, 2015). In the middle Eocene, the majority of at

least low to mid latitude SSTs are likely at or above the limit of calibrations based on the modern core-top dataset, ~30 °C, so uncertainties are going to be high whichever calibration is used (Inglis et al., 2015). Additionally, recent culture experiments above 30 °C show little relationship between GDGT distribution and temperature, or higher influence of other factors than temperature (Bale et al., 2019; Elling et al., 2015) hence extrapolation of TEX_{86} calibrations above 30 °C may be highly uncertain. TEX_{86} has also been shown to be less sensitive to temperature change as temperature increases (Cramwinckel et al., 2018). The linear calibration used by BAYSPAR may therefore overestimate temperatures in the middle Eocene, particularly across the peak MECO interval. However, comparisons of TEX_{86} calibrations from Site 1172 show that across the MECO, BAYSPAR SSTs are lower than an exponential calibration (Bijl et al., 2021), indicating that the linear calibration method BAYSPAR does not always result in the highest SSTs.

In this compilation, SSTs predicted by Mg/Ca for low latitude ODP Sites 1260 and 865 reach >30 °C (Figs. 4.7, 4.12), and $\delta^{18}O$ from well-preserved planktic foraminiferal carbonate from the Baskil Section also predicts similarly high SSTs over the peak MECO (Fig. 4.14). The range of the clumped isotope SST compilation for the middle Eocene also extends beyond 30 °C (Evans et al., 2018). Therefore, while SSTs derived from TEX_{86} (and particularly via the BAYSPAR method) may be overestimated to some extent, the absolute temperatures of 30+ °C are not unrealistic particularly given wider knowledge of Eocene climates from fossil evidence, for example the presence of polar forests (e.g. Jahren, 2007; Poole et al., 2001).

4.4.1.6 High variability in TEX_{86} SST reconstructions

Of the three proxies, TEX_{86} SST reconstructions show the highest variability across the MECO, both between the two TEX_{86} palaeothermometry methods (OPTiMAL and

BAYSPAR) and between TEX_{86} and other proxies. The TEX_{86} proxy produces both the warmest (~38 °C, in peak and post-MECO intervals at DSDP Site 516) and coldest (~ -1.5 °C, in the MECO onset interval at ODP Site 913) absolute SSTs of all proxies in this compilation. TEX_{86} SSTs also show the greatest variation in temperature change, ΔT, across the MECO, from -11 °C at DSDP Site 516 to 23.1 °C at ODP Site 913 (Fig. 4.18). We note that extreme apparent warming and cooling across the MECO at DSDP Site 516 and ODP Site 913 are based on single, poor quality data points where BAYSPAR and OPTiMAL both predict near-zero (<5 °C) or negative (~ -1.5 °C) temperatures based on TEX_{86} values. We do not consider these realistic. For DSDP Site 516, SSTs of <5 °C are extremely unlikely to have occurred as this site was at a mid-latitude, ~33 °S, in the middle Eocene and such low SSTs are rare even at high latitudes at this time (Douglas et al., 2014; Evans et al., 2018). MECO SSTs predicted by BAYSPAR are much higher than the low temperatures predicted by OPTiMAL for DSDP Site 516 but all of these data fail the quality test for OPTiMAL so do not accurately reproduce middle Eocene SSTs at this site. ΔT across the MECO is more likely to be close to ~5 °C for this site, as shown by the BAYSPAR record and in line with ΔT for other mid-latitude sites (~3 – 5 °C, Fig. 4.18) and typical MECO warming (Bohaty et al., 2009). Similarly, MECO warming of ~23 °C at ODP Site 913 is based on one sample in the MECO onset interval where the BAYSPAR method predicts SSTs of ~ -0.7 °C. While ODP Site 913 has a very high palaeolatitude of ~69 °N, negative SSTs are not seen for any other samples at this site and are unlikely to occur at the ocean surface in the warm middle Eocene (Evans et al., 2018). Additionally, quality control metrics indicate this this sample has high (above threshold) MI, %GDGT-0 and ΔRI values (Supplementary Table 4.3), indicating significant influence of methanotrophic and methanogenic archaea on GDGT distributions (Weijers et al., 2006;

Zhang et al., 2011), along with bias through non-thermal influences such as microbial community structure or nutrient levels (Zhang et al., 2016). We therefore discount this sample and assume that actual MECO temperature change at this site was more conservative. The majority of variability outside of typical middle Eocene values in TEX_{86} SSTs is therefore due to poor data quality, and not reflective of actual conditions.

4.4.2 Site specific responses to MECO warming

MECO warming is typically reconstructed as ~3 – 6 °C based on a mix of SST proxy methods and sites (e.g. Bijl et al., 2010; Bohaty et al., 2009; Cramwinckel et al., 2018; Rivero-Cuesta et al., 2019). Following removal of suspect data points discussed in sections above that also corresponded with very high and low SST estimates, MECO ΔT in this study is relatively modest and ranges from -5.6 °C (ODP Site 647) to 7.5 °C (ODP Site 1172). It is surprising that several sites in this compilation appear to show overall cooling across the MECO: ODP Sites, 702, 959 and the Belaya River section. As discussed above, the cooling shown in TEX_{86} records for ODP Site 959 is based on poor quality data and can therefore be discounted here.

At the Belaya River Section, both BAYSPAR and OPTiMAL reconstruct temperature declines of -0.2 and -1.5 °C, respectively (Fig. 4.18). However, bulk $\delta^{18}O$ records from the Belaya River section used to define the different MECO intervals (see Methods) indicates minimum $\delta^{18}O$ values and inferred peak temperatures after the TEX_{86}-based temperature maximum. Indeed, Cramwinckel et al. (2022) used the TEX_{86} record rather than $\delta^{18}O$ trends to define the peak of the MECO and quantify MECO warming, giving a warming of 2 – 3 °C at the MECO. At the Baskil Section, peak SSTs according to planktic foraminiferal $\delta^{18}O$ values occur ~160 kyrs before the minimum in the benthic foraminiferal $\delta^{18}O$ record (Fig. 4.14; Giorgioni et al., 2019). Interestingly, peak MECO SSTs in other proxies are coincident

with minimum bulk or benthic $\delta^{18}O$ values at other sites in this compilation, e.g. ODP Sites 702, 748, 865, 1260 (Mg/Ca SSTs) and 1263 implying that this is a generally robust approach to MECO identification, but these are notably all deep-sea sites. The Baskil Section and Belaya River are recording conditions in the western Neotethys and northern Peri-Tethys respectively and are relatively shallow water, shelf settings (Cramwinckel et al., 2022; Giorgioni et al., 2019). Thus, MECO surface warming may have occurred earlier in restricted Tethyan basins than other open ocean sites, where coincident surface and deep water warming occurs and/or there may be additional secondary controls on $\delta^{18}O_{sw}$ due to local changes in the hydrological regime.

We also reconstruct overall cooling in $\delta^{18}O$ and Mg/Ca records at ODP Site 702. These records are low resolution, and the cooling signature is possibly biased by a single high SST value in the pre-MECO interval. Additionally, the highest SSTs in the $\delta^{18}O$ reconstruction occur in the post-MECO interval according to the high-resolution bulk $\delta^{18}O$ record (Bohaty et al., 2009). Hence, SST change from the pre- to peak MECO intervals does not capture the SST maximum experienced at this site. The cooling signature at ODP Site 702 is therefore more likely an artefact of offset in timing between maximum SSTs at the site in Mg/Ca and planktic $\delta^{18}O$, and the minimum bulk $\delta^{18}O$ values used to identify MECO intervals.

4.4.3 Polar amplification and the role of pCO_2

This compilation allows an estimate of the spatial (interbasinal) and latitudinal variation in warming, as well as the impact of warming on background latitudinal gradients (Figs. 4.18, 4.19), which has been a focus of much recent research (e.g. Bijl et al., 2009; Dunkley Jones et al., 2013; Evans et al., 2018; Hollis et al., 2012, 2019; Tierney et al., 2022). It is well established that the Eocene had a reduced latitudinal temperature gradient relative to modern (Bijl et al., 2009; Hollis et al., 2012, 2019), which may have been due to an intensified

hydrological cycle facilitating enhanced ocean overturning and allowing greater heat transport, keeping polar regions warm (Thomas et al., 2014). Increased poleward heat transport may also be related to greater frequency and intensity of tropical cyclones in warmer climates, which result in increased vertical mixing and heat transport from surface to deeper waters which then travel poleward and thus transport warmth to high latitudes (Sriver & Huber, 2007). As these heat transport mechanisms decline with cooling global temperatures, high latitudes experienced greater post-EECO cooling than low latitudes. This leads to a temperature difference of ~14 °C by the late middle Eocene, 41.3 – 38 Ma and steepening of the latitudinal temperature gradient (Inglis et al., 2015). While absolute SSTs cannot easily be compared with latitude due to different controls on different SST proxies employed here we assess the difference between the highest and lowest latitude site for each proxy based on good quality data. For the pre-MECO interval, we reconstruct a latitudinal difference of ~7 °C for Mg/Ca, ~9 °C for TEX_{86} and ~10 °C for $\delta^{18}O$ (Fig. 4.19). These differences increase to ~10 °C for Mg/Ca, ~10 °C for TEX_{86} and ~13 °C for $\delta^{18}O$ across the peak MECO interval when the same low latitude and high latitude sites are compared (Fig. 4.19). This indicates that MECO warming may have strengthened the Eocene latitudinal gradient by ~1 – 3 °C. This is an unexpected result, as warming is typically associated with reduced latitudinal gradients over both short, e.g., PETM and longer timescales, e.g. EECO (Hollis et al., 2019; Inglis et al., 2015). We do not necessarily capture true maximum SSTs in our peak MECO interval at many sites, due to low resolution records and our averaging strategy. Hence, overall latitudinal patterns are not fully characterised in this compilation and further evidence is needed to assess the impact of MECO warming on latitudinal gradients. We do not reconstruct significant polar amplification of warming. Where ice sheets are present, polar amplification is driven by ice-albedo feedbacks (Lunt et al., 2012). Lack of large ice sheets

may limit this effect in the middle Eocene, thus MECO warming is similar for all latitudes in this compilation. One exception is warming of ~7.5 °C seen at ODP Site 1172 (Fig. 4.18). As this is a high southern latitude site, the warming signal expressed by all proxies from high latitude sites may be influenced by small volumes of snow and ice on Antarctica due to ice-albedo feedbacks (e.g. Tierney et al., 2022). However, sites 702 and 748 do not show a similar enhanced warming despite similarly high latitudes.

MECO warming has been linked to atmospheric pCO_2 rise of ~320 ppm (Bijl et al., 2009; Henehan et al., 2020). We record warming at all latitudes in our study in screened datasets which supports a greenhouse gas forcing mechanism for the MECO, as increased pCO_2 should cause a warming signal globally. Excluding sites which show cooling and the extreme warming of >20 degrees at ODP 913, MECO warming across this compilation is between ~1 – 7.5 °C, which is slightly wider than the range of ~3 – 6 °C typically quoted for this event (Bijl et al., 2010; Bohaty et al., 2009; Cramwinckel et al., 2018; Rivero-Cuesta et al., 2019). While the proxies here can underestimate (e.g. $\delta^{18}O$) and overestimate (e.g. TEX_{86}) absolute temperatures, the relative temperature change across warming events is more comparable. The surface ocean response to the MECO is more variable than previously constrained. Variability in SSTs across warming events has been previous reconstructed for Eocene compilations (e.g. Dunkley Jones et al., 2013; Tierney et al., 2022). Warming has been shown to have profound effects on continental hydrological cycles (Carmichael et al., 2017; Pagani et al., 2006; Schmitz & Pujalte, 2007). Hydrological variations over the MECO would have had a significant effect on local SST, salinity and pH, thus affecting both absolute temperature values and the magnitude of overall warming reconstructed.

Reconstruction of the impact of the MECO on latitudinal temperature gradients may be improved by adding constraints from terrestrial records. However, few terrestrial temperature

records have been created to characterise the scale of MECO warming on land. One record of clumped stable isotopes from soil carbonate suggests MECO warming of ~9 °C in mid-latitude continental North America (Methner et al., 2016). This scale of warming is large compared to our reconstructed MECO SST increase of ~1 – 7.5 °C (excluding poor quality data), and is much greater than our reconstructed warming for mid-latitudes (Fig. 4.18). However, temperature records from the continental interior can be profoundly affected by hydrological cycle changes which accompany periods of global warming and hence may show greater variation than SSTs. More temperature records from land would allow for greater characterisation of the impact of the MECO in the terrestrial realm, and thus greater understanding of the overall latitudinal temperature evolution across the MECO.

4.5 CONCLUSIONS AND AREAS FOR FUTURE WORK

We compile $\delta^{18}O$, Mg/Ca and TEX_{86} SST records from 17 globally distributed sites to capture surface temperature evolution across the MECO. We recalculate temperatures using consistent methods to improve comparison of trends between sites, and interrogate the strengths and weaknesses of common palaeotemperature calibrations when applied to middle Eocene records. This is the first global compilation of SSTs created across the MECO using all available records and the results presented here may be used in future to calculate global climate sensitivity.

Any palaeoclimate study may be improved with more data, but it is particularly pertinent in this case. While we have a wide latitudinal spread of sites, our compilation lacks records from the Pacific Ocean (4 of 17 sites here are located in the Pacific) and the Indian Ocean (one of 17 sites is located in the Indian Ocean). The southwest Pacific was an important source of global deep waters in the Eocene (Sijp et al., 2014), therefore is it important to

constrain environmental change here across climate events such as the MECO. Additionally, SST records from TEX_{86} at latitudes higher than 60 °N and 60 °S are shown here to be unreliable. We therefore require further high latitude records to assess the response to MECO warming in sub-polar regions.

All proxies included in this compilation have drawbacks which impact final temperature reconstructions. SSTs from all of our planktic foraminiferal $\delta^{18}O$ records, except the Baskil Section record, are likely artificially lowered by post-depositional alteration. Until there is conclusive evidence for greater volumes of ice across the middle Eocene, we suggest that the offset between $\delta^{18}O$ and other proxies is caused largely by diagenetic alteration and not mischaracterisation of $\delta^{18}O_{sw}$, though there is also inherent uncertainty in this value. Our compilation shows evidence for anomalously cool $\delta^{18}O$ SSTs at both high and low latitude sites, showing that in the warm middle Eocene, diagenetic recrystallisation of planktic foraminiferal carbonate is a potential problem for all latitudes. None of our sites have records of all three SST proxies, and it is not realistic to obtain $\delta^{18}O$ values or Mg/Ca from sites where carbonate preservation is poor. However, we may better quantify the impact of alteration by adding TEX_{86} SST records to sites where $\delta^{18}O$ and Mg/Ca SSTs have been already created, where organic matter concentrations and sedimentary conditions permit. Our records highlight the importance of including site-specific pH correction in Mg/Ca temperature calibrations. Further study into regional variations in middle Eocene surface ocean pH is needed to better constrain this factor.

We apply a consistent definition of MECO intervals to characterise the evolution of the event based on high resolution bulk or benthic foraminiferal $\delta^{18}O$ records. This allows us to compare average temperatures in each MECO interval across sites without invoking age model discrepancies that would affect a direct comparison. Whilst this is generally robust, at

several sites we find that the timing of SST maxima is not necessarily aligned with the timing of bulk or benthic foraminiferal $\delta^{18}O$ minima used to define the peak MECO interval. Our strategy may therefore underestimate peak MECO warmth in some sites. Nevertheless, we constrain MECO warming to ~1 – 7.5 °C. We do not identify any strong evidence for polar amplification of warming, or evidence that the MECO decreases latitudinal temperature gradients. However, due to poor high latitude TEX_{86} records, more evidence is needed to quantify the latitudinal patterns shown in this compilation.

Combining records from multiple palaeotemperature proxies with model reconstructions where possible (e.g. Lunt et al., 2021) will avoid incorrect characterisations of environmental change based on a single proxy which may be significantly affected by problems as described above. This compilation could be supplemented in future by expanding the SST proxy data included, e.g., clumped isotopes (Evans et al., 2018), alkenone ($U^{K'}_{37}$) palaeothermometry (Bijl et al., 2009), $\delta^{18}O$ from bivalve (Douglas et al., 2014) and coral carbonate (Brachert et al., 2022) and temperatures from halite fluid inclusions (Xu et al., 2021). Additionally, estimates of terrestrial temperatures are needed to allow further expansion of this compilation towards estimates of climate sensitivity across the middle Eocene.

CHAPTER 5: CONCLUSIONS

5.4 Summary of main findings

Here, new geochemical (X-ray fluorescence) and benthic stable isotope ($\delta^{18}O$ and $\delta^{13}C$) records are presented for IODP Site U1514 in the high latitude Indian Ocean across the Early Eocene Climatic Optimum (EECO) and early Eocene hyperthermal events P to U. A new compilation of available $\delta^{18}O$, Mg/Ca and TEX_{86} sea surface temperature (SST) estimates across the Middle Eocene Climatic Optimum (MECO) is also presented. These records provide new insights into environmental evolution across key Eocene warming events, and comprise the first high-resolution climate records of early Eocene hyperthermals between 50 – 51 Ma from the Indian Ocean. The main findings of this thesis are summarised below with reference to the aims stated in Chapter 1.

5.4.1 Chapter 2: Sediment chemistry at IODP Site U1514: Implications for environmental dynamics of the early Eocene 'hothouse' in the high latitude Indian Ocean

The aim of Chapter 2 was to document the environmental and geochemical signals across the build-up, peak and close of the EECO (~49 – 53 Ma), and use these records to assess any impacts of Southern Ocean circulation on high latitude Indian Ocean geochemistry. To address this aim, a ~9 Myr-long, high-resolution X-ray fluorescence (XRF) record of sediment chemistry from IODP Site U1514 is presented. These records span ~46 – 55 Ma to capture the rise of global temperatures into the EECO, as well as subsequent global cooling as the EECO collapses. XRF records provide only a semi-quantitative picture of sedimentary components. To reduce this problem, XRF datasets are converted into multiple forms: ratios of elements normalised to Ti, individual element concentrations and individual element mass

accumulation rates. This high resolution (~2 – 5 kyr) long-term (9 Myr) record of sediment chemistry from the Indian Ocean highlights the many uses of XRF data beyond simply Ca/Fe variations, which are typically assessed in deep sea records. XRF data from seven key elements are highlighted in this chapter: Ti, Fe, K and Si, which document part of the lithogenic input to this site, and Ca, Ba and Sr, which are biogenic in origin in this case. Based on these records, sedimentary variations at Site U1514 across the EECO are driven by local changes in productivity and weathering fluxes, induced largely by hydrological changes on the Australian continent. An additional peak in productivity occurs at the end of the EECO, at the same time as global temperatures begin to cool. This may indicate a response in the southern Indian Ocean to the initiation of a surface water connection through the Tasmanian Gateway, however other mechanisms to increase productivity cannot be discounted. Heightened primary productivity may provide a mechanism for post-EECO pCO_2 drawdown, however evidence suggests that this was a temporary and localised process at Site U1514 so further estimates of post-EECO Southern Ocean productivity are needed to examine the impact of this mechanism on a global scale.

5.4.2 Chapter 3: Orbital forcing of early Eocene hyperthermal events: A new benthic foraminiferal record from the Indian Ocean, 50-51 Ma

In Chapter 3, the aim was to identify the impact, phasing and evolution of Earth's orbital cycles on benthic foraminiferal stable isotope records of Early Eocene hyperthermals. In this chapter, a high-resolution benthic stable isotope ($\delta^{18}O$ and $\delta^{13}C$) record was created from IODP Site U1514 between 50 – 51 Ma. This interval incorporates six early Eocene hyperthermals, events P – U by the typical hyperthermal naming scheme. These 'later' early Eocene hyperthermals are not as frequently studied as larger, earlier hyperthermal events such

as the Palaeocene-Eocene Thermal Maximum and Eocene Thermal Maximum-2. Additionally, these records make up some of the first records of hyperthermal events P to U from the Indian Ocean, which is underrepresented in existing Eocene climate records. $\delta^{18}O$ and $\delta^{13}C$ records show that hyperthermals in the high latitude Indian Ocean vary in character, but are associated with bottom water warming of ~1.75 – 4 °C.

Time series analysis is used to identify the influence of orbital cycles on $\delta^{18}O$, $\delta^{13}C$ and a longer (~49 – 52 Ma) XRF Ca/Fe record. High power at periodicities of ~1.25 m in stable isotopes and Ca/Fe indicates the persistent influence of the short (~100-kyr) eccentricity cycle on hyperthermal timing. The Ca/Fe record also shows high power at a periodicity of ~4.4 m, which can be linked to the long (~405-kyr) eccentricity cycle. This is consistent with previous studies, which have identified that early Eocene hyperthermals are paced by the long and short eccentricity cycles. High power is also seen at a periodicity of ~0.4 – 0.6 m between ~232 – 234 m CCSF. This can be tied to the transient influence of the ~41-kyr obliquity cycle on Indian Ocean climate records. While the importance of obliquity is thought to be reduced in an ice-free world, strong obliquity cycles have been identified periodically throughout the Palaeocene and early Eocene which may be tied to minor ice volume variations or hydrological cycling. These records confirm some influence of high latitude climate dynamics on the Indian Ocean even during peak temperautres of the EECO.

5.4.3 Chapter 4: Proxy constraints on sea surface temperature evolution across the Middle Eocene Climatic Optimum

The aim of Chapter 4 was to compile existing sea surface temperature (SST) data across the Middle Eocene Climatic Optimum (MECO) from $\delta^{18}O$, Mg/Ca and TEX_{86} proxies to assess both latitudinal and methodological variation in MECO warming. $\delta^{18}O$, Mg/Ca and TEX_{86}

data across the MECO were compiled from 17 sites with a global spread. To facilitate comparisons between sites with different age models, records were converted to the GTS2012 timescale. SST's were then re-calculated from original $\delta^{18}O$, Mg/Ca and TEX_{86} records using consistent and up-to-date methods. The resulting compilation indicates MECO warming of ~1 – 7.5 °C, excluding poor-quality data. The reduced latitudinal thermal gradient of the middle Eocene relative to the modern case is also reconstructed, whereby high latitude sites are much warmer than modern. However, the MECO itself does not appear to significantly reduce latitudinal temperature gradients any further.

This compilation highlights major sources of uncertainty that need to be considered when these proxies are used to analyse past temperature variations. Post-depositional diagenesis causes artificially cool temperature estimates from $\delta^{18}O$ records from all latitudes in the middle Eocene. Additionally, uncertainties in middle Eocene ice volume and geographic variations in surface ocean pH impact estimates of $\delta^{18}O_{sw}$ and seawater carbonate ion concentrations. This affects final $\delta^{18}O$ and Mg/Ca temperature reconstructions. Additionally, not accounting for the impact MECO warming may have had on $\delta^{18}O_{sw}$ and pH evolution may cause peak-MECO surface temperatures to be underestimated. TEX_{86}-based temperature reconstructions also highlight the limits of the OPTiMAL tool when applied to middle Eocene temperatures.

5.5 Future directions for Eocene palaeoclimate research

The Eocene is and will likely always be a key interval of Earth's history in palaeoclimatology. Scientific drilling over the past three decades has allowed researchers to document Eocene climate evolution across a wide range of latitudes and ocean basins, as demonstrated in the spread of MECO records presented in Chapter 4 of this thesis. The

timing, duration and magnitude of major Eocene climate events, such as the PETM, EECO, early Eocene hyperthermals and the MECO are by now relatively well-constrained in most ocean basins through numerous proxies. However, this thesis highlights unknowns which still limit our understanding of this dynamic interval of Earth's history, and areas which should be targeted in future to complete the picture of Eocene climate evolution.

This thesis identifies the Indian Ocean as a key geographical gap in Eocene climate studies. Datasets presented here from IODP Site U1514 contribute somewhat to this problem, however conclusions made in this thesis would be strengthened with additional sedimentary evidence from elsewhere in Indian Ocean. Additional proxy records from Site U1514 would also contribute to our understanding of Indian Ocean climate in the Eocene. In particular, clay mineralogy studies alongside the XRF records presented in Chapter 2 would allow a complete picture of sedimentary providence to be drawn. Furthermore, planktic and benthic foraminiferal stable isotope records across the MECO from Site U1514, in combination with foraminiferal Mg/Ca SST estimates, would contribute to a prominent gap in the compilation of MECO proxy records presented in Chapter 4. The high-resolution benthic stable isotope record presented in Chapter 3 should be extended back to at least the PETM to incorporate the full range of early Eocene hyperthermals, and identify whether orbital signals identified between 50 – 51 Ma hold up for earlier events.

Aside from Ca/Fe variations, XRF records from the Eocene are relatively underutilised. Chapter 2 demonstrates that long-term XRF records can contribute to our understanding of hydrological cycling on continents, though there are many caveats with interpreting XRF in this way. Long-term XRF records from sites such as the South Pacific and Kerguelen Plateau would complement the record from IODP Site U1514, and highlight which sedimentary

changes are local signals, versus more geographically extensive signals which have the potential to impact global climate evolution.

A major source of uncertainty in Eocene climate reconstructions is the geochemical evolution of the ocean. New boron isotope records of pH have been presented across the MECO (Henehan et al., 2020), however the geographic variation of pH needs to be assessed further across the MECO and other climate events to increase the accuracy of proxy temperature reconstructions. Additionally, better estimates of Eocene $\delta^{18}O_{sw}$ may improve our understanding of ice volume change throughout the Eocene.

References

Anagnostou, E., John, E. H., Babila, T. L., Sexton, P. F., Ridgwell, A., Lunt, D. J., Pearson, P. N., Chalk, T. B., Pancost, R. D., & Foster, G. L. (2020). Proxy evidence for state-dependence of climate sensitivity in the Eocene greenhouse. *Nature Communications*, *11*(1), 4436. https://doi.org/10.1038/s41467-020-17887-x

Anagnostou, E., John, E. H., Edgar, K. M., Foster, G. L., Ridgwell, A., Inglis, G. N., Pancost, R. D., Lunt, D. J., & Pearson, P. N. (2016). Changing atmospheric CO2 concentration was the primary driver of early Cenozoic climate. *Nature*, *533*(7603), 380–384. https://doi.org/10.1038/nature17423

Anand, P., Elderfield, H., & Conte, M. H. (2003). Calibration of Mg/Ca thermometry in planktonic foraminifera from a sediment trap time series. *Paleoceanography*, *18*(2), n/a-n/a. https://doi.org/10.1029/2002PA000846

Anand, R. R., & Paine, M. (2002). Regolith geology of the Yilgarn Craton, Western Australia: Implications for exploration. *Australian Journal of Earth Sciences*, *49*(1), 3–162. https://doi.org/10.1046/j.1440-0952.2002.00912.x

Anderson, R. F., Ali, S., Bradtmiller, L. I., Nielsen, S. H. H., Fleisher, M. Q., Anderson, B. E., & Burckle, L. H. (2009). Wind-Driven Upwelling in the Southern Ocean and the Deglacial Rise in Atmospheric CO_2. *Science*, *323*(5920), 1443–1448. https://doi.org/10.1126/science.1167441

Aze, T., Ezard, T. H. G., Purvis, A., Coxall, H. K., Stewart, D. R. M., Wade, B. S., & Pearson, P. N. (2011). A phylogeny of Cenozoic macroperforate planktonic foraminifera from fossil data. *Biological Reviews*, *86*(4), 900–927. https://doi.org/10.1111/j.1469-185X.2011.00178.x

Aze, T., Pearson, P. N., Dickson, A. J., Badger, M. P. S., Bown, P. R., Pancost, R. D., Gibbs, S. J., Huber, B. T., Leng, M. J., Coe, A. L., Cohen, A. S., & Foster, G. L. (2014). Extreme warming of tropical waters during the Paleocene–Eocene Thermal Maximum. *Geology*, *42*(9), 739–742. https://doi.org/10.1130/G35637.1

Bale, N. J., Palatinszky, M., Rijpstra, W. I. C., Herbold, C. W., Wagner, M., & Sinninghe Damsté, J. S. (2019). Membrane Lipid Composition of the Moderately Thermophilic Ammonia-Oxidizing Archaeon "*Candidatus* Nitrosotenuis uzonensis" at Different Growth Temperatures. *Applied and Environmental Microbiology*, *85*(20). https://doi.org/10.1128/AEM.01332-19

Barker, P. F., Filippelli, G. M., Florindo, F., Martin, E. E., & Scher, H. D. (2007). Onset and role of the Antarctic Circumpolar Current. *Deep Sea Research Part II: Topical Studies in Oceanography*, *54*(21–22), 2388–2398. https://doi.org/10.1016/j.dsr2.2007.07.028

Barker, S., Greaves, M., & Elderfield, H. (2003). A study of cleaning procedures used for foraminiferal Mg/Ca paleothermometry. *Geochemistry, Geophysics, Geosystems*, *4*(9), n/a-n/a. https://doi.org/10.1029/2003GC000559

Barnet, J. S. K., Littler, K., Westerhold, T., Kroon, D., Leng, M. J., Bailey, I., Röhl, U., & Zachos, J. C. (2019). A High-Fidelity Benthic Stable Isotope Record of Late Cretaceous–Early Eocene Climate Change and Carbon-Cycling. *Paleoceanography and Paleoclimatology*, *34*(4), 672–691. https://doi.org/10.1029/2019PA003556

Batenburg, S. J., Sprovieri, M., Gale, A. S., Hilgen, F. J., Hüsing, S., Laskar, J., Liebrand, D., Lirer, F., Orue-Etxebarria, X., Pelosi, N., & Smit, J. (2012). Cyclostratigraphy and astronomical tuning of the Late Maastrichtian at Zumaia (Basque country, Northern Spain). *Earth and Planetary Science Letters*, *359–360*, 264–278. https://doi.org/10.1016/j.epsl.2012.09.054

Beasley, C., Parvaz, D. B., Cotton, L., & Littler, K. (2020). Liberating microfossils from indurated carbonates: comparison of three disaggregation methods. *Journal of Micropalaeontology*, *39*(2), 169–181. https://doi.org/10.5194/jm-39-169-2020

Bemis, B. E., Spero, H. J., Bijma, J., & Lea, D. W. (1998). Reevaluation of the oxygen isotopic composition of planktonic foraminifera: Experimental results and revised paleotemperature equations. *Paleoceanography*, *13*(2), 150–160. https://doi.org/10.1029/98PA00070

Berggren, W. A., Kent, D. v., Swisher, C. C., & Aubry, M.-P. (1995). A Revised Cenozoic Geochronology and Chronostratigraphy. In *Geochronology, Time Scales and Global Stratigraphic Correlation*. SEPM Society for Sedimentary Geology. https://doi.org/10.2110/pec.95.04.0129

Bernard, S., Daval, D., Ackerer, P., Pont, S., & Meibom, A. (2017). Burial-induced oxygen-isotope re-equilibration of fossil foraminifera explains ocean paleotemperature paradoxes. *Nature Communications*, *8*(1), 1134. https://doi.org/10.1038/s41467-017-01225-9

Berner, R. A. (1992). Weathering, plants, and the long-term carbon cycle. *Geochimica et Cosmochimica Acta*, *56*(8), 3225–3231. https://doi.org/10.1016/0016-7037(92)90300-8

Bice, K. L., & Marotzke, J. (2002). Could changing ocean circulation have destabilized methane hydrate at the Paleocene/Eocene boundary? *Paleoceanography*, *17*(2), 8-1-8–12. https://doi.org/10.1029/2001PA000678

Bijl, P. K., Bendle, J. A. P., Bohaty, S. M., Pross, J., Schouten, S., Tauxe, L., Stickley, C. E., McKay, R. M., Rohl, U., Olney, M., Sluijs, A., Escutia, C., Brinkhuis, H., Klaus, A., Fehr, A., Williams, T., Carr, S. A., Dunbar, R. B., Gonzalez, J. J., … Yamane, M. (2013). Eocene cooling linked to early flow across the Tasmanian Gateway. *Proceedings of the National Academy of Sciences*, *110*(24), 9645–9650. https://doi.org/10.1073/pnas.1220872110

Bijl, P. K., Frieling, J., Cramwinckel, M. J., Boschman, C., Sluijs, A., & Peterse, F. (2021). Maastrichtian–Rupelian paleoclimates in the southwest Pacific – a critical re-evaluation of biomarker paleothermometry and dinoflagellate cyst paleoecology at Ocean Drilling Program Site 1172. *Climate of the Past*, *17*(6), 2393–2425. https://doi.org/10.5194/cp-17-2393-2021

Bijl, P. K., Houben, A. J. P., Schouten, S., Bohaty, S. M., Sluijs, A., Reichart, G.-J., Sinninghe Damsté, J. S., & Brinkhuis, H. (2010). Transient Middle Eocene Atmospheric CO 2 and Temperature Variations. *Science*, *330*(6005), 819–821. https://doi.org/10.1126/science.1193654

Bijl, P. K., Schouten, S., Sluijs, A., Reichart, G. J., Zachos, J. C., & Brinkhuis, H. (2009). Early palaeogene temperature evolution of the southwest Pacific Ocean. *Nature*, *461*(7265), 776–779. https://doi.org/10.1038/nature08399

Bijma, J., Spero, H. J., & Lea, D. W. (1999). Reassessing Foraminiferal Stable Isotope Geochemistry: Impact of the Oceanic Carbonate System (Experimental Results). In *Use of Proxies in Paleoceanography* (pp. 489–512). Springer Berlin Heidelberg. https://doi.org/10.1007/978-3-642-58646-0_20

Bogus, K., Batenburg, S., Jones, M., Edgar, K., de Vleeschouwer, D., Tagliaro, G., Martinez, M., Hanson, E., Walker-Trivett, C., Levay, B., & Schoemann, M. (2019). Shore-based X-ray fluorescence core scanning of IODP Expedition 369 (Australia Cretaceous Climate and Tectonics) material. In *Australia Cretaceous Climate and Tectonics. Proceedings of the International Ocean Discovery Program, 369 : Supplementary material.* (Vol. 369). Integrated Ocean Drilling Program Management International, Inc.,.

Bohaty, S. M., & Zachos, J. C. (2003). Significant Southern Ocean warming event in the late middle Eocene. *Geology*, *31*(11), 1017. https://doi.org/10.1130/G19800.1

Bohaty, S. M., Zachos, J. C., Florindo, F., & Delaney, M. L. (2009). Coupled greenhouse warming and deep-sea acidification in the middle Eocene. *Paleoceanography*, *24*(2), n/a-n/a. https://doi.org/10.1029/2008PA001676

Bornemann, A., D'haenens, S., Norris, R. D., & Speijer, R. P. (2016). The demise of the early Eocene greenhouse – Decoupled deep and surface water cooling in the eastern North Atlantic. *Global and Planetary Change*, *145*, 130–140. https://doi.org/10.1016/j.gloplacha.2016.08.010

Borrelli, C., Cramer, B. S., & Katz, M. E. (2014). Bipolar Atlantic deepwater circulation in the middle-late Eocene: Effects of Southern Ocean gateway openings. *Paleoceanography*, *29*(4), 308–327. https://doi.org/10.1002/2012PA002444

Boscolo Galazzo, F., Thomas, E., Pagani, M., Warren, C., Luciani, V., & Giusberti, L. (2014). The middle Eocene climatic optimum (MECO): A multiproxy record of paleoceanographic changes in the southeast Atlantic (ODP Site 1263, Walvis Ridge). *Paleoceanography*, *29*(12), 1143–1161. https://doi.org/10.1002/2014PA002670

Bosmans, J. H. C., Drijfhout, S. S., Tuenter, E., Hilgen, F. J., Lourens, L. J., & Rohling, E. J. (2015). Precession and obliquity forcing of the freshwater budget over the Mediterranean. *Quaternary Science Reviews*, *123*, 16–30. https://doi.org/10.1016/j.quascirev.2015.06.008

Bosmans, J. H. C., Hilgen, F. J., Tuenter, E., & Lourens, L. J. (2015). Obliquity forcing of low-latitude climate. *Climate of the Past*, *11*(10), 1335–1346. https://doi.org/10.5194/cp-11-1335-2015

Boulila, S., Vahlenkamp, M., de Vleeschouwer, D., Laskar, J., Yamamoto, Y., Pälike, H., Kirtland Turner, S., Sexton, P. F., Westerhold, T., & Röhl, U. (2018). Towards a robust and consistent middle Eocene astronomical timescale. *Earth and Planetary Science Letters*, *486*, 94–107. https://doi.org/10.1016/j.epsl.2018.01.003

Brachert, T. C., Felis, T., Gagnaison, C., Hoehle, M., Reuter, M., & Spreter, P. M. (2022). Slow-growing reef corals as climate archives: A case study of the Middle Eocene Climatic Optimum 40 Ma ago. *Science Advances*, *8*(20). https://doi.org/10.1126/sciadv.abm3875

Bralower, T. J., Kelly, D. C., Gibbs, S., Farley, K., Eccles, L., Lindemann, T. L., & Smith, G. J. (2014). Impact of dissolution on the sedimentary record of the Paleocene–Eocene thermal maximum. *Earth and Planetary Science Letters*, *401*, 70–82. https://doi.org/10.1016/j.epsl.2014.05.055

Browning, J. V., Miller, K. G., & Pak, D. K. (1996). Global implications of lower to middle Eocene sequence boundaries on the New Jersey coastal plain: The icehouse cometh. *Geology*, *24*(7), 639. https://doi.org/10.1130/0091-7613(1996)024<0639:GIOLTM>2.3.CO;2

Burke, K. D., Williams, J. W., Chandler, M. A., Haywood, A. M., Lunt, D. J., & Otto-Bliesner, B. L. (2018). Pliocene and Eocene provide best analogs for near-future climates. *Proceedings of the National Academy of Sciences*, *115*(52), 13288–13293. https://doi.org/10.1073/pnas.1809600115

Cande, S. C., & Kent, D. v. (1995). Revised calibration of the geomagnetic polarity timescale for the Late Cretaceous and Cenozoic. *Journal of Geophysical Research: Solid Earth*, *100*(B4), 6093–6095. https://doi.org/10.1029/94JB03098

Carmichael, M. J., Inglis, G. N., Badger, M. P. S., Naafs, B. D. A., Behrooz, L., Remmelzwaal, S., Monteiro, F. M., Rohrssen, M., Farnsworth, A., Buss, H. L., Dickson, A. J., Valdes, P. J., Lunt, D. J., & Pancost, R. D. (2017). Hydrological and associated biogeochemical consequences of rapid global warming during the Paleocene-Eocene Thermal Maximum. *Global and Planetary Change*, *157*, 114–138. https://doi.org/10.1016/j.gloplacha.2017.07.014

Carmichael, M. J., Lunt, D. J., Huber, M., Heinemann, M., Kiehl, J., LeGrande, A., Loptson, C. A., Roberts, C. D., Sagoo, N., Shields, C., Valdes, P. J., Winguth, A., Winguth, C., & Pancost, R. D. (2016). A model–model and data–model comparison for the early Eocene hydrological cycle. *Climate of the Past*, *12*(2), 455–481. https://doi.org/10.5194/cp-12-455-2016

Carter, S. C., Paytan, A., & Griffith, E. M. (2020). Toward an Improved Understanding of the Marine Barium Cycle and the Application of Marine Barite as a Paleoproductivity Proxy. *Minerals*, *10*(5), 421. https://doi.org/10.3390/min10050421

Chen, Z., Ding, Z., Yang, S., Zhang, C., & Wang, X. (2016). Increased precipitation and weathering across the Paleocene-Eocene Thermal Maximum in central China. *Geochemistry, Geophysics, Geosystems*, *17*(6), 2286–2297. https://doi.org/10.1002/2016GC006333

Church, M. J., Wai, B., Karl, D. M., & DeLong, E. F. (2010). Abundances of crenarchaeal *amoA* genes and transcripts in the Pacific Ocean. *Environmental Microbiology*, *12*(3), 679–688. https://doi.org/10.1111/j.1462-2920.2009.02108.x

Colin, C., Siani, G., Liu, Z., Blamart, D., Skonieczny, C., Zhao, Y., Bory, A., Frank, N., Duchamp-Alphonse, S., Thil, F., Richter, T., Kissel, C., & Gargani, J. (2014). Late Miocene to early Pliocene climate variability off NW Africa (ODP Site 659). *Palaeogeography, Palaeoclimatology, Palaeoecology*, *401*, 81–95. https://doi.org/10.1016/j.palaeo.2014.02.015

Coxall, H. K., Wilson, P. A., Pälike, H., Lear, C. H., & Backman, J. (2005). Rapid stepwise onset of Antarctic glaciation and deeper calcite compensation in the Pacific Ocean. *Nature*, *433*(7021), 53–57. https://doi.org/10.1038/nature03135

Craig, H. (1957). Isotopic standards for carbon and oxygen and correction factors for mass-spectrometric analysis of carbon dioxide. *Geochimica et Cosmochimica Acta*, *12*(1–2), 133–149. https://doi.org/10.1016/0016-7037(57)90024-8

Cramer, B. S., Miller, K. G., Barrett, P. J., & Wright, J. D. (2011). Late Cretaceous–Neogene trends in deep ocean temperature and continental ice volume: Reconciling records of benthic foraminiferal geochemistry (δ^{18} O and Mg/Ca) with sea level history. *Journal of Geophysical Research*, *116*(C12), C12023. https://doi.org/10.1029/2011JC007255

Cramer, B. S., Toggweiler, J. R., Wright, J. D., Katz, M. E., & Miller, K. G. (2009). Ocean overturning since the late cretaceous: Inferences from a new benthic foraminiferal isotope compilation. *Paleoceanography*, *24*(4), 1–15. https://doi.org/10.1029/2008PA001683

Cramer, B. S., Wright, J. D., Kent, D. v., & Aubry, M.-P. (2003). Orbital climate forcing of δ^{13} C excursions in the late Paleocene-early Eocene (chrons C24n-C25n). *Paleoceanography*, *18*(4), n/a-n/a. https://doi.org/10.1029/2003PA000909

Cramwinckel, M. J., Coxall, H. K., Śliwińska, K. K., Polling, M., Harper, D. T., Bijl, P. K., Brinkhuis, H., Eldrett, J. S., Houben, A. J. P., Peterse, F., Schouten, S., Reichart, G., Zachos, J. C., & Sluijs, A. (2020). A Warm, Stratified, and Restricted Labrador Sea Across the Middle Eocene and Its Climatic Optimum. *Paleoceanography and Paleoclimatology*, *35*(10). https://doi.org/10.1029/2020PA003932

Cramwinckel, M. J., Huber, M., Kocken, I. J., Agnini, C., Bijl, P. K., Bohaty, S. M., Frieling, J., Goldner, A., Hilgen, F. J., Kip, E. L., Peterse, F., van der Ploeg, R., Röhl, U., Schouten, S., & Sluijs, A. (2018). Synchronous tropical and polar temperature evolution in the Eocene. *Nature*, *559*(7714), 382–386. https://doi.org/10.1038/s41586-018-0272-2

Cramwinckel, M. J., van der Ploeg, R., van Helmond, N. A. G. M., Waarlo, N., Agnini, C., Bijl, P. K., van der Boon, A., Brinkhuis, H., Frieling, J., Krijgsman, W., Mather, T. A., Middelburg, J. J., Peterse, F., Slomp, C. P., & Sluijs, A. (2022). Deoxygenation and organic carbon sequestration in the Tethyan realm associated with the middle Eocene climatic optimum. *GSA Bulletin*. https://doi.org/10.1130/B36280.1

Cramwinckel, M. J., Woelders, L., Huurdeman, E. P., Peterse, F., Gallagher, S. J., Pross, J., Burgess, C. E., Reichart, G.-J., Sluijs, A., & Bijl, P. K. (2020). Surface-circulation change in the southwest Pacific Ocean across the Middle Eocene Climatic Optimum: inferences from dinoflagellate cysts and biomarker paleothermometry. *Climate of the Past*, *16*(5), 1667–1689. https://doi.org/10.5194/cp-16-1667-2020

Crouch, E. M., Shepherd, C. L., Morgans, H. E. G., Naafs, B. D. A., Dallanave, E., Phillips, A., Hollis, C. J., & Pancost, R. D. (2020). Climatic and environmental changes across the early Eocene climatic optimum at mid-Waipara River, Canterbury Basin, New Zealand. *Earth-Science Reviews*, *200*, 102961. https://doi.org/10.1016/j.earscirev.2019.102961

Crowley, T. J., & Hyde, W. T. (2008). Transient nature of late Pleistocene climate variability. *Nature*, *456*(7219), 226–230. https://doi.org/10.1038/nature07365

Dawber, C. F., & Tripati, A. K. (2011). Constraints on glaciation in the middle Eocene (46-37 Ma) from Ocean Drilling Program (ODP) Site 1209 in the tropical Pacific Ocean. *Paleoceanography*, *26*(2), n/a-n/a. https://doi.org/10.1029/2010PA002037

DeConto, R. M., Galeotti, S., Pagani, M., Tracy, D., Schaefer, K., Zhang, T., Pollard, D., & Beerling, D. J. (2012). Past extreme warming events linked to massive carbon release from thawing permafrost. *Nature*, *484*(7392), 87–91. https://doi.org/10.1038/nature10929

DeConto, R. M., & Pollard, D. (2003). A coupled climate–ice sheet modeling approach to the Early Cenozoic history of the Antarctic ice sheet. *Palaeogeography, Palaeoclimatology, Palaeoecology*, *198*(1–2), 39–52. https://doi.org/10.1016/S0031-0182(03)00393-6

Delaney, M. L., W.H.Bé, A., & Boyle, E. A. (1985). Li, Sr, Mg, and Na in foraminiferal calcite shells from laboratory culture, sediment traps, and sediment cores. *Geochimica et Cosmochimica Acta*, *49*(6), 1327–1341. https://doi.org/10.1016/0016-7037(85)90284-4

Dickens, G. R. (2011). Down the Rabbit Hole: toward appropriate discussion of methane release from gas hydrate systems during the Paleocene-Eocene thermal maximum and other past hyperthermal events. *Climate of the Past*, *7*(3), 831–846. https://doi.org/10.5194/cp-7-831-2011

Dickens, G. R., Castillo, M. M., & Walker, J. C. G. (1997). A blast of gas in the latest Paleocene: Simulating first-order effects of massive dissociation of oceanic methane hydrate. *Geology*, *25*(3), 259. https://doi.org/10.1130/0091-7613(1997)025<0259:ABOGIT>2.3.CO;2

Dickens, G. R., O'Neil, J. R., Rea, D. K., & Owen, R. M. (1995). Dissociation of oceanic methane hydrate as a cause of the carbon isotope excursion at the end of the Paleocene. *Paleoceanography*, *10*(6), 965–971. https://doi.org/10.1029/95PA02087

Diester-Haass, L., & Faul, K. (2019). Paleoproductivity Reconstructions for the Paleogene Southern Ocean: A Direct Comparison of Geochemical and Micropaleontological Proxies. *Paleoceanography and Paleoclimatology*, *34*(1), 79–97. https://doi.org/10.1029/2018PA003384

Douglas, P. M. J., Affek, H. P., Ivany, L. C., Houben, A. J. P., Sijp, W. P., Sluijs, A., Schouten, S., & Pagani, M. (2014). Pronounced zonal heterogeneity in Eocene southern high-latitude sea surface temperatures. *Proceedings of the National Academy of Sciences*, *111*(18), 6582–6587. https://doi.org/10.1073/pnas.1321441111

Dunkley Jones, T., Eley, Y. L., Thomson, W., Greene, S. E., Mandel, I., Edgar, K., & Bendle, J. A. (2020). OPTiMAL: a new machine learning approach for GDGT-based palaeothermometry. *Climate of the Past*, *16*(6), 2599–2617. https://doi.org/10.5194/cp-16-2599-2020

Dunkley Jones, T., Lunt, D. J., Schmidt, D. N., Ridgwell, A., Sluijs, A., Valdes, P. J., & Maslin, M. (2013). Climate model and proxy data constraints on ocean warming across the Paleocene–Eocene Thermal Maximum. *Earth-Science Reviews*, *125*, 123–145. https://doi.org/10.1016/j.earscirev.2013.07.004

Dutton, A. L., Lohmann, K. C., & Zinsmeister, W. J. (2002). Stable isotope and minor element proxies for Eocene climate of Seymour Island, Antarctica. *Paleoceanography*, *17*(2), 6-1-6–13. https://doi.org/10.1029/2000PA000593

Dymond, J., Suess, E., & Lyle, M. (1992). Barium in Deep-Sea Sediment: A Geochemical Proxy for Paleoproductivity. *Paleoceanography*, *7*(2), 163–181. https://doi.org/10.1029/92PA00181

Eagle, M., Paytan, A., Arrigo, K. R., van Dijken, G., & Murray, R. W. (2003). A comparison between excess barium and barite as indicators of carbon export. *Paleoceanography*, *18*(1), n/a-n/a. https://doi.org/10.1029/2002PA000793

Edgar, K. M., Anagnostou, E., Pearson, P. N., & Foster, G. L. (2015). Assessing the impact of diagenesis on δ11B, δ13C, δ18O, Sr/Ca and B/Ca values in fossil planktic foraminiferal calcite. *Geochimica et Cosmochimica Acta*, *166*, 189–209. https://doi.org/10.1016/j.gca.2015.06.018

Edgar, K. M., Bohaty, S. M., Coxall, H. K., Bown, P. R., Batenburg, S. J., Lear, C. H., & Pearson, P. N. (2020). New composite bio- and isotope stratigraphies spanning the Middle Eocene Climatic Optimum at tropical ODP Site 865 in the Pacific Ocean. *Journal of Micropalaeontology*, *39*(2), 117–138. https://doi.org/10.5194/jm-39-117-2020

Edgar, K. M., Bohaty, S. M., Gibbs, S. J., Sexton, P. F., Norris, R. D., & Wilson, P. A. (2013). Symbiont "bleaching" in planktic foraminifera during the Middle Eocene Climatic Optimum. *Geology*, *41*(1), 15–18. https://doi.org/10.1130/G33388.1

Edgar, K. M., MacLeod, K. G., Hasegawa, T., Hanson, E. M., Boomer, I., & Kirby, N. (2022). *Data report: Cenozoic and Upper Cretaceous bulk carbonate stable carbon and oxygen isotopes from IODP Expedition 369 Sites U1513, U1514, and U1516 in the southeast Indian Ocean*. https://doi.org/10.14379/iodp.proc.369.206.2022

Edgar, K. M., Pälike, H., & Wilson, P. A. (2013). Testing the impact of diagenesis on the δ^{18}O and δ^{13}C of benthic foraminiferal calcite from a sediment burial depth transect in the equatorial Pacific. *Paleoceanography*, *28*(3), 468–480. https://doi.org/10.1002/palo.20045

Edgar, K. M., Wilson, P. A., Sexton, P. F., Gibbs, S. J., Roberts, A. P., & Norris, R. D. (2010). New biostratigraphic, magnetostratigraphic and isotopic insights into the Middle Eocene Climatic Optimum in low latitudes. *Palaeogeography, Palaeoclimatology, Palaeoecology*, *297*(3–4), 670–682. https://doi.org/10.1016/j.palaeo.2010.09.016

Edgar, K. M., Wilson, P. A., Sexton, P. F., & Suganuma, Y. (2007). No extreme bipolar glaciation during the main Eocene calcite compensation shift. *Nature*, *448*(7156), 908–911. https://doi.org/10.1038/nature06053

Elderfield, H., & Ganssen, G. (2000). Past temperature and δ18O of surface ocean waters inferred from foraminiferal Mg/Ca ratios. *Nature*, *405*(6785), 442–445. https://doi.org/10.1038/35013033

Elling, F. J., Könneke, M., Mußmann, M., Greve, A., & Hinrichs, K.-U. (2015). Influence of temperature, pH, and salinity on membrane lipid composition and TEX86 of marine planktonic thaumarchaeal isolates. *Geochimica et Cosmochimica Acta*, *171*, 238–255. https://doi.org/10.1016/j.gca.2015.09.004

Elliot Smith, M., Carroll, A. R., & Mueller, E. R. (2008). Elevated weathering rates in the Rocky Mountains during the Early Eocene Climatic Optimum. *Nature Geoscience*, *1*(6), 370–374. https://doi.org/10.1038/ngeo205

Ellis, B., Grant, K., Mallela, J., & Abram, N. (2019). Is XRF core scanning a viable method for coral palaeoclimate temperature reconstructions? *Quaternary International*, *514*, 97–107. https://doi.org/10.1016/j.quaint.2018.11.044

Elsworth, G., Galbraith, E., Halverson, G., & Yang, S. (2017). Enhanced weathering and CO2 drawdown caused by latest Eocene strengthening of the Atlantic meridional overturning circulation. *Nature Geoscience*, *10*(3), 213–216. https://doi.org/10.1038/ngeo2888

Evans, D., & Müller, W. (2012). Deep time foraminifera Mg/Ca paleothermometry: Nonlinear correction for secular change in seawater Mg/Ca. *Paleoceanography*, *27*(4). https://doi.org/10.1029/2012PA002315

Evans, D., Sagoo, N., Renema, W., Cotton, L. J., Müller, W., Todd, J. A., Saraswati, P. K., Stassen, P., Ziegler, M., Pearson, P. N., Valdes, P. J., & Affek, H. P. (2018). Eocene greenhouse climate revealed by coupled clumped isotope-Mg/Ca thermometry. *Proceedings of the National Academy of Sciences*, *115*(6), 1174–1179. https://doi.org/10.1073/pnas.1714744115

Evans, D., Wade, B. S., Henehan, M., Erez, J., & Müller, W. (2016). Revisiting carbonate chemistry controls on planktic foraminifera Mg / Ca: implications for sea surface temperature and hydrology shifts over the Paleocene–Eocene Thermal Maximum and Eocene–Oligocene transition. *Climate of the Past*, *12*(4), 819–835. https://doi.org/10.5194/cp-12-819-2016

Evans, G., Augustinus, P., Gadd, P., Zawadzki, A., Ditchfield, A., & Shane, P. (2021). A multi-proxy record of environmental change through the last 53,000 years recorded in the sediments of Lake Kanono, Northland, New Zealand. *Journal of Sedimentary Research*, *91*(10), 1094–1111. https://doi.org/10.2110/jsr.2020.021

Faul, K. L., & Delaney, M. L. (2010). A comparison of early Paleogene export productivity and organic carbon burial flux for Maud Rise, Weddell Sea, and Kerguelen Plateau, south Indian Ocean. *Paleoceanography*, *25*(3). https://doi.org/10.1029/2009PA001916

Fogwill, C. J., Turney, C. S. M., Menviel, L., Baker, A., Weber, M. E., Ellis, B., Thomas, Z. A., Golledge, N. R., Etheridge, D., Rubino, M., Thornton, D. P., van Ommen, T. D., Moy, A. D., Curran, M. A. J., Davies, S., Bird, M. I., Munksgaard, N. C., Rootes, C. M., Millman, H., … Cooper, A. (2020). Southern Ocean carbon sink enhanced by sea-ice feedbacks at the Antarctic Cold Reversal. *Nature Geoscience*, *13*(7), 489–497. https://doi.org/10.1038/s41561-020-0587-0

Forster, P., Storelvmo, T., Armour, K., Collins, W., Dufresne, J.-L., Frame, D., Lunt, D. J., Mauritsen, T., Palmer, M. D., Watanabe, M., Wild, M., & Zhang, H. (2021). The Earth's Energy Budget, Climate Feedbacks, and Climate Sensitivity. In v. Masson-Delmotte, P. Zhai, A. Pirani, S.L. Connors, C. Péan, S. Berger, N. Caud, Y. Chen, L. Goldfarb, M.I. Gomis, M. Huang, K. Leitzell, E. Lonnoy, J.B.R. Matthews, T.K. Maycock, T. Waterfield, O. Yelekçi, R. Yu, & B. Zhou (Eds.), *Climate Change 2021: The Physical Science Basis. Contribution of Working Group I to the Sixth Assessment Report of the Intergovernmental Panel on Climate Change* (pp. 923–1054). Cambridge University Press.

Francescone, F., Lauretano, V., Bouligand, C., Moretti, M., Sabatino, N., Schrader, C., Catanzariti, R., Hilgen, F., Lanci, L., Turtù, A., Sprovieri, M., Lourens, L., & Galeotti, S. (2019). A 9 million-year-long astrochronological record of the early–middle Eocene corroborated by seafloor spreading rates. *GSA Bulletin*, *131*(3–4), 499–520. https://doi.org/10.1130/B32050.1

Froelich, F., & Misra, S. (2014). Was the Late Paleocene-Early Eocene Hot Because Earth Was Flat? An Ocean Lithium Isotope View of Mountain Building, Continental Weathering, Carbon Dioxide, and Earth's Cenozoic Clima. *Oceanography*, *27*(1), 36–49. https://doi.org/10.5670/oceanog.2014.06

Frölicher, T. L., Sarmiento, J. L., Paynter, D. J., Dunne, J. P., Krasting, J. P., & Winton, M. (2015). Dominance of the Southern Ocean in Anthropogenic Carbon and Heat Uptake in CMIP5 Models. *Journal of Climate*, *28*(2), 862–886. https://doi.org/10.1175/JCLI-D-14-00117.1

Gaillardet, J., Dupré, B., & Allègre, C. J. (1999). Geochemistry of large river suspended sediments: silicate weathering or recycling tracer? *Geochimica et Cosmochimica Acta*, *63*(23–24), 4037–4051. https://doi.org/10.1016/S0016-7037(99)00307-5

Galeotti, S., Krishnan, S., Pagani, M., Lanci, L., Gaudio, A., Zachos, J. C., Monechi, S., Morelli, G., & Lourens, L. (2010). Orbital chronology of Early Eocene hyperthermals from the Contessa Road section, central Italy. *Earth and Planetary Science Letters*, *290*(1–2), 192–200. https://doi.org/10.1016/j.epsl.2009.12.021

Gasson, E., Lunt, D. J., DeConto, R., Goldner, A., Heinemann, M., Huber, M., LeGrande, A. N., Pollard, D., Sagoo, N., Siddall, M., Winguth, A., & Valdes, P. J. (2014). Uncertainties in the modelled CO₂ threshold for Antarctic glaciation. *Climate of the Past*, *10*(2), 451–466. https://doi.org/10.5194/cp-10-451-2014

Gasson, E., Siddall, M., Lunt, D. J., Rackham, O. J. L., Lear, C. H., & Pollard, D. (2012). Exploring uncertainties in the relationship between temperature, ice volume, and sea level over the past 50 million years. *Reviews of Geophysics*, *50*(1), RG1005. https://doi.org/10.1029/2011RG000358

Gibbs, S. J., Bown, P. R., Murphy, B. H., Sluijs, A., Edgar, K. M., Pälike, H., Bolton, C. T., & Zachos, J. C. (2012). Scaled biotic disruption during early Eocene global warming events. *Biogeosciences*, *9*(11), 4679–4688. https://doi.org/10.5194/bg-9-4679-2012

Giorgioni, M., Jovane, L., Rego, E. S., Rodelli, D., Frontalini, F., Coccioni, R., Catanzariti, R., & Özcan, E. (2019). Carbon cycle instability and orbital forcing during the Middle Eocene Climatic Optimum. *Scientific Reports*, *9*(1), 9357. https://doi.org/10.1038/s41598-019-45763-2

Gottschalk, J., Skinner, L. C., Lippold, J., Vogel, H., Frank, N., Jaccard, S. L., & Waelbroeck, C. (2016). Biological and physical controls in the Southern Ocean on past millennial-scale atmospheric CO2 changes. *Nature Communications*, *7*(1), 11539. https://doi.org/10.1038/ncomms11539

Gradstein, F. M., Ogg, J. G., Schmitz, M., & Ogg, G. (2012). *The Geologic Time Scale 2012*. Elsevier.

Greene, S. E., Ridgwell, A., Kirtland Turner, S., Schmidt, D. N., Pälike, H., Thomas, E., Greene, L. K., & Hoogakker, B. A. A. (2019). Early Cenozoic Decoupling of Climate and Carbonate Compensation Depth Trends. *Paleoceanography and Paleoclimatology*, *34*(6), 930–945. https://doi.org/10.1029/2019PA003601

Griffith, E. M., Thomas, E., Lewis, A. R., Penman, D. E., Westerhold, T., & Winguth, A. M. E. (2021). Bentho-Pelagic Decoupling: The Marine Biological Carbon Pump During Eocene Hyperthermals. *Paleoceanography and Paleoclimatology*, *36*(3). https://doi.org/10.1029/2020PA004053

Grinsted, A., Moore, J. C., & Jevrejeva, S. (2004). Application of the cross wavelet transform and wavelet coherence to geophysical time series. *Nonlinear Processes in Geophysics*, *11*(5/6), 561–566. https://doi.org/10.5194/npg-11-561-2004

Gutjahr, M., Ridgwell, A., Sexton, P. F., Anagnostou, E., Pearson, P. N., Pälike, H., Norris, R. D., Thomas, E., & Foster, G. L. (2017). Very large release of mostly volcanic carbon during the Palaeocene–Eocene Thermal Maximum. *Nature*, *548*(7669), 573–577. https://doi.org/10.1038/nature23646

Hammer, Ø., Harper, D. A. T., & Ryan, P. D. (2001). Past: Paleontological Statistics Software Package for Education and Data Analysis. *Palaeontologia Electronica*, *4*(1), 9.

Hasiuk, F. J., & Lohmann, K. C. (2010). Application of calcite Mg partitioning functions to the reconstruction of paleocean Mg/Ca. *Geochimica et Cosmochimica Acta*, *74*(23), 6751–6763. https://doi.org/10.1016/j.gca.2010.07.030

Haywood, A. M., Hill, D. J., Dolan, A. M., Otto-Bliesner, B. L., Bragg, F., Chan, W.-L., Chandler, M. A., Contoux, C., Dowsett, H. J., Jost, A., Kamae, Y., Lohmann, G., Lunt, D. J., Abe-Ouchi, A., Pickering, S. J., Ramstein, G., Rosenbloom, N. A., Salzmann, U., Sohl, L., … Zhang, Z. (2013). Large-scale features of Pliocene climate: results from the Pliocene Model Intercomparison Project. *Climate of the Past*, *9*(1), 191–209. https://doi.org/10.5194/cp-9-191-2013

Henehan, M. J., Edgar, K. M., Foster, G. L., Penman, D. E., Hull, P. M., Greenop, R., Anagnostou, E., & Pearson, P. N. (2020). Revisiting the Middle Eocene Climatic Optimum "Carbon Cycle Conundrum" With

New Estimates of Atmospheric pCO 2 From Boron Isotopes. *Paleoceanography and Paleoclimatology*, *35*(6). https://doi.org/10.1029/2019PA003713

Hobbs, R. W., Huber, B. T., & Bogus, K. A. (2019). *Volume 369: Australia Cretaceous Climate and Tectonics* (Vol. 369). International Ocean Discovery Program. https://doi.org/10.14379/iodp.proc.369.2019

Hodell, D. A., Evans, H. F., Channell, J. E. T., & Curtis, J. H. (2010). Phase relationships of North Atlantic ice-rafted debris and surface-deep climate proxies during the last glacial period. *Quaternary Science Reviews*, *29*(27–28), 3875–3886. https://doi.org/10.1016/j.quascirev.2010.09.006

Holbourn, A. E. L., Henderson, A. S., & MacLeod, N. (2013). *Atlas of benthic foraminifera*. Wiley-Blackwell.

Hollis, C. J., Dunkley Jones, T., Anagnostou, E., Bijl, P. K., Cramwinckel, M. J., Cui, Y., Dickens, G. R., Edgar, K. M., Eley, Y., Evans, D., Foster, G. L., Frieling, J., Inglis, G. N., Kennedy, E. M., Kozdon, R., Lauretano, V., Lear, C. H., Littler, K., Lourens, L., … Lunt, D. J. (2019). The DeepMIP contribution to PMIP4: methodologies for selection, compilation and analysis of latest Paleocene and early Eocene climate proxy data, incorporating version 0.1 of the DeepMIP database. *Geoscientific Model Development*, *12*(7), 3149–3206. https://doi.org/10.5194/gmd-12-3149-2019

Hollis, C. J., Taylor, K. W. R., Handley, L., Pancost, R. D., Huber, M., Creech, J. B., Hines, B. R., Crouch, E. M., Morgans, H. E. G., Crampton, J. S., Gibbs, S., Pearson, P. N., & Zachos, J. C. (2012). Early Paleogene temperature history of the Southwest Pacific Ocean: Reconciling proxies and models. *Earth and Planetary Science Letters*, *349–350*, 53–66. https://doi.org/10.1016/j.epsl.2012.06.024

Hönisch, B., Ridgwell, A., Schmidt, D. N., Thomas, E., Gibbs, S. J., Sluijs, A., Zeebe, R., Kump, L., Martindale, R. C., Greene, S. E., Kiessling, W., Ries, J., Zachos, J. C., Royer, D. L., Barker, S., Marchitto, T. M., Moyer, R., Pelejero, C., Ziveri, P., … Williams, B. (2012). The Geological Record of Ocean Acidification. *Science*, *335*(6072), 1058–1063. https://doi.org/10.1126/science.1208277

Hopmans, E. C., Weijers, J. W. H., Schefuß, E., Herfort, L., Sinninghe Damsté, J. S., & Schouten, S. (2004). A novel proxy for terrestrial organic matter in sediments based on branched and isoprenoid tetraether lipids. *Earth and Planetary Science Letters*, *224*(1–2), 107–116. https://doi.org/10.1016/j.epsl.2004.05.012

Huber, B. T., Hobbs, R. W., Bogus, K. A., Batenburg, S. J., Brumsack, H. J., do Monte Guerra, R., Edgar, K. M., Edvardsen, T., Garcia Tejada, M. L., Harry, D. L., Hasegawa, T., Haynes, S. J., Jiang, T., Jones, M. M., Kuroda, J., Lee, E. Y., Li, Y. X., MacLeod, K. G., Maritati, A., … Xu, Z. (2019a). *Expedition 369 methods*. https://doi.org/10.14379/iodp.proc.369.102.2019

Huber, B. T., Hobbs, R. W., Bogus, K. A., Batenburg, S. J., Brumsack, H. J., do Monte Guerra, R., Edgar, K. M., Edvardsen, T., Garcia Tejada, M. L., Harry, D. L., Hasegawa, T., Haynes, S. J., Jiang, T., Jones, M. M., Kuroda, J., Lee, E. Y., Li, Y. X., MacLeod, K. G., Maritati, A., … Xu, Z. (2019b). *Site U1514*. https://doi.org/10.14379/iodp.proc.369.105.2019

Huber, M., Brinkhuis, H., Stickley, C. E., Döös, K., Sluijs, A., Warnaar, J., Schellenberg, S. A., & Williams, G. L. (2004). Eocene circulation of the Southern Ocean: Was Antarctica kept warm by subtropical waters? *Paleoceanography*, *19*(4), n/a-n/a. https://doi.org/10.1029/2004PA001014

Huber, M., & Goldner, A. (2012). Eocene monsoons. *Journal of Asian Earth Sciences*, *44*, 3–23. https://doi.org/10.1016/j.jseaes.2011.09.014

Huck, C. E., van de Flierdt, T., Bohaty, S. M., & Hammond, S. J. (2017). Antarctic climate, Southern Ocean circulation patterns, and deep water formation during the Eocene. *Paleoceanography*, *32*(7), 674–691. https://doi.org/10.1002/2017PA003135

Hyland, E. G., & Sheldon, N. D. (2013). Coupled CO2-climate response during the Early Eocene Climatic Optimum. *Palaeogeography, Palaeoclimatology, Palaeoecology*, *369*, 125–135. https://doi.org/10.1016/j.palaeo.2012.10.011

Ingall, E. D., Diaz, J. M., Longo, A. F., Oakes, M., Finney, L., Vogt, S., Lai, B., Yager, P. L., Twining, B. S., & Brandes, J. A. (2013). Role of biogenic silica in the removal of iron from the Antarctic seas. *Nature Communications*, *4*(1), 1981. https://doi.org/10.1038/ncomms2981

Inglis, G. N., Bragg, F., Burls, N. J., Cramwinckel, M. J., Evans, D., Foster, G. L., Huber, M., Lunt, D. J., Siler, N., Steinig, S., Tierney, J. E., Wilkinson, R., Anagnostou, E., de Boer, A. M., Dunkley Jones, T., Edgar, K. M., Hollis, C. J., Hutchinson, D. K., & Pancost, R. D. (2020). Global mean surface temperature and

climate sensitivity of the early Eocene Climatic Optimum (EECO), Paleocene–Eocene Thermal Maximum (PETM), and latest Paleocene. *Climate of the Past*, *16*(5), 1953–1968. https://doi.org/10.5194/cp-16-1953-2020

Inglis, G. N., Farnsworth, A., Lunt, D., Foster, G. L., Hollis, C. J., Pagani, M., Jardine, P. E., Pearson, P. N., Markwick, P., Galsworthy, A. M. J., Raynham, L., Taylor, Kyle. W. R., & Pancost, R. D. (2015). Descent toward the Icehouse: Eocene sea surface cooling inferred from GDGT distributions. *Paleoceanography*, *30*(7), 1000–1020. https://doi.org/10.1002/2014PA002723

Jacques, F. M. B., Shi, G., Li, H., & Wang, W. (2014). An early–middle Eocene Antarctic summer monsoon: Evidence of 'fossil climates.' *Gondwana Research*, *25*(4), 1422–1428. https://doi.org/10.1016/j.gr.2012.08.007

Jahren, A. H. (2007). The Arctic Forest of the Middle Eocene. *Annual Review of Earth and Planetary Sciences*, *35*(1), 509–540. https://doi.org/10.1146/annurev.earth.35.031306.140125

Jenkyns, H. C., Schouten-Huibers, L., Schouten, S., & Sinninghe Damsté, J. S. (2012). Warm Middle Jurassic–Early Cretaceous high-latitude sea-surface temperatures from the Southern Ocean. *Climate of the Past*, *8*(1), 215–226. https://doi.org/10.5194/cp-8-215-2012

Johnson, T. C., Brown, E. T., & Shi, J. (2011). Biogenic silica deposition in Lake Malawi, East Africa over the past 150,000years. *Palaeogeography, Palaeoclimatology, Palaeoecology*, *303*(1–4), 103–109. https://doi.org/10.1016/j.palaeo.2010.01.024

Jolley, D. W., & Bell, B. R. (2002). The evolution of the North Atlantic Igneous Province and the opening of the NE Atlantic rift. *Geological Society, London, Special Publications*, *197*(1), 1–13. https://doi.org/10.1144/GSL.SP.2002.197.01.01

Jones, S. M., Hoggett, M., Greene, S. E., & Dunkley Jones, T. (2019). Large Igneous Province thermogenic greenhouse gas flux could have initiated Paleocene-Eocene Thermal Maximum climate change. *Nature Communications*, *10*(1), 5547. https://doi.org/10.1038/s41467-019-12957-1

Judd, E. J., Ivany, L. C., DeConto, R. M., Halberstadt, A. R. W., Miklus, N. M., Junium, C. K., & Uveges, B. T. (2019). Seasonally Resolved Proxy Data From the Antarctic Peninsula Support a Heterogeneous Middle Eocene Southern Ocean. *Paleoceanography and Paleoclimatology*, 2019PA003581. https://doi.org/10.1029/2019PA003581

Katz, M. E., Katz, D. R., Wright, J. D., Miller, K. G., Pak, D. K., Shackleton, N. J., & Thomas, E. (2003). Early Cenozoic benthic foraminiferal isotopes: Species reliability and interspecies correction factors. *Paleoceanography*, *18*(2), n/a-n/a. https://doi.org/10.1029/2002PA000798

Kennett, J. P. (1977). Cenozoic evolution of Antarctic glaciation, the circum-Antarctic Ocean, and their impact on global paleoceanography. *Journal of Geophysical Research*, *82*(27), 3843–3860. https://doi.org/10.1029/JC082i027p03843

Khider, D., Huerta, G., Jackson, C., Stott, L. D., & Emile-Geay, J. (2015). A Bayesian, multivariate calibration for *G lobigerinoides ruber* Mg/Ca. *Geochemistry, Geophysics, Geosystems*, *16*(9), 2916–2932. https://doi.org/10.1002/2015GC005844

Kim, J.-H., Schouten, S., Hopmans, E. C., Donner, B., & Sinninghe Damsté, J. S. (2008). Global sediment core-top calibration of the TEX86 paleothermometer in the ocean. *Geochimica et Cosmochimica Acta*, *72*(4), 1154–1173. https://doi.org/10.1016/j.gca.2007.12.010

Kim, J.-H., van der Meer, J., Schouten, S., Helmke, P., Willmott, V., Sangiorgi, F., Koç, N., Hopmans, E. C., & Damsté, J. S. S. (2010). New indices and calibrations derived from the distribution of crenarchaeal isoprenoid tetraether lipids: Implications for past sea surface temperature reconstructions. *Geochimica et Cosmochimica Acta*, *74*(16), 4639–4654. https://doi.org/10.1016/j.gca.2010.05.027

Kim, S.-T., & O'Neil, J. R. (1997). Equilibrium and nonequilibrium oxygen isotope effects in synthetic carbonates. *Geochimica et Cosmochimica Acta*, *61*(16), 3461–3475. https://doi.org/10.1016/S0016-7037(97)00169-5

Kirtland Turner, S. (2014). Pliocene switch in orbital-scale carbon cycle/climate dynamics. *Paleoceanography*, *29*(12), 1256–1266. https://doi.org/10.1002/2014PA002651

Kirtland Turner, S., Sexton, P. F., Charles, C. D., & Norris, R. D. (2014). Persistence of carbon release events through the peak of early Eocene global warmth. *Nature Geoscience*, *7*(10), 748–751. https://doi.org/10.1038/ngeo2240

Kleiven, H. (Kikki) F., Kissel, C., Laj, C., Ninnemann, U. S., Richter, T. O., & Cortijo, E. (2008). Reduced North Atlantic Deep Water Coeval with the Glacial Lake Agassiz Freshwater Outburst. *Science*, *319*(5859), 60–64. https://doi.org/10.1126/science.1148924

Kodama, K. P., & Hinnov, L. A. (2014). *Rock Magnetic Cyclostratigraphy*. John Wiley & Sons, Ltd. https://doi.org/10.1002/9781118561294

Kuhlmann, H., Meggers, H., Freudenthal, T., & Wefer, G. (2004). The transition of the monsoonal and the N Atlantic climate system off NW Africa during the Holocene. *Geophysical Research Letters*, *31*(22). https://doi.org/10.1029/2004GL021267

Kump, L. R., Brantley, S. L., & Arthur, M. A. (2000). Chemical Weathering, Atmospheric CO_2, and Climate. *Annual Review of Earth and Planetary Sciences*, *28*(1), 611–667. https://doi.org/10.1146/annurev.earth.28.1.611

Laskar, J., Fienga, A., Gastineau, M., & Manche, H. (2011). La2010: a new orbital solution for the long-term motion of the Earth. *Astronomy & Astrophysics*, *532*, A89. https://doi.org/10.1051/0004-6361/201116836

Lauretano, V., Hilgen, F. J., Zachos, J. C., & Lourens, L. J. (2016). Astronomically tuned age model for the early Eocene carbon isotope events: A new high-resolution δ13 Cbenthic record of ODP Site 1263 between ~ 49 and ~ 54 Ma. *Newsletters on Stratigraphy*, *49*(2), 383–400. https://doi.org/10.1127/nos/2016/0077

Lauretano, V., Kennedy-Asser, A. T., Korasidis, V. A., Wallace, M. W., Valdes, P. J., Lunt, D. J., Pancost, R. D., & Naafs, B. D. A. (2021). Eocene to Oligocene terrestrial Southern Hemisphere cooling caused by declining pCO2. *Nature Geoscience*, *14*(9), 659–664. https://doi.org/10.1038/s41561-021-00788-z

Lauretano, V., Littler, K., Polling, M., Zachos, J. C., & Lourens, L. J. (2015). Frequency, magnitude and character of hyperthermal events at the onset of the Early Eocene Climatic Optimum. *Climate of the Past*, *11*(10), 1313–1324. https://doi.org/10.5194/cp-11-1313-2015

Lauretano, V., Zachos, J. C., & Lourens, L. J. (2018). Orbitally Paced Carbon and Deep-Sea Temperature Changes at the Peak of the Early Eocene Climatic Optimum. *Paleoceanography and Paleoclimatology*, *33*(10), 1050–1065. https://doi.org/10.1029/2018PA003422

Lea, D. W., Mashiotta, T. A., & Spero, H. J. (1999). Controls on magnesium and strontium uptake in planktonic foraminifera determined by live culturing. *Geochimica et Cosmochimica Acta*, *63*(16), 2369–2379. https://doi.org/10.1016/S0016-7037(99)00197-0

Lear, C. H., Bailey, T. R., Pearson, P. N., Coxall, H. K., & Rosenthal, Y. (2008). Cooling and ice growth across the Eocene-Oligocene transition. *Geology*, *36*(3), 251. https://doi.org/10.1130/G24584A.1

LeGrande, A. N., & Schmidt, G. A. (2006). Global gridded data set of the oxygen isotopic composition in seawater. *Geophysical Research Letters*, *33*(12), L12604. https://doi.org/10.1029/2006GL026011

Leon-Rodriguez, L., & Dickens, G. R. (2010). Constraints on ocean acidification associated with rapid and massive carbon injections: The early Paleogene record at ocean drilling program site 1215, equatorial Pacific Ocean. *Palaeogeography, Palaeoclimatology, Palaeoecology*, *298*(3–4), 409–420. https://doi.org/10.1016/j.palaeo.2010.10.029

L'Homme, N. (2005). Global budget of water isotopes inferred from polar ice sheets. *Geophysical Research Letters*, *32*(20), L20502. https://doi.org/10.1029/2005GL023774

Li, M., Hinnov, L., & Kump, L. (2019). Acycle: Time-series analysis software for paleoclimate research and education. *Computers & Geosciences*, *127*, 12–22. https://doi.org/10.1016/j.cageo.2019.02.011

Licht, A., van Cappelle, M., Abels, H. A., Ladant, J.-B., Trabucho-Alexandre, J., France-Lanord, C., Donnadieu, Y., Vandenberghe, J., Rigaudier, T., Lécuyer, C., Terry Jr, D., Adriaens, R., Boura, A., Guo, Z., Soe, A. N., Quade, J., Dupont-Nivet, G., & Jaeger, J.-J. (2014). Asian monsoons in a late Eocene greenhouse world. *Nature*, *513*(7519), 501–506. https://doi.org/10.1038/nature13704

Littler, K., Röhl, U., Westerhold, T., & Zachos, J. C. (2014). A high-resolution benthic stable-isotope record for the South Atlantic: Implications for orbital-scale changes in Late Paleocene–Early Eocene climate and

carbon cycling. *Earth and Planetary Science Letters*, *401*, 18–30. https://doi.org/10.1016/j.epsl.2014.05.054

Liu, Z., Pagani, M., Zinniker, D., DeConto, R., Huber, M., Brinkhuis, H., Shah, S. R., Leckie, R. M., & Pearson, A. (2009). Global Cooling During the Eocene-Oligocene Climate Transition. *Science*, *323*(5918), 1187–1190. https://doi.org/10.1126/science.1166368

Lourens, L. J., Sluijs, A., Kroon, D., Zachos, J. C., Thomas, E., Röhl, U., Bowles, J., & Raffi, I. (2005). Astronomical pacing of late Palaeocene to early Eocene global warming events. *Nature*, *435*(7045), 1083–1087. https://doi.org/10.1038/nature03814

Luciani, V., Dickens, G. R., Backman, J., Fornaciari, E., Giusberti, L., Agnini, C., & D'Onofrio, R. (2016). Major perturbations in the global carbon cycle and photosymbiont-bearing planktic foraminifera during the early Eocene. *Climate of the Past*, *12*(4), 981–1007. https://doi.org/10.5194/cp-12-981-2016

Lunt, D. J., Bragg, F., Chan, W.-L., Hutchinson, D. K., Ladant, J.-B., Morozova, P., Niezgodzki, I., Steinig, S., Zhang, Z., Zhu, J., Abe-Ouchi, A., Anagnostou, E., de Boer, A. M., Coxall, H. K., Donnadieu, Y., Foster, G., Inglis, G. N., Knorr, G., Langebroek, P. M., … Otto-Bliesner, B. L. (2021). DeepMIP: model intercomparison of early Eocene climatic optimum (EECO) large-scale climate features and comparison with proxy data. *Climate of the Past*, *17*(1), 203–227. https://doi.org/10.5194/cp-17-203-2021

Lunt, D. J., Dunkley Jones, T., Heinemann, M., Huber, M., LeGrande, A., Winguth, A., Loptson, C., Marotzke, J., Roberts, C. D., Tindall, J., Valdes, P., & Winguth, C. (2012). A model–data comparison for a multi-model ensemble of early Eocene atmosphere–ocean simulations: EoMIP. *Climate of the Past*, *8*(5), 1717–1736. https://doi.org/10.5194/cp-8-1717-2012

Lunt, D. J., Elderfield, H., Pancost, R., Ridgwell, A., Foster, G. L., Haywood, A., Kiehl, J., Sagoo, N., Shields, C., Stone, E. J., & Valdes, P. (2013). Warm climates of the past—a lesson for the future? *Philosophical Transactions of the Royal Society A: Mathematical, Physical and Engineering Sciences*, *371*(2001), 20130146. https://doi.org/10.1098/rsta.2013.0146

Lunt, D. J., Haywood, A. M., Schmidt, G. A., Salzmann, U., Valdes, P. J., Dowsett, H. J., & Loptson, C. A. (2012). On the causes of mid-Pliocene warmth and polar amplification. *Earth and Planetary Science Letters*, *321–322*, 128–138. https://doi.org/10.1016/j.epsl.2011.12.042

Lyle, M., Olivarez Lyle, A., Backman, J., & Tripati, A. (2005). Biogenic Sedimentation in the Eocene Equatorial Pacific-The Stuttering Greenhouse and Eocene Carbonate Compensation Depth. In *Proceedings of the Ocean Drilling Program, 199 Scientific Results*. Ocean Drilling Program. https://doi.org/10.2973/odp.proc.sr.199.219.2005

Mackensen, A., & Schmiedl, G. (2019). Stable carbon isotopes in paleoceanography: atmosphere, oceans, and sediments. *Earth-Science Reviews*, *197*, 102893. https://doi.org/10.1016/j.earscirev.2019.102893

Malevich, S. B., Vetter, L., & Tierney, J. E. (2019). Global Core Top Calibration of δ18O in Planktic Foraminifera to Sea Surface Temperature. *Paleoceanography and Paleoclimatology*, *34*(8), 1292–1315. https://doi.org/10.1029/2019PA003576

Mann, M. E., & Lees, J. M. (1996). Robust estimation of background noise and signal detection in climatic time series. *Climatic Change*, *33*(3), 409–445. https://doi.org/10.1007/BF00142586

Mantsis, D. F., Clement, A. C., Broccoli, A. J., & Erb, M. P. (2011). Climate Feedbacks in Response to Changes in Obliquity. *Journal of Climate*, *24*(11), 2830–2845. https://doi.org/10.1175/2010JCLI3986.1

Marinov, I., Gnanadesikan, A., Toggweiler, J. R., & Sarmiento, J. L. (2006). The Southern Ocean biogeochemical divide. *Nature*, *441*(7096), 964–967. https://doi.org/10.1038/nature04883

Martin, H. A. (2006). Cenozoic climatic change and the development of the arid vegetation in Australia. *Journal of Arid Environments*, *66*(3), 533–563. https://doi.org/10.1016/j.jaridenv.2006.01.009

Matys Grygar, T., Hošek, M., Mach, K., Schnabl, P., & Martinez, M. (2017). Climatic instability before the Miocene Climatic Optimum reflected in a Central European lacustrine record from the Most Basin in the Czech Republic. *Palaeogeography, Palaeoclimatology, Palaeoecology*, *485*, 930–945. https://doi.org/10.1016/j.palaeo.2017.08.011

Matys Grygar, T., Mach, K., Schnabl, P., Martinez, M., & Zeeden, C. (2019). Orbital forcing and abrupt events in a continental weathering proxy from central Europe (Most Basin, Czech Republic, 17.7–15.9 Ma)

recorded beginning of the Miocene Climatic Optimum. *Palaeogeography, Palaeoclimatology, Palaeoecology*, *514*, 423–440. https://doi.org/10.1016/j.palaeo.2018.10.034

McCarren, H., Thomas, E., Hasegawa, T., Röhl, U., & Zachos, J. C. (2008). Depth dependency of the Paleocene-Eocene carbon isotope excursion: Paired benthic and terrestrial biomarker records (Ocean Drilling Program Leg 208, Walvis Ridge). *Geochemistry, Geophysics, Geosystems*, *9*(10), n/a-n/a. https://doi.org/10.1029/2008GC002116

McGowran, B., & Hill, R. S. (2015). Cenozoic climatic shifts in southern Australia. *Transactions of the Royal Society of South Australia*, *139*(1), 19–37. https://doi.org/10.1080/03721426.2015.1035215

McInerney, F. A., & Wing, S. L. (2011). The Paleocene-Eocene Thermal Maximum: A Perturbation of Carbon Cycle, Climate, and Biosphere with Implications for the Future. *Annual Review of Earth and Planetary Sciences*, *39*(1), 489–516. https://doi.org/10.1146/annurev-earth-040610-133431

McManus, J., Berelson, W. M., Hammond, D. E., & Klinkhammer, G. P. (1999). Barium Cycling in the North Pacific: Implications for the Utility of Ba as a Paleoproductivity and Paleoalkalinity Proxy. *Paleoceanography*, *14*(1), 53–61. https://doi.org/10.1029/1998PA900007

McManus, J., Berelson, W. M., Klinkhammer, G. P., Johnson, K. S., Coale, K. H., Anderson, R. F., Kumar, N., Burdige, D. J., Hammond, D. E., Brumsack, H. J., McCorkle, D. C., & Rushdi, A. (1998). Geochemistry of barium in marine sediments: implications for its use as a paleoproxy. *Geochimica et Cosmochimica Acta*, *62*(21–22), 3453–3473. https://doi.org/10.1016/S0016-7037(98)00248-8

Meckler, A. N., Sexton, P. F., Piasecki, A. M., Leutert, T. J., Marquardt, J., Ziegler, M., Agterhuis, T., Lourens, L. J., Rae, J. W. B., Barnet, J., Tripati, A., & Bernasconi, S. M. (2022). Cenozoic evolution of deep ocean temperature from clumped isotope thermometry. *Science*, *377*(6601), 86–90. https://doi.org/10.1126/science.abk0604

Methner, K., Mulch, A., Fiebig, J., Wacker, U., Gerdes, A., Graham, S. A., & Chamberlain, C. P. (2016). Rapid Middle Eocene temperature change in western North America. *Earth and Planetary Science Letters*, *450*, 132–139. https://doi.org/10.1016/j.epsl.2016.05.053

Miller, K. G., Wright, J. D., & Fairbanks, R. G. (1991). Unlocking the Ice House: Oligocene-Miocene oxygen isotopes, eustasy, and margin erosion. *Journal of Geophysical Research: Solid Earth*, *96*(B4), 6829–6848. https://doi.org/10.1029/90JB02015

Miller, K. G., Wright, J. D., & Browning, J. v. (2005). Visions of ice sheets in a greenhouse world. *Marine Geology*, *217*(3–4), 215–231. https://doi.org/10.1016/j.margeo.2005.02.007

Müller, R. D., Cannon, J., Qin, X., Watson, R. J., Gurnis, M., Williams, S., Pfaffelmoser, T., Seton, M., Russell, S. H. J., & Zahirovic, S. (2018). GPlates: Building a Virtual Earth Through Deep Time. *Geochemistry, Geophysics, Geosystems*, *19*(7), 2243–2261. https://doi.org/10.1029/2018GC007584

Müller, R. D., Zahirovic, S., Williams, S. E., Cannon, J., Seton, M., Bower, D. J., Tetley, M. G., Heine, C., le Breton, E., Liu, S., Russell, S. H. J., Yang, T., Leonard, J., & Gurnis, M. (2019). A Global Plate Model Including Lithospheric Deformation Along Major Rifts and Orogens Since the Triassic. *Tectonics*, *38*(6), 1884–1907. https://doi.org/10.1029/2018TC005462

Murphy, B. H., Farley, K. A., & Zachos, J. C. (2010). An extraterrestrial 3He-based timescale for the Paleocene–Eocene thermal maximum (PETM) from Walvis Ridge, IODP Site 1266. *Geochimica et Cosmochimica Acta*, *74*(17), 5098–5108. https://doi.org/10.1016/j.gca.2010.03.039

Nicolo, M. J., Dickens, G. R., Hollis, C. J., & Zachos, J. C. (2007). Multiple early Eocene hyperthermals: Their sedimentary expression on the New Zealand continental margin and in the deep sea. *Geology*, *35*(8), 699. https://doi.org/10.1130/G23648A.1

Nürnberg, D., Bijma, J., & Hemleben, C. (1996). Assessing the reliability of magnesium in foraminiferal calcite as a proxy for water mass temperatures. *Geochimica et Cosmochimica Acta*, *60*(5), 803–814. https://doi.org/10.1016/0016-7037(95)00446-7

Ortiz, S., & Thomas, E. (2015). Deep-sea benthic foraminiferal turnover during the early–middle Eocene transition at Walvis Ridge (SE Atlantic). *Palaeogeography, Palaeoclimatology, Palaeoecology*, *417*, 126–136. https://doi.org/10.1016/j.palaeo.2014.10.023

Pagani, M., Pedentchouk, N., Huber, M., Sluijs, A., Schouten, S., Brinkhuis, H., Sinninghe Damsté, J. S., & Dickens, G. R. (2006). Arctic hydrology during global warming at the Palaeocene/Eocene thermal maximum. *Nature*, *442*(7103), 671–675. https://doi.org/10.1038/nature05043

Pagani, M., Zachos, J. C., Freeman, K. H., Tipple, B., & Bohaty, S. (2005). Marked Decline in Atmospheric Carbon Dioxide Concentrations During the Paleogene. *Science*, *309*(5734), 600–603. https://doi.org/10.1126/science.1110063

Pälike, H., Frazier, J., & Zachos, J. C. (2006). Extended orbitally forced palaeoclimatic records from the equatorial Atlantic Ceara Rise. *Quaternary Science Reviews*, *25*(23–24), 3138–3149. https://doi.org/10.1016/j.quascirev.2006.02.011

Pälike, H., Lyle, M. W., Nishi, H., Raffi, I., Ridgwell, A., Gamage, K., Klaus, A., Acton, G., Anderson, L., Backman, J., Baldauf, J., Beltran, C., Bohaty, S. M., Bown, P., Busch, W., Channell, J. E. T., Chun, C. O. J., Delaney, M., Dewangan, P., … Zeebe, R. E. (2012). A Cenozoic record of the equatorial Pacific carbonate compensation depth. *Nature*, *488*(7413), 609–614. https://doi.org/10.1038/nature11360

Payros, A., Tosquella, J., Bernaola, G., Dinarès-Turell, J., Orue-Etxebarria, X., & Pujalte, V. (2009). Filling the North European Early/Middle Eocene (Ypresian/Lutetian) boundary gap: Insights from the Pyrenean continental to deep-marine record. *Palaeogeography, Palaeoclimatology, Palaeoecology*, *280*(3–4), 313–332. https://doi.org/10.1016/j.palaeo.2009.06.018

Paytan, A., & Kastner, M. (1996). Benthic Ba fluxes in the central Equatorial Pacific, implications for the oceanic Ba cycle. *Earth and Planetary Science Letters*, *142*(3–4), 439–450. https://doi.org/10.1016/0012-821X(96)00120-3

Pearson, P. N. (2012). Oxygen Isotopes in Foraminifera: Overview and Historical Review. *The Paleontological Society Papers*, *18*, 1–38. https://doi.org/10.1017/S1089332600002539

Pearson, P. N., Ditchfield, P. W., Singano, J., Harcourt-Brown, K. G., Nicholas, C. J., Olsson, R. K., Shackleton, N. J., & Hall, M. A. (2001). Warm tropical sea surface temperatures in the Late Cretaceous and Eocene epochs. *Nature*, *413*(6855), 481–487. https://doi.org/10.1038/35097000

Pingitore, N. E., Lytle, F. W., Davies, B. M., Eastman, M. P., Eller, P. G., & Larson, E. M. (1992). Mode of incorporation of Sr2+ in calcite: Determination by X-ray absorption spectroscopy. *Geochimica et Cosmochimica Acta*, *56*(4), 1531–1538. https://doi.org/10.1016/0016-7037(92)90222-5

Pogge von Strandmann, P. A. E., Jones, M. T., West, A. J., Murphy, M. J., Stokke, E. W., Tarbuck, G., Wilson, D. J., Pearce, C. R., & Schmidt, D. N. (2021). Lithium isotope evidence for enhanced weathering and erosion during the Paleocene-Eocene Thermal Maximum. *Science Advances*, *7*(42). https://doi.org/10.1126/sciadv.abh4224

Poole, I., Hunt, R. J., & Cantrill, D. J. (2001). A Fossil Wood Flora from King George Island: Ecological Implications for an Antarctic Eocene Vegetation. *Annals of Botany*, *88*(1), 33–54. https://doi.org/10.1006/anbo.2001.1425

Quilty, P. G. (1994). The background: 144 million years of Australian palaeoclimate and palaeogeography. In R. S. Hill (Ed.), *History of the Australian vegetation: Cretaceous to Recent* (pp. 14–43). Cambridge University Press.

Rae, J. W. B., Zhang, Y. G., Liu, X., Foster, G. L., Stoll, H. M., & Whiteford, R. D. M. (2021). Atmospheric CO_2 over the Past 66 Million Years from Marine Archives. *Annual Review of Earth and Planetary Sciences*, *49*(1), 609–641. https://doi.org/10.1146/annurev-earth-082420-063026

Regenberg, M., Regenberg, A., Garbe-Schönberg, D., & Lea, D. W. (2014). Global dissolution effects on planktonic foraminiferal Mg/Ca ratios controlled by the calcite-saturation state of bottom waters. *Paleoceanography*, *29*(3), 127–142. https://doi.org/10.1002/2013PA002492

Richter, T. O., van der Gaast, S., Koster, B., Vaars, A., Gieles, R., de Stigter, H. C., de Haas, H., & van Weering, T. C. E. (2006). The Avaatech XRF Core Scanner: technical description and applications to NE Atlantic sediments. *Geological Society, London, Special Publications*, *267*(1), 39–50. https://doi.org/10.1144/GSL.SP.2006.267.01.03

Rivero-Cuesta, L., Westerhold, T., Agnini, C., Dallanave, E., Wilkens, R. H., & Alegret, L. (2019). Paleoenvironmental Changes at ODP Site 702 (South Atlantic): Anatomy of the Middle Eocene Climatic

Optimum. *Paleoceanography and Paleoclimatology*, *34*(12), 2047–2066. https://doi.org/10.1029/2019PA003806

Röhl, U., Westerhold, T., Bralower, T. J., & Zachos, J. C. (2007). On the duration of the Paleocene-Eocene thermal maximum (PETM). *Geochemistry, Geophysics, Geosystems*, *8*(12), n/a-n/a. https://doi.org/10.1029/2007GC001784

Rohling, E. J., Yu, J., Heslop, D., Foster, G. L., Opdyke, B., & Roberts, A. P. (2021). Sea level and deep-sea temperature reconstructions suggest quasi-stable states and critical transitions over the past 40 million years. *Science Advances*, *7*(26). https://doi.org/10.1126/sciadv.abf5326

Rosenthal, Y., Boyle, E. A., & Slowey, N. (1997). Temperature control on the incorporation of magnesium, strontium, fluorine, and cadmium into benthic foraminiferal shells from Little Bahama Bank: Prospects for thermocline paleoceanography. *Geochimica et Cosmochimica Acta*, *61*(17), 3633–3643. https://doi.org/10.1016/S0016-7037(97)00181-6

Rosenthal, Y., & Lohmann, G. P. (2002). Accurate estimation of sea surface temperatures using dissolution-corrected calibrations for Mg/Ca paleothermometry. *Paleoceanography*, *17*(3), 16-1-16–6. https://doi.org/10.1029/2001PA000749

Rothwell, R. G., & Croudace, I. w. (2015). *Twenty Years of XRF Core Scanning Marine Sediments: What Do Geochemical Proxies Tell Us?* (pp. 25–102). https://doi.org/10.1007/978-94-017-9849-5_2

Sabine, C. L., Feely, R. A., Gruber, N., Key, R. M., Lee, K., Bullister, J. L., Wanninkhof, R., Wong, C. S., Wallace, D. W. R., Tilbrook, B., Millero, F. J., Peng, T.-H., Kozyr, A., Ono, T., & Rios, A. F. (2004). The Oceanic Sink for Anthropogenic CO_2. *Science*, *305*(5682), 367–371. https://doi.org/10.1126/science.1097403

Sarkar, S., Basak, C., Frank, M., Berndt, C., Huuse, M., Badhani, S., & Bialas, J. (2019). Late Eocene onset of the Proto-Antarctic Circumpolar Current. *Scientific Reports*, *9*(1), 10125. https://doi.org/10.1038/s41598-019-46253-1

Schaller, M. F., & Fung, M. K. (2018). The extraterrestrial impact evidence at the Palaeocene–Eocene boundary and sequence of environmental change on the continental shelf. *Philosophical Transactions of the Royal Society A: Mathematical, Physical and Engineering Sciences*, *376*(2130), 20170081. https://doi.org/10.1098/rsta.2017.0081

Scheffer, M., Bascompte, J., Brock, W. A., Brovkin, V., Carpenter, S. R., Dakos, V., Held, H., van Nes, E. H., Rietkerk, M., & Sugihara, G. (2009). Early-warning signals for critical transitions. *Nature*, *461*(7260), 53–59. https://doi.org/10.1038/nature08227

Scher, H. D., & Martin, E. E. (2004). Circulation in the Southern Ocean during the Paleogene inferred from neodymium isotopes. *Earth and Planetary Science Letters*, *228*(3–4), 391–405. https://doi.org/10.1016/j.epsl.2004.10.016

Scher, H. D., & Martin, E. E. (2006). Timing and Climatic Consequences of the Opening of Drake Passage. *Science*, *312*(5772), 428–430. https://doi.org/10.1126/science.1120044

Scher, H. D., Whittaker, J. M., Williams, S. E., Latimer, J. C., Kordesch, W. E. C., & Delaney, M. L. (2015). Onset of Antarctic Circumpolar Current 30 million years ago as Tasmanian Gateway aligned with westerlies. *Nature*, *523*(7562), 580–583. https://doi.org/10.1038/nature14598

Schmittner, A., & Galbraith, E. D. (2008). Glacial greenhouse-gas fluctuations controlled by ocean circulation changes. *Nature*, *456*(7220), 373–376. https://doi.org/10.1038/nature07531

Schmitz, B., & Pujalte, V. (2007). Abrupt increase in seasonal extreme precipitation at the Paleocene-Eocene boundary. *Geology*, *35*(3), 215. https://doi.org/10.1130/G23261A.1

Schneider, L. J., Bralower, T. J., & Kump, L. R. (2011). Response of nannoplankton to early Eocene ocean destratification. *Palaeogeography, Palaeoclimatology, Palaeoecology*, *310*(3–4), 152–162. https://doi.org/10.1016/j.palaeo.2011.06.018

Schouten, S., Hopmans, E. C., Schefuß, E., & Sinninghe Damsté, J. S. (2002). Distributional variations in marine crenarchaeotal membrane lipids: a new tool for reconstructing ancient sea water temperatures? *Earth and Planetary Science Letters*, *204*(1–2), 265–274. https://doi.org/10.1016/S0012-821X(02)00979-2

Schrag, D. P., DePaolo, D. J., & Richter, F. M. (1995). Reconstructing past sea surface temperatures: Correcting for diagenesis of bulk marine carbonate. *Geochimica et Cosmochimica Acta*, *59*(11), 2265–2278. https://doi.org/10.1016/0016-7037(95)00105-9

Sexton, P. F., Norris, R. D., Wilson, P. A., Pälike, H., Westerhold, T., Röhl, U., Bolton, C. T., & Gibbs, S. (2011). Eocene global warming events driven by ventilation of oceanic dissolved organic carbon. *Nature*, *471*(7338), 349–352. https://doi.org/10.1038/nature09826

Sexton, P. F., Wilson, P. A., & Norris, R. D. (2006). Testing the Cenozoic multisite composite δ^{18}O and δ^{13}C curves: New monospecific Eocene records from a single locality, Demerara Rise (Ocean Drilling Program Leg 207). *Paleoceanography*, *21*(2), n/a-n/a. https://doi.org/10.1029/2005PA001253

Sexton, P. F., Wilson, P. A., & Pearson, P. N. (2006). Microstructural and geochemical perspectives on planktic foraminiferal preservation: "Glassy" versus "Frosty." *Geochemistry, Geophysics, Geosystems*, *7*(12), n/a-n/a. https://doi.org/10.1029/2006GC001291

Shackleton, N. J., & Kennett, J. P. (1975). Paleotemperature history of the Cenozoic and the initiation of Antarctic glaciation: oxygen and carbon isotope analyses in DSDP Sites 277, 279, and 281. In J. P. Kennett, R. E. Houtz, P. B. Andrews, A. R. Edwards, V. A. Gostin, M. Hajós, M. A. Hampton, D. G. Jenkins, S. v. Margolis, A. T. Ovenshine, & K. Perch-Nielsen (Eds.), *Initial reports of the Deep See Drilling Project, Volume 29* (pp. 743–755). U.S. Government Printing Office.

Sigman, D. M., & Boyle, E. A. (2000). Glacial/interglacial variations in atmospheric carbon dioxide. *Nature*, *407*(6806), 859–869. https://doi.org/10.1038/35038000

Sijp, W. P., England, M. H., & Toggweiler, J. R. (2009). Effect of Ocean Gateway Changes under Greenhouse Warmth. *Journal of Climate*, *22*(24), 6639–6652. https://doi.org/10.1175/2009JCLI3003.1

Sijp, W. P., von der Heydt, A. S., Dijkstra, H. A., Flögel, S., Douglas, P. M. J., & Bijl, P. K. (2014). The role of ocean gateways on cooling climate on long time scales. *Global and Planetary Change*, *119*, 1–22. https://doi.org/10.1016/j.gloplacha.2014.04.004

Sinninghe Damsté, J. S., Ossebaar, J., Schouten, S., & Verschuren, D. (2012). Distribution of tetraether lipids in the 25-ka sedimentary record of Lake Challa: extracting reliable TEX86 and MBT/CBT palaeotemperatures from an equatorial African lake. *Quaternary Science Reviews*, *50*, 43–54. https://doi.org/10.1016/j.quascirev.2012.07.001

Slotnick, B. S., Dickens, G. R., Nicolo, M. J., Hollis, C. J., Crampton, J. S., Zachos, J. C., & Sluijs, A. (2012). Large-Amplitude Variations in Carbon Cycling and Terrestrial Weathering during the Latest Paleocene and Earliest Eocene: The Record at Mead Stream, New Zealand. *The Journal of Geology*, *120*(5), 487–505. https://doi.org/10.1086/666743

Sluijs, A., Frieling, J., Inglis, G. N., Nierop, K. G. J., Peterse, F., Sangiorgi, F., & Schouten, S. (2020). Late Paleocene–early Eocene Arctic Ocean sea surface temperatures: reassessing biomarker paleothermometry at Lomonosov Ridge. *Climate of the Past*, *16*(6), 2381–2400. https://doi.org/10.5194/cp-16-2381-2020

Sluijs, A., Schouten, S., Donders, T. H., Schoon, P. L., Röhl, U., Reichart, G.-J., Sangiorgi, F., Kim, J.-H., Sinninghe Damsté, J. S., & Brinkhuis, H. (2009). Warm and wet conditions in the Arctic region during Eocene Thermal Maximum 2. *Nature Geoscience*, *2*(11), 777–780. https://doi.org/10.1038/ngeo668

Sluijs, A., Zeebe, R. E., Bijl, P. K., & Bohaty, S. M. (2013). A middle Eocene carbon cycle conundrum. *Nature Geoscience*, *6*(6), 429–434. https://doi.org/10.1038/ngeo1807

Spaggiari, C. v., Bodorkos, S., Barquero-Molina, M., Tyler, I. M., & Wingate, M. T. D. (2009). *Interpreted bedrock geology of the South Yilgarn and central Albany–Fraser Orogen, Western Australia: Vol. Record 2009* (10th ed.). Geological Survey of Western Australia.

SPEELMAN, E. N., van KEMPEN, M. M. L., BARKE, J., BRINKHUIS, H., REICHART, G. J., SMOLDERS, A. J. P., ROELOFS, J. G. M., SANGIORGI, F., de LEEUW, J. W., LOTTER, A. F., & SINNINGHE DAMSTÉ, J. S. (2009). The Eocene Arctic *Azolla* bloom: environmental conditions, productivity and carbon drawdown. *Geobiology*, *7*(2), 155–170. https://doi.org/10.1111/j.1472-4669.2009.00195.x

Speijer, R. P., Scheibner, C., Stassen, P., & Morsi, A.-M. M. (2012). Response of marine ecosystems to deep-time global warming: a synthesis of biotic patterns across the Paleocene-Eocene thermal maximum (PETM). *Austrian Journal of Earth Sciences*, *105*(1), 6–16.

Spero, H. J., Bijma, J., Lea, D. W., & Bemis, B. E. (1997). Effect of seawater carbonate concentration on foraminiferal carbon and oxygen isotopes. *Nature*, *390*(6659), 497–500. https://doi.org/10.1038/37333

Spero, H. J., Bijma, J., Lea, D. W., & Russell, A. D. (1999). Deconvolving Glacial Ocean Carbonate Chemistry from the Planktonic Foraminifera Carbon Isotope Record. In *Reconstructing Ocean History* (pp. 329–342). Springer US. https://doi.org/10.1007/978-1-4615-4197-4_19

Spicer, R. A., Yang, J., Herman, A. B., Kodrul, T., Maslova, N., Spicer, T. E. V., Aleksandrova, G., & Jin, J. (2016). Asian Eocene monsoons as revealed by leaf architectural signatures. *Earth and Planetary Science Letters*, *449*, 61–68. https://doi.org/10.1016/j.epsl.2016.05.036

Spofforth, D. J. A., Pälike, H., & Green, D. (2008). Paleogene record of elemental concentrations in sediments from the Arctic Ocean obtained by XRF analyses. *Paleoceanography*, *23*(1), 1–13. https://doi.org/10.1029/2007PA001489

Sriver, R. L., & Huber, M. (2007). Observational evidence for an ocean heat pump induced by tropical cyclones. *Nature*, *447*(7144), 577–580. https://doi.org/10.1038/nature05785

Stap, L., Lourens, L. J., Thomas, E., Sluijs, A., Bohaty, S., & Zachos, J. C. (2010). High-resolution deep-sea carbon and oxygen isotope records of Eocene Thermal Maximum 2 and H2. *Geology*, *38*(7), 607–610. https://doi.org/10.1130/G30777.1

Stickley, C. E., Brinkhuis, H., Schellenberg, S. A., Sluijs, A., Röhl, U., Fuller, M., Grauert, M., Huber, M., Warnaar, J., & Williams, G. L. (2004). Timing and nature of the deepening of the Tasmanian Gateway. *Paleoceanography*, *19*(4), n/a-n/a. https://doi.org/10.1029/2004PA001022

Stickley, C. E., St John, K., Koç, N., Jordan, R. W., Passchier, S., Pearce, R. B., & Kearns, L. E. (2009). Evidence for middle Eocene Arctic sea ice from diatoms and ice-rafted debris. *Nature*, *460*(7253), 376–379. https://doi.org/10.1038/nature08163

Stoll, H. M., & Schrag, D. P. (2000). Coccolith Sr/Ca as a new indicator of coccolithophorid calcification and growth rate. *Geochemistry, Geophysics, Geosystems*, *1*(5). https://doi.org/10.1029/1999GC000015

Stoll, H. M., & Schrag, D. P. (2001). Sr/Ca variations in Cretaceous carbonates: relation to productivity and sea level changes. *Palaeogeography, Palaeoclimatology, Palaeoecology*, *168*(3–4), 311–336. https://doi.org/10.1016/S0031-0182(01)00205-X

Stoll, H. M., & Ziveri, P. (2004). Coccolithophorid-based geochemical paleoproxies. In *Coccolithophores* (pp. 529–562). Springer Berlin Heidelberg. https://doi.org/10.1007/978-3-662-06278-4_20

Stoll, H. M., Ziveri, P., Geisen, M., Probert, I., & Young, J. R. (2002). Potential and limitations of Sr/Ca ratios in coccolith carbonate: new perspectives from cultures and monospecific samples from sediments. *Philosophical Transactions of the Royal Society of London. Series A: Mathematical, Physical and Engineering Sciences*, *360*(1793), 719–747. https://doi.org/10.1098/rsta.2001.0966

Thomas, D. J., Korty, R., Huber, M., Schubert, J. A., & Haines, B. (2014). Nd isotopic structure of the Pacific Ocean 70-30 Ma and numerical evidence for vigorous ocean circulation and ocean heat transport in a greenhouse world. *Paleoceanography*, *29*(5), 454–469. https://doi.org/10.1002/2013PA002535

Thomas, D. J., Zachos, J. C., Bralower, T. J., Thomas, E., & Bohaty, S. (2002). Warming the fuel for the fire: Evidence for the thermal dissociation of methane hydrate during the Paleocene-Eocene thermal maximum. *Geology*, *30*(12), 1067. https://doi.org/10.1130/0091-7613(2002)030<1067:WTFFTF>2.0.CO;2

Tierney, J. E., Sinninghe Damsté, J. S., Pancost, R. D., Sluijs, A., & Zachos, J. C. (2017). Eocene temperature gradients. *Nature Geoscience*, *10*(8), 538–539. https://doi.org/10.1038/ngeo2997

Tierney, J. E., & Tingley, M. P. (2014). A Bayesian, spatially-varying calibration model for the TEX86 proxy. *Geochimica et Cosmochimica Acta*, *127*, 83–106. https://doi.org/10.1016/j.gca.2013.11.026

Tierney, J. E., & Tingley, M. P. (2015). A TEX86 surface sediment database and extended Bayesian calibration. *Scientific Data*, *2*(1), 150029. https://doi.org/10.1038/sdata.2015.29

Tierney, J. E., Zhu, J., Li, M., Ridgwell, A., Hakim, G. J., Poulsen, C. J., Whiteford, R. D. M., Rae, J. W. B., & Kump, L. R. (2022). Spatial patterns of climate change across the Paleocene–Eocene Thermal Maximum. *Proceedings of the National Academy of Sciences*, *119*(42). https://doi.org/10.1073/pnas.2205326119

Tjallingii, R., Röhl, U., Kölling, M., & Bickert, T. (2007). Influence of the water content on X-ray fluorescence core-scanning measurements in soft marine sediments. *Geochemistry, Geophysics, Geosystems*, *8*(2), n/a-n/a. https://doi.org/10.1029/2006GC001393

Toggweiler, J. R., Russell, J. L., & Carson, S. R. (2006). Midlatitude westerlies, atmospheric CO_2, and climate change during the ice ages. *Paleoceanography*, *21*(2), n/a-n/a. https://doi.org/10.1029/2005PA001154

Tripati, A., & Darby, D. (2018). Evidence for ephemeral middle Eocene to early Oligocene Greenland glacial ice and pan-Arctic sea ice. *Nature Communications*, *9*(1), 1038. https://doi.org/10.1038/s41467-018-03180-5

Tripati, A. K., Eagle, R. A., Morton, A., Dowdeswell, J. A., Atkinson, K. L., Bahé, Y., Dawber, C. F., Khadun, E., Shaw, R. M. H., Shorttle, O., & Thanabalasundaram, L. (2008). Evidence for glaciation in the Northern Hemisphere back to 44 Ma from ice-rafted debris in the Greenland Sea. *Earth and Planetary Science Letters*, *265*(1–2), 112–122. https://doi.org/10.1016/j.epsl.2007.09.045

Tyrrell, T., & Zeebe, R. E. (2004). History of carbonate ion concentration over the last 100 million years. *Geochimica et Cosmochimica Acta*, *68*(17), 3521–3530. https://doi.org/10.1016/j.gca.2004.02.018

Vahlenkamp, M., de Vleeschouwer, D., Batenburg, S. J., Edgar, K. M., Hanson, E., Martinez, M., Pälike, H., MacLeod, K. G., Li, Y.-X., Richter, C., Bogus, K., Hobbs, R. W., & Huber, B. T. (2020). A lower to middle Eocene astrochronology for the Mentelle Basin (Australia) and its implications for the geologic time scale. *Earth and Planetary Science Letters*, *529*, 115865. https://doi.org/10.1016/j.epsl.2019.115865

van Andel, T. H., Heath, G. R., & Moore, T. C. (1975). *Cenozoic History and Paleoceanography of the Central Equatorial Pacific Ocean* (pp. 1–223). https://doi.org/10.1130/MEM143-p1

van der Boon, A., Kuiper, K. F., van der Ploeg, R., Cramwinckel, M. J., Honarmand, M., Sluijs, A., & Krijgsman, W. (2021). Exploring a link between the Middle Eocene Climatic Optimum and Neotethys continental arc flare-up. *Climate of the Past*, *17*(1), 229–239. https://doi.org/10.5194/cp-17-229-2021

van der Ploeg, R., Selby, D., Cramwinckel, M. J., Li, Y., Bohaty, S. M., Middelburg, J. J., & Sluijs, A. (2018). Middle Eocene greenhouse warming facilitated by diminished weathering feedback. *Nature Communications*, *9*(1), 2877. https://doi.org/10.1038/s41467-018-05104-9

Wade, B. S., Al-Sabouni, N., Hemleben, C., & Kroon, D. (2008). Symbiont bleaching in fossil planktonic foraminifera. *Evolutionary Ecology*, *22*(2), 253–265. https://doi.org/10.1007/s10682-007-9176-6

Walker, J. C. G., Hays, P. B., & Kasting, J. F. (1981). A negative feedback mechanism for the long-term stabilization of Earth's surface temperature. *Journal of Geophysical Research*, *86*(C10), 9776. https://doi.org/10.1029/JC086iC10p09776

Weijers, J. W. H., Schouten, S., Hopmans, E. C., Geenevasen, J. A. J., David, O. R. P., Coleman, J. M., Pancost, R. D., & Sinninghe Damste, J. S. (2006). Membrane lipids of mesophilic anaerobic bacteria thriving in peats have typical archaeal traits. *Environmental Microbiology*, *8*(4), 648–657. https://doi.org/10.1111/j.1462-2920.2005.00941.x

Weltje, G. J., & Tjallingii, R. (2008). Calibration of XRF core scanners for quantitative geochemical logging of sediment cores: Theory and application. *Earth and Planetary Science Letters*, *274*(3–4), 423–438. https://doi.org/10.1016/j.epsl.2008.07.054

West, A., Galy, A., & Bickle, M. (2005). Tectonic and climatic controls on silicate weathering. *Earth and Planetary Science Letters*, *235*(1–2), 211–228. https://doi.org/10.1016/j.epsl.2005.03.020

Westerhold, T., Marwan, N., Drury, A. J., Liebrand, D., Agnini, C., Anagnostou, E., Barnet, J. S. K., Bohaty, S. M., de Vleeschouwer, D., Florindo, F., Frederichs, T., Hodell, D. A., Holbourn, A. E., Kroon, D., Lauretano, V., Littler, K., Lourens, L. J., Lyle, M., Pälike, H., … Zachos, J. C. (2020). An astronomically dated record of Earth's climate and its predictability over the last 66 million years. *Science*, *369*(6509), 1383–1387. https://doi.org/10.1126/science.aba6853

Westerhold, T., & Röhl, U. (2009). High resolution cyclostratigraphy of the early Eocene – new insights into the origin of the Cenozoic cooling trend. *Climate of the Past*, *5*(3), 309–327. https://doi.org/10.5194/cp-5-309-2009

Westerhold, T., & Röhl, U. (2013). Orbital pacing of Eocene climate during the Middle Eocene Climate Optimum and the chron C19r event: Missing link found in the tropical western Atlantic. *Geochemistry, Geophysics, Geosystems*, *14*(11), 4811–4825. https://doi.org/10.1002/ggge.20293

Westerhold, T., Röhl, U., Donner, B., McCarren, H. K., & Zachos, J. C. (2011). A complete high-resolution Paleocene benthic stable isotope record for the central Pacific (ODP Site 1209). *Paleoceanography*, *26*(2), n/a-n/a. https://doi.org/10.1029/2010PA002092

Westerhold, T., Röhl, U., Donner, B., & Zachos, J. C. (2018). Global Extent of Early Eocene Hyperthermal Events: A New Pacific Benthic Foraminiferal Isotope Record From Shatsky Rise (ODP Site 1209). *Paleoceanography and Paleoclimatology*, *33*(6), 626–642. https://doi.org/10.1029/2017PA003306

Westerhold, T., Röhl, U., Frederichs, T., Agnini, C., Raffi, I., Zachos, J. C., & Wilkens, R. H. (2017). Astronomical calibration of the Ypresian timescale: implications for seafloor spreading rates and the chaotic behavior of the solar system? *Climate of the Past*, *13*(9), 1129–1152. https://doi.org/10.5194/cp-13-1129-2017

Wilkinson, C. M., Ganerød, M., Hendriks, B. W. H., & Eide, E. A. (2017). Compilation and appraisal of geochronological data from the North Atlantic Igneous Province (NAIP). *Geological Society, London, Special Publications*, *447*(1), 69–103. https://doi.org/10.1144/SP447.10

Witkowski, J., Penman, D. E., Bryłka, K., Wade, B. S., Matting, S., Harwood, D. M., & Bohaty, S. M. (2020). Early Paleogene biosiliceous sedimentation in the Atlantic Ocean: Testing the inorganic origin hypothesis for Paleocene and Eocene chert and porcellanite. *Palaeogeography, Palaeoclimatology, Palaeoecology*, *556*, 109896. https://doi.org/10.1016/j.palaeo.2020.109896

Wright, N. M., Scher, H. D., Seton, M., Huck, C. E., & Duggan, B. D. (2018). No Change in Southern Ocean Circulation in the Indian Ocean From the Eocene Through Late Oligocene. *Paleoceanography and Paleoclimatology*, *33*(2), 152–167. https://doi.org/10.1002/2017PA003238

Xu, Y., Cao, Y., & Liu, C. (2021). Mid-Eocene sea surface cooling in the easternmost proto-Paratethys sea: constraints from quantitative temperatures in halite fluid inclusions. *International Journal of Earth Sciences*, *110*(5), 1713–1727. https://doi.org/10.1007/s00531-021-02037-5

Zachos, J. C., Breza, J. R., & Wise, S. W. (1992). Early Oligocene ice-sheet expansion on Antarctica: Stable isotope and sedimentological evidence from Kerguelen Plateau, southern Indian Ocean. *Geology*, *20*(6), 569. https://doi.org/10.1130/0091-7613(1992)020<0569:EOISEO>2.3.CO;2

Zachos, J. C., Dickens, G. R., & Zeebe, R. E. (2008). An early Cenozoic perspective on greenhouse warming and carbon-cycle dynamics. *Nature*, *451*(7176), 279–283. https://doi.org/10.1038/nature06588

Zachos, J. C., McCarren, H., Murphy, B., Röhl, U., & Westerhold, T. (2010). Tempo and scale of late Paleocene and early Eocene carbon isotope cycles: Implications for the origin of hyperthermals. *Earth and Planetary Science Letters*, *299*(1–2), 242–249. https://doi.org/10.1016/j.epsl.2010.09.004

Zachos, J. C., Röhl, U., Schellenberg, S. A., Sluijs, A., Hodell, D. A., Kelly, D. C., Thomas, E., Nicolo, M., Raffi, I., Lourens, L. J., McCarren, H., & Kroon, D. (2005). Rapid Acidification of the Ocean During the Paleocene-Eocene Thermal Maximum. *Science*, *308*(5728), 1611–1615. https://doi.org/10.1126/science.1109004

Zachos, J. C., Schouten, S., Bohaty, S., Quattlebaum, T., Sluijs, A., Brinkhuis, H., Gibbs, S. J., & Bralower, T. J. (2006). Extreme warming of mid-latitude coastal ocean during the Paleocene-Eocene Thermal Maximum: Inferences from TEX86 and isotope data. *Geology*, *34*(9), 737. https://doi.org/10.1130/G22522.1

Zachos, J. C., Stott, L. D., & Lohmann, K. C. (1994). Evolution of Early Cenozoic marine temperatures. *Paleoceanography*, *9*(2), 353–387. https://doi.org/10.1029/93PA03266

Zachos, J., Pagani, M., Sloan, L., Thomas, E., & Billups, K. (2001). Trends, Rhythms, and Aberrations in Global Climate 65 Ma to Present. *Science*, *292*(5517), 686–693. https://doi.org/10.1126/science.1059412

Zeebe, R. E., & Tyrrell, T. (2019). History of carbonate ion concentration over the last 100 million years II: Revised calculations and new data. *Geochimica et Cosmochimica Acta*, *257*, 373–392. https://doi.org/10.1016/j.gca.2019.02.041

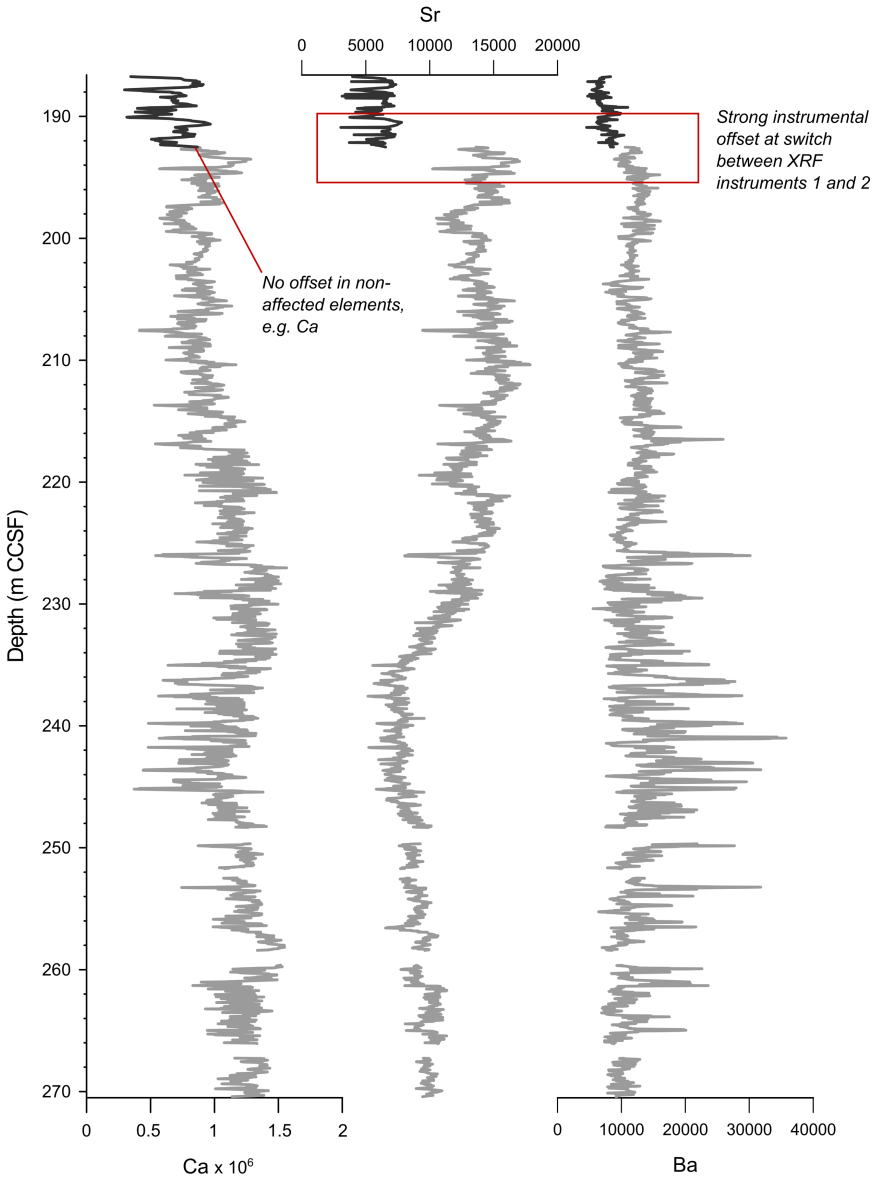
Zhang, Y. G., Pagani, M., & Wang, Z. (2016). Ring Index: A new strategy to evaluate the integrity of TEX_{86} paleothermometry. *Paleoceanography*, *31*(2), 220–232. https://doi.org/10.1002/2015PA002848

Zhang, Y. G., Zhang, C. L., Liu, X.-L., Li, L., Hinrichs, K.-U., & Noakes, J. E. (2011). Methane Index: A tetraether archaeal lipid biomarker indicator for detecting the instability of marine gas hydrates. *Earth and Planetary Science Letters*, *307*(3–4), 525–534. https://doi.org/10.1016/j.epsl.2011.05.031

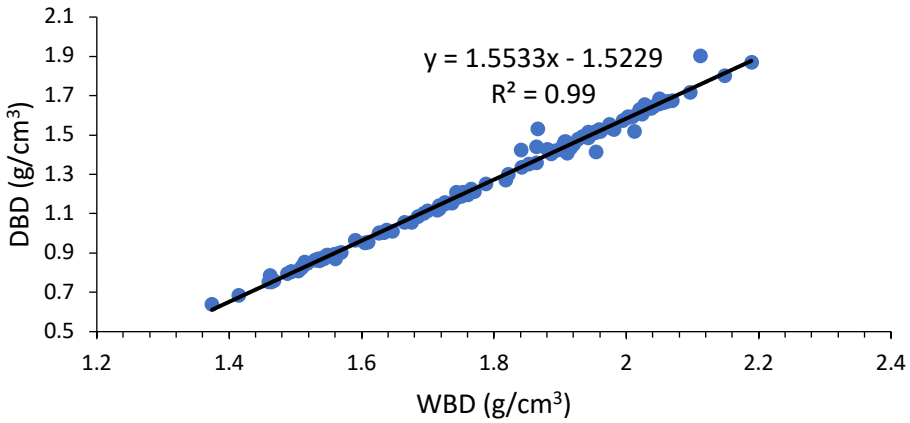
Zhou, Y., Retallack, G. J., & Huang, C. (2015). Early Eocene paleosol developed from basalt in southeastern Australia: implications for paleoclimate. *Arabian Journal of Geosciences*, *8*(3), 1281–1290. https://doi.org/10.1007/s12517-014-1328-8

Appendices

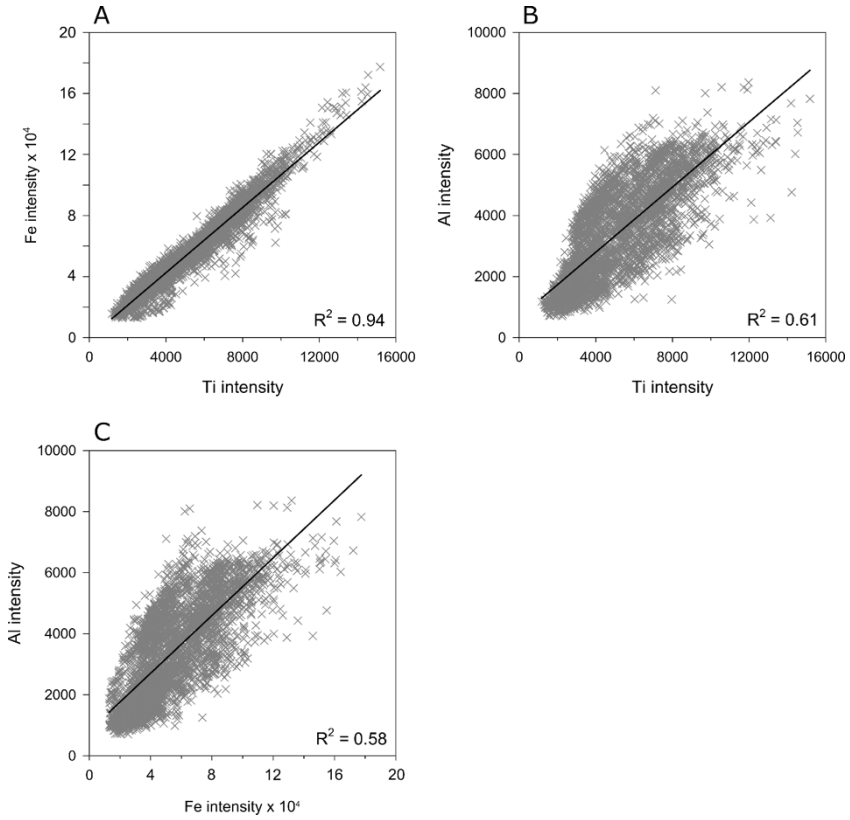
Appendix 1: Supplementary material for Chapter 2



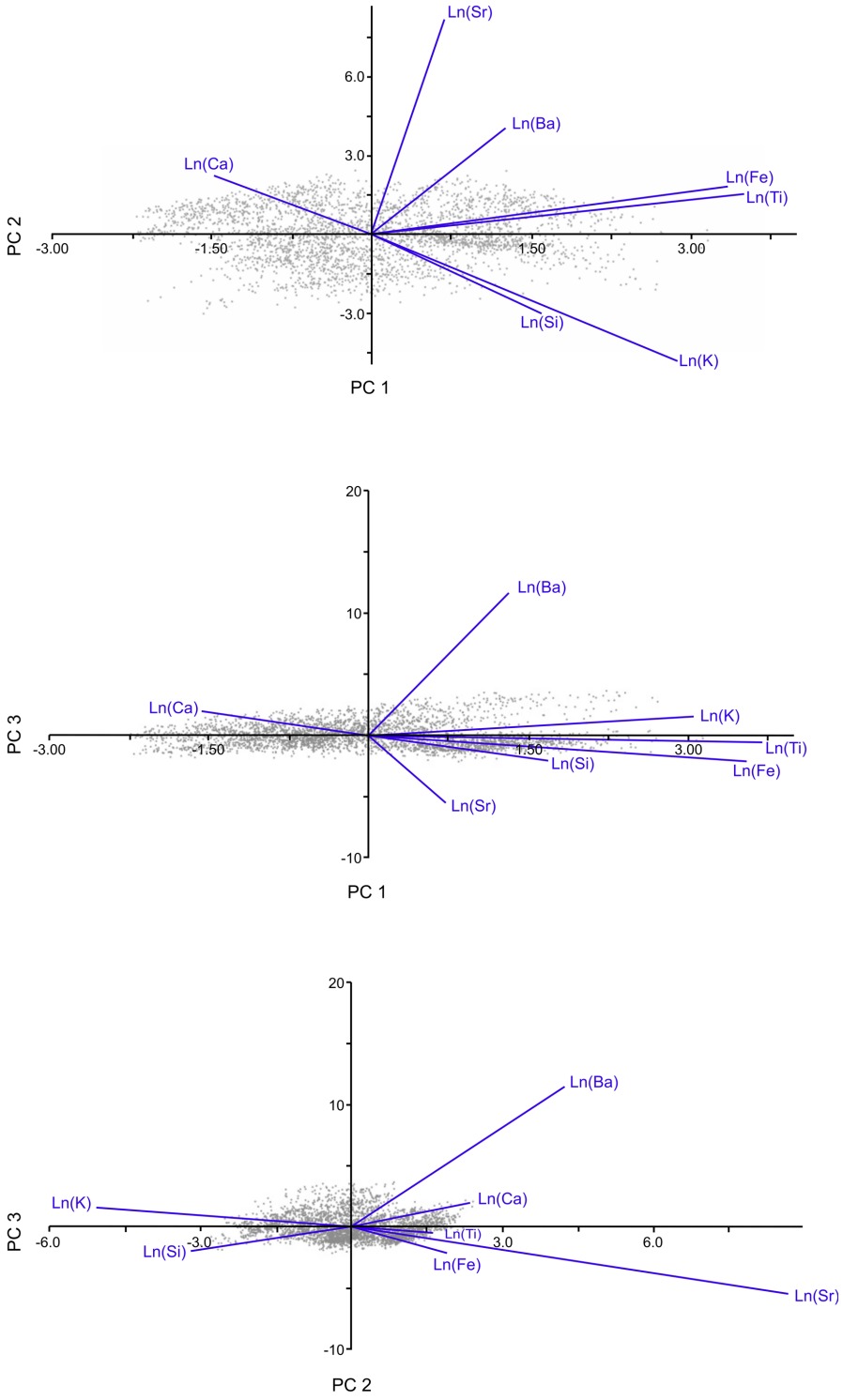
Supplementary Figure 2.1: XRF intensities across the study interval for selected elements showing switch points between XRF instruments '1' (pale grey) and '2' (dark grey). Strong instrumental offset is seen in Sr and Ba (as highlighted in figure), and weak/no offset in Ca, Fe, K, Ti, Si.



Supplementary Figure 2.2: Relationship between wet bulk density (WBD) and dry bulk density (DBD) from shipboard moisture and density dataset for Site U1514. This relationship is then applied to gamma ray attenuation (GRA) density measurements to obtain a high-resolution dry bulk density dataset.



Supplementary Figure 2.3: Relationships between XRF intensities for Fe and Ti (A), Al and Ti (B) and Al and Fe (C).



Supplementary Figure 2.4: Biplots between PC1 and PC2 (top), PC1 and PC3 (middle) and PC2 and PC3 (bottom). Eigenvectors for elements are indicated with the blue lines.

Supplementary Table 2.1*: XRF data and concentrations of elements from 46 – 55 Ma.

Supplementary Table 2.2*: Mass accumulation rates for elements referenced in this study, from 46 – 55 Ma.

Supplementary Table 2.3*: PCA results including dataset analysed for principle components in PAST4 software, and the resulting principle components 1 to 3.

**Due to large file sizes, Supplementary Tables 2.1 to 2.3 have been deposited online at the University of Birmingham eData Repository. These data tables have been titled, 'Kirby, Nicola (2022) Research data supporting PhD thesis,"Climatic, oceanographic and environmental change in the early to middle Eocene" by Nicola Kirby'. A DOI and link to this dataset will be issued pending approval, which will be available to examiners on request and will be inserted into this thesis.*

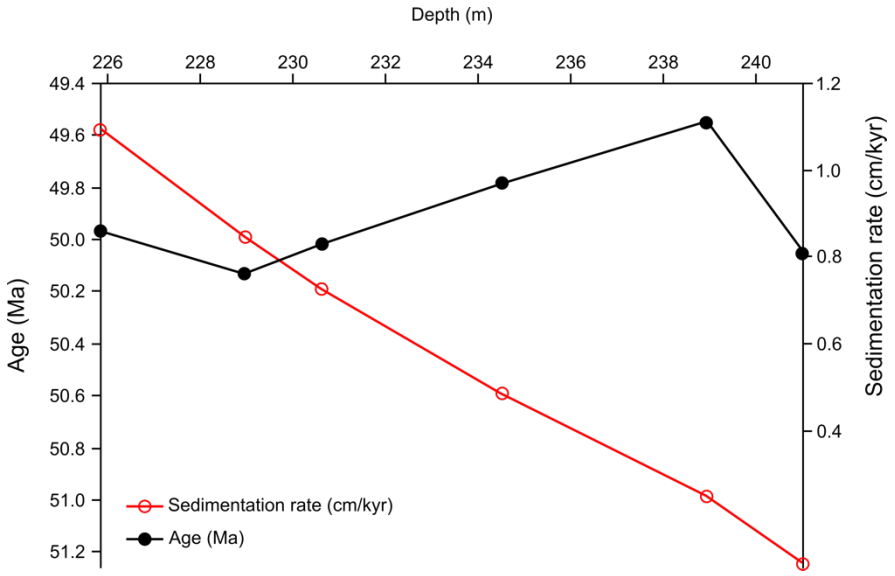
Supplementary Table 2.4: Discrete concentration measurements for elements referenced in this study, used to calibrate XRF data to concentration.

Site	Hole	Core	Type	Sec	Top	Bot	CSF-A (m)	SiO2 (%)	TiO2 (%)	Al2O3 (%)	Fe2O3 (%)	CaO (%)	K2O (%)	Ba (ppm)	Sr (ppm)
U1514	A	7	H	4	141	151	61.51	17.61	0.063	1	0.64	42.88	0.22	497	1179
U1514	A	8	H	4	141	151	71.02	39.36	0.33	4.92	2.25	25.16	0.63	710	
U1514	A	9	H	4	141	151	80.52	31.36	0.257	4.39	2.12	30.66	0.66	793	1010
U1514	A	10	H	4	140	150	90.02	36.05	0.262	4.45	2.62	27.23	0.93	787	922
U1514	A	11	H	4	142	152	99.54	56.09	0.477	8.09	3.88	11.02	2.54	1243	542
U1514	A	12	H	4	141	151	109.05	38.31	0.317	5.18	2.85	25.3	1.21	724	892
U1514	A	13	H	4	48	50	117.62	47.87	0.287	4.4	2.53	20.03	1.02	768	725
U1514	A	13	H	4	141	151	118.54	48.63	0.311	4.74	2.61	19.47	1.02	913	735
U1514	A	13	H	5	97	99	119.62	43.06	0.279	4.23	2.3	23.48	1.02	666	837
U1514	A	13	H	6	118	120	121.34	50.33	0.331	5.22	2.91	17.24	1.01	878	659
U1514	A	14	H	1	75	77	122.86	38.48	0.275	4.35	2.51	25.47	0.79	718	947
U1514	A	14	H	2	28	30	123.89	47.46	0.324	5.21	3.04	18.56	0.98	931	691
U1514	A	14	H	2	130	132	124.89	40.08	0.276	4.82	2.55	24.01	0.85	812	910
U1514	A	14	H	4	28	30	126.9	49.91	0.339	5.37	2.96	11.81	0.95	938	459
U1514	A	14	H	4	139	149	128	57.16	0.407	6.08	3.47	11.96	1.14	1112	483
U1514	A	14	H	6	28	30	129.89	47.65	0.288	4.48	2.31	19.69	0.8	1119	696
U1514	A	15	H	1	77	79	132.38	48.84	0.344	5.81	3.28	17.18	0.97	1012	661
U1514	A	15	H	2	148	150	134.59	28.69	0.181	2.89	1.56	33.88	0.48	858	1214
U1514	A	15	H	4	48	50	136.61	40.5	0.301	5.71	3.21	22.57	0.92	1491	915
U1514	A	15	H	4	142	152	137.54	41.25	0.245	4.09	2.2	24.43	0.69	802	936
U1514	A	15	H	6	47	49	139.63	35.35	0.209	3.55	1.93	24.02	0.58	721	869
U1514	A	16	H	1	48	50	141.59	34.69	0.195	3.56	1.93	29.29	0.6	849	1085
U1514	A	16	H	2	23	25	142.84	29.11	0.181	3.21	1.85	30.31	0.55	820	1087
U1514	A	16	H	2	148	150	144.09	52.56	0.286	4.82	2.82	13.04	0.86	830	531
U1514	A	16	H	4	140	150	147.01	43.8	0.244	4.12	2.36	23.04	0.7	932	891
U1514	A	16	H	6	118	120	149.82	24.64	0.186	3.43	1.64	35.94	0.5	924	1354
U1514	A	17	H	1	148	150	152.09	47.31	0.298	4.98	2.42	19.74	0.75	910	732
U1514	A	17	H	4	23	25	155.36	42.18	0.287	4.73	2.56	23.68	0.69	936	825
U1514	A	17	H	4	141	151	156.53	35.63	0.257	4.44	2.33	27.99	0.62	948	1036
U1514	A	17	H	6	43	45	158.57	53.32	0.284	4.77	2.39	16.4	0.74	1301	618
U1514	A	18	H	1	23	25	160.34	46.01	0.311	5.55	2.74	20.34	0.85	1126	759
U1514	A	18	H	2	78	80	162.39	36.19	0.248	4.72	2.41	27.35	0.69	701	970
U1514	A	18	H	3	124	126	164.34	31.53	0.205	3.54	1.46	32.19	0.61	882	1133
U1514	A	18	H	4	140	150	166	42.8	0.28	4.5	2.33	23.96	0.85	691	860
U1514	A	18	H	6	97	99	168.58	24.24	0.137	2.59	1.48	35.83	0.47	518	1209
U1514	A	19	H	3	50	52	172.15	30.95	0.25	4.52	2.55	30.22	0.68	817	1073
U1514	A	19	H	4	143	145	174.58	50.69	0.39	6.53	3.8	14.93	0.91	925	583
U1514	A	19	H	5	140	150	176.05	51.08	0.404	6.51	3.68	16.37	0.92	976	662
U1514	A	20	F	1	98	100	179.09	28.82	0.2	3.45	1.87	30.36	0.55	649	1078
U1514	A	20	F	3	70	72	181.86	47.98	0.379	6.71	3.81	18.38	1.03	933	729
U1514	A	20	F	CC	9	11	183.03	35.69	0.242	4.18	2.31	25.88	0.67	783	939
U1514	A	21	F	1	140	150	184.3	36.96	0.27	4.72	2.61	28.02	0.72	738	1059
U1514	A	21	F	3	96	98	186.89	40.2	0.256	4.25	2.57	21.96	0.69	696	797
U1514	A	21	F	CC	12	14	187.81	36.6		4.19		24.74	0.61	697	929
U1514	A	22	F	1	110	112	188.81	36.62	0.3	5.11	2.81	23.29	0.7	711	879
U1514	A	22	F	3	70	72	191.25	38.93	0.372	6.26	3.15	24.51	0.92	1043	930
U1514	A	23	F	1	140	150	193.9	25.86	0.197	3.44	1.57	36.28	0.54	749	1258
U1514	A	23	F	3	40	42	195.91	33.53	0.252	4.12	2.57	26.62	0.62	831	930
U1514	A	24	F	1	78	80	198.09	43.31	0.362	5.81	3.28	21.54	0.88	1094	802

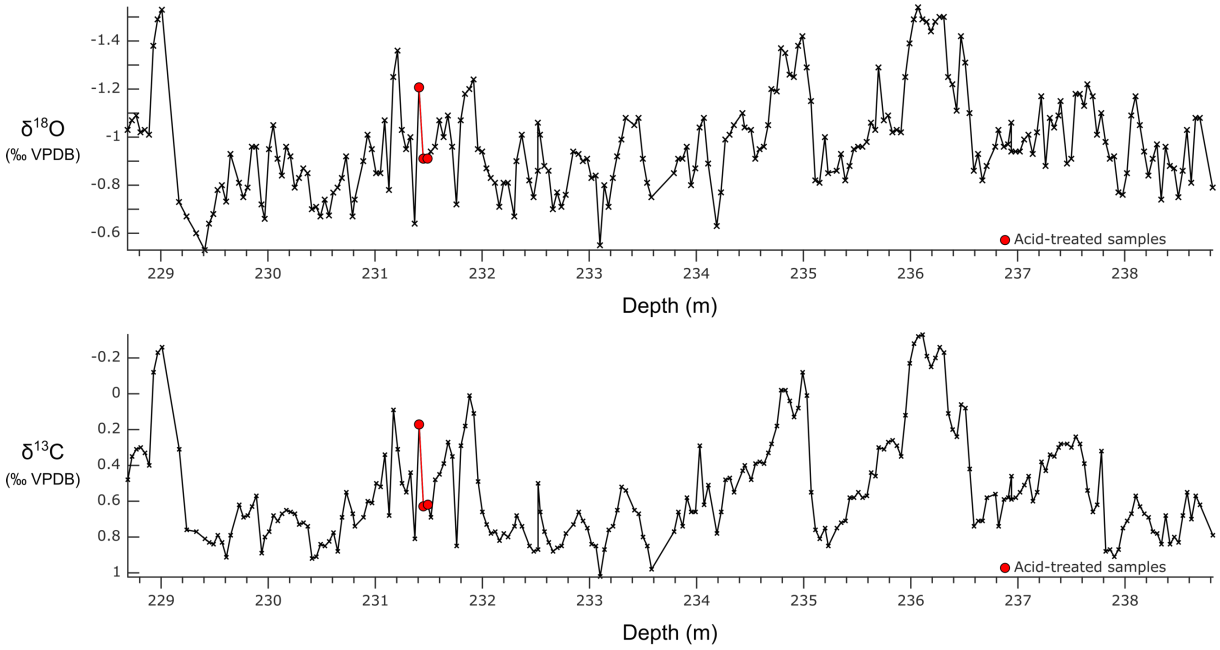
Site	Hole	Core	Type	Sec	Top	Bot	CSF-A (m)	SiO2 (%)	TiO2 (%)	Al2O3 (%)	Fe2O3 (%)	CaO (%)	K2O (%)	Ba (ppm)	Sr (ppm)
U1514	A	24	F	3	72	74	201.01	33	0.244	4.15	2.17	30.32	0.7	950	1069
U1514	A	25	X	1	86	88	202.97	31.34	0.216	3.73	1.92	29.04	0.63	781	1041
U1514	A	25	X	2	140	150	205	28.73	0.247	4.12	2.05	33.75	0.78	790	1185
U1514	A	25	X	4	40	42	207.01	30.36	0.269	4.6	2.18	31.01	0.8	858	1109
U1514	A	26	X	3	99	101	212.2	25.41	0.242	4.27	2.2	32.79	0.62	946	1161
U1514	A	26	X	4	140	150	214.1	35.78	0.367	6.34	3.49	26.78	0.81	1112	1025
U1514	A	26	X	6	36	38	216.07	26.93	0.231	4.13	2.24	34.34	0.46	1016	1060
U1514	A	26	X	CC	49	51	217.29		0.263	4.76	2.33	30.41	0.51	839	1038
U1514	A	27	X	2	21	23	219.52	13.65	0.085	1.55	0.8	45.15	0.17	859	968
U1514	A	27	X	4	141	151	223.72	23.02	0.183	3.44	1.63	38.02	0.38	789	1150
U1514	A	27	X	6	103	105	226.37	18.93	0.14	2.55	1.27	39.26	0.3	652	1106
U1514	A	28	X	3	88	90	231.3	23.4	0.18	3.56	1.69	36	0.48	1084	694
U1514	A	28	X	4	141	151	233.33	15.85	0.095	1.94	1.06	43.71	0.24	774	791
U1514	A	29	X	1	23	25	237.24	30.19	0.204	4.13	2.07	30.83	0.68	1032	432
U1514	A	29	X	1	137	147	238.37	22.9	0.121	2.5	1.29	38.79	0.43	1255	595
U1514	A	29	X	3	27	29	240.11	20.89	0.13	2.9	1.37	37.82	0.53	750	566
U1514	A	30	X	1	115	125	247.75	23.44	0.187	3.73	1.86	37.52	0.62	854	710
U1514	A	31	X	1	54	56	250.18	22.73	0.175	3.38	1.68	36.02	0.69	931	648
U1514	A	31	X	2	65	67	251.28	24.25		2.64	1.22	36.66			644
U1514	A	31	X	2	120	121	251.825	32.04	0.103	1.93	0.77	34.01	0.53	586	552
U1514	A	31	X	2	140	142	252.06	28.07	0.124	2.38	0.94	35.56	0.62	665	570
U1514	C	3	R	4	145	147	209.56	22.3	0.196	3.39	1.74	37.76	0.56	748	1357
U1514	C	3	R	5	144	146	211.05	24.95	0.243	4.24	2	32.32	0.6	958	1144
U1514	C	4	R	4	70	72	218.42	12.89	0.088	1.57	0.78	45	0.21	941	962
U1514	C	7	R	4	100	102	243.02	54.02	0.301	6.24	2.04	14.78	1.43	2287	341
U1514	C	7	R	6	26	28	244.61	24.3	0.145	3.03	1.41	37.52	0.6		657
U1514	C	8	R	3	3	5	250.52	29.76	0.214	3.91	1.21	31.91	1.08	814	576
U1514	C	8	R	5	98	100	253.88	31.05	0.25	4.93	2.11	29.83	1.15	812	614
U1514	C	8	R	6	57	67	254.96	23.96	0.199	4	1.93	36.81	0.75	756	745
U1514	C	9	R	1	126	136	258.86	18.17	0.153	3.26	1.41	41.32	0.52	812	745
U1514	C	9	R	3	95	97	261.42	17.19	0.107	2.23	1.09	41.32	0.37	608	776
U1514	C	9	R	5	48	50	263.96	21.12	0.141	2.93	1.48	38.19	0.5	631	777
U1514	C	10	R	1	100	102	268.21	21.08	0.185	3.7	1.81	38.45	0.5	628	759
U1514	C	10	R	2	140	150	269.94	18.27	0.146	2.82	1.28	41.82	0.41	741	800
U1514	C	10	R	5	101	103	273.18	22.44	0.166	3.21	1.5	37.92	0.46	717	736
U1514	C	10	R	8	28	30	276.04	26.47	0.177	3.42	1.67	34.65	0.52	691	763
U1514	C	11	R	2	104	105	279.025	22.86	0.154	2.99	1.58	37.61	0.44	523	806
U1514	C	11	R	2	125	126	279.235	25.27	0.238	4.59	2.41	34.72	0.64	719	781
U1514	C	11	R	3	1	2	279.495	15.93	0.17	3.6	1.7	41.3	0.5	749	842
U1514	C	11	R	3	29	30	279.775	11.24	0.086	1.87	0.93	46.5	0.29	664	838
U1514	C	11	R	3	55	56	280.035	15	0.184	3.94	1.94	41.17	0.56	566	742
U1514	C	11	R	3	61	62	280.095	17.62	0.221	4.71	2.3	39.9	0.69	552	712
U1514	C	11	R	3	81	82	280.295	23.77	0.298	5.93	2.44	34.27	0.82	1461	686
U1514	C	11	R	3	86	87	280.345	26.28	0.264	5.45	2.51	33.61	0.58	2184	614
U1514	C	11	R	3	89	90	280.375	32.48	0.315	6.61	3.32	27.44	0.72	1935	522
U1514	C	11	R	3	93	94	280.415	41.11	0.401	7.98	4.04	20.28	0.89	1460	398
U1514	C	11	R	3	101	102	280.495	33.99	0.188	3.85	1.82	29.47	0.45	868	584
U1514	C	11	R	3	104	105	280.525	32.74	0.14	2.77	1.33	33.5	0.34	1020	657
U1514	C	11	R	3	117	118	280.655	27.4	0.205	4	1.95	34.14	0.49	959	714
U1514	C	11	R	3	128	129	280.765	42.83	0.117	2.34	0.91	27.42	0.32	770	555
U1514	C	11	R	3	144	145	280.925	25.66	0.209	3.95	1.91	35.38	0.46	1128	727
U1514	C	11	R	4	52	53	281.505	20.56	0.141	2.71	1.31	39.34	0.33	1059	805
U1514	C	11	R	5	38	41	282.605	23.7	0.1	1.95	0.84	39.06	0.24	497	886
U1514	C	12	R	1	125	127	287.66	18.65	0.111	2.19	0.92	41.47	0.23	434	858

Site	Hole	Core	Type	Sec	Top	Bot	CSF-A (m)	SiO2 (%)	TiO2 (%)	Al2O3 (%)	Fe2O3 (%)	CaO (%)	K2O (%)	Ba (ppm)	Sr (ppm)
U1514	C	12	R	4	55	57	290.21	25.61	0.112	2.19	0.92	37.39	0.28	482	803
U1514	C	12	R	5	80	90	291.3	23.58	0.106	1.99	0.76	39.75	0.24	592	836
U1514	C	12	R	7	74	76	293.64	26.19	0.178	3.42	1.42	35.32	0.42	757	736
U1514	C	13	R	2	127	129	298.6	17.38	0.126	2.44	1.08	41.94	0.34	484	922
U1514	C	13	R	4	132	142	301.53	17.8	0.203	3.51	1.44	41.26	0.36	345	966
U1514	C	13	R	7	36	38	304.22	16.16	0.097	1.91	0.73	43	0.21	496	973
U1514	C	14	R	1	112	114	306.73	30.74	0.079	1.57	0.58	35.81	0.18	526	821
U1514	C	14	R	3	28	30	308.84	14.5	0.099	1.92	0.74	44.94	0.22	584	1024
U1514	C	14	R	3	142	152	309.97	28.04	0.162	3.07	1.23	35.95	0.36	698	877
U1514	C	14	R	5	2	3	311.055	20.14	0.105	2.03	0.77	41.14	0.25	901	910
U1514	C	14	R	5	82	83	311.855	64.3		5.86	2.7	8.41	0.88	1557	318
U1514	C	14	R	6	49	51	313.03	34.18	0.139	2.49	1.08	31.19	0.34	544	761
U1514	C	14	R	7	44	46	314.09	33.05	0.21	3.97	1.78	30.76	0.53	980	774
U1514	C	15	R	1	17	19	315.38	25.4	0.23	3.71	1.64	34.79	0.5	610	908
U1514	C	15	R	1	117	119	316.38	24.7	0.171	2.8	1.31	36.81	0.42	576	863
U1514	C	15	R	2	83	85	317.54	24.64	0.192	3.06	1.42	36.64	0.45	844	839
U1514	C	15	R	3	68	70	318.89	28	0.147	2.51	1.13	35.73	0.38	549	800
U1514	C	15	R	4	113	115	320.85	29.43	0.183	3.23	1.53	33.71	0.46	1097	812
U1514	C	15	R	5	140	150	322.64	28.86	0.221	3.4	1.63	34.8	0.48	725	848
U1514	C	15	R	6	67	69	323.42	30.16	0.267	4.32	2.04	31.14	0.62	1000	771
U1514	C	16	R	1	109	111	325.9	39.94	0.287	4.58	2.54	25.24	0.7	1198	634
U1514	C	16	R	3	87	97	328.3	32.46	0.244	3.88	1.98	32	0.6	1055	760
U1514	C	17	R	1	104	106	335.45	26.2	0.207	3.39	1.68	35.09	0.48	918	884
U1514	C	17	R	2	142	152	337.14	28.45	0.22	3.73	1.77	34.7	0.51	752	844
U1514	C	17	R	4	40	42	338.85	27.74	0.219	3.72	1.7	33.82	0.51	797	752
U1514	C	18	R	1	62	64	344.63	30.38	0.26	4.39	2.13	32.25	0.62	1190	740
U1514	C	18	R	2	73	83	346.18	27.23	0.189	3.27	1.62	35.94	0.46	1027	719
U1514	C	18	R	5	25	27	349.25	24.51	0.167	2.94	1.4	37.47	0.42	620	780
U1514	C	19	R	1	148	150	355.09	29.87	0.228	3.89	1.58	32.32	0.53	665	759
U1514	C	19	R	5	81	91	359.32	22.98	0.172	2.98	1.36	38.85	0.39	432	737
U1514	C	19	R	7	147	149	362.18	21.88	0.173	3.04	1.52	38.27	0.41	418	653
U1514	C	20	R	2	58	68	365.29	21.09	0.202	3.42	1.5	39.63	0.43	396	684
U1514	C	21	R	3	53	55	375.87	19.09	0.176	3.17	1.6	40.73	0.44	589	701
U1514	C	22	R	2	128	138	385.09	32.61	0.277	4.65	2.01	31.44	0.59	634	520
U1514	C	23	R	4	143	153	397.3	29.17	0.396	6.76	3.48	30.44	1.16	1246	651

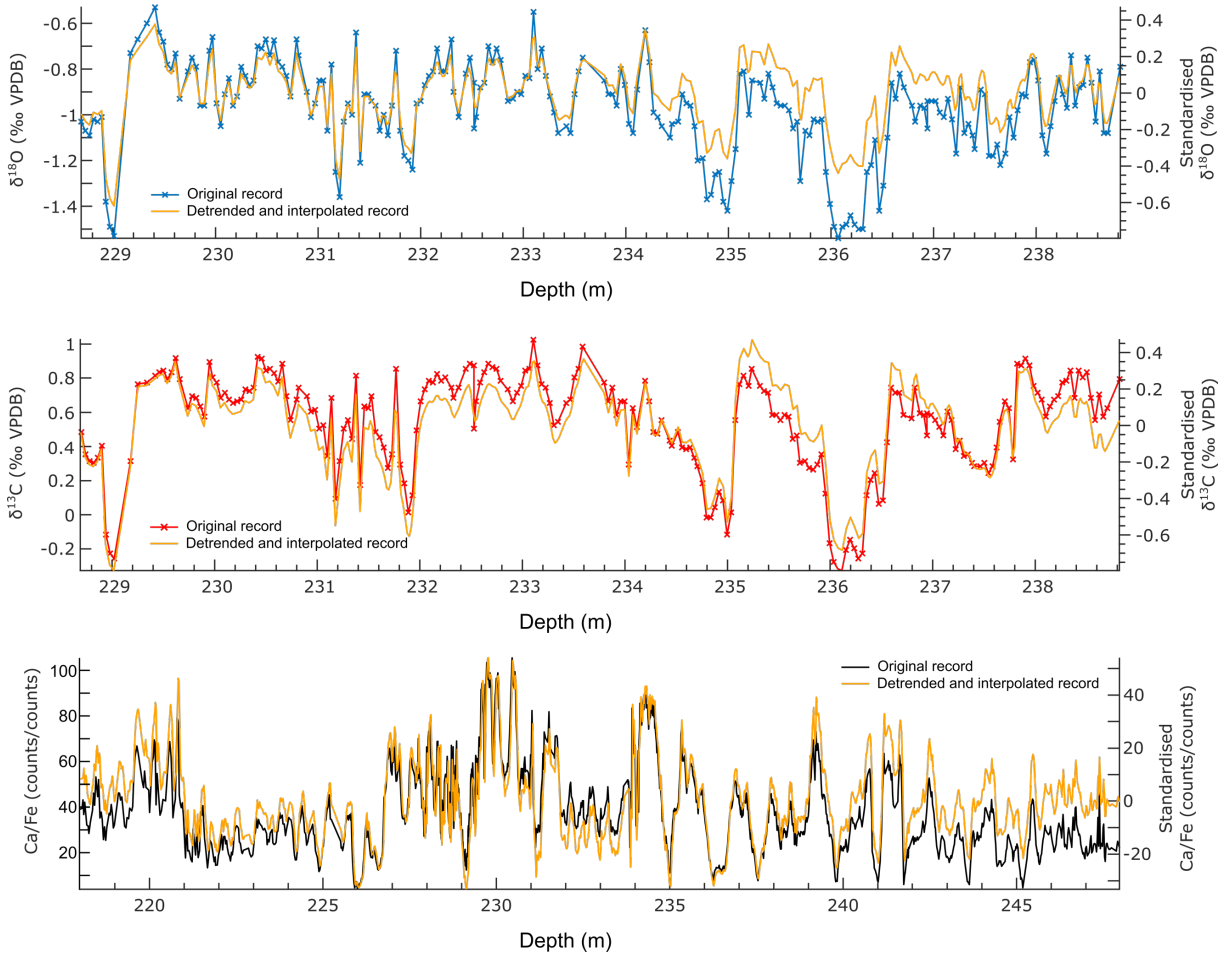
Appendix 2: Supplementary material for Chapter 3



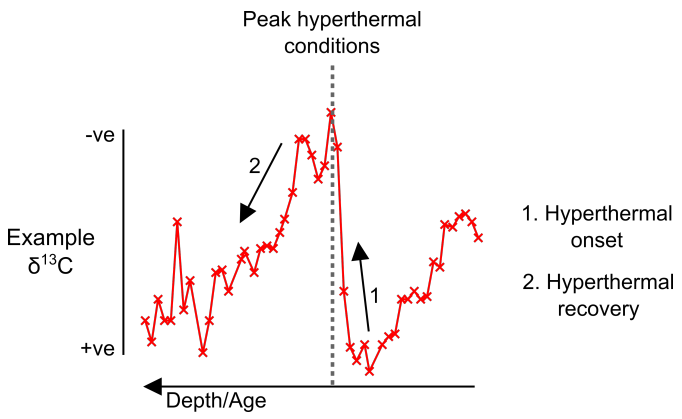
Supplementary Figure 3.1: Linear sedimentation rate (black line with filled circles) for Site U1514 between 226 – 241 m CCSF, and age-depth relationship (red line with unfilled circles). Linear sedimentation rates are based on age-depth tie points published in Vahlenkamp et al., 2020.



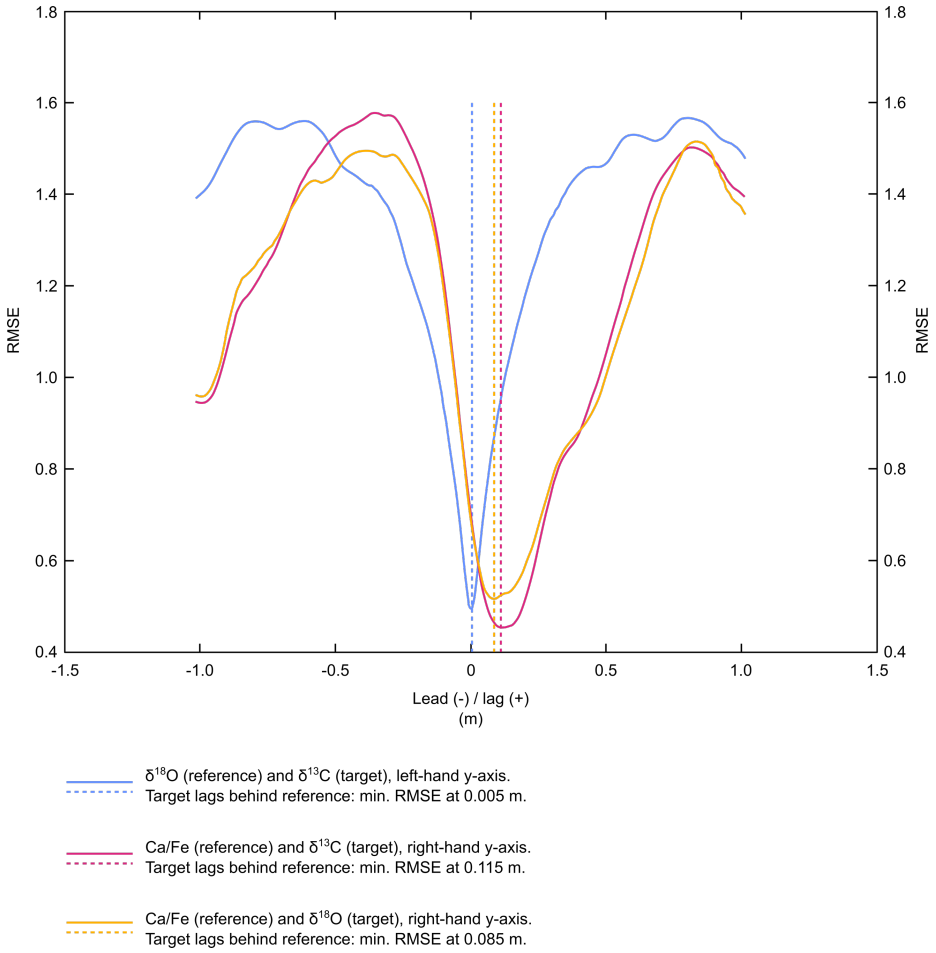
Supplementary Figure 3.2: Oxygen (top) and carbon (bottom) stable isotope results for Site U1514 with acid-treated samples highlighted in red.



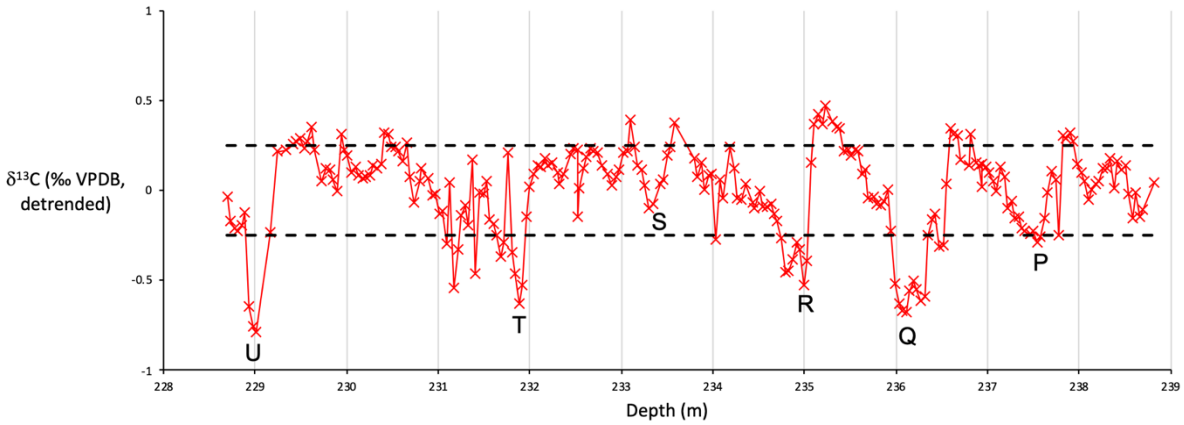
Supplementary Figure 3.3: Comparisons between original $\delta^{18}O$ (blue, top), $\delta^{13}C$ (red, middle) and Ca/Fe (black, bottom) datasets and their interpolated and detrended counterparts (all yellow).



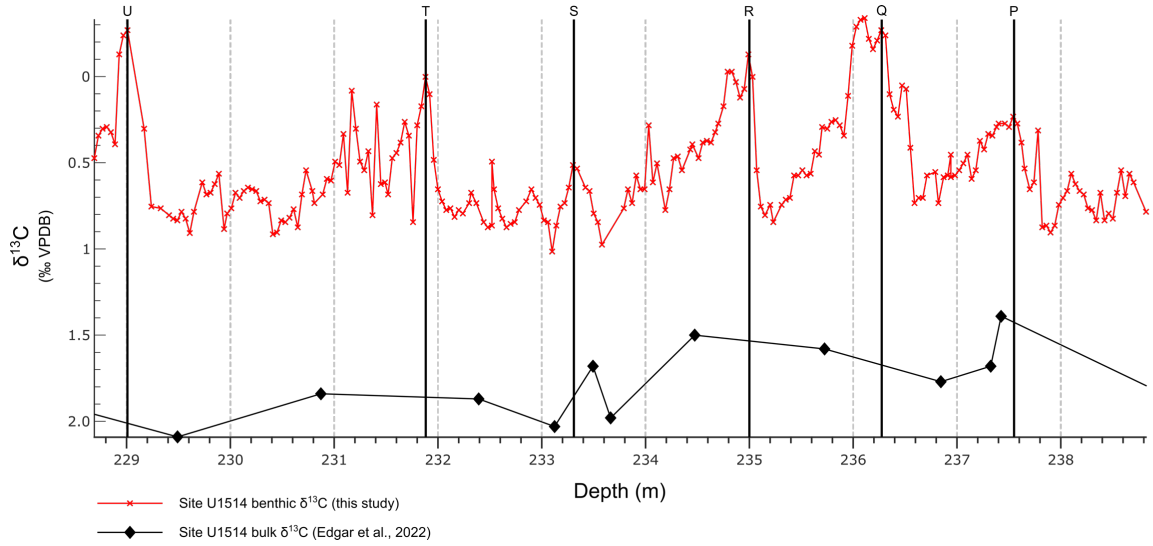
Supplementary Figure 3.4: Schematic of an example hyperthermal excursion in a $\delta^{13}C$ dataset, showing how hyperthermal excursions are identified and classified. Hyperthermal onset refers to the beginning of a strong decline in $\delta^{13}C$, peak hyperthermal indicates the initial low point in $\delta^{13}C$ and hyperthermal recovery begins at the onset of a strong, sustained rise in $\delta^{13}C$.



Supplementary Figure 3.5: Lead-lag analysis for $\delta^{18}O$ and $\delta^{13}C$ (blue), Ca/Fe and $\delta^{13}C$ (pink) and Ca/Fe and $\delta^{18}O$ (yellow). Curves show root mean squared error (RMSE) for curve fit between target and reference curves. Dotted lines show point of minimum RMSE, i.e. the best fit between target and reference curves, where negative values indicate that the target leads the reference and positive values indicate the target lags behind the reference.



Supplementary Figure 3.6: Detrended $\delta^{13}C$ record from Site U1514. Black dashed lines show one standard deviation above and below the mean of the detrended record. Hyperthermals P to U have been identified.



Supplementary Figure 3.7: Benthic $\delta^{13}C$ from Site U1514 (red line, crosses) compared to low-resolution bulk $\delta^{13}C$ (Black line with diamonds, Edgar et al., 2022).

Supplementary Table 3.1: Stable isotope results from IODP Site U1514, 50 – 51 Ma.

Site	Hole	Core	Type	Sect	Half	Top (cm)	Bottom (cm)	Depth CCSF (m)	Sample ID	No. tests	Approx. mass (mg)	$\delta^{13}C$ ‰ VPDB	$\delta^{18}O$ ‰ VPDB
U1514	C	5	R	4	W	16	18	228.69	NK 96	20	0.141	0.485	-1.028
U1514	C	5	R	4	W	20	22	228.73	NK 97	20	0.148	0.346	-1.068
U1514	C	5	R	4	W	24	26	228.77	NK 98	20	0.148	0.311	-1.088
U1514	C	5	R	4	W	28	30	228.81	NK 99	20	0.148	0.303	-1.017
U1514	C	5	R	4	W	32	34	228.85	NK 100	20	0.148	0.331	-1.028
U1514	C	5	R	4	W	36	38	228.89	NK 101	20	0.148	0.396	-1.014
U1514	C	5	R	4	W	40	42	228.93	NK 102	20	0.148	-0.124	-1.379
U1514	C	5	R	4	W	44	46	228.97	NK 103	20	0.148	-0.227	-1.488
U1514	C	5	R	4	W	48	50	229.01	NK 104	20	0.148	-0.262	-1.529
U1514	C	5	R	4	W	52	54	229.05	NK 105	3	0.052	0.853	-0.522
U1514	C	5	R	4	W	56	58	229.09	NK 106	7	0.052		
U1514	C	5	R	4	W	60	62	229.13	NK 107	4	0.042		
U1514	C	5	R	4	W	64	66	229.17	NK 108	4	0.0296	0.310	-0.730
U1514	C	5	R	4	W	68	70	229.21	NK 109	1	0.0074		
U1514	C	5	R	4	W	71	73	229.24	NK 110	9	0.0666	0.758	-0.674
U1514	C	5	R	4	W	80	82	229.33	NK 111	7	0.0518	0.771	-0.597
U1514	C	5	R	4	W	84	86	229.37	NK 112	2	0.0148	0.316	-1.844
U1514	C	5	R	4	W	88	90	229.41	NK 113	8	0.0592	0.814	-0.531
U1514	C	5	R	4	W	92	94	229.45	NK 114	5	0.037	0.834	-0.643
U1514	C	5	R	4	W	96	98	229.49	NK 115	15	0.111	0.842	-0.676
U1514	C	5	R	4	W	100	102	229.53	NK 116	11	0.0814	0.786	-0.781
U1514	C	5	R	4	W	104	106	229.57	NK 117	15	0.111	0.829	-0.799
U1514	C	5	R	4	W	108	110	229.61	NK 118	12	0.0888	0.913	-0.732
U1514	C	5	R	4	W	112	114	229.65	NK 119	10	0.074	0.786	-0.929
U1514	C	5	R	4	W	116	118	229.69	NK 120	20	0.148		
U1514	C	5	R	4	W	120	122	229.73	NK 121	20	0.148	0.616	-0.814
U1514	C	5	R	4	W	124	126	229.77	NK 122	20	0.148	0.692	-0.752
U1514	C	5	R	4	W	128	130	229.81	NK 123	20	0.148	0.680	-0.792
U1514	C	5	R	4	W	132	134	229.85	NK 124	20	0.148	0.634	-0.964
U1514	C	5	R	4	W	136	138	229.89	NK 125	21	0.1554	0.566	-0.961
U1514	C	5	R	4	W	141	143	229.94	NK 240	20	0.148	0.887	-0.721

Site	Hole	Core	Type	Sect	Half	Top (cm)	Bottom (cm)	Depth CCSF (m)	Sample ID	No. tests	Approx. mass (mg)	$\delta^{13}C$ ‰ VPDB	$\delta^{18}O$ ‰ VPDB
U1514	C	5	R	4	W	144	146	229.97	NK 126	20	0.148	0.796	-0.662
U1514	C	5	R	4	W	148	150	230.01	NK 127	20	0.148	0.768	-0.948
U1514	C	5	R	5	W	2	4	230.05	NK 128	20	0.148	0.683	-1.052
U1514	C	5	R	5	W	6	8	230.09	NK 129	20	0.148	0.715	-0.907
U1514	C	5	R	5	W	10	12	230.13	NK 130	21	0.1554	0.673	-0.845
U1514	C	5	R	5	W	14	16	230.17	NK 131	20	0.148	0.652	-0.963
U1514	C	5	R	5	W	18	20	230.21	NK 132	20	0.148	0.656	-0.917
U1514	C	5	R	5	W	22	24	230.25	NK 133	20	0.148	0.668	-0.788
U1514	C	5	R	5	W	26	28	230.29	NK 134	20	0.148	0.728	-0.828
U1514	C	5	R	5	W	30	32	230.33	NK 135	20	0.148	0.721	-0.873
U1514	C	5	R	5	W	34	36	230.37	NK 136	20	0.148	0.739	-0.845
U1514	C	5	R	5	W	38	40	230.41	NK 137	14	0.1036	0.919	-0.699
U1514	C	5	R	5	W	42	44	230.45	NK 138	20	0.148	0.906	-0.715
U1514	C	5	R	5	W	46	48	230.49	NK 139	14	0.1036	0.843	-0.671
U1514	C	5	R	5	W	50	52	230.53	NK 140	13	0.0962	0.845	-0.739
U1514	C	5	R	5	W	54	56	230.57	NK 141	13	0.0962	0.825	-0.674
U1514	C	5	R	5	W	58	60	230.61	NK 142	14	0.1036	0.775	-0.769
U1514	C	5	R	5	W	62	64	230.65	NK 143	9	0.0666	0.879	-0.793
U1514	C	5	R	5	W	66	68	230.69	NK 144	13	0.0962	0.693	-0.831
U1514	C	5	R	5	W	70	72	230.73	NK 145	10	0.074	0.552	-0.919
U1514	C	5	R	5	W	76	78	230.79	NK 146	7	0.0518	0.673	-0.667
U1514	C	5	R	5	W	78	80	230.81	NK 147	9	0.0666	0.742	-0.740
U1514	C	5	R	5	W	82	84	230.85	NK 241	20	0.148		
U1514	C	5	R	5	W	86	88	230.89	NK 148	20	0.148	0.691	-0.903
U1514	C	5	R	5	W	90	92	230.93	NK 149	20	0.148	0.602	-1.014
U1514	C	5	R	5	W	94	96	230.97	NK 150	20	0.148	0.607	-0.950
U1514	C	5	R	5	W	98	100	231.01	NK 151	20	0.148	0.498	-0.854
U1514	C	5	R	5	W	102	104	231.05	NK 152	8	0.0592	0.516	-0.848
U1514	C	5	R	5	W	106	108	231.09	NK 153	7	0.0518	0.336	-1.074
U1514	C	5	R	5	W	110	112	231.13	NK 154	9	0.0666	0.684	-0.776
U1514	C	5	R	5	W	114	116	231.17	NK 155	10	0.074	0.086	-1.248
U1514	C	5	R	5	W	118	120	231.21	NK 156	14	0.1036	0.306	-1.358
U1514	C	5	R	5	W	122	124	231.25	NK 157	20	0.148	0.495	-1.031

Site	Hole	Core	Type	Sect	Half	Top (cm)	Bottom (cm)	Depth CCSF (m)	Sample ID	No. tests	Approx. mass (mg)	$\delta^{13}C$ ‰ VPDB	$\delta^{18}O$ ‰ VPDB
U1514	C	5	R	5	W	126	128	231.29	NK 158	20	0.148	0.548	-0.947
U1514	C	5	R	5	W	130	132	231.33	NK 159	14	0.1036	0.442	-1.001
U1514	C	5	R	5	W	134	136	231.37	NK 160	14	0.1036	0.810	-0.644
U1514	C	5	R	5	W	138	140	231.41	NK 161	10	0.074	0.172	-1.208
U1514	C	5	R	5	W	142	144	231.45	NK 162	2	0.0148	0.625	-0.913
U1514	C	5	R	5	W	146	148	231.49	NK 163	6	0.0444	0.622	-0.909
U1514	C	5	R	5	W	149	151	231.52	NK 164	8	0.0592	0.688	-0.937
U1514	C	5	R	6	W	2	4	231.56	NK 165	15	0.111	0.483	-0.958
U1514	C	5	R	6	W	6	8	231.6	NK 242	20	0.148	0.452	-1.066
U1514	C	5	R	6	W	10	12	231.64	NK 166	7	0.0518	0.392	-1.002
U1514	C	5	R	6	W	14	16	231.68	NK 167	7	0.0518	0.275	-1.087
U1514	C	5	R	6	W	18	20	231.72	NK 168	12	0.0888	0.354	-0.956
U1514	C	5	R	6	W	22	24	231.76	NK 169	10	0.074	0.852	-0.720
U1514	C	5	R	6	W	26	28	231.80	NK 170	14	0.1036	0.285	-1.072
U1514	C	5	R	6	W	30	32	231.84	NK 171	8	0.0592	0.179	-1.182
U1514	C	5	R	6	W	34	36	231.88	NK 172	8	0.0592	0.008	-1.203
U1514	C	5	R	6	W	38	40	231.92	NK 173	8	0.0592	0.112	-1.242
U1514	C	5	R	6	W	42	44	231.96	NK 174	15	0.111	0.491	-0.947
U1514	C	5	R	6	W	46	48	232.00	NK 175	20	0.148	0.663	-0.938
U1514	C	5	R	6	W	50	52	232.04	NK 176	20	0.148	0.729	-0.869
U1514	C	5	R	6	W	54	56	232.08	NK 177	20	0.148	0.777	-0.829
U1514	C	5	R	6	W	58	60	232.12	NK 178	21	0.1554	0.769	-0.809
U1514	C	5	R	6	W	62	64	232.16	NK 179	20	0.148	0.816	-0.712
U1514	C	5	R	6	W	66	68	232.20	NK 180	20	0.148	0.779	-0.807
U1514	C	5	R	6	W	70	72	232.24	NK 181	20	0.148	0.796	-0.815
U1514	C	5	R	6	W	76	78	232.30	NK 182	20	0.148	0.742	-0.669
U1514	C	5	R	6	W	78	80	232.32	NK 183	20	0.148	0.684	-0.905
U1514	C	5	R	6	W	83	85	232.37	NK 243	20	0.148	0.745	-1.007
U1514	C	5	R	6	W	90	92	232.44	NK 184	20	0.148	0.854	-0.821
U1514	C	5	R	6	W	94	96	232.48	NK 185	20	0.148	0.878	-0.747
U1514	C	5	R	6	W	98	100	232.52	NK 186	20	0.148	0.873	-0.864
U1514	A	28	X	4	W	24	26	232.52	NK 1	6	0.047	0.501	-1.058
U1514	A	28	X	4	W	28	30	232.54	NK 2	20	0.148	0.656	-1.010

Site	Hole	Core	Type	Sect	Half	Top (cm)	Bottom (cm)	Depth CCSF (m)	Sample ID	No. tests	Approx. mass (mg)	$\delta^{13}C$ ‰ VPDB	$\delta^{18}O$ ‰ VPDB
U1514	A	28	X	4	W	32	34	232.58	NK 3	15	0.111	0.766	-0.882
U1514	A	28	X	4	W	36	38	232.62	NK 4	15	0.111	0.829	-0.858
U1514	A	28	X	4	W	40	42	232.66	NK 5	20	0.148	0.881	-0.703
U1514	A	28	X	4	W	44	46	232.70	NK 6	20	0.148	0.863	-0.765
U1514	A	28	X	4	W	48	50	232.74	NK 7	20	0.148	0.846	-0.709
U1514	A	28	X	4	W	52	54	232.78	NK 8	15	0.111	0.783	-0.759
U1514	A	28	X	4	W	57	59	232.85	NK 230	19	0.1406	0.726	-0.937
U1514	A	28	X	4	W	64	66	232.90	NK 9	19	0.141	0.660	-0.928
U1514	A	28	X	4	W	68	70	232.94	NK 10	20	0.148	0.712	-0.898
U1514	A	28	X	4	W	72	74	232.98	NK 11	20	0.133	0.752	-0.909
U1514	A	28	X	4	W	76	78	233.02	NK 12	20	0.148	0.841	-0.833
U1514	A	28	X	4	W	80	82	233.06	NK 13	20	0.148	0.849	-0.836
U1514	A	28	X	4	W	82	84	233.1	NK 231	20	0.148	1.023	-0.551
U1514	A	28	X	4	W	88	90	233.14	NK 14	20	0.148	0.872	-0.798
U1514	A	28	X	4	W	92	94	233.18	NK 15	20	0.148	0.755	-0.710
U1514	A	28	X	4	W	96	98	233.22	NK 16	20	0.148	0.742	-0.832
U1514	A	28	X	4	W	100	102	233.26	NK 17	20	0.148	0.645	-0.920
U1514	A	28	X	4	W	104	106	233.30	NK 18	20	0.148	0.524	-0.990
U1514	A	28	X	4	W	108	110	233.34	NK 19	20	0.148	0.544	-1.077
U1514	A	28	X	4	W	113	115	233.42	NK 232	20	0.148	0.651	-1.047
U1514	A	28	X	4	W	120	122	233.46	NK 20	20	0.148	0.672	-1.081
U1514	A	28	X	4	W	124	126	233.50	NK 21	20	0.078	0.797	-0.906
U1514	A	28	X	4	W	128	130	233.54	NK 22	20	0.148	0.851	-0.808
U1514	A	28	X	4	W	132	134	233.58	NK 23	20	0.148	0.983	-0.750
U1514	A	28	X	5	W	0	2	233.79	NK 24	20	0.148	0.775	-0.846
U1514	A	28	X	5	W	4	6	233.83	NK 25	20	0.148	0.661	-0.910
U1514	A	28	X	5	W	8	10	233.87	NK 26	20	0.148	0.738	-0.909
U1514	A	28	X	5	W	12	14	233.91	NK 27	20	0.148	0.577	-0.955
U1514	A	28	X	5	W	16	18	233.95	NK 28	20	0.148	0.660	-0.797
U1514	A	28	X	5	W	20	22	233.99	NK 29	20	0.148	0.656	-0.870
U1514	A	28	X	5	W	24	26	234.03	NK 30	6	0.044	0.294	-1.039
U1514	A	28	X	5	W	28	30	234.07	NK 31	20	0.167	0.624	-1.077
U1514	A	28	X	5	W	32	34	234.11	NK 32	20	0.148	0.512	-0.889

Site	Hole	Core	Type	Sect	Half	Top (cm)	Bottom (cm)	Depth CCSF (m)	Sample ID	No. tests	Approx. mass (mg)	$\delta^{13}C$ ‰ VPDB	$\delta^{18}O$ ‰ VPDB
U1514	A	28	X	5	W	40	42	234.19	NK 33	20	0.148	0.782	-0.627
U1514	A	28	X	5	W	44	46	234.23	NK 34	20	0.148	0.664	-0.773
U1514	A	28	X	5	W	48	50	234.27	NK 35	20	0.148	0.481	-0.989
U1514	A	28	X	5	W	52	54	234.31	NK 36	20	0.148	0.475	-1.007
U1514	A	28	X	5	W	56	58	234.35	NK 37	4	0.052	0.545	-1.054
U1514	A	28	X	5	W	60	62	234.39	NK 38				
U1514	A	28	X	5	W	64	66	234.43	NK 39	5	0.0518	0.426	-1.095
U1514	A	28	X	5	W	66	68	234.45	NK 233	20	0.148	0.397	-1.041
U1514	A	28	X	5	W	72	74	234.51	NK 40	18	0.134	0.479	-1.029
U1514	A	28	X	5	W	76	78	234.55	NK 41	10	0.095	0.392	-0.915
U1514	A	28	X	5	W	80	82	234.59	NK 42	17	0.126	0.377	-0.947
U1514	A	28	X	5	W	84	86	234.63	NK 43	20	0.148	0.392	-0.960
U1514	A	28	X	5	W	88	90	234.67	NK 44	20	0.148	0.325	-1.048
U1514	A	28	X	5	W	91	93	234.7	NK 234	20	0.148	0.284	-1.198
U1514	A	28	X	5	W	96	98	234.75	NK 45	22	0.163	0.177	-1.194
U1514	A	28	X	5	W	100	102	234.79	NK 46	15	0.111	-0.016	-1.370
U1514	A	28	X	5	W	104	106	234.83	NK 47	20	0.148	-0.024	-1.347
U1514	A	28	X	5	W	108	110	234.87	NK 48	20	0.148	0.040	-1.262
U1514	A	28	X	5	W	112	114	234.91	NK 49	10	0.099	0.126	-1.250
U1514	A	28	X	5	W	116	118	234.95	NK 235	20	0.148	0.080	-1.383
U1514	A	28	X	5	W	120	122	234.99	NK 50	2	0.03	-0.119	-1.416
U1514	A	28	X	5	W	124	126	235.03	NK 51	20	0.148	0.015	-1.286
U1514	A	28	X	5	W	128	130	235.07	NK 52	20	0.148	0.549	-1.150
U1514	A	28	X	5	W	132	134	235.11	NK 53	18	0.134	0.760	-0.825
U1514	A	28	X	5	W	136	138	235.15	NK 54	20	0.148	0.807	-0.814
U1514	A	28	X	5	W	141	143	235.2	NK 236	20	0.148	0.747	-0.997
U1514	A	28	X	5	W	144	146	235.23	NK 55	20	0.148	0.848	-0.851
U1514	A	28	X	5	W	148	150	235.27	NK 56				
U1514	A	28	X	6	W	2	4	235.31	NK 57	20	0.148	0.753	-0.865
U1514	A	28	X	6	W	6	8	235.35	NK 58	10	0.095	0.716	-0.929
U1514	A	28	X	6	W	10	12	235.39	NK 59	17	0.126	0.710	-0.822
U1514	A	28	X	6	W	14	16	235.43	NK 60	20	0.148	0.584	-0.884
U1514	A	28	X	6	W	18	20	235.47	NK 61	6	0.044	0.582	-0.951

Site	Hole	Core	Type	Sect	Half	Top (cm)	Bottom (cm)	Depth CCSF (m)	Sample ID	No. tests	Approx. mass (mg)	$\delta^{13}C$ ‰ VPDB	$\delta^{18}O$ ‰ VPDB
U1514	A	28	X	6	W	22	24	235.51	NK 62	20	0.148	0.548	-0.963
U1514	A	28	X	6	W	26	28	235.55	NK 63	20	0.148	0.578	-0.960
U1514	A	28	X	6	W	30	32	235.59	NK 64	10	0.07	0.566	-0.977
U1514	A	28	X	6	W	34	36	235.63	NK 65	20	0.148	0.438	-1.062
U1514	A	28	X	6	W	38	40	235.67	NK 66	18	0.134	0.463	-1.032
U1514	A	28	X	6	W	41	43	235.7	NK 237	20	0.148	0.304	-1.294
U1514	A	28	X	6	W	46	48	235.75	NK 67	20	0.148	0.314	-1.073
U1514	A	28	X	6	W	50	52	235.79	NK 68	20	0.148	0.275	-1.093
U1514	A	28	X	6	W	54	56	235.83	NK 69	20	0.148	0.264	-1.022
U1514	A	28	X	6	W	58	60	235.87	NK 70	20	0.148	0.288	-1.033
U1514	A	28	X	6	W	62	64	235.91	NK 71	20	0.148	0.350	-1.020
U1514	A	28	X	6	W	66	68	235.95	NK 238	15	0.111	0.122	-1.249
U1514	A	28	X	6	W	70	72	235.99	NK 72	20	0.148	-0.174	-1.385
U1514	A	28	X	6	W	74	76	236.03	NK 73	20	0.148	-0.280	-1.494
U1514	A	28	X	6	W	78	80	236.07	NK 74	20	0.148	-0.320	-1.536
U1514	A	28	X	6	W	82	84	236.11	NK 75	20	0.148	-0.329	-1.494
U1514	A	28	X	6	W	86	88	236.15	NK 76	20	0.148	-0.214	-1.480
U1514	A	28	X	6	W	90	92	236.19	NK 77	20	0.148	-0.151	-1.440
U1514	A	28	X	6	W	94	96	236.23	NK 78	15	0.118	-0.196	-1.479
U1514	A	28	X	6	W	98	100	236.27	NK 79	20	0.148	-0.260	-1.502
U1514	A	28	X	6	W	102	104	236.31	NK 80	20	0.148	-0.234	-1.498
U1514	A	28	X	6	W	106	108	236.35	NK 81	18	0.134	0.105	-1.249
U1514	A	28	X	6	W	110	112	236.39	NK 82	20	0.148	0.199	-1.222
U1514	A	28	X	6	W	114	116	236.43	NK 83	20	0.148	0.239	-1.112
U1514	A	28	X	6	W	118	120	236.47	NK 84	20	0.148	0.055	-1.416
U1514	A	28	X	6	W	122	124	236.51	NK 85	13	0.096	0.080	-1.309
U1514	A	28	X	6	W	126	128	236.55	NK 86	6	0.035	0.418	-1.103
U1514	A	28	X	6	W	130	132	236.59	NK 87	20	0.148	0.742	-0.862
U1514	A	28	X	7	W	2	4	236.63	NK 88	20	0.148	0.709	-0.926
U1514	A	28	X	7	W	6	8	236.67	NK 89	20	0.148	0.706	-0.819
U1514	A	28	X	7	W	10	12	236.71	NK 90	20	0.148	0.584	-0.881
U1514	A	28	X	7	W	14	16	236.75	NK 91	11	0.081		
U1514	A	28	X	7	W	18	20	236.79	NK 92	20	0.148	0.555	-0.959

Site	Hole	Core	Type	Sect	Half	Top (cm)	Bottom (cm)	Depth CCSF (m)	Sample ID	No. tests	Approx. mass (mg)	$\delta^{13}C$ ‰ VPDB	$\delta^{18}O$ ‰ VPDB
U1514	A	28	X	7	W	21	23	236.82	NK 239	20	0.148	0.742	-1.026
U1514	A	28	X	7	W	26	28	236.87	NK 93	20	0.148	0.588	-0.957
U1514	A	28	X	7	W	30	32	236.91	NK 94	20	0.148	0.580	-0.973
U1514	A	28	X	7	W	33	35	236.94	NK 95	20	0.148	0.456	-1.058
U1514	C	6	R	3	W	36	38	236.94	NK 187	14	0.1036	0.594	-0.941
U1514	C	6	R	3	W	40	42	236.98	NK 188	16	0.1184	0.583	-0.936
U1514	C	6	R	3	W	44	46	237.02	NK 189	15	0.111	0.551	-0.939
U1514	C	6	R	3	W	48	50	237.06	NK 190	14	0.1036	0.512	-0.991
U1514	C	6	R	3	W	52	54	237.10	NK 191	20	0.148	0.462	-1.007
U1514	C	6	R	3	W	56	58	237.14	NK 192	17	0.1258	0.605	-0.934
U1514	C	6	R	3	W	60	62	237.18	NK 193	9	0.0666	0.555	-1.023
U1514	C	6	R	3	W	64	66	237.22	NK 194	21	0.1554	0.377	-1.170
U1514	C	6	R	3	W	68	70	237.26	NK 195	12	0.0888	0.432	-0.880
U1514	C	6	R	3	W	72	74	237.30	NK 196	20	0.148	0.337	-1.082
U1514	C	6	R	3	W	76	78	237.34	NK 197	20	0.148	0.346	-1.045
U1514	C	6	R	3	W	80	82	237.38	NK 198	20	0.148	0.303	-1.090
U1514	C	6	R	3	W	82	84	237.4	NK 244	14	0.1036	0.284	-1.149
U1514	C	6	R	3	W	88	90	237.46	NK 199	20	0.148	0.275	-0.892
U1514	C	6	R	3	W	92	94	237.50	NK 200	20	0.148	0.298	-0.905
U1514	C	6	R	3	W	96	98	237.54	NK 201	20	0.148	0.236	-1.182
U1514	C	6	R	3	W	100	102	237.58	NK 202	20	0.148	0.284	-1.181
U1514	C	6	R	3	W	104	106	237.62	NK 203	7	0.0518	0.393	-1.133
U1514	C	6	R	3	W	107	109	237.65	NK 245	7	0.0518	0.538	-1.218
U1514	C	6	R	3	W	112	114	237.70	NK 204	8	0.0592	0.659	-1.168
U1514	C	6	R	3	W	116	118	237.74	NK 205	20	0.148	0.619	-1.011
U1514	C	6	R	3	W	120	122	237.78	NK 206	10	0.074	0.319	-1.100
U1514	C	6	R	3	W	124	126	237.82	NK 207	9	0.0666	0.880	-0.977
U1514	C	6	R	3	W	128	130	237.86	NK 208	14	0.1036	0.874	-0.913
U1514	C	6	R	3	W	132	134	237.90	NK 209	8	0.0592	0.908	-0.924
U1514	C	6	R	3	W	136	138	237.94	NK 210	20	0.148	0.873	-0.766
U1514	C	6	R	3	W	140	142	237.98	NK 211	20	0.148	0.749	-0.760
U1514	C	6	R	3	W	144	146	238.02	NK 212	20	0.148	0.705	-0.849
U1514	C	6	R	3	W	148	150	238.06	NK 213	8	0.0592	0.675	-1.091

Site	Hole	Core	Type	Sect	Half	Top (cm)	Bottom (cm)	Depth CCSF (m)	Sample ID	No. tests	Approx. mass (mg)	$\delta^{13}C$ ‰ VPDB	$\delta^{18}O$ ‰ VPDB
U1514	C	6	R	4	W	1	3	238.10	NK 214	12	0.0888	0.567	-1.174
U1514	C	6	R	4	W	5	7	238.14	NK 215	17	0.1258	0.628	-1.054
U1514	C	6	R	4	W	9	11	238.18	NK 216	20	0.148	0.666	-0.943
U1514	C	6	R	4	W	13	15	238.22	NK 217	21	0.1554	0.693	-0.836
U1514	C	6	R	4	W	17	19	238.26	NK 218	20	0.148	0.773	-0.907
U1514	C	6	R	4	W	21	23	238.30	NK 219	20	0.148	0.776	-0.972
U1514	C	6	R	4	W	25	27	238.34	NK 220	20	0.148	0.841	-0.744
U1514	C	6	R	4	W	29	31	238.38	NK 221	12	0.0888	0.679	-0.963
U1514	C	6	R	4	W	33	35	238.42	NK 222	21	0.1554	0.840	-0.879
U1514	C	6	R	4	W	37	39	238.46	NK 223	15	0.111	0.802	-0.867
U1514	C	6	R	4	W	41	43	238.50	NK 224	20	0.148	0.829	-0.754
U1514	C	6	R	4	W	45	47	238.54	NK 225	18	0.1332	0.676	-0.859
U1514	C	6	R	4	W	49	51	238.58	NK 226	20	0.148	0.548	-1.026
U1514	C	6	R	4	W	53	55	238.62	NK 227	21	0.1554	0.697	-0.808
U1514	C	6	R	4	W	57	59	238.66	NK 228	20	0.148	0.570	-1.079
U1514	C	6	R	4	W	61	63	238.70	NK 229	14	0.1036	0.621	-1.079
U1514	C	6	R	4	W	73	75	238.82	NK 246	21	0.1554	0.791	-0.790

Supplementary Table 3.2: Ca/Fe from XRF. Data has been split between 3 tables to conserve space.

XRF data 1: 228.795 – 231.737 m CCSF		
CCSF (m)	**Age (Ma)**	**Ca/Fe (counts/counts)**
228.795	50.0017	30.68
228.805	50.0034	39.94
228.815	50.0051	51.52
228.825	50.0068	50.12
228.835	50.0085	58.22
228.845	50.0102	46.43
228.855	50.0119	39.11
228.865	50.0136	62.96
228.875	50.0153	68.97
228.885	50.0171	46.04
228.915	50.0222	50.05
228.925	50.0239	46.37
228.935	50.0256	48.31
228.965	50.0308	35.37
228.975	50.0325	36.48
228.985	50.0342	37.04
228.995	50.0359	37.42
229.005	50.0376	32.04
229.015	50.0393	30.08
229.025	50.0410	29.20
229.035	50.0427	28.68
229.045	50.0444	30.03
229.05	50.0453	24.98
229.055	50.0462	24.89
229.06	50.0470	23.59
229.065	50.0479	18.95
229.07	50.0487	18.14
229.075	50.0496	18.19
229.08	50.0504	20.30
229.085	50.0513	20.64
229.09	50.0522	19.01
229.095	50.0530	20.43
229.1	50.0539	18.65
229.105	50.0547	16.64
229.11	50.0556	16.21
229.115	50.0564	18.59
229.12	50.0573	21.47
229.125	50.0581	15.28
229.13	50.0590	14.22
229.135	50.0596	15.84
229.14	50.0602	17.20
229.145	50.0608	17.71
229.15	50.0613	14.98
229.155	50.0619	12.40

XRF data 2: 231.757 – 235.03 m CCSF		
CCSF (m)	**Age (Ma)**	**Ca/Fe (counts/counts)**
231.757	50.3282	71.35
231.777	50.3299	70.26
231.873	50.3379	37.23
231.893	50.3395	37.37
231.913	50.3412	36.08
231.923	50.3420	35.89
231.965	50.3455	38.74
232.002	50.3486	33.18
232.022	50.3502	33.42
232.042	50.3519	32.12
232.062	50.3535	35.83
232.082	50.3552	40.30
232.102	50.3569	41.65
232.122	50.3585	45.24
232.142	50.3602	49.51
232.162	50.3618	50.88
232.182	50.3635	44.56
232.202	50.3652	43.91
232.245	50.3687	40.25
232.265	50.3704	37.62
232.285	50.3721	31.99
232.305	50.3737	31.92
232.325	50.3754	30.59
232.345	50.3770	31.45
232.365	50.3787	31.37
232.385	50.3804	35.95
232.405	50.3820	37.65
232.425	50.3837	36.40
232.435	50.3845	37.02
232.462	50.3868	41.91
232.482	50.3884	39.93
232.502	50.3901	42.77
232.53	50.3924	42.79
232.533	50.3926	35.33
232.573	50.3960	33.79
232.593	50.3976	32.57
232.613	50.3993	33.06
232.633	50.4009	36.41
232.653	50.4026	36.07
232.673	50.4043	40.64
232.693	50.4059	44.74
232.713	50.4076	48.64
232.733	50.4092	43.90
232.753	50.4109	44.76

XRF data 3: 235.04 – 238.51 m CCSF		
CCSF (m)	**Age (Ma)**	**Ca/Fe (counts/counts)**
235.04	50.5962	14.72
235.05	50.5970	20.24
235.06	50.5978	22.97
235.07	50.5985	27.23
235.08	50.5993	27.79
235.09	50.6001	28.62
235.1	50.6008	32.72
235.11	50.6016	34.41
235.12	50.6024	35.39
235.13	50.6031	38.58
235.14	50.6039	34.43
235.155	50.6050	39.37
235.165	50.6058	38.30
235.175	50.6066	39.18
235.185	50.6073	38.97
235.195	50.6081	37.24
235.205	50.6089	38.68
235.215	50.6096	38.96
235.225	50.6104	38.92
235.24	50.6116	40.06
235.25	50.6123	40.16
235.26	50.6131	41.63
235.27	50.6139	41.77
235.28	50.6146	45.68
235.305	50.6165	53.26
235.323	50.6179	57.82
235.341	50.6193	71.95
235.359	50.6211	73.97
235.38	50.6237	60.53
235.4	50.6262	60.14
235.42	50.6286	61.31
235.44	50.6311	62.49
235.46	50.6336	58.18
235.505	50.6391	46.08
235.526	50.6417	50.34
235.547	50.6443	50.45
235.572	50.6474	53.92
235.59	50.6496	56.73
235.607	50.6517	59.33
235.624	50.6538	59.19
235.645	50.6563	58.02
235.665	50.6588	57.68
235.685	50.6613	53.85
235.701	50.6632	53.07

CCSF (m)	Age (Ma)	Ca/Fe (counts/counts)
229.16	50.0625	13.47
229.165	50.0631	17.77
229.17	50.0637	18.38
229.175	50.0643	19.50
229.18	50.0648	19.71
229.185	50.0654	18.25
229.19	50.0660	19.78
229.195	50.0666	18.17
229.2	50.0672	19.58
229.205	50.0678	29.61
229.21	50.0683	30.79
229.215	50.0689	31.87
229.22	50.0695	28.89
229.225	50.0701	27.10
229.23	50.0707	32.92
229.235	50.0713	34.16
229.24	50.0718	36.99
229.254	50.0735	37.06
229.269	50.0752	36.52
229.279	50.0764	50.60
229.289	50.0776	54.39
229.299	50.0787	51.86
229.309	50.0799	56.67
229.319	50.0811	54.49
229.329	50.0822	55.53
229.339	50.0834	59.35
229.349	50.0846	53.42
229.359	50.0857	40.33
229.369	50.0869	44.66
229.379	50.0881	37.02
229.388	50.0891	32.85
229.397	50.0902	41.79
229.406	50.0912	33.59
229.415	50.0923	46.17
229.425	50.0935	62.66
229.435	50.0946	61.96
229.445	50.0958	58.51
229.455	50.0970	56.12
229.465	50.0981	61.33
229.475	50.0993	55.91
229.485	50.1005	45.63
229.522	50.1048	70.73
229.532	50.1059	66.67
229.542	50.1071	67.44
229.552	50.1083	67.64
229.562	50.1095	69.96
229.572	50.1106	82.25
229.582	50.1118	91.69
229.592	50.1130	90.61

CCSF (m)	Age (Ma)	Ca/Fe (counts/counts)
232.773	50.4126	46.27
232.793	50.4142	48.96
232.813	50.4159	47.29
232.833	50.4175	44.62
232.853	50.4192	40.55
232.873	50.4209	37.20
232.893	50.4225	35.73
232.913	50.4242	33.85
232.933	50.4259	34.52
232.953	50.4275	29.48
232.973	50.4292	28.67
232.993	50.4308	27.07
233.013	50.4325	32.06
233.033	50.4342	39.37
233.053	50.4358	34.78
233.073	50.4375	34.89
233.093	50.4391	35.47
233.113	50.4408	36.35
233.133	50.4425	36.91
233.153	50.4441	39.69
233.173	50.4458	40.93
233.193	50.4474	42.20
233.213	50.4491	43.52
233.233	50.4508	48.90
233.253	50.4524	43.23
233.273	50.4541	35.31
233.293	50.4557	32.25
233.313	50.4574	34.22
233.333	50.4591	29.32
233.353	50.4607	29.17
233.373	50.4624	31.28
233.393	50.4640	30.25
233.413	50.4657	29.89
233.433	50.4674	27.69
233.453	50.4690	29.47
233.473	50.4707	29.62
233.493	50.4723	28.26
233.513	50.4740	29.47
233.533	50.4757	33.12
233.545	50.4767	34.34
233.57	50.4787	36.67
233.59	50.4804	37.27
233.61	50.4821	39.88
233.63	50.4837	43.63
233.65	50.4854	43.04
233.67	50.4870	45.33
233.688	50.4885	49.20
233.81	50.4987	52.00
233.82	50.4995	50.01

CCSF (m)	Age (Ma)	Ca/Fe (counts/counts)
235.763	50.6709	47.96
235.781	50.6731	42.16
235.799	50.6753	42.03
235.817	50.6775	42.53
235.835	50.6798	37.09
235.853	50.6820	42.98
235.875	50.6847	45.74
235.897	50.6874	45.68
235.919	50.6901	45.38
235.94	50.6927	47.01
235.96	50.6952	47.75
235.98	50.6976	41.58
236	50.7001	38.56
236.02	50.7026	36.13
236.04	50.7050	32.97
236.06	50.7075	31.09
236.08	50.7099	28.68
236.1	50.7124	26.73
236.12	50.7149	23.02
236.14	50.7173	19.93
236.16	50.7198	16.52
236.18	50.7223	16.61
236.2	50.7247	12.83
236.22	50.7272	11.44
236.24	50.7297	10.42
236.26	50.7321	7.71
236.28	50.7346	8.75
236.3	50.7371	11.08
236.32	50.7395	12.32
236.34	50.7420	12.62
236.357	50.7441	13.49
236.377	50.7465	13.42
236.399	50.7493	13.25
236.421	50.7520	13.40
236.441	50.7544	14.47
236.461	50.7569	12.35
236.481	50.7591	12.86
236.501	50.7611	11.88
236.523	50.7633	12.56
236.543	50.7653	13.20
236.563	50.7673	14.09
236.583	50.7693	12.86
236.605	50.7715	13.59
236.625	50.7735	14.87
236.645	50.7755	18.10
236.665	50.7775	20.71
236.685	50.7795	23.70
236.705	50.7815	28.09
236.712	50.7822	29.24

CCSF (m)	Age (Ma)	Ca/Fe (counts/counts)
229.602	50.1141	92.88
229.612	50.1153	94.28
229.622	50.1165	92.00
229.632	50.1176	90.96
229.642	50.1188	82.83
229.652	50.1200	80.58
229.662	50.1211	68.86
229.672	50.1223	52.50
229.682	50.1235	55.86
229.692	50.1246	80.02
229.702	50.1258	93.86
229.715	50.1273	91.15
229.73	50.1291	96.61
229.745	50.1308	103.40
229.76	50.1326	101.25
229.775	50.1343	103.80
229.79	50.1361	95.90
229.805	50.1378	96.36
229.82	50.1396	92.47
229.835	50.1413	98.93
229.87	50.1454	92.59
229.885	50.1472	81.13
229.9	50.1489	69.41
229.915	50.1507	59.32
229.93	50.1524	58.57
229.945	50.1542	68.23
229.96	50.1559	73.01
229.975	50.1577	82.69
229.99	50.1594	89.25
230.005	50.1612	91.83
230.02	50.1629	96.47
230.045	50.1659	96.04
230.065	50.1682	98.90
230.085	50.1705	83.36
230.105	50.1729	82.61
230.125	50.1752	71.33
230.145	50.1775	66.57
230.165	50.1799	61.30
230.19	50.1828	59.68
230.225	50.1869	58.00
230.245	50.1892	50.74
230.265	50.1916	54.30
230.285	50.1939	54.06
230.305	50.1962	55.55
230.325	50.1986	55.51
230.345	50.2009	59.20
230.365	50.2032	57.76
230.385	50.2056	66.41
230.405	50.2079	72.95

CCSF (m)	Age (Ma)	Ca/Fe (counts/counts)
233.83	50.5003	51.41
233.84	50.5012	48.14
233.85	50.5020	45.78
233.86	50.5028	29.62
233.87	50.5036	22.26
233.88	50.5045	46.73
233.89	50.5053	43.73
233.9	50.5061	39.66
233.91	50.5070	40.40
233.92	50.5078	53.05
233.93	50.5086	83.41
233.94	50.5095	80.66
233.95	50.5103	76.61
233.96	50.5111	78.18
233.97	50.5119	77.48
233.98	50.5128	71.39
233.99	50.5136	63.32
234	50.5144	65.89
234.01	50.5153	67.23
234.02	50.5161	64.53
234.046	50.5183	31.74
234.06	50.5194	32.15
234.07	50.5202	39.07
234.08	50.5211	31.35
234.09	50.5219	51.84
234.1	50.5227	58.45
234.11	50.5236	64.82
234.12	50.5244	37.78
234.13	50.5252	67.62
234.14	50.5261	70.99
234.15	50.5269	74.35
234.16	50.5277	85.55
234.17	50.5285	85.46
234.18	50.5294	83.60
234.187	50.5300	82.76
234.205	50.5315	78.82
234.21	50.5319	76.03
234.22	50.5327	78.96
234.23	50.5335	80.49
234.24	50.5344	82.76
234.25	50.5352	86.01
234.26	50.5360	87.87
234.27	50.5368	82.74
234.28	50.5377	87.87
234.29	50.5385	88.93
234.3	50.5393	89.90
234.31	50.5402	86.36
234.33	50.5418	88.97
234.34	50.5425	83.55

CCSF (m)	Age (Ma)	Ca/Fe (counts/counts)
236.731	50.7841	33.69
236.75	50.7860	37.51
236.775	50.7885	39.30
236.795	50.7905	39.40
236.815	50.7925	40.52
236.837	50.7947	43.15
236.859	50.7969	48.32
236.89	50.8000	50.81
236.901	50.8011	51.43
236.933	50.8043	50.46
236.94	50.8050	46.60
236.96	50.8070	44.97
236.98	50.8090	44.26
237	50.8110	45.09
237.02	50.8130	41.74
237.04	50.8150	40.14
237.06	50.8170	36.65
237.08	50.8190	39.84
237.09	50.8200	35.52
237.13	50.8240	36.45
237.14	50.8250	41.91
237.16	50.8270	42.23
237.18	50.8290	42.72
237.2	50.8310	41.76
237.22	50.8330	46.22
237.24	50.8350	44.37
237.26	50.8370	38.98
237.28	50.8390	38.49
237.29	50.8400	35.65
237.32	50.8430	30.09
237.34	50.8450	25.89
237.36	50.8470	28.60
237.38	50.8490	22.15
237.4	50.8510	20.14
237.41	50.8520	21.70
237.44	50.8550	20.01
237.46	50.8570	18.46
237.52	50.8630	10.06
237.54	50.8650	9.00
237.56	50.8678	7.72
237.58	50.8706	10.73
237.6	50.8734	13.12
237.62	50.8762	14.59
237.64	50.8790	17.38
237.66	50.8818	19.84
237.68	50.8845	19.40
237.7	50.8873	19.48
237.72	50.8901	17.53
237.74	50.8929	24.18

CCSF (m)	Age (Ma)	Ca/Fe (counts/counts)
230.425	50.2102	81.94
230.455	50.2137	96.44
230.475	50.2161	105.47
230.495	50.2184	100.74
230.515	50.2203	93.77
230.535	50.2220	92.21
230.555	50.2238	99.41
230.575	50.2255	91.88
230.595	50.2273	76.42
230.625	50.2299	67.66
230.645	50.2316	53.23
230.665	50.2334	50.62
230.685	50.2351	45.69
230.72	50.2382	52.32
230.74	50.2399	56.96
230.76	50.2417	52.68
230.78	50.2434	56.88
230.8	50.2452	50.15
230.82	50.2469	58.83
230.84	50.2486	61.97
230.86	50.2504	55.48
230.88	50.2521	56.06
230.907	50.2545	56.05
230.927	50.2562	55.59
230.947	50.2580	54.94
230.967	50.2597	47.83
230.987	50.2615	48.77
231.007	50.2632	62.94
231.027	50.2649	62.24
231.047	50.2667	82.37
231.063	50.2681	69.81
231.09	50.2704	40.88
231.11	50.2722	35.83
231.13	50.2739	31.01
231.15	50.2757	22.39
231.17	50.2774	30.58
231.19	50.2792	29.96
231.21	50.2809	28.78
231.23	50.2826	32.09
231.245	50.2839	32.01
231.265	50.2857	29.14
231.285	50.2874	31.71
231.305	50.2892	44.64
231.325	50.2909	49.15
231.345	50.2927	52.80
231.365	50.2944	63.58
231.385	50.2962	56.60
231.4	50.2975	72.95
231.435	50.3005	70.44

CCSF (m)	Age (Ma)	Ca/Fe (counts/counts)
234.35	50.5433	84.49
234.36	50.5441	84.38
234.37	50.5448	84.90
234.38	50.5456	84.70
234.39	50.5464	79.49
234.4	50.5471	77.70
234.41	50.5479	74.21
234.42	50.5487	77.97
234.43	50.5494	85.28
234.44	50.5502	78.65
234.45	50.5510	79.78
234.458	50.5516	79.28
234.48	50.5533	86.09
234.514	50.5559	80.99
234.524	50.5566	80.18
234.534	50.5574	85.24
234.544	50.5582	80.11
234.554	50.5589	81.72
234.564	50.5597	79.43
234.574	50.5605	84.63
234.584	50.5612	74.63
234.595	50.5621	75.27
234.635	50.5652	68.32
234.645	50.5659	63.87
234.655	50.5667	69.07
234.665	50.5675	65.02
234.675	50.5682	63.26
234.685	50.5690	59.28
234.695	50.5698	57.04
234.705	50.5705	53.70
234.715	50.5713	53.24
234.725	50.5721	48.18
234.735	50.5728	48.90
234.75	50.5740	53.78
234.76	50.5747	46.40
234.77	50.5755	44.94
234.78	50.5763	43.01
234.79	50.5770	41.13
234.8	50.5778	33.75
234.81	50.5786	36.56
234.82	50.5793	35.95
234.83	50.5801	33.22
234.84	50.5809	31.50
234.85	50.5816	30.82
234.86	50.5824	29.92
234.87	50.5832	25.26
234.88	50.5840	26.50
234.89	50.5847	25.50
234.9	50.5855	27.22

CCSF (m)	Age (Ma)	Ca/Fe (counts/counts)
237.75	50.8943	24.48
237.77	50.8971	23.77
237.78	50.8985	26.49
237.8	50.9013	27.15
237.82	50.9041	31.58
237.84	50.9069	35.26
237.86	50.9097	33.17
237.88	50.9125	41.03
237.9	50.9152	45.48
237.94	50.9208	45.85
237.95	50.9222	41.69
237.98	50.9264	43.46
238	50.9292	41.23
238.02	50.9320	40.25
238.04	50.9348	36.35
238.06	50.9376	37.56
238.08	50.9404	37.92
238.11	50.9446	29.81
238.13	50.9474	31.81
238.15	50.9501	30.04
238.16	50.9515	28.62
238.18	50.9543	24.97
238.21	50.9585	21.55
238.23	50.9613	21.62
238.24	50.9627	30.95
238.27	50.9669	26.45
238.29	50.9697	28.65
238.31	50.9725	30.58
238.33	50.9753	28.83
238.35	50.9781	29.46
238.37	50.9809	26.63
238.38	50.9823	29.17
238.39	50.9836	26.99
238.44	50.9906	33.38
238.45	50.9920	40.49
238.47	50.9948	42.89
238.49	50.9976	39.03
238.51	51.0002	42.37

CCSF (m)	Age (Ma)	Ca/Fe (counts/counts)
231.497	50.3059	68.54
231.517	50.3077	72.02
231.537	50.3094	81.83
231.557	50.3111	68.57
231.577	50.3129	63.61
231.597	50.3146	65.14
231.617	50.3164	64.13
231.637	50.3181	63.77
231.657	50.3199	63.22
231.677	50.3216	63.09
231.697	50.3232	61.45
231.717	50.3249	71.08
231.737	50.3266	71.17

CCSF (m)	Age (Ma)	Ca/Fe (counts/counts)
234.91	50.5863	27.18
234.92	50.5870	25.07
234.93	50.5878	23.64
234.94	50.5886	22.82
234.95	50.5893	20.04
234.96	50.5901	21.03
234.97	50.5909	16.69
234.98	50.5916	14.04
234.99	50.5924	12.72
235	50.5932	11.61
235.01	50.5939	11.54
235.02	50.5947	11.39
235.03	50.5955	11.19

Supplementary Table 3.3: Data summary for other records across this study interval, used in site comparison, Fig. 3.6.

Site	Location	Palaeolatitude	Palaeowater Depth	Data available	Material	Average sedimentation rate between 50-51 Ma	Reference
ODP 1263	Southeastern Atlantic (Walvis Ridge)	30° S	1500 m	Benthic $\delta^{13}C$	Foraminiferal carbonate from *.N truempyi*	1.21 cm/ka	Lauretano et al., 2016 Westerhold et al., 2017
ODP 1209	Northwestern Pacific (Shatsky Rise)	30° N	2387 m	Benthic $\delta^{13}C$ and $\delta^{18}O$	Foraminiferal carbonate from *N. truempyi*	0.64 cm/ka	Westerhold et al., 2018
ODP 1258	Equatorial Atlantic (Demerara Rise)	1° S	3000 m	Bulk $\delta^{13}C$ and $\delta^{18}O$	Bulk carbonate	1.18 cm/ka	Kirtland Turner et al., 2014
IODP U1514	Southern Indian Ocean (Mentelle Basin)	60° S	>2500 m	Benthic $\delta^{13}C$ and $\delta^{18}O$	Foraminiferal carbonate from *N. truempyi*	0.97 cm/ka	This study

Appendix 3: Supplementary material for Chapter 4

Supplementary Table 4.1: $\delta^{18}O$ data tables for sites in this compilation: ODP Site 647 (Supplementary Table 4.1.1), ODP Site 702 (Supplementary Table 4.1.2), ODP Site 748 (Supplementary Table 4.1.3), ODP Site 865 (Supplementary Table 4.1.4), ODP Site 1051 (Supplementary Table 4.1.5), ODP Site 1052 (Supplementary Table 4.1.6), ODP Site 1260 (Supplementary Table 4.1.7), ODP Site 1263 (Supplementary Table 4.1.8), Baskil Section (Supplementary Table 4.1.9), IODP Site U1408 (Supplementary Table 4.1.10)

Supplementary Table 4.1.1: ODP Site 647

Depth (mbsf)	Age (Ma) GTS2012	$\delta^{13}C$ (‰ VPDB)	$\delta^{18}O$ (‰ VPDB)	$\delta^{18}O_{sw}$ (‰ VSMOW)	$\delta^{18}O_{sw}$ (‰ VPDB)	$[CO_3^{2-}]$ ($\mu mol\ kg^{-1}$)	$\delta^{18}O_c$'	SST - Equation 1 (°C)	SST - Bayfox (°C)			Species	Size fraction (µm)	MECO interval
									0.05	0.50	0.95			
470.70	40.76	2.86	-2.62	-1.07	-1.34	99.51	-2.81	23.11	19.91	23.80	27.49	*Acarinina bullbrooki*	150-300	N/A
474.58	40.89	0.86	-1.98	-1.07	-1.34	99.44	-2.17	20.01	17.14	20.98	24.92	*Acarinina cf. collactea 5-chambers*	150-300	N/A
470.80	40.76	2.81	-2.70	-1.07	-1.34	99.51	-2.89	23.51	20.27	24.07	27.97	*Acarinina cf. collactea 5-chambers*	150-300	N/A
436.08	39.67	0.50	-2.63	-1.07	-1.34	100.57	-2.82	23.15	19.89	23.79	27.70	*Acarinina cf. mcgowrani 4-chambers*	150-300	N/A
460.55	40.41	1.08	-1.76	-1.07	-1.34	99.69	-1.95	18.96	16.17	20.05	23.93	*Acarinina cf. mcgowrani 4-chambers*	150-300	Pre
460.55	40.41	1.13	-2.02	-1.07	-1.34	99.69	-2.21	20.20	17.37	21.14	25.02	*Acarinina cf. mcgowrani 4-chambers*	63-150	Pre
467.25	40.64	2.48	-3.30	-1.07	-1.34	99.57	-3.49	26.49	22.83	26.70	30.53	*Acarinina cf. mcgowrani 4-chambers*	150-300	N/A
468.83	40.69	2.32	-2.45	-1.07	-1.34	99.55	-2.64	22.28	19.12	22.99	26.92	*Acarinina cf. mcgowrani 4-chambers*	150-300	N/A
470.80	40.76	2.61	-2.75	-1.07	-1.34	99.51	-2.94	23.75	20.43	24.30	28.14	*Acarinina cf. mcgowrani 4-chambers*	150-300	N/A
476.16	40.95	1.63	-2.55	-1.07	-1.34	99.42	-2.74	22.77	19.57	23.45	27.30	*Acarinina cf. mcgowrani 4-chambers*	63-300	N/A
483.25	41.19	0.44	-2.35	-1.07	-1.34	99.30	-2.54	21.80	18.71	22.56	26.41	*Acarinina cf. mcgowrani 4-chambers*	150-300	N/A
457.55	40.30	1.40	-2.14	-1.07	-1.34	99.75	-2.33	20.78	17.83	21.70	25.52	*Acarinina mix*	63-300	Pre
463.76	40.52	0.77	-1.64	-1.07	-1.34	99.64	-1.83	18.39	15.75	19.59	23.44	*Acarinina mix*	63-300	Pre

Depth (mbsf)	Age (Ma) GTS2012	$\delta^{13}C$ (‰ VPDB)	$\delta^{18}O$ (‰ VPDB)	$\delta^{18}O_{sw}$ (‰ VSMOW)	$\delta^{18}O_{sw}$ (‰ VPDB)	$[CO_3^{2-}]$ (µmol kg^{-1})	$\delta^{18}O_c$'	SST - Equation 1 (°C)	SST - Bayfox (°C)			Species	Size fraction (µm)	MECO interval
									0.05	0.50	0.95			
472.53	40.82	2.23	-2.05	-1.07	-1.34	99.48	-2.24	20.35	17.39	21.29	25.17	*Acarinina mix*	150-300	N/A
436.08	39.67	0.89	-4.23	-1.07	-1.34	100.57	-4.42	31.23	26.78	30.60	34.44	*Chiloguembelina ototara*	63-150	N/A
439.15	39.75	0.76	-2.13	-1.07	-1.34	100.40	-2.32	20.73	17.91	21.64	25.54	*Chiloguembelina ototara*	63-150	N/A
442.97	39.86	0.06	-1.62	-1.07	-1.34	100.18	-1.81	18.29	15.66	19.46	23.36	*Chiloguembelina ototara*	63-150	Post
447.57	39.99	0.48	-2.05	-1.07	-1.34	99.92	-2.24	20.34	17.41	21.35	25.22	*Chiloguembelina ototara*	63-150	Post
456.80	40.28	0.48	-2.11	-1.07	-1.34	99.76	-2.30	20.63	17.76	21.56	25.38	*Chiloguembelina ototara*	63-150	Onset
457.55	40.30	-0.73	-1.24	-1.07	-1.34	99.75	-1.43	16.52	14.00	17.89	21.68	*Chiloguembelina ototara*	63-150	Pre
460.55	40.41	-0.14	-1.58	-1.07	-1.34	99.69	-1.77	18.11	15.42	19.29	23.06	*Chiloguembelina ototara*	63-150	Pre
463.76	40.52	-0.15	-1.52	-1.07	-1.34	99.64	-1.71	17.83	15.25	19.05	22.89	*Chiloguembelina ototara*	63-150	Pre
465.36	40.57	-0.06	-1.59	-1.07	-1.34	99.61	-1.78	18.16	15.50	19.33	23.17	*Chiloguembelina ototara*	63-150	N/A
467.25	40.64	0.07	-1.35	-1.07	-1.34	99.57	-1.54	17.03	14.53	18.32	22.19	*Chiloguembelina ototara*	63-150	N/A
468.83	40.69	0.14	-1.85	-1.07	-1.34	99.55	-2.04	19.39	16.63	20.48	24.38	*Chiloguembelina ototara*	63-150	N/A
470.70	40.76	-0.18	-1.82	-1.07	-1.34	99.51	-2.01	19.25	16.48	20.33	24.21	*Chiloguembelina ototara*	63-150	N/A
472.53	40.82	0.12	-1.83	-1.07	-1.34	99.48	-2.02	19.30	16.56	20.39	24.18	*Chiloguembelina ototara*	63-150	N/A
474.58	40.89	-0.01	-1.67	-1.07	-1.34	99.44	-1.86	18.54	15.78	19.65	23.50	*Chiloguembelina ototara*	63-150	N/A
476.16	40.95	-0.36	-1.42	-1.07	-1.34	99.42	-1.61	17.36	14.75	18.66	22.43	*Chiloguembelina ototara*	63-150	N/A
477.82	41.00	-0.81	-2.09	-1.07	-1.34	99.39	-2.28	20.54	17.61	21.47	25.38	*Chiloguembelina ototara*	63-150	N/A
479.62	41.07	0.63	-2.82	-1.07	-1.34	99.36	-3.01	24.10	20.76	24.60	28.44	*Chiloguembelina ototara*	63-150	N/A
480.59	41.10	0.34	-1.66	-1.07	-1.34	99.34	-1.85	18.49	15.62	19.58	23.43	*Chiloguembelina ototara*	63-150	N/A
481.42	41.13	0.52	-2.35	-1.07	-1.34	99.32	-2.54	21.80	18.78	22.54	26.39	*Chiloguembelina ototara*	63-150	N/A
483.25	41.19	0.00	-2.43	-1.07	-1.34	99.30	-2.62	22.19	19.10	22.94	26.81	*Chiloguembelina ototara*	63-150	N/A
485.05	41.24	0.18	-1.83	-1.07	-1.34	99.27	-2.02	19.30	16.54	20.36	24.21	*Chiloguembelina ototara*	63-150	N/A
486.76	41.29	0.01	-1.51	-1.07	-1.34	99.24	-1.70	17.78	15.17	19.03	22.80	*Chiloguembelina ototara*	63-150	N/A
488.21	41.33	0.11	-1.59	-1.07	-1.34	99.22	-1.78	18.16	15.48	19.37	23.19	*Chiloguembelina ototara*	63-150	N/A

Depth (mbsf)	Age (Ma) GTS2012	$\delta^{13}C$ (‰ VPDB)	$\delta^{18}O$ (‰ VPDB)	$\delta^{18}O_{sw}$ (‰ VSMOW)	$\delta^{18}O_{sw}$ (‰ VPDB)	$[CO_3^{2-}]$ (µmol kg^{-1})	$\delta^{18}O_c$'	SST - Equation 1 (°C)	SST - Bayfox (°C)			Species	Size fraction (µm)	MECO interval
									0.05	0.50	0.95			
424.70	39.35	1.39	-1.32	-1.07	-1.34	101.22	-1.51	16.88	14.32	18.19	22.04	*Globigerinatheka index*	150-300	N/A
445.72	39.94	1.80	-2.01	-1.07	-1.34	100.02	-2.20	20.15	17.29	21.11	24.99	*Globoturborotalita cf. ouachitaensis*	150-300	Post
447.57	39.99	1.12	-1.93	-1.07	-1.34	99.92	-2.12	19.77	16.92	20.79	24.60	*Globoturborotalita cf. ouachitaensis*	150-300	Post
449.33	40.04	0.82	-1.95	-1.07	-1.34	99.88	-2.14	19.87	16.98	20.84	24.77	*Globoturborotalita cf. ouachitaensis*	150-300	Post
436.08	39.67	0.25	-3.56	-1.07	-1.34	100.57	-3.75	27.79	23.95	27.81	31.65	*Pseudohastigerina micra*	63-150	N/A
439.15	39.75	0.21	-3.19	-1.07	-1.34	100.40	-3.38	25.93	22.38	26.17	30.06	*Pseudohastigerina micra*	63-150	N/A
442.97	39.86	0.43	-2.90	-1.07	-1.34	100.18	-3.09	24.49	21.01	24.94	28.77	*Pseudohastigerina micra*	63-150	Post
445.72	39.94	0.04	-3.25	-1.07	-1.34	100.02	-3.44	26.24	22.54	26.37	30.23	*Pseudohastigerina micra*	63-150	Post
456.80	40.28	-0.12	-3.09	-1.07	-1.34	99.76	-3.28	25.44	21.90	25.79	29.58	*Pseudohastigerina micra*	63-150	Onset
457.55	40.30	0.25	-2.85	-1.07	-1.34	99.75	-3.04	24.25	20.89	24.70	28.58	*Pseudohastigerina micra*	63-150	Pre
460.55	40.41	0.18	-3.67	-1.07	-1.34	99.69	-3.86	28.36	24.38	28.25	32.02	*Pseudohastigerina micra*	63-150	Pre
463.76	40.52	0.41	-3.70	-1.07	-1.34	99.64	-3.89	28.52	24.53	28.33	32.23	*Pseudohastigerina micra*	63-150	Pre
467.25	40.64	0.68	-3.38	-1.07	-1.34	99.57	-3.57	26.89	23.20	26.99	30.85	*Pseudohastigerina micra*	63-150	N/A
468.83	40.69	0.10	-2.64	-1.07	-1.34	99.55	-2.83	23.21	20.01	23.84	27.63	*Pseudohastigerina micra*	63-150	N/A
472.53	40.82	0.39	-3.41	-1.07	-1.34	99.48	-3.60	27.05	23.33	27.11	30.95	*Pseudohastigerina micra*	63-150	N/A
474.58	40.89	0.01	-3.44	-1.07	-1.34	99.44	-3.63	27.20	23.35	27.24	31.11	*Pseudohastigerina micra*	63-150	N/A
476.16	40.95	0.58	-3.12	-1.07	-1.34	99.42	-3.31	25.59	22.05	25.91	29.70	*Pseudohastigerina micra*	63-150	N/A
483.25	41.19	0.39	-3.42	-1.07	-1.34	99.30	-3.61	27.10	23.36	27.13	31.04	*Pseudohastigerina micra*	63-150	N/A
485.05	41.24	0.25	-3.31	-1.07	-1.34	99.27	-3.50	26.54	22.90	26.75	30.57	*Pseudohastigerina micra*	63-150	N/A
479.62	41.07	1.16	-1.98	-1.07	-1.34	99.36	-2.17	20.01	17.08	21.01	24.82	*Turborotalia pomeroli*	150-300	N/A

Supplementary Table 4.1.2: ODP Site 702

Depth (mbsf)	Age (Ma) GTS2012	$\delta^{13}C$ (‰ VPDB)	$\delta^{18}O$ (‰ VPDB)	$\delta^{18}O_{sw}$ (‰ VSMOW)	$\delta^{18}O_{sw}$ (‰ VPDB)	$[CO_3^{2-}]$ (µmol kg^{-1})	$\delta^{18}O_c$'	SST - Equation 1 (°C)	SST - Bayfox (°C)			Species	Size fraction (µm)	MECO interval
									0.05	0.50	0.95			
66.33	39.92	3.63	0.16	-0.91	-1.18	100.06	-0.03	10.89	8.79	12.56	16.38	*Globigerinatheka index*	250-300	Post
70.53	40.09	2.57	-0.09	-0.91	-1.18	99.85	-0.28	12.00	9.72	13.59	17.42	*Globigerinatheka index*	250-300	Post
71.03	40.11	2.99	0.65	-0.91	-1.18	99.84	0.46	8.74	6.59	10.45	14.31	*Globigerinatheka index*	250-300	Peak
71.72	40.14	2.55	0.10	-0.91	-1.18	99.83	-0.09	11.16	8.89	12.79	16.58	*Globigerinatheka index*	250-300	Peak
73.21	40.25	2.55	0.17	-0.91	-1.18	99.77	-0.02	10.85	8.60	12.51	16.39	*Globigerinatheka index*	250-300	Onset
77.54	40.61	3.03	0.03	-0.91	-1.18	99.59	-0.16	11.47	9.23	13.07	17.00	*Globigerinatheka index*	250-300	Pre
80.13	40.82	2.08	0.67	-0.91	-1.18	99.48	0.48	8.65	6.53	10.41	14.27	*Globigerinatheka index*	250-300	N/A

Supplementary Table 4.1.3: ODP Site 748

Depth (mbsf)	Age (Ma) GTS2012	$\delta^{13}C$ (‰ VPDB)	$\delta^{18}O$ (‰ VPDB)	$\delta^{18}O_{sw}$ (‰ VSMOW)	$\delta^{18}O_{sw}$ (‰ VPDB)	$[CO_3^{2-}]$ (µmol kg^{-1})	$\delta^{18}O_c$'	SST - Equation 1 (°C)	SST - Bayfox (°C)			Species	Size fraction (µm)	MECO interval
									0.05	0.50	0.95			
161.33	39.45	2.39	0.07	-0.91	-1.18	101.02	-0.12	11.28	9.08	12.95	16.74	*Acarinina primitiva*	150-180	N/A
161.33	39.45	2.55	0.00	-0.91	-1.18	101.02	-0.19	11.59	9.37	13.24	17.14	*Acarinina primitiva*	180-212	N/A
161.33	39.45	2.84	0.01	-0.91	-1.18	101.02	-0.18	11.55	9.33	13.21	17.04	*Acarinina primitiva*	212-250	N/A
161.33	39.45	3.19	-0.02	-0.91	-1.18	101.02	-0.21	11.68	9.49	13.37	17.23	*Acarinina primitiva*	250-300	N/A
161.33	39.45	3.01	-0.12	-0.91	-1.18	101.02	-0.31	12.13	9.96	13.75	17.55	*Acarinina primitiva*	300-355	N/A
161.42	39.45	2.21	-0.03	-0.91	-1.18	101.00	-0.22	11.72	9.49	13.34	17.27	*Acarinina primitiva*	150-180	N/A
161.42	39.45	2.33	-0.07	-0.91	-1.18	101.00	-0.26	11.90	9.63	13.51	17.40	*Acarinina primitiva*	150-180	N/A
161.42	39.45	2.58	-0.08	-0.91	-1.18	101.00	-0.27	11.95	9.71	13.56	17.45	*Acarinina primitiva*	150-180	N/A
161.42	39.45	2.47	0.19	-0.91	-1.18	101.00	0.00	10.75	8.58	12.37	16.29	*Acarinina primitiva*	180-212	N/A
161.42	39.45	2.46	0.07	-0.91	-1.18	101.00	-0.12	11.28	9.14	12.92	16.69	*Acarinina primitiva*	180-212	N/A
161.42	39.45	2.52	-0.14	-0.91	-1.18	101.00	-0.33	12.22	9.89	13.84	17.70	*Acarinina primitiva*	180-212	N/A
161.42	39.45	2.65	-0.01	-0.91	-1.18	101.00	-0.20	11.64	9.42	13.29	17.10	*Acarinina primitiva*	180-212	N/A

Depth (mbsf)	Age (Ma) GTS2012	$\delta^{13}C$ (‰ VPDB)	$\delta^{18}O$ (‰ VPDB)	$\delta^{18}O_{sw}$ (‰ VSMOW)	$\delta^{18}O_{sw}$ (‰ VPDB)	$[CO_3^{2-}]$ (µmol kg^{-1})	$\delta^{18}O_c$'	SST - Equation 1 (°C)	SST - Bayfox (°C)			Species	Size fraction (µm)	MECO interval
									0.05	0.50	0.95			
161.42	39.45	2.63	-0.11	-0.91	-1.18	101.00	-0.30	12.08	9.96	13.71	17.62	*Acarinina primitiva*	180-212	N/A
161.42	39.45	2.81	-0.06	-0.91	-1.18	101.00	-0.25	11.86	9.64	13.42	17.29	*Acarinina primitiva*	212-250	N/A
161.42	39.45	2.97	-0.19	-0.91	-1.18	101.00	-0.38	12.44	10.08	14.02	17.88	*Acarinina primitiva*	212-250	N/A
161.42	39.45	2.88	-0.24	-0.91	-1.18	101.00	-0.43	12.67	10.43	14.26	18.08	*Acarinina primitiva*	212-250	N/A
161.42	39.45	2.66	-0.10	-0.91	-1.18	101.00	-0.29	12.04	9.89	13.66	17.55	*Acarinina primitiva*	212-250	N/A
161.42	39.45	2.79	0.07	-0.91	-1.18	101.00	-0.12	11.28	9.08	12.96	16.80	*Acarinina primitiva*	250-300	N/A
161.42	39.45	2.86	0.10	-0.91	-1.18	101.00	-0.09	11.15	8.95	12.82	16.64	*Acarinina primitiva*	250-300	N/A
161.42	39.45	3.07	-0.05	-0.91	-1.18	101.00	-0.24	11.81	9.63	13.40	17.32	*Acarinina primitiva*	250-300	N/A
164.37	40.06	1.86	-0.65	-0.91	-1.18	99.87	-0.84	14.54	12.18	15.99	19.84	*Acarinina primitiva*	150-180	Peak
164.37	40.06	1.94	-0.52	-0.91	-1.18	99.87	-0.71	13.94	11.60	15.49	19.38	*Acarinina primitiva*	180-212	Peak
164.37	40.06	1.95	-0.41	-0.91	-1.18	99.87	-0.60	13.44	11.11	14.99	18.77	*Acarinina primitiva*	212-250	Peak
164.37	40.06	2.25	-0.38	-0.91	-1.18	99.87	-0.57	13.31	10.96	14.90	18.77	*Acarinina primitiva*	250-300	Peak
164.37	40.06	2.10	-0.26	-0.91	-1.18	99.87	-0.45	12.77	10.48	14.40	18.27	*Acarinina primitiva*	300-355	Peak
164.91	40.10	1.80	-0.38	-0.91	-1.18	99.85	-0.57	13.31	10.99	14.83	18.65	*Acarinina primitiva*	150-180	Onset
164.91	40.10	1.90	-0.47	-0.91	-1.18	99.85	-0.66	13.72	11.41	15.26	19.07	*Acarinina primitiva*	180-212	Onset
164.91	40.10	1.81	-0.59	-0.91	-1.18	99.85	-0.78	14.26	11.87	15.78	19.58	*Acarinina primitiva*	212-250	Onset
164.91	40.10	1.92	-0.42	-0.91	-1.18	99.85	-0.61	13.49	11.21	15.05	18.85	*Acarinina primitiva*	250-300	Onset
164.91	40.10	2.07	-0.40	-0.91	-1.18	99.85	-0.59	13.40	11.08	14.94	18.80	*Acarinina primitiva*	300-355	Onset
165.63	40.15	2.08	-0.50	-0.91	-1.18	99.83	-0.69	13.85	11.49	15.32	19.29	*Acarinina primitiva*	125-150	Onset
165.63	40.15	2.21	-0.63	-0.91	-1.18	99.83	-0.82	14.45	12.12	15.91	19.68	*Acarinina primitiva*	150-180	Onset
165.63	40.15	2.10	-0.34	-0.91	-1.18	99.83	-0.53	13.13	10.83	14.71	18.57	*Acarinina primitiva*	180-212	Onset
165.63	40.15	1.93	-0.18	-0.91	-1.18	99.83	-0.37	12.41	10.21	13.99	17.94	*Acarinina primitiva*	212-250	Onset
165.63	40.15	1.86	-0.15	-0.91	-1.18	99.83	-0.34	12.27	10.06	13.86	17.75	*Acarinina primitiva*	250-300	Onset
165.63	40.15	2.11	-0.14	-0.91	-1.18	99.83	-0.33	12.23	10.02	13.87	17.66	*Acarinina primitiva*	300-355	Onset
167.13	40.24	1.99	-0.16	-0.91	-1.18	99.78	-0.35	12.32	10.16	13.90	17.75	*Acarinina primitiva*	125-150	Onset

Depth (mbsf)	Age (Ma) GTS2012	$\delta^{13}C$ (‰ VPDB)	$\delta^{18}O$ (‰ VPDB)	$\delta^{18}O_{sw}$ (‰ VSMOW)	$\delta^{18}O_{sw}$ (‰ VPDB)	$[CO_3^{2-}]$ (µmol kg^{-1})	$\delta^{18}O_c$'	SST - Equation 1 (°C)	SST - Bayfox (°C)			Species	Size fraction (µm)	MECO interval
									0.05	0.50	0.95			
167.13	40.24	1.84	0.23	-0.91	-1.18	99.78	0.04	10.58	8.45	12.25	16.00	*Acarinina primitiva*	150-180	Onset
167.13	40.24	1.78	0.10	-0.91	-1.18	99.78	-0.09	11.16	8.92	12.80	16.67	*Acarinina primitiva*	180-212	Onset
167.13	40.24	1.89	0.04	-0.91	-1.18	99.78	-0.15	11.42	9.21	13.07	17.03	*Acarinina primitiva*	250-300	Onset
167.13	40.24	2.27	0.24	-0.91	-1.18	99.78	0.05	10.54	8.38	12.14	16.08	*Acarinina primitiva*	300-355	Onset
168.31	40.30	1.75	0.14	-0.91	-1.18	99.75	-0.05	10.98	8.83	12.63	16.56	*Acarinina primitiva*	150-180	Onset
168.31	40.30	1.90	0.00	-0.91	-1.18	99.75	-0.19	11.60	9.31	13.25	17.08	*Acarinina primitiva*	180-212	Onset
168.31	40.30	1.94	0.07	-0.91	-1.18	99.75	-0.12	11.29	9.10	12.92	16.88	*Acarinina primitiva*	212-250	Onset
168.31	40.30	1.94	0.11	-0.91	-1.18	99.75	-0.08	11.11	8.84	12.81	16.64	*Acarinina primitiva*	250-300	Onset
168.31	40.30	2.04	0.12	-0.91	-1.18	99.75	-0.07	11.07	8.89	12.74	16.60	*Acarinina primitiva*	300-355	Onset
169.65	40.37	1.72	0.19	-0.91	-1.18	99.71	0.00	10.76	8.54	12.41	16.27	*Acarinina primitiva*	125-150	Onset
169.65	40.37	1.62	0.09	-0.91	-1.18	99.71	-0.10	11.20	9.01	12.87	16.68	*Acarinina primitiva*	150-180	Onset
169.65	40.37	1.95	-0.29	-0.91	-1.18	99.71	-0.48	12.90	10.50	14.49	18.31	*Acarinina primitiva*	180-212	Onset
169.65	40.37	1.79	0.08	-0.91	-1.18	99.71	-0.11	11.25	9.07	12.90	16.69	*Acarinina primitiva*	212-250	Onset
169.65	40.37	2.06	0.03	-0.91	-1.18	99.71	-0.16	11.47	9.21	13.15	17.06	*Acarinina primitiva*	300-355	Onset
169.65	40.37	2.03	0.11	-0.91	-1.18	99.71	-0.08	11.11	8.91	12.73	16.66	*Acarinina primitiva*	250-300	Onset
171.26	41.29	1.37	-0.14	-0.91	-1.18	99.24	-0.33	12.23	9.96	13.84	17.71	*Acarinina primitiva*	150-180	N/A
171.26	41.29	1.46	0.29	-0.91	-1.18	99.24	0.10	10.32	8.15	11.95	15.79	*Acarinina primitiva*	180-212	N/A
171.26	41.29	1.63	0.25	-0.91	-1.18	99.24	0.06	10.50	8.28	12.21	15.97	*Acarinina primitiva*	212-250	N/A
171.26	41.29	1.85	0.22	-0.91	-1.18	99.24	0.03	10.63	8.43	12.31	16.17	*Acarinina primitiva*	250-300	N/A
171.26	41.29	1.93	0.42	-0.91	-1.18	99.24	0.23	9.75	7.66	11.52	15.34	*Acarinina primitiva*	300-355	N/A
174.86	41.63	0.79	-0.44	-0.91	-1.18	99.07	-0.63	13.59	11.44	15.13	18.89	*Acarinina primitiva*	150-180	N/A
174.86	41.63	0.85	-0.26	-0.91	-1.18	99.07	-0.45	12.77	10.51	14.34	18.19	*Acarinina primitiva*	180-212	N/A
174.86	41.63	0.92	-0.33	-0.91	-1.18	99.07	-0.52	13.09	10.78	14.70	18.52	*Acarinina primitiva*	180-212	N/A
174.86	41.63	0.92	-0.27	-0.91	-1.18	99.07	-0.46	12.82	10.56	14.41	18.21	*Acarinina primitiva*	212-250	N/A
174.86	41.63	1.11	-0.21	-0.91	-1.18	99.07	-0.40	12.55	10.28	14.14	17.97	*Acarinina primitiva*	212-250	N/A

Depth (mbsf)	Age (Ma) GTS2012	$\delta^{13}C$ (‰ VPDB)	$\delta^{18}O$ (‰ VPDB)	$\delta^{18}O_{sw}$ (‰ VSMOW)	$\delta^{18}O_{sw}$ (‰ VPDB)	$[CO_3^{2-}]$ (µmol kg^{-1})	$\delta^{18}O_c$'	SST - Equation 1 (°C)	SST - Bayfox (°C)			Species	Size fraction (µm)	MECO interval
									0.05	0.50	0.95			
174.86	41.63	1.57	-0.32	-0.91	-1.18	99.07	-0.51	13.04	10.75	14.65	18.50	*Acarinina primitiva*	300-355	N/A
174.86	41.63	1.25	-0.32	-0.91	-1.18	99.07	-0.51	13.04	10.74	14.61	18.46	*Acarinina primitiva*	250-300	N/A
161.33	39.45	3.18	0.16	-0.91	-1.18	101.02	-0.03	10.88	8.71	12.51	16.38	*Globigerinatheka index*	>425	N/A
161.33	39.45	2.33	0.22	-0.91	-1.18	101.02	0.03	10.61	8.37	12.31	16.15	*Globigerinatheka index*	150-180	N/A
161.33	39.45	2.55	0.28	-0.91	-1.18	101.02	0.09	10.35	8.17	12.02	15.92	*Globigerinatheka index*	180-212	N/A
161.33	39.45	2.66	0.22	-0.91	-1.18	101.02	0.03	10.61	8.41	12.21	16.05	*Globigerinatheka index*	212-250	N/A
161.33	39.45	2.77	0.40	-0.91	-1.18	101.02	0.21	9.82	7.65	11.54	15.37	*Globigerinatheka index*	250-300	N/A
161.33	39.45	2.91	0.42	-0.91	-1.18	101.02	0.23	9.73	7.48	11.44	15.35	*Globigerinatheka index*	300-355	N/A
161.33	39.45	2.98	0.44	-0.91	-1.18	101.02	0.25	9.64	7.49	11.36	15.10	*Globigerinatheka index*	355-425	N/A
161.42	39.45	2.08	0.30	-0.91	-1.18	101.00	0.11	10.26	8.06	11.94	15.73	*Globigerinatheka index*	150-180	N/A
161.42	39.45	2.25	0.13	-0.91	-1.18	101.00	-0.06	11.01	8.82	12.71	16.52	*Globigerinatheka index*	150-180	N/A
161.42	39.45	2.41	0.01	-0.91	-1.18	101.00	-0.18	11.55	9.28	13.16	17.11	*Globigerinatheka index*	150-180	N/A
161.42	39.45	2.42	0.17	-0.91	-1.18	101.00	-0.02	10.83	8.58	12.49	16.31	*Globigerinatheka index*	180-212	N/A
161.42	39.45	2.47	0.12	-0.91	-1.18	101.00	-0.07	11.06	8.90	12.68	16.54	*Globigerinatheka index*	180-212	N/A
161.42	39.45	2.44	0.04	-0.91	-1.18	101.00	-0.15	11.41	9.20	13.09	16.98	*Globigerinatheka index*	180-212	N/A
161.42	39.45	2.34	0.40	-0.91	-1.18	101.00	0.21	9.82	7.67	11.45	15.35	*Globigerinatheka index*	212-250	N/A
161.42	39.45	2.54	0.23	-0.91	-1.18	101.00	0.04	10.57	8.36	12.30	16.22	*Globigerinatheka index*	212-250	N/A
161.42	39.45	2.63	0.20	-0.91	-1.18	101.00	0.01	10.70	8.58	12.36	16.20	*Globigerinatheka index*	212-250	N/A
161.42	39.45	2.73	0.36	-0.91	-1.18	101.00	0.17	10.00	7.83	11.70	15.57	*Globigerinatheka index*	250-300	N/A
161.42	39.45	2.73	0.19	-0.91	-1.18	101.00	0.00	10.75	8.48	12.43	16.29	*Globigerinatheka index*	250-300	N/A
161.42	39.45	2.61	0.35	-0.91	-1.18	101.00	0.16	10.04	7.92	11.74	15.58	*Globigerinatheka index*	250-300	N/A
161.42	39.45	2.73	0.31	-0.91	-1.18	101.00	0.12	10.22	8.09	11.88	15.75	*Globigerinatheka index*	300-355	N/A
161.42	39.45	2.77	0.39	-0.91	-1.18	101.00	0.20	9.86	7.79	11.49	15.32	*Globigerinatheka index*	300-355	N/A
161.42	39.45	2.94	0.29	-0.91	-1.18	101.00	0.10	10.30	8.09	12.00	15.89	*Globigerinatheka index*	300-355	N/A

Depth (mbsf)	Age (Ma) GTS2012	$\delta^{13}C$ (‰ VPDB)	$\delta^{18}O$ (‰ VPDB)	$\delta^{18}O_{sw}$ (‰ VSMOW)	$\delta^{18}O_{sw}$ (‰ VPDB)	$[CO_3^{2-}]$ (µmol kg^{-1})	$\delta^{18}O_c$'	SST - Equation 1 (°C)	SST - Bayfox (°C)			Species	Size fraction (µm)	MECO interval
									0.05	0.50	0.95			
161.42	39.45	2.70	0.34	-0.91	-1.18	101.00	0.15	10.08	7.98	11.82	15.53	*Globigerinatheka index*	300-355	N/A
161.42	39.45	2.74	0.38	-0.91	-1.18	101.00	0.19	9.91	7.80	11.65	15.46	*Globigerinatheka index*	355-425	N/A
161.42	39.45	2.97	0.25	-0.91	-1.18	101.00	0.06	10.48	8.38	12.21	16.14	*Globigerinatheka index*	355-425	N/A
161.42	39.45	2.85	0.30	-0.91	-1.18	101.00	0.11	10.26	8.14	11.99	15.86	*Globigerinatheka index*	355-425	N/A
164.37	40.06	1.40	-0.43	-0.91	-1.18	99.87	-0.62	13.54	11.21	15.08	19.03	*Globigerinatheka index*	150-180	Peak
164.37	40.06	1.85	-0.23	-0.91	-1.18	99.87	-0.42	12.63	10.28	14.19	18.06	*Globigerinatheka index*	180-212	Peak
164.37	40.06	1.92	-0.34	-0.91	-1.18	99.87	-0.53	13.13	10.91	14.72	18.47	*Globigerinatheka index*	212-250	Peak
164.37	40.06	1.78	-0.32	-0.91	-1.18	99.87	-0.51	13.04	10.67	14.56	18.47	*Globigerinatheka index*	250-300	Peak
164.37	40.06	1.94	-0.38	-0.91	-1.18	99.87	-0.57	13.31	11.07	14.86	18.73	*Globigerinatheka index*	300-355	Peak
164.37	40.06	2.17	-0.32	-0.91	-1.18	99.87	-0.51	13.04	10.72	14.65	18.51	*Globigerinatheka index*	300-355	Peak
164.37	40.06	1.99	-0.38	-0.91	-1.18	99.87	-0.57	13.31	11.03	14.87	18.70	*Globigerinatheka index*	355-400	Peak
164.37	40.06	1.98	-0.27	-0.91	-1.18	99.87	-0.46	12.81	10.58	14.32	18.15	*Globigerinatheka index*	355-425	Peak
164.91	40.10	2.24	-0.33	-0.91	-1.18	99.85	-0.52	13.08	10.80	14.63	18.49	*Globigerinatheka index*	>400	Onset
164.91	40.10	1.49	-0.20	-0.91	-1.18	99.85	-0.39	12.50	10.17	14.07	17.98	*Globigerinatheka index*	125-150	Onset
164.91	40.10	1.76	-0.19	-0.91	-1.18	99.85	-0.38	12.45	10.23	14.07	18.01	*Globigerinatheka index*	150-180	Onset
164.91	40.10	1.87	-0.40	-0.91	-1.18	99.85	-0.59	13.40	11.11	14.94	18.74	*Globigerinatheka index*	180-212	Onset
164.91	40.10	1.76	-0.30	-0.91	-1.18	99.85	-0.49	12.95	10.67	14.53	18.41	*Globigerinatheka index*	212-250	Onset
164.91	40.10	1.79	-0.35	-0.91	-1.18	99.85	-0.54	13.17	10.96	14.70	18.52	*Globigerinatheka index*	250-300	Onset
164.91	40.10	1.83	-0.36	-0.91	-1.18	99.85	-0.55	13.22	10.98	14.77	18.66	*Globigerinatheka index*	300-355	Onset
164.91	40.10	2.02	-0.40	-0.91	-1.18	99.85	-0.59	13.40	11.08	14.95	18.70	*Globigerinatheka index*	355-400	Onset
171.26	41.29	1.38	0.23	-0.91	-1.18	99.24	0.04	10.58	8.40	12.27	16.12	*Globigerinatheka index*	150-180	N/A
171.26	41.29	1.80	0.16	-0.91	-1.18	99.24	-0.03	10.89	8.63	12.59	16.40	*Globigerinatheka index*	180-212	N/A
171.26	41.29	1.90	0.15	-0.91	-1.18	99.24	-0.04	10.94	8.74	12.59	16.44	*Globigerinatheka index*	212-250	N/A
171.26	41.29	2.23	0.05	-0.91	-1.18	99.24	-0.14	11.38	9.14	13.02	16.90	*Globigerinatheka index*	250-300	N/A
171.26	41.29	2.46	-0.06	-0.91	-1.18	99.24	-0.25	11.87	9.55	13.50	17.28	*Globigerinatheka index*	300-355	N/A

Depth (mbsf)	Age (Ma) GTS2012	$\delta^{13}C$ (‰ VPDB)	$\delta^{18}O$ (‰ VPDB)	$\delta^{18}O_{sw}$ (‰ VSMOW)	$\delta^{18}O_{sw}$ (‰ VPDB)	$[CO_3^{2-}]$ (µmol kg^{-1})	$\delta^{18}O_c$'	SST - Equation 1 (°C)	SST - Bayfox (°C)			Species	Size fraction (µm)	MECO interval
									0.05	0.50	0.95			
171.26	41.29	2.52	0.12	-0.91	-1.18	99.24	-0.07	11.07	8.97	12.76	16.68	*Globigerinatheka index*	355-400	N/A
174.86	41.63	0.81	-0.31	-0.91	-1.18	99.07	-0.50	13.00	10.74	14.60	18.44	*Globigerinatheka index*	150-180	N/A
174.86	41.63	1.14	-0.31	-0.91	-1.18	99.07	-0.50	13.00	10.67	14.51	18.39	*Globigerinatheka index*	180-212	N/A
174.86	41.63	1.17	-0.28	-0.91	-1.18	99.07	-0.47	12.86	10.61	14.46	18.35	*Globigerinatheka index*	212-250	N/A
174.86	41.63	1.37	-0.35	-0.91	-1.18	99.07	-0.54	13.18	10.86	14.76	18.55	*Globigerinatheka index*	250-300	N/A
174.86	41.63	1.39	-0.36	-0.91	-1.18	99.07	-0.55	13.23	10.97	14.75	18.58	*Globigerinatheka index*	300-355	N/A
174.86	41.63	1.60	-0.38	-0.91	-1.18	99.07	-0.57	13.32	10.98	14.87	18.76	*Globigerinatheka index*	355-400	N/A
161.33	39.45	1.74	0.54	-0.91	-1.18	101.02	0.35	9.21	7.02	10.91	14.78	*Subbotina spp.*	150-180	N/A
161.33	39.45	1.81	0.66	-0.91	-1.18	101.02	0.47	8.68	6.50	10.35	14.25	*Subbotina spp.*	180-212	N/A
161.33	39.45	1.82	0.81	-0.91	-1.18	101.02	0.62	8.04	5.96	9.78	13.61	*Subbotina spp.*	212-250	N/A
161.33	39.45	1.88	0.79	-0.91	-1.18	101.02	0.60	8.12	5.94	9.82	13.64	*Subbotina spp.*	250-300	N/A
161.33	39.45	1.87	0.75	-0.91	-1.18	101.02	0.56	8.29	6.16	9.99	13.88	*Subbotina spp.*	300-355	N/A
161.33	39.45	1.88	0.77	-0.91	-1.18	101.02	0.58	8.21	6.18	9.94	13.80	*Subbotina spp.*	355-425	N/A
161.42	39.45	1.54	0.39	-0.91	-1.18	101.00	0.20	9.86	7.70	11.58	15.41	*Subbotina spp.*	150-180	N/A
161.42	39.45	1.59	0.46	-0.91	-1.18	101.00	0.27	9.56	7.37	11.21	15.14	*Subbotina spp.*	150-180	N/A
161.42	39.45	1.47	0.64	-0.91	-1.18	101.00	0.45	8.77	6.72	10.49	14.43	*Subbotina spp.*	180-212	N/A
161.42	39.45	1.67	0.54	-0.91	-1.18	101.00	0.35	9.21	7.09	10.92	14.85	*Subbotina spp.*	180-212	N/A
161.42	39.45	1.69	0.50	-0.91	-1.18	101.00	0.31	9.38	7.26	11.07	14.95	*Subbotina spp.*	180-212	N/A
161.42	39.45	1.53	0.65	-0.91	-1.18	101.00	0.46	8.73	6.62	10.44	14.26	*Subbotina spp.*	180-212	N/A
161.42	39.45	1.69	0.65	-0.91	-1.18	101.00	0.46	8.73	6.56	10.47	14.30	*Subbotina spp.*	212-250	N/A
161.42	39.45	1.69	0.67	-0.91	-1.18	101.00	0.48	8.64	6.45	10.33	14.19	*Subbotina spp.*	212-250	N/A
161.42	39.45	1.70	0.65	-0.91	-1.18	101.00	0.46	8.73	6.64	10.50	14.38	*Subbotina spp.*	212-250	N/A
161.42	39.45	1.67	0.63	-0.91	-1.18	101.00	0.44	8.82	6.71	10.52	14.33	*Subbotina spp.*	250-300	N/A
161.42	39.45	1.69	0.69	-0.91	-1.18	101.00	0.50	8.55	6.43	10.29	14.18	*Subbotina spp.*	250-300	N/A

Depth (mbsf)	Age (Ma) GTS2012	$\delta^{13}C$ (‰ VPDB)	$\delta^{18}O$ (‰ VPDB)	$\delta^{18}O_{sw}$ (‰ VSMOW)	$\delta^{18}O_{sw}$ (‰ VPDB)	$[CO_3^{2-}]$ (µmol kg^{-1})	$\delta^{18}O_c$'	SST - Equation 1 (°C)	SST - Bayfox (°C)			Species	Size fraction (µm)	MECO interval
									0.05	0.50	0.95			
161.42	39.45	1.75	0.67	-0.91	-1.18	101.00	0.48	8.64	6.45	10.39	14.25	*Subbotina spp.*	250-300	N/A
164.37	40.06	1.25	-0.24	-0.91	-1.18	99.87	-0.43	12.68	10.42	14.26	18.10	*Subbotina spp.*	150-180	Peak
164.37	40.06	1.20	-0.18	-0.91	-1.18	99.87	-0.37	12.41	10.20	14.02	17.88	*Subbotina spp.*	180-212	Peak
164.37	40.06	1.28	-0.16	-0.91	-1.18	99.87	-0.35	12.32	10.06	13.96	17.82	*Subbotina spp.*	212-250	Peak
164.37	40.06	1.10	-0.32	-0.91	-1.18	99.87	-0.51	13.04	10.77	14.62	18.44	*Subbotina spp.*	250-300	Peak
164.37	40.06	1.00	-0.21	-0.91	-1.18	99.87	-0.40	12.54	10.27	14.12	17.93	*Subbotina spp.*	300-355	Peak
164.91	40.10	1.27	-0.13	-0.91	-1.18	99.85	-0.32	12.18	10.01	13.81	17.69	*Subbotina spp.*	150-180	Onset
164.91	40.10	1.31	0.00	-0.91	-1.18	99.85	-0.19	11.60	9.33	13.24	17.07	*Subbotina spp.*	180-212	Onset
164.91	40.10	1.18	0.12	-0.91	-1.18	99.85	-0.07	11.07	8.87	12.75	16.64	*Subbotina spp.*	212-250	Onset
164.91	40.10	1.22	-0.03	-0.91	-1.18	99.85	-0.22	11.73	9.61	13.36	17.13	*Subbotina spp.*	250-300	Onset
164.91	40.10	1.12	-0.14	-0.91	-1.18	99.85	-0.33	12.23	10.01	13.79	17.71	*Subbotina spp.*	300-355	Onset
171.26	41.29	0.95	0.39	-0.91	-1.18	99.24	0.20	9.88	7.78	11.57	15.44	*Subbotina spp.*	150-180	N/A
171.26	41.29	1.20	0.50	-0.91	-1.18	99.24	0.31	9.40	7.31	11.10	14.94	*Subbotina spp.*	180-212	N/A
171.26	41.29	1.16	0.39	-0.91	-1.18	99.24	0.20	9.88	7.75	11.60	15.47	*Subbotina spp.*	212-250	N/A
171.26	41.29	1.25	0.40	-0.91	-1.18	99.24	0.21	9.84	7.71	11.53	15.48	*Subbotina spp.*	250-300	N/A
171.26	41.29	1.15	0.53	-0.91	-1.18	99.24	0.34	9.27	7.15	11.01	14.87	*Subbotina spp.*	300-355	N/A
174.86	41.63	0.68	0.02	-0.91	-1.18	99.07	-0.17	11.52	9.24	13.14	16.98	*Subbotina spp.*	150-180	N/A
174.86	41.63	0.54	-0.05	-0.91	-1.18	99.07	-0.24	11.83	9.67	13.43	17.22	*Subbotina spp.*	180-212	N/A
174.86	41.63	0.50	-0.08	-0.91	-1.18	99.07	-0.27	11.96	9.76	13.59	17.48	*Subbotina spp.*	212-250	N/A
174.86	41.63	0.56	-0.03	-0.91	-1.18	99.07	-0.22	11.74	9.57	13.43	17.30	*Subbotina spp.*	250-300	N/A
174.86	41.63	0.33	-0.01	-0.91	-1.18	99.07	-0.20	11.65	9.36	13.33	17.19	*Subbotina spp.*	300-355	N/A

Supplementary Table 4.1.4: ODP Site 865

Depth (amcd)	Age (Ma) GTS2012	$\delta^{13}C$ (‰ VPDB)	$\delta^{18}O$ (‰ VPDB)	$\delta^{18}O_{sw}$ (‰ VSMOW)	$\delta^{18}O_{sw}$ (‰ VPDB)	$[CO_3^{2-}]$ (µmol kg^{-1})	$\delta^{18}O_c$'	SST - Equation 1 (°C)	SST - Bayfox (°C)			Species	Size fraction (µm)	MECO interval
									0.05	0.50	0.95			
29.00	39.12	3.32	-0.43	-0.33	-0.60	101.67	-0.62	16.18	13.69	17.50	21.31	*Acarinina praetopilensis*	250-300	N/A
33.68	39.96	3.46	-0.44	-0.33	-0.60	99.98	-0.63	16.24	13.69	17.59	21.48	*Acarinina praetopilensis*	250-300	Post
34.19	40.00													
34.59	40.03	3.49	-0.33	-0.33	-0.60	99.88	-0.52	15.74	13.22	17.13	21.04	*Acarinina praetopilensis*	250-300	Post
34.89	40.09	3.34	-0.41	-0.33	-0.60	99.85	-0.60	16.11	13.58	17.52	21.32	*Acarinina praetopilensis*	250-300	Post
35.08	40.14	2.76	-0.38	-0.33	-0.60	99.83	-0.57	15.97	13.44	17.30	21.12	*Acarinina praetopilensis*	250-300	Post
35.17	40.17	3.16	-0.71	-0.33	-0.60	99.81	-0.90	17.51	14.89	18.73	22.54	*Acarinina praetopilensis*	250-300	Peak
35.42	40.24	3.30	-0.89	-0.33	-0.60	99.78	-1.08	18.35	15.59	19.52	23.37	*Acarinina praetopilensis*	250-300	Peak
35.63	40.31													
35.87	40.38	3.26	-0.72	-0.33	-0.60	99.71	-0.91	17.55	14.96	18.78	22.62	*Acarinina praetopilensis*	250-300	Onset
36.36	40.52	3.20	-0.63	-0.33	-0.60	99.64	-0.82	17.13	14.52	18.36	22.30	*Acarinina praetopilensis*	250-300	Pre
36.77	40.63	3.24	-0.78	-0.33	-0.60	99.58	-0.97	17.84	15.21	19.05	22.87	*Acarinina praetopilensis*	250-300	Pre
37.57	40.81	3.30	-0.50	-0.33	-0.60	99.49	-0.69	16.53	13.98	17.85	21.64	*Acarinina praetopilensis*	250-300	N/A
38.27	40.92	2.84	-0.42	-0.33	-0.60	99.43	-0.61	16.16	13.72	17.54	21.44	*Acarinina praetopilensis*	250-300	N/A
39.67	41.13	3.46	-0.26	-0.33	-0.60	99.32	-0.45	15.42	12.94	16.83	20.72	*Acarinina praetopilensis*	250-300	N/A
30.08	39.33	3.18	-0.40	-0.33	-0.60	101.26	-0.59	16.05	13.63	17.43	21.24	*Morozovelloides crassatus*	250-300	N/A
35.08	40.14	2.79	-0.56	-0.33	-0.60	99.83	-0.75	16.80	14.26	18.12	21.94	*Morozovelloides crassatus*	250-300	Post
42.14	41.53	2.94	-0.40	-0.33	-0.60	99.12	-0.59	16.07	13.53	17.38	21.23	*Morozovelloides crassatus*	250-300	N/A

Supplementary Table 4.1.5: ODP Site 1051

Depth (mbsf)	Age (Ma) GTS2012	$\delta^{13}C$ (‰ VPDB)	$\delta^{18}O$ (‰ VPDB)	$\delta^{18}O_{sw}$ (‰ VSMOW)	$\delta^{18}O_{sw}$ (‰ VPDB)	$[CO_3^{2-}]$ (µmol kg^{-1})	$\delta^{18}O_c$'	SST - Equation 1 (°C)	SST - Bayfox (°C)			Species	Size fraction (µm)	MECO interval
									0.05	0.50	0.95			
69.14	39.94	2.89	-0.92	-0.22	-0.49	100.02	-1.11	19.01	16.13	20.10	24.00	*Acarinina topilensis*	180-212	Post
69.14	39.94	2.87	-0.95	-0.22	-0.49	100.02	-1.14	19.13	16.36	20.22	24.08	*Acarinina topilensis*	212-250	Post
69.14	39.94	3.37	-1.05	-0.22	-0.49	100.02	-1.24	19.61	16.76	20.69	24.52	*Acarinina topilensis*	250-300	Post
69.14	39.94	3.70	-1.10	-0.22	-0.49	100.02	-1.29	19.89	17.07	20.89	24.79	*Acarinina topilensis*	300-355	Post
77.35	40.07	2.46	-0.71	-0.22	-0.49	99.86	-0.90	18.01	15.35	19.17	23.02	*Acarinina topilensis*	180-212	Peak
77.35	40.07	2.53	-0.88	-0.22	-0.49	99.86	-1.07	18.83	16.13	19.96	23.83	*Acarinina topilensis*	212-250	Peak
77.35	40.07	2.57	-0.91	-0.22	-0.49	99.86	-1.10	18.95	16.18	20.08	23.88	*Acarinina topilensis*	250-300	Peak
79.47	40.17	1.82	-1.94	-0.22	-0.49	99.81	-2.13	23.97	20.63	24.45	28.25	*Acarinina topilensis*	180-212	Onset
79.47	40.17	2.94	-0.01	-0.22	-0.49	99.81	-0.20	14.76	12.50	16.28	20.06	*Acarinina topilensis*	212-250	Onset
79.47	40.17	2.92	-0.74	-0.22	-0.49	99.81	-0.93	18.16	15.31	19.31	23.21	*Acarinina topilensis*	250-300	Onset
79.47	40.17	3.28	-0.70	-0.22	-0.49	99.81	-0.89	17.96	15.29	19.16	22.97	*Acarinina topilensis*	300-355	Onset
92.25	40.39	2.83	-0.81	-0.22	-0.49	99.70	-1.00	18.47	15.74	19.62	23.55	*Acarinina topilensis*	180-212	Onset
92.25	40.39	2.81	-1.19	-0.22	-0.49	99.70	-1.38	20.29	17.37	21.24	25.08	*Acarinina topilensis*	212-250	Onset
92.25	40.39	3.38	-1.09	-0.22	-0.49	99.70	-1.28	19.84	17.04	20.84	24.66	*Acarinina topilensis*	250-300	Onset
92.25	40.39	3.33	-1.51	-0.22	-0.49	99.70	-1.70	21.86	18.72	22.67	26.55	*Acarinina topilensis*	300-355	Onset
92.25	40.39	3.82	-1.62	-0.22	-0.49	99.70	-1.81	22.39	19.21	23.07	27.05	*Acarinina topilensis*	355-400	Onset
105.12	40.73	2.15	-0.52	-0.22	-0.49	99.53	-0.71	17.13	14.56	18.40	22.29	*Acarinina topilensis*	180-212	Pre
105.12	40.73	2.68	-0.51	-0.22	-0.49	99.53	-0.70	17.09	14.51	18.40	22.24	*Acarinina topilensis*	212-250	Pre
105.12	40.73	2.99	-0.20	-0.22	-0.49	99.53	-0.39	15.64	13.29	17.03	20.90	*Acarinina topilensis*	250-300	Pre
105.12	40.73	3.30	-0.34	-0.22	-0.49	99.53	-0.53	16.29	13.69	17.68	21.58	*Acarinina topilensis*	300-355	Pre
105.12	40.73	3.30	-0.47	-0.22	-0.49	99.53	-0.66	16.90	14.20	18.20	21.96	*Acarinina topilensis*	355-400	Pre
111.43	40.81	2.48	-0.71	-0.22	-0.49	99.49	-0.90	18.00	15.39	19.19	23.10	*Acarinina topilensis*	180-212	N/A
111.43	40.81	2.63	-0.68	-0.22	-0.49	99.49	-0.87	17.89	15.26	19.09	22.91	*Acarinina topilensis*	212-250	N/A
111.43	40.81	3.20	-0.51	-0.22	-0.49	99.49	-0.70	17.09	14.53	18.30	22.16	*Acarinina topilensis*	250-300	N/A

Depth (mbsf)	Age (Ma) GTS2012	$\delta^{13}C$ (‰ VPDB)	$\delta^{18}O$ (‰ VPDB)	$\delta^{18}O_{sw}$ (‰ VSMOW)	$\delta^{18}O_{sw}$ (‰ VPDB)	$[CO_3^{2-}]$ (µmol kg^{-1})	$\delta^{18}O_c$'	SST - Equation 1 (°C)	SST - Bayfox (°C)			Species	Size fraction (µm)	MECO interval
									0.05	0.50	0.95			
111.43	40.81	3.33	-0.68	-0.22	-0.49	99.49	-0.87	17.89	15.26	19.09	22.91	*Acarinina topilensis*	300-355	N/A
69.14	39.94	1.49	-1.81	-0.22	-0.49	100.02	-2.00	23.30	20.10	23.92	27.73	*Globigerinatheka spp*	180-212	Post
69.14	39.94	2.00	-1.60	-0.22	-0.49	100.02	-1.79	22.30	19.12	23.03	26.78	*Globigerinatheka spp*	212-250	Post
69.14	39.94	2.32	-1.44	-0.22	-0.49	100.02	-1.62	21.48	18.39	22.30	26.12	*Globigerinatheka spp*	250-300	Post
69.14	39.94	2.73	-1.45	-0.22	-0.49	100.02	-1.64	21.56	18.52	22.37	26.16	*Globigerinatheka spp*	300-355	Post
69.14	39.94	3.04	-1.45	-0.22	-0.49	100.02	-1.64	21.56	18.42	22.40	26.32	*Globigerinatheka spp*	355-400	Post
77.35	40.07	1.34	-1.41	-0.22	-0.49	99.86	-1.60	21.35	18.29	22.26	26.15	*Globigerinatheka spp*	180-212	Peak
77.35	40.07	1.91	-1.38	-0.22	-0.49	99.86	-1.57	21.22	18.28	22.01	25.90	*Globigerinatheka spp*	212-250	Peak
77.35	40.07	2.30	-0.96	-0.22	-0.49	99.86	-1.15	19.20	16.37	20.30	24.17	*Globigerinatheka spp*	250-300	Peak
77.35	40.07	2.00	-1.79	-0.22	-0.49	99.86	-1.98	23.20	19.99	23.83	27.59	*Globigerinatheka spp*	300-355	Peak
77.35	40.07	2.13	-0.96	-0.22	-0.49	99.86	-1.15	19.20	16.44	20.27	24.18	*Globigerinatheka spp*	355-400	Peak
79.47	40.17	1.39	-1.28	-0.22	-0.49	99.81	-1.47	20.75	17.88	21.60	25.59	*Globigerinatheka spp*	180-212	Onset
79.47	40.17	1.85	-1.24	-0.22	-0.49	99.81	-1.43	20.53	17.62	21.45	25.33	*Globigerinatheka spp*	212-250	Onset
79.47	40.17	2.19	-1.04	-0.22	-0.49	99.81	-1.23	19.59	16.84	20.64	24.45	*Globigerinatheka spp*	250-300	Onset
79.47	40.17	2.40	-0.84	-0.22	-0.49	99.81	-1.03	18.65	15.94	19.79	23.68	*Globigerinatheka spp*	300-355	Onset
79.47	40.17	2.60	-0.85	-0.22	-0.49	99.81	-1.04	18.70	15.95	19.80	23.66	*Globigerinatheka spp*	355-400	Onset
79.47	40.17	2.54	-1.25	-0.22	-0.49	99.81	-1.44	20.60	17.65	21.47	25.31	*Globigerinatheka spp*	400-450	Onset
92.25	40.39	1.56	-1.47	-0.22	-0.49	99.70	-1.66	21.67	18.60	22.46	26.36	*Globigerinatheka spp*	180-212	Onset
92.25	40.39	1.91	-1.31	-0.22	-0.49	99.70	-1.50	20.89	17.99	21.78	25.71	*Globigerinatheka spp*	212-250	Onset
92.25	40.39	2.15	-1.16	-0.22	-0.49	99.70	-1.35	20.16	17.22	21.09	24.91	*Globigerinatheka spp*	250-300	Onset
92.25	40.39	2.55	-0.88	-0.22	-0.49	99.70	-1.07	18.82	16.10	19.96	23.75	*Globigerinatheka spp*	300-355	Onset
92.25	40.39	2.76	-0.96	-0.22	-0.49	99.70	-1.15	19.19	16.42	20.28	24.09	*Globigerinatheka spp*	355-400	Onset
105.12	40.73	2.08	-0.23	-0.22	-0.49	99.53	-0.42	15.76	13.36	17.17	21.05	*Globigerinatheka spp*	212-250	Pre
105.12	40.73	1.22	-1.18	-0.22	-0.49	99.53	-1.37	20.27	17.38	21.20	25.02	*Globigerinatheka spp*	180-212	Pre

Depth (mbsf)	Age (Ma) GTS2012	$\delta^{13}C$ (‰ VPDB)	$\delta^{18}O$ (‰ VPDB)	$\delta^{18}O_{sw}$ (‰ VSMOW)	$\delta^{18}O_{sw}$ (‰ VPDB)	$[CO_3^{2-}]$ (µmol kg^{-1})	$\delta^{18}O_c$'	SST - Equation 1 (°C)	SST - Bayfox (°C)			Species	Size fraction (µm)	MECO interval
									0.05	0.50	0.95			
105.12	40.73	2.20	-0.67	-0.22	-0.49	99.53	-0.86	17.84	15.09	19.04	22.90	*Globigerinatheka spp*	250-300	Pre
105.12	40.73	2.75	-0.86	-0.22	-0.49	99.53	-1.05	18.73	15.98	19.89	23.66	*Globigerinatheka spp*	300-355	Pre
111.43	40.81	1.44	-1.14	-0.22	-0.49	99.49	-1.33	20.07	17.18	21.02	24.91	*Globigerinatheka spp*	180-212	N/A
111.43	40.81	1.76	-0.81	-0.22	-0.49	99.49	-1.00	18.50	15.81	19.63	23.51	*Globigerinatheka spp*	212-250	N/A
111.43	40.81	2.41	-0.72	-0.22	-0.49	99.49	-0.91	18.08	15.44	19.29	23.13	*Globigerinatheka spp*	250-300	N/A
111.43	40.81	2.43	-0.66	-0.22	-0.49	99.49	-0.85	17.78	15.13	18.99	22.94	*Globigerinatheka spp*	300-355	N/A
69.14	39.94	2.53	-1.08	-0.22	-0.49	100.02	-1.27	19.78	16.88	20.81	24.69	*Morozovelloides crassatus*	150-180	Post
69.14	39.94	2.79	-1.13	-0.22	-0.49	100.02	-1.32	20.01	17.12	21.06	24.86	*Morozovelloides crassatus*	180-212	Post
69.14	39.94	2.92	-1.03	-0.22	-0.49	100.02	-1.22	19.53	16.78	20.61	24.42	*Morozovelloides crassatus*	212-250	Post
69.14	39.94	3.26	-1.38	-0.22	-0.49	100.02	-1.57	21.21	18.19	22.10	26.02	*Morozovelloides crassatus*	250-300	Post
77.35	40.07	2.08	-0.86	-0.22	-0.49	99.86	-1.05	18.72	16.07	19.84	23.64	*Morozovelloides crassatus*	150-180	Peak
77.35	40.07	2.37	-0.67	-0.22	-0.49	99.86	-0.86	17.82	15.22	19.00	22.89	*Morozovelloides crassatus*	180-212	Peak
77.35	40.07	2.59	-0.70	-0.22	-0.49	99.86	-0.89	17.98	15.23	19.14	23.00	*Morozovelloides crassatus*	212-250	Peak
77.35	40.07	2.70	-0.78	-0.22	-0.49	99.86	-0.97	18.33	15.66	19.47	23.42	*Morozovelloides crassatus*	250-300	Peak
77.35	40.07	2.95	-1.20	-0.22	-0.49	99.86	-1.39	20.34	17.50	21.32	25.07	*Morozovelloides crassatus*	300-355	Peak
79.47	40.17	1.80	-1.09	-0.22	-0.49	99.81	-1.28	19.80	16.97	20.82	24.68	*Morozovelloides crassatus*	150-180	Onset
79.47	40.17	2.40	-0.80	-0.22	-0.49	99.81	-0.99	18.46	15.77	19.57	23.50	*Morozovelloides crassatus*	180-212	Onset
79.47	40.17	2.06	-1.91	-0.22	-0.49	99.81	-2.10	23.83	20.54	24.37	28.29	*Morozovelloides crassatus*	212-250	Onset
79.47	40.17	2.90	-0.87	-0.22	-0.49	99.81	-1.06	18.75	16.03	19.86	23.76	*Morozovelloides crassatus*	250-300	Onset
79.47	40.17	3.10	-1.15	-0.22	-0.49	99.81	-1.34	20.12	17.23	21.07	24.92	*Morozovelloides crassatus*	355-400	Onset
79.47	40.17	3.46	-0.71	-0.22	-0.49	99.81	-0.90	18.03	15.43	19.24	23.12	*Morozovelloides crassatus*	400-450	Onset
92.25	40.39	2.16	-0.88	-0.22	-0.49	99.70	-1.07	18.82	16.12	19.98	23.83	*Morozovelloides crassatus*	150-180	Onset
92.25	40.39	2.61	-0.89	-0.22	-0.49	99.70	-1.08	18.88	16.08	19.94	23.84	*Morozovelloides crassatus*	180-212	Onset
92.25	40.39	2.73	-1.23	-0.22	-0.49	99.70	-1.42	20.51	17.52	21.44	25.24	*Morozovelloides crassatus*	212-250	Onset

Depth (mbsf)	Age (Ma) GTS2012	$\delta^{13}C$ (‰ VPDB)	$\delta^{18}O$ (‰ VPDB)	$\delta^{18}O_{sw}$ (‰ VSMOW)	$\delta^{18}O_{sw}$ (‰ VPDB)	$[CO_3^{2-}]$ (µmol kg^{-1})	$\delta^{18}O_c$'	SST - Equation 1 (°C)	SST - Bayfox (°C)			Species	Size fraction (µm)	MECO interval
									0.05	0.50	0.95			
92.25	40.39	3.10	-0.41	-0.22	-0.49	99.70	-0.60	16.61	14.07	17.94	21.87	*Morozovelloides crassatus*	250-300	Onset
92.25	40.39	3.29	-1.07	-0.22	-0.49	99.70	-1.26	19.71	16.83	20.66	24.51	*Morozovelloides crassatus*	300-355	Onset
105.12	40.73	2.17	-0.43	-0.22	-0.49	99.53	-0.62	16.71	14.14	17.97	21.79	*Morozovelloides crassatus*	150-180	Pre
105.12	40.73	2.35	-0.45	-0.22	-0.49	99.53	-0.64	16.82	14.18	18.12	21.91	*Morozovelloides crassatus*	180-212	Pre
105.12	40.73	2.50	-0.73	-0.22	-0.49	99.53	-0.92	18.11	15.51	19.26	23.16	*Morozovelloides crassatus*	212-250	Pre
105.12	40.73	2.56	-0.90	-0.22	-0.49	99.53	-1.09	18.92	16.18	20.04	23.90	*Morozovelloides crassatus*	250-300	Pre
105.12	40.73	2.88	-0.52	-0.22	-0.49	99.53	-0.71	17.13	14.52	18.39	22.32	*Morozovelloides crassatus*	300-355	Pre
111.43	40.81	2.48	-0.54	-0.22	-0.49	99.49	-0.73	17.21	14.56	18.50	22.28	*Morozovelloides crassatus*	150-180	N/A
111.43	40.81	2.87	-0.33	-0.22	-0.49	99.49	-0.52	16.24	13.74	17.60	21.41	*Morozovelloides crassatus*	180-212	N/A
111.43	40.81	2.96	-0.50	-0.22	-0.49	99.49	-0.69	17.05	14.43	18.41	22.24	*Morozovelloides crassatus*	212-250	N/A
111.43	40.81	2.69	-0.78	-0.22	-0.49	99.49	-0.97	18.35	15.65	19.50	23.35	*Morozovelloides crassatus*	250-300	N/A
111.43	40.81	2.58	-0.71	-0.22	-0.49	99.49	-0.90	18.00	15.40	19.21	23.07	*Morozovelloides crassatus*	300-355	N/A
69.14	39.94	1.52	-0.27	-0.22	-0.49	100.02	-0.46	15.97	13.42	17.31	21.15	*Subbotina spp*	180-212	Post
69.14	39.94	1.21	-0.27	-0.22	-0.49	100.02	-0.46	15.97	13.51	17.37	21.20	*Subbotina spp*	212-250	Post
69.14	39.94	1.24	-0.24	-0.22	-0.49	100.02	-0.43	15.83	13.41	17.22	21.03	*Subbotina spp*	250-300	Post
69.14	39.94	1.46	-0.33	-0.22	-0.49	100.02	-0.52	16.25	13.72	17.60	21.46	*Subbotina spp*	300-355	Post
77.35	40.07	1.08	-0.92	-0.22	-0.49	99.86	-1.11	19.03	16.21	20.09	23.96	*Subbotina spp*	180-212	Peak
77.35	40.07	1.26	-1.16	-0.22	-0.49	99.86	-1.35	20.17	17.27	21.14	25.04	*Subbotina spp*	212-250	Peak
77.35	40.07	1.25	-0.39	-0.22	-0.49	99.86	-0.58	16.51	13.93	17.80	21.72	*Subbotina spp*	250-300	Peak
79.47	40.17	1.48	-0.17	-0.22	-0.49	99.81	-0.36	15.48	13.06	16.85	20.78	*Subbotina spp*	180-212	Onset
79.47	40.17	1.91	0.31	-0.22	-0.49	99.81	0.12	13.31	11.04	14.88	18.70	*Subbotina spp*	212-250	Onset
79.47	40.17	1.49	-0.17	-0.22	-0.49	99.81	-0.36	15.50	13.05	16.87	20.71	*Subbotina spp*	250-300	Onset
79.47	40.17	1.50	-0.39	-0.22	-0.49	99.81	-0.58	16.50	14.04	17.86	21.65	*Subbotina spp*	300-355	Onset
79.47	40.17	1.67	-0.27	-0.22	-0.49	99.81	-0.46	15.98	13.44	17.36	21.26	*Subbotina spp*	355-400	Onset

Depth (mbsf)	Age (Ma) GTS2012	$\delta^{13}C$ (‰ VPDB)	$\delta^{18}O$ (‰ VPDB)	$\delta^{18}O_{sw}$ (‰ VSMOW)	$\delta^{18}O_{sw}$ (‰ VPDB)	$[CO_3^{2-}]$ (µmol kg^{-1})	$\delta^{18}O_c$'	SST - Equation 1 (°C)	SST - Bayfox (°C)			Species	Size fraction (µm)	MECO interval
									0.05	0.50	0.95			
92.25	40.39	1.12	-0.35	-0.22	-0.49	99.70	-0.54	16.34	13.86	17.66	21.52	*Subbotina spp*	180-212	Onset
92.25	40.39	1.56	-0.37	-0.22	-0.49	99.70	-0.56	16.44	13.90	17.76	21.76	*Subbotina spp*	212-250	Onset
92.25	40.39	1.41	-0.69	-0.22	-0.49	99.70	-0.88	17.94	15.26	19.19	22.90	*Subbotina spp*	250-300	Onset
92.25	40.39	1.54	-0.67	-0.22	-0.49	99.70	-0.86	17.83	15.20	19.04	22.89	*Subbotina spp*	300-355	Onset
105.12	40.73	1.59	-0.09	-0.22	-0.49	99.53	-0.28	15.12	12.73	16.57	20.41	*Subbotina spp*	180-212	Pre
105.12	40.73	1.33	-0.15	-0.22	-0.49	99.53	-0.34	15.41	12.88	16.77	20.57	*Subbotina spp*	212-250	Pre
105.12	40.73	1.36	-0.26	-0.22	-0.49	99.53	-0.45	15.92	13.47	17.34	21.14	*Subbotina spp*	250-300	Pre
105.12	40.73	1.19	-0.09	-0.22	-0.49	99.53	-0.28	15.14	12.66	16.56	20.45	*Subbotina spp*	300-355	Pre
105.12	40.73	1.39	-0.22	-0.22	-0.49	99.53	-0.41	15.75	13.37	17.18	21.02	*Subbotina spp*	355-400	Pre
105.12	40.73	1.52	-0.25	-0.22	-0.49	99.53	-0.44	15.89	13.38	17.32	21.16	*Subbotina spp*	400-450	Pre
111.43	40.81	1.72	-0.30	-0.22	-0.49	99.49	-0.49	16.08	13.63	17.46	21.28	*Subbotina spp*	212-250	N/A
111.43	40.81	1.19	-0.05	-0.22	-0.49	99.49	-0.24	14.95	12.61	16.39	20.36	*Subbotina spp*	250-300	N/A

Supplementary Table 4.1.6: ODP Site 1052

Depth (mcd)	Age (Ma) GTS2012	$\delta^{13}C$ (‰ VPDB)	$\delta^{18}O$ (‰ VPDB)	$\delta^{18}O_{sw}$ (‰ VSMOW)	$\delta^{18}O_{sw}$ (‰ VPDB)	$[CO_3^{2-}]$ (µmol kg^{-1})	$\delta^{18}O_c$'	SST - Equation 1 (°C)	SST - Bayfox (°C)			Species	Size fraction (µm)	MECO interval
									0.05	0.50	0.95			
127.21	39.61	2.18	-1.04	-0.22	-0.49	100.69	-1.23	19.58	16.77	20.61	24.52	*Morozovelloides crassatus*	137.5	N/A
127.21	39.61	2.50	-1.02	-0.22	-0.49	100.69	-1.21	19.48	16.78	20.55	24.29	*Morozovelloides crassatus*	165	N/A
127.21	39.61	2.78	-0.83	-0.22	-0.49	100.69	-1.02	18.58	15.89	19.76	23.62	*Morozovelloides crassatus*	196	N/A
127.21	39.61	3.07	-1.16	-0.22	-0.49	100.69	-1.35	20.15	17.32	21.13	24.97	*Morozovelloides crassatus*	231	N/A
127.21	39.61	3.52	-1.16	-0.22	-0.49	100.69	-1.35	20.15	17.23	21.13	24.92	*Morozovelloides crassatus*	275	N/A
112.50	38.90	2.11	-1.06	-0.22	-0.49	102.12	-1.25	19.66	16.81	20.65	24.50	*Morozovelloides crassatus*	137.5	N/A
112.50	38.90	2.51	-1.09	-0.22	-0.49	102.12	-1.28	19.80	17.03	20.80	24.62	*Morozovelloides crassatus*	165	N/A
112.50	38.90	2.57	-1.19	-0.22	-0.49	102.12	-1.38	20.28	17.44	21.23	25.03	*Morozovelloides crassatus*	196	N/A

Depth (mcd)	Age (Ma) GTS2012	$\delta^{13}C$ (‰ VPDB)	$\delta^{18}O$ (‰ VPDB)	$\delta^{18}O_{sw}$ (‰ VSMOW)	$\delta^{18}O_{sw}$ (‰ VPDB)	$[CO_3^{2-}]$ (µmol kg^{-1})	$\delta^{18}O_c$'	SST - Equation 1 (°C)	SST - Bayfox (°C)			Species	Size fraction (µm)	MECO interval
									0.05	0.50	0.95			
112.50	38.90	3.00	-1.13	-0.22	-0.49	102.12	-1.32	19.99	17.15	21.01	24.79	*Morozovelloides crassatus*	231	N/A
112.50	38.90	3.11	-1.08	-0.22	-0.49	102.12	-1.27	19.75	16.89	20.77	24.71	*Morozovelloides crassatus*	275	N/A
112.50	38.90	3.34	-1.10	-0.22	-0.49	102.12	-1.29	19.85	16.96	20.88	24.71	*Morozovelloides crassatus*	327.5	N/A
93.07	38.27	2.01	-0.50	-0.22	-0.49	103.39	-0.68	17.00	14.44	18.28	22.10	*Morozovelloides crassatus*	118	N/A
93.07	38.27	2.36	-0.36	-0.22	-0.49	103.39	-0.54	16.35	13.83	17.65	21.52	*Morozovelloides crassatus*	137.5	N/A
93.07	38.27	2.54	-0.46	-0.22	-0.49	103.39	-0.64	16.81	14.32	18.11	22.00	*Morozovelloides crassatus*	165	N/A
93.07	38.27	2.75	-0.41	-0.22	-0.49	103.39	-0.59	16.58	14.08	17.91	21.72	*Morozovelloides crassatus*	196	N/A
93.07	38.27	2.91	-0.54	-0.22	-0.49	103.39	-0.72	17.19	14.62	18.47	22.28	*Morozovelloides crassatus*	231	N/A
92.67	38.26	2.53	-0.41	-0.22	-0.49	103.41	-0.59	16.58	14.01	17.89	21.72	*Morozovelloides crassatus*	137.5	N/A
92.67	38.26	2.61	-0.38	-0.22	-0.49	103.41	-0.56	16.44	13.94	17.79	21.66	*Morozovelloides crassatus*	137.5	N/A
92.67	38.26	2.83	-0.34	-0.22	-0.49	103.41	-0.52	16.26	13.79	17.63	21.43	*Morozovelloides crassatus*	165	N/A
92.67	38.26	2.77	-0.30	-0.22	-0.49	103.41	-0.48	16.07	13.64	17.46	21.28	*Morozovelloides crassatus*	165	N/A
92.67	38.26	3.07	-0.39	-0.22	-0.49	103.41	-0.57	16.49	13.97	17.77	21.67	*Morozovelloides crassatus*	196	N/A
92.67	38.26	3.31	-0.37	-0.22	-0.49	103.41	-0.55	16.40	13.88	17.71	21.51	*Morozovelloides crassatus*	231	N/A
92.67	38.26	3.41	-0.57	-0.22	-0.49	103.41	-0.75	17.33	14.79	18.57	22.37	*Morozovelloides crassatus*	275	N/A
92.67	38.26	3.39	-0.44	-0.22	-0.49	103.41	-0.62	16.72	14.15	18.04	21.94	*Morozovelloides crassatus*	327.5	N/A
92.57	38.26	2.67	-0.75	-0.22	-0.49	103.41	-0.93	18.18	15.46	19.29	23.13	*Morozovelloides crassatus*	95	N/A
92.57	38.26	2.95	-0.72	-0.22	-0.49	103.41	-0.90	18.03	15.46	19.22	23.09	*Morozovelloides crassatus*	185	N/A
92.57	38.26	3.05	-0.81	-0.22	-0.49	103.41	-0.99	18.46	15.76	19.66	23.53	*Morozovelloides crassatus*	275	N/A
92.57	38.26	3.23	-0.75	-0.22	-0.49	103.41	-0.93	18.18	15.46	19.38	23.18	*Morozovelloides crassatus*	327.5	N/A

Supplementary Table 4.1.7: ODP Site 1260

Depth (rmcd)	Age (Ma) GTS2012	$\delta^{13}C$ (‰ VPDB)	$\delta^{18}O$ (‰ VPDB)	$\delta^{18}O_{sw}$ (‰ VSMOW)	$\delta^{18}O_{sw}$ (‰ VPDB)	$[CO_3^{2-}]$ (µmol kg^{-1})	$\delta^{18}O_c$'	SST - Equation 1 (°C)	SST - Bayfox (°C)			Species	Size fraction (µm)	MECO interval
									0.05	0.50	0.95			
38.27	39.81	3.43	-1.18	-0.32	-0.59	100.29	-1.37	19.76	16.94	20.78	24.61	*Morozovelloides crassatus*	250-300	N/A
40.48	39.91	3.73	-1.94	-0.32	-0.59	100.08	-2.13	23.45	20.20	24.04	27.96	*Morozovelloides crassatus*	250-300	Post
41.98	39.98	3.78	-2.41	-0.32	-0.59	99.93	-2.60	25.78	22.20	26.06	29.94	*Morozovelloides crassatus*	250-300	Post
43.43	40.06	3.77	-2.30	-0.32	-0.59	99.87	-2.49	25.23	21.75	25.56	29.39	*Morozovelloides crassatus*	250-300	Post
44.28	40.11	3.20	-1.87	-0.32	-0.59	99.84	-2.06	23.11	19.86	23.69	27.63	*Morozovelloides crassatus*	250-300	Peak
47.08	40.25	3.12	-1.36	-0.32	-0.59	99.77	-1.55	20.63	17.78	21.62	25.45	*Morozovelloides crassatus*	250-300	Onset
49.28	40.39	3.01	-1.37	-0.32	-0.59	99.70	-1.56	20.68	17.79	21.59	25.50	*Morozovelloides crassatus*	250-300	Onset
51.58	40.52	2.97	-1.29	-0.32	-0.59	99.64	-1.48	20.29	17.40	21.29	25.01	*Morozovelloides crassatus*	250-300	Onset
52.88	40.65	2.88	-1.49	-0.32	-0.59	99.57	-1.68	21.26	18.31	22.12	26.02	*Morozovelloides crassatus*	250-300	Pre

Supplementary Table 4.1.8: ODP Site 1263

Depth (mbsf)	Age (Ma) GTS2012	$\delta^{13}C$ (‰ VPDB)	$\delta^{18}O$ (‰ VPDB)	$\delta^{18}O_{sw}$ (‰ VSMOW)	$\delta^{18}O_{sw}$ (‰ VPDB)	$[CO_3^{2-}]$ (µmol kg^{-1})	$\delta^{18}O_c$'	SST - Equation 1 (°C)	SST - Bayfox (°C)			Species	Size fraction (µm)	MECO interval
									0.05	0.50	0.95			
131.81	39.76	3.16	0.28	-0.13	-0.40	100.39	0.09	13.84	11.56	15.39	19.05	*Acarinina spp.*	180-250	N/A
132.20	39.77	3.10	0.45	-0.13	-0.40	100.36	0.26	13.09	10.81	14.68	18.45	*Acarinina spp.*	180-250	N/A
132.60	39.79	3.17	0.42	-0.13	-0.40	100.33	0.23	13.23	10.91	14.81	18.70	*Acarinina spp.*	180-250	N/A
133.01	39.80	3.11	0.38	-0.13	-0.40	100.30	0.19	13.40	11.07	14.93	18.77	*Acarinina spp.*	180-250	N/A
133.40	39.82	3.16	0.20	-0.13	-0.40	100.27	0.01	14.23	11.94	15.72	19.55	*Acarinina spp.*	180-250	N/A
133.80	39.83	3.25	0.32	-0.13	-0.40	100.24	0.13	13.68	11.29	15.26	19.14	*Acarinina spp.*	180-250	N/A
134.21	39.85	3.49	0.38	-0.13	-0.40	100.21	0.19	13.40	11.17	14.98	18.85	*Acarinina spp.*	180-250	N/A
134.60	39.86	3.10	0.34	-0.13	-0.40	100.18	0.15	13.57	11.23	15.08	19.05	*Acarinina spp.*	180-250	Post
135.00	39.88	2.97	0.24	-0.13	-0.40	100.15	0.05	14.02	11.68	15.52	19.37	*Acarinina spp.*	180-250	Post
135.41	39.89	2.96	0.31	-0.13	-0.40	100.12	0.12	13.74	11.42	15.21	19.04	*Acarinina spp.*	180-250	Post

Depth (mbsf)	Age (Ma) GTS2012	$\delta^{13}C$ (‰ VPDB)	$\delta^{18}O$ (‰ VPDB)	$\delta^{18}O_{sw}$ (‰ VSMOW)	$\delta^{18}O_{sw}$ (‰ VPDB)	$[CO_3^{2-}]$ (µmol kg^{-1})	$\delta^{18}O_c$'	SST - Equation 1 (°C)	SST - Bayfox (°C)			Species	Size fraction (µm)	MECO interval
									0.05	0.50	0.95			
135.80	39.91	2.75	-0.07	-0.13	-0.40	100.09	-0.26	15.45	12.98	16.90	20.73	*Acarinina spp.*	180-250	Post
136.20	39.92	3.27	0.16	-0.13	-0.40	100.06	-0.03	14.39	12.02	15.87	19.76	*Acarinina spp.*	180-250	Post
136.61	39.94	3.21	0.29	-0.13	-0.40	100.03	0.10	13.83	11.49	15.38	19.23	*Acarinina spp.*	180-250	Post
137.00	39.95	3.17	0.14	-0.13	-0.40	100.00	-0.05	14.49	12.09	16.00	19.86	*Acarinina spp.*	180-250	Post
137.40	39.96	3.34	0.15	-0.13	-0.40	99.97	-0.04	14.46	12.12	15.92	19.85	*Acarinina spp.*	180-250	Post
137.81	39.98	3.26	0.01	-0.13	-0.40	99.94	-0.18	15.10	12.59	16.52	20.37	*Acarinina spp.*	180-250	Post
138.20	39.99	3.21	0.31	-0.13	-0.40	99.91	0.12	13.72	11.42	15.26	19.08	*Acarinina spp.*	180-250	Post
138.60	40.01	3.04	0.13	-0.13	-0.40	99.90	-0.07	14.57	12.15	16.05	19.93	*Acarinina spp.*	180-250	Post
139.00	40.02	2.70	-0.10	-0.13	-0.40	99.89	-0.29	15.61	13.12	16.98	20.86	*Acarinina spp.*	180-250	Post
139.40	40.04	3.10	0.04	-0.13	-0.40	99.88	-0.15	14.96	12.56	16.42	20.30	*Acarinina spp.*	180-250	Post
139.80	40.05	2.98	0.00	-0.13	-0.40	99.87	-0.19	15.15	12.82	16.62	20.43	*Acarinina spp.*	180-250	Post
140.20	40.06	2.83	0.11	-0.13	-0.40	99.87	-0.08	14.62	12.27	16.10	19.93	*Acarinina spp.*	180-250	Post
140.59	40.08	3.35	0.16	-0.13	-0.40	99.86	-0.04	14.43	12.09	15.86	19.76	*Acarinina spp.*	180-250	Post
140.99	40.10	3.21	-0.18	-0.13	-0.40	99.85	-0.37	15.99	13.50	17.39	21.24	*Acarinina spp.*	180-250	Post
141.39	40.12	2.98	0.22	-0.13	-0.40	99.84	0.02	14.15	11.77	15.63	19.52	*Acarinina spp.*	180-250	Peak
141.78	40.15	2.83	-0.21	-0.13	-0.40	99.82	-0.40	16.10	13.56	17.45	21.27	*Acarinina spp.*	180-250	Peak
142.20	40.18	3.01	0.14	-0.13	-0.40	99.81	-0.05	14.51	12.10	15.98	19.79	*Acarinina spp.*	180-250	Peak
142.60	40.21	2.97	0.13	-0.13	-0.40	99.79	-0.06	14.55	12.10	16.03	19.92	*Acarinina spp.*	180-250	Onset
143.00	40.24	2.87	0.35	-0.13	-0.40	99.78	0.16	13.54	11.21	15.06	18.99	*Acarinina spp.*	180-250	Onset
143.40	40.30	2.77	0.11	-0.13	-0.40	99.75	-0.08	14.62	12.22	16.09	19.96	*Acarinina spp.*	180-250	Onset
143.80	40.36	3.09	0.10	-0.13	-0.40	99.72	-0.09	14.68	12.36	16.13	20.02	*Acarinina spp.*	180-250	Onset
144.20	40.43	3.14	-0.09	-0.13	-0.40	99.68	-0.28	15.54	13.14	16.93	20.87	*Acarinina spp.*	180-250	Onset
144.60	40.49	2.82	0.03	-0.13	-0.40	99.65	-0.17	15.03	12.62	16.47	20.36	*Acarinina spp.*	180-250	Onset
145.00	40.55	2.87	0.37	-0.13	-0.40	99.62	0.18	13.45	11.21	15.01	18.91	*Acarinina spp.*	180-250	Onset

Depth (mbsf)	Age (Ma) GTS2012	$\delta^{13}C$ (‰ VPDB)	$\delta^{18}O$ (‰ VPDB)	$\delta^{18}O_{sw}$ (‰ VSMOW)	$\delta^{18}O_{sw}$ (‰ VPDB)	$[CO_3^{2-}]$ ($\mu mol\ kg^{-1}$)	$\delta^{18}O_c$'	SST - Equation 1 (°C)	SST - Bayfox (°C)			Species	Size fraction (µm)	MECO interval
									0.05	0.50	0.95			
136.61	39.94	2.74	0.15	-0.13	-0.40	100.03	-0.04	14.45	12.16	15.97	19.81	*Globigerinatheka spp.*	>500	Post
137.00	39.95	2.75	0.10	-0.13	-0.40	100.00	-0.09	14.66	12.30	16.10	19.94	*Globigerinatheka spp.*	>500	Post
137.40	39.96	2.71	0.53	-0.13	-0.40	99.97	0.34	12.72	10.43	14.33	18.13	*Globigerinatheka spp.*	>500	Post
137.81	39.98	2.82	0.54	-0.13	-0.40	99.94	0.35	12.70	10.36	14.25	18.15	*Globigerinatheka spp.*	>500	Post
138.20	39.99	2.81	0.42	-0.13	-0.40	99.91	0.23	13.21	10.91	14.81	18.64	*Globigerinatheka spp.*	>500	Post
138.60	40.01	2.90	-0.22	-0.13	-0.40	99.90	-0.41	16.16	13.67	17.49	21.36	*Globigerinatheka spp.*	>500	Post
139.00	40.02	3.02	-0.44	-0.13	-0.40	99.89	-0.63	17.19	14.62	18.44	22.30	*Globigerinatheka spp.*	>500	Post
139.40	40.04	3.16	-0.29	-0.13	-0.40	99.88	-0.48	16.49	13.92	17.88	21.63	*Globigerinatheka spp.*	>500	Post
139.80	40.05	2.76	0.09	-0.13	-0.40	99.87	-0.10	14.74	12.41	16.23	20.04	*Globigerinatheka spp.*	>500	Post
140.20	40.06	2.93	-0.17	-0.13	-0.40	99.87	-0.36	15.95	13.55	17.31	21.19	*Globigerinatheka spp.*	>500	Post
140.59	40.08	2.57	0.39	-0.13	-0.40	99.86	0.20	13.36	11.06	14.94	18.81	*Globigerinatheka spp.*	>500	Post
140.99	40.10	0.95	0.34	-0.13	-0.40	99.85	0.15	13.57	11.33	15.10	18.96	*Globigerinatheka spp.*	>500	Post
141.39	40.12	2.47	0.16	-0.13	-0.40	99.84	-0.03	14.41	12.05	15.85	19.72	*Globigerinatheka spp.*	>500	Peak
141.78	40.15	2.35	0.07	-0.13	-0.40	99.82	-0.12	14.81	12.36	16.25	20.24	*Globigerinatheka spp.*	>500	Peak
142.20	40.18	2.55	0.49	-0.13	-0.40	99.81	0.30	12.89	10.57	14.49	18.34	*Globigerinatheka spp.*	>500	Peak
142.60	40.21	2.48	0.30	-0.13	-0.40	99.79	0.11	13.76	11.47	15.29	19.12	*Globigerinatheka spp.*	>500	Onset
143.00	40.24	2.52	0.52	-0.13	-0.40	99.78	0.33	12.76	10.51	14.35	18.30	*Globigerinatheka spp.*	>500	Onset
143.40	40.30	2.28	0.23	-0.13	-0.40	99.75	0.04	14.09	11.81	15.63	19.43	*Globigerinatheka spp.*	>500	Onset
143.80	40.36	2.77	0.31	-0.13	-0.40	99.72	0.12	13.72	11.34	15.21	19.06	*Globigerinatheka spp.*	>500	Onset
144.20	40.43	2.38	0.38	-0.13	-0.40	99.68	0.19	13.42	11.10	14.99	18.84	*Globigerinatheka spp.*	>500	Onset
144.60	40.49	2.49	0.44	-0.13	-0.40	99.65	0.25	13.15	10.88	14.71	18.54	*Globigerinatheka spp.*	>500	Onset
145.00	40.55	2.45	0.53	-0.13	-0.40	99.62	0.34	12.72	10.41	14.29	18.11	*Globigerinatheka spp.*	>500	Onset
136.57	39.93	3.17	0.14	-0.13	-0.40	100.03	-0.05	14.50	12.14	15.96	19.82	*Globigerinatheka kugleri*	250-300	Post
138.08	39.99	3.31	-0.18	-0.13	-0.40	99.92	-0.37	15.97	13.50	17.36	21.22	*Globigerinatheka kugleri*	250-300	Post

Depth (mbsf)	Age (Ma) GTS2012	$\delta^{13}C$ (‰ VPDB)	$\delta^{18}O$ (‰ VPDB)	$\delta^{18}O_{sw}$ (‰ VSMOW)	$\delta^{18}O_{sw}$ (‰ VPDB)	$[CO_3^{2-}]$ (µmol kg^{-1})	$\delta^{18}O_c$'	SST - Equation 1 (°C)	SST - Bayfox (°C)			Species	Size fraction (µm)	MECO interval
									0.05	0.50	0.95			
140.46	40.07	3.18	-0.09	-0.13	-0.40	99.86	-0.28	15.55	13.09	17.00	20.82	*Globigerinatheka kugleri*	250-300	Post
141.28	40.12	2.79	-0.41	-0.13	-0.40	99.84	-0.60	17.04	14.52	18.36	22.24	*Globigerinatheka kugleri*	250-300	Peak
141.48	40.13	2.88	-0.18	-0.13	-0.40	99.84	-0.37	15.97	13.43	17.35	21.24	*Globigerinatheka kugleri*	250-300	Peak
143.00	40.24	1.94	-0.35	-0.13	-0.40	99.78	-0.54	16.76	14.31	18.08	21.87	*Globigerinatheka kugleri*	250-300	Onset
143.65	40.34	2.91	-0.31	-0.13	-0.40	99.73	-0.50	16.58	13.98	17.89	21.72	*Globigerinatheka kugleri*	250-300	Onset
146.08	40.73	2.78	0.18	-0.13	-0.40	99.53	-0.01	14.32	11.98	15.82	19.64	*Globigerinatheka kugleri*	250-300	Onset

Supplementary Table 4.1.9: Baskil Section

Depth (thickness, m)	Age (Ma) GTS2012	$\delta^{13}C$ (‰ VPDB)	$\delta^{18}O$ (‰ VPDB)	$\delta^{18}O_{sw}$ (‰ VSMOW)	$\delta^{18}O_{sw}$ (‰ VPDB)	$[CO_3^{2-}]$ (µmol kg^{-1})	$\delta^{18}O_c$'	SST - Equation 1 (°C)	SST - Bayfox (°C)			Species	Size fraction (µm)	MECO interval
									0.05	0.50	0.95			
0.00	42.14	1.05	-3.46	-0.22	-0.49	98.81	-3.65	31.67	27.07	30.95	34.79	*Acarinina spp.*	150-250	N/A
2.00	42.11	1.12	-3.32	-0.22	-0.49	98.82	-3.51	30.95	26.52	30.37	34.15	*Acarinina spp.*	150-250	N/A
3.00	42.09	1.28	-3.87	-0.22	-0.49	98.83	-4.06	33.82	28.88	32.75	36.59	*Acarinina spp.*	150-250	N/A
5.00	42.06	1.63	-3.61	-0.22	-0.49	98.85	-3.80	32.46	27.78	31.63	35.48	*Acarinina spp.*	150-250	N/A
8.00	42.01	1.52	-3.71	-0.22	-0.49	98.87	-3.90	32.98	28.20	32.07	35.85	*Acarinina spp.*	150-250	N/A
11.00	41.96	1.42	-3.44	-0.22	-0.49	98.90	-3.63	31.57	26.96	30.94	34.72	*Acarinina spp.*	150-250	N/A
15.00	41.90	1.56	-3.18	-0.22	-0.49	98.93	-3.37	30.22	25.95	29.79	33.68	*Acarinina spp.*	150-250	N/A
18.00	41.85	1.86	-3.04	-0.22	-0.49	98.96	-3.23	29.50	25.36	29.18	32.93	*Acarinina spp.*	150-250	N/A
24.00	41.75	1.12	-3.53	-0.22	-0.49	99.01	-3.72	32.04	27.43	31.25	35.07	*Acarinina spp.*	150-250	N/A
28.00	41.69	1.41	-3.65	-0.22	-0.49	99.04	-3.84	32.66	27.92	31.77	35.66	*Acarinina spp.*	150-250	N/A
31.00	41.64	1.22	-3.35	-0.22	-0.49	99.06	-3.54	31.10	26.69	30.44	34.33	*Acarinina spp.*	150-250	N/A
35.00	41.57	1.26	-3.08	-0.22	-0.49	99.10	-3.27	29.70	25.61	29.36	33.20	*Acarinina spp.*	150-250	N/A
38.00	41.53	1.16	-3.40	-0.22	-0.49	99.12	-3.59	31.36	26.92	30.74	34.54	*Acarinina spp.*	150-250	N/A
42.00	41.46	1.98	-3.61	-0.22	-0.49	99.16	-3.80	32.45	27.77	31.61	35.45	*Acarinina spp.*	150-250	N/A

Depth (thickness, m)	Age (Ma) GTS2012	$\delta^{13}C$ (‰ VPDB)	$\delta^{18}O$ (‰ VPDB)	$\delta^{18}O_{sw}$ (‰ VSMOW)	$\delta^{18}O_{sw}$ (‰ VPDB)	$[CO_3^{2-}]$ (µmol kg^{-1})	$\delta^{18}O_c$'	SST - Equation 1 (°C)	SST - Bayfox (°C)			Species	Size fraction (µm)	MECO interval
									0.05	0.50	0.95			
45.50	41.40	1.67	-3.60	-0.22	-0.49	99.19	-3.79	32.40	27.77	31.59	35.41	*Acarinina spp.*	150-250	N/A
50.00	41.33	1.24	-2.83	-0.22	-0.49	99.22	-3.02	28.42	24.43	28.25	32.22	*Acarinina spp.*	150-250	N/A
54.00	41.27	1.13	-2.75	-0.22	-0.49	99.25	-2.94	28.02	24.15	27.95	31.80	*Acarinina spp.*	150-250	N/A
58.00	41.20	0.84	-3.11	-0.22	-0.49	99.29	-3.30	29.86	25.66	29.48	33.36	*Acarinina spp.*	150-250	N/A
60.00	41.19	0.90	-3.27	-0.22	-0.49	99.29	-3.46	30.68	26.34	30.11	33.91	*Acarinina spp.*	150-250	N/A
61.00	41.18	1.12	-3.17	-0.22	-0.49	99.30	-3.36	30.16	25.88	29.71	33.54	*Acarinina spp.*	150-250	N/A
62.00	41.18	1.01	-2.77	-0.22	-0.49	99.30	-2.96	28.12	24.18	28.03	31.92	*Acarinina spp.*	150-250	N/A
63.50	41.17	1.00	-2.61	-0.22	-0.49	99.30	-2.80	27.31	23.46	27.31	31.20	*Acarinina spp.*	150-250	N/A
65.00	41.16	0.54	-3.15	-0.22	-0.49	99.31	-3.34	30.06	25.86	29.65	33.57	*Acarinina spp.*	150-250	N/A
66.00	41.16	0.93	-2.31	-0.22	-0.49	99.31	-2.50	25.80	22.17	26.09	29.91	*Acarinina spp.*	150-250	N/A
68.00	41.15	0.53	-2.44	-0.22	-0.49	99.31	-2.63	26.45	22.66	26.66	30.52	*Acarinina spp.*	150-250	N/A
69.50	41.14	0.84	-2.87	-0.22	-0.49	99.32	-3.06	28.63	24.58	28.46	32.33	*Acarinina spp.*	150-250	N/A
71.00	41.13	1.06	-3.23	-0.22	-0.49	99.32	-3.42	30.47	26.10	29.96	33.84	*Acarinina spp.*	150-250	N/A
72.00	41.12	1.02	-2.76	-0.22	-0.49	99.33	-2.95	28.07	24.17	28.03	31.86	*Acarinina spp.*	150-250	N/A
73.00	41.12	0.79	-3.15	-0.22	-0.49	99.33	-3.34	30.06	25.84	29.65	33.54	*Acarinina spp.*	150-250	N/A
74.00	41.11	0.92	-3.33	-0.22	-0.49	99.33	-3.52	30.99	26.58	30.43	34.28	*Acarinina spp.*	150-250	N/A
75.00	41.11	0.85	-3.18	-0.22	-0.49	99.33	-3.37	30.22	25.96	29.79	33.61	*Acarinina spp.*	150-250	N/A
76.00	41.10	1.13	-2.83	-0.22	-0.49	99.34	-3.02	28.42	24.35	28.27	32.10	*Acarinina spp.*	150-250	N/A
77.00	41.10	0.62	-3.03	-0.22	-0.49	99.34	-3.22	29.44	25.22	29.12	32.97	*Acarinina spp.*	150-250	N/A
78.00	41.09	0.78	-2.87	-0.22	-0.49	99.34	-3.06	28.63	24.55	28.49	32.28	*Acarinina spp.*	150-250	N/A
79.00	41.09	1.17	-2.88	-0.22	-0.49	99.34	-3.07	28.68	24.69	28.54	32.32	*Acarinina spp.*	150-250	N/A
80.00	41.08	0.55	-2.36	-0.22	-0.49	99.35	-2.55	26.05	22.44	26.28	30.01	*Acarinina spp.*	150-250	N/A
82.00	41.07	1.13	-2.31	-0.22	-0.49	99.35	-2.50	25.80	22.23	26.02	29.85	*Acarinina spp.*	150-250	N/A
84.00	41.06	0.54	-3.23	-0.22	-0.49	99.36	-3.42	30.47	26.04	29.92	33.78	*Acarinina spp.*	150-250	N/A
85.00	41.05	0.50	-2.63	-0.22	-0.49	99.36	-2.82	27.41	23.47	27.41	31.25	*Acarinina spp.*	150-250	N/A

Depth (thickness, m)	Age (Ma) GTS2012	$\delta^{13}C$ (‰ VPDB)	$\delta^{18}O$ (‰ VPDB)	$\delta^{18}O_{sw}$ (‰ VSMOW)	$\delta^{18}O_{sw}$ (‰ VPDB)	$[CO_3^{2-}]$ ($\mu mol\ kg^{-1}$)	$\delta^{18}O_c$'	SST - Equation 1 (°C)	SST - Bayfox (°C)			Species	Size fraction (µm)	MECO interval
									0.05	0.50	0.95			
86.00	41.05	0.62	-2.04	-0.22	-0.49	99.36	-2.23	24.45	20.99	24.93	28.72	*Acarinina spp.*	150-250	N/A
87.00	41.04	0.35	-2.89	-0.22	-0.49	99.37	-3.08	28.73	24.76	28.55	32.36	*Acarinina spp.*	150-250	N/A
88.00	41.04	0.64	-2.24	-0.22	-0.49	99.37	-2.43	25.45	21.93	25.77	29.52	*Acarinina spp.*	150-250	N/A
89.00	41.03	0.36	-3.56	-0.22	-0.49	99.37	-3.75	32.19	27.51	31.38	35.17	*Acarinina spp.*	150-250	N/A
90.00	41.03	0.86	-2.97	-0.22	-0.49	99.37	-3.16	29.14	24.95	28.87	32.72	*Acarinina spp.*	150-250	N/A
95.00	41.00	0.83	-2.73	-0.22	-0.49	99.39	-2.92	27.91	24.02	27.86	31.75	*Acarinina spp.*	150-250	N/A
105.00	40.95	1.37	-2.23	-0.22	-0.49	99.42	-2.42	25.40	21.88	25.65	29.55	*Acarinina spp.*	150-250	N/A
115.00	40.89	1.44	-2.60	-0.22	-0.49	99.45	-2.79	27.25	23.42	27.30	31.23	*Acarinina spp.*	150-250	N/A
120.00	40.86	1.53	-2.21	-0.22	-0.49	99.46	-2.40	25.30	21.75	25.63	29.45	*Acarinina spp.*	150-250	N/A
125.00	40.84	1.53	-2.43	-0.22	-0.49	99.47	-2.62	26.40	22.64	26.52	30.39	*Acarinina spp.*	150-250	N/A
130.00	40.81	1.39	-2.40	-0.22	-0.49	99.49	-2.59	26.25	22.67	26.44	30.25	*Acarinina spp.*	150-250	N/A
135.00	40.78	1.87	-2.03	-0.22	-0.49	99.50	-2.22	24.40	20.98	24.86	28.75	*Acarinina spp.*	150-250	N/A
141.00	40.75	1.72	-2.35	-0.22	-0.49	99.52	-2.54	25.99	22.39	26.27	30.12	*Acarinina spp.*	150-250	N/A
142.00	40.69	1.65	-2.56	-0.22	-0.49	99.55	-2.75	27.05	23.31	27.06	30.90	*Acarinina spp.*	150-250	N/A
143.00	40.63	1.78	-2.57	-0.22	-0.49	99.58	-2.76	27.10	23.30	27.14	31.02	*Acarinina spp.*	150-250	Pre
144.00	40.56	1.58	-2.95	-0.22	-0.49	99.61	-3.14	29.03	24.94	28.80	32.62	*Acarinina spp.*	150-250	Pre
145.00	40.50	1.57	-3.67	-0.22	-0.49	99.64	-3.86	32.76	28.06	31.86	35.74	*Acarinina spp.*	150-250	Pre
146.00	40.46	1.60	-2.53	-0.22	-0.49	99.67	-2.72	26.90	23.10	26.98	30.93	*Acarinina spp.*	150-250	Pre
147.00	40.43	1.60	-2.80	-0.22	-0.49	99.68	-2.99	28.27	24.29	28.14	31.96	*Acarinina spp.*	150-250	Pre
148.00	40.39	1.34	-3.87	-0.22	-0.49	99.70	-4.06	33.81	28.87	32.76	36.61	*Acarinina spp.*	150-250	Onset
151.00	40.29	0.99	-2.61	-0.22	-0.49	99.75	-2.80	27.30	23.51	27.33	31.21	*Acarinina spp.*	150-250	Onset
152.00	40.25	1.44	-2.80	-0.22	-0.49	99.77	-2.99	28.26	24.45	28.15	31.96	*Acarinina spp.*	150-250	Onset
153.00	40.21	1.30	-3.35	-0.22	-0.49	99.79	-3.54	31.09	26.71	30.54	34.29	*Acarinina spp.*	150-250	Onset
155.00	40.20	1.24	-3.24	-0.22	-0.49	99.80	-3.43	30.52	26.17	29.98	33.81	*Acarinina spp.*	150-250	Onset
156.00	40.19	0.92	-3.11	-0.22	-0.49	99.80	-3.30	29.85	25.71	29.46	33.40	*Acarinina spp.*	150-250	Onset

Depth (thickness, m)	Age (Ma) GTS2012	$\delta^{13}C$ (‰ VPDB)	$\delta^{18}O$ (‰ VPDB)	$\delta^{18}O_{sw}$ (‰ VSMOW)	$\delta^{18}O_{sw}$ (‰ VPDB)	$[CO_3^{2-}]$ (µmol kg^{-1})	$\delta^{18}O_c$'	SST - Equation 1 (°C)	SST - Bayfox (°C)			Species	Size fraction (µm)	MECO interval
									0.05	0.50	0.95			
157.00	40.19	0.60	-3.73	-0.22	-0.49	99.80	-3.92	33.08	28.19	32.08	36.01	*Acarinina spp.*	150-250	Onset
158.00	40.19	0.58	-3.61	-0.22	-0.49	99.80	-3.80	32.45	27.74	31.63	35.54	*Acarinina spp.*	150-250	Onset
162.00	40.18	0.97	-3.01	-0.22	-0.49	99.81	-3.20	29.34	25.23	29.04	32.91	*Acarinina spp.*	150-250	Onset
165.00	40.17	1.25	-4.03	-0.22	-0.49	99.81	-4.22	34.66	29.54	33.38	37.24	*Acarinina spp.*	150-250	Onset
166.00	40.17	1.24	-4.26	-0.22	-0.49	99.81	-4.45	35.89	30.58	34.38	38.25	*Acarinina spp.*	150-250	Onset
167.00	40.16	0.87	-4.87	-0.22	-0.49	99.82	-5.06	39.19	33.20	37.00	40.87	*Acarinina spp.*	150-250	Peak
172.00	40.15	1.16	-4.15	-0.22	-0.49	99.82	-4.34	35.30	29.99	33.92	37.74	*Acarinina spp.*	150-250	Peak
175.00	40.14	1.96	-3.71	-0.22	-0.49	99.83	-3.90	32.97	28.20	32.03	35.86	*Acarinina spp.*	150-250	Peak
177.00	40.14	2.16	-3.66	-0.22	-0.49	99.83	-3.85	32.71	27.90	31.81	35.64	*Acarinina spp.*	150-250	Peak
178.00	40.13	2.04	-3.18	-0.22	-0.49	99.83	-3.37	30.21	25.93	29.70	33.54	*Acarinina spp.*	150-250	Peak
179.00	40.13	1.51	-3.39	-0.22	-0.49	99.83	-3.58	31.30	26.73	30.62	34.57	*Acarinina spp.*	150-250	Peak
191.00	40.00	1.58	-3.00	-0.22	-0.49	99.90	-3.19	29.29	25.13	29.02	32.91	*Acarinina spp.*	150-250	Peak
193.00	39.76	1.74	-3.09	-0.22	-0.49	100.38	-3.28	29.74	25.58	29.41	33.24	*Acarinina spp.*	150-250	Post
194.00	39.75	2.35	-2.99	-0.22	-0.49	100.40	-3.18	29.23	25.06	28.94	32.76	*Acarinina spp.*	150-250	Post
196.00	39.73	1.87	-2.93	-0.22	-0.49	100.45	-3.12	28.92	24.84	28.72	32.58	*Acarinina spp.*	150-250	N/A
201.00	39.59	2.12	-2.27	-0.22	-0.49	100.73	-2.46	25.58	22.10	25.85	29.66	*Acarinina spp.*	150-250	N/A
206.00	39.52	2.26	-3.22	-0.22	-0.49	100.87	-3.41	30.41	26.17	29.92	33.74	*Acarinina spp.*	150-250	N/A
215.00	39.40	2.38	-3.04	-0.22	-0.49	101.11	-3.23	29.48	25.27	29.13	32.95	*Acarinina spp.*	150-250	N/A
220.00	39.33	2.08	-4.13	-0.22	-0.49	101.25	-4.32	35.18	29.96	33.81	37.68	*Acarinina spp.*	150-250	N/A
230.00	39.20	1.51	-4.39	-0.22	-0.49	101.52	-4.58	36.57	31.10	34.96	38.78	*Acarinina spp.*	150-250	N/A
260.00	38.78	2.34	-2.92	-0.22	-0.49	102.36	-3.11	28.85	24.81	28.62	32.49	*Acarinina spp.*	150-250	N/A
265.00	38.72	2.11	-2.24	-0.22	-0.49	102.49	-2.43	25.42	21.90	25.75	29.56	*Acarinina spp.*	150-250	N/A
275.00	38.55	2.12	-2.42	-0.22	-0.49	102.83	-2.60	26.31	22.60	26.50	30.32	*Acarinina spp.*	150-250	N/A
277.00	38.52	1.83	-3.84	-0.22	-0.49	102.89	-4.02	33.62	28.71	32.56	36.40	*Acarinina spp.*	150-250	N/A
280.00	38.47	2.03	-2.97	-0.22	-0.49	102.99	-3.15	29.10	24.93	28.86	32.66	*Acarinina spp.*	150-250	N/A

Depth (thickness, m)	Age (Ma) GTS2012	$\delta^{13}C$ (‰ VPDB)	$\delta^{18}O$ (‰ VPDB)	$\delta^{18}O_{sw}$ (‰ VSMOW)	$\delta^{18}O_{sw}$ (‰ VPDB)	$[CO_3^{2-}]$ (µmol kg^{-1})	$\delta^{18}O_c$'	SST - Equation 1 (°C)	SST - Bayfox (°C)			Species	Size fraction (µm)	MECO interval
									0.05	0.50	0.95			
288.00	38.35	1.99	-2.22	-0.22	-0.49	103.23	-2.40	25.31	21.75	25.61	29.50	*Acarinina spp.*	150-250	N/A
298.00	38.24	1.97	-3.15	-0.22	-0.49	103.46	-3.33	30.02	25.76	29.64	33.49	*Acarinina spp.*	150-250	N/A
316.00	37.87	1.68	-3.37	-0.22	-0.49	104.20	-3.55	31.15	26.71	30.60	34.45	*Acarinina spp.*	150-250	N/A
321.00	37.78	1.86	-3.37	-0.22	-0.49	104.38	-3.55	31.15	26.76	30.55	34.48	*Acarinina spp.*	150-250	N/A

Supplementary Table 4.1.10: U1408

Depth (rmcd)	Age (Ma) GTS2012	$\delta^{13}C$ (‰ VPDB)	$\delta^{18}O$ (‰ VPDB)	$\delta^{18}O_{sw}$ (‰ VSMOW)	$\delta^{18}O_{sw}$ (‰ VPDB)	$[CO_3^{2-}]$ (µmol kg^{-1})	$\delta^{18}O_c$'	SST - Equation 1 (°C)	SST - Bayfox (°C)			Species	Size fraction (µm)	MECO interval
									0.05	0.50	0.95			
83.50	40.92	2.66	-1.28	-0.41	-0.68	99.43	-1.47	19.82	16.98	20.87	24.73	*Acarinina bullbrooki*	280-330	N/A
84.49	40.96	2.18	-1.38	-0.41	-0.68	99.41	-1.58	20.34	17.41	21.28	25.13	*Acarinina bullbrooki*	280-330	N/A
85.47	41.00	2.37	-1.21	-0.41	-0.68	99.39	-1.40	19.48	16.64	20.53	24.47	*Acarinina bullbrooki*	280-330	N/A
86.47	41.04	2.61	-1.33	-0.41	-0.68	99.37	-1.52	20.07	17.15	21.05	24.88	*Acarinina bullbrooki*	280-330	N/A
87.46	41.08	2.17	-1.30	-0.41	-0.68	99.35	-1.49	19.91	17.12	20.92	24.81	*Acarinina bullbrooki*	280-330	N/A
88.48	41.12	1.92	-1.07	-0.41	-0.68	99.33	-1.27	18.86	16.23	20.00	23.88	*Acarinina bullbrooki*	280-330	N/A
89.47	41.16	1.44	-0.93	-0.41	-0.68	99.31	-1.12	18.19	15.49	19.35	23.14	*Acarinina bullbrooki*	280-330	N/A
90.46	41.20	1.53	-0.98	-0.41	-0.68	99.29	-1.17	18.42	15.71	19.58	23.53	*Acarinina bullbrooki*	280-330	N/A
91.60	41.25	2.05	-1.06	-0.41	-0.68	99.26	-1.25	18.80	16.11	19.92	23.72	*Acarinina bullbrooki*	280-330	N/A
92.61	41.29	1.59	-0.93	-0.41	-0.68	99.24	-1.12	18.18	15.56	19.38	23.27	*Acarinina bullbrooki*	280-330	N/A
93.61	41.33	1.74	-1.02	-0.41	-0.68	99.22	-1.22	18.62	15.94	19.81	23.65	*Acarinina bullbrooki*	280-330	N/A
94.60	41.37	1.55	-0.86	-0.41	-0.68	99.20	-1.05	17.83	15.26	19.05	22.97	*Acarinina bullbrooki*	280-330	N/A
95.70	41.42	1.42	-0.84	-0.41	-0.68	99.18	-1.03	17.74	15.12	18.93	22.83	*Acarinina bullbrooki*	280-330	N/A
96.69	41.46	1.50	-0.89	-0.41	-0.68	99.16	-1.08	17.99	15.41	19.25	23.07	*Acarinina bullbrooki*	280-330	N/A
97.70	41.50	1.43	-1.17	-0.41	-0.68	99.14	-1.37	19.33	16.54	20.40	24.23	*Acarinina bullbrooki*	280-330	N/A
99.52	41.57	1.47	-0.96	-0.41	-0.68	99.10	-1.15	18.30	15.62	19.47	23.35	*Acarinina bullbrooki*	280-330	N/A

Depth (rmcd)	Age (Ma) GTS2012	$\delta^{13}C$ (‰ VPDB)	$\delta^{18}O$ (‰ VPDB)	$\delta^{18}O_{sw}$ (‰ VSMOW)	$\delta^{18}O_{sw}$ (‰ VPDB)	$[CO_3^{2-}]$ (µmol kg^{-1})	$\delta^{18}O_c$'	SST - Equation 1 (°C)	SST - Bayfox (°C)			Species	Size fraction (µm)	MECO interval
									0.05	0.50	0.95			
100.51	41.61	1.56	-1.01	-0.41	-0.68	99.08	-1.21	18.57	15.83	19.68	23.62	*Acarinina bullbrooki*	280-330	N/A
101.52	41.65	1.48	-1.15	-0.41	-0.68	99.06	-1.34	19.23	16.51	20.32	24.09	*Acarinina bullbrooki*	280-330	N/A
102.52	41.69	1.51	-1.18	-0.41	-0.68	99.04	-1.38	19.38	16.65	20.49	24.38	*Acarinina bullbrooki*	280-330	N/A
103.51	41.73	1.61	-1.29	-0.41	-0.68	99.02	-1.48	19.87	17.02	20.92	24.75	*Acarinina bullbrooki*	280-330	N/A
105.52	41.81	1.41	-1.02	-0.41	-0.68	98.97	-1.21	18.60	15.90	19.80	23.54	*Acarinina bullbrooki*	280-330	N/A
106.25	41.84	1.77	-1.34	-0.41	-0.68	98.96	-1.53	20.11	17.27	21.09	24.99	*Acarinina bullbrooki*	280-330	N/A
107.26	41.89	1.57	-1.22	-0.41	-0.68	98.94	-1.41	19.55	16.73	20.59	24.47	*Acarinina bullbrooki*	280-330	N/A
108.23	41.92	1.94	-1.48	-0.41	-0.68	98.92	-1.67	20.79	17.83	21.72	25.51	*Acarinina bullbrooki*	280-330	N/A
109.23	41.97	2.12	-1.18	-0.41	-0.68	98.90	-1.37	19.35	16.61	20.43	24.31	*Acarinina bullbrooki*	280-330	N/A
110.24	42.01	2.20	-1.49	-0.41	-0.68	98.88	-1.69	20.87	17.91	21.79	25.60	*Acarinina bullbrooki*	280-330	N/A
111.24	42.05	1.88	-1.62	-0.41	-0.68	98.86	-1.81	21.48	18.55	22.39	26.29	*Acarinina bullbrooki*	280-330	N/A
112.23	42.09	1.88	-1.50	-0.41	-0.68	98.84	-1.70	20.91	17.90	21.82	25.69	*Acarinina bullbrooki*	280-330	N/A
113.24	42.13	1.99	-1.28	-0.41	-0.68	98.81	-1.47	19.84	17.06	20.89	24.74	*Acarinina bullbrooki*	280-330	N/A
113.96	42.16	1.92	-1.30	-0.41	-0.68	98.80	-1.50	19.96	17.10	20.94	24.91	*Acarinina bullbrooki*	280-330	N/A
114.96	42.20	2.00	-1.39	-0.41	-0.68	98.78	-1.58	20.36	17.42	21.32	25.17	*Acarinina bullbrooki*	280-330	N/A
115.94	42.24	1.66	-1.20	-0.41	-0.68	98.76	-1.40	19.48	16.76	20.56	24.45	*Acarinina bullbrooki*	280-330	N/A
117.96	42.31	1.44	-1.15	-0.41	-0.68	98.72	-1.34	19.22	16.51	20.30	24.14	*Acarinina bullbrooki*	280-330	N/A
118.72	42.33	1.49	-1.12	-0.41	-0.68	98.71	-1.32	19.10	16.34	20.23	24.08	*Acarinina bullbrooki*	280-330	N/A
119.72	42.36	1.20	-1.06	-0.41	-0.68	98.70	-1.25	18.79	16.06	19.93	23.72	*Acarinina bullbrooki*	280-330	N/A
120.70	42.39	1.69	-1.12	-0.41	-0.68	98.68	-1.32	19.09	16.40	20.24	24.13	*Acarinina bullbrooki*	280-330	N/A
121.72	42.41	1.31	-1.22	-0.41	-0.68	98.67	-1.41	19.57	16.77	20.63	24.45	*Acarinina bullbrooki*	280-330	N/A
122.72	42.44	1.56	-1.00	-0.41	-0.68	98.66	-1.19	18.50	15.83	19.62	23.48	*Acarinina bullbrooki*	280-330	N/A
123.70	42.46	1.57	-1.13	-0.41	-0.68	98.64	-1.32	19.14	16.36	20.18	24.16	*Acarinina bullbrooki*	280-330	N/A
40.39	39.03	4.22	-1.08	-0.41	-0.68	101.86	-1.26	18.85	16.13	19.94	23.78	*Acarinina praetopilensis*	280-330	N/A

Depth (rmcd)	Age (Ma) GTS2012	$\delta^{13}C$ (‰ VPDB)	$\delta^{18}O$ (‰ VPDB)	$\delta^{18}O_{sw}$ (‰ VSMOW)	$\delta^{18}O_{sw}$ (‰ VPDB)	$[CO_3^{2-}]$ (µmol kg^{-1})	$\delta^{18}O_c$'	SST - Equation 1 (°C)	SST - Bayfox (°C)			Species	Size fraction (µm)	MECO interval
									0.05	0.50	0.95			
42.85	39.16	3.71	-1.79	-0.41	-0.68	101.60	-1.98	22.29	19.20	23.03	26.87	*Acarinina praetopilensis*	280-330	N/A
44.38	39.24	3.85	-2.23	-0.41	-0.68	101.43	-2.41	24.42	20.99	24.92	28.76	*Acarinina praetopilensis*	280-330	N/A
50.33	39.56	3.39	-1.82	-0.41	-0.68	100.79	-2.01	22.44	19.31	23.21	27.05	*Acarinina praetopilensis*	280-330	N/A
51.33	39.61	3.24	-1.71	-0.41	-0.68	100.68	-1.90	21.89	18.85	22.66	26.63	*Acarinina praetopilensis*	280-330	N/A
52.32	39.64	3.62	-1.71	-0.41	-0.68	100.62	-1.90	21.90	18.76	22.67	26.48	*Acarinina praetopilensis*	280-330	N/A
53.33	39.67	4.04	-1.85	-0.41	-0.68	100.58	-2.04	22.58	19.40	23.28	27.10	*Acarinina praetopilensis*	280-330	N/A
54.33	39.69	3.30	-1.75	-0.41	-0.68	100.53	-1.94	22.09	19.05	22.85	26.70	*Acarinina praetopilensis*	280-330	N/A
56.37	39.76	3.12	-1.65	-0.41	-0.68	100.38	-1.84	21.62	18.64	22.42	26.22	*Acarinina praetopilensis*	280-330	Post
57.36	39.81	3.63	-1.63	-0.41	-0.68	100.28	-1.82	21.53	18.55	22.40	26.19	*Acarinina praetopilensis*	280-330	Post
58.38	39.86	3.56	-1.88	-0.41	-0.68	100.18	-2.07	22.71	19.55	23.40	27.21	*Acarinina praetopilensis*	280-330	Post
59.37	39.91	3.33	-1.56	-0.41	-0.68	100.09	-1.75	21.17	18.26	22.05	25.79	*Acarinina praetopilensis*	280-330	Post
60.34	39.95	3.10	-1.80	-0.41	-0.68	100.00	-1.99	22.36	19.18	23.08	26.92	*Acarinina praetopilensis*	280-330	Post
61.18	39.99	3.41	-1.70	-0.41	-0.68	99.92	-1.89	21.83	18.81	22.64	26.62	*Acarinina praetopilensis*	280-330	Post
61.67	40.02	3.68	-2.03	-0.41	-0.68	99.89	-2.22	23.48	20.25	24.08	27.90	*Acarinina praetopilensis*	280-330	Peak
62.18	40.04	2.98	-1.57	-0.41	-0.68	99.88	-1.76	21.22	18.28	22.14	25.96	*Acarinina praetopilensis*	280-330	Peak
62.68	40.06	2.94	-1.80	-0.41	-0.68	99.87	-1.99	22.33	19.28	23.13	27.05	*Acarinina praetopilensis*	280-330	Peak
64.18	40.13	3.67	-1.71	-0.41	-0.68	99.83	-1.90	21.92	18.86	22.73	26.65	*Acarinina praetopilensis*	280-330	Onset
65.68	40.20	3.32	-1.96	-0.41	-0.68	99.80	-2.15	23.11	19.89	23.75	27.55	*Acarinina praetopilensis*	280-330	Onset
66.17	40.22	3.02	-2.05	-0.41	-0.68	99.79	-2.24	23.57	20.31	24.15	28.05	*Acarinina praetopilensis*	280-330	Onset
66.68	40.24	2.99	-2.05	-0.41	-0.68	99.78	-2.24	23.57	20.38	24.13	27.97	*Acarinina praetopilensis*	280-330	Onset
67.47	40.27	3.07	-1.86	-0.41	-0.68	99.76	-2.05	22.63	19.49	23.41	27.29	*Acarinina praetopilensis*	280-330	Onset
68.49	40.31	3.19	-2.99	-0.41	-0.68	99.74	-3.18	28.28	24.35	28.23	32.04	*Acarinina praetopilensis*	280-330	Onset
68.99	40.33	3.73	-2.29	-0.41	-0.68	99.73	-2.49	24.78	21.34	25.20	29.03	*Acarinina praetopilensis*	280-330	Onset
69.48	40.35	2.47	-1.62	-0.41	-0.68	99.72	-1.81	21.45	18.46	22.24	26.07	*Acarinina praetopilensis*	280-330	Onset
69.99	40.37	3.03	-1.80	-0.41	-0.68	99.71	-1.99	22.33	19.19	23.06	26.99	*Acarinina praetopilensis*	280-330	Onset

Depth (rmcd)	Age (Ma) GTS2012	$\delta^{13}C$ (‰ VPDB)	$\delta^{18}O$ (‰ VPDB)	$\delta^{18}O_{sw}$ (‰ VSMOW)	$\delta^{18}O_{sw}$ (‰ VPDB)	$[CO_3^{2-}]$ (µmol kg^{-1})	$\delta^{18}O_c$'	SST - Equation 1 (°C)	SST - Bayfox (°C)			Species	Size fraction (µm)	MECO interval
									0.05	0.50	0.95			
70.47	40.39	3.35	-1.66	-0.41	-0.68	99.70	-1.85	21.67	18.63	22.49	26.35	*Acarinina praetopilensis*	280-330	Onset
71.17	40.42	2.98	-1.85	-0.41	-0.68	99.69	-2.04	22.60	19.43	23.28	27.11	*Acarinina praetopilensis*	280-330	Onset
72.67	40.48	2.94	-2.04	-0.41	-0.68	99.66	-2.23	23.51	20.24	24.11	27.92	*Acarinina praetopilensis*	280-330	Onset
73.16	40.50	3.24	-1.73	-0.41	-0.68	99.64	-1.92	21.99	18.99	22.77	26.71	*Acarinina praetopilensis*	280-330	Onset
73.67	40.52	2.60	-1.76	-0.41	-0.68	99.63	-1.95	22.15	19.07	22.95	26.78	*Acarinina praetopilensis*	280-330	Onset
74.17	40.54	2.97	-1.81	-0.41	-0.68	99.62	-2.00	22.37	19.31	23.11	26.97	*Acarinina praetopilensis*	280-330	Onset
74.66	40.56	2.90	-1.65	-0.41	-0.68	99.61	-1.84	21.60	18.57	22.44	26.27	*Acarinina praetopilensis*	280-330	Onset
75.17	40.58	2.78	-1.63	-0.41	-0.68	99.60	-1.82	21.52	18.47	22.31	26.20	*Acarinina praetopilensis*	280-330	Onset
76.16	40.62	3.01	-1.60	-0.41	-0.68	99.58	-1.79	21.36	18.44	22.22	26.04	*Acarinina praetopilensis*	280-330	Onset
76.67	40.64	2.71	-1.47	-0.41	-0.68	99.57	-1.66	20.74	17.82	21.67	25.56	*Acarinina praetopilensis*	280-330	Pre
77.06	40.66	2.66	-1.51	-0.41	-0.68	99.56	-1.70	20.93	17.97	21.83	25.64	*Acarinina praetopilensis*	280-330	Pre
77.57	40.68	2.88	-1.31	-0.41	-0.68	99.55	-1.50	19.97	17.12	20.97	24.83	*Acarinina praetopilensis*	280-330	Pre
78.07	40.70	2.89	-1.32	-0.41	-0.68	99.54	-1.51	20.05	17.22	21.02	24.88	*Acarinina praetopilensis*	280-330	Pre
78.56	40.72	2.98	-1.28	-0.41	-0.68	99.53	-1.47	19.85	17.00	20.85	24.68	*Acarinina praetopilensis*	280-330	Pre
79.07	40.74	2.82	-1.38	-0.41	-0.68	99.52	-1.57	20.30	17.49	21.32	25.13	*Acarinina praetopilensis*	280-330	Pre
80.50	40.80	3.21	-1.55	-0.41	-0.68	99.49	-1.74	21.14	18.18	22.02	25.83	*Acarinina praetopilensis*	280-330	Pre
81.49	40.84	2.82	-1.45	-0.41	-0.68	99.47	-1.64	20.66	17.75	21.59	25.51	*Acarinina praetopilensis*	280-330	Pre
82.50	40.88	2.58	-1.53	-0.41	-0.68	99.45	-1.72	21.02	18.09	21.92	25.73	*Acarinina praetopilensis*	280-330	Pre
83.50	40.92	3.12	-1.74	-0.41	-0.68	99.43	-1.93	22.04	19.01	22.86	26.68	*Acarinina praetopilensis*	280-330	N/A
84.49	40.96	2.59	-1.52	-0.41	-0.68	99.41	-1.71	21.01	18.05	21.90	25.70	*Acarinina praetopilensis*	280-330	N/A
85.47	41.00	3.32	-1.94	-0.41	-0.68	99.39	-2.13	23.02	19.90	23.68	27.57	*Acarinina praetopilensis*	280-330	N/A
86.47	41.04	3.23	-1.78	-0.41	-0.68	99.37	-1.97	22.27	19.26	23.04	26.91	*Acarinina praetopilensis*	280-330	N/A
87.46	41.08	3.08	-1.46	-0.41	-0.68	99.35	-1.65	20.71	17.70	21.64	25.45	*Acarinina praetopilensis*	280-330	N/A
88.48	41.12	3.44	-1.69	-0.41	-0.68	99.33	-1.88	21.83	18.81	22.66	26.50	*Acarinina praetopilensis*	280-330	N/A
91.60	41.25	3.15	-1.43	-0.41	-0.68	99.26	-1.62	20.56	17.64	21.54	25.41	*Acarinina praetopilensis*	280-330	N/A

Depth (rmcd)	Age (Ma) GTS2012	$\delta^{13}C$ (‰ VPDB)	$\delta^{18}O$ (‰ VPDB)	$\delta^{18}O_{sw}$ (‰ VSMOW)	$\delta^{18}O_{sw}$ (‰ VPDB)	$[CO_3^{2-}]$ (µmol kg^{-1})	$\delta^{18}O_c$'	SST - Equation 1 (°C)	SST - Bayfox (°C)			Species	Size fraction (µm)	MECO interval
									0.05	0.50	0.95			
48.83	39.48	2.27	-1.22	-0.41	-0.68	100.95	-1.41	19.53	16.74	20.58	24.37	*Globigerinatheka index*	300-350	N/A
53.33	39.67	2.23	-1.05	-0.41	-0.68	100.58	-1.24	18.73	15.97	19.84	23.81	*Globigerinatheka index*	300-350	N/A
55.38	39.72	2.31	-1.19	-0.41	-0.68	100.47	-1.38	19.38	16.61	20.48	24.29	*Globigerinatheka index*	300-350	N/A
58.38	39.86	1.92	-1.40	-0.41	-0.68	100.18	-1.59	20.42	17.58	21.36	25.17	*Globigerinatheka index*	300-350	Post
60.34	39.95	2.35	-1.06	-0.41	-0.68	100.00	-1.25	18.78	16.03	19.97	23.75	*Globigerinatheka index*	300-350	Post
61.18	39.99	2.46	-1.08	-0.41	-0.68	99.92	-1.27	18.86	16.13	20.00	23.87	*Globigerinatheka index*	300-350	Post
63.17	40.09	2.40	-1.37	-0.41	-0.68	99.86	-1.56	20.27	17.41	21.26	25.15	*Globigerinatheka index*	300-350	Peak
63.68	40.11	2.47	-1.22	-0.41	-0.68	99.84	-1.41	19.56	16.71	20.58	24.49	*Globigerinatheka index*	300-350	Onset
64.18	40.13	2.51	-1.29	-0.41	-0.68	99.83	-1.48	19.89	17.09	20.92	24.79	*Globigerinatheka index*	300-350	Onset
65.68	40.20	1.92	-1.33	-0.41	-0.68	99.80	-1.52	20.05	17.23	21.07	25.01	*Globigerinatheka index*	300-350	Onset
66.17	40.22	1.86	-1.57	-0.41	-0.68	99.79	-1.76	21.20	18.22	22.03	25.92	*Globigerinatheka index*	300-350	Onset
67.47	40.27	2.42	-1.57	-0.41	-0.68	99.76	-1.76	21.22	18.23	22.08	25.96	*Globigerinatheka index*	300-350	Onset
69.99	40.37	2.01	-1.63	-0.41	-0.68	99.71	-1.82	21.51	18.59	22.38	26.15	*Globigerinatheka index*	300-350	Onset
71.17	40.42	1.65	-1.22	-0.41	-0.68	99.69	-1.41	19.55	16.82	20.59	24.43	*Globigerinatheka index*	300-350	Onset
76.16	40.62	1.76	-0.84	-0.41	-0.68	99.58	-1.03	17.74	15.17	19.02	22.89	*Globigerinatheka index*	300-350	Onset
80.50	40.80	1.94	-0.84	-0.41	-0.68	99.49	-1.03	17.76	15.16	19.02	22.92	*Globigerinatheka index*	300-350	Pre
82.50	40.88	1.75	-0.73	-0.41	-0.68	99.45	-0.92	17.24	14.64	18.56	22.34	*Globigerinatheka index*	300-350	Pre
84.49	40.96	1.75	-1.31	-0.41	-0.68	99.41	-1.50	19.96	17.14	20.99	24.79	*Globigerinatheka index*	300-350	N/A
86.47	41.04	2.16	-1.24	-0.41	-0.68	99.37	-1.43	19.64	16.82	20.69	24.53	*Globigerinatheka index*	300-350	N/A
90.46	41.20	2.28	-1.03	-0.41	-0.68	99.29	-1.22	18.66	15.92	19.81	23.68	*Globigerinatheka index*	300-350	N/A
93.61	41.33	2.53	-1.34	-0.41	-0.68	99.22	-1.53	20.13	17.21	21.20	24.93	*Globigerinatheka index*	300-350	N/A
95.70	41.42	2.13	-0.92	-0.41	-0.68	99.18	-1.11	18.12	15.53	19.34	23.32	*Globigerinatheka index*	300-350	N/A
99.52	41.57	1.77	-1.14	-0.41	-0.68	99.10	-1.34	19.19	16.45	20.28	24.12	*Globigerinatheka index*	300-350	N/A
114.96	42.20	2.34	-1.28	-0.41	-0.68	98.78	-1.47	19.83	17.04	20.88	24.70	*Globigerinatheka index*	300-350	N/A

Depth (rmcd)	Age (Ma) GTS2012	$\delta^{13}C$ (‰ VPDB)	$\delta^{18}O$ (‰ VPDB)	$\delta^{18}O_{sw}$ (‰ VSMOW)	$\delta^{18}O_{sw}$ (‰ VPDB)	$[CO_3^{2-}]$ (µmol kg^{-1})	$\delta^{18}O_c$'	SST - Equation 1 (°C)	SST - Bayfox (°C)			Species	Size fraction (µm)	MECO interval
									0.05	0.50	0.95			
60.34	39.95	2.54	-1.18	-0.41	-0.68	100.00	-1.37	19.38	16.54	20.43	24.30	*Globigerinatheka mexicana*	300-350	Post
62.18	40.04	2.61	-1.43	-0.41	-0.68	99.88	-1.62	20.56	17.71	21.57	25.45	*Globigerinatheka mexicana*	300-350	Peak
63.17	40.09	2.56	-1.25	-0.41	-0.68	99.86	-1.44	19.68	16.83	20.75	24.56	*Globigerinatheka mexicana*	300-350	Peak
64.67	40.16	2.29	-1.37	-0.41	-0.68	99.82	-1.56	20.26	17.41	21.22	25.11	*Globigerinatheka mexicana*	300-350	Onset
65.18	40.18	2.14	-1.82	-0.41	-0.68	99.81	-2.01	22.46	19.39	23.17	27.07	*Globigerinatheka mexicana*	300-350	Onset
65.68	40.20	2.18	-1.62	-0.41	-0.68	99.80	-1.81	21.45	18.40	22.26	26.16	*Globigerinatheka mexicana*	300-350	Onset
66.17	40.22	2.16	-1.52	-0.41	-0.68	99.79	-1.71	20.99	17.99	21.88	25.67	*Globigerinatheka mexicana*	300-350	Onset
66.68	40.24	2.00	-1.52	-0.41	-0.68	99.78	-1.71	20.96	18.07	21.95	25.69	*Globigerinatheka mexicana*	300-350	Onset
66.99	40.25	2.21	-1.44	-0.41	-0.68	99.77	-1.63	20.62	17.65	21.54	25.36	*Globigerinatheka mexicana*	300-350	Onset
67.47	40.27	2.46	-1.42	-0.41	-0.68	99.76	-1.61	20.51	17.55	21.46	25.29	*Globigerinatheka mexicana*	300-350	Onset
68.49	40.31	2.16	-1.40	-0.41	-0.68	99.74	-1.59	20.40	17.51	21.37	25.19	*Globigerinatheka mexicana*	300-350	Onset
68.99	40.33	2.36	-1.45	-0.41	-0.68	99.73	-1.64	20.65	17.75	21.61	25.44	*Globigerinatheka mexicana*	300-350	Onset
69.48	40.35	1.90	-1.50	-0.41	-0.68	99.72	-1.69	20.88	18.05	21.85	25.67	*Globigerinatheka mexicana*	300-350	Onset
69.99	40.37	2.35	-1.53	-0.41	-0.68	99.71	-1.72	21.01	18.09	21.92	25.76	*Globigerinatheka mexicana*	300-350	Onset
72.17	40.46	2.00	-1.45	-0.41	-0.68	99.67	-1.64	20.65	17.78	21.62	25.48	*Globigerinatheka mexicana*	300-350	Onset
73.67	40.52	2.33	-1.44	-0.41	-0.68	99.63	-1.63	20.58	17.60	21.49	25.35	*Globigerinatheka mexicana*	300-350	Onset
74.66	40.56	2.52	-1.27	-0.41	-0.68	99.61	-1.46	19.77	16.99	20.81	24.69	*Globigerinatheka mexicana*	300-350	Onset
75.67	40.60	2.51	-1.29	-0.41	-0.68	99.59	-1.49	19.90	17.08	20.94	24.79	*Globigerinatheka mexicana*	300-350	Onset
76.67	40.64	2.40	-1.38	-0.41	-0.68	99.57	-1.57	20.33	17.38	21.28	25.16	*Globigerinatheka mexicana*	300-350	Pre
77.06	40.66	2.40	-1.34	-0.41	-0.68	99.56	-1.53	20.10	17.19	21.11	24.92	*Globigerinatheka mexicana*	300-350	Pre
77.57	40.68	2.40	-1.09	-0.41	-0.68	99.55	-1.28	18.91	16.25	20.05	23.84	*Globigerinatheka mexicana*	300-350	Pre
78.07	40.70	1.82	-1.06	-0.41	-0.68	99.54	-1.25	18.76	16.12	19.93	23.79	*Globigerinatheka mexicana*	300-350	Pre
78.56	40.72	2.60	-1.40	-0.41	-0.68	99.53	-1.59	20.42	17.58	21.38	25.31	*Globigerinatheka mexicana*	300-350	Pre

Supplementary Table 4.2: Mg/Ca data for sites in this compilation: ODP Site 702 (Supplementary Table 4.2.1), ODP Site 1260 (Supplementary Table 4.2.2), ODP Site 1263 (Supplementary Table 4.2.3), ODP Site 865 (Supplementary Table 4.2.4).

Supplementary Table 4.2.1: Site 702

	Depth (mbsf)	Age - GTS2012 (Ma)	Mg/Ca_c (mmol/mol)	Species	Mg/Ca_{sw} (mol/mol, Evans et al., 2018)	B'	T (°C)	T - Henehan et al., 2020 (°C)	MECO interval
Site 702	66.33	39.92	2.22	*Globigerinatheka index*	2.09	0.26	23.86	21.04	Post
	70.53	40.09	2.39	*Globigerinatheka index*	2.09	0.26	24.69	22.75	Post
	71.03	40.11	2.45	*Globigerinatheka index*	2.09	0.26	24.96	23.14	Peak
	71.72	40.14	2.25	*Globigerinatheka index*	2.09	0.26	24.02	20.46	Peak
	73.21	40.25	2.22	*Globigerinatheka index*	2.09	0.26	23.87	21.54	Onset
	77.54	40.61	2.40	*Globigerinatheka index*	2.08	0.26	24.75	23.61	Pre
	80.13	40.82	2.21	*Globigerinatheka index*	2.08	0.26	23.83	21.12	N/A

Supplementary Table 4.2.2: Site 1260

	Depth (mbsf)	Age - GTS2012 (Ma)	Mg/Ca_c (mmol/mol)	Species	Mg/Ca_{sw} (mol/mol, Evans et al., 2018)	B'	T (°C)	T - Henehan et al., 2020 (°C)	MECO interval
Site 1260	38.27	39.81	3.85	*Morozovelloides crassatus*	2.10	0.26	29.97	30.71	N/A
	40.48	39.91	3.58	*Morozovelloides crassatus*	2.09	0.26	29.17	29.99	Post
	41.98	39.98	3.30	*Morozovelloides crassatus*	2.09	0.26	28.27	28.69	Post
	43.43	40.06	3.25	*Morozovelloides crassatus*	2.09	0.26	28.10	27.73	Post
	44.28	40.11	4.26	*Morozovelloides crassatus*	2.09	0.26	31.11	32.18	Peak
	47.08	40.25	3.70	*Morozovelloides crassatus*	2.09	0.26	29.55	30.34	Onset
	49.28	40.39	4.14	*Morozovelloides crassatus*	2.09	0.26	30.80	32.24	Onset
	51.58	40.52	3.80	*Morozovelloides crassatus*	2.08	0.26	29.85	30.84	Onset
	52.88	40.65	3.74	*Morozovelloides crassatus*	2.08	0.26	29.68	30.66	Pre
	59.98	41.01	4.14	*Acarinina praetopilensis*	2.08	0.26	30.81	31.76	N/A

Supplementary Table 4.2.3: Site 1263

	Depth (mbsf)	Age - GTS2012 (Ma)	Mg/Ca_c (mmol/mol)	Species	Mg/Ca_{sw} (mol/mol, Evans et al., 2018)	B'	T (°C)	T - Henehan et al., 2020 (°C)	MECO interval
Site 1263	136.57	39.93	2.99	*Globigerinatheka kugleri*	2.09	0.26	27.17	26.40	Post
	138.08	39.99	3.12	*Globigerinatheka kugleri*	2.09	0.26	27.65	27.37	Post
	140.46	40.07	3.14	*Globigerinatheka kugleri*	2.09	0.26	27.72	27.33	Post
	141.28	40.12	3.15	*Globigerinatheka kugleri*	2.09	0.26	27.76	26.92	Peak
	141.48	40.13	3.50	*Globigerinatheka kugleri*	2.09	0.26	28.93	28.62	Peak
	143.00	40.24	2.88	*Globigerinatheka kugleri*	2.09	0.26	26.76	25.40	Onset
	143.65	40.34	2.85	*Globigerinatheka kugleri*	2.09	0.26	26.65	25.58	Onset
	146.08	40.73	2.72	*Globigerinatheka kugleri*	2.08	0.26	26.14	25.35	Onset
	148.29	41.06	2.84	*Globigerinatheka kugleri*	2.08	0.26	26.62	25.91	N/A

Supplementary Table 4.2.4: Site 865

	Depth (mbsf)	Age - GTS2012 (Ma)	Mg/Ca_c (mmol/mol)	Species	Mg/Ca_{sw} (mol/mol, Evans et al., 2018)	B'	T (°C)	T - Henehan et al., 2020 (°C)	MECO interval
Site 865 - 1	29.00	39.12	4.04	*Acarinina praetopilensis*	2.13	0.26	30.44	32.24	N/A
	30.08	39.33	3.51	*Morozovelloides crassatus*	2.12	0.26	28.90	29.63	N/A
	33.68	39.96	4.25	*Acarinina praetopilensis*	2.09	0.26	31.08	32.72	Post
	34.19	40.00	4.30	*Acarinina praetopilensis*	2.09	0.26	31.21	32.98	Post
	34.59	40.03	4.32	*Acarinina praetopilensis*	2.09	0.26	31.26	32.71	Post
	34.89	40.09	4.43	*Acarinina praetopilensis*	2.09	0.26	31.54	32.54	Post
	35.08	40.14	4.73	*Acarinina praetopilensis*	2.09	0.26	32.27	33.54	Post
	35.08	40.14	4.40	*Morozovelloides crassatus*	2.09	0.26	31.47	32.45	Post
	35.17	40.17	4.99	*Acarinina praetopilensis*	2.09	0.26	32.87	33.83	Peak
	35.42	40.24	3.93	*Acarinina praetopilensis*	2.09	0.26	30.22	31.42	Peak
	35.63	40.31	3.92	*Acarinina praetopilensis*	2.09	0.26	30.19	31.30	Onset
	35.87	40.38	3.99	*Acarinina praetopilensis*	2.09	0.26	30.39	31.71	Onset

	36.36	40.52	3.89	*Acarinina praetopilensis*	2.08	0.26	30.11	31.04	Pre
	36.77	40.63	3.97	*Acarinina praetopilensis*	2.08	0.26	30.34	31.13	Pre
	37.57	40.81	4.09	*Acarinina praetopilensis*	2.08	0.26	30.67	31.71	N/A
	38.27	40.92	3.98	*Acarinina praetopilensis*	2.08	0.26	30.37	31.58	N/A
	39.67	41.13	3.93	*Acarinina praetopilensis*	2.08	0.26	30.23	31.59	N/A
	42.14	41.53	4.60	*Morozovelloides crassatus*	2.08	0.26	31.98	34.27	N/A

	Depth (mbsf)	Age - GTS2012 (Ma)	Mg/Ca_c (mmol/mol)	Species	Mg/Ca_{sw} (mol/mol, Evans et al., 2018)	B'	T (°C)	T - Henehan et al., 2020 (°C)	MECO interval
Site 865 - 2	24.45	38.55	4.04	*Acarinina praetopilensis*	2.08	0.26	30.54		N/A
	25.95	38.61	3.70	*Acarinina praetopilensis*	2.08	0.26	29.56		N/A
	28.45	38.70	3.83	*Acarinina praetopilensis*	2.08	0.26	29.95		N/A
	28.95	38.71	3.76	*Acarinina praetopilensis*	2.08	0.26	29.74		N/A
	35.27	40.20	3.76	*Acarinina praetopilensis*	2.08	0.26	29.74		Peak
	35.57	40.29	3.84	*Acarinina praetopilensis*	2.08	0.26	29.98		Onset
	35.67	40.32	3.67	*Acarinina praetopilensis*	2.08	0.26	29.47		Onset
	35.77	40.35	3.73	*Acarinina praetopilensis*	2.08	0.26	29.65		Onset
	35.97	40.41	3.79	*Acarinina praetopilensis*	2.08	0.26	29.83		Onset
	36.07	40.43	3.76	*Acarinina praetopilensis*	2.08	0.26	29.74		Onset
	36.17	40.46	3.71	*Acarinina praetopilensis*	2.08	0.26	29.58		Onset
	36.57	40.58	3.68	*Acarinina praetopilensis*	2.09	0.26	29.49		Pre
	37.17	40.74	3.72	*Acarinina praetopilensis*	2.09	0.26	29.61		Pre
	37.87	40.86	3.64	*Acarinina praetopilensis*	2.09	0.26	29.37		N/A
	38.67	40.98	3.77	*Acarinina praetopilensis*	2.09	0.26	29.76		N/A
	39.17	41.05	3.73	*Acarinina praetopilensis*	2.09	0.26	29.64		N/A
	40.17	41.21	3.54	*Acarinina praetopilensis*	2.09	0.26	29.06		N/A
	40.67	41.29	4.05	*Acarinina praetopilensis*	2.09	0.26	30.55		N/A

	41.17	41.38	4.02	*Acarinina praetopilensis*	2.15	0.26	30.34	N/A
	41.67	41.46	3.87	*Acarinina praetopilensis*	2.15	0.26	29.91	N/A
	42.27	41.56	3.92	*Acarinina praetopilensis*	2.15	0.26	30.04	N/A
	42.64	41.60	3.99	*Acarinina praetopilensis*	2.16	0.26	30.23	N/A

Supplementary Table 4.3: GDGT abundances for sites in this compilation: DSDP Site 516 (Supplementary Table 4.3.1), ODP Site 647 (Supplementary Table 4.3.2), ODP Site 913 (Supplementary Table 4.3.3), ODP Site 959 (Supplementary Table 4.3.4), ODP Site 1170 (Supplementary Table 4.3.5), ODP Site 1172 (Supplementary Table 4.3.6), ODP Site 1209 (Supplementary Table 4.3.7), Belaya River Section (Supplementary Table 4.3.8)

Supplementary Table 4.3.1: Site 516 (fractional abundances)

Depth (mbsf)	Age (Ma)	MECO interval	Relative abundance						Fractional abundance						TEX86
			1302	1300	1298	1296	1292	1292'	1302	1300	1298	1296	1292	1292'	
			GDGT0	GDGT1	GDGT2	GDGT3	CREN	CREN'	GDGT0	GDGT1	GDGT2	GDGT3	CREN	CREN'	TEX86
618.12	38.12	N/A	586216	142339	209204	42300	1362508	174368	0.23	0.06	0.08	0.02	0.54	0.07	0.75
626.54	38.96	N/A	650882	83991	166114	21149	1357791	110212	0.27	0.04	0.07	0.01	0.57	0.05	0.78
634.61	39.77	N/A	174114	14185	19887	3469	95829	15523	0.54	0.04	0.06	0.01	0.30	0.05	0.73
637.20	40.03	N/A	4982170	631812	924338	205957	7353674	1093753	0.33	0.04	0.06	0.01	0.48	0.07	0.78
647.52	40.50	Post	2288773	174260	225029	62522	1519185	195238	0.51	0.04	0.05	0.01	0.34	0.04	0.73
650.29	40.54	Post	2371026	83882	199794	77390	1226042	193503	0.57	0.02	0.05	0.02	0.30	0.05	0.85
654.47	40.60	Post	506279	56427	92450	21149	622042	97129	0.36	0.04	0.07	0.02	0.45	0.07	0.79
659.90	40.68	Peak	2411763	99308	212100	25997	1338668	311698	0.55	0.02	0.05	0.01	0.30	0.07	0.85
668.44	40.80	Onset	493561	152444	254682	66723	2750936	453173	0.12	0.04	0.06	0.02	0.66	0.11	0.84
675.43	40.91	Onset	9011088	751264	1065444	281806	8081500	1008448	0.45	0.04	0.05	0.01	0.40	0.05	0.76
682.34	41.01	Onset	1658462	483183	665605	158644	4563025	586962	0.20	0.06	0.08	0.02	0.56	0.07	0.74
691.60	41.14	Pre	12645617	284653	446394	86893	2994092	403299	0.75	0.02	0.03	0.01	0.18	0.02	0.77
696.34	41.21	Pre	3545359	1203686	2032503	539959	13821388	2199474	0.15	0.05	0.09	0.02	0.59	0.09	0.80
710.62	41.42	N/A	1739587	139058	237908	53997	592408	114727	0.60	0.05	0.08	0.02	0.21	0.04	0.75
712.30	41.45	N/A	517713	196756	372015	75752	2839663	444404	0.12	0.04	0.08	0.02	0.64	0.10	0.82
717.13	41.52	N/A	6918096	342282	659381	114749	4658518	639145	0.52	0.03	0.05	0.01	0.35	0.05	0.81
724.28	41.62	N/A	17804991	6886291	12440988	3188021	76480269	15145404	0.13	0.05	0.09	0.02	0.58	0.11	0.82
731.28	41.81	N/A	1768763	589247	1018536	214774	7223903	1059472	0.15	0.05	0.09	0.02	0.61	0.09	0.80
738.25	42.05	N/A	98057	11313	21854	5115	116281	16694	0.36	0.04	0.08	0.02	0.43	0.06	0.79
747.10	42.34	N/A	21958	8240	10689	2756	169312	32973	0.09	0.03	0.04	0.01	0.69	0.13	0.85
751.67	42.50	N/A	181594	73444	128288	25820	966535	123326	0.12	0.05	0.09	0.02	0.64	0.08	0.79

Supplementary Table 4.3.2: Site 647 (fractional abundances)

Depth (mbsf)	Age (Ma)	MECO interval	Relative abundance						Fractional abundance						TEX86
			1302	1300	1298	1296	1292	1292'	1302	1300	1298	1296	1292	1292'	
			GDGT0	GDGT1	GDGT2	GDGT3	CREN	CREN'	GDGT0	GDGT1	GDGT2	GDGT3	CREN	CREN'	TEX86
397.60	38.57	N/A	105888.00	23679.40	23229.00	4909.98	193898.00	17511.50	0.29	0.06	0.06	0.01	0.53	0.05	0.66
402.00	38.71	N/A	125026.00	29528.40	33526.60	8099.35	262967.00	27332.80	0.26	0.06	0.07	0.02	0.54	0.06	0.70
402.40	38.72	N/A	38047.80	8828.59	8692.81	1907.38	64362.00	5664.81	0.30	0.07	0.07	0.01	0.50	0.04	0.65
405.50	38.81	N/A	170397.00	39044.30	40912.90	9726.09	338390.00	29133.90	0.27	0.06	0.07	0.02	0.54	0.05	0.67
407.58	38.86	N/A	87442.50	21771.20	23322.50	5401.09	188176.00	18049.40	0.25	0.06	0.07	0.02	0.55	0.05	0.68
410.00	38.93	N/A	160687.00	34837.60	32913.30	8095.26	284818.00	23394.40	0.29	0.06	0.06	0.01	0.52	0.04	0.65
411.50	38.97	N/A	155874.00	40500.10	41907.60	10452.70	305440.00	21577.10	0.27	0.07	0.07	0.02	0.53	0.04	0.65
412.00	38.99	N/A	580323.00	122169.00	117168.00	28350.70	1206230.00	90058.70	0.27	0.06	0.05	0.01	0.56	0.04	0.66
416.00	39.10	N/A	32353.80	6832.23	6020.33	1430.07	54379.40	4350.24	0.31	0.06	0.06	0.01	0.52	0.04	0.63
416.00	39.10	N/A	58188.40	11744.70	11194.70	2737.94	93250.30	8162.56	0.31	0.06	0.06	0.01	0.50	0.04	0.65
419.95	39.21	N/A	41699.90	8379.16	7583.56	1189.28	69250.00	5355.92	0.31	0.06	0.06	0.01	0.52	0.04	0.63
420.90	39.24	N/A	175550.00	56755.00	56136.80	12921.30	328667.00	12379.70	0.27	0.09	0.09	0.02	0.51	0.02	0.59
425.49	39.37	N/A	74658.00	15403.80	13219.50	3772.31	140779.00	9848.15	0.29	0.06	0.05	0.01	0.55	0.04	0.64
426.80	39.41	N/A	249921.00	50668.00	43614.40	10313.70	454801.00	32790.30	0.30	0.06	0.05	0.01	0.54	0.04	0.63
428.30	39.45	N/A	225933.00	46000.50	48111.80	11849.00	365660.00	29056.60	0.31	0.06	0.07	0.02	0.50	0.04	0.66
428.55	39.46	N/A	821471.00	116242.00	120935.00	34204.10	1081100.00	89162.30	0.36	0.05	0.05	0.02	0.48	0.04	0.68
433.80	39.60	N/A	510613.00	120634.00	130941.00	40918.40	1277210.00	110158.00	0.23	0.06	0.06	0.02	0.58	0.05	0.70
435.10	39.64	N/A	52268.30	12571.80	13136.50	4589.08	123605.00	10576.10	0.24	0.06	0.06	0.02	0.57	0.05	0.69
437.19	39.70	N/A	176885.00	58445.40	62649.90	16840.30	389056.00	24546.00	0.24	0.08	0.09	0.02	0.53	0.03	0.64
439.29	39.76	N/A	278957.00	75449.30	88393.40	28465.90	719835.00	70580.20	0.22	0.06	0.07	0.02	0.57	0.06	0.71
440.40	39.79	N/A	242277.00	67214.10	81500.50	24343.30	709202.00	69010.10	0.20	0.06	0.07	0.02	0.59	0.06	0.72
441.10	39.81	N/A	116738.00	37032.40	41270.90	11396.50	265678.00	17958.60	0.24	0.08	0.08	0.02	0.54	0.04	0.66
442.90	39.86	Post	89824.80	25422.00	26501.10	9368.96	217529.00	20909.20	0.23	0.07	0.07	0.02	0.56	0.05	0.69
443.90	39.89	Post	134742.00	46978.60	49631.00	12901.50	291733.00	13710.60	0.25	0.09	0.09	0.02	0.53	0.02	0.62
445.92	39.95	Post	309383.00	88635.70	113732.00	33124.90	955524.00	101446.00	0.19	0.06	0.07	0.02	0.60	0.06	0.74
446.60	39.96	Post	262609.00	88850.60	103339.00	29899.80	642154.00	49878.60	0.22	0.08	0.09	0.03	0.55	0.04	0.67
448.10	40.01	Post	344453.00	90046.60	107356.00	33085.90	988983.00	100491.00	0.21	0.05	0.06	0.02	0.59	0.06	0.73
449.60	40.05	Post	51884.80	13254.80	16337.40	4532.99	129720.00	13054.60	0.23	0.06	0.07	0.02	0.57	0.06	0.72
451.40	40.10	Peak	55450.80	16556.80	25358.90	8895.73	150737.00	19248.30	0.20	0.06	0.09	0.03	0.55	0.07	0.76

452.30	40.13	Peak	545385.00	187770.00	228823.00	77805.80	1354130.00	115786.00	0.22	0.07	0.09	0.03	0.54	0.05	0.69
452.77	40.14	Peak	65037.60	19845.90	26966.10	11162.60	203215.00	24021.50	0.19	0.06	0.08	0.03	0.58	0.07	0.76
454.20	40.19	Onset	66487.30	18111.30	22010.90	6513.23	179844.00	18658.80	0.21	0.06	0.07	0.02	0.58	0.06	0.72
455.10	40.22	Onset	19581.30	5316.03	6491.22	2113.78	53838.20	5328.19	0.21	0.06	0.07	0.02	0.58	0.06	0.72
455.77	40.24	Onset	192098.00	55165.00	70844.40	20539.40	617876.00	62223.30	0.19	0.05	0.07	0.02	0.61	0.06	0.74
456.60	40.27	Onset	108810.00	26520.80	29722.20	7953.95	263303.00	23794.40	0.24	0.06	0.06	0.02	0.57	0.05	0.70
458.40	40.33	Pre	85250.50	23471.90	25185.50	7814.17	220694.00	21693.40	0.22	0.06	0.07	0.02	0.57	0.06	0.70
459.90	40.38	Pre	317993.00	82112.80	91268.50	26770.60	927453.00	80570.90	0.21	0.05	0.06	0.02	0.61	0.05	0.71
464.03	40.53	Pre	154676.00	39667.00	45454.50	12669.60	428753.00	40593.80	0.21	0.05	0.06	0.02	0.59	0.06	0.71
467.42	40.65	N/A	98825.90	26241.00	31200.50	8952.97	264327.00	25984.90	0.22	0.06	0.07	0.02	0.58	0.06	0.72
468.10	40.67	N/A	158110.00	39841.80	47462.10	13487.10	432776.00	42831.60	0.22	0.05	0.06	0.02	0.59	0.06	0.72
471.42	40.78	N/A	32111.10	8563.61	9702.20	2899.54	81442.40	7349.33	0.23	0.06	0.07	0.02	0.57	0.05	0.70
474.62	40.89	N/A	82299.20	22281.20	26879.90	6902.13	230923.00	22949.30	0.21	0.06	0.07	0.02	0.59	0.06	0.72
476.12	40.95	N/A	96424.20	23775.20	27389.60	7450.50	241943.00	23226.30	0.23	0.06	0.07	0.02	0.58	0.06	0.71
476.41	40.96	N/A	270818.00	70364.80	86241.80	22889.90	832390.00	84147.40	0.20	0.05	0.06	0.02	0.61	0.06	0.73
477.62	41.00	N/A	86430.50	23996.20	29076.30	8448.91	252287.00	28035.20	0.20	0.06	0.07	0.02	0.59	0.07	0.73
478.60	41.03	N/A	37115.00	9962.54	12328.50	2974.58	99503.40	10149.00	0.22	0.06	0.07	0.02	0.58	0.06	0.72
479.61	41.07	N/A	302407.00	93019.00	151197.00	35866.50	1246650.00	153445.00	0.15	0.05	0.08	0.02	0.63	0.08	0.79
480.11	41.08	N/A	159787.00	51162.90	79311.70	18619.60	631143.00	76745.80	0.16	0.05	0.08	0.02	0.62	0.08	0.77
480.72	41.11	N/A	116757.00	37281.70	54960.80	13431.70	438095.00	52848.30	0.16	0.05	0.08	0.02	0.61	0.07	0.76
480.95	41.11	N/A	42015.70	11682.60	14870.20	3910.84	125835.00	12859.20	0.20	0.06	0.07	0.02	0.60	0.06	0.73
481.12	41.12	N/A	58272.40	17030.10	20843.40	5564.62	171282.00	17752.60	0.20	0.06	0.07	0.02	0.59	0.06	0.72
481.65	41.14	N/A	73737.20	16482.60	17091.20	4493.32	151637.00	13135.00	0.27	0.06	0.06	0.02	0.55	0.05	0.68
481.67	41.14	N/A	285214.00	93245.20	171774.00	33489.70	1437140.00	180496.00	0.13	0.04	0.08	0.02	0.65	0.08	0.81
482.97	41.18	N/A	32441.80	8697.36	10562.80	3154.60	78842.40	9255.08	0.23	0.06	0.07	0.02	0.55	0.06	0.73
484.75	41.23	N/A	297656.00	94937.70	134236.00	36334.50	1171850.00	131723.00	0.16	0.05	0.07	0.02	0.63	0.07	0.76
485.00	41.24	N/A	78630.50	22669.60	28967.70	7522.61	253818.00	24759.90	0.19	0.05	0.07	0.02	0.61	0.06	0.73
486.96	41.29	N/A	73606.10	21260.90	28009.80	7269.43	234642.00	26529.30	0.19	0.05	0.07	0.02	0.60	0.07	0.74
490.95	41.40	N/A	33226.00	7255.96	6763.09	1958.61	61404.70	5456.06	0.29	0.06	0.06	0.02	0.53	0.05	0.66
493.75	41.43	N/A	42801.70	11951.70	15751.80	4311.60	132323.00	14469.30	0.19	0.05	0.07	0.02	0.60	0.07	0.74

Supplementary Table 4.3.3: Site 913 (fractional abundances)

Depth (mbsf)	Age (Ma)	MECO interval	Relative abundance						Fractional abundance						TEX_{86}
			1302 GDGT0	1300 GDGT1	1298 GDGT2	1296 GDGT3	1292 CREN	1292' CREN'	1302 GDGT0	1300 GDGT1	1298 GDGT2	1296 GDGT3	1292 CREN	1292' CREN'	TEX_{86}
488.65	38.16	N/A	32221629	5530647	4261322	440398	34149808	2183935	0.41	0.07	0.05	0.01	0.43	0.03	0.55
489.68	38.28	N/A	9584836	1526568	1109356	91793	5410909	380441	0.53	0.08	0.06	0.01	0.30	0.02	0.51
492.53	38.60	N/A	22452614	4463983	3748336	367957	19762438	1745071	0.43	0.08	0.07	0.01	0.38	0.03	0.57
507.99	39.63	N/A	387530	46022	31462	3432	163385	10952	0.60	0.07	0.05	0.01	0.25	0.02	0.50
508.65	39.69	N/A	2921030	227384	224845	18594	475567	43394	0.75	0.06	0.06	0.00	0.12	0.01	0.56
511.49	39.94	Post	43619451	8141139	2903390	353573	16047587	1369118	0.60	0.11	0.04	0.00	0.22	0.02	0.36
512.49	40.01	Post	21787654	2966410	2426934	309836	17309324	1292353	0.47	0.06	0.05	0.01	0.38	0.03	0.58
514.32	40.13	Peak	84060898	14490079	13780120	1359260	82842848	6537485	0.41	0.07	0.07	0.01	0.41	0.03	0.60
516.72	40.30	Onset	170353	54768	17578	1407	58378	4546	0.55	0.18	0.06	0.00	0.19	0.01	0.30
532.67	41.40	N/A	75817696	15240714	17597154	1850374	111595012	10218329	0.33	0.07	0.08	0.01	0.48	0.04	0.66
538.34	41.79	N/A	49396877	9953333	11984820	1435266	75044140	5982444	0.32	0.06	0.08	0.01	0.49	0.04	0.66
551.05	42.31	N/A	35586708	5783732	5336602	661690	44389373	3353989	0.37	0.06	0.06	0.01	0.47	0.04	0.62

Supplementary Table 4.3.4: Site 959 (fractional abundances)

Depth (mbsf)	Age (Ma)	MECO interval	Relative abundance						Fractional abundance						TEX86
			1302 GDGT0	1300 GDGT1	1298 GDGT2	1296 GDGT3	1292 CREN	1292' CREN'	1302 GDGT0	1300 GDGT1	1298 GDGT2	1296 GDGT3	1292 CREN	1292' CREN'	TEX86
543.34	38.36	N/A	0.2	0.06	0.07	0.02	0.61	0.05	0.20	0.06	0.07	0.02	0.60	0.05	0.70
552.37	38.78	N/A	0.2	0.06	0.07	0.02	0.6	0.05	0.20	0.06	0.07	0.02	0.60	0.05	0.70
554.86	38.90	N/A	0.19	0.05	0.06	0.02	0.63	0.05	0.19	0.05	0.06	0.02	0.63	0.05	0.72
557.19	39.01	N/A	0.18	0.05	0.06	0.02	0.63	0.06	0.18	0.05	0.06	0.02	0.63	0.06	0.74
562.04	39.24	N/A	0.21	0.06	0.07	0.02	0.59	0.05	0.21	0.06	0.07	0.02	0.59	0.05	0.70
564.01	39.33	N/A	0.18	0.05	0.06	0.02	0.63	0.05	0.18	0.05	0.06	0.02	0.64	0.05	0.72
565.89	39.42	N/A	0.26	0.04	0.05	0.02	0.58	0.05	0.26	0.04	0.05	0.02	0.58	0.05	0.75
567.71	39.50	N/A	0.17	0.05	0.06	0.02	0.63	0.06	0.17	0.05	0.06	0.02	0.64	0.06	0.74
569.21	39.57	N/A	0.15	0.05	0.07	0.02	0.64	0.07	0.15	0.05	0.07	0.02	0.64	0.07	0.76

571.56	39.68	N/A	0.13	0.04	0.07	0.02	0.67	0.07	0.13	0.04	0.07	0.02	0.67	0.07	0.80
573.31	39.76	N/A	0.15	0.05	0.07	0.02	0.65	0.06	0.15	0.05	0.07	0.02	0.65	0.06	0.75
574.99	39.84	Post	0.12	0.05	0.07	0.02	0.67	0.07	0.12	0.05	0.07	0.02	0.67	0.07	0.76
576.06	39.89	Post	0.15	0.05	0.07	0.02	0.65	0.06	0.15	0.05	0.07	0.02	0.65	0.06	0.75
577.03	39.94	Post	0.10	0.04	0.08	0.02	0.68	0.08	0.10	0.04	0.08	0.02	0.68	0.08	0.82
578.26	40.00	Post	0.10	0.04	0.07	0.02	0.68	0.09	0.10	0.04	0.07	0.02	0.68	0.09	0.82
581.19	40.11	Peak	0.10	0.03	0.06	0.02	0.70	0.09	0.10	0.03	0.06	0.02	0.70	0.09	0.85
581.53	40.12	Peak	0.11	0.04	0.07	0.02	0.68	0.08	0.11	0.04	0.07	0.02	0.68	0.08	0.81
590.86	40.47	Onset	0.13	0.04	0.07	0.02	0.67	0.07	0.13	0.04	0.07	0.02	0.67	0.07	0.80
592.88	40.55	Pre	0.16	0.05	0.06	0.02	0.66	0.06	0.16	0.05	0.06	0.02	0.65	0.06	0.74
595.07	40.63	Pre	0.16	0.05	0.07	0.02	0.64	0.06	0.16	0.05	0.07	0.02	0.64	0.06	0.75
600.36	40.83	N/A	0.17	0.05	0.07	0.02	0.64	0.06	0.17	0.05	0.07	0.02	0.63	0.06	0.75
602.11	40.90	N/A	0.18	0.06	0.08	0.02	0.61	0.06	0.18	0.06	0.08	0.02	0.60	0.06	0.73
603.78	40.96	N/A	0.16	0.05	0.06	0.02	0.64	0.07	0.16	0.05	0.06	0.02	0.64	0.07	0.75
606.36	41.06	N/A	0.18	0.05	0.06	0.02	0.63	0.06	0.18	0.05	0.06	0.02	0.63	0.06	0.74
608.85	41.15	N/A	0.18	0.05	0.06	0.02	0.63	0.06	0.18	0.05	0.06	0.02	0.63	0.06	0.74
610.68	41.22	N/A	0.17	0.05	0.06	0.02	0.64	0.07	0.17	0.05	0.06	0.02	0.63	0.07	0.75
615.42	41.40	N/A	0.17	0.05	0.06	0.02	0.62	0.08	0.17	0.05	0.06	0.02	0.62	0.08	0.76
619.83	41.56	N/A	0.17	0.05	0.06	0.02	0.64	0.06	0.17	0.05	0.06	0.02	0.64	0.06	0.74
623.19	41.69	N/A	0.16	0.05	0.05	0.02	0.65	0.07	0.16	0.05	0.05	0.02	0.65	0.07	0.74
629.29	41.92	N/A	0.15	0.05	0.06	0.02	0.65	0.08	0.15	0.05	0.06	0.02	0.64	0.08	0.76
639.11	42.29	N/A	0.12	0.04	0.06	0.02	0.67	0.09	0.12	0.04	0.06	0.02	0.67	0.09	0.81
644.09	42.47	N/A	0.11	0.04	0.06	0.02	0.69	0.09	0.11	0.04	0.06	0.02	0.68	0.09	0.81

Supplementary Table 4.3.5: Site 1170 (fractional abundances)

Depth (mbsf)	Age (Ma)	MECO interval	Relative abundance						Fractional abundance						TEX_{86}
			1302	1300	1298	1296	1292	1292'	1302	1300	1298	1296	1292	1292'	
			GDGT0	GDGT1	GDGT2	GDGT3	CREN	CREN'	GDGT0	GDGT1	GDGT2	GDGT3	CREN	CREN'	TEX_{86}
503.06	N/A	N/A	0.45	0.05	0.03	0.01	0.44	0.02	0.45	0.05	0.03	0.01	0.44	0.02	0.56
523.66	N/A	N/A	0.34	0.06	0.05	0.01	0.50	0.03	0.34	0.06	0.05	0.01	0.50	0.03	0.61
542.96	N/A	N/A	0.42	0.06	0.03	0.01	0.46	0.02	0.42	0.06	0.03	0.01	0.46	0.02	0.53
551.06	N/A	N/A	0.43	0.06	0.03	0.01	0.45	0.02	0.43	0.06	0.03	0.01	0.45	0.02	0.54
552.56	N/A	N/A	0.47	0.06	0.04	0.01	0.41	0.02	0.47	0.06	0.04	0.01	0.41	0.02	0.55
559.16	N/A	N/A	0.41	0.06	0.04	0.01	0.45	0.02	0.41	0.06	0.04	0.01	0.45	0.02	0.56
563.65	N/A	N/A	0.41	0.06	0.04	0.01	0.46	0.03	0.41	0.06	0.04	0.01	0.46	0.03	0.55
568.76	N/A	N/A	0.39	0.06	0.05	0.01	0.46	0.04	0.39	0.06	0.05	0.01	0.46	0.04	0.59
573.26	N/A	N/A	0.50	0.08	0.05	0.01	0.34	0.02	0.50	0.08	0.05	0.01	0.34	0.02	0.51
574.76	N/A	N/A	0.31	0.07	0.07	0.02	0.49	0.06	0.31	0.07	0.07	0.02	0.49	0.06	0.68
576.26	N/A	N/A	0.32	0.07	0.06	0.01	0.48	0.05	0.32	0.07	0.06	0.01	0.48	0.05	0.65
577.57	N/A	N/A	0.41	0.06	0.04	0.01	0.44	0.03	0.41	0.06	0.04	0.01	0.44	0.03	0.57
578.36	N/A	N/A	0.41	0.06	0.04	0.01	0.45	0.04	0.41	0.06	0.04	0.01	0.45	0.04	0.57
579.86	N/A	N/A	0.36	0.07	0.05	0.02	0.47	0.04	0.36	0.07	0.05	0.02	0.47	0.04	0.59
581.36	N/A	N/A	0.23	0.06	0.07	0.01	0.57	0.06	0.23	0.06	0.07	0.01	0.57	0.06	0.72
582.86	N/A	N/A	0.34	0.06	0.05	0.01	0.48	0.05	0.34	0.06	0.05	0.01	0.48	0.05	0.63
584.36	N/A	N/A	0.32	0.07	0.06	0.01	0.49	0.05	0.32	0.07	0.06	0.01	0.49	0.05	0.66
585.10	N/A	N/A	0.41	0.06	0.03	0.01	0.45	0.03	0.41	0.06	0.03	0.01	0.45	0.03	0.55
587.20	N/A	N/A	0.36	0.06	0.04	0.01	0.48	0.04	0.36	0.06	0.04	0.01	0.48	0.04	0.60
588.38	N/A	N/A	0.35	0.06	0.05	0.01	0.48	0.04	0.35	0.06	0.05	0.01	0.48	0.04	0.61
589.88	N/A	N/A	0.33	0.06	0.06	0.01	0.49	0.05	0.33	0.06	0.06	0.01	0.49	0.05	0.65
591.38	N/A	N/A	0.35	0.07	0.05	0.01	0.48	0.04	0.35	0.07	0.05	0.01	0.48	0.04	0.61
592.88	N/A	N/A	0.36	0.06	0.04	0.01	0.49	0.04	0.36	0.06	0.04	0.01	0.49	0.04	0.61
594.41	N/A	N/A	0.34	0.06	0.05	0.01	0.48	0.05	0.34	0.06	0.05	0.01	0.48	0.05	0.65
595.88	N/A	N/A	0.37	0.06	0.05	0.01	0.47	0.04	0.37	0.06	0.05	0.01	0.47	0.04	0.61
596.73	N/A	N/A	0.34	0.06	0.05	0.01	0.47	0.05	0.34	0.06	0.05	0.01	0.47	0.05	0.64
597.61	N/A	N/A	0.39	0.06	0.03	0.01	0.47	0.04	0.39	0.06	0.03	0.01	0.47	0.04	0.58
599.09	N/A	N/A	0.35	0.07	0.05	0.01	0.47	0.05	0.35	0.07	0.05	0.01	0.47	0.05	0.63
600.59	N/A	N/A	0.36	0.06	0.05	0.01	0.46	0.05	0.36	0.06	0.05	0.01	0.46	0.05	0.64

602.09	N/A	N/A	0.34	0.07	0.05	0.01	0.48	0.05	0.34	0.07	0.05	0.01	0.48	0.05	0.64
603.59	N/A	N/A	0.43	0.06	0.03	0.01	0.44	0.03	0.43	0.06	0.03	0.01	0.44	0.03	0.55
605.09	N/A	N/A	0.40	0.06	0.04	0.01	0.45	0.04	0.40	0.06	0.04	0.01	0.45	0.04	0.57
606.59	N/A	N/A	0.32	0.06	0.06	0.01	0.48	0.06	0.32	0.06	0.06	0.01	0.48	0.06	0.68
607.16	N/A	N/A	0.41	0.06	0.03	0.01	0.45	0.03	0.41	0.06	0.03	0.01	0.45	0.03	0.55
608.66	N/A	N/A	0.40	0.07	0.04	0.01	0.44	0.05	0.40	0.07	0.04	0.01	0.44	0.05	0.59
613.16	N/A	N/A	0.40	0.06	0.04	0.01	0.45	0.04	0.40	0.06	0.04	0.01	0.45	0.04	0.58
613.16	N/A	N/A	0.39	0.06	0.04	0.01	0.46	0.04	0.39	0.06	0.04	0.01	0.46	0.04	0.58
618.61	N/A	N/A	0.38	0.06	0.04	0.01	0.47	0.04	0.38	0.06	0.04	0.01	0.47	0.04	0.60
621.61	N/A	N/A	0.35	0.06	0.05	0.01	0.47	0.05	0.35	0.06	0.05	0.01	0.47	0.05	0.64
627.96	N/A	N/A	0.37	0.06	0.04	0.01	0.48	0.04	0.37	0.06	0.04	0.01	0.48	0.04	0.60
633.96	N/A	N/A	0.36	0.07	0.05	0.01	0.47	0.05	0.36	0.07	0.05	0.01	0.47	0.05	0.63
633.96	N/A	N/A	0.35	0.07	0.05	0.01	0.47	0.05	0.35	0.07	0.05	0.01	0.47	0.05	0.62
637.66	N/A	N/A	0.35	0.06	0.04	0.01	0.49	0.05	0.35	0.06	0.04	0.01	0.49	0.05	0.63
650.16	N/A	N/A	0.31	0.07	0.05	0.01	0.50	0.06	0.31	0.07	0.05	0.01	0.50	0.06	0.66
662.96	N/A	N/A	0.29	0.06	0.05	0.01	0.53	0.06	0.29	0.06	0.05	0.01	0.53	0.06	0.68
669.56	N/A	Peak	0.24	0.07	0.07	0.02	0.53	0.08	0.24	0.07	0.07	0.02	0.53	0.08	0.72
678.65	N/A	N/A	0.28	0.06	0.05	0.01	0.53	0.06	0.28	0.06	0.05	0.01	0.53	0.06	0.68
688.72	N/A	N/A	0.28	0.06	0.05	0.02	0.53	0.06	0.28	0.06	0.05	0.02	0.53	0.06	0.69
696.91	N/A	N/A	0.35	0.06	0.04	0.01	0.49	0.05	0.35	0.06	0.04	0.01	0.49	0.05	0.65
701.22	N/A	N/A	0.29	0.06	0.05	0.02	0.53	0.05	0.29	0.06	0.05	0.02	0.53	0.05	0.66

Supplementary Table 4.3.6: Site 1172 (fractional abundances)

Depth (mbsf)	Age (Ma)	MECO interval	Relative abundance						Fractional abundance						TEX_{86}
			1302	1300	1298	1296	1292	1292'	1302	1300	1298	1296	1292	1292'	
			GDGT0	GDGT1	GDGT2	GDGT3	CREN	CREN'	GDGT0	GDGT1	GDGT2	GDGT3	CREN	CREN'	TEX_{86}
373.30	38.21	N/A	27600000	4960000	3400000	1290000	31500000	2050000	0.39	0.07	0.05	0.02	0.44	0.03	0.58
379.80	38.54	N/A	14400000	2550000	1700000	616000	16800000	1130000	0.39	0.07	0.05	0.02	0.45	0.03	0.57
385.00	38.73	N/A	22000000	4170000	2950000	1050000	25200000	1850000	0.38	0.07	0.05	0.02	0.44	0.03	0.58
391.00	38.97	N/A	67000000	13800000	9950000	4240000	66600000	4790000	0.40	0.08	0.06	0.03	0.40	0.03	0.58
394.92	39.12	N/A	28700000	6040000	4840000	1690000	35000000	2710000	0.36	0.08	0.06	0.02	0.44	0.03	0.60
396.85	39.20	N/A	4440000	846000	570000	200000	5340000	372000	0.38	0.07	0.05	0.02	0.45	0.03	0.57
402.37	39.41	N/A	13700000	2890000	2390000	785000	18300000	1590000	0.35	0.07	0.06	0.02	0.46	0.04	0.62
404.20	39.48	N/A	27300000	5700000	4550000	1790000	31000000	2510000	0.37	0.08	0.06	0.02	0.43	0.03	0.61
406.62	39.58	N/A	9630000	2100000	1690000	632000	14200000	1260000	0.33	0.07	0.06	0.02	0.48	0.04	0.63
407.72	39.62	Post	19400000	4430000	4170000	1750000	26900000	2630000	0.33	0.07	0.07	0.03	0.45	0.04	0.66
408.70	39.66	Post	10400000	2250000	1870000	758000	14600000	1240000	0.33	0.07	0.06	0.02	0.47	0.04	0.63
411.70	39.78	Post	5520000	1220000	1080000	425000	8200000	683000	0.32	0.07	0.06	0.02	0.48	0.04	0.64
412.52	39.81	Post	31500000	8200000	7440000	3080000	44700000	4550000	0.32	0.08	0.07	0.03	0.45	0.05	0.65
413.22	39.84	Post	15500000	3920000	4300000	1190000	24300000	3040000	0.30	0.08	0.08	0.02	0.47	0.06	0.69
414.12	39.87	Peak	21100000	5160000	6570000	1910000	35000000	4460000	0.28	0.07	0.09	0.03	0.47	0.06	0.71
414.68	39.89	Peak	9170000	2380000	2790000	787000	17900000	2040000	0.26	0.07	0.08	0.02	0.51	0.06	0.70
415.52	39.93	Peak	14300000	3470000	4280000	1130000	26400000	3010000	0.27	0.07	0.08	0.02	0.50	0.06	0.71
416.22	39.95	Peak	17300000	4240000	4530000	1190000	28600000	3160000	0.29	0.07	0.08	0.02	0.48	0.05	0.68
416.80	39.98	Onset	9790000	2160000	2030000	665000	14900000	1390000	0.32	0.07	0.07	0.02	0.48	0.04	0.65
417.72	40.01	Onset	19100000	4680000	4900000	1520000	29000000	3290000	0.31	0.07	0.08	0.02	0.46	0.05	0.67
418.30	40.03	Onset	9190000	2150000	2140000	590000	14600000	1520000	0.30	0.07	0.07	0.02	0.48	0.05	0.66
419.12	40.07	Onset	22700000	5050000	4250000	1460000	30500000	2790000	0.34	0.08	0.06	0.02	0.46	0.04	0.63
420.02	40.10	Onset	19100000	4020000	3110000	1250000	23700000	1880000	0.36	0.08	0.06	0.02	0.45	0.04	0.61
420.92	40.14	Onset	25100000	4640000	3470000	1260000	35300000	2110000	0.35	0.06	0.05	0.02	0.49	0.03	0.60
421.62	40.21	Onset	24600000	4690000	3800000	1180000	35600000	2280000	0.34	0.07	0.05	0.02	0.49	0.03	0.61
421.90	40.24	Pre	16400000	3020000	2100000	655000	19900000	1340000	0.38	0.07	0.05	0.02	0.46	0.03	0.58
422.92	40.36	Pre	37800000	7650000	5550000	2050000	44200000	3480000	0.38	0.08	0.06	0.02	0.44	0.03	0.59
423.40	40.41	Pre	16100000	3550000	2700000	1030000	20500000	1650000	0.35	0.08	0.06	0.02	0.45	0.04	0.60
424.22	40.50	N/A	19300000	3810000	2770000	1030000	24200000	1850000	0.36	0.07	0.05	0.02	0.46	0.03	0.60

424.90	40.58	N/A	6790000	1410000	1270000	369000	9920000	835000	0.33	0.07	0.06	0.02	0.48	0.04	0.64
425.62	40.66	N/A	33600000	6920000	5110000	1890000	39600000	3300000	0.37	0.08	0.06	0.02	0.44	0.04	0.60
426.40	40.75	N/A	18400000	3730000	2880000	1050000	22600000	1840000	0.36	0.07	0.06	0.02	0.45	0.04	0.61
427.22	40.84	N/A	17400000	3600000	2720000	1040000	21700000	1670000	0.36	0.07	0.06	0.02	0.45	0.03	0.60
427.90	40.91	N/A	47400000	12000000	9900000	3470000	61700000	6940000	0.34	0.08	0.07	0.02	0.44	0.05	0.63
428.96	41.03	N/A	36800000	8400000	6680000	2360000	46000000	4320000	0.35	0.08	0.06	0.02	0.44	0.04	0.61
430.90	41.26	N/A	27400000	5490000	5020000	1670000	35900000	3290000	0.35	0.07	0.06	0.02	0.46	0.04	0.65
433.00	41.47	N/A	14900000	3450000	2920000	998000	21200000	2030000	0.33	0.08	0.06	0.02	0.47	0.04	0.63
437.50	41.81	N/A	23700000	5630000	5030000	1820000	32600000	3300000	0.33	0.08	0.07	0.03	0.45	0.05	0.64
444.10	42.31	N/A	15900000	3400000	3250000	953000	21600000	1880000	0.34	0.07	0.07	0.02	0.46	0.04	0.64

Supplementary Table 4.3.7: Site 1209 (fractional abundances)

Depth (mbsf)	Age (Ma)	MECO interval	Relative abundance						Fractional abundance						TEX_{86}
			1302	1300	1298	1296	1292	1292'	1302	1300	1298	1296	1292	1292'	
			GDGT0	GDGT1	GDGT2	GDGT3	CREN	CREN'	GDGT0	GDGT1	GDGT2	GDGT3	CREN	CREN'	TEX_{86}
134.77	38.29	N/A	0.23	0.08	0.09	0.01	0.54	0.06	0.23	0.08	0.09	0.01	0.54	0.06	0.67
136.81	39.34	N/A	0.28	0.09	0.15	0.01	0.45	0.02	0.28	0.09	0.15	0.01	0.45	0.02	0.66
137.78	39.82	N/A	0.45	0.06	0.08	0.02	0.36	0.04	0.45	0.06	0.08	0.02	0.36	0.04	0.67
140.23	40.98	N/A	0.19	0.06	0.06	0.03	0.63	0.03	0.19	0.06	0.06	0.03	0.63	0.03	0.66

Supplementary Table 4.3.8: Belaya River section (fractional abundances)

Depth (mbsf)	Age (Ma)	MECO interval	Relative abundance						Fractional abundance						TEX_{86}
			1302	1300	1298	1296	1292	1292'	1302	1300	1298	1296	1292	1292'	
			GDGT0	GDGT1	GDGT2	GDGT3	CREN	CREN'	GDGT0	GDGT1	GDGT2	GDGT3	CREN	CREN'	TEX_{86}
20.85	41.26	N/A	611268	225699	410942	142360	3214590	403053	0.12	0.05	0.08	0.03	0.64	0.08	0.81
21.43	41.20	N/A	300656	107912	202656	39732	1585230	203247	0.12	0.04	0.08	0.02	0.65	0.08	0.81
21.99	41.15	N/A	400917	145868	283684	49307	2113930	292683	0.12	0.04	0.09	0.02	0.64	0.09	0.81
22.81	41.07	N/A	363768	136979	290775	50006	2142870	290079	0.11	0.04	0.09	0.02	0.65	0.09	0.82
23.33	41.02	N/A	300079	117604	246905	41435.3	1825560	247113	0.11	0.04	0.09	0.01	0.66	0.09	0.82
23.93	40.96	N/A	324060	125370	266546	43981.3	1974000	272724	0.11	0.04	0.09	0.01	0.66	0.09	0.82
24.58	40.90	N/A	271883	100067	200592	31076.9	1586490	217221	0.11	0.04	0.08	0.01	0.66	0.09	0.82
25.13	40.85	N/A	317147	116965	229902	37460.6	1762580	229113	0.12	0.04	0.09	0.01	0.65	0.09	0.81
25.58	40.80	N/A	306279	116645	225389	44397.1	1796160	233136	0.11	0.04	0.08	0.02	0.66	0.09	0.81
26.25	40.74	Pre	366076	133163	248526	48879	2001600	249303	0.12	0.04	0.08	0.02	0.66	0.08	0.80
26.77	40.69	Pre	349688	132257	240272	48738.7	1975970	248844	0.12	0.04	0.08	0.02	0.66	0.08	0.80
27.47	40.62	Pre	317040	117699	225751	46510	1798510	227823	0.12	0.04	0.08	0.02	0.66	0.08	0.81
28.03	40.57	Pre	218797	86662	166175	37211	1396630	180562	0.10	0.04	0.08	0.02	0.67	0.09	0.82
28.65	40.51	Pre	212635	85689	177527	40745	1486060	203025	0.10	0.04	0.08	0.02	0.67	0.09	0.83
29.22	40.45	Onset	223546	90651	207630	44260	1603210	231224	0.09	0.04	0.09	0.02	0.67	0.10	0.84
29.88	40.38	Onset	56221	22087	46576	10307	342208	48531	0.11	0.04	0.09	0.02	0.65	0.09	0.83
29.88	40.38	Onset	234365	95112	194962	46695	1593650	233678	0.10	0.04	0.08	0.02	0.66	0.10	0.83
30.35	40.34	Onset	210934	89115	201971	46806	1745790	269112	0.08	0.03	0.08	0.02	0.68	0.10	0.85
30.82	40.33	Onset	42848	18068	42622	9078	314687	47117	0.09	0.04	0.09	0.02	0.66	0.10	0.85
31.37	40.32	Onset	821453	86888	210748	44809	1784430	274794	0.25	0.03	0.07	0.01	0.55	0.09	0.86
31.81	40.31	Onset	52420	20689	50205	10999	390066	61922	0.09	0.04	0.09	0.02	0.67	0.11	0.86
31.81	40.31	Onset	186901	79051	190283	43522	1661460	259824	0.08	0.03	0.08	0.02	0.69	0.11	0.86
32.50	40.30	Onset	174613	77178	168083	45607	1531580	220233	0.08	0.03	0.08	0.02	0.69	0.10	0.85
33.00	40.29	Onset	62205	23845	51634	11323	387536	58375	0.10	0.04	0.09	0.02	0.65	0.10	0.84
33.65	40.27	Onset	61707	22206	43011	11272	350495	50971	0.11	0.04	0.08	0.02	0.65	0.09	0.83
34.04	40.26	Onset	74953	30376	66147	15653	528709	76355	0.09	0.04	0.08	0.02	0.67	0.10	0.84
34.28	40.26	Peak	61540	24092	49045	12553	407680	53154	0.10	0.04	0.08	0.02	0.67	0.09	0.83
34.65	40.25	Peak	316680	121703	244018	62384	2138290	293591	0.10	0.04	0.08	0.02	0.67	0.09	0.83
34.90	40.24	Peak	86537	32934	61299	15915	491888	63957	0.11	0.04	0.08	0.02	0.65	0.08	0.81

35.36	40.23	Peak	103905	35000	59743	14683	459406	52815	0.14	0.05	0.08	0.02	0.63	0.07	0.78
35.55	40.23	Peak	76863	28576	48315	12551	380530	46741	0.13	0.05	0.08	0.02	0.64	0.08	0.79
35.83	40.22	Peak	140552	54776	107905	29308	875729	111503	0.11	0.04	0.08	0.02	0.66	0.08	0.82
36.33	40.21	Post	242832	22471	43464	9939	300977	38998	0.37	0.03	0.07	0.02	0.46	0.06	0.80
36.70	40.21	Post	72282	26111	45956	11028	336925	39985	0.14	0.05	0.09	0.02	0.63	0.08	0.79
37.10	40.20	Post	60149	21962	39082	8919	272270	33316	0.14	0.05	0.09	0.02	0.62	0.08	0.79
37.91	40.18	Post	91855	31206	64676	13402	441896	59608	0.13	0.04	0.09	0.02	0.63	0.08	0.82
38.34	40.17	Post	288339	112410	205462	46315	1680770	209549	0.11	0.04	0.08	0.02	0.66	0.08	0.80
39.15	40.15	Post	44559	18002	33498	7340	250876	32482	0.12	0.05	0.09	0.02	0.65	0.08	0.80
39.76	40.14	Post	479604	184023	353356	75955	2800650	352606	0.11	0.04	0.08	0.02	0.66	0.08	0.81
40.40	40.12	Post	115719	38705	62245	14413	467467	60977	0.15	0.05	0.08	0.02	0.62	0.08	0.78
40.40	40.12	Post	639502	224425	354122	90440	3034030	382476	0.14	0.05	0.07	0.02	0.64	0.08	0.79
41.00	40.11	Post	534870	174497	308762	72671	2537680	302265	0.14	0.04	0.08	0.02	0.65	0.08	0.80
41.65	40.09	Post	409785	129062	236745	56628	1932480	245155	0.14	0.04	0.08	0.02	0.64	0.08	0.81
42.68	40.06	Post	45532	15965	24703	5660	182811	21366	0.15	0.05	0.08	0.02	0.62	0.07	0.76
43.58	40.04	Post	510225	176771	298811	69050	2382340	289801	0.14	0.05	0.08	0.02	0.64	0.08	0.79
44.28	40.02	Post	603389	235580	470162	95541	3658680	478112	0.11	0.04	0.08	0.02	0.66	0.09	0.82
45.40	39.99	Post	734995	285420	601764	120168	4538060	637134	0.11	0.04	0.09	0.02	0.66	0.09	0.83
46.05	39.98	Post	857225	316949	557788	120548	4646770	570267	0.12	0.04	0.08	0.02	0.66	0.08	0.80
46.90	39.95	N/A	191178	73534	139036	25279	945756	127006	0.13	0.05	0.09	0.02	0.63	0.08	0.80
48.60	39.91	N/A	360947	137783	277302	51281	2083530	293955	0.11	0.04	0.09	0.02	0.65	0.09	0.82

Supplementary Table 4.4: Quality control metrics and SSTs from TEX_{86} for sites in this compilation: DSDP Site 516 (Supplementary Table 4.4.1), ODP Site 647 (Supplementary Table 4.4.2), ODP Site 913 (Supplementary Table 4.4.3), ODP Site 959 (Supplementary Table 4.4.4), ODP Site 1170 (Supplementary Table 4.4.5), ODP Site 1172 (Supplementary Table 4.4.6), ODP Site 1209 (Supplementary Table 4.4.7), Belaya River Section (Supplementary Table 4.4.8). Samples which fail various quality control metrics have been highlighted in red.

Supplementary Table 4.4.1: Site 516 (quality control metrics and TEX_{86} SSTs)

Depth (mbsf)	Age (Ma)	MECO interval	Quality Control									OPTiMAL SST			BAYSPAR SST (°C)		
			RI	>0.5 BIT	>0.5 MI	>67% %GDGT-0	%GDGT_RS	Cren'	GDGT2:GDGT3	Abundance of cren'	>0.3 ΔRI	>0.5 D_nearest	SST (°C)	StDev on SST	5th	50th	95th
618.12	38.12	N/A	2.72	0.11	0.20	30.08	22.93	0.11	4.95	0.31	0.16	0.51	29.0	4.2	25.1	30.7	37.2
626.54	38.96	N/A	2.66	0.11	0.16	32.40	14.48	0.08	7.85	0.29	0.35	0.70	20.6	5.2	27.0	32.7	39.7
634.61	39.77	N/A	1.58	0.20	0.25	64.50	8.19	0.14	5.73	0.29	1.23	1.16	14.1	7.2	24.1	29.7	36.0
637.20	40.03	N/A	2.43	0.03	0.17	40.39	18.00	0.13	4.49	0.38	0.58	0.82	26.2	5.9	26.9	32.5	39.5
647.52	40.50	Post	1.72	0.18	0.21	60.10	7.86	0.11	3.60	0.30	1.10	1.05	7.2	6.9	24.1	29.8	36.3
650.29	40.54	Post	1.54	0.20	0.20	65.92	7.55	0.14	2.58	0.35	1.79	1.38	10.1	8.3	30.9	37.1	45.1
654.47	40.60	Post	2.28	0.14	0.19	44.87	16.10	0.14	4.37	0.36	0.77	1.06	24.3	6.8	27.5	33.2	40.4
659.90	40.68	Peak	1.64	0.08	0.17	64.31	11.44	0.19	8.16	0.48	1.68	1.15	6.1	7.0	30.8	36.9	45.0
668.44	40.80	Onset	3.28	0.04	0.13	15.21	47.87	0.14	3.82	0.49	-0.01	0.92	25.2	6.2	30.1	36.2	44.0
675.43	40.91	Onset	1.98	0.03	0.19	52.72	10.06	0.11	3.78	0.32	0.93	0.99	14.1	6.7	25.6	31.2	38.0
682.34	41.01	Onset	2.82	0.05	0.20	26.66	26.14	0.11	4.20	0.31	0.04	0.55	27.8	4.2	24.8	30.4	36.9
691.60	41.14	Pre	0.89	0.05	0.19	80.86	3.09	0.12	5.14	0.33	2.06	0.64	9.2	6.1	26.2	31.8	38.7
696.34	41.21	Pre	3.04	0.07	0.19	20.41	38.29	0.14	3.76	0.37	0.05	0.57	26.0	4.4	28.1	33.8	41.1
710.62	41.42	N/A	1.25	0.18	0.38	74.60	6.19	0.16	4.41	0.21	1.61	1.60	12.5	8.6	24.8	30.4	37.1
712.30	41.45	N/A	3.22	0.04	0.16	15.42	46.19	0.14	4.91	0.41	-0.03	0.51	27.9	4.6	29.2	35.1	42.7
717.13	41.52	N/A	1.74	0.06	0.17	59.76	8.46	0.12	5.75	0.36	1.38	0.88	4.6	6.4	28.4	34.2	41.6
724.28	41.62	N/A	3.09	0.02	0.20	18.88	45.96	0.17	3.90	0.40	0.09	0.51	26.1	4.8	29.2	34.9	42.6
731.28	41.81	N/A	3.07	0.05	0.18	19.67	37.46	0.13	4.74	0.37	0.01	0.47	27.4	4.3	27.9	33.6	40.9
738.25	42.05	N/A	2.24	0.17	0.22	45.75	14.55	0.13	4.27	0.30	0.84	1.37	21.6	7.6	27.7	33.5	40.8
747.10	42.34	N/A	3.44	0.02	0.10	11.48	60.03	0.16	3.88	0.60	-0.11	1.54	18.4	8.3	31.0	37.0	45.2
751.67	42.50	N/A	3.18	0.05	0.17	15.82	40.45	0.11	4.97	0.35	-0.12	0.41	28.3	4.0	27.5	33.3	40.5

Supplementary Table 4.4.2: Site 647 (quality control metrics and TEX_{86} SSTs)

Depth (mbsf)	Age (Ma)	MECO interval	Quality Control									OPTiMAL			BAYSPAR SST (°C)		
				>0.5	>0.5	>67%					>0.3	>0.5					
			RI	BIT	MI	%GDGT-0	%GDGT_RS	Cren'	GDGT2:GDGT3	Abundance of cren'	ΔRI	D_nearest	SST (°C)	StDev on SST	5th	50th	95th
397.60	38.57	N/A	2.52	0.47	0.20	35.32	14.19	0.08	4.73	0.25	0.00	0.23	24.3	3.5	19.3	25.2	31.1
402.00	38.71	N/A	2.64	0.40	0.20	32.22	17.94	0.09	4.14	0.28	0.04	0.44	27.5	3.9	22.1	27.8	34.3
402.40	38.72	N/A	2.45	0.62	0.22	37.15	12.96	0.08	4.56	0.23	0.04	0.29	25.1	3.6	18.6	24.5	30.4
405.50	38.81	N/A	2.58	0.30	0.20	33.49	14.60	0.08	4.21	0.25	-0.01	0.28	25.7	3.6	20.2	26.0	32.2
407.58	38.86	N/A	2.64	0.27	0.20	31.73	17.11	0.09	4.32	0.26	-0.03	0.36	26.9	3.7	20.9	26.7	33.0
410.00	38.93	N/A	2.49	0.30	0.20	36.07	12.71	0.08	4.07	0.24	0.00	0.33	24.1	3.6	18.6	24.6	30.5
411.50	38.97	N/A	2.54	0.28	0.22	33.79	12.16	0.07	4.01	0.19	-0.06	0.28	25.6	3.6	18.4	24.4	30.4
412.00	38.99	N/A	2.62	0.15	0.17	32.48	13.43	0.07	4.13	0.25	-0.10	0.36	23.5	3.6	19.2	25.2	31.2
416.00	39.10	N/A	2.45	0.51	0.20	37.30	11.85	0.07	4.21	0.23	-0.02	0.21	22.9	3.6	17.5	23.6	29.4
416.00	39.10	N/A	2.42	0.53	0.20	38.42	12.30	0.08	4.09	0.24	0.08	0.36	24.4	3.7	18.9	24.8	30.9
419.95	39.21	N/A	2.44	0.28	0.19	37.58	11.38	0.07	6.38	0.24	-0.02	0.22	19.6	3.5	17.2	23.2	29.0
420.90	39.24	N/A	2.45	0.20	0.27	34.82	6.59	0.04	4.34	0.09	-0.16	0.79	23.7	5.6	14.4	20.8	26.4
425.49	39.37	N/A	2.54	0.25	0.18	34.65	11.65	0.07	3.50	0.23	-0.10	0.38	22.5	3.7	17.6	23.7	29.5
426.80	39.41	N/A	2.52	0.17	0.18	35.46	11.60	0.07	4.23	0.24	-0.09	0.33	21.5	3.6	17.3	23.4	29.2
428.30	39.45	N/A	2.42	0.27	0.21	38.19	11.40	0.07	4.06	0.22	0.11	0.41	25.0	3.8	19.3	25.2	31.2
428.55	39.46	N/A	2.27	0.24	0.19	43.18	9.79	0.08	3.54	0.25	0.32	0.64	23.3	4.8	20.6	26.4	32.6
433.80	39.60	N/A	2.76	0.11	0.17	28.56	17.75	0.08	3.20	0.27	-0.08	0.54	26.2	4.5	22.1	27.8	34.3
435.10	39.64	N/A	2.72	0.11	0.18	29.72	16.83	0.08	2.86	0.26	-0.07	0.66	24.8	5.1	21.5	27.3	33.8
437.19	39.70	N/A	2.59	0.30	0.25	31.26	12.19	0.06	3.72	0.15	-0.13	0.90	24.5	6.0	18.0	24.0	29.9
439.29	39.76	N/A	2.77	0.18	0.20	27.93	20.19	0.09	3.11	0.27	-0.04	0.81	25.6	5.3	22.9	28.6	35.3
440.40	39.79	N/A	2.86	0.12	0.18	25.46	22.17	0.09	3.35	0.29	-0.10	0.70	27.0	4.7	23.6	29.2	36.0
441.10	39.81	N/A	2.63	0.24	0.24	30.53	13.33	0.06	3.62	0.17	-0.12	0.86	24.9	5.7	19.1	25.0	31.1
442.90	39.86	Post	2.72	0.23	0.20	29.23	18.88	0.09	2.83	0.25	-0.08	0.92	24.2	5.9	21.4	27.2	33.6
443.90	39.89	Post	2.56	0.21	0.26	31.59	9.24	0.04	3.85	0.11	-0.17	1.10	23.2	6.8	16.5	22.6	28.4
445.92	39.95	Post	2.90	0.15	0.18	24.46	24.69	0.10	3.43	0.30	-0.07	0.72	27.0	4.8	24.5	30.1	37.2
446.60	39.96	Post	2.68	0.15	0.24	29.03	15.96	0.07	3.46	0.18	-0.10	0.87	23.5	6.5	20.2	26.1	32.2
448.10	40.01	Post	2.86	0.11	0.17	25.83	22.59	0.09	3.24	0.30	-0.07	0.75	26.8	4.9	23.8	29.5	36.4
449.60	40.05	Post	2.76	0.20	0.19	28.57	20.10	0.09	3.60	0.28	0.00	0.53	27.2	4.5	23.3	29.0	35.8

451.40	40.10	Peak	2.80	0.28	0.23	26.89	25.77	0.11	2.85	0.27	0.14	1.35	22.1	7.9	26.1	31.8	39.3
452.30	40.13	Peak	2.69	0.22	0.25	28.71	17.51	0.08	2.94	0.19	-0.04	1.52	20.6	8.2	21.6	27.3	33.7
452.77	40.14	Peak	2.90	0.25	0.20	24.24	26.97	0.11	2.42	0.29	0.01	1.38	22.5	7.8	25.7	31.5	38.8
454.20	40.19	Onset	2.81	0.19	0.19	26.99	21.91	0.09	3.38	0.29	-0.04	0.64	26.9	4.8	23.5	29.3	36.1
455.10	40.22	Onset	2.82	0.12	0.19	26.67	21.39	0.09	3.07	0.28	-0.05	0.81	25.5	5.4	23.6	29.3	36.2
455.77	40.24	Onset	2.92	0.10	0.18	23.72	24.47	0.09	3.45	0.30	-0.10	0.74	27.2	4.7	24.3	30.1	37.2
456.60	40.27	Onset	2.73	0.11	0.18	29.24	17.94	0.08	3.74	0.27	-0.06	0.30	27.2	4.0	22.0	27.7	34.2
458.40	40.33	Pre	2.78	0.13	0.19	27.86	20.28	0.09	3.22	0.28	-0.10	0.49	26.9	4.5	22.1	27.8	34.3
459.90	40.38	Pre	2.87	0.09	0.17	25.53	20.22	0.08	3.41	0.29	-0.16	0.44	27.3	4.2	22.5	28.3	34.9
464.03	40.53	Pre	2.83	0.13	0.17	26.51	20.79	0.09	3.59	0.29	-0.10	0.41	27.6	4.2	22.8	28.6	35.4
467.42	40.65	N/A	2.80	0.17	0.19	27.21	20.82	0.09	3.48	0.28	-0.06	0.57	27.3	4.4	23.0	28.8	35.6
468.10	40.67	N/A	2.83	0.14	0.17	26.76	21.32	0.09	3.52	0.30	-0.06	0.55	27.4	4.4	23.5	29.2	36.0
471.42	40.78	N/A	2.76	0.15	0.19	28.28	18.62	0.08	3.35	0.26	-0.08	0.48	26.8	4.5	22.0	27.8	34.2
474.62	40.89	N/A	2.84	0.11	0.18	26.28	21.80	0.09	3.89	0.29	-0.09	0.44	28.2	4.0	23.1	28.9	35.8
476.12	40.95	N/A	2.76	0.11	0.18	28.50	19.41	0.09	3.68	0.28	-0.05	0.39	27.4	4.1	22.6	28.4	35.1
476.41	40.96	N/A	2.91	0.10	0.16	24.55	23.71	0.09	3.77	0.32	-0.10	0.56	28.0	4.2	24.2	29.9	37.0
477.62	41.00	N/A	2.87	0.10	0.18	25.52	24.49	0.10	3.44	0.31	-0.06	0.69	27.3	4.6	24.1	29.8	36.8
478.60	41.03	N/A	2.80	0.17	0.19	27.17	21.47	0.09	4.14	0.29	-0.05	0.41	28.4	3.9	23.2	29.0	35.7
479.61	41.07	N/A	3.08	0.07	0.17	19.52	33.66	0.11	4.22	0.35	-0.05	0.48	27.8	4.2	27.3	33.2	41.2
480.11	41.08	N/A	3.05	0.12	0.17	20.20	32.45	0.11	4.26	0.34	-0.07	0.53	27.9	4.1	26.7	32.4	40.2
480.72	41.11	N/A	3.02	0.17	0.18	21.04	31.16	0.11	4.09	0.33	-0.07	0.59	27.7	4.2	26.1	31.9	39.4
480.95	41.11	N/A	2.88	0.12	0.18	25.03	23.43	0.09	3.80	0.30	-0.08	0.59	28.1	4.2	24.0	29.7	36.7
481.12	41.12	N/A	2.86	0.08	0.19	25.39	23.35	0.09	3.75	0.29	-0.10	0.53	28.0	4.2	23.4	29.2	36.0
481.65	41.14	N/A	2.61	0.21	0.19	32.72	15.12	0.08	3.80	0.26	-0.02	0.41	25.7	3.8	20.5	26.4	32.7
481.67	41.14	N/A	3.18	0.06	0.16	16.56	38.76	0.11	5.13	0.38	-0.06	0.53	28.0	4.4	28.5	34.4	42.7
482.97	41.18	N/A	2.74	0.32	0.20	29.15	22.20	0.11	3.35	0.29	0.04	0.71	26.2	5.2	23.7	29.4	36.3
484.75	41.23	N/A	3.05	0.08	0.17	20.26	30.68	0.10	3.69	0.33	-0.12	0.59	27.3	4.4	25.9	31.7	39.1
485.00	41.24	N/A	2.92	0.08	0.18	23.65	23.95	0.09	3.85	0.30	-0.13	0.62	28.2	4.1	24.0	29.6	36.6
486.96	41.29	N/A	2.92	0.11	0.18	23.88	26.49	0.10	3.85	0.32	-0.07	0.66	27.9	4.3	24.8	30.5	37.8
490.95	41.40	N/A	2.53	0.22	0.19	35.11	14.10	0.08	3.45	0.25	0.00	0.50	24.6	4.0	19.5	25.4	31.5
493.75	41.43	N/A	2.90	0.10	0.18	24.44	25.26	0.10	3.65	0.31	-0.05	0.72	27.5	4.5	24.7	30.5	37.7

Supplementary Table 4.4.3: Site 913 (quality control metrics and TEX_{86} SSTs)

Depth (mbsf)	Age (Ma)	MECO interval	Quality Control									OPTiMAL			BAYSPAR SST (°C)		
			RI	>0.5 BIT	>0.5 MI	>67% %GDGT-0	%GDGT_RS	Cren'	GDGT2:GDGT3	Abundance of cren'	>0.3 ΔRI	>0.5 D_nearest	SST (°C)	StDev on SST	5th	50th	95th
488.65	38.16	N/A	2.04	0.33	0.22	48.55	6.35	0.06	9.68	0.18	0.14	0.32	18.3	3.5	11.6	19.0	28.2
489.68	38.28	N/A	1.50	0.02	0.32	63.92	3.82	0.07	12.09	0.12	0.56	0.68	15.9	4.5	7.9	15.5	23.5
492.53	38.60	N/A	1.89	0.18	0.29	53.19	7.21	0.08	10.19	0.17	0.34	0.39	22.4	4.0	12.7	20.0	29.6
507.99	39.63	N/A	1.27	0.12	0.32	70.34	2.75	0.06	9.17	0.12	0.76	0.56	11.7	4.4	7.2	14.8	22.5
508.65	39.69	N/A	0.72	0.28	0.48	86.00	1.46	0.08	12.09	0.08	1.48	1.17	11.4	7.2	11.9	19.2	28.5
511.49	39.94	Post	1.17	0.69	0.40	73.10	3.04	0.08	8.21	0.11	0.58	0.95	8.6	6.6	-5.7	4.1	11.9
512.49	40.01	Post	1.80	0.32	0.23	55.73	5.60	0.07	7.83	0.18	0.44	0.33	18.6	3.8	13.2	20.6	30.5
514.32	40.13	Peak	1.99	0.42	0.25	50.36	7.22	0.07	10.14	0.18	0.33	0.52	22.7	4.0	15.0	22.4	33.2
516.72	40.30	Onset	1.13	NA	0.54	74.48	2.60	0.07	12.49	0.06	0.53	2.79	15.5	8.9	-12.4	-0.7	8.0
532.67	41.40	N/A	2.34	0.15	0.22	40.45	11.88	0.08	9.51	0.23	0.19	0.31	22.3	3.7	19.3	26.9	40.4
538.34	41.79	N/A	2.36	0.16	0.22	39.70	10.80	0.07	8.35	0.20	0.18	0.33	22.0	3.6	19.3	26.9	40.3
551.05	42.31	N/A	2.20	0.24	0.20	44.50	8.61	0.07	8.07	0.22	0.18	0.25	20.8	3.6	16.4	23.7	35.2

Supplementary Table 4.4.4: Site 959 (quality control metrics and TEX_{86} SSTs)

Depth (mbsf)	Age (Ma)	MECO interval	Quality Control									OPTiMAL			BAYSPAR SST (°C)		
			RI	>0.5 BIT	>0.5 MI	>67% %GDGT-0	%GDGT_RS	Cren'	GDGT2:GDGT3	Abundance of cren'	>0.3 ΔRI	>0.5 D_nearest	SST (°C)	StDev on SST	5th	50th	95th
543.34	38.36	N/A	2.87	NA	0.19	24.69	20.00	0.08	3.50	0.25	-0.19	0.60	27.6	4.3	20.7	27.6	34.3
552.37	38.78	N/A	2.86	NA	0.19	25.00	20.00	0.08	3.50	0.25	-0.18	0.58	27.6	4.3	20.8	27.6	34.2
554.86	38.90	N/A	2.95	NA	0.16	23.17	20.83	0.07	3.00	0.28	-0.18	0.95	26.2	5.2	22.1	29.0	36.0
557.19	39.01	N/A	2.99	NA	0.16	22.22	25.00	0.09	3.00	0.32	-0.16	0.93	26.3	5.2	22.9	29.9	37.0
562.04	39.24	N/A	2.82	NA	0.19	26.25	19.23	0.08	3.50	0.25	-0.14	0.51	27.5	4.3	20.9	27.6	34.2
564.01	39.33	N/A	2.98	NA	0.16	22.22	21.74	0.07	3.00	0.28	-0.21	0.97	26.2	5.2	22.1	29.0	36.0
565.89	39.42	N/A	2.72	NA	0.15	30.95	16.13	0.08	2.50	0.31	0.16	1.09	21.4	6.7	23.8	30.7	38.2
567.71	39.50	N/A	3.02	NA	0.16	21.25	26.09	0.09	3.00	0.32	-0.20	0.88	26.3	5.1	23.0	29.9	37.2

569.21	39.57	N/A	3.09	NA	0.16	18.99	31.82	0.10	3.50	0.33	-0.16	0.55	26.9	4.5	24.4	31.5	39.1
571.56	39.68	N/A	3.20	NA	0.15	16.25	35.00	0.09	3.50	0.35	-0.10	0.45	26.5	4.8	26.7	33.9	42.1
573.31	39.76	N/A	3.09	NA	0.16	18.75	28.57	0.08	3.50	0.30	-0.21	0.62	27.0	4.6	23.7	30.7	38.1
574.99	39.84	Post	3.21	NA	0.16	15.19	36.84	0.09	3.50	0.33	-0.28	0.40	26.7	4.4	24.5	31.5	39.0
576.06	39.89	Post	3.09	NA	0.16	18.75	28.57	0.08	3.50	0.30	-0.21	0.62	27.0	4.6	23.7	30.7	38.2
577.03	39.94	Post	3.30	NA	0.16	12.82	44.44	0.11	4.00	0.36	-0.12	0.34	27.6	4.1	27.5	35.0	43.4
578.26	40.00	Post	3.32	NA	0.14	12.82	47.37	0.12	3.50	0.41	-0.14	0.42	26.8	4.7	27.7	35.0	43.7
581.19	40.11	Peak	3.37	NA	0.12	12.50	47.37	0.11	3.00	0.45	-0.04	0.76	25.0	6.1	29.3	37.0	46.2
581.53	40.12	Peak	3.28	NA	0.15	13.92	42.11	0.11	3.50	0.38	-0.14	0.37	26.8	4.6	27.1	34.5	42.9
590.86	40.47	Onset	3.20	NA	0.15	16.25	35.00	0.09	3.50	0.35	-0.10	0.45	26.5	4.8	26.7	33.9	42.0
592.88	40.55	Pre	3.08	NA	0.15	19.51	27.27	0.08	3.00	0.32	-0.25	0.78	26.4	5.1	23.0	29.9	37.2
595.07	40.63	Pre	3.05	NA	0.17	20.00	27.27	0.09	3.50	0.30	-0.17	0.70	27.0	4.7	23.8	30.7	38.1
600.36	40.83	N/A	3.02	NA	0.17	20.99	26.09	0.09	3.50	0.30	-0.14	0.76	27.1	4.7	23.7	30.7	38.1
602.11	40.90	N/A	2.93	NA	0.19	22.78	25.00	0.09	4.00	0.27	-0.14	0.55	27.9	4.1	22.4	29.3	36.4
603.78	40.96	N/A	3.07	NA	0.15	20.00	30.43	0.10	3.00	0.35	-0.19	0.74	26.2	5.1	23.8	30.7	38.2
606.36	41.06	N/A	2.99	NA	0.16	22.22	25.00	0.09	3.00	0.32	-0.16	0.93	26.3	5.2	22.9	29.9	37.0
608.85	41.15	N/A	2.99	NA	0.16	22.22	25.00	0.09	3.00	0.32	-0.16	0.93	26.3	5.2	23.1	29.9	37.1
610.68	41.22	N/A	3.04	NA	0.15	20.99	29.17	0.10	3.00	0.35	-0.16	0.80	26.3	5.2	23.8	30.7	38.0
615.42	41.40	N/A	3.03	NA	0.16	21.52	32.00	0.11	3.00	0.38	-0.10	0.79	25.8	5.3	24.5	31.5	39.0
619.83	41.56	N/A	3.03	NA	0.16	20.99	26.09	0.09	3.00	0.32	-0.20	0.86	26.4	5.1	22.9	29.9	37.1
623.19	41.69	N/A	3.09	NA	0.14	19.75	30.43	0.10	2.50	0.37	-0.26	0.88	25.2	5.7	23.0	29.9	37.1
629.29	41.92	N/A	3.12	NA	0.15	18.75	34.78	0.11	3.00	0.38	-0.19	0.62	25.9	5.1	24.4	31.5	39.0
639.11	42.29	N/A	3.26	NA	0.14	15.19	42.86	0.12	3.00	0.43	-0.12	0.54	25.5	5.4	27.1	34.4	42.8
644.09	42.47	N/A	3.31	NA	0.13	13.75	45.00	0.12	3.00	0.43	-0.16	0.54	25.6	5.4	27.2	34.5	42.7

Supplementary Table 4.4.5: Site 1170 (quality control metrics and TEX_{86} SSTs)

Depth (mbsf)	Age (Ma)	MECO interval	Quality Control									OPTiMAL			BAYSPAR SST (°C)		
				>0.5	>0.5	>67%					>0.3	>0.5					
			RI	BIT	MI	%GDGT-0	%GDGT_RS	Cren'	GDGT2:GDGT3	Abundance of cren'	ΔRI	D_nearest	SST (°C)	StDev on SST	5th	50th	95th
503.06	N/A	N/A	1.99	0.14	0.15	50.62	5.13	0.05	4.53	0.23	0.21	0.32	11.8	3.7	12.1	19.1	25.0
523.66	N/A	N/A	2.32	0.17	0.20	40.89	8.36	0.06	3.63	0.20	0.03	0.38	22.1	3.7	15.8	22.4	28.6
542.96	N/A	N/A	2.06	0.11	0.17	48.05	4.97	0.05	3.50	0.18	0.04	0.16	13.9	3.6	9.5	16.8	22.5
551.06	N/A	N/A	2.03	0.08	0.17	49.03	5.46	0.05	3.93	0.20	0.10	0.33	13.7	3.6	10.6	17.7	23.5
552.56	N/A	N/A	1.89	0.10	0.19	53.04	4.85	0.05	4.41	0.19	0.28	0.44	12.3	3.7	11.3	18.4	24.2
559.16	N/A	N/A	2.07	0.11	0.19	47.87	5.26	0.05	3.42	0.17	0.12	0.29	15.5	3.8	11.9	18.8	24.7
563.65	N/A	N/A	2.10	0.10	0.19	47.15	6.09	0.05	4.04	0.19	0.07	0.22	16.2	3.6	11.5	18.5	24.3
568.76	N/A	N/A	2.15	0.12	0.20	45.99	8.36	0.07	4.02	0.23	0.15	0.31	19.1	3.8	14.9	21.5	27.6
573.26	N/A	N/A	1.66	0.18	0.26	59.63	4.51	0.07	4.79	0.15	0.40	0.42	15.8	4.1	8.1	15.5	21.5
574.76	N/A	N/A	2.43	0.19	0.21	38.31	15.27	0.10	4.06	0.27	0.16	0.40	26.1	4.1	20.8	27.0	34.0
576.26	N/A	N/A	2.36	0.17	0.21	40.09	12.78	0.09	4.25	0.25	0.13	0.40	24.8	3.8	19.0	25.3	31.9
577.57	N/A	N/A	2.06	0.12	0.19	48.54	7.26	0.07	4.04	0.22	0.18	0.29	15.9	3.8	13.3	20.1	26.0
578.36	N/A	N/A	2.10	0.11	0.19	47.60	8.08	0.07	4.04	0.24	0.13	0.36	16.0	3.8	12.9	19.7	25.6
579.86	N/A	N/A	2.25	0.10	0.21	43.21	9.18	0.07	2.66	0.21	0.04	0.69	21.0	4.8	14.3	21.0	27.0
581.36	N/A	N/A	2.78	0.13	0.17	28.41	22.12	0.10	4.89	0.32	-0.02	0.42	28.4	3.7	23.8	29.8	37.7
582.86	N/A	N/A	2.32	0.15	0.20	41.31	11.70	0.09	4.35	0.26	0.09	0.37	21.8	3.8	17.2	23.7	29.9
584.36	N/A	N/A	2.39	0.21	0.20	39.59	14.56	0.10	4.05	0.28	0.12	0.45	24.2	4.0	19.2	25.6	32.3
585.10	N/A	N/A	2.08	0.08	0.18	48.07	6.98	0.06	3.65	0.23	0.09	0.24	14.6	3.7	11.4	18.4	24.2
587.20	N/A	N/A	2.26	0.12	0.19	43.13	10.85	0.08	4.03	0.27	0.07	0.47	19.9	3.9	15.5	22.1	28.1
588.38	N/A	N/A	2.29	0.15	0.19	42.06	10.10	0.08	3.59	0.24	0.07	0.41	22.0	3.8	16.2	22.7	28.9
589.88	N/A	N/A	2.38	0.16	0.20	40.00	13.47	0.09	4.14	0.28	0.11	0.40	23.5	3.9	18.7	25.1	31.7
591.38	N/A	N/A	2.28	0.13	0.20	42.54	10.87	0.08	3.92	0.25	0.08	0.44	21.2	3.8	16.0	22.6	28.6
592.88	N/A	N/A	2.30	0.11	0.17	42.32	10.57	0.08	3.79	0.28	0.07	0.32	20.7	3.8	16.3	22.7	28.8
594.41	N/A	N/A	2.34	0.13	0.19	41.27	13.04	0.10	3.97	0.29	0.16	0.48	23.3	4.1	19.1	25.4	32.1
595.88	N/A	N/A	2.23	0.10	0.19	43.98	9.91	0.08	4.14	0.25	0.11	0.39	20.3	3.8	15.7	22.2	28.3
596.73	N/A	N/A	2.31	0.13	0.20	42.02	12.29	0.09	3.80	0.27	0.15	0.46	23.4	4.1	18.2	24.6	31.0
597.61	N/A	N/A	2.18	0.09	0.17	45.49	9.13	0.08	3.51	0.27	0.08	0.41	17.6	3.9	13.8	20.5	26.4
599.09	N/A	N/A	2.29	0.12	0.20	42.53	11.93	0.09	3.93	0.27	0.14	0.49	22.6	4.0	17.5	23.9	30.3

600.59	N/A	N/A	2.25	0.08	0.19	44.12	13.00	0.11	4.00	0.31	0.19	0.60	21.1	4.3	17.9	24.2	30.6
602.09	N/A	N/A	2.32	0.13	0.19	41.70	13.22	0.10	4.05	0.29	0.12	0.48	22.2	4.1	18.0	24.3	30.6
603.59	N/A	N/A	2.03	0.07	0.18	49.35	6.94	0.07	3.42	0.24	0.13	0.25	12.8	3.8	11.3	18.3	24.2
605.09	N/A	N/A	2.11	0.09	0.19	47.35	8.43	0.08	3.65	0.25	0.11	0.37	16.0	3.9	12.9	19.7	25.5
606.59	N/A	N/A	2.39	0.21	0.20	40.15	16.25	0.12	4.03	0.31	0.20	0.60	25.2	4.4	20.8	27.0	33.9
607.16	N/A	N/A	2.09	0.08	0.18	47.74	7.19	0.07	3.48	0.23	0.08	0.27	14.8	3.8	11.4	18.4	24.3
608.66	N/A	N/A	2.13	0.09	0.19	47.54	11.04	0.10	3.73	0.30	0.18	0.55	16.6	4.4	14.7	21.4	27.4
613.16	N/A	N/A	2.12	0.09	0.19	47.15	8.81	0.08	3.53	0.26	0.12	0.41	16.5	4.0	13.4	20.2	26.1
613.16	N/A	N/A	2.16	0.09	0.18	46.19	9.65	0.08	3.56	0.27	0.11	0.46	17.4	4.0	13.9	20.6	26.6
618.61	N/A	N/A	2.21	0.08	0.18	44.65	9.55	0.08	3.37	0.26	0.10	0.44	19.6	3.9	15.0	21.6	27.6
621.61	N/A	N/A	2.29	0.10	0.19	42.89	12.83	0.10	3.77	0.29	0.17	0.55	22.5	4.2	18.1	24.5	31.0
627.96	N/A	N/A	2.25	0.08	0.18	43.48	10.17	0.08	3.80	0.27	0.06	0.39	19.7	3.8	15.1	21.6	27.7
633.96	N/A	N/A	2.27	0.09	0.19	43.22	12.87	0.10	3.80	0.30	0.13	0.57	21.4	4.2	17.1	23.6	29.9
633.96	N/A	N/A	2.30	0.09	0.19	42.49	12.78	0.10	3.78	0.29	0.11	0.53	21.5	4.2	17.1	23.5	29.8
637.66	N/A	N/A	2.33	0.07	0.18	41.61	12.13	0.09	3.87	0.29	0.09	0.48	21.5	3.9	17.4	23.7	30.1
650.16	N/A	N/A	2.43	0.07	0.19	38.74	15.85	0.11	3.65	0.31	0.08	0.49	23.8	4.3	19.3	25.6	32.3
662.96	N/A	N/A	2.55	0.05	0.18	35.27	17.57	0.10	4.25	0.32	0.04	0.45	24.5	4.0	20.8	27.0	34.1
669.56	N/A	Peak	2.69	0.07	0.19	31.29	25.67	0.14	4.32	0.36	0.06	0.52	27.5	4.5	23.7	29.7	37.6
678.65	N/A	N/A	2.57	0.05	0.18	34.80	18.19	0.11	3.55	0.33	0.03	0.56	24.9	4.4	21.0	27.1	34.2
688.72	N/A	N/A	2.57	0.04	0.18	34.82	17.93	0.10	3.25	0.32	0.06	0.67	25.3	4.7	21.6	27.7	35.0
696.91	N/A	N/A	2.35	0.05	0.17	41.11	12.09	0.09	3.23	0.30	0.13	0.46	23.1	4.2	18.6	24.9	31.5
701.22	N/A	N/A	2.52	0.02	0.18	35.96	14.61	0.09	2.99	0.28	0.01	0.65	23.7	4.5	19.5	25.7	32.5

Supplementary Table 4.4.6: Site 1172 (quality control metrics and TEX_{86} SSTs)

Depth (mbsf)	Age (Ma)	MECO interval	Quality Control									OPTiMAL			BAYSPAR SST (°C)		
			RI	>0.5 BIT	>0.5 MI	>67% %GDGT-0	%GDGT_RS	Cren'	GDGT2:GDGT3	Abundance of cren'	>0.3 ΔRI	>0.5 D_nearest	SST (°C)	StDev on SST	5th	50th	95th
373.30	38.21	N/A	2.12	0.33	0.22	46.70	6.91	0.06	2.64	0.18	0.13	0.75	19.4	5.2	13.3	20.0	25.9
379.80	38.54	N/A	2.14	0.33	0.21	46.15	7.28	0.06	2.76	0.19	0.11	0.46	19.2	4.7	13.3	19.9	25.8
385.00	38.73	N/A	2.12	0.36	0.23	46.61	7.76	0.07	2.81	0.18	0.15	0.82	20.4	5.3	13.8	20.5	26.5
391.00	38.97	N/A	2.00	0.44	0.28	50.15	6.67	0.07	2.35	0.15	0.26	1.13	19.1	7.6	13.6	20.2	26.1
394.92	39.12	N/A	2.17	0.34	0.25	45.05	8.63	0.07	2.86	0.18	0.17	1.06	21.4	6.1	15.6	22.1	28.2
396.85	39.20	N/A	2.16	0.30	0.22	45.40	7.73	0.07	2.85	0.19	0.08	0.56	20.2	4.8	13.2	19.9	25.8
402.37	39.41	N/A	2.26	0.33	0.23	42.81	10.40	0.08	3.04	0.21	0.14	0.83	22.5	5.4	16.9	23.4	29.6
404.20	39.48	N/A	2.12	0.40	0.26	46.83	8.42	0.07	2.54	0.17	0.23	1.12	19.7	7.3	15.6	22.1	28.3
406.62	39.58	N/A	2.35	0.32	0.22	40.41	11.57	0.08	2.67	0.22	0.08	0.91	21.7	5.8	17.3	23.8	30.2
407.72	39.62	Post	2.30	0.40	0.26	41.90	11.94	0.09	2.38	0.20	0.23	1.93	17.3	8.7	19.5	25.7	32.5
408.70	39.66	Post	2.30	0.37	0.24	41.60	10.65	0.08	2.47	0.20	0.13	1.07	19.7	7.1	17.6	24.0	30.4
411.70	39.78	Post	2.35	0.38	0.23	40.23	11.01	0.08	2.54	0.20	0.12	1.07	19.6	7.2	18.2	24.3	30.9
412.52	39.81	Post	2.31	0.43	0.28	41.34	12.62	0.09	2.42	0.20	0.18	2.10	17.1	8.8	18.6	25.0	31.6
413.22	39.84	Post	2.40	0.34	0.26	38.94	16.40	0.11	3.61	0.24	0.22	1.02	23.5	6.5	21.3	27.5	34.5
414.12	39.87	Peak	2.45	0.34	0.26	37.61	17.45	0.11	3.44	0.25	0.29	1.43	21.2	7.8	23.3	29.4	37.0
414.68	39.89	Peak	2.57	0.28	0.23	33.88	18.20	0.10	3.55	0.26	0.12	0.75	25.3	5.6	22.5	28.6	36.0
415.52	39.93	Peak	2.53	0.26	0.23	35.14	17.39	0.10	3.79	0.25	0.18	0.68	25.6	5.3	22.8	29.0	36.6
416.22	39.95	Peak	2.44	0.26	0.24	37.69	15.44	0.10	3.81	0.24	0.15	0.61	25.6	4.8	20.7	26.9	34.0
416.80	39.98	Onset	2.37	0.30	0.23	39.65	12.43	0.09	3.05	0.22	0.13	0.94	22.7	5.7	19.0	25.1	31.9
417.72	40.01	Onset	2.37	0.34	0.26	39.71	14.69	0.10	3.22	0.23	0.21	1.28	21.4	7.3	20.5	26.8	33.8
418.30	40.03	Onset	2.41	0.31	0.23	38.63	14.19	0.09	3.63	0.24	0.14	0.63	25.0	4.7	19.6	25.7	32.6
419.12	40.07	Onset	2.26	0.33	0.24	42.67	10.95	0.08	2.91	0.21	0.15	1.07	21.7	6.2	17.1	23.7	30.0
420.02	40.10	Onset	2.19	0.32	0.25	44.63	8.96	0.07	2.49	0.18	0.16	1.13	20.1	6.9	15.7	22.4	28.5
420.92	40.14	Onset	2.30	0.26	0.20	41.56	7.75	0.06	2.75	0.18	0.01	0.53	21.1	4.5	15.0	21.6	27.6
421.62	40.21	Onset	2.32	0.25	0.20	40.86	8.48	0.06	3.22	0.19	0.03	0.43	22.2	4.0	15.7	22.3	28.4
421.90	40.24	Pre	2.17	0.22	0.21	45.18	7.55	0.06	3.21	0.19	0.08	0.35	20.0	4.1	13.3	20.0	25.9
422.92	40.36	Pre	2.14	0.29	0.24	46.10	8.43	0.07	2.71	0.19	0.16	1.01	21.1	5.9	14.5	21.2	27.2
423.40	40.41	Pre	2.21	0.27	0.25	43.99	9.30	0.07	2.62	0.18	0.12	1.12	20.6	6.6	15.3	21.8	27.9

424.22	40.50	N/A	2.20	0.28	0.23	44.37	8.75	0.07	2.69	0.20	0.11	0.95	21.2	5.5	14.9	21.6	27.7
424.90	40.58	N/A	2.33	0.28	0.22	40.63	10.95	0.08	3.44	0.21	0.11	0.47	23.8	4.4	17.8	24.0	30.5
425.62	40.66	N/A	2.15	0.32	0.24	45.90	8.94	0.08	2.70	0.19	0.17	1.02	21.2	6.0	15.1	21.7	27.7
426.40	40.75	N/A	2.19	0.32	0.24	44.88	9.09	0.08	2.74	0.19	0.16	1.06	21.4	5.9	15.6	22.1	28.2
427.22	40.84	N/A	2.19	0.33	0.24	44.50	8.76	0.07	2.62	0.18	0.13	1.06	21.0	6.1	15.2	21.9	27.9
427.90	40.91	N/A	2.24	0.38	0.27	43.45	12.77	0.10	2.85	0.21	0.18	1.42	19.8	7.8	17.2	23.4	29.7
428.96	41.03	N/A	2.20	0.32	0.26	44.44	10.51	0.09	2.83	0.20	0.17	1.22	21.0	6.8	16.2	22.7	28.9
430.90	41.26	N/A	2.25	0.31	0.24	43.29	10.72	0.08	3.01	0.21	0.22	1.08	22.1	5.9	18.4	24.8	31.4
433.00	41.47	N/A	2.31	0.31	0.24	41.27	11.99	0.09	2.93	0.22	0.12	1.03	22.0	6.2	17.4	23.7	30.1
437.50	41.81	N/A	2.29	0.33	0.26	42.10	12.22	0.09	2.76	0.21	0.18	1.33	19.6	7.8	18.1	24.4	31.0
444.10	42.31	N/A	2.27	0.22	0.24	42.40	10.57	0.08	3.41	0.20	0.19	0.84	23.2	5.3	18.1	24.2	30.8

Supplementary Table 4.4.7: Site 1209 (quality control metrics and TEX_{86} SSTs)

Depth (mbsf)	Age (Ma)	MECO interval	Quality Control									OPTiMAL			BAYSPAR SST (°C)		
				>0.5	>0.5	>67%					>0.3	>0.5					
			RI	BIT	MI	%GDGT-0	%GDGT_RS	Cren'	GDGT2:GDGT3	Abundance of cren'	ΔRI	D_nearest	SST (°C)	StDev on SST	5th	50th	95th
134.77	38.29	N/A	2.66	0.00	0.23	29.98	19.51	0.09	7.55	0.24	-0.10	0.29	25.5	3.58	19.1	25.9	33.0
136.81	39.34	N/A	2.31	0.13	0.35	38.11	7.63	0.05	13.27	0.08	0.21	1.35	23.7	7.31	18.4	25.2	32.1
137.78	39.82	N/A	1.85	0.00	0.28	55.49	7.34	0.09	4.32	0.18	0.70	1.05	17.2	6.58	18.8	25.7	32.6
140.23	40.98	N/A	2.91	0.00	0.19	23.16	13.86	0.05	1.96	0.17	-0.40	1.41	20.4	7.98	18.2	25.0	31.8

Supplementary Table 4.4.8: Belaya River (quality control metrics and TEX_{86} SSTs)

Depth (mbsf)	Age (Ma)	MECO interval	Quality Control									OPTiMAL			BAYSPAR SST (°C)		
			RI	>0.5 BIT	>0.5 MI	>67% %GDGT-0	%GDGT_RS	Cren'	GDGT2:GDGT3	Abundance of cren'	>0.3 ΔRI	>0.5 D_nearest	SST (°C)	StDev on SST	5th	50th	95th
20.85	41.26	N/A	3.18	NA	0.18	15.98	39.74	0.11	2.89	0.34	-0.04	0.70	25.8	5.6	22.1	25.7	29.2
21.43	41.20	N/A	3.19	NA	0.16	15.94	40.33	0.11	5.10	0.37	-0.07	0.59	28.5	4.2	21.6	25.3	29.3
21.99	41.15	N/A	3.19	NA	0.17	15.94	42.20	0.12	5.75	0.38	-0.04	0.61	27.8	4.7	21.9	25.8	29.3
22.81	41.07	N/A	3.24	NA	0.16	14.51	44.36	0.12	5.81	0.38	-0.04	0.72	28.0	4.8	22.5	26.3	29.9
23.33	41.02	N/A	3.25	NA	0.16	14.12	45.16	0.12	5.96	0.38	-0.06	0.70	27.8	4.9	22.5	26.2	29.7
23.93	40.96	N/A	3.25	NA	0.16	14.10	45.70	0.12	6.06	0.38	-0.05	0.72	27.5	5.1	22.5	26.2	29.9
24.58	40.90	N/A	3.24	NA	0.16	14.63	44.41	0.12	6.45	0.40	-0.06	0.66	26.1	5.4	22.2	25.9	29.7
25.13	40.85	N/A	3.21	NA	0.16	15.25	41.94	0.12	6.14	0.37	-0.07	0.55	27.2	4.8	22.0	25.5	29.2
25.58	40.80	N/A	3.24	NA	0.16	14.57	43.22	0.11	5.08	0.38	-0.09	0.58	28.5	4.3	21.9	25.7	29.5
26.25	40.74	Pre	3.21	NA	0.16	15.46	40.51	0.11	5.08	0.37	-0.09	0.58	28.5	4.2	21.6	25.2	29.1
26.77	40.69	Pre	3.22	NA	0.16	15.04	41.58	0.11	4.93	0.37	-0.11	0.58	28.5	4.2	21.6	25.1	28.7
27.47	40.62	Pre	3.22	NA	0.16	14.99	41.81	0.11	4.85	0.37	-0.08	0.43	28.6	4.1	21.6	25.4	29.2
28.03	40.57	Pre	3.28	NA	0.16	13.54	45.21	0.11	4.47	0.38	-0.11	0.31	28.5	4.1	21.8	25.8	29.4
28.65	40.51	Pre	3.32	NA	0.15	12.52	48.84	0.12	4.36	0.40	-0.08	0.37	28.4	4.2	23.1	26.7	30.2
29.22	40.45	Onset	3.32	NA	0.16	12.24	50.84	0.13	4.69	0.40	-0.03	0.39	28.6	4.1	23.6	27.2	30.6
29.88	40.38	Onset	3.25	NA	0.17	14.11	46.33	0.12	4.52	0.38	-0.03	0.28	28.0	3.8	23.0	26.4	30.0
29.88	40.38	Onset	3.31	NA	0.16	12.82	49.93	0.13	4.18	0.41	-0.05	0.38	27.9	4.2	23.4	26.8	30.5
30.35	40.34	Onset	3.39	NA	0.14	10.78	56.06	0.13	4.32	0.44	-0.04	0.55	27.9	4.9	24.0	27.7	31.4
30.82	40.33	Onset	3.33	NA	0.16	11.98	52.37	0.13	4.70	0.40	-0.01	0.29	28.5	3.9	23.7	27.3	31.1
31.37	40.32	Onset	2.76	NA	0.14	31.52	25.07	0.13	4.70	0.45	0.62	1.29	24.7	7.2	24.5	28.2	31.9
31.81	40.31	Onset	3.35	NA	0.15	11.85	54.16	0.14	4.56	0.43	0.02	0.40	28.2	4.4	24.4	28.0	31.5
31.81	40.31	Onset	3.42	NA	0.14	10.11	58.16	0.14	4.37	0.45	-0.03	0.59	27.6	5.2	24.8	28.2	32.0
32.5	40.30	Onset	3.41	NA	0.14	10.23	55.78	0.13	3.69	0.43	-0.08	0.55	26.9	4.8	23.9	27.6	31.3
33	40.29	Onset	3.27	NA	0.16	13.83	48.41	0.13	4.56	0.40	0.00	0.34	28.2	4.0	23.2	27.0	30.7
33.65	40.27	Onset	3.24	NA	0.16	14.97	45.24	0.13	3.82	0.40	-0.02	0.38	26.9	4.3	22.7	26.5	30.1
34.04	40.26	Onset	3.32	NA	0.16	12.42	50.46	0.13	4.23	0.40	-0.04	0.37	28.0	4.1	23.5	27.1	30.8
34.28	40.26	Peak	3.29	NA	0.16	13.12	46.34	0.12	3.91	0.38	-0.07	0.42	27.3	4.1	22.6	26.3	29.7
34.65	40.25	Peak	3.31	NA	0.15	12.90	48.11	0.12	3.91	0.41	-0.07	0.38	27.6	4.4	22.8	26.7	30.1

34.9	40.24	Peak	3.22	NA	0.17	14.96	42.50	0.12	3.85	0.37	-0.08	0.28	26.8	4.0	21.7	25.4	29.0
35.36	40.23	Peak	3.10	NA	0.18	18.45	33.70	0.10	4.07	0.33	-0.07	0.45	27.0	4.1	20.7	24.4	28.2
35.55	40.23	Peak	3.15	NA	0.17	16.80	37.81	0.11	3.85	0.34	-0.10	0.34	26.6	4.0	20.8	24.4	28.2
35.83	40.22	Peak	3.26	NA	0.16	13.83	44.24	0.11	3.68	0.37	-0.08	0.26	26.6	4.1	22.4	26.1	29.7
36.33	40.21	Post	2.28	NA	0.18	44.65	13.84	0.11	4.37	0.34	0.84	1.18	22.7	7.1	21.6	25.3	29.1
36.7	40.21	Post	3.12	NA	0.18	17.66	35.62	0.11	4.17	0.32	-0.07	0.38	26.8	4.0	20.8	24.4	27.9
37.1	40.20	Post	3.10	NA	0.19	18.09	35.65	0.11	4.38	0.32	-0.05	0.40	26.9	3.9	20.6	24.5	27.9
37.91	40.18	Post	3.14	NA	0.18	17.21	39.35	0.12	4.83	0.35	0.03	0.30	27.7	4.0	22.1	25.8	29.4
38.34	40.17	Post	3.23	NA	0.16	14.64	42.09	0.11	4.44	0.37	-0.12	0.18	28.4	3.9	21.5	25.2	28.9
39.15	40.15	Post	3.21	NA	0.17	15.08	42.16	0.11	4.56	0.36	-0.10	0.13	28.0	3.8	21.6	25.2	28.9
39.76	40.14	Post	3.23	NA	0.16	14.62	42.37	0.11	4.65	0.37	-0.09	0.26	28.6	4.0	21.8	25.5	29.2
40.4	40.12	Post	3.05	NA	0.18	19.84	34.51	0.12	4.32	0.35	-0.04	0.46	27.4	4.1	20.4	24.1	27.8
40.4	40.12	Post	3.15	NA	0.16	17.41	37.43	0.11	3.92	0.36	-0.11	0.27	27.4	4.2	20.5	24.3	28.0
41	40.11	Post	3.15	NA	0.16	17.41	36.11	0.11	4.25	0.35	-0.06	0.28	27.9	4.1	21.4	25.0	28.3
41.65	40.09	Post	3.15	NA	0.16	17.50	37.43	0.11	4.18	0.37	-0.02	0.26	27.6	4.2	21.6	25.4	29.3
42.68	40.06	Post	3.04	NA	0.18	19.94	31.94	0.10	4.36	0.32	-0.10	0.47	27.6	4.0	19.6	23.3	26.9
43.58	40.04	Post	3.13	NA	0.17	17.64	36.22	0.11	4.33	0.35	-0.09	0.28	27.9	4.0	20.7	24.6	28.0
44.28	40.02	Post	3.25	NA	0.16	14.16	44.21	0.12	4.92	0.37	-0.08	0.41	28.7	4.1	22.3	25.9	29.6
45.4	39.99	Post	3.26	NA	0.16	13.94	46.43	0.12	5.01	0.39	-0.04	0.44	28.6	4.2	22.5	26.4	30.2
46.05	39.98	Post	3.21	NA	0.16	15.57	39.95	0.11	4.63	0.36	-0.12	0.42	28.5	4.0	21.0	25.1	28.5
46.9	39.95	N/A	3.14	NA	0.18	16.82	39.92	0.12	5.50	0.35	-0.05	0.55	28.1	4.2	21.2	24.9	28.7
48.6	39.91	N/A	3.23	NA	0.16	14.77	44.89	0.12	5.41	0.39	-0.05	0.67	28.2	4.6	22.5	26.0	29.5

Supplementary Table 4.5: Average temperatures within pre-, onset, peak and post-MECO intervals. Samples which lie outside these intervals are not included. Intervals without any samples present from a particular site have been excluded. H2020 refers to Henehan et al. (2020).

ODP 516							
	Interval	**Mean OPTiMAL SST (°C)**	**Standard deviation**	**No. of samples**	**Mean BAYSPAR SST (°C)**	**Standard deviation**	**No. of samples**
TEX_{86}	Pre	17.6	8.4	2	32.8	1.0	2
	Onset	22.4	5.9	3	32.6	2.5	3
	Peak	6.1	0.0	1	36.9	0.0	1
	Post	13.9	7.5	3	33.4	3.0	3
ODP 647							
	Interval	**Mean OPTiMAL SST (°C)**	**Standard deviation**	**No. of samples**	**Mean BAYSPAR SST (°C)**	**Standard deviation**	**No. of samples**
TEX_{86}	Pre	27.3	0.3	3	28.2	0.4	3
	Onset	26.7	0.7	4	29.1	0.9	4
	Peak	21.7	0.8	3	30.2	2.1	3
	Post	25.3	1.7	6	27.4	2.6	6
$\delta^{18}O$: *Acarinina* spp.	**Interval**	**Mean SST - Equation 1 (°C)**	**Standard deviation**	**No. of samples**	**Mean Bayfox SST (°C)**	**Standard deviation**	**No. samples**
	Pre	19.58	0.95	4	20.62	0.84	4
$\delta^{18}O$: *Chiloguembelina ototara*	**Interval**	**Mean SST - Equation 1 (°C)**	**Standard deviation**	**No. of samples**	**Mean Bayfox SST (°C)**	**Standard deviation**	**No. samples**
	Pre	17.48	0.69	3	18.74	0.61	3
	Onset	20.63	0.00	1	21.56	0.00	1
	Post	19.32	1.03	2	20.40	0.94	2
$\delta^{18}O$: *Pseudohastigerina micra*	**Interval**	**Mean SST - Equation 1 (°C)**	**Standard deviation**	**No. of samples**	**Mean Bayfox SST (°C)**	**Standard deviation**	**No. samples**
	Pre	27.04	1.98	3	27.09	1.69	3
	Onset	25.44	0.00	1	25.79	0.00	1
	Post	25.36	0.87	2	25.66	0.71	2
$\delta^{18}O$: *Globoturborotalia cf. ouachitaensis*	**Interval**	**Mean SST - Equation 1 (°C)**	**Standard deviation**	**No. of samples**	**Mean Bayfox SST (°C)**	**Standard deviation**	**No. samples**
	Post	19.9	0.16	3	20.9	0.14	3
ODP 702							
	Interval	**Mean SST: Equation 1 (°C)**	**Standard deviation**	**No. of samples**	**Mean Bayfox SST (°C)**	**Standard deviation**	**No. of samples**
$\delta^{18}O$: *Globigerinatheka index*	Pre	11.5	0.0	1	13.1	0	1
	Onset	10.8	0.0	1	12.5	0	1
	Peak	9.9	1.2	2	11.6	1.2	2
	Post	11.4	0.6	2	13.1	0.5	2

	Interval	Mean SST: no pH correction (°C)	Standard deviation	No. of samples	Mean SST: H2020 (°C)	Standard deviation	No. of samples
Mg/Ca: *Globigerinatheka index*	Pre	24.7	0.0	1	23.6	0.0	1
	Onset	23.9	0.0	1	21.5	0.0	1
	Peak	24.5	0.5	2	21.8	1.3	2
	Post	24.3	0.4	2	21.9	0.9	2
ODP 748							
$\delta^{18}O$: *Acarinina primitiva*	**Interval**	**Mean SST: Equation 1 (°C)**	**Standard deviation**	**No. of samples**	**Mean Bayfox SST (°C)**	**Standard deviation**	**No. samples**
	Onset	12.1	1.2	27	13.7	1.1	27
	Peak	13.6	0.6	5	15.2	0.5	5
$\delta^{18}O$: *Globigerinatheka index*	**Interval**	**Mean SST: Equation 1 (°C)**	**Standard deviation**	**No. of samples**	**Mean Bayfox SST (°C)**	**Standard deviation**	**No. samples**
	Onset	13.0	0.4	8	14.6	0.3	8
	Peak	13.1	0.3	8	14.7	0.3	8
$\delta^{18}O$: *Subbotina* spp.	**Interval**	**Mean SST: Equation 1 (°C)**	**Standard deviation**	**No. of samples**	**Mean Bayfox SST (°C)**	**Standard deviation**	**No. samples**
	Onset	11.8	0.4	5	13.4	0.4	5
	Peak	12.6	0.3	5	14.2	0.2	5
ODP 865							
$\delta^{18}O$: *Acarinina praetopilensis*	**Interval**	**Mean SST: Equation 1 (°C)**	**Standard deviation**	**No. of samples**	**Mean Bayfox SST (°C)**	**Standard deviation**	**No. of samples**
	Pre	17.5	0.4	2	18.7	0.3	2
	Onset	17.6	0.0	1	18.8	0.0	1
	Peak	17.9	0.4	2	19.1	0.4	2
	Post	16.0	0.2	4	17.4	0.2	4
$\delta^{18}O$: *Morozovelloides crassatus*	**Interval**	**Mean SST: Equation 1 (°C)**	**Standard deviation**	**No. of samples**	**Mean Bayfox SST (°C)**	**Standard deviation**	**No. of samples**
	Post	16.8	0	1	18.1	0	1
Mg/Ca: *Acarinina praetopilensis*	**Interval**	**Mean SST: no pH correction (°C)**	**Standard deviation**	**No. of samples**	**Mean SST: H2020 (°C)**	**Standard deviation**	**No. of samples**
	Pre	29.9	0.3	4	31.1	0.0	2
	Onset	29.9	0.3	8	31.5	0.2	2
	Peak	30.9	1.4	3	32.6	1.2	2
	Post	31.5	0.4	5	32.9	0.3	5
Mg/Ca: *Morozovelloides crassatus*	**Interval**	**Mean SST: no pH correction (°C)**	**Standard deviation**	**No. of samples**	**Mean SST: H2020 (°C)**	**Standard deviation**	**No. of samples**
	Post	31.5	0	1	32.4	0	1
ODP 913							

	Interval	Mean OPTiMAL SST (°C)	Standard deviation	No. of samples	Mean BAYSPAR SST (°C)	Standard deviation	No. of samples
TEX_{86}	Onset	15.5	0.0	1	-0.7	0.0	1
	Peak	22.7	0.0	1	22.4	0.0	1
	Post	13.6	5.0	2	12.4	8.2	2
ODP 959							
	Interval	**Mean OPTiMAL SST (°C)**	**Standard deviation**	**No. of samples**	**Mean BAYSPAR SST (°C)**	**Standard deviation**	**No. of samples**
TEX_{86}	Pre	26.7	0.3	2	30.3	0.4	2
	Onset	26.5	0.0	1	33.9	0.0	1
	Peak	25.9	0.9	2	35.7	1.3	2
	Post	27.0	0.4	4	33.1	2.0	4
ODP 1051							
	Interval	**Mean SST Equation 1 (°C)**	**Standard deviation**	**No. of samples**	**Mean Bayfox SST (°C)**	**Standard deviation**	**No. samples**
$\delta^{18}O$: *Acarinina topilensis*	Pre	16.6	0.6	5	17.9	0.5	5
	Onset	19.7	2.6	9	20.7	2.3	9
	Peak	18.6	0.4	3	19.7	0.4	3
	Post	19.4	0.4	4	20.5	0.3	4
	Interval	**Mean SST Equation 1 (°C)**	**Standard deviation**	**No. of samples**	**Mean Bayfox SST (°C)**	**Standard deviation**	**No. samples**
$\delta^{18}O$: *Globigerinatheka spp.*	Pre	18.2	1.6	4	19.3	1.5	4
	Onset	20.0	1.0	11	20.9	0.9	11
	Peak	20.8	1.5	5	21.7	1.3	5
	Post	22.0	0.7	5	22.8	0.6	5
	Interval	**Mean SST Equation 1 (°C)**	**Standard deviation**	**No. of samples**	**Mean Bayfox SST (°C)**	**Standard deviation**	**No. samples**
$\delta^{18}O$: *Morozovelloides crassatus*	Pre	17.5	0.9	5	18.8	0.8	5
	Onset	19.4	1.7	11	20.4	1.6	11
	Peak	18.6	0.9	5	19.8	0.8	5
	Post	20.1	0.6	4	21.2	0.6	4
	Interval	**Mean SST Equation 1 (°C)**	**Standard deviation**	**No. of samples**	**Mean Bayfox SST (°C)**	**Standard deviation**	**No. samples**
$\delta^{18}O$: *Subbotina spp.*	Pre	15.5	0.3	6	17.0	0.3	6
	Onset	16.2	1.3	9	17.5	1.2	9
	Peak	18.6	1.5	3	19.7	1.4	3
	Post	16.0	0.2	4	17.4	0.1	4
ODP 1170							
	Interval	**Mean OPTiMAL SST (°C)**	**Standard deviation**	**No. of samples**	**Mean BAYSPAR SST (°C)**	**Standard deviation**	**No. of samples**
TEX_{86}	Peak	27.5	0.0	1	29.7	0.0	1

ODP 1172							
	Interval	**Mean OPTiMAL SST (°C)**	**Standard deviation**	**No. of samples**	**Mean BAYSPAR SST (°C)**	**Standard deviation**	**No. of samples**
TEX_{86}	Pre	20.6	0.4	3	21.0	0.7	3
	Onset	22.0	1.4	7	23.9	1.8	7
	Peak	24.4	1.9	4	28.5	1.0	4
	Post	19.4	2.3	5	25.3	1.2	5
ODP 1260							
	Interval	**Mean SST Equation 1 (°C)**	**Standard deviation**	**No. of samples**	**Mean Bayfox SST (°C)**	**Standard deviation**	**No. of samples**
$\delta^{18}O$: *Morozovelloides crassatus*	Pre	21.3	0.0	1	22.1	0	1
	Onset	20.5	0.2	3	21.5	0.2	3
	Peak	23.1	0.0	1	23.7	0	1
	Post	24.8	1.0	3	25.2	0.9	3
	Interval	**Mean SST: no pH correction (°C)**	**Standard deviation**	**No. of samples**	**Mean SST: H2020 (°C)**	**Standard deviation**	**No. of samples**
Mg/Ca: *Morozovelloides crassatus*	Pre	29.7	0.0	1	30.7	0.0	1
	Onset	30.1	0.5	3	31.1	0.8	3
	Peak	31.1	0.0	1	32.2	0.0	1
	Post	28.5	0.5	3	28.8	0.9	3
ODP 1263							
	Interval	**Mean SST: no pH correction (°C)**	**Standard deviation**	**No. of samples**	**Mean SST: H2020 (°C)**	**Standard deviation**	**No. of samples**
Mg/Ca: *Globigerinatheka kugleri*	Onset	26.5	0.3	3	25.4	0.1	3
	Peak	28.3	0.6	2	27.8	0.8	2
	Post	27.5	0.2	3	27.0	0.4	3
	Interval	**Mean SST Equation 1 (°C)**	**Standard deviation**	**No. of samples**	**Mean Bayfox SST (°C)**	**Standard deviation**	**No. samples**
$\delta^{18}O$: *Acarinina spp.*	Onset	14.5	0.7	7	16.0	0.7	7
	Peak	14.9	0.8	3	16.4	0.8	3
	Post	14.6	0.7	17	16.1	0.7	17
	Interval	**Mean SST Equation 1 (°C)**	**Standard deviation**	**No. of samples**	**Mean Bayfox SST (°C)**	**Standard deviation**	**No. samples**
$\delta^{18}O$: *Globigerinatheka spp.*	Onset	14.1	1.4	10	15.6	1.3	10
	Peak	15.0	1.4	5	16.5	1.3	5
	Post	14.8	1.4	15	16.2	1.3	15
Baskil Section							

	Interval	Mean SST Equation 1 (°C)	Standard deviation	No. of samples	Mean Bayfox SST (°C)	Standard deviation	No. samples
$\delta^{18}O$: *Acarinina spp.*	Pre	28.8	2.1	5	28.6	1.8	5
	Onset	31.5	2.6	11	30.8	2.1	11
	Peak	33.0	3.1	7	32.0	2.5	7
	Post	29.5	0.3	2	29.2	0.2	2
Belaya River							
	Interval	**Mean OPTiMAL SST (°C)**	**Standard deviation**	**No. of samples**	**Mean BAYSPAR SST (°C)**	**Standard deviation**	**No. of samples**
TEX_{86}	Pre	28.5	0.1	5	25.7	0.6	5
	Onset	27.6	1.0	12	27.3	0.6	12
	Peak	27.0	0.4	6	25.5	0.9	6
	Post	27.5	1.4	16	25.0	0.7	16
U1408							
	Interval	**Mean SST Equation 1 (°C)**	**Standard deviation**	**No. of samples**	**Mean Bayfox SST (°C)**	**Standard deviation**	**No. samples**
$\delta^{18}O$: *Acarinina praetopilensis*	Pre	20.5	0.5	9	21.5	0.4	9
	Onset	22.8	1.6	18	23.5	1.4	18
	Peak	22.3	0.9	3	23.1	0.8	3
	Post	21.9	0.5	6	22.7	0.5	6
	Interval	**Mean SST Equation 1 (°C)**	**Standard deviation**	**No. of samples**	**Mean Bayfox SST (°C)**	**Standard deviation**	**No. samples**
$\delta^{18}O$: *Globigerinatheka index*	Pre	17.5	0.3	2	18.8	0.2	2
	Onset	20.1	1.2	8	21.1	1.0	8
	Peak	20.3	0.0	1	21.3	0.0	1
	Post	19.4	0.8	3	20.4	0.7	3
	Interval	**Mean SST Equation 1 (°C)**	**Standard deviation**	**No. of samples**	**Mean Bayfox SST (°C)**	**Standard deviation**	**No. samples**
$\delta^{18}O$: *Globigerinatheka mexicana*	Pre	19.7	0.7	5	20.8	0.6	5
	Onset	20.7	0.6	15	21.7	0.6	15
	Peak	20.1	0.4	2	21.2	0.4	2
	Post	19.4	0.0	1	20.4	0.0	1